are four maxima, and a *broadside* and an *end-fire* array have been formed simultaneously.

It is often desired in some Dolph-Tschebyscheff designs to take advantage of the largest possible spacing between the elements while maintaining the same level of all minor lobes, including the one toward $\theta = 0°$ and 180°. In general, as well as in Example 6.8, the only minor lobe that can exceed the level of the others, when the spacing exceeds a certain maximum spacing between the elements, is the one toward end-fire ($\theta = 0°$ or 180° or $z = -1$ in Figure 6.19 or Figure 6.20). The maximum spacing which can be used while meeting the requirements is obtained using (6-72) or

$$z = z_0 \cos(u) = z_0 \cos\left(\frac{\pi d}{\lambda} \cos\theta\right) \tag{6-75}$$

The requirement not to introduce a minor lobe with a level exceeding the others is accomplished by utilizing the Tschebyscheff polynomial up to, but not going beyond $z = -1$. Therefore, for $\theta = 0°$ or 180°

$$-1 \geq z_0 \cos\left(\frac{\pi d_{\max}}{\lambda}\right) \tag{6-76}$$

or

$$\boxed{d_{\max} \leq \frac{\lambda}{\pi} \cos^{-1}\left(-\frac{1}{z_0}\right)} \tag{6-76a}$$

The excitation coefficients of a Dolph-Tschebyscheff array can be derived using various documented techniques [9]–[11] and others. One method, whose results are suitable for computer calculations, is that by Barbiere [9]. The coefficients using this method can be obtained using

$$a_n = \begin{cases} \displaystyle\sum_{q=n}^{M} (-1)^{M-q} (z_0)^{2q-1} \frac{(q+M-2)!(2M-1)}{(q-n)!(q+n-1)!(M-q)!} & \text{(6-77a)} \\ \qquad \text{for even } 2M \text{ elements} \\ \qquad n = 1, 2, \ldots M \\ \displaystyle\sum_{q=n}^{M+1} (-1)^{M-q+1} (z_0)^{2(q-1)} \frac{(q+M-2)!(2M)}{\epsilon_n (q-n)!(q+n-2)!(M-q+1)!} \\ \qquad \text{for odd } 2M+1 \text{ elements} \\ \qquad n = 1, 2, \ldots M+1 \end{cases}$$

(6-77b)

$$\text{where } \epsilon_n = \begin{cases} 2 & n = 1 \\ 1 & n \neq 1 \end{cases}$$

C. Beamwidth and Directivity

For large Dolph-Tschebyscheff arrays scanned not too close to end-fire and with side lobes in the range from -20 to -60 dB, the half-power beamwidth and directivity can be found by introducing a beam broadening factor given approximately by [2]

INTEL-1045
U.S. Patent 7,151,430

$$f = 1 + 0.636\left\{\frac{2}{R_0}\cosh\left[\sqrt{(\cosh^{-1} R_0)^2 - \pi^2}\right]\right\}^2 \tag{6-78}$$

where R_0 is the major-to-side lobe voltage ratio. The beam broadening factor is plotted in Figure 6.22(a) as a function of side lobe level (in dB).

The half-power beamwidth of a Dolph-Tschebyscheff array can be determined by

1. calculating the beamwidth of a uniform array (of the same number of elements and spacing) using (6-22a) or reading it off Figure 6.11
2. multiplying the beamwidth of part (1) by the appropriate beam broadening factor f computed using (6-78) or reading it off Figure 6.22(a)

The same procedure can be used to determine the beamwidth of arrays with a cosine-on-pedestal distribution [2].

The beam broadening factor f can also be used to determine the directivity of large Dolph-Tschebyscheff arrays, scanned near broadside, with side lobes in the -20 to -60 dB range [2]. That is,

$$D_0 = \frac{2R_0^2}{1 + (R_0^2 - 1)f\dfrac{\lambda}{(L + d)}} \tag{6-79}$$

which is shown plotted in Figure 6.22(b) as a function of $L + d$ (in wavelengths).

From the data in Figure 6.22(b) it can be concluded that:

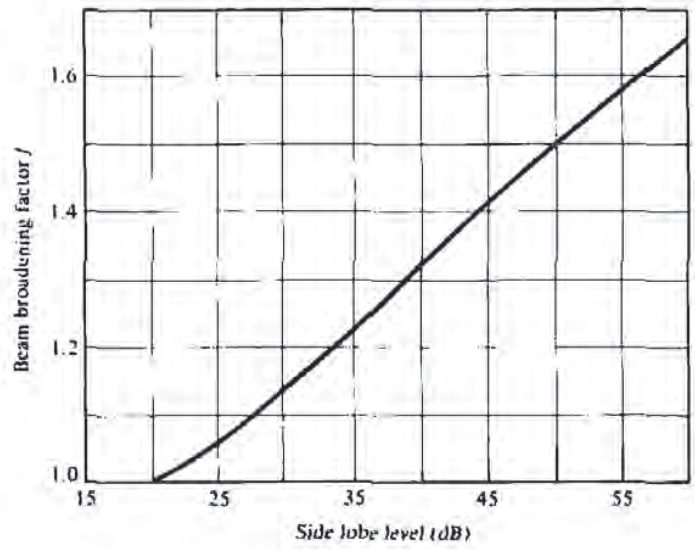
1. The directivity of a Dolph-Tschebyscheff array, with a given side lobe level, increases as the array size or number of elements increases.
2. For a given array length, or a given number of elements in the array, the directivity does not necessarily increase as the side lobe level decreases. As a matter of fact, a -15 dB side lobe array has smaller directivity than a -20 dB side lobe array. This may not be the case for all other side lobe levels.

The beamwidth and the directivity of an array depend linearly, but not necessarily at the same rate, on the overall length or total number of elements of the array. Therefore, the beamwidth and directivity must be related to each other. For a uniform broadside array this relation is [2]

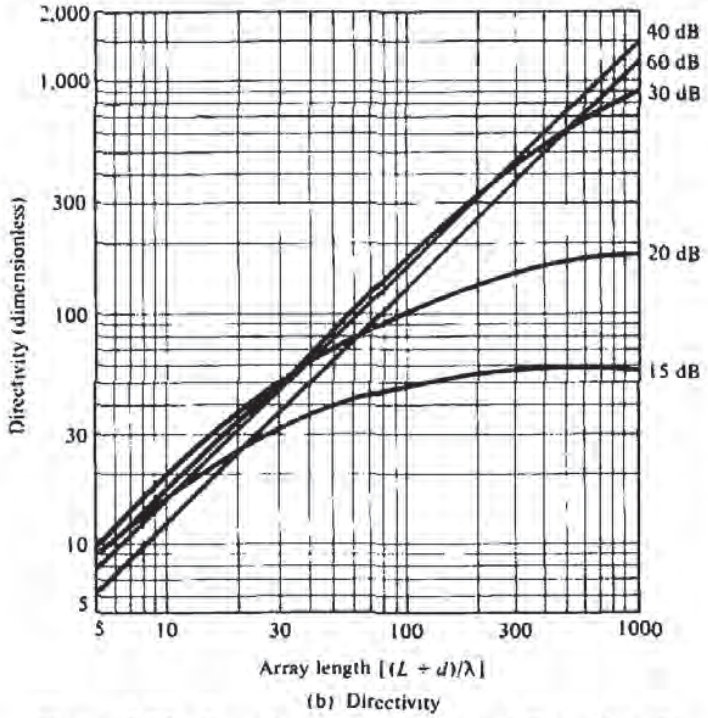
$$D_0 = \frac{101.5}{\Theta_d} \tag{6-80}$$

where Θ_d is the 3-dB beamwidth (in degrees). The above relation can be used as a good approximation betwen beamwidth and directivity for most linear broadside arrays with practical distributions (including the Dolph-Tschebyscheff array). Equation (6-80) states that for a linear broadside array the product of the 3-dB beamwidth and the directivity is approximately equal to 100. This is analogous to the product of the gain and bandwidth for electronic amplifiers.

INTEL-1045
U.S. Patent 7,151,430



(a) Beam broadening factor



(b) Directivity

Figure 6.22 Beam broadening factor and directivity of Tschebyscheff arrays. (SOURCE: R. S. Elliott, "Beamwidth and Directivity of Large Scanning Arrays," First of Two Parts, *The Microwave Journal*, December 1963).

INTEL-1045
U.S. Patent 7,151,430

D. Design

The design of a Dolph-Tschebyscheff array is very similar to those of other methods. Usually a certain number of parameters is specified, and the remaining are obtained following a certain procedure. In this section we will outline an alternate method that can be used, in addition to the one outlined and followed in Example 6.9, to design a Dolph-Tschebyscheff array. This method leads to the excitation coefficients more directly.

Specify

a. The side lobe level (in dB).
b. The number of elements.

Design Procedure

a. Transform the side lobe level from decibels to a voltage ratio using

$$R_0(\text{Voltage Ratio}) = [R_0(VR)] = 10^{R_0(dB)/20} \tag{6-81}$$

b. Calculate P, which also represents the order of the Tschebyscheff polynomial, using

$$P = \text{number of elements} - 1$$

c. Determine z_0 using (6-73) or

$$z_0 = \cosh\left[\frac{1}{P}\cosh^{-1}(R_0(VR))\right] \tag{6-82}$$

d. Calculate the excitation coefficients using (6-77a) or (6-77b).
e. Determine the beam broadening factor using (6-78).
f. Calculate the half-power beamwidth of a uniform array with the same number of elements and spacing between them.
g. Find the half-power beamwidth of the Tschebyscheff array by multiplying the half-power beamwidth of the uniform array by the beam broadening factor.
h. The maximum spacing between the elements should not exceed that of (6-76a).
i. Determine the directivity using (6-79).
j. The number of complete minor lobes for the three-dimensional pattern on either side of the main maximum, using the maximum permissible spacing, is equal to $N - 1$.
k. Calculate the array factor using (6-61a) or (6-61b).

This procedure leads to the same results as any other.

Example 6.10

Calculate the half-power beamwidth and the directivity for the Dolph-Tschebyscheff array of Example 6.9 for a spacing of $\lambda/2$ between the elements.

SOLUTION

From Example 6.9,

$$R_0 = 26 \text{ dB} \Rightarrow R_0 = 20 \quad \text{(voltage ratio)}$$

INTEL-1045
U.S. Patent 7,151,430

Using (6-78) or Figure 6.22(a), the beam broadening factor f is equal to

$$f = 1.079$$

According to (6-22a) or Figure 6.11, the beamwidth of a uniform broadside array with $L + d = 5\lambda$ is equal to

$$\Theta_h = 10.17^\circ$$

Thus the beamwidth of a Dolph-Tschebyscheff array is equal to

$$\Theta_h = 10.17^\circ f = 10.17^\circ(1.079) = 10.97^\circ$$

The directivity can be obtained using (6-79), and it is equal to

$$D_0 = \frac{2(20)^2}{1 + [(20)^2 - 1]\dfrac{1.079}{5}} = 9.18(\text{dimensionless}) = 9.63 \text{ dB}$$

which closely agrees with the results of Figure 6.22(b).

6.9 SUPERDIRECTIVITY

Antennas whose directivities are much larger than the directivity of a reference antenna of the same size are known as superdirective antennas. Thus a superdirective array is one whose directivity is larger than that of a reference array (usually a uniform array of the same length). In an array, superdirectivity is accomplished by inserting more elements within a fixed length (decreasing the spacing). Doing this, leads eventually to very large magnitudes and rapid changes of phase in the excitation coefficients of the elements of the array. Thus adjacent elements have very large and oppositely directed currents. This necessitates a very precise adjustment of their values. Associated with this are increases in reactive power (relative to the radiated power) and the Q of the array.

6.9.1 Efficiency and Directivity

Because of the very large currents in the elements of superdirective arrays, the ohmic losses increase and the antenna efficiency decreases very sharply. Although practically the ohmic losses can be reduced by the use of superconductive materials, there is no easy solution for the precise adjustment of the amplitudes and phases of the array elements. High radiation efficiency superdirective arrays can be designed utilizing array functions that are insensitive to changes in element values [12].

In practice, superdirective arrays are usually called *supergain*. However, supergain is a misnomer because such antennas have actual overall gains (because of very low efficiencies) less than uniform arrays of the same length. Although significant superdirectivity is very difficult and usually very impractical, a moderate amount can be accomplished. Superdirective antennas are very intriguing, and they have received much attention in the literature.

The length of the array is usually the limiting factor to the directivity of an array. Schelkunoff [13] pointed out that theoretically very high directivities can be obtained from linear end-fire arrays. Bowkamp and de Bruijn [14], however, concluded that

INTEL-1045
U.S. Patent 7,151,430

theoretically there is no limit in the directivity of a linear antenna. More specifically, Riblet [8] showed that Dolph-Tschebyscheff arrays with element spacing less than $\lambda/2$ can yield any desired directivity. A numerical example of a Dolph-Tschebyscheff array of nine elements, $\lambda/32$ spacing between the elements (total length of $\lambda/4$), and a 1/19.5 (-25.8 dB) side lobe level was carried out by Yaru [6]. It was found that to produce a directivity of 8.5 times greater than that of a single element, the currents on the individual elements must be on the order of 14×10^6 amperes and their values adjusted to an accuracy of better than one part in 10^{11}. The maximum radiation intensity produced by such an array is equivalent to that of a single element with a current of only 19.5×10^{-3} amperes. If the elements of such an array are 1-cm diameter, copper, $\lambda/2$ dipoles operating at 10 MHz, the efficiency of the array is less than $10^{-14}\%$.

6.9.2 Designs With Constraints

To make the designs more practical, applications that warrant some superdirectivity should incorporate constraints. One constraint is based on the sensitivity factor, and it was utilized for the design of superdirective arrays [15]. The sensitivity factor (designated as K) is an important parameter which is related to the electrical and mechanical tolerances of an antenna, and it can be used to describe its performance (especially its practical implementation). For an N-element array, such as that shown in Figure 6.5(a), it can be written as [15]

$$K = \frac{\sum_{n=1}^{N} |a_n|^2}{\left| \sum_{n=1}^{N} a_n e^{-jkr_n'} \right|^2} \tag{6-83}$$

where a_n is the current excitation of the nth element, and r_n' is the distance from the nth element to the far-field observation point (*in the direction of maximum radiation*).

In practice, the excitation coefficients and the positioning of the elements, which result in a desired pattern, cannot be achieved as specified. A certain amount of error, both electrical and mechanical, will always be present. Therefore the desired pattern will not be realized exactly, as required. However, if the design is accomplished based on specified constraints, the realized pattern will approximate the desired one within a specified deviation.

To derive design constraints, the realized current excitation coefficients c_n's are related to the desired ones a_n's by

$$c_n = a_n + \alpha_n a_n = a_n(1 + \alpha_n) \tag{6-83a}$$

where $\alpha_n a_n$ represents the error in the nth excitation coefficient. The mean square value of α_n is denoted by

$$\epsilon^2 = \langle |\alpha_n| \rangle^2 \tag{6-83b}$$

To take into account the error associated with the positioning of the elements, we introduce

$$\delta^2 = \frac{(k\sigma)^2}{3} \tag{6-83c}$$

INTEL-1045
U.S. Patent 7,151,430

where σ is the root-mean-square value of the element position error. Combining (6-83b) and (6-83c) reduces to

$$\Delta^2 = \delta^2 + \epsilon^2 \tag{6-83d}$$

where Δ is a measure of the combined electrical and mechanical errors.

For uncorrelated errors [15]

$$K\Delta^2 = \frac{\text{average radiation intensity of realized pattern}}{\text{maximum radiation intensity of desired pattern}}$$

If the realized pattern is to be very close to the desired one, then

$$K\Delta^2 \ll 1 \Rightarrow \Delta \ll \frac{1}{\sqrt{K}} \tag{6-83e}$$

Equation (6-83e) can be rewritten, by introducing a safety factor S, as

$$\boxed{\Delta = \frac{1}{\sqrt{SK}}} \tag{6-83f}$$

S is chosen large enough so that (6-83e) is satisfied. When Δ is multiplied by 100, 100Δ represents the percent tolerance for combined electrical and mechanical errors.

The choice of the value of S depends largely on the required accuracy between the desired and realized patterns. For example, if the focus is primarily on the realization of the main beam, a value of $S = 10$ will probably be satisfactory. For side lobes of 20 dB down, S should be about 1,000. In general, an approximate value of S should be chosen according to

$$S \simeq 10 \times 10^{b/10} \tag{6-83g}$$

where b represents the pattern level (in dB down) whose shape is to be accurately realized.

The above method can be used to design, with the safety factor K constrained to a certain value, arrays with maximum directivity. Usually one first plots, for each selected excitation distribution and positioning of the elements, the directivity D of the array under investigation versus the corresponding sensitivity factor K (using 6-83) of the same array. The design usually begins with the excitation and positioning of a uniform array (i.e., uniform amplitudes, a progressive phase, and equally spaced elements). The directivity associated with it is designated as D_0 while the corresponding sensitivity factor, computed using (6-83), is equal to $K_0 = 1/N$.

As the design deviates from that of the uniform array and becomes superdirective, the values of the directivity increase monotonically with increases in K. Eventually a maximum directivity is attained (designated as D_{max}), and it corresponds to a $K = K_{max}$; beyond that point ($K > K_{max}$), the directivity decreases monotonically. The antenna designer should then select the design for which $D_0 < D < D_{max}$ and $K_0 = 1/N < K < K_{max}$.

The value of D is chosen subject to the constraint that K is a certain number whose corresponding tolerance error Δ of (6-83f), for the desired safety factor S, can be achieved practically. Tolerance errors of less than about 0.3 percent are usually not achievable in practice. In general, the designer must trade-off between directivity and sensitivity factor; larger D's (provided $D \leq D_{max}$) result in larger K's ($K \leq K_{max}$), and vice-versa.

INTEL-1045
U.S. Patent 7,151,430

A number of constrained designs can be found in [15]. For example, an array of cylindrical monopoles above an infinite and perfectly conducting ground plane was designed for optimum directivity at $f = 30$ MHz, with a constraint on the sensitivity factor. The spacing d between the elements was maintained uniform.

For a four-element array, it was found that for $d = 0.3\lambda$ the maximum directivity was 14.5 dB and occurred at a sensitivity factor of $K = 1$. However for $d = 0.1\lambda$ the maximum directivity was up to 15.8 dB, with the corresponding sensitivity factor up to about 10^3. At $K_0 = 1/N = 1/4$, the directivities for $d = 0.3\lambda$ and 0.1λ were about 11.3 and 8 dB, respectively. When the sensitivity factor was maintained constant and equal to $K = 1$, the directivity for $d = 0.3\lambda$ was 14.5 dB and only 11.6 dB for $d = 0.1\lambda$. It should be noted that the directivity of a single monopole above an infinite ground plane is twice that of the corresponding dipole in free-space and equal to about 3.25 (or about 5.1 dB).

6.10 PLANAR ARRAY

In addition to placing elements along a line (to form a linear array), individual radiators can be positioned along a rectangular grid to form a rectangular or planar array. Planar arrays provide additional variables which can be used to control and shape the pattern of the array. Planar arrays are more versatile and can provide more symmetrical patterns with lower side lobes. In addition, they can be used to scan the main beam of the antenna toward any point in space. Applications include tracking radar, search radar, remote sensing, communications, and many others.

6.10.1 Array Factor

To derive the array factor for a planar array, let us refer to Figure 6.23. If M elements are initially placed along the x-axis, as shown in Figure 6.23(a), the array factor of it can be written according to (6-52) and (6-54) as

$$\text{AF} = \sum_{m=1}^{M} I_{m1} e^{j(m-1)(kd_x \sin\theta\cos\phi + \beta_x)} \tag{6-84}$$

where I_{m1} is the excitation coefficient of each element. The spacing and progressive phase shift between the elements along the x-axis are represented, respectively, by d_x and β_x. If N such arrays are placed next to each other in the y-direction, a distance d_y apart and with a progressive phase β_y, a rectangular array will be formed as shown in Figure 6.23(b). The array factor for the entire planar array can be written as

$$\text{AF} = \sum_{n=1}^{N} I_{1n} \left[\sum_{m=1}^{M} I_{m1} e^{j(m-1)(kd_x \sin\theta\cos\phi + \beta_x)} \right] e^{j(n-1)(kd_y \sin\theta\sin\phi + \beta_y)} \tag{6-84a}$$

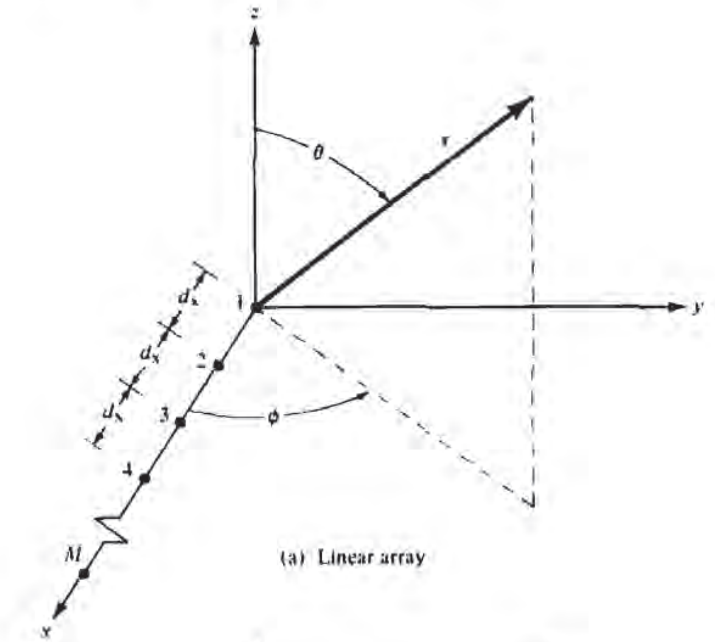
or

$$\text{AF} = S_{xm} S_{yn} \tag{6-85}$$

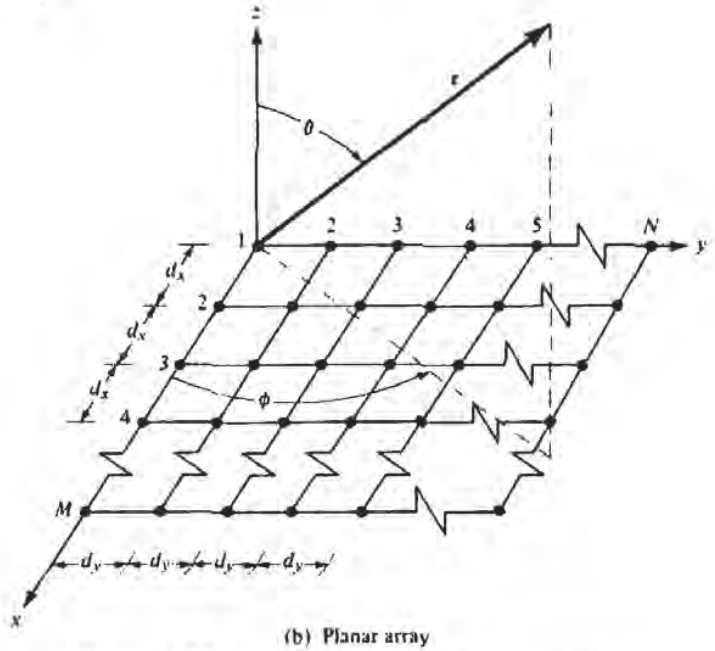
where

$$S_{xm} = \sum_{m=1}^{M} I_{m1} e^{j(m-1)(kd_x \sin\theta\cos\phi + \beta_x)} \tag{6-85a}$$

INTEL-1045
U.S. Patent 7,151,430



(a) Linear array



(b) Planar array

Figure 6.23 Linear and planar array geometries.

$$S_{yn} = \sum_{n=1}^{N} I_{1n} e^{j(n-1)(kd_y \sin\theta \sin\phi + \beta_y)} \tag{6-85b}$$

Equation (6-85) indicates that the pattern of a rectangular array is the product of the array factors of the arrays in the x- and y-directions.

If the amplitude excitation coefficients of the elements of the array in the y-

INTEL-1045
U.S. Patent 7,151,430

direction are proportional to those along the x, the amplitude of the (m, n)th element can be written as

$$I_{mn} = I_{m1} I_{1n} \tag{6-86}$$

If in addition the amplitude excitation of the entire array is uniform ($I_{mn} = I_0$), (6-84a) can be expressed as

$$\text{AF} = I_0 \sum_{m=1}^{M} e^{j(m-1)(kd_x \sin\theta\cos\phi + \beta_x)} \sum_{n=1}^{N} e^{j(n-1)(kd_y \sin\theta\sin\phi + \beta_y)} \tag{6-87}$$

According to (6-6), (6-10), and (6-10c), the normalized form of (6-87) can also be written as

$$\text{AF}_n(\theta, \phi) = \left\{ \frac{1}{M} \frac{\sin\left(\frac{M}{2}\psi_x\right)}{\sin\left(\frac{\psi_x}{2}\right)} \right\} \left\{ \frac{1}{N} \frac{\sin\left(\frac{N}{2}\psi_y\right)}{\sin\left(\frac{\psi_y}{2}\right)} \right\} \tag{6-88}$$

where

$$\psi_x = kd_x \sin\theta\cos\phi + \beta_x \tag{6-88a}$$

$$\psi_y = kd_y \sin\theta\sin\phi + \beta_y \tag{6-88b}$$

When the spacing between the elements is equal or greater than $\lambda/2$, multiple maxima of equal magnitude can be formed. The principal maximum is referred to as the *major lobe* and the remaining as the *grating lobes*. A *grating lobe* is defined as "a lobe, other than the main lobe, produced by an array antenna when the inter element spacing is sufficiently large to permit the in-phase addition of radiated fields in more than one direction." To form or avoid grating lobes in a rectangular array, the same principles must be satisfied as for a linear array. To avoid grating lobes in the x-z and y-z planes, the spacing between the elements in the x- and y-directions, respectively, must be less than $\lambda/2$ ($d_x < \lambda/2$ and $d_y < \lambda/2$).

For a rectangular array, the major lobe and grating lobes of S_{xm} and S_{yn} in (6-85a) and (6-85b) are located at

$$kd_x \sin\theta\cos\phi + \beta_x = \pm 2m\pi \qquad m = 0, 1, 2, \ldots \tag{6-89a}$$

$$kd_y \sin\theta\sin\phi + \beta_y = \pm 2n\pi \qquad n = 0, 1, 2, \ldots \tag{6-89b}$$

The phases β_x and β_y are independent of each other, and they can be adjusted so that the main beam of S_{xm} is not the same as that of S_{yn}. However, in most practical applications it is required that the conical main beams of S_{xm} and S_{yn} intersect and their maxima be directed toward the same direction. If it is desired to have only one main beam that is directed along $\theta = \theta_0$ and $\phi = \phi_0$, the progressive phase shift between the elements in the x- and y-directions must be equal to

$$\beta_x = -kd_x \sin\theta_0\cos\phi_0 \tag{6-90a}$$

$$\beta_y = -kd_y \sin\theta_0\sin\phi_0 \tag{6-90b}$$

INTEL-1045
U.S. Patent 7,151,430

When solved simultaneously, (6-90a) and (6-90b) can also be expressed as

$$\tan \phi_0 = \frac{\beta_y d_x}{\beta_x d_y} \tag{6-91a}$$

$$\sin^2 \theta_0 = \left(\frac{\beta_x}{kd_x}\right)^2 + \left(\frac{\beta_y}{kd_y}\right)^2 \tag{6-91b}$$

The principal maximum ($m = n = 0$) and the grating lobes can be located by

$$kd_x(\sin \theta \cos \phi - \sin \theta_0 \cos \phi_0) = \pm 2m\pi, \qquad m = 0, 1, 2, \ldots \tag{6-92a}$$

$$kd_y(\sin \theta \sin \phi - \sin \theta_0 \sin \phi_0) = \pm 2n\pi, \qquad n = 0, 1, 2, \ldots \tag{6-92b}$$

or

$$\sin \theta \cos \phi - \sin \theta_0 \cos \phi_0 = \pm \frac{m\lambda}{d_x}, \qquad m = 0, 1, 2, \ldots \tag{6-93a}$$

$$\sin \theta \sin \phi - \sin \theta_0 \sin \phi_0 = \pm \frac{n\lambda}{d_y}, \qquad n = 0, 1, 2, \ldots \tag{6-93b}$$

which, when solved simultaneously, reduce to

$$\boxed{\phi = \tan^{-1}\left[\frac{\sin \theta_0 \sin \phi_0 \pm n\lambda/d_y}{\sin \theta_0 \cos \phi_0 \pm m\lambda/d_x}\right]} \tag{6-94a}$$

and

$$\boxed{\theta = \sin^{-1}\left[\frac{\sin \theta_0 \cos \phi_0 \pm m\lambda/d_x}{\cos \phi}\right] = \sin^{-1}\left[\frac{\sin \theta_0 \sin \phi_0 \pm n\lambda/d_y}{\sin \phi}\right]} \tag{6-94b}$$

In order for a true grating lobe to occur, both forms of (6-94b) must be satisfied simultaneously (i.e., lead to the same θ value).

To demonstrate the principles of planar array theory, the three-dimensional pattern of a 5×5 element array of uniform amplitude, $\beta_x = \beta_y = 0$, and $d_x = d_y = \lambda/4$, is shown in Figure 6.24. The maximum is oriented along $\theta_0 = 0°$ and only the pattern above the x-y plane is shown. An identical pattern is formed in the lower hemisphere which can be diminished by the use of a ground plane.

To examine the pattern variation as a function of the element spacing, the three-dimensional pattern of the same 5×5 element array of isotropic sources with $d_x = d_y = \lambda/2$ and $\beta_x = \beta_y = 0$ is displayed in Figure 6.25. As contrasted with Figure 6.24, the pattern of Figure 6.25 exhibits complete minor lobes in all planes. Figure 6.26 displays the corresponding two-dimensional elevation patterns with cuts at $\phi = 0°$ (x-z plane), $\phi = 90°$ (y-z plane), and $\phi = 45°$. The two principal patterns ($\phi = 0°$ and $\phi = 90°$) are identical. The patterns of Figures 6.24 and 6.25 display a four-fold symmetry.

As discussed previously, arrays possess wide versatility in their radiation characteristics. The most common characteristic of an array is its scanning mechanism. To illustrate that, the three-dimensional pattern of the same 5×5 element array, with its maximum oriented along the $\theta_0 = 30°$, $\phi_0 = 45°$, is plotted in Figure 6.27. The

INTEL-1045
U.S. Patent 7,151,430

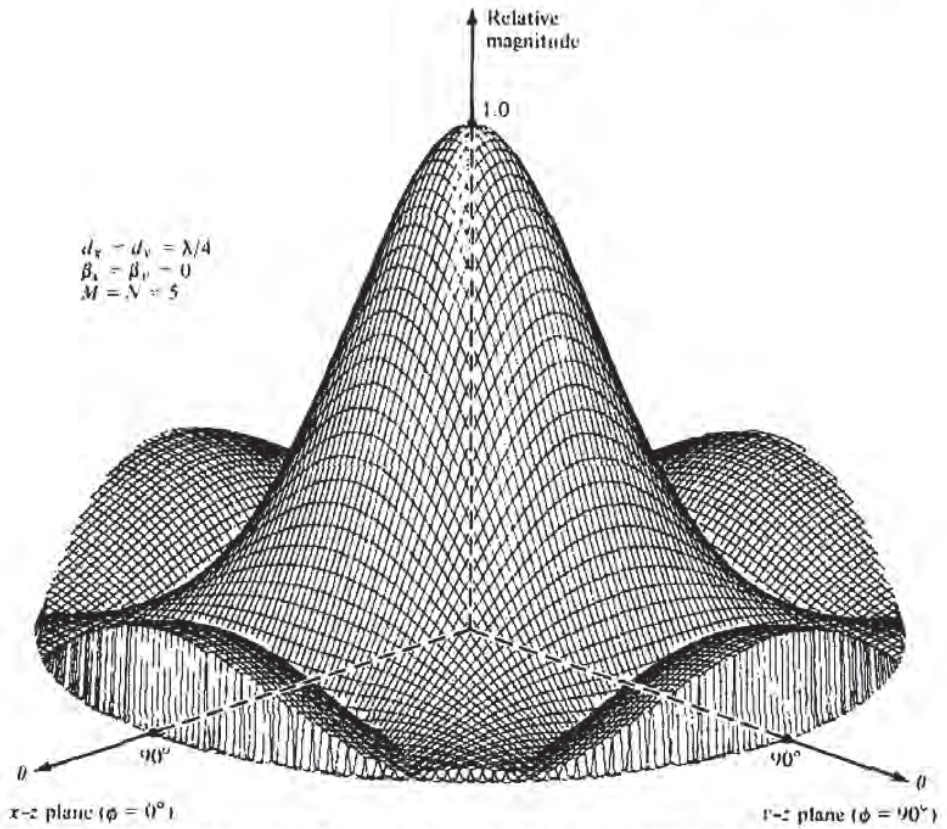


Figure 6.24 Three-dimensional antenna pattern of a planar array of isotropic elements with a spacing of $d_x = d_y = \lambda/4$, and equal amplitude and phase excitations.

element spacing is $d_x = d_y = \lambda/2$. The maximum is found in the first quadrant of the upper hemisphere. The small ring around the vertical axis indicates the maximum value of the pattern along that axis ($\theta = 0°$). The two-dimensional patterns are shown in Figure 6.28, and they exhibit only a two-fold symmetry. The principal plane pattern ($\phi = 0°$ or $\phi = 90°$) is normalized relative to the maximum which occurs at $\theta_0 = 30°$, $\phi_0 = 45°$. Its maximum along the principal planes ($\phi = 0°$ or $\phi = 90°$) occurs when $\theta = 21°$ and it is 17.37 dB down from the maximum at $\theta_0 = 30°$, $\phi_0 = 45°$.

To illustrate the formation of the grating lobes, when the spacing between the elements is large, the three-dimensional pattern of the 5×5 element array with $d_x = d_y = \lambda$ and $\beta_x = \beta_y = 0$ are displayed in Figure 6.29. Its corresponding two-dimensional elevation patterns at $\phi = 0°$ ($\phi = 90°$) and $\phi = 45°$ are exhibited in Figure 6.30. Besides the maxima along $\theta = 0°$ and $\theta = 180°$, additional maxima with equal intensity, referred to as *grating lobes*, appear along the principal planes (x-z and y-z planes) when $\theta = 90°$. Further increase of the spacing to $d_x = d_y = 2\lambda$ would result in additional grating lobes.

The array factor of the planar array has been derived assuming that each element is an isotropic source. If the antenna is an array of *identical* elements, the total field can be obtained by applying the pattern multiplication rule of (6-5) in a manner similar as for the linear array.

When only the central element of a large planar array is excited and the others

INTEL-1045
U.S. Patent 7,151,430

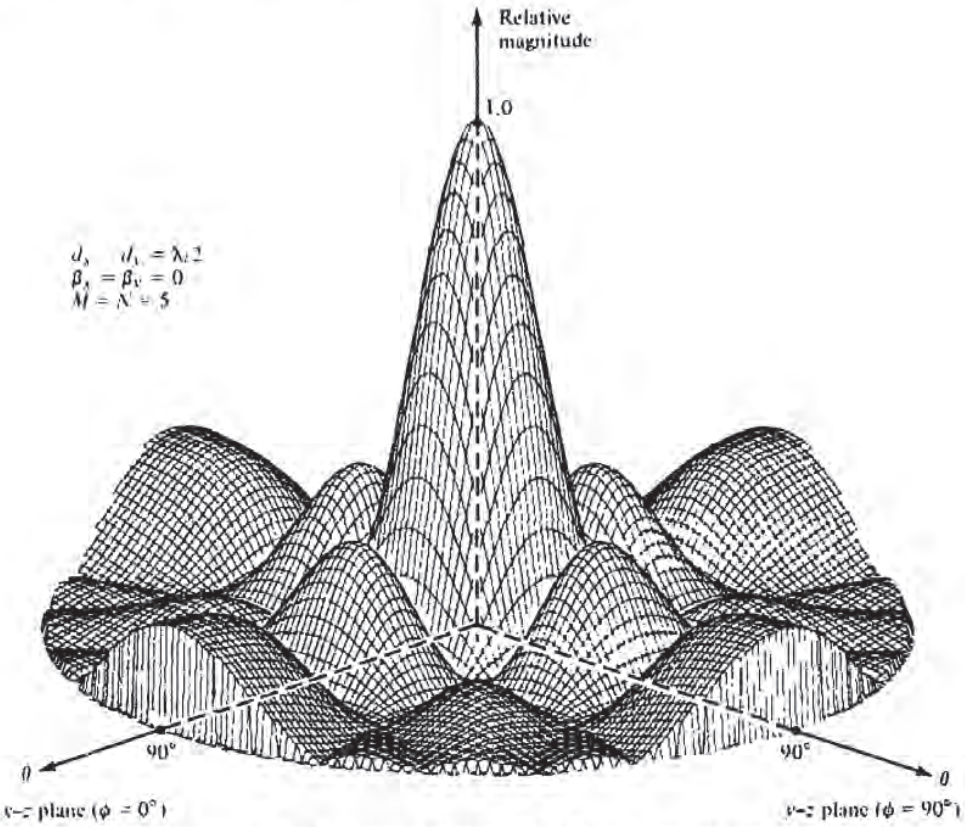


Figure 6.25 Three-dimensional antenna pattern of a planar array of isotropic elements with a spacing of $d_x = d_y = \lambda/2$, and equal amplitude and phase excitations.

are passively terminated, it has been observed experimentally that additional nulls in the pattern of the element are developed which are not accounted for by theory which does not include coupling. The nulls were observed to become deeper and narrower [16] as the number of elements surrounding the excited element increased and approached a large array. These effects became more noticeable for arrays of open waveguides. It has been demonstrated [17] that dips at angles interior to grating lobes are formed by coupling through surface wave propagation. The coupling decays very slowly with distance, so that even distant elements from the driven elements experience substantial parasitic excitation. The angles where these large variations occur can be placed outside scan angles of interest by choosing smaller element spacing than would be used in the absence of such coupling. Because of the complexity of the problem, it will not be pursued here any further but the interested reader is referred to the published literature.

6.10.2 Beamwidth

The task of finding the beamwidth of nonuniform amplitude planar arrays is quite formidable. Instead, a very simple procedure will be outlined which can be used to compute these parameters for large arrays whose maximum is not scanned too far off

INTEL-1045
U.S. Patent 7,151,430

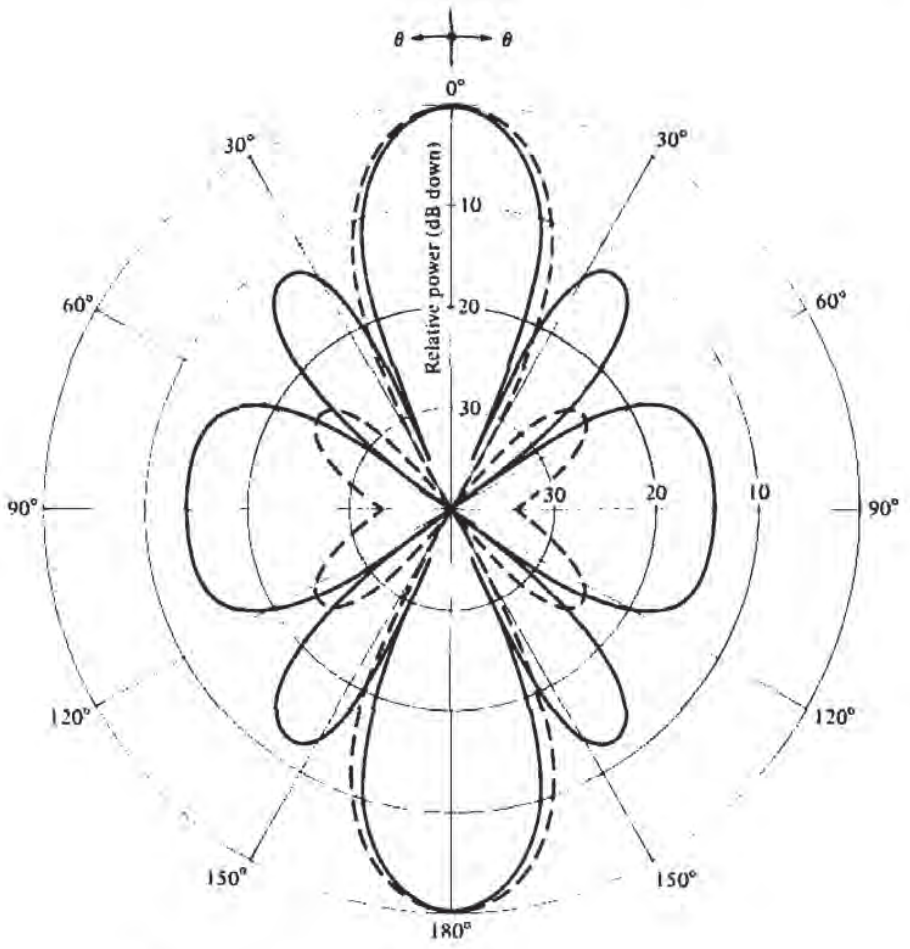


Figure 6.26 Two-dimensional antenna patterns of a planar array of isotropic elements with a spacing of $d_x = d_y = \lambda/2$, and equal amplitude and phase excitations.

broadside. The method [18] utilizes results of a uniform linear array and the beam broadening factor of the amplitude distribution.

The maximum of the conical main beam of the array is assumed to be directed toward θ_0, ϕ_0 as shown in Figure 6.31. To define a beamwidth, two planes are chosen. One is the elevation plane defined by the angle $\phi = \phi_0$ and the other is a plane that is perpendicular to it. The corresponding half-power beamwidth of each is designated, respectively, by Θ_h and Ψ_h. For example, if the array maximum is pointing along $\theta_0 = \pi/2$ and $\phi_0 = \pi/2$, Θ_h represents the beamwidth in the y-z plane and Ψ_h, the beamwidth in the x-y plane.

For a large array, with its maximum near broadside, the elevation plane half-power beamwidth Θ_h is given approximately by [18]

INTEL-1045
U.S. Patent 7,151,430

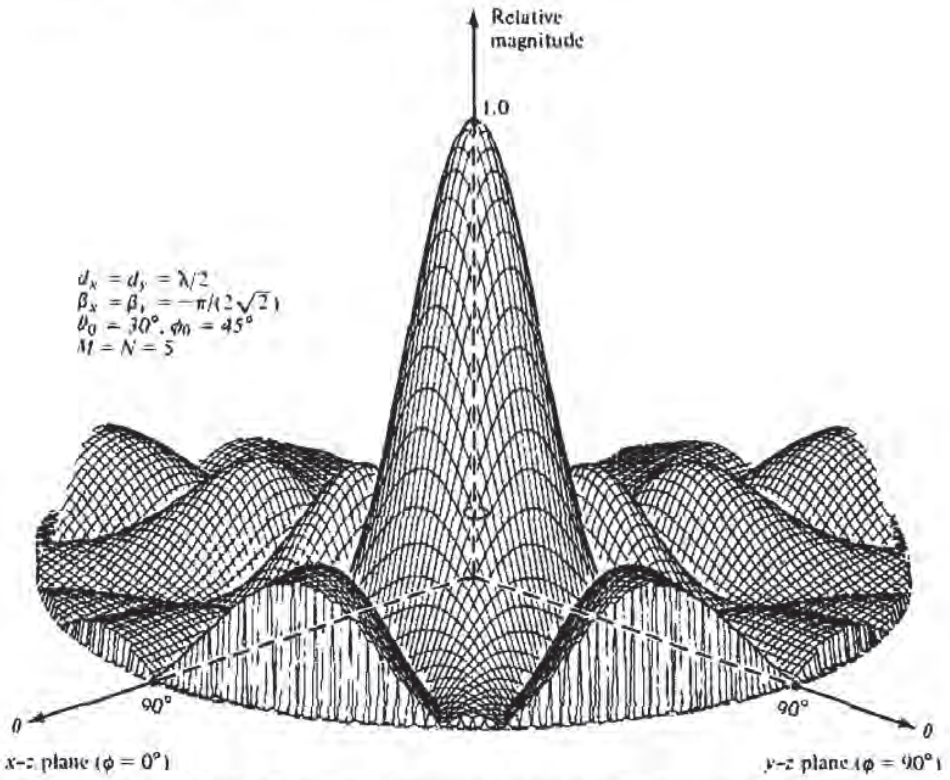


Figure 6.27 Three-dimensional antenna pattern of a planar array of isotropic elements with a spacing of $d_x = d_y = \lambda/2$, equal amplitude, and progressive phase excitation.

$$\Theta_h = \sqrt{\frac{1}{\cos^2\theta_0[\Theta_{x0}^{-2}\cos^2\phi_0 + \Theta_{y0}^{-2}\sin^2\phi_0]}} \tag{6-95}$$

where Θ_{x0} represents the half-power beamwidth of a *broadside* linear array of M elements. Similarly, Θ_{y0} represents the half-power beamwidth of a *broadside* array of N elements.

The values of Θ_{x0} and Θ_{y0} can be obtained by using previous results. For a uniform distribution, for example, the values of Θ_{x0} and Θ_{y0} can be obtained by using, respectively, the lengths $(L_x + d_x)/\lambda$ and $(L_y + d_y)/\lambda$ and reading the values from the broadside curve of Figure 6.11. For a Tschebyscheff distribution, the values of Θ_{x0} and Θ_{y0} are obtained by multiplying each uniform distribution value by the beam broadening factor of (6-78) or Figure 6.22(a). The same concept can be used to obtain the beamwidth of other distributions as long as their corresponding beam broadening factors are available.

For a square array ($M = N$, $\Theta_{x0} = \Theta_{y0}$), (6-95) reduces to

$$\Theta_h = \Theta_{x0}\sec\theta_0 = \Theta_{y0}\sec\theta_0 \tag{6-95a}$$

Equation (6-95a) indicates that for $\theta_0 > 0$ the beamwidth increases proportionally to $\sec\theta_0 = 1/\cos\theta_0$. The broadening of the beamwidth by $\sec\theta_0$, as θ_0 increases, is

INTEL-1045
U.S. Patent 7,151,430

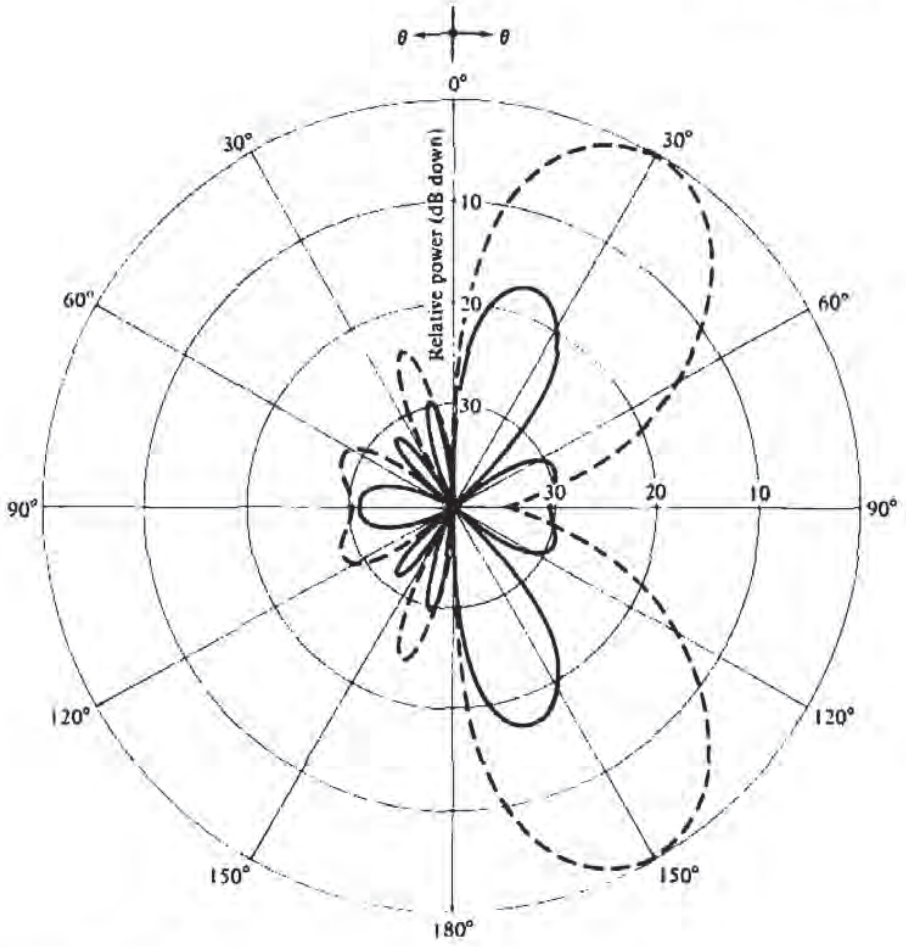


Figure 6.28 Two-dimensional antenna patterns of a planar array of isotropic elements with a spacing of $d_x = d_y = \lambda/2$, equal amplitude, and progressive phase excitation.

consistent with the reduction by $\cos\theta_0$ of the projected area of the array in the pointing direction.

The half-power beamwidth Ψ_h, in the plane that is perpendicular to the $\phi = \phi_0$ elevation, is given by [18]

$$\Psi_h = \sqrt{\frac{1}{\Theta_{x0}^{-2}\sin^2\phi_0 + \Theta_{y0}^{-2}\cos^2\phi_0}} \tag{6-96}$$

and it does not depend on θ_0. For a square array, (6-96) reduces to

$$\Psi_h = \Theta_{x0} = \Theta_{y0} \tag{6-96a}$$

INTEL-1045
U.S. Patent 7,151,430

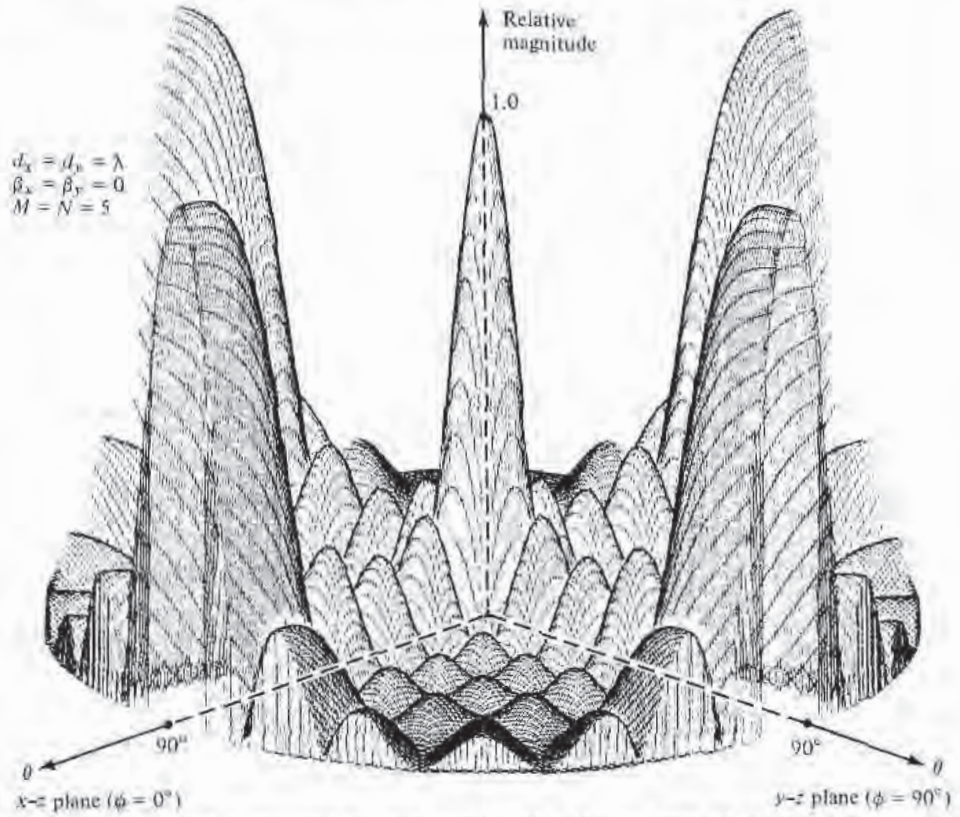


Figure 6.29 Three-dimensional antenna pattern of a planar array of isotropic elements with a spacing of $d_x = d_y = \lambda$, and equal amplitude and phase excitations.

The values of Θ_{x0} and Θ_{y0} are the same as in (6-95) and (6-95a).

For a planar array, it is useful to define a beam solid angle Ω_A by

$$\Omega_A = \Theta_h \Psi_h \tag{6-97}$$

as it was done in (2-23), (2-24), and (2-26a). Using (6-95) and (6-96), (6-97) can be expressed as

$$\Omega_A = \frac{\Theta_{x0}\Theta_{y0} \sec\theta_0}{\left[\sin^2\phi_0 + \dfrac{\Theta_{x0}^2}{\Theta_{y0}^2}\cos^2\phi_0\right]^{1/2}\left[\sin^2\phi_0 + \dfrac{\Theta_{x0}^2}{\Theta_{y0}^2}\cos^2\phi_0\right]^{1/2}} \tag{6-98}$$

6.10.3 Directivity

The directivity of the array factor $AF(\theta, \phi)$ whose major beam is pointing in the $\theta = \theta_0$ and $\phi = \phi_0$ direction, can be obtained by employing the definition of (2-22) and writing it as

$$D_0 = \frac{4\pi[AF(\theta_0, \phi_0)]\,[AF(\theta_0, \phi_0)]^*|_{max}}{\displaystyle\int_0^{2\pi}\int_0^{\pi}[AF(\theta, \phi)]\,[AF(\theta, \phi)]^* \sin\theta\, d\theta\, d\phi} \tag{6-99}$$

INTEL-1045
U.S. Patent 7,151,430

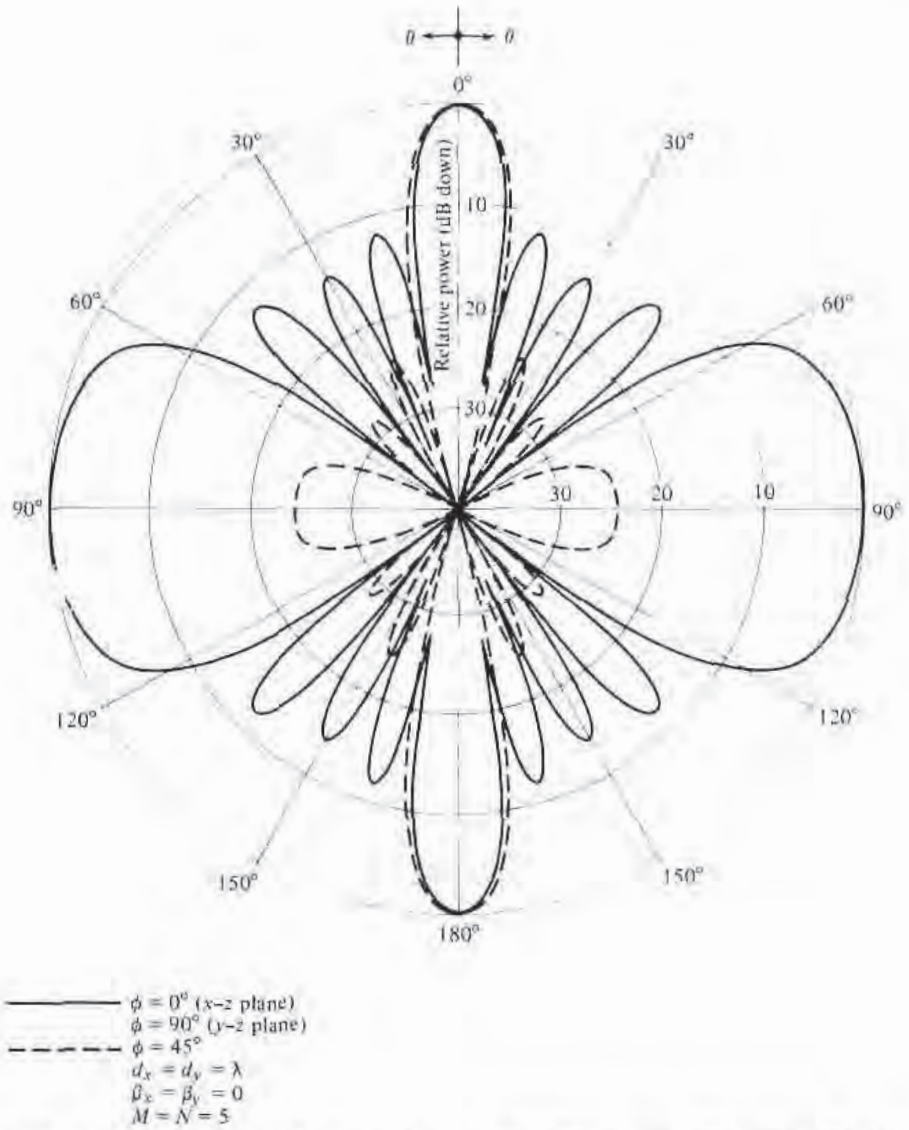


Figure 6.30 Two-dimensional antenna patterns of a planar array of isotropic elements with a spacing of $d_x = d_y = \lambda$, and equal amplitude and phase excitations.

A novel method has been introduced [19] for integrating the terms of the directivity expression for isotropic and conical patterns.

As in the case of the beamwidth, the task of evaluating (6-99) for nonuniform amplitude distribution is formidable. Instead, a very simple procedure will be outlined to compute the directivity of a planar array using data from linear arrays.

It should be pointed out that the directivity of an array with bidirectional (two-sided pattern in free space) would be half the directivity of the same array with unidirectional (one-sided pattern) elements (e.g., dipoles over ground plane).

For large planar arrays, which are nearly broadside, the directivity reduces to [18]

$$D_0 = \pi \cos \theta_0 D_x D_y \tag{6-100}$$

INTEL-1045
U.S. Patent 7,151,430

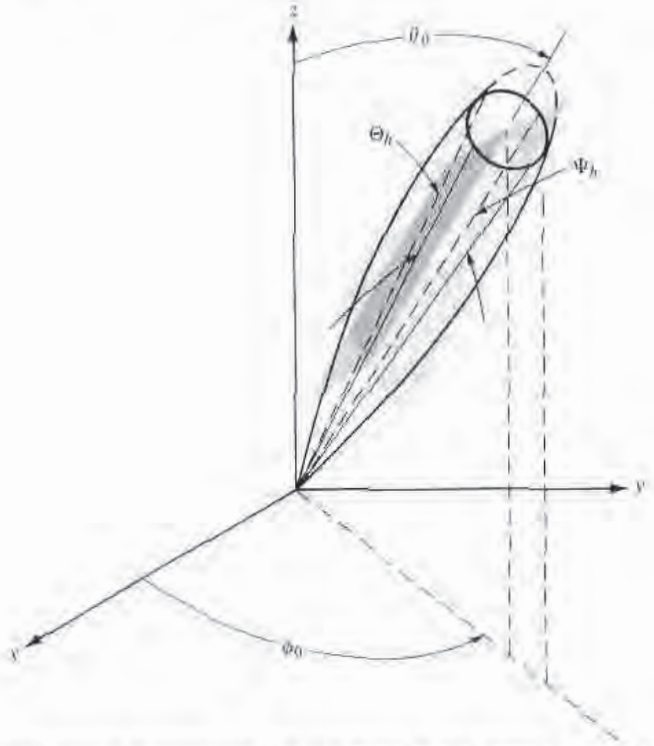


Figure 6.31 Half-power beamwidths for a conical main beam oriented toward $\theta = \theta_0$, $\phi = \phi_0$. (SOURCE: R. S. Elliott, "Beamwidth and Directivity of Large Scanning Arrays," Last of Two Parts, *The Microwave Journal*, January 1964)

where D_x and D_y are the directivities of broadside linear arrays each, respectively, of length and number of elements L_x, M and L_y, N. The factor $\cos\theta_0$ accounts for the decrease of the directivity because of the decrease of the projected area of the array. Each of the values, D_x and D_y, can be obtained by using (6-79) with the appropriate beam broadening factor f. For Tschebyscheff arrays, D_x and D_y can be obtained using (6-78) or Figure 6-22(a) and (6-79). Alternatively, they can be obtained using the graphical data of Figure 6.22(b).

For most practical amplitude distributions, the directivity of (6-100) is related to the beam solid angle of the same array by

$$D_0 \simeq \frac{\pi^2}{\Omega_A(\text{rads}^2)} = \frac{32{,}400}{\Omega_A(\text{degrees}^2)} \tag{6-101}$$

where Ω_A is expressed in square radians or square degrees. Equation (6-101) should be compared with (2-26) or (2-27) given by Kraus.

Example 6.11

Compute the half-power beamwidths, beam solid angle, and directivity of a planar square array of 100 isotropic elements (10×10). Assume a Tschebyscheff distribution, $\lambda/2$ spacing between the elements, -26 dB side lobe level, and the maximum oriented along $\theta_0 = 30°$, $\phi_0 = 45°$.

INTEL-1045
U.S. Patent 7,151,430

SOLUTION

Since in the x- and y-directions

$$L_x + d_x = L_y + d_y = 5\lambda$$

and each is equal to $L + d$ of Example 6.10, then

$$\Theta_{x0} = \Theta_{y0} = 10.97°$$

According to (6-95a)

$$\Theta_h = \Theta_{x0} \sec \theta_0 = 10.97° \sec(30°) = 12.67°$$

and (6-96a)

$$\Psi_h = \Theta_{x0} = 10.97°$$

and (6-97)

$$\Omega_A = \Theta_h \Psi_h = 12.67(10.97) = 138.96 \quad (\text{degrees}^2)$$

The directivity can be obtained using (6-100). Since the array is square, $D_x = D_y$, each one is equal to the directivity of Example 6.10. Thus

$$D_0 = \pi \cos(30°)(9.18)(9.18) = 229.28(\text{dimensionless}) = 23.60 \text{ dB}$$

Using (6-101)

$$D_0 \simeq \frac{32{,}400}{\Omega_A(\text{degrees}^2)} = \frac{32{,}400}{138.96} = 233.16(\text{dimensionless}) = 23.67 \text{ dB}$$

Obviously we have an excellent agreement.

6.11 DESIGN CONSIDERATIONS

Antenna arrays can be designed to control their radiation characteristics by properly selecting the phase and/or amplitude distribution between the elements. It has already been shown that a control of the phase can significantly alter the radiation pattern of an array. In fact, the principle of scanning arrays, where the maximum of the array pattern can be pointed in different directions, is based primarily on control of the phase excitation of the elements. In addition, it has been shown that a proper amplitude excitation taper between the elements can be used to control the beamwidth and sidelobe level. Typically the level of the minor lobes can be controlled by tapering the distribution across the array; the smoother the taper from the center of the array toward the edges, the lower the sidelobe level and the larger the half-power beamwidth, and conversely. Therefore a very smooth taper, such as that represented by a binomial distribution or others, would result in very low sidelobe but larger half-power beamwidth. In contrast, an abrupt distribution, such as that of uniform illumination, exhibits the smaller half-power beamwidth but the highest sidelobe level (about -13.5 dB). Therefore, if it is desired to achieve simultaneously both a very low sidelobe level, as well as a small half-power beamwidth, a compromise design has to be selected. The Dolph-Tschebyscheff design of Section 6.8.3 is one such distribution. There are other designs that can be used effectively to achieve a good compromise between sidelobe level and beamwidth. Two such examples are the Taylor Line-

INTEL-1045
U.S. Patent 7,151,430

Source (Tschebyscheff Error) and the Taylor Line-Source (One-Parameter). These are discussed in detail in Sections 7.6 and 7.7 of Chapter 7, respectively. Both of these are very similar to the Dolph-Tschebyscheff, with primarily the following exceptions.

For the Taylor Tschebyscheff Error design, the number of minor lobes with the same level can be controlled as part of the design; the level of the remaining one is monotonically decreasing. This is in contrast to the Dolph-Tschebyscheff where all the minor lobes are of the same level. Therefore, given the same sidelobe level, the half-power beamwidth of the Taylor Tschebyscheff Error is slightly greater than that of the Dolph-Tschebyscheff. For the Taylor One-Parameter design, the level of the first minor lobe (closest to the major lobe) is controlled as part of the design; the level of the remaining ones are monotonically decreasing. Therefore, given the same sidelobe level, the half-power beamwidth of the Taylor One-Parameter is slightly greater than that of the Taylor Tschebyscheff Error, which in turn is slightly greater than that of the Dolph-Tschebyscheff design. More details of these two methods, and other ones, can be found in Chapter 7. However there are some other characteristics that can be used to design arrays.

Uniform arrays are usually preferred in design of direct-radiating active-planar arrays with a large number of elements [20]. One design consideration in satellite antennas is the beamwidth which can be used to determine the "footprint" area of the coverage. It is important to relate the beamwidth to the size of the antenna. In addition, it is also important to maximize the directivity of the antenna within the angular sector defined by the beamwidth, especially at the edge-of-the-coverage (EOC) [20]. For engineering design purposes, closed-form expressions would be desirable.

To relate the half-power beamwidth, or any other beamwidth, to the length of the array in closed form, it is easier to represent the uniform array with a large number of elements as an aperture. The normalized array factor for a rectangular array is that of (6-88). For broadside radiation ($\theta_0 = 0°$) and small spacings between the elements ($d_x \ll \lambda$ and $d_y \ll \lambda$), (6-88) can be used to spproximate the pattern of a uniform illuminated aperture. In one principal plane (i.e., x-z plane: $\phi = 0°$) of Figure 6.23, (6-88) reduces for small element spacing and large number of elements to

$$
\begin{aligned}
(AF)_n(\theta, \phi = 0) &= \frac{1}{M} \frac{\sin\left(\frac{Mkd_x}{2} \sin\theta\right)}{\sin\left(\frac{kd_x}{2} \sin\theta\right)} \\
&\simeq \frac{\sin\left(\frac{Mkd_x}{2} \sin\theta\right)}{\frac{Mkd_x}{2} \sin\theta} \\
&\simeq \frac{\sin\left(\frac{kL_x}{2} \sin\theta\right)}{\frac{kL_x}{2} \sin\theta}
\end{aligned}
\tag{6-102}
$$

INTEL-1045
U.S. Patent 7,151,430

where L_x is the length of the array in the x direction. The array factor of (6-102) can be used to represent the field in a principal plane of a uniform aperture (see Sections 12.5.1, 12.5.2 and Table 12.1). Since the maximum effective area of a uniform array is equal to its physical area $A_{em} = A_p$ [see (12-37)], the maximum directivity is equal to

$$D_0 = \frac{4\pi}{\lambda^2} A_{em} = \frac{4\pi}{\lambda^2} A_p = \frac{4\pi}{\lambda^2} L_x L_y \tag{6-103}$$

Therefore the normalized power pattern in the xz-plane, multiplied by the maximum directivity, can be written as the product of (6-102) and (6-103), and it can be expressed as

$$P(\theta, \phi = 0) = \left(\frac{4\pi L_x L_y}{\lambda^2}\right)\left[\frac{\sin\left(\frac{kL_x}{2}\sin\theta\right)}{\frac{kL_x}{2}\sin\theta}\right]^2 \tag{6-104}$$

The maximum of (6-104) occurs when $\theta = 0°$. However, for any other angle $\theta = \theta_i$, the maximum of the pattern occurs when

$$\sin\left(\frac{kL_x}{2}\sin\theta_c\right) = 1 \tag{6-105}$$

or

$$\boxed{L_x = \frac{\pi}{k\sin\theta_c} = \frac{\lambda}{2\sin\theta_i}} \tag{6-105a}$$

Therefore to maximize the directivity at the edge $\theta = \theta_i$ of a given angular sector $0° \le \theta \le \theta_c$, the optimum aperture dimension must be chosen according to (6-105a). Doing otherwise leads to a decrease in directivity at the edge-of-the-coverage.

For a square aperture ($L_y = L_x$) the value of the normalized power pattern of (6-104) occurs when $\theta = 0°$, and it is equal to

$$P(\theta = 0°)|_{\max} = 4\pi\left(\frac{L_x}{\lambda}\right)^2 \tag{6-106}$$

while that at the edge of the covering, using the optimum dimension, is

$$P(\theta = \theta_c) = 4\pi\left(\frac{L_x}{\lambda}\right)^2\left(\frac{2}{\pi}\right)^2 \tag{6-107}$$

Therefore the value of the directivity at the edge of the desired coverage ($\theta = \theta_i$), relative to its maximum value at $\theta = 0°$, is

$$\frac{P(\theta = \theta_c)}{P(\theta = 0°)} = \left(\frac{2}{\pi}\right)^2 = 0.4053(\text{dimensionless}) = -3.92\ \text{dB} \tag{6-108}$$

Thus the variation of the directivity within the desired coverage ($0° \le \theta \le \theta_c$) is less than 4 dB.

If, for example, the length of the array for a maximum half-power beamwidth coverage is changed from the optimum or chosen to be optimized at another angle,

INTEL-1045
U.S. Patent 7,151,430

then the directivity at the edge of the half-power beamwidth is reduced from the optimum.

Similar expressions have been derived for circular apertures with uniform, parabolic and parabolic with -10 dB pedestal [20], and they can be found in Chapter 12, Section 12.7.

6.12 CIRCULAR ARRAY

The circular array, in which the elements are placed in a circular ring, is an array configuration of very practical interest. Its applications span radio direction finding, air and space navigation, underground propagation, radar, sonar, and many other systems.

6.12.1 Array Factor

Referring to Figure 6.32, let us assume that N isotropic elements are equally spaced on the x-y plane along a circular ring of the radius a. The normalized field of the array can be written as

$$E_n(r, \theta, \phi) = \sum_{n=1}^{N} a_n \frac{e^{-jkR_n}}{R_n} \tag{6-109}$$

where R_n is the distance from the nth element to the observation point. In general

$$R_n = (r^2 + a^2 - 2ar\cos\psi)^{1/2} \tag{6-109a}$$

which for $r \gg a$ reduces to

$$R_n \simeq r - a\cos\psi_n = r - a(\hat{\mathbf{a}}_\rho \cdot \hat{\mathbf{a}}_r) = r - a\sin\theta\cos(\phi - \phi_n) \tag{6-109b}$$

where

$$\begin{aligned}\hat{\mathbf{a}}_\rho \cdot \hat{\mathbf{a}}_r &= (\hat{\mathbf{a}}_x\cos\phi_n + \hat{\mathbf{a}}_y\sin\phi_n) \cdot (\hat{\mathbf{a}}_x\sin\theta\cos\phi + \hat{\mathbf{a}}_y\sin\theta\sin\phi + \hat{\mathbf{a}}_z\cos\theta) \\ &= \sin\theta\cos(\phi - \phi_n)\end{aligned} \tag{6-109c}$$

Thus (6-109) reduces, assuming that for amplitude variations $R_n \simeq r$, to

$$E_n(r, \theta, \phi) = \frac{e^{-jkr}}{r} \sum_{n=1}^{N} a_n e^{+jka\sin\theta\cos(\phi - \phi_n)} \tag{6-110}$$

where

a_n = excitation coefficients (amplitude and phase) of nth element

$\phi_n = 2\pi\left(\frac{n}{N}\right)$ = angular position of nth element on x-y plane

In general, the excitation coefficient of the nth element can be written as

$$a_n = I_n e^{j\alpha_n} \tag{6-111}$$

INTEL-1045
U.S. Patent 7,151,430

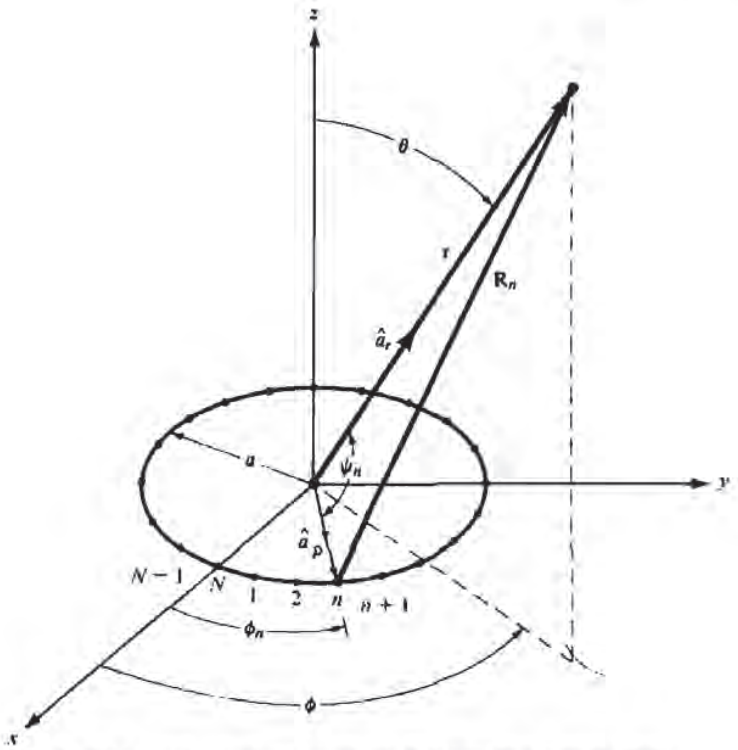


Figure 6.32 Geometry of an N-element circular array.

where

I_n = amplitude excitation of the nth element

α_n = phase excitation (relative to the array center) of the nth element

With (6-111), (6-110) can be expressed as

$$E_n(r, \theta, \phi) = \frac{e^{-jkr}}{r}[\mathrm{AF}(\theta, \phi)] \tag{6-112}$$

where

$$\mathrm{AF}(\theta, \phi) = \sum_{n=1}^{N} I_n e^{j[ka \sin\theta \cos(\phi - \phi_n) + \alpha_n]} \tag{6-112a}$$

Equation (6-112a) represents the array factor of a circular array of N equally spaced elements. To direct the peak of the main beam in the (θ_0, ϕ_0) direction, the phase excitation of the nth element can be chosen to be

$$\alpha_n = -ka \sin\theta_0 \cos(\phi_0 - \phi_n) \tag{6-113}$$

Thus the array factor of (6-112a) can be written as

$$\begin{aligned} \mathrm{AF}(\theta, \phi) &= \sum_{n=1}^{N} I_n e^{jka[\sin\theta\cos(\phi - \phi_n) - \sin\theta_0\cos(\phi_0 - \phi_n)]} \\ &= \sum_{n=1}^{N} I_n e^{jka(\cos\psi - \cos\psi_0)} \end{aligned} \tag{6-114}$$

INTEL-1045
U.S. Patent 7,151,430

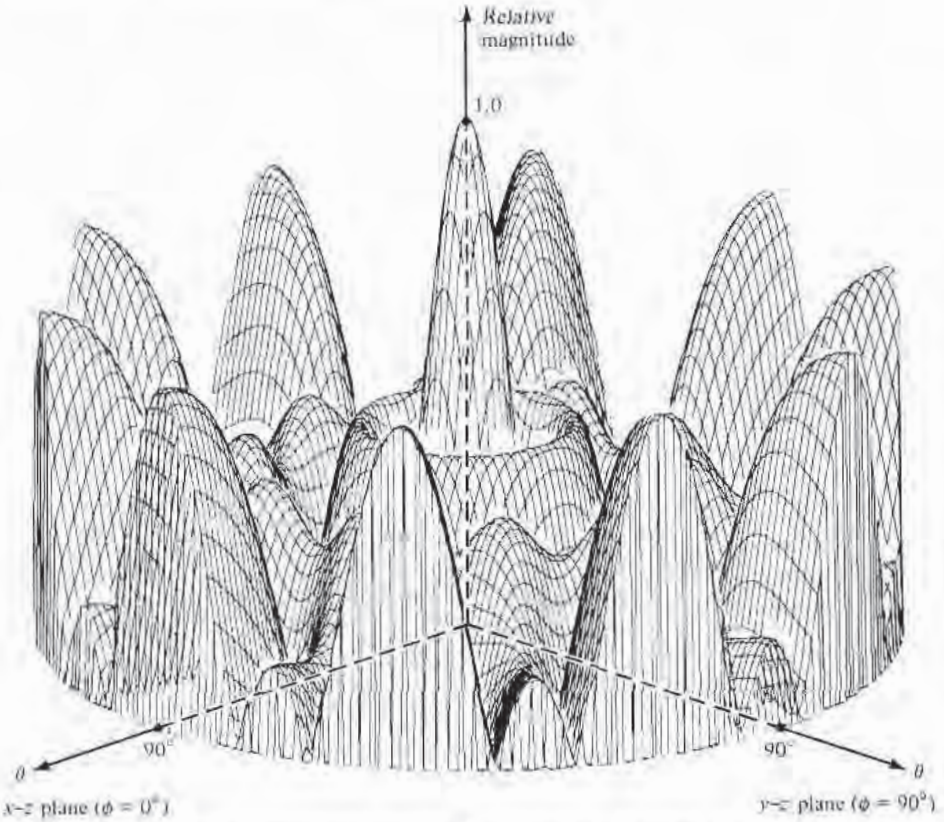


Figure 6.33 Three-dimensional amplitude pattern of the array factor for a uniform circular array of 10 elements ($C = ka = 10$).

To reduce (6-114) to a simpler form, we define ρ_0 as

$$\rho_0 = a[(\sin\theta\cos\phi - \sin\theta_0\cos\phi_0)^2 + (\sin\theta\sin\phi - \sin\theta_0\sin\phi_0)^2]^{1/2} \tag{6-115}$$

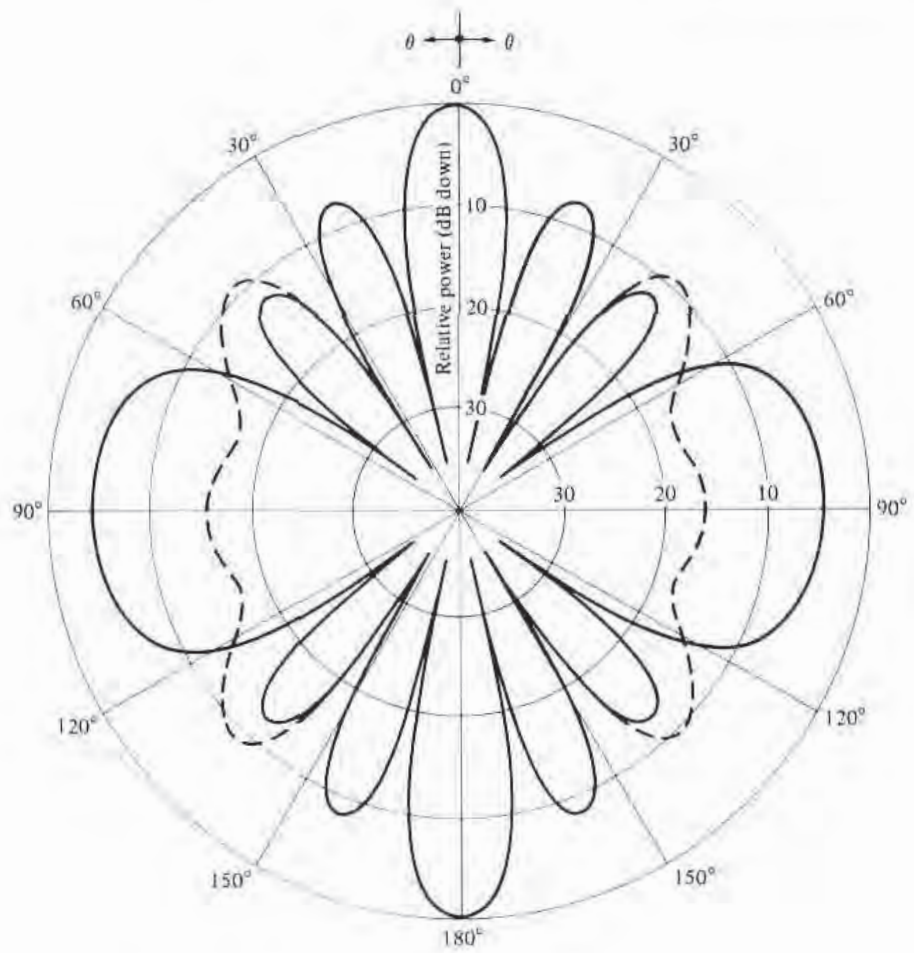
Thus the exponential in (6-114) takes the form of

$$ka(\cos\psi - \cos\psi_0) = \frac{k\rho_0[\sin\theta\cos(\phi - \phi_n) - \sin\theta_0\cos(\phi_0 - \phi_n)]}{[(\sin\theta\cos\phi - \sin\theta_0\cos\phi_0)^2 + (\sin\theta\sin\phi - \sin\theta_0\sin\phi_0)^2]^{1/2}} \tag{6-116}$$

which when expanded reduces to

$$ka(\cos\psi - \cos\psi_0) = k\rho_0\left\{\frac{\cos\phi_n(\sin\theta\cos\phi - \sin\theta_0\cos\phi_0) + \sin\phi_n(\sin\theta\sin\phi - \sin\theta_0\sin\phi_0)}{[(\sin\theta\cos\phi - \sin\theta_0\cos\phi_0)^2 + (\sin\theta\sin\phi - \sin\theta_0\sin\phi_0)^2]^{1/2}}\right\} \tag{6-116a}$$

INTEL-1045
U.S. Patent 7,151,430



——— $x-z$ plane ($\phi = 0°$)

– – – – $y-z$ plane ($\phi = 90°$)

Figure 6.34 Principal plane amplitude patterns of the array factor for a uniform circular array of 10 elements ($ka = 10$).

Defining

$$\cos \xi = \frac{\sin \theta \cos \phi - \sin \theta_0 \cos \phi_0}{[(\sin \theta \cos \phi - \sin \theta_0 \cos \phi_0)^2 + (\sin \theta \sin \phi - \sin \theta_0 \sin \phi_0)^2]^{1/2}} \tag{6-117}$$

then

$$\sin \xi = [1 - \cos^2 \xi]^{1/2} = \frac{\sin \theta \sin \phi - \sin \theta_0 \sin \phi_0}{[(\sin \theta \cos \phi - \sin \theta_0 \cos \phi_0)^2 + (\sin \theta \sin \phi - \sin \theta_0 \sin \phi_0)^2]^{1/2}} \tag{6-118}$$

INTEL-1045
U.S. Patent 7,151,430

Thus (6-116a) and (6-114) can be rewritten, respectively, as

$$ka(\cos\psi - \cos\psi_0) = k\rho_0(\cos\phi_n\cos\xi + \sin\phi_n\sin\xi) = k\rho_0\cos(\phi_n - \xi) \tag{6-119}$$

$$\mathrm{AF}(\theta, \phi) = \sum_{n=1}^{N} I_n e^{jka(\cos\psi - \cos\psi_0)} = \sum_{n=1}^{N} I_n e^{jk\rho_0\cos(\phi_n - \xi)} \tag{6-120}$$

where

$$\xi = \tan^{-1}\left[\frac{\sin\theta\sin\phi - \sin\theta_0\sin\phi_0}{\sin\theta\cos\phi - \sin\theta_0\cos\phi_0}\right] \tag{6-120a}$$

and ρ_0 is defined by (6-115).

Equations (6-120), (6-115), and (6-120a) can be used to calculate the array factor once N, I_n, a, θ_0, and ϕ_0 are specified. This is usually very time consuming, even for moderately large values of N. The three-dimensional pattern of the array factor for a 10-element uniform circular array of $ka = 10$ is shown in Figure 6.33. The corresponding two-dimensional principal plane patterns are displayed in Figure 6.34. As the radius of the array becomes very large, the directivity of a uniform circular array approaches the value of N, where N is equal to the number of elements. An excellent discussion on circular arrays can be found in [21].

For a uniform amplitude excitation of each element ($I_n = I_0$), (6-120) can be written as

$$\mathrm{AF}(\theta, \phi) = NI_0 \sum_{m=-\infty}^{+\infty} J_{mN}(k\rho_0)e^{jmN(\pi/2 - \xi)} \tag{6-121}$$

where $J_p(x)$ is the Bessel function of the first kind (see Appendix V). The part of the array factor associated with the zero order Bessel function $J_0(k\rho_0)$ is called the *principal term* and the remaining terms are noted as the *residuals*. For a circular array with a large number of elements, the term $J_0(k\rho_0)$ alone can be used to approximate the two-dimensional principal plane patterns. The remaining terms in (6-121) contribute negligibly because Bessel functions of larger orders are very small.

References

1. G. Aspley, L. Coltum and M. Rabinowitz, "Quickly Devise a Fast Diode Phase Shifter," *Microwaves*, May 1979, pp. 67–68.
2. R. S. Elliott, "Beamwidth and Directivity of Large Scanning Arrays," First of Two Parts, *The Microwave Journal*, December 1963, pp. 53–60.
3. W. W. Hansen and J. R. Woodyard, "A New Principle in Directional Antenna Design," *Proc. IRE*, Vol. 26, No. 3, March 1938, pp. 333–345.
4. J. S. Stone, United States Patents No. 1,643,323 and No. 1,715,433.
5. C. L. Dolph, "A Current Distribution for Broadside Arrays Which Optimizes the Relationship Between Beamwidth and Side-Lobe Level," *Proc. IRE and Waves and Electrons*, June 1946.
6. N. Yaru, "A Note on Super-Gain Arrays," *Proc. IRE*, Vol. 39, September 1951, pp. 1081–1085.
7. L. J. Ricardi, "Radiation Properties of the Binomial Array," *Microwave Journal*, Vol. 15, No. 12, December 1972, pp. 20–21.
8. H. J. Riblet, Discussion on "A Current Distribution for Broadside Arrays Which Opti-

INTEL-1045
U.S. Patent 7,151,430

mizes the Relationship Between Beamwidth and Side-Lobe Level," *Proc. IRE*, May 1947, pp. 489–492.
9. D. Barbiere, "A Method for Calculating the Current Distribution of Tschebyscheff Arrays," *Proc. IRE*, January 1952, pp. 78–82.
10. R. J. Stegen, "Excitation Coefficients and Beamwidths of Tschebyscheff Arrays," *Proc. IRE*, November 1953, pp. 1671–1674.
11. C. J. Drane, Jr., "Useful Approximations for the Directivity and Beamwidth of Large Scanning Dolph-Chebyshev Arrays," *Proc. IEEE*, November 1968, pp. 1779–1787.
12. M. M. Dawoud and A. P. Anderson, "Design of Superdirective Arrays with High Radiation Efficiency," *IEEE Trans. Antennas Propagat.*, Vol. AP-26, No. 6, January 1978, pp. 819–823.
13. S. A. Schelkunoff, "A Mathematical Theory of Linear Arrays," *Bell System Tech. Journal*, Vol. 22, January 1943, pp. 80–87.
14. C. J. Bowkamp and N. G. de Bruijn, "The Problem of Optimum Antenna Current Distribution," *Phillips Res. Rept.*, Vol. 1, January 1946, pp. 135–158.
15. E. H. Newman, J. H. Richmond, and C. H. Walter, "Superdirective Receiving Arrays," *IEEE Trans. Antennas Propagat.*, Vol. AP-26, No. 5, September 1978, pp. 629–635.
16. J. L. Allen, "On Surface-Wave Coupling Between Elements of Large Arrays," *IEEE Trans. Antennas Propagat.*, Vol. AP-13, No. 4, July 1965, pp. 638–639.
17. R. H. T. Bates, "Mode Theory Approach to Arrays," *IEEE Trans. Antennas Propagat.*, Vol. AP-13, No. 2, March 1965, pp. 321–322.
18. R. S. Elliott, "Beamwidth and Directivity of Large Scanning Arrays," Last of Two Parts, *The Microwave Journal*, January 1964, pp. 74–82.
19. B. J. Forman, "A Novel Directivity Expression for Planar Antenna Arrays," *Radio Science*, Vol. 5, No. 7, July 1970, pp. 1077–1083.
20. K. Praba, "Optimal Aperture for Maximum Edge-of-Coverage (EOC) Directivity," *IEEE Antennas & Propagation Magazine*, Vol. 36, No. 3, pp. 72–74, June 1994.
21. M. T. Ma, *Theory and Application of Antenna Arrays*, Wiley, 1974, Chapter 3, pp. 191–202.

PROBLEMS

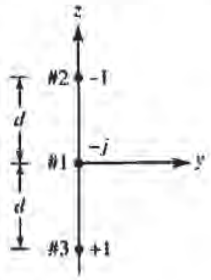
6.1. Three isotropic sources, with spacing d between them, are placed along the z-axis. The excitation coefficient of each outside element is unity while that of the center element is 2. For a spacing of $d = \lambda/4$ between the elements, find the
(a) array factor
(b) angles (in degrees) where the nulls of the pattern occur ($0° \le \theta \le 180°$)
(c) angles (in degrees) where the maxima of the pattern occur ($0° \le \theta \le 180°$)

6.2. Two very short dipoles ("infinitesimal") of equal length are equidistant from the origin with their centers lying on the y-axis, and oriented parallel to the z-axis. They are excited with currents of equal amplitude. The current in dipole 1 (at $y = -d/2$) leads the current in dipole 2 (at $y = +d/2$) by 90° in phase. The spacing between dipoles is one quarter wavelength. To simplify the notation, let E_0 equal the maximum magnitude of the far field at distance r due to either source alone.
(a) Derive expressions for the following six principal plane patterns:
1. $|E_\theta(\theta)|$ for $\phi = 0°$
2. $|E_\theta(\theta)|$ for $\phi = 90°$
3. $|E_\theta(\phi)|$ for $\theta = 90°$
4. $|E_\phi(\theta)|$ for $\phi = 0°$
5. $|E_\phi(\theta)|$ for $\phi = 90°$
6. $|E_\phi(\phi)|$ for $\theta = 90°$

(b) Sketch the six field patterns.

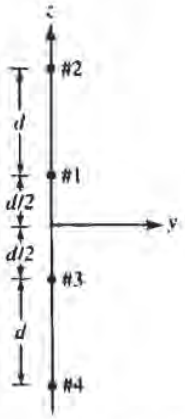
INTEL-1045
U.S. Patent 7,151,430

6.3. A three-element array of isotropic sources has the phase and magnitude relationships shown. The spacing between the elements is $d = \lambda/2$.
(a) Find the array factor.
(b) Find all the nulls.

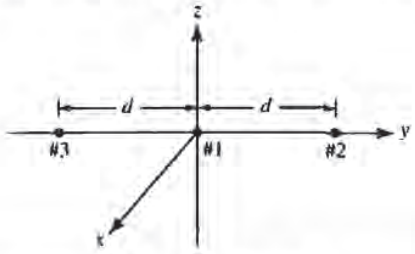


6.4. Repeat Problem 6.3 when the excitation coefficients for elements #1, #2 and #3 are, respectively, $+1$, $+j$ and $-j$.

6.5. Four isotropic sources are placed along the z-axis as shown. Assuming that the amplitudes of elements #1 and #2 are $+1$ and the amplitudes of elements #3 and #4 are -1 (or 180 degrees out of phase with #1 and #2), find
(a) the array factor *in simplified form*
(b) all the nulls when $d = \lambda/2$



6.6. Three isotropic elements of equal excitation phase are placed along the y-axis, as shown in the figure. If the relative amplitude of #1 is $+2$ and of #2 and #3 is $+1$, find a *simplified* expression for the three-dimensional unnormalized array factor.



6.7. Design a two-element uniform array of isotropic sources, positioned along the z-axis a distance $\lambda/4$ apart, so that its only maximum occurs along $\theta = 0°$. Assuming ordinary end-fire conditions, find the
(a) relative phase excitation of each element
(b) array factor of the array
(c) directivity using the computer program DIRECTIVITY at the end of Chapter 2. Compare it with Kraus' approximate formula

INTEL-1045
U.S. Patent 7,151,430

6.8. Repeat the design of Problem 6.7 so that its only maximum occurs along $\theta = 180°$.

6.9. Design a four-element ordinary end-fire array with the elements placed along the z-axis a distance d apart and with the maximum of the array factor directed toward $\theta = 0°$. For a spacing of $d = \lambda/2$ between the elements find the
(a) progressive phase excitation between the elements to accomplish this
(b) angles (in degrees) where the nulls of the array factor occur
(c) angles (in degrees) where the maximum of the array factor occur
(d) beamwidth (in degrees) between the first nulls of the array factor
(e) directivity (in dB) of the array factor. Verify using the computer program DIRECTIVITY at the end of the chapter.

6.10. Design an ordinary end-fire uniform linear array with only one maximum so that its directivity is 20 dB (above isotropic). The spacing between the elements is $\lambda/4$, and its length is much greater than the spacing. Determine the
(a) number of elements
(b) overall length of the array (in wavelengths)
(c) approximate half-power beamwidth (in degrees)
(d) amplitude level (compared to the maximum of the major lobe) of the first minor lobe (in dB)
(e) progressive phase shift between the elements (in degrees).

6.11. Redesign the ordinary end-fire uniform array of Problem 6.10 in order to increase its directivity while maintaining the same, as in Problem 6.10, the uniformity, number of elements, spacing between them, and end-fire radiation.
(a) What different from the design of Problem 6.10 are you going to do to achieve this? Be very specific, and give values.
(b) By how many decibels (maximum) can you increase the directivity, compared to the design of Problem 6.10?
(c) Are you expecting the half-power beamwidth to increase or decrease? Why increase or decrease and by how much?
(d) What antenna figure-of-merit will be degraded by this design? Be very specific in naming it, and why is it degraded?

6.12. Ten isotropic elements are placed along the z-axis. Design a Hansen-Woodyard end-fire array with the maximum directed toward $\theta = 180°$. Find the:
(a) desired spacing
(b) progressive phase shift β (in radians)
(c) location of all the nulls (in degrees)
(d) first null beamwidth (in degrees)
(e) directivity; verify using the computer program DIRECTIVITY at the end of the chapter

6.13. An array of 10 isotropic elements are placed along the z-axis a distance d apart. Assuming uniform distribution, find the progressive phase (in degrees), half-power beamwidth (in degrees), first null beamwidth (in degrees), first side lobe level maximum beamwidth (in degrees), relative side lobe level maximum (in dB), and directivity (in dB) (using equations and the computer program DIRECTIVITY at the end of Chapter 2, and compare) for
(a) broadside
(b) ordinary end-fire
(c) Hansen-Woodyard end-fire
arrays when the spacing between the elements is $d = \lambda/4$.

6.14. Find the beamwidth and directivity of a 10-element uniform scanning array of isotropic sources placed along the z-axis. The spacing between the elements is $\lambda/4$ and the maximum is directed at 45° from its axis.

6.15. Show that in order for a uniform array of N elements not to have any minor lobes, the spacing and the progressive phase shift between the elements must be
(a) $d = \lambda/N$, $\beta = 0$ for a broadside array.
(b) $d = \lambda/(2N)$, $\beta = \pm kd$ for an ordinary end-fire array.

INTEL-1045
U.S. Patent 7,151,430

6.16. A uniform array of 20 isotropic elements is placed along the z-axis a distance $\lambda/4$ apart with a progressive phase shift of β rad. Calculate β (give the answer in radians) for the following array types:
(a) broadside
(b) end-fire with maximum at $\theta = 0°$
(c) end-fire with maximum at $\theta = 180°$
(d) phased array with maximum aimed at $\theta = 30°$
(e) Hansen-Woodyard with maximum at $\theta = 0°$
(f) Hansen-Woodyard with maximum at $\theta = 180°$

6.17. Design a 19-element uniform linear scanning array with a spacing of $\lambda/4$ between the elements.
(a) What is the progressive phase excitation between the elements so that the maximum of the array factor is 30° from the line where the elements are placed?
(b) What is the half-power beamwidth (in degrees) of the array factor of part a? Verify using the computer program at the end of this chapter.
(c) What is the value (in dB) of the maximum of the first minor lobe?

6.18. For a uniform broadside linear array of 10 isotropic elements, determine the approximate directivity (in dB) when the spacing between the elements is
(a) $\lambda/4$
(b) $\lambda/2$
(c) $3\lambda/4$
(d) λ
Compare the values with those obtained using the computer program at the end of this chapter.

6.19. The maximum distance d between the elements in a linear scanning array to suppress grating lobes is

$$d_{\max} = \frac{\lambda}{1 + |\cos(\theta_0)|}$$

where θ_0 is the direction of the pattern maximum. What is the maximum distance between the elements, without introducing grating lobes, when the array is designed to scan to maximum angles of
(a) $\theta_0 = 30°$
(b) $\theta_0 = 45°$
(c) $\theta_0 = 60°$

6.20. An array of 4 isotropic sources is formed by placing one at the origin, and one along the x-, y-, and z-axes a distance d from the origin. Find the array factor for all space. The excitation coefficient of each element is identical.

6.21. Design a linear array of isotropic elements placed along the z-axis such that the nulls of the array factor occur at $\theta = 0°$ and $\theta = 45°$. Assume that the elements are spaced a distance of $\lambda/4$ apart and that $\beta = 0°$.
(a) Sketch and label the visible region on the unit circle
(b) Find the required number of elements
(c) Determine their excitation coefficients

6.22. Design a linear array of isotropic elements placed along the z-axis such that the zeros of the array factor occur at $\theta = 10°$, 70°, and 110°. Assume that the elements are spaced a distance of $\lambda/4$ apart and that $\beta = 45°$.
(a) Sketch and label the visible region on the unit circle
(b) Find the required number of elements
(c) Determine their excitation coefficients

6.23. Repeat Problem 6.22 so that the nulls occur at $\theta = 0°$, 50° and 100°. Assume a spacing of $\lambda/5$ and $\beta = 0°$ between the elements.

INTEL-1045
U.S. Patent 7,151,430

6.24. Design a three-element binomial array of isotropic elements positioned along the z-axis a distance d apart. Find the
(a) normalized excitation coefficients
(b) array factor
(c) nulls of the array factor for $d = \lambda$
(d) maxima of the array factor for $d = \lambda$

6.25. Show that a three-element binomial array with a spacing of $d \leq \lambda/2$ between the elements does not have a side lobe.

6.26. Four isotropic sources are placed symmetrically along the z-axis a distance d apart. Design a binomial array. Find the
(a) normalized excitation coefficients
(b) array factor
(c) angles (in degrees) where the array factor nulls occur when $d = 3\lambda/4$

6.27. Five isotropic sources are placed symmetrically along the z-axis, each separated from its neighbor by an electrical distance $kd = 5\pi/4$. For a binomial array, find
(a) the excitation coefficients
(b) the array factor
(c) the normalized power pattern
(d) the angles (in degrees) where the nulls (if any) occur
Verify parts of the problem using the computer program at the end of this chapter.

6.28. Design a four-element binomial array of $\lambda/2$ dipoles, placed symmetrically along the x-axis a distance d apart. The length of each dipole is parallel to the z-axis.
(a) Find the normalized excitation coefficients.
(b) Write the array factor for all space.
(c) Write expressions for the E-fields for all space.

6.29. Repeat the design of Problem 6.28 when the $\lambda/2$ dipoles are placed along the y-axis.

6.30. Design a broadside binomial array of six elements placed along the z-axis separated by a distance $d = \lambda/2$.
(a) Find the amplitude excitation coefficients (a_n's).
(b) What is the progressive phase excitation between the elements?
(c) Write the array factor.
(d) Now assume that the elements are $\lambda/4$ dipoles oriented in the z-direction. Write the expression for the electric field *vector* in the far field.
Verify parts of the problem using the computer program at the end of this chapter.

6.31. Repeat Problem 6.30 for an array of seven elements.

6.32. Five isotropic elements, with spacing d between them, are placed along the z-axis. For a binomial amplitude distribution,
(a) write the array factor in its most simplified form
(b) compute the directivity (in dB) using the computer program at the end of this chapter ($d = \lambda/2$)
(c) find the nulls of the array when $d = \lambda (0° \leq \theta \leq 180°)$

6.33. Repeat the design of Problem 6.24 for a Dolph-Tschebyscheff array with a side lobe level of -20 dB.

6.34. Design a three-element, -40 dB side lobe level Dolph-Tschebyscheff array of isotropic elements placed symmetrically along the z-axis. Find the
(a) amplitude excitation coefficients
(b) array factor
(c) angles where the nulls occur for $d = 3\lambda/4$ $(0° \leq \theta \leq 180°)$
(d) directivity for $d = 3\lambda/4$
(e) half-power beamwidth for $d = 3\lambda/4$

6.35. Design a four-element, -40 dB side lobe level Dolph-Tschebyscheff array of isotropic elements placed symmetrically about the z-axis. Find the
(a) amplitude excitation coefficients
(b) array factor
(c) angles where the nulls occur for $d = 3\lambda/4$.
Verify parts of the problem using the computer program at the end of this chapter.

INTEL-1045
U.S. Patent 7,151,430

6.36. Repeat the design of Problem 6.35 for a five-element, −20 dB Dolph-Tschebyscheff array.

6.37. Repeat the design of Problem 6.35 for a six-element, −20 dB Dolph-Tschebyscheff array.

6.38. Repeat the design of Problem 6.28 for a Dolph-Tschebyscheff distribution of −40 dB side lobe level and $\lambda/4$ spacing between the elements. In addition, find the
(a) directivity of the entire array
(b) half-power beamwidths of the entire array in the x-y and y-z planes

6.39. Repeat the design of Problem 6.29 for a Dolph-Tschebyscheff distribution of −40 dB side lobe level and $\lambda/4$ spacing between the elements. In addition, find the
(a) directivity of the entire array
(b) half-power beamwidths of the entire array in the x-y and x-z planes

6.40. Design a five-element, −40 dB side lobe level Dolph-Tschebyscheff array of isotropic elements. The elements are placed along the x-axis with a spacing of $\lambda/4$ between them. Determine the
(a) normalized amplitude coefficients
(b) array factor
(c) directivity
(d) half-power beamwidth

6.41. The total length of a discrete-element array is 4λ. For a −30 dB side lobe level Dolph-Tschebyscheff design and a spacing of $\lambda/2$ between the elements along the z-axis, find the
(a) number of elements
(b) excitation coefficients
(c) directivity
(d) half-power beamwidth

6.42. Design a broadside three-element, −26 dB side lobe level Dolph-Tschebyscheff array of isotopic sources placed along the z-axis. For this design, find the
(a) normalized excitation coefficients
(b) array factor
(c) nulls of the array factor when $d = \lambda/2$ (in degrees)
(d) maxima of the array factor when $d = \lambda/2$ (in degrees)
(e) beamwidth (in degrees) of the array factor when $d = \lambda/2$
(f) directivity (in dB) of the array factor when $d = \lambda/2$

6.43. Design a broadside uniform array, with its elements placed along the z axis, so that the directivity of the array factor is 33 dB (above isotropic). Assuming the spacing between the elements is $\lambda/16$, and it is very small compared to the overall length of the array, determine the:
(a) Closest number of integer elements to achieve this.
(b) Overall length of the array (in wavelengths).
(c) Half-power beamwidth (in degrees).
(d) Amplitude level (in dB) of the maximum of the first minor lobe compared to the maximum of the major lobe.

6.44. The design of Problem 6.43 needs to be changed to a nonuniform Dolph-Tschebyscheff so that to lower the side lobe amplitude level to −30 dB, while maintaining the same number of elements and spacing. For the new nonuniform design, what is the:
(a) Half-power beamwidth (in degrees).
(b) Directivity (in dB).

6.45. Design a Dolph-Tschebyscheff linear array of N elements with uniform spacing between them. The array factor must meet the following specifications:
(1) −40 dB sidelobe level.
(2) Four complete minor lobes from $0° \leq \theta \leq 90°$; all of the same level.

INTEL-1045
U.S. Patent 7,151,430

(3) Largest allowable spacing between the elements (in wavelengths) and still meet above specifications.

Determine:

(a) Number of elements
(b) Excitation coefficients, normalized so that the ones of the edge elements is unity.
(c) Maximum allowable spacing (in wavelengths) between the elements and still meet specifications.
(d) Plot (in 1° increments) the normalized (max = 0 dB) array factor (in dB). Check to see that the array factor meets the specifications. If not, find out what is wrong with it.

Verify parts of the problem using the computer program at the end of this chapter.

6.46. In high-performance radar arrays low-sidelobes are very desirable. In a particular application it is desired to design a broadside linear array which maintains all the sidelobes at the same level of -30 dB. The number of elements must be 3 and the spacing between them must be $\lambda/4$.

(a) State the design that will meet the specifications.
(b) What are the amplitude excitations of the elements?
(c) What is the half-power beamwidth (in degrees) of the main lobe?
(d) What is the directivity (in dB) of the array?

6.47. Design a nonuniform amplitude broadside linear array of 5 elements. The total length of the array is 2λ. To meet the sidelobe and half-power beamwidth specifications, the amplitude excitations of the elements must be that of a cosine-on-a-pedestal distribution represented by

$$\text{Amplitude distribution} = 1 + \cos(\pi x_n/L)$$

where x_n is the position of the nth element (in terms of L) measured from the center of the array. Determine the amplitude excitation coefficients a_n's of the five elements. Assume uniform spacing between the elements and the end elements are located at the edges of the array length.

6.48. It is desired to design a uniform square scanning array whose elevation half-power beamwidth is 2°. Determine the minimum dimensions of the array when the scan maximum angle is

(a) $\theta_0 = 30°$
(b) $\theta_0 = 45°$
(c) $\theta_0 = 60°$

6.49. Determine the azimuthal and elevation angles of the grating lobes for a 10×10 element uniform planar array when the spacing between the elements is λ. The maximum of the main beam is directed toward $\theta_0 = 60°$, $\phi_0 = 90°$ and the array is located on the x-y plane.

6.50. Design a 10×8 (10 in the x direction and 8 in the y) element uniform planar array so that the main maximum is oriented along $\theta_0 = 10°$, $\phi_0 = 90°$. For a spacing of $d_x = d_y = \lambda/8$ between the elements, find the

(a) progressive phase shift between the elements in the x and y directions
(b) directivity of the array
(c) half-power beamwidths (in two perpendicular planes) of the array

Verify the design using the computer program at the end of this chapter.

6.51. The main beam maximum of a 10×10 planar array of isotropic elements (100 elements) is directed toward $\theta_0 = 10°$ and $\phi_0 = 45°$. Find the directivity, beamwidths (in two perpendicular planes), and beam solid angle for a Tschebyscheff distribution design with side lobes of -26 dB. The array is placed on the x-y plane and the elements are equally spaced with $d = \lambda/4$. It should be noted that an array with bidirectional (two-sided pattern) elements would have a directivity which would be half of that of

INTEL-1045
U.S. Patent 7,151,430

the same array but with unidirectional (one-sided pattern) elements. Verify the design using the computer program at the end of this chapter.

6.52. Repeat Problem 6.50 for a Tschebyscheff distribution array of -30 dB side lobes.

6.53. In the design of uniform linear arrays, the maximum usually occurs at $\theta = \theta_0$ at the design frequency $f = f_0$, which has been used to determine the progressive phase between the elements. As the frequency shifts from the designed center frequency f_0 to f_h, the maximum amplitude of the array factor at $f = f_h$ is 0.707 the normalized maximum amplitude of unity at $f = f_0$. The frequency f_h is referred to as the half-power frequency, and it is used to determine the frequency bandwidth over which the pattern maximum varies over an amplitude of 3 dB. Using the array factor of linear uniform array, determine an expression for the 3-dB frequency bandwidth in terms of the length L of the array and the scan angle θ_0.

INTEL-1045
U.S. Patent 7,151,430

```
C*****************************************************************
C
C THIS IS A FORTRAN PROGRAM THAT COMPUTES THE
C RADIATION CHARACTERISTICS OF:
C
C   I.  LINEAR ARRAYS (UNIFORM & BROADSIDE NONUNIFORM)
C   II. PLANAR  ARRAY (BROADSIDE UNIFORM)
C
C THE UNIFORM AND BROADSIDE NONUNIFORM LINEAR ARRAYS HAVE N
C ELEMENTS PLACED EQUIDISTANTLY ALONG THE Z-AXIS.
C
C BROADSIDE PLANAR UNIFORM ARRAY HAS M x N ELEMENTS PLACED
C EQUIDISTANTLY ALONG THE X AND Y AXES
C
C
C     OPTION I.  LINEAR ARRAYS
C
C        OPTION A. UNIFORM
C
C          **CHOICES: ARRAY TYPE
C          1. BROADSIDE (Maximum along θ = 90°)
C          2. ORDINARY END-FIRE (Maximum along θ = 0° or 180°)
C          3. HANSEN WOODYARD END-FIRE (Maximum along θ = 0° or 180°)
C          4. SCANNING (Maximum along θ = θmax)
C
C          **ARRAY INPUT PARAMETERS
C          1. NUMBER OF ELEMENTS
C          2. SPACING BETWEEN THE ELEMENTS (in λ)
C          3. DIRECTION OF ARRAY MAXIMUM θmax (in degrees)
C
C          ** PROGRAM OUTPUT:
C          1. NORMALIZED ARRAY FACTOR
C          2. DIRECTIVITY (dimensionless and in dB) USING
C             NUMERICAL INTEGRATION OF THE ARRAY FACTOR
C          3. HALF-POWER BEAMWIDTH (in degrees) USING AN
C             ITERATIVE METHOD (for all maxima in the pattern)
C
C        OPTION B. NONUNIFORM (BROADSIDE)
C
C          **CHOICES: ARRAY TYPE
C          1. BINOMIAL
C          2. DOLPH-TSCHEBYSCHEFF
C
C          **BINOMIAL ARRAY INPUT PARAMETERS
C          1. NUMBER OF ELEMENTS
C          2. SPACING BETWEEN THE ELEMENTS (in λ)
C
C
C
```

(continued on next page)

INTEL-1045
U.S. Patent 7,151,430

```
C                                                          (continued)
C
C
C       **DOLPH-TSCHEBYSCHEFF ARRAY INPUT PARAMETERS
C       1. NUMBER OF ELEMENTS
C       2. SPACING BETWEEN THE ELEMENTS (in λ)
C       3. SIDE LOBE LEVEL (in positive dB; i.e., 30 dB)
C
C       **PROGRAM OUTPUT:
C       1. NORMALIZED EXCITATION COEFFICIENTS (a_n)
C       2. NORMALIZED ARRAY FACTOR
C       3. DIRECTIVITY (in dB) USING NUMERICAL
C          INTEGRATION OF THE ARRAY FACTOR
C       4. HALF-POWER BEAMWIDTH (in degrees) USING
C          AN ITERATIVE METHOD (for all maxima in the pattern)
C
C
C    OPTION II.  PLANAR ARRAY (BROADSIDE UNIFORM)
C
C       **ARRAY INPUT PARAMETERS
C       1. NUMBER OF ARRAY ELEMENTS IN X-DIRECTION
C       2. SPACING BETWEEN ELEMENTS IN X-DIRECTION (in λ)
C       3. NUMBER OF ARRAY ELEMENTS IN Y-DIRECTION
C       4. SPACING BETWEEN ELEMENTS IN Y-DIRECTION (in λ)
C       5. MAXIMUM BEAM DIRECTION ANGLE θ_o
C       6. MAXIMUM BEAM DIRECTION ANGLE φ_o
C       7. THE AZIMUTHAL ANGLE φ_elevation (in degrees) AT WHICH
C          THE 2-D ANTENNA PATTERN NEEDS TO BE EVALUATED
C
C       **NOTE
C       ONLY THE ELEVATION ANTENNA PATTERN IS
C       EVALUATED.  THIS PATTERN RANGES FROM θ=0° TO
C       θ=180°, WHEREAS φ REMAINS CONSTANT  AT
C       φ_elevation.  IF THE PATTERN NEEDS TO BE EVALUATED
C       IN THE BACKSIDE REGION OF THE 2-D ARRAY, THEN
C       THE PROGRAM NEEDS TO BE RE-RUN FOR A NEW
C       AZIMUTHAL ANGLE φ'_elevation = φ_elevation + 180°.
C
C       **PROGRAM OUTPUT:
C       1. NORMALIZED ARRAY FACTOR EVALUATED AT
C          A GIVEN ANGLE .
C       2. DIRECTIVITY (in dB) USING NUMERICAL
C          INTEGRATION OF THE ARRAY FACTOR
C       3. HALF-POWER BEAMWIDTH (in degrees) FOR ALL
C          MAXIMA THAT OCCUR IN THE ELEVATION PLANE
C          OF THE 2-D ARRAY PATTERN
C
C*************************************************************
```


INTEL-1045
U.S. Patent 7,151,430

CHAPTER 7

ANTENNA SYNTHESIS AND CONTINUOUS SOURCES

7.1 INTRODUCTION

Thus far in the book we have concentrated primarily on the analysis and design of antennas. In the analysis problem an antenna model is chosen, and it is analyzed for its radiation characteristics (pattern, directivity, impedance, beamwidth, efficiency, polarization, and bandwidth). This is usually accomplished by initially specifying the current distribution of the antenna, and then analyzing it using standard procedures. If the antenna current is not known, it can usually be determined from integral equation formulations. Numerical techniques, such as the Moment Method of Chapter 8, can be used to numerically solve the integral equations.

In practice, it is often necessary to design an antenna system that will yield desired radiation characteristics. For example, a very common request is to design an antenna whose far-field pattern possesses nulls in certain directions. Other common requests are for the pattern to exhibit a desired distribution, narrow beamwidth and low side lobes, decaying minor lobes, and so forth. The task, in general, is to find not only the antenna configuration but also its geometrical dimensions and excitation distribution. The designed system should yield, either exactly or approximately, an acceptable radiation pattern, and it should satisfy other system constraints. This method of design is usually referred to as *synthesis*. Although synthesis, in its broadest definition, usually refers to antenna pattern synthesis, it is often used interchangeably with design. Since design methods have been outlined and illustrated previously, in this chapter we want to introduce and illustrate antenna pattern synthesis methods.

Antenna pattern synthesis usually requires that first an approximate analytical model is chosen to represent, either exactly or approximately, the desired pattern. The second step is to realize the analytical model by an antenna model. Generally speaking, antenna pattern synthesis can be classified into three categories. One group requires that the antenna patterns possess nulls in desired directions. The method introduced by Schelkunoff [1] can be used to accomplish this; it will be discussed in Section 7.3. Another category requires that the patterns exhibit a desired distribution in the entire visible region. This is referred to as *beam shaping*, and it can be accomplished using the Fourier transform [2] and the Woodward-Lawson [3], [4] methods. They will be discussed and illustrated in Sections 7.4 and 7.5, respectively. A third group includes

INTEL-1045
U.S. Patent 7,151,430

techniques that produce patterns with narrow beams and low side lobes. Some methods that accomplish this have aleady been discussed: namely the binomial method (Section 6.8.2) and the Dolph-Tschebyscheff method (also spelled Tchebyscheff or Chebyshev) of Section 6.8.3. Other techniques that belong to this family are the Taylor line-source (Tschebyscheff error) [5] and the Taylor line-source (one-parameter) [6]. They will be outlined and illustrated in Sections 7.6 and 7.7, respectively.

The synthesis methods will be utilized to design line-sources and linear arrays whose space factors [as defined by (4-58a)] and array factors [as defined by (6-52)] will yield desired far-field radiation patterns. The total pattern is formed by multiplying the space factor (or array factor) by the element factor (or element pattern) as dictated by (4-59) [or (6-5)]. For very narrow beam patterns, the total pattern is nearly the same as the space factor or array factor. This is demonstrated by the dipole antenna ($l \leq \lambda$) of Figure 4.5 whose element factor, as given by (4-58a), is $\sin\theta$; for values of θ near 90° ($\theta \simeq 90°$), $\sin\theta \simeq 1$.

The synthesis techniques will be followed with a brief discussion of some very popular line-source distributions (triangular, cosine, cosine-squared) and continuous aperture distributions (rectangular and circular).

7.2 CONTINUOUS SOURCES

Very long (in terms of a wavelength) arrays of discrete elements usually are more difficult to implement, more costly, and have narrower bandwidths. For such applications, antennas with continuous distributions would be convenient to use. A very long wire and a large reflector represent, respectively, antennas with continuous line and aperture distributions. Continuous distribution antennas usually have larger side lobes, are more difficult to scan, and in general, they are not as versatile as arrays of discrete elements. The characteristics of continuously distributed sources can be approximated by discrete-element arrays, and vice-versa, and their development follows and parallels that of discrete-element arrays.

7.2.1 Line-Source

Continuous line-source distributions are functions of only one coordinate, and they can be used to approximate linear arrays of discrete elements and vice-versa.

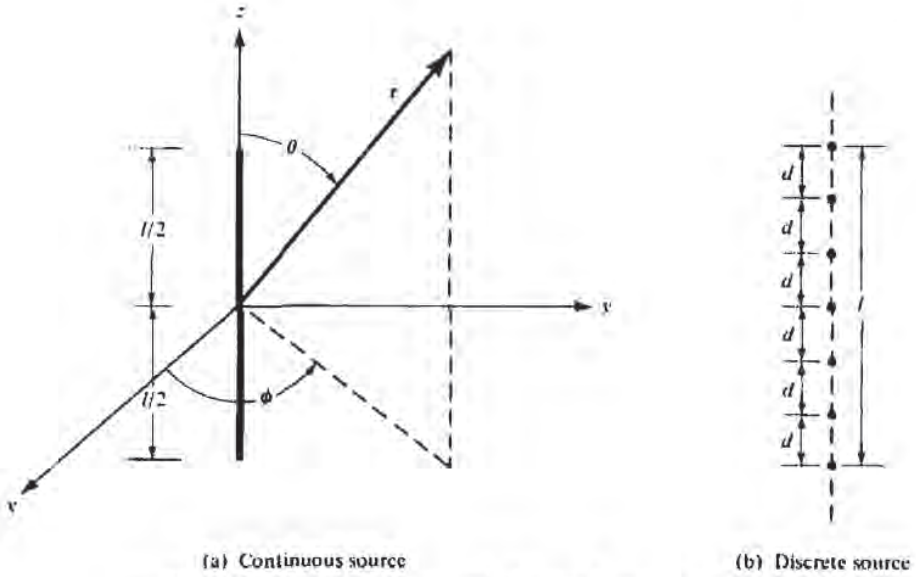
The array factor of a discrete-element array, placed along the z-axis, is given by (6-52) and (6-52a). As the number of elements increases in a fixed-length array, the source approaches a continuous distribution. In the limit, the array factor summation reduces to an integral. For a continuous distribution, the factor that corresponds to the array factor is known as the *space factor*. For a line-source distribution of length l placed symmetrically along the z-axis as shown in Figure 7.1(a), the space factor (SF) is given by

$$\boxed{\mathrm{SF}(\theta) = \int_{-l/2}^{+l/2} I_n(z') e^{j[kz'\cos\theta + \phi_n(z')]}\, dz'} \tag{7-1}$$

where $I_n(z')$ and $\phi_n(z')$ represent, respectively, the amplitude and phase distributions along the souce. For a constant phase distribution $\phi_n(z') = 0$.

Equation (7-1) is a finite one-dimensional Fourier transform relating the far-field pattern of the source to its excitation distribution. Two-dimensional Fourier transforms are used to represent the space factors for two-dimensional source distributions. These relations are results of the angular spectrum concept for plane waves, introduced first

INTEL-1045
U.S. Patent 7,151,430



(a) Continuous source (b) Discrete source

Figure 7.1 Continuous and discrete linear sources.

by Booker and Clemmow [2], and it relates the angular spectrum of a wave to the excitation distribution of the source.

For a continuous source distribution, the total field is given by the product of the *element* and *space* factors as defined in (4-59). This is analogous to the pattern multiplication of (6-5) for arrays. *The type of current and its direction of flow on a source determine the element factor.* For a finite length linear dipole, for example, the toal field of (4-58a) is obtained by summing the contributions of small infinitesimal elements which are used to represent the entire dipole. In the limit, as the infinitesimal lengths become very small, the summation reduces to an integration. In (4-58a), the factor outside the brackets is the element factor and the one within the brackets is the space factor and corresponds to (7-1).

7.2.2 Discretization of Continuous Sources

The radiation characteristics of continuous sources can be approximated by discrete-element arrays, and vice-versa. This is illustrated in Figure 7.1(b) whereby discrete elements, with a spacing d between them, are placed along the length of the continuous source. Smaller spacings between the elements yield better approximations, and they can even capture the fine details of the continuous distribution radiation characteristics. For example, the continuous line-source distribution $I_n(z')$ of (7-1) can be approximated by a discrete-element array whose element excitation coefficients, at the specified element positions within $-l/2 \leq z' \leq l/2$, are determined by the sampling of $I_n(z')e^{j\phi_n(z')}$. The radiation pattern of the digitized discrete-element array will approximate the pattern of the continuous source.

The technique can be used for the discretization of any continuous distribution. The accuracy increases as the element spacing decreases; in the limit, the two patterns will be identical. For large element spacing, the patterns of the two antennas will not match well. To avoid this, another method known as *root-matching* can be used [7]. Instead of sampling the continuous current distribution to determine the element excitation coefficients, the root-matching method requires that the nulls of the contin-

INTEL-1045
U.S. Patent 7,151,430

uous distribution pattern also appear in the initial pattern of the discrete-element array. If the synthesized pattern using this method still does not yield (within an acceptable accuracy) the desired pattern, a perturbation technique [7] can then be applied to the distribution of the discrete-element array to improve its accuracy.

7.3 SCHELKUNOFF POLYNOMIAL METHOD

A method that is conducive to the synthesis of arrays whose patterns possess nulls in desired directions is that introduced by Schelkunoff [1]. To complete the design, this method requires information on the number of nulls and their locations. The number of elements and their excitation coefficients are then derived. The analytical formation of the technique follows.

Referring to Figure 6.5(a), the array factor for an N-element, equally spaced, nonuniform amplitude, and progressive phase excitation is given by (6-52) as

$$\text{AF} = \sum_{n=1}^{N} a_n e^{j(n-1)(kd\cos\theta+\beta)} = \sum_{n=1}^{N} a_n e^{j(n-1)\psi} \tag{7-2}$$

where a_n accounts for the nonuniform amplitude excitation of each element. The spacing between the elements is d and β is the progressive phase shift.

Letting

$$z = x + jy = e^{j\psi} = e^{j(kd\cos\theta+\beta)} \tag{7-3}$$

we can rewrite (7-2) as

$$\text{AF} = \sum_{n=1}^{N} a_n z^{n-1} = a_1 + a_2 z + a_3 z^2 + \cdots + a_N z^{N-1} \tag{7-4}$$

which is a polynomial of degree $(N-1)$. From the mathematics of complex variables and algebra, any polynomial of degree $(N-1)$ has $(N-1)$ roots and can be expressed as a product of $(N-1)$ linear terms. Thus we can write (7-4) as

$$\boxed{\text{AF} = a_n(z-z_1)(z-z_2)(z-z_3)\cdots(z-z_{N-1})} \tag{7-5}$$

where $z_1, z_2, z_3, \ldots, z_{N-1}$ are the roots, which may be complex, of the polynomial. The magnitude of (7-5) can be expressed as

$$\boxed{|\text{AF}| = |a_n||z-z_1||z-z_2||z-z_3|\cdots|z-z_{N-1}|} \tag{7-6}$$

Some very interesting observations can be drawn from (7-6) which can be used judiciously for the analysis and synthesis of arrays. Before tackling that phase of the problem, let us first return and examine the properties of (7-3).

The complex variable z of (7-3) can be written in another form as

$$z = |z|e^{j\psi} = |z|\angle\psi = 1\angle\psi \tag{7-7}$$

$$\psi = kd\cos\theta + \beta = \frac{2\pi}{\lambda}d\cos\theta + \beta \tag{7-7a}$$

It is clear that for any value of d, θ, or β the magnitude of z lies always on a *unit* circle; however its phase depends upon d, θ, and β. For $\beta = 0$, we have plotted in Figures 7-2(a)–(d) the value of z, magnitude and phase, as θ takes values of 0 to π rad. It is observed that for $d = \lambda/8$ the values of z, for all the physically observable

INTEL-1045
U.S. Patent 7,151,430

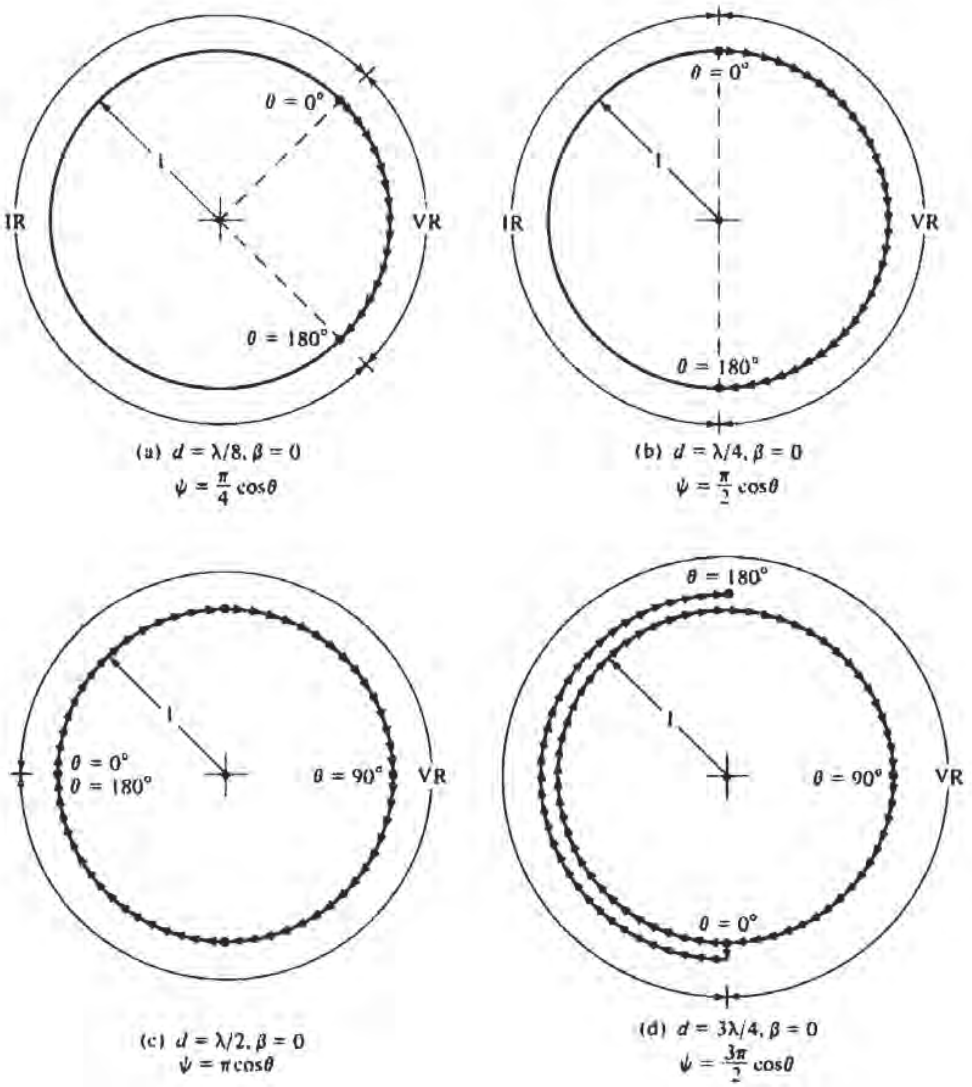


Figure 7.2 *V*isible *R*egion (VR) and *I*nvisible *R*egion (IR) boundaries for complex variable z when $\beta = 0$.

angles of θ, only exist over the part of the circle shown in Figure 7.2(a). Any values of z outside that arc are not realizable by any observation angle θ for the spacing $d = \lambda/8$. We refer to the realizable part of the circle as the *visible region* and the remaining as the *invisible region*. In Figure 7.2(a) we also observe the path of the z values as θ changes from 0° to 180°.

In Figures 7.2(b)–(d) we have plotted the values of z when the spacing between the elements is $\lambda/4$, $\lambda/2$, and $3\lambda/4$. It is obvious that the visible region can be extended by increasing the spacing between the elements. It requires a spacing of at least $\lambda/2$ to encompass, at least once, the entire circle. Any spacing greater than $\lambda/2$ leads to multiple values for z. In Figure 7.2(d) we have double values for z for half of the circle when $d = 3\lambda/4$.

To demonstrate the versatility of the arrays, in Figures 7.3(a)–(d) we have plotted the values of z for the same spacings as in Figures 7.2(a)–(d) but with a $\beta = \pi/4$. A comparison between the corresponding figures indicates that the overall visible region

INTEL-1045
U.S. Patent 7,151,430

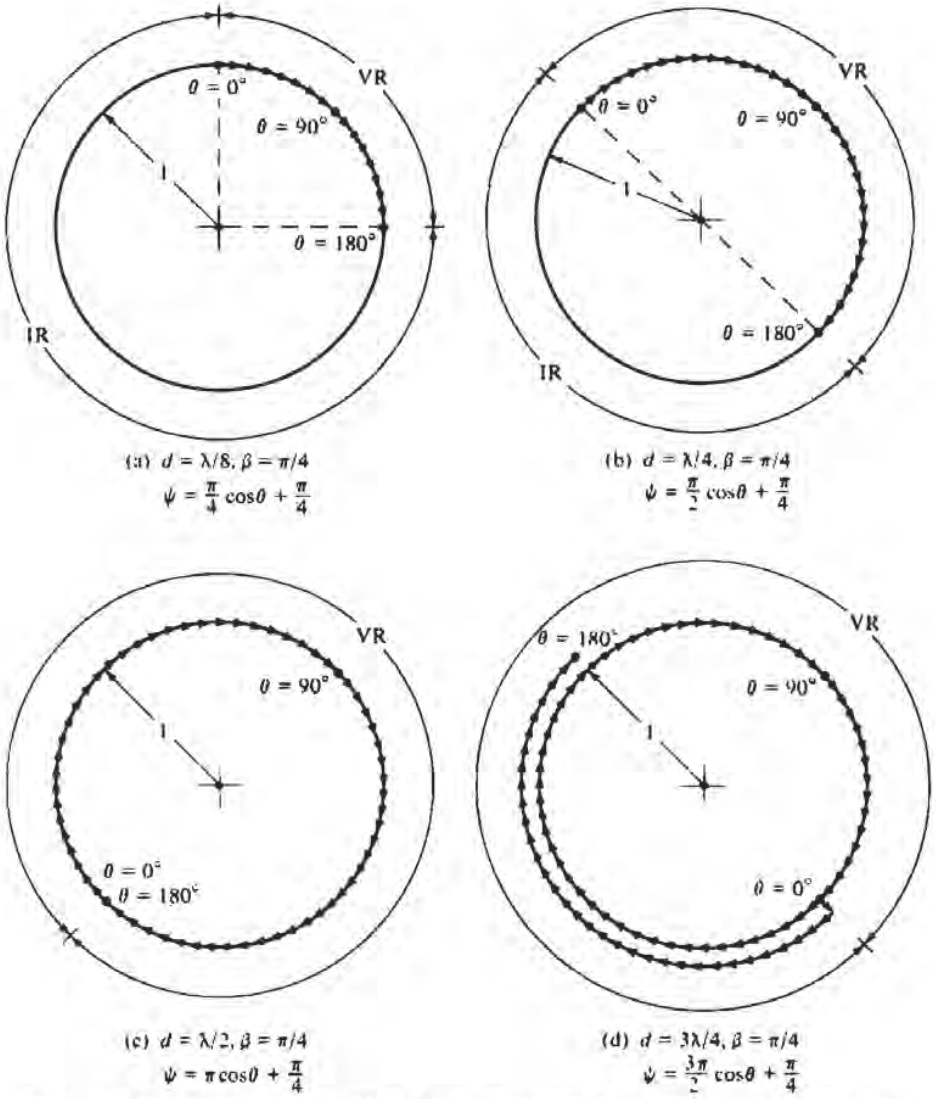


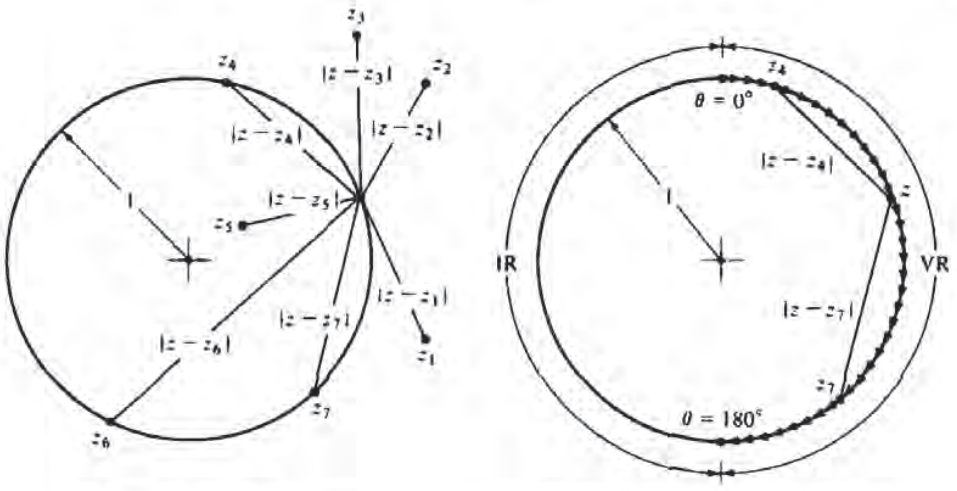
Figure 7.3 *Visible Region* (VR) and *Invisible Region* (IR) boundaries for complex variable z when $\beta = \pi/4$.

for each spacing has not changed but its relative position on the circle has rotated counterclockwise by an amount equal to β.

We can conclude then that the overall extent of the visible region can be controlled by the spacing between the elements and its relative position on the circle by the progressive phase excitation of the elements. These two can be used effectively in the design of the array factors.

Now let us return to (7-6). The magnitude of the array factor, its form as shown in (7-6), has a geometrical interpretation. For a given value of z in the visible region of the unit circle, corresponding to a value of θ as determined by (7-3), $|AF|$ is proportional to the product of the distances between z and $z_1, z_2, z_3, \ldots, z_{N-1}$, the roots of AF. In addition, apart from a constant, the phase of AF is equal to the sum of the phases between z and each of the zeros (roots). This is best demonstrated geometrically in Figure 7.4(a). If all the roots $z_1, z_2, z_3, \ldots, z_{N-1}$ are located in the visible region of the unit circle, then each one corresponds to a null in the pattern of

INTEL-1045
U.S. Patent 7,151,430



(a) Roots of array factor

(b) Roots of array factor on unit circle and within visible region

Figure 7.4 Array factor roots within and outside unit circle, and visible and invisible regions.

|AF| because as θ changes z changes and eventually passes through each of the z_n's. When it does, the length between z and that z_n is zero and (7-6) vanishes. When all the zeros (roots) are not in the visible region of the unit circle, but some lie outside it and/or any other point not on the unit circle, then only those zeros on the visible region will contribute to the nulls of the pattern. This is shown geometrically in Figure 7.4(b). If no zeros exist in the visible region of the unit circle, then that particular array factor has no nulls for any value of θ. However, if a given zero lies on the unit circle but not in its visible region, that zero can be included in the pattern by changing the phase excitation β so that the visible region is rotated until it encompasses that root. Doing this, and not changing d, may exclude some other zero(s).

To demonstrate all the principles, we will consider an example along with some computations.

Example 7.1

Design a linear array with a spacing between the elements of $d = \lambda/4$ such that it has zeros at $\theta = 0°, 90°$, and $180°$. Determine the number of elements, their excitation, and plot the derived pattern. Use Schelkunoff's method.

SOLUTION

For a spacing of $\lambda/4$ between the elements and a phase shift $\beta = 0°$, the visible region is shown in Figure 7.2(b). If the desired zeros of the array factor must occur at $\theta = 0°, 90°$, and $180°$, then these correspond to $z = j, 1, -j$ on the unit circle. Thus a normalized form of the array factor is given by

$$AF = (z - z_1)(z - z_2)(z - z_3) = (z - j)(z - 1)(z + j)$$
$$AF = z^3 - z^2 + z - 1$$

INTEL-1045
U.S. Patent 7,151,430

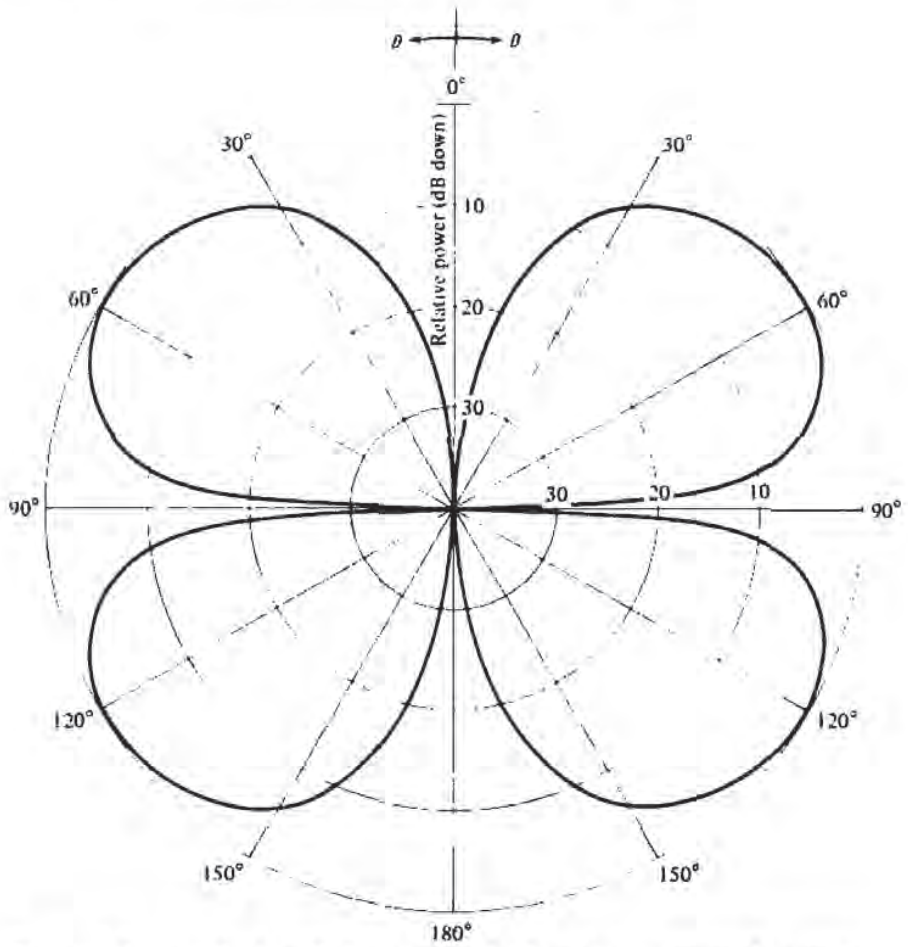


Figure 7.5 Amplitude radiation pattern of a four-element array of isotropic sources with a spacing of $\lambda/4$ between them, zero degrees progressive phase shift, and zeros at $\theta = 0°$, 90°, and 180°.

Referring to (7-4), the above array factor and the desired radiation characteristics can be obtained when there are four elements and their excitation coefficients are equal to

$$a_1 = -1$$
$$a_2 = +1$$
$$a_3 = -1$$
$$a_4 = +1$$

To illustrate the method, we plotted in Figure 7.5 the pattern of that array; it clearly meets the desired specifications. Because of the symmetry of the array, the pattern of the left hemisphere is identical to that of the right.

7.4 FOURIER TRANSFORM METHOD

This method can be used to determine, given a complete description of the desired pattern, the excitation distribution of a continuous or a discrete source antenna system.

INTEL-1045
U.S. Patent 7,151,430

The derived excitation will yield, either exactly or approximately, the desired antenna pattern. The pattern synthesis using this method is referred to as *beam shaping*.

7.4.1 Line-Source

For a continuous line-source distribution of length l, as shown in Figure 7.1, the normalized space factor of (7-1) can be written as

$$\mathrm{SF}(\theta) = \int_{-l/2}^{l/2} I(z')e^{j(k\cos\theta - k_z)z'}\,dz' = \int_{-l/2}^{l/2} I(z')e^{j\xi z'}\,dz' \tag{7-8}$$

$$\xi = k\cos\theta - k_z \Rightarrow \theta = \cos^{-1}\left(\frac{\xi + k_z}{k}\right) \tag{7-8a}$$

where k_z is the excitation phase constant of the source. For a normalized uniform current distribution of the form $I(z') = I_0/l$, (7-8) reduces to

$$\mathrm{SF}(\theta) = I_0 \frac{\sin\left[\dfrac{kl}{2}\left(\cos\theta - \dfrac{k_z}{k}\right)\right]}{\dfrac{kl}{2}\left(\cos\theta - \dfrac{k_z}{k}\right)} \tag{7-9}$$

The observation angle θ of (7-9) will have real values (visible region) provided that $-(k + k_z) \le \xi \le (k - k_z)$ as obtained from (7-8a).

Since the current distribution of (7-8) extends only over $-l/2 \le z' \le l/2$ (and it is zero outside it), the limits can be extended to infinity and (7-8) can be written as

$$\boxed{\mathrm{SF}(\theta) = \mathrm{SF}(\xi) = \int_{-\infty}^{+\infty} I(z')e^{j\xi z'}\,dz'} \tag{7-10a}$$

The form of (7-10a) is a Fourier transform, and it relates the excitation distribution $I(z')$ of a continuous source to its far-field space factor $\mathrm{SF}(\theta)$. The transform pair of (7-10a) is given by

$$\boxed{I(z') = \frac{1}{2\pi}\int_{-\infty}^{+\infty} \mathrm{SF}(\xi)e^{-jz'\xi}\,d\xi = \frac{1}{2\pi}\int_{-\infty}^{+\infty} \mathrm{SF}(\theta)e^{-jz'\xi}\,d\xi} \tag{7-10b}$$

Whether (7-10a) represents the direct transform and (7-10b) the inverse transform, or vice-versa, does not matter here. The most important thing is that the excitation distribution and the far-field space factor are related by Fourier transforms.

Equation (7-10b) indicates that if $\mathrm{SF}(\theta)$ represents the desired pattern, the excitation distribution $I(z')$ that will yield the exact desired pattern must in general exist for all values of z' ($-\infty \le z' \le \infty$). Since physically only sources of finite dimensions are realizable, the excitation distribution of (7-10b) is truncated at $z' = \pm l/2$ (beyond $z' = \pm l/2$ it is set to zero). Thus the approximate source distribution is given by

$$I_a(z') = \begin{cases} I(z') = \dfrac{1}{2\pi}\displaystyle\int_{-\infty}^{+\infty} \mathrm{SF}(\xi)e^{-jz'\xi}\,d\xi & -l/2 \le z' \le l/2 \\ 0 & \text{elsewhere} \end{cases} \tag{7-11}$$

INTEL-1045
U.S. Patent 7,151,430

and it yields an approximate pattern $SF(\theta)_a$. The approximate pattern is used to represent, within certain error, the desired pattern $SF(\theta)_d$. Thus

$$\boxed{SF(\theta)_d = SF(\theta)_a = \int_{-l/2}^{l/2} I_a(z')e^{j\xi z'}\,dz'} \tag{7-12}$$

It can be shown that, over all values of ξ, the synthesized approximate pattern $SF(\theta)_a$ yields the least mean square error or deviation from the desired pattern $SF(\theta)_d$. However that criterion is not satisfied when the values of ξ are restricted only in the visible region [8], [9].

To illustrate the principles of this design method, an example is taken.

Example 7.2

Determine the current distribution and the approximate radiation pattern of a line-source placed along the z-axis whose desired radiation pattern is symmetrical about $\theta = \pi/2$, and it is given by

$$SF(\theta) = \begin{cases} 1 & \pi/4 \le \theta \le 3\pi/4 \\ 0 & \text{elsewhere} \end{cases}$$

This is referred to as a sectoral pattern, and it is widely used in radar search and communication applications.

SOLUTION

Since the pattern is symmetrical, $k_z = 0$. The values of ξ, as determined by (7-8a), are given by $k/\sqrt{2} \ge \xi \ge -k/\sqrt{2}$. In turn, the current distribution is given by (7-10b) or

$$I(z') = \frac{1}{2\pi}\int_{-\infty}^{+\infty} SF(\xi)e^{-j\xi z'}\,d\xi$$

$$= \frac{1}{2\pi}\int_{-k/\sqrt{2}}^{k/\sqrt{2}} e^{-j\xi z'}\,d\xi = \frac{k}{\pi\sqrt{2}}\left[\frac{\sin\left(\frac{kz'}{\sqrt{2}}\right)}{\frac{kz'}{\sqrt{2}}}\right]$$

and it exists over all values of z' ($-\infty \le z' \le \infty$). Over the extent of the line source, the current distribution is approximated by

$$I_a(z') = I(z'), \qquad -l/2 \le z' \le l/2$$

If the derived current distribution $I(z')$ is used in conjunction with (7-10a) and it is assumed to exist over all values of z', the exact and desired sectoral pattern will result. If however it is truncated at $z' = \pm l/2$ (and assumed to be zero outside), then the desired pattern is approximated by (7-12) or

$$SF(\theta)_d = SF(\theta)_a = \int_{-l/2}^{l/2} I_a(z')e^{j\xi z'}\,dz'$$

INTEL-1045
U.S. Patent 7,151,430

$$= \frac{1}{\pi}\left\{ S_i\left[\frac{l}{\lambda}\pi\left(\cos\theta + \frac{1}{\sqrt{2}}\right)\right] - S_i\left[\frac{l}{\lambda}\pi\left(\cos\theta - \frac{1}{\sqrt{2}}\right)\right]\right\}$$

where $S_i(x)$ is the sine integral of (4-68b).

The approximate current distribution (normalized so that its maximum is unity) is plotted in Figure 7.6(a) for $l = 5\lambda$ and $l = 10\lambda$. The corresponding approximate normalized patterns are shown in Figure 7.6(b) where they are compared with the desired pattern. A very good reconstruction is indicated. The longer line source ($l = 10\lambda$) provides a better realization. The side lobes are about 0.102 (-19.83 dB) for $l = 5\lambda$ and 0.081 (-21.83 dB) for $l = 10\lambda$ (relative to the pattern at $\theta = 90°$).

7.4.2 Linear Array

The array factor of an N-element linear array of equally spaced elements and non-uniform excitation is given by (7-2). If the reference point is taken at the physical center of the array, the array factor can also be written as

Odd Number of Elements (N = 2M + 1)

$$\boxed{\mathrm{AF}(\theta) = \mathrm{AF}(\psi) = \sum_{m=-M}^{M} a_m e^{jm\psi}} \tag{7-13a}$$

Even Number of Elements (N = 2M)

$$\boxed{\mathrm{AF}(\theta) = \mathrm{AF}(\psi) = \sum_{m=-M}^{-1} a_m e^{j[(2m-1)/2]\psi} + \sum_{m=1}^{M} a_m e^{j[(2m-1)/2]\psi}} \tag{7-13b}$$

where

$$\boxed{\psi = kd\cos\theta + \beta} \tag{7-13c}$$

For an odd number of elements ($N = 2M + 1$), the elements are placed at

$$z'_m = md, \qquad m = 0, \pm 1, \pm 2, \ldots, \pm M \tag{7-13d}$$

and for an even number ($N = 2M$) at

$$z'_m = \begin{cases} \dfrac{2m-1}{2}d, & 1 \le m \le M \\ \dfrac{2m+1}{2}d, & -M \le m \le -1 \end{cases} \tag{7-13e}$$

An odd number of elements must be utilized to synthesize a desired pattern whose average value, over all angles, is not equal to zero. The $m = 0$ term of (7-13a) is analogous to the d.c. term in a Fourier series expansion of functions whose average value is not zero.

In general, the array factor of an antenna is a periodic function of ψ, and it must repeat for every 2π radians. In order for the array factor to satisfy the periodicity requirements for real values of θ (visible region), then $2kd = 2\pi$ or $d = \lambda/2$. The periodicity and visible region requirement of $d = \lambda/2$ can be relaxed; in fact, it can be made $d < \lambda/2$. However, the array factor $\mathrm{AF}(\psi)$ must be made pseudoperiodic by using fill-in functions, as is customarily done in Fourier series analysis. Such a

INTEL-1045
U.S. Patent 7,151,430

construction leads to nonunique solutions, because each new fill-in function will result in a different solution. In addition, spacings smaller than $\lambda/2$ lead to superdirective arrays that are undesirable and impractical. If $d > \lambda/2$, the derived patterns exhibit undesired grating lobes; in addition, they must be restricted to satisfy the periodicity requirements.

If $AF(\psi)$ represents the desired array factor, the excitation coefficients of the array can be obtained by the Fourier formula of

Odd Number of Elements (N = 2M + 1)

$$a_m = \frac{1}{T}\int_{-T/2}^{T/2} AF(\psi)e^{-jm\psi}d\psi = \frac{1}{2\pi}\int_{-\pi}^{\pi} AF(\psi)e^{-jm\psi}d\psi \qquad -M \le m \le M \tag{7-14a}$$

Even Number of Elements (N = 2M)

$$a_m = \begin{cases} \dfrac{1}{T}\displaystyle\int_{-T/2}^{T/2} AF(\psi)e^{-j[(2m+1)/2]\psi}d\psi \\ \qquad = \dfrac{1}{2\pi}\displaystyle\int_{-\pi}^{\pi} AF(\psi)e^{-j[(2m+1)/2]\psi}d\psi \qquad -M \le m \le -1 & (7\text{-}14b) \\ \dfrac{1}{T}\displaystyle\int_{-T/2}^{T/2} AF(\psi)e^{j[(2m-1)/2]\psi}d\psi \\ \qquad = \dfrac{1}{2\pi}\displaystyle\int_{-\pi}^{\pi} AF(\psi)e^{j[(2m-1)/2]\psi}d\psi \qquad 1 \le m \le M & (7\text{-}14c) \end{cases}$$

Simplifications in the forms of (7-13a)–(7-13b) and (7-14a)–(7-14c) can be obtained when the excitations are symmetrical about the physical center of the array.

Example 7.3

Determine the excitation coefficients and the resultant pattern for a broadside discrete element array whose array factor closely approximates the desired symmetrical sectoral pattern of Example 7.2. Use 11 elements with a spacing of $d = \lambda/2$ between them. Repeat the design for 21 elements.

SOLUTION

Since the array is broadside, the progressive phase shift between the elements as required by (6-18a) is zero ($\beta = 0$). Since the pattern is nonzero only for $\pi/4 \le \theta \le 3\pi/4$, the corresponding values of ψ are obtained from (7-13c) or $\pi/\sqrt{2} \ge \psi \ge -\pi/\sqrt{2}$. The excitation coefficients are obtained from (7-14a) or

$$a_m = \frac{1}{2\pi}\int_{-\pi/\sqrt{2}}^{\pi/\sqrt{2}} e^{-jm\psi}\,d\psi = \frac{1}{\sqrt{2}}\left[\frac{\sin\left(\dfrac{m\pi}{\sqrt{2}}\right)}{\dfrac{m\pi}{\sqrt{2}}}\right]$$

INTEL-1045
U.S. Patent 7,151,430

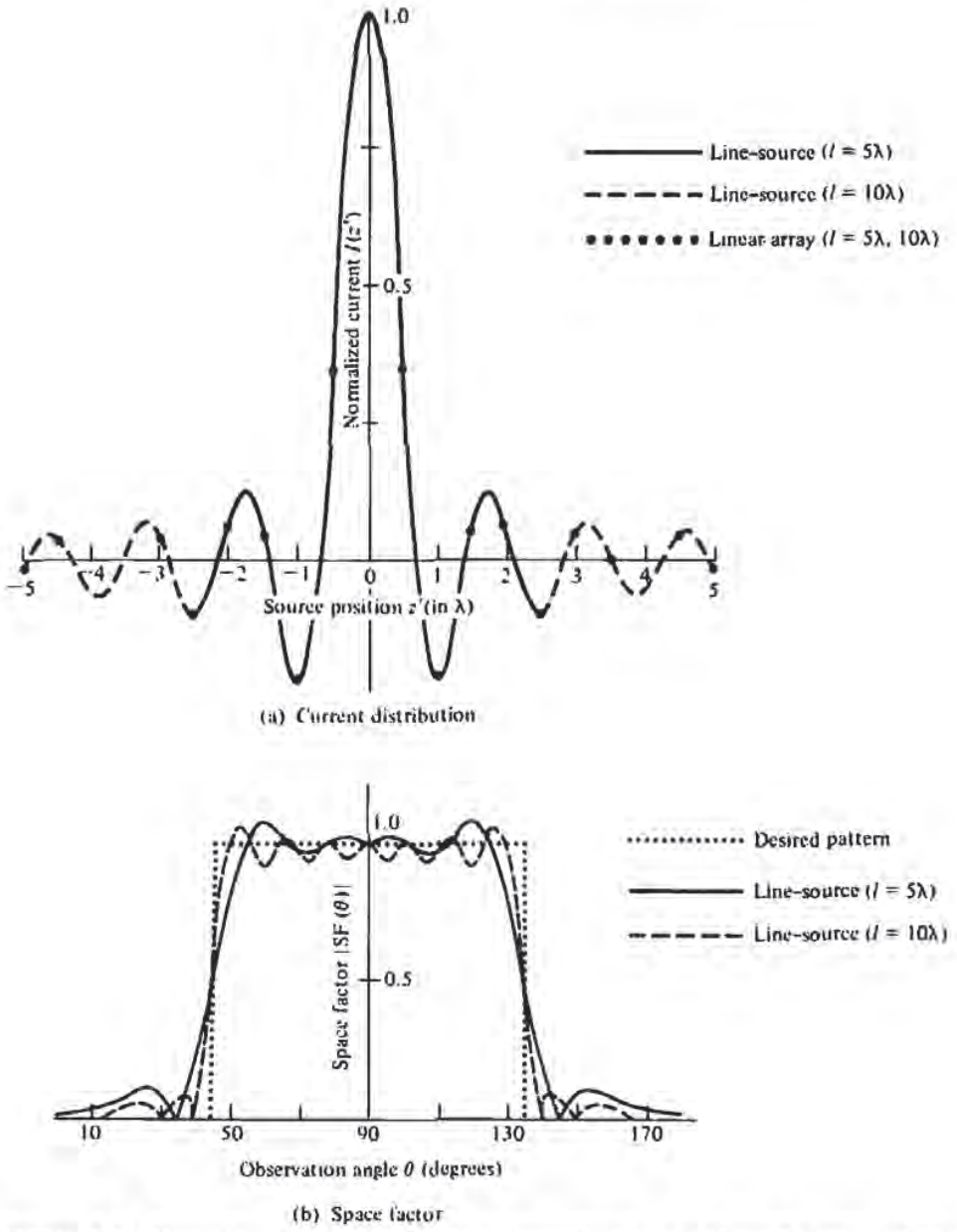


Figure 7.6 Normalized current distribution, desired pattern, and synthesized patterns using the Fourier transform method.

and they are symmetrical about the physical center of the array $[a_m(-z'_m) = a_m(z'_m)]$. The corresponding array factor is given by (7-13a).

The normalized excitation coefficients are

a_0	1.0000	$a_{\pm 4}$	0.0578	$a_{\pm 8}$	−0.0496
$a_{\pm 1}$	0.3582	$a_{\pm 5}$	−0.0895	$a_{\pm 9}$	0.0455
$a_{\pm 2}$	−0.2170	$a_{\pm 6}$	0.0518	$a_{\pm 10}$	−0.0100
$a_{\pm 3}$	0.0558	$a_{\pm 7}$	0.0101		

They are displayed graphically by a dot (•) in Figure 7.6(a) where they are compared with the continuous current distribution of Example 7.2. It is apparent that at the

INTEL-1045
U.S. Patent 7,151,430

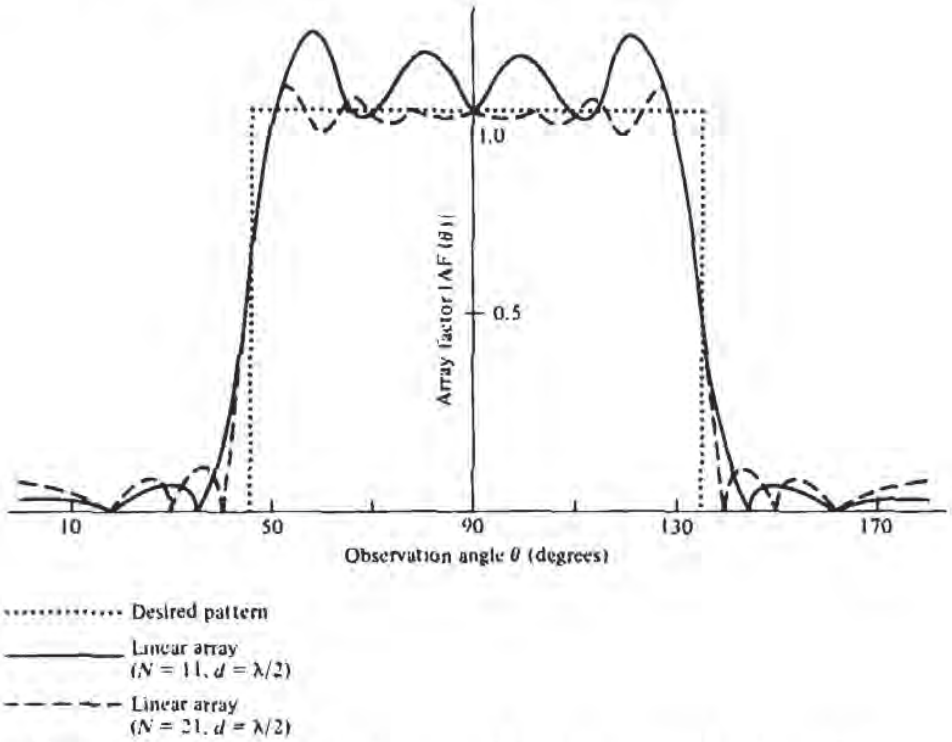


Figure 7.7 Desired array factor and synthesized normalized patterns for linear array of 11 and 21 elements using the Fourier transform method.

element positions, the line-source and linear array excitation values are identical. This is expected since the two antennas are of the same length (for $N = 11$, $d = \lambda/2 \Rightarrow l = 5\lambda$ and for $N = 21$, $d = \lambda/2 \Rightarrow l = 10\lambda$).

The corresponding normalized array factors are displayed in Figure 7.7. As it should be expected, the larger array ($N = 21$, $d = \lambda/2$) provides a better reconstruction of the desired pattern. The side lobe levels, relative to the value of the pattern at $\theta = 90°$, are 0.061 (-24.29 dB) for $N = 11$ and 0.108 (-19.33 dB) for $N = 21$.

Discrete element linear arrays only approximate continuous line-sources. Therefore, their patterns shown in Figure 7.7 do not approximate as well the desired pattern as the corresponding patterns of the line-source distributions shown in Figure 7.6(b).

Whenever the desired pattern contains discontinuities or its values in a given region change very rapidly, the reconstruction pattern will exhibit oscillatory overshoots which are referred to as *Gibbs' phenomena*. Since the desired sectoral patterns of Examples 7.2 and 7.3 are discontinuous at $\theta = \pi/4$ and $3\pi/4$, the reconstructed patterns displayed in Figures 7.6(b) and 7.7 exhibit these oscillatory overshoots.

7.5 WOODWARD-LAWSON METHOD

A very popular antenna pattern synthesis method used for beam shaping was introduced by Woodward and Lawson [3], [4], [10]. The synthesis is accomplished by sampling the desired pattern at various discrete locations. Associated with each pattern sample is a harmonic current of uniform amplitude distribution and uniform progres-

INTEL-1045
U.S. Patent 7,151,430

sive phase, whose corresponding field is referred to as a *composing function*. For a line-source, each composing function is of an $b_m \sin(\psi_m)/\psi_m$ form whereas for a linear array it takes an $b_m \sin(N\phi_m)/N \sin(\phi_m)$ form. The excitation coefficient b_m of each harmonic current is such that its field strength is equal to the amplitude of the desired pattern at its corresponding sampled point. The total excitation of the source is comprised of a finite summation of space harmonics. The corresponding synthesized pattern is represented by a finite summation of composing functions with each term representing the field of a current harmonic with uniform amplitude distribution and uniform progressive phase.

The formation of the overall pattern using the Woodward-Lawson method is accomplished as follows. The first composing function produces a pattern whose main beam placement is determined by the value of its uniform progressive phase while its intermost side lobe level is about -13.5 dB; the level of the remaining side lobes monotonically decreases. The second composing function has also a similar pattern except that its uniform progressive phase is adjusted so that its main lobe maximum coincides with the intermost null of the first composing function. This results in the filling-in of the intermost null of the pattern of the first composing function; the amount of filling-in is controlled by the amplitude excitation of the second composing function. Similarly, the uniform progressive phase of the third composing function is adjusted so that the maximum of its main lobe occurs at the second intermost null of the first composing function; it also results in filling-in of the second intermost null of the first composing function. This process continues with the remaining finite number of composing functions.

The Woodward-Lawson method is simple, elegant and provides insight into the process of pattern synthesis. However, because the pattern of each composing function perturbs the entire pattern to be synthesized, it lacks local control over the side lobe level in the unshaped region of the entire pattern. In 1988 and 1989 a spirited and welcomed dialogue developed concerning the Woodward-Lawson method [11]–[14]. The dialogue centered whether the Woodward-Lawson method should be taught and even appear in textbooks, and whether it should be replaced by an alternate method [15] which overcomes some of the shortcomings of the Woodward-Lawson method. The alternate method of [15] is more of a numerical and iterative extension of Schelkunoff's polynomial method which may be of greater practical value because it provides superior beamshape and pattern control. One of the distinctions of the two methods is that the Woodward-Lawson method deals with the synthesis of *field patterns* while that of [15] deals with the synthesis of *power patterns*.

The analytical formulation of this method is similar to the Shannon sampling theorem used in communications which states that "if a function $g(t)$ is band-limited, with its highest frequency being f_h, the function $g(t)$ can be reconstructed using samples taken at a frequency f_s. To faithfully reproduce the original function $g(t)$, the sampling frequency f_s should be at least twice the highest frequency f_h ($f_s = 2f_h$) or the function should be sampled at points separated by no more than $\Delta t = 1/f_s = 1/(2\,f_h) = T_h/2$ where T_h is the period of the highest frequency f_h." In a similar manner, the radiation pattern of an antenna can be synthesized by sampling functions whose samples are separated by λ/l rad, where l is the length of the source [9], [10].

7.5.1 Line-Source

Let the current distribution of a continuous source be represented, within $-l/2 \leq z' \leq l/2$, by a finite summation of normalized sources each of constant amplitude and linear phase of the form

INTEL-1045
U.S. Patent 7,151,430

$$i_m(z') = \frac{b_m}{l} e^{-jkz'\cos\theta_m} \qquad -l/2 \le z' \le l/2 \tag{7-15}$$

As it will be shown later, θ_m represents the angles where the desired pattern is sampled. The total current $I(z')$ is given by a finite summation of $2M$ (even samples) or $2M + 1$ (odd samples) current sources each of the form of (7-15). Thus

$$\boxed{I(z') = \frac{1}{l} \sum_{m=-M}^{M} b_m e^{-jkz'\cos\theta_m}} \tag{7-16}$$

where

$$m = 0, \pm 1, \pm 2, \ldots, \pm M \text{ (for } 2M + 1 \text{ odd number of samples)} \tag{7-16a}$$

For simplicity always use odd number of samples.

Associated with each current source of (7-15) is a corresponding field pattern of the form given by (7-9) or

$$s_m(\theta) = b_m \left\{ \frac{\sin\left[\frac{kl}{2}(\cos\theta - \cos\theta_m)\right]}{\frac{kl}{2}(\cos\theta - \cos\theta_m)} \right\} \tag{7-17}$$

whose maximum occurs when $\theta = \theta_m$. The total pattern is obtained by summing $2M + 1$ (odd samples) terms each of the form given by (7-17). Thus

$$\boxed{\mathrm{SF}(\theta) = \sum_{m=-M}^{M} b_m \left\{ \frac{\sin\left[\frac{kl}{2}(\cos\theta - \cos\theta_m)\right]}{\frac{kl}{2}(\cos\theta - \cos\theta_m)} \right\}} \tag{7-18}$$

The maximum of each individual term in (7-18) occurs when $\theta = \theta_m$, and it is equal to $\mathrm{SF}(\theta = \theta_m)$. In addition, when one term in (7-18) attains its maximum value at its sample at $\theta = \theta_m$, all other terms of (7-18) which are associated with the other samples are zero at $\theta = \theta_m$. In other words, all sampling terms (composing functions) of (7-18) are zero at all sampling points other than at their own. Thus at each sampling point the total field is equal to that of the sample. This is one of the most appealing properties of this method. If the desired space factor is sampled at $\theta = \theta_m$, the excitation coefficients b_m can be made equal to its value at the sample points θ_m. Thus

$$\boxed{b_m = \mathrm{SF}(\theta = \theta_m)_d} \tag{7-19}$$

The reconstructed pattern is then given by (7-18), and it approximates closely the desired pattern.

In order for the synthesized pattern to satisfy the periodicity requirements of 2π for real values of θ (visible region) and to faithfully reconstruct the desired pattern, each sample should be separated by

$$kz'\Delta|_{|z'|=l} = 2\pi \Rightarrow \Delta = \frac{\lambda}{l} \tag{7-19a}$$

INTEL-1045
U.S. Patent 7,151,430

The location of each sample is given by

$$\cos\theta_m = m\Delta = m\left(\frac{\lambda}{l}\right),\ m = 0, \pm 1, \pm 2, \ldots \quad \text{for } \textit{odd} \text{ samples} \tag{7-19b}$$

$$\cos\theta_m = \begin{cases} \dfrac{(2m-1)}{2}\Delta = \dfrac{(2m-1)}{2}\left(\dfrac{\lambda}{l}\right), & m = +1, +2, \ldots \quad \text{for } \textit{even} \text{ samples} \\ \dfrac{(2m+1)}{2}\Delta = \dfrac{(2m+1)}{2}\left(\dfrac{\lambda}{l}\right), & m = -1, -2, \ldots \quad \text{for } \textit{even} \text{ samples} \end{cases} \tag{7-19c}$$

Therefore, M should be the closest integer to $M = l/\lambda$.

As long as the location of each sample is determined by (7-19b), the pattern value at the sample points is determined solely by that of one sample and it is not correlated to the field of the other samples.

Example 7.4

Repeat the design of Example 7.2 for $l = 5\lambda$ using odd samples and the Woodward-Lawson line-source synthesis method.

SOLUTION

Since $l = 5\lambda$, $M = 5$ and the sampling separation is 0.2. The total number of sampling points is 11. The angles where the sampling is performed are given, according to (7-19b), by

$$\theta_m = \cos^{-1}\left(m\frac{\lambda}{l}\right) = \cos^{-1}(0.2m), \qquad m = 0, \pm 1, \ldots, \pm 5$$

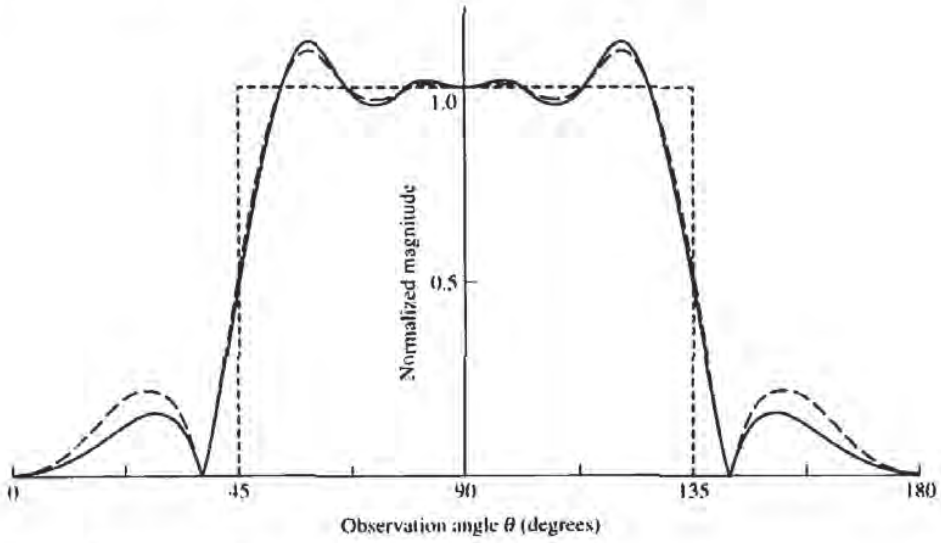
The angles and the excitation coefficients at the sample points are listed below.

m	θ_m	$b_m = \mathrm{SF}(\theta_m)_d$	m	θ_m	$b_m = \mathrm{SF}(\theta_m)_d$
0	90°	1			
1	78.46°	1	−1	101.54°	1
2	66.42°	1	−2	113.58°	1
3	53.13°	1	−3	126.87°	1
4	36.87°	0	−4	143.13°	0
5	0°	0	−5	180°	0

The computed pattern is shown in Figure 7.8(a) where it is compared with the desired pattern. A good reconstruction is indicated. The side lobe level, relative to the value of the pattern at $\theta = 90°$, is 0.160 (-15.92 dB).

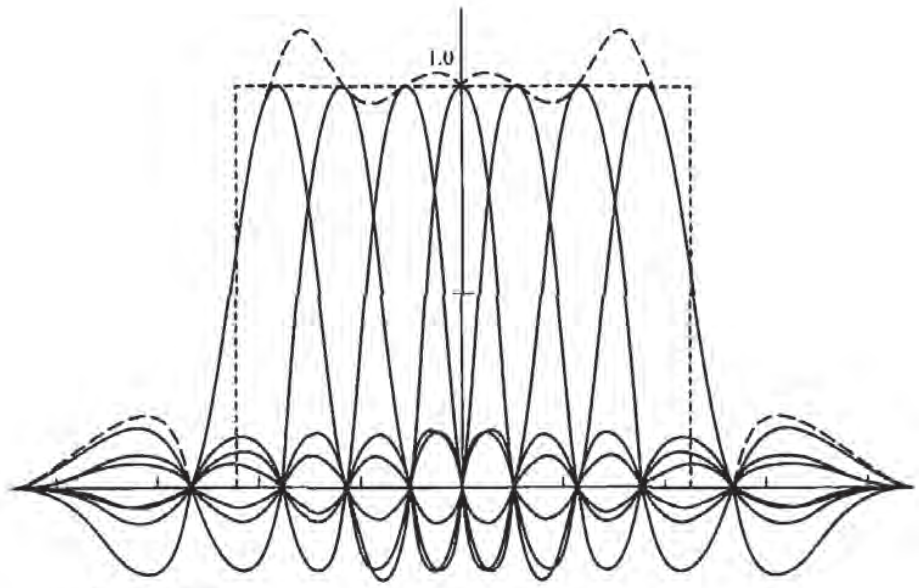
To demonstrate the synthesis of the pattern using the sampling concept, we have plotted in Figure 7.8(b) all seven nonzero composing functions $s_m(\theta)$ used for the reconstruction of the $l = 5\lambda$ line-source pattern of Figure 7.8(a). Each nonzero $s_m(\theta)$ composing function was computed using (7-17) for $m = 0, \pm 1, \pm 2, \pm 3$. It is evident that at each sampling point all the composing functions are zero, except the one that represents that sample. Thus the value of the desired pattern at each sampling point is determined solely by the maximum value of a single composing function. The angles where the composing functions attain their maximum values are listed in the previous table.

INTEL-1045
U.S. Patent 7,151,430



------ Desired pattern
——— Line-source |SF (θ)| (l = 5λ)
— — — Linear array |AF (θ)| (N = 10, d = λ/2)

(a) Normalized amplitude patterns



----- Desired pattern
— — — Line-source |SF (θ)| (l = 5λ)
——— Composing functions $s_m(\theta)$, $m = 0, \pm 1, \pm 2, \pm 3$

(b) Composing functions for line-source (l = 5λ)

Figure 7.8 Desired and synthesized patterns, and composing functions for Woodward-Lawson designs.

INTEL-1045
U.S. Patent 7,151,430

7.5.2 Linear Array

The Woodward-Lawson method can also be implemented to synthesize discrete linear arrays. The technique is similar to the Woodward-Lawson method for line sources except that the pattern of each sample, as given by (7-17), is replaced by the array factor of a uniform array as given by (6-10c). The pattern of each sample can be written as

$$f_m(\theta) = b_m \frac{\sin\left[\frac{N}{2}kd(\cos\theta - \cos\theta_m)\right]}{N\sin\left[\frac{1}{2}kd(\cos\theta - \cos\theta_m)\right]} \tag{7-20}$$

$\ell = Nd$ assumes the array is equal to the length of the line source *(the length ℓ of the line includes a distance $d/2$ beyond each end element)*. The total array factor can be written as a superposition of $2M + 1$ sampling, terms (as was done for the line source) each of the form of (7-20). Thus

$$\boxed{\mathrm{AF}(\theta) = \sum_{m=-M}^{M} b_m \frac{\sin\left[\frac{N}{2}kd(\cos\theta - \cos\theta_m)\right]}{N\sin\left[\frac{1}{2}kd(\cos\theta - \cos\theta_m)\right]}} \tag{7-21}$$

As for the line sources, the excitation coefficients of the array elements at the sample points are equal to the value of the desired array factor at the sample points. That is,

$$\boxed{b_m = \mathrm{AF}(\theta = \theta_m)_d} \tag{7-22}$$

The sample points are taken at

$$\boxed{\cos\theta_m = m\Delta = m\left(\frac{\lambda}{l}\right),\ m = 0, \pm 1, \pm 2, \ldots \quad \text{for } \textit{odd} \text{ samples}} \tag{7-23a}$$

$$\boxed{\cos\theta_m = \begin{cases} \dfrac{(2m-1)}{2}\Delta = \dfrac{(2m-1)}{2}\left(\dfrac{\lambda}{Nd}\right), \\ \qquad m = +1, +2, \ldots \quad \text{for } \textit{even} \text{ samples} \\ \dfrac{(2m+1)}{2}\Delta = \dfrac{(2m+1)}{2}\left(\dfrac{\lambda}{Nd}\right), \\ \qquad m = -1, -2, \ldots \quad \text{for } \textit{even} \text{ samples} \end{cases}} \tag{7-23b}$$

The normalized excitation coefficient of each array element, required to give the desired pattern, is given by

$$\boxed{a_n(z') = \frac{1}{N}\sum_{m=-M}^{M} b_m e^{-jkz_n'\cos\theta_m}} \tag{7-24}$$

where z_n' indicates the position of the nth element (element in question) symmetrically placed about the geometrical center of the array.

Example 7.5

Repeat the design of Example 7.4 for a linear array of 10 elements using the Woodward-Lawson method with odd samples and an element spacing of $d = \lambda/2$.

INTEL-1045
U.S. Patent 7,151,430

SOLUTION

According to (7-19), (7-19b), (7-22) and (7-23a), the excitation coefficients of the array at the sampling points are the same as those of the line source. Using the values of b_m as listed in Example 7.4, the computed array factor pattern using (7-21) is shown in Figure 7.8(a). A good synthesis of the desired pattern is displayed. The side lobe level, relative to the pattern value at $\theta = 90°$, is 0.221 (-13.1 dB). The agreement between the line-source and the linear array Woodward-Lawson designs are also good.

The normalized pattern of the symmetrical discrete array can also be generated using the array factor of (6-61a) or (6-61b), where the normalized excitation coefficients a_n's of the array elements are obtained using (7-24). For this example, the excitation coefficients of the 10-element array, along with their symmetrical position, are listed below. To achieve the normalized amplitude pattern of unity at $\theta = 90°$ in Figure 7.8(a), the array factor of (6-61a) must be multiplied by $1/\Sigma a_n = 1/0.5 = 2.0$.

Element Number n	Element Position z'_n	Excitation Coefficient a_n
± 1	$\pm 0.25\lambda$	0.5695717
± 2	$\pm 0.75\lambda$	-0.0344577
± 3	$\pm 1.25\lambda$	-0.0999999
± 4	$\pm 1.75\lambda$	0.1108508
± 5	$\pm 2.25\lambda$	-0.0459650

In general, the Fourier transform synthesis method yields reconstructed patterns whose mean-square error (or deviation) from the desired pattern is a minimum. However, the Woodward-Lawson synthesis method reconstructs patterns whose values at the sampled points are identical to the ones of the desired pattern; it does not have any control of the pattern between the sample points, and it does not yield a pattern with least mean-square deviation.

Ruze [9] points out that the least-mean-square error design is not necessarily the best. The particular application will dictate the preference between the two. However, the Fourier transform method is best suited for reconstruction of desired patterns which are analytically simple and which allow the integrations to be performed in closed form. Today, with the advent of high-speed computers, this is not a major restriction since integration can be performed (with high efficiency) numerically. In contrast, the Woodward-Lawson method is more flexible, and it can be used to synthesize any desired pattern. In fact, it can even be used to reconstruct patterns which, because of their complicated nature, cannot be expressed analytically. Measured patterns, either of analog or digital form, can also be synthesized using the Woodward-Lawson method.

7.6 TAYLOR LINE-SOURCE (TSCHEBYSCHEFF ERROR)

In Chapter 6 we discussed the classic Dolph-Tschebyscheff array design which yields, for a given side lobe level, the smallest possible first null beamwidth (or the smallest possible side lobe level for a given first null beamwidth). Another classic design that

INTEL-1045
U.S. Patent 7,151,430

is closely related to it, but is more applicable for continuous distributions, is that by Taylor [5] (this method is different from that by Taylor [6] which will be discussed in the next section).

The Taylor design [5] yields a pattern that is an optimum compromise between beamwidth and side lobe level. In an ideal design, the minor lobes are maintained at an equal and specific level. Since the minor lobes are of equal ripple and extend to infinity, this implies an infinite power. More realistically, however, the technique as introduced by Taylor leads to a pattern whose first few minor lobes (closest to the main lobe) are maintained at an equal and specified level; the remaining lobes decay monotonically. Practically, even the level of the closest minor lobes exhibits a slight monotonic decay. This decay is a function of the space u over which these minor lobes are required to be maintained at an equal level. As this space increases, the rate of decay of the closest minor lobes decreases. For a very large space of u (over which the closest minor lobes are required to have an equal ripple), the rate of decay is negligible. It should be pointed out, however, that the other method by Taylor [6] (of Section 7.7) yields minor lobes, all of which decay monotomically.

The details of the analytical formulation are somewhat complex (for the average reader) and lengthy, and they will not be included here. The interested reader is referred to the literature [5], [16]. Instead, a succinct outline of the salient points of the method and of the design procedure will be included. The design is for far-field patterns, and it is based on the formulation of (7-1).

Ideally the normalized space factor that yields a pattern with equal-ripple minor lobes is given by

$$\mathrm{SF}(\theta) = \frac{\cosh\left[\sqrt{(\pi A)^2 - u^2}\right]}{\cosh(\pi A)} \tag{7-25}$$

$$u = \pi \frac{l}{\lambda} \cos\theta \tag{7-25a}$$

whose maximum value occurs when $u = 0$. The constant A is related to the maximum desired side lobe level R_0 by

$$\cosh(\pi A) = R_0 \text{ (voltage ratio)} \tag{7-26}$$

The space factor of (7-25) can be derived from the Dolph-Tschebyscheff array formulation of Section 6.8.3, if the number of elements of the array are allowed to become infinite.

Since (7-25) is ideal and cannot be realized physically, Taylor [5] suggested that it be approximated (within a certain error) by a space factor comprised of a product of factors whose roots are the zeros of the pattern. Because of its approximation to the ideal Tschebyscheff design, it is also referred to as *Tschebyscheff error*. The Taylor space factor is given by

$$\boxed{\mathrm{SF}(u, A, \bar{n}) = \frac{\sin(u)}{u} \frac{\prod_{n=1}^{\bar{n}-1}\left[1 - \left(\frac{u}{u_n}\right)^2\right]}{\prod_{n=1}^{\bar{n}-1}\left[1 - \left(\frac{u}{n\pi}\right)^2\right]}} \tag{7-27}$$

INTEL-1045
U.S. Patent 7,151,430

$$u = \pi v = \pi \frac{l}{\lambda} \cos\theta \tag{7-27a}$$

$$u_n = \pi v_n = \pi \frac{l}{\lambda} \cos\theta_n \tag{7-27b}$$

where θ_n represents the locations of the nulls. The parameter $\bar{n}$ is a constant chosen by the designer so that the minor lobes for $|v| = |u/\pi| \le \bar{n}$ are maintained at a nearly constant voltage level of $1/R_0$; for $|v| = |u/\pi| > \bar{n}$ the envelope, through the maxima of the remaining minor lobes, decays at a rate of $1/v = \pi/u$. In addition, the nulls of the pattern for $|v| \ge \bar{n}$ occur at integer values of v.

In general, there are $\bar{n} - 1$ inner nulls for $|v| < \bar{n}$ and an infinite number of outer nulls for $|v| \ge \bar{n}$. To provide a smooth transition between the inner and the outer nulls (at the expense of slight beam broadening), Taylor introduced a parameter σ. It is usually referred to as the *scaling factor*, and it spaces the inner nulls so that they blend smoothly with the outer ones. In addition, it is the factor by which the beamwidth of the Taylor design is greater than that of the Dolph-Tschebyscheff, and it is given by

$$\sigma = \frac{\bar{n}}{\sqrt{A^2 + (\bar{n} - \frac{1}{2})^2}} \tag{7-28}$$

The location of the nulls are obtained using

$$u_n = \pi v_n = \pi \frac{l}{\lambda} \cos\theta_n \simeq \begin{cases} \pm\pi\sigma\sqrt{A^2 + (n - \frac{1}{2})^2} & 1 \le n < \bar{n} \\ \pm n\pi & \bar{n} \le n \le \infty \end{cases} \tag{7-29}$$

The normalized line-source distribution, which yields the desired pattern, is given by

$$I(z') = \frac{\lambda}{l}\left[1 + 2\sum_{p=1}^{\bar{n}-1} \mathrm{SF}(p, A, \bar{n}) \cos\left(2\pi p \frac{z'}{l}\right)\right] \tag{7-30}$$

The coefficients $\mathrm{SF}(p, A, \bar{n})$ represent samples of the Taylor pattern, and they can be obtained from (7-27) with $u = \pi p$. They can also be found using

$$\mathrm{SF}(p, A, \bar{n}) = \begin{cases} \dfrac{[(\bar{n} - 1)!]^2}{(\bar{n} - 1 + p)!(\bar{n} - 1 - p)!} \displaystyle\prod_{m=1}^{\bar{n}-1}\left[1 - \left(\frac{\pi p}{u_m}\right)^2\right] & |p| < \bar{n} \\ 0 & |p| \ge \bar{n} \end{cases} \tag{7-30a}$$

with $\mathrm{SF}(-p, A, \bar{n}) = \mathrm{SF}(p, A, \bar{n})$.

The half-power beamwidth is given approximately by [8]

$$\Theta_0 \simeq 2\sin^{-1}\left\{\frac{\lambda\sigma}{\pi l}\left[(\cosh^{-1} R_0)^2 - \left(\cosh^{-1}\frac{R_0}{\sqrt{2}}\right)^2\right]^{1/2}\right\} \tag{7-31}$$

7.6.1 Design Procedure

To initiate a Taylor design, you must

1. specify the normalized maximum tolerable side lobe level $1/R_0$ of the pattern.

INTEL-1045
U.S. Patent 7,151,430

2. choose a positive integer value for $\bar{n}$ such that for $|v| = |(l/\lambda)\cos\theta| \leq \bar{n}$ the normalized level of the minor lobes is nearly constant at $1/R_0$. For $|v| > \bar{n}$, the minor lobes decrease monotonically. In addition, for $|v| < \bar{n}$ there exist $(\bar{n} - 1)$ nulls. The position of all the nulls is found using (7-29). Small values of $\bar{n}$ yield source distributions which are maximum at the center and monotonically decrease toward the edges. In contrast, large values of $\bar{n}$ result in sources which are peaked simultaneously at the center and at the edges, and they yield sharper main beams. Therefore, very small and very large values of $\bar{n}$ should be avoided. Typically, the value of $\bar{n}$ should be at least 3 and at least 6 for designs with side lobes of -25 and -40 dB, respectively.

To complete the design, you do the following:

1. Determine A using (7-26), σ using (7-28), and the nulls using (7-29).
2. Compute the space factor using (7-27), the source distribution using (7-30) and (7-30a), and the half-power beamwidth using (7-31).

Example 7.6

Design a -20 dB Taylor distribution line-source with $\bar{n} = 5$. Plot the pattern and the current distribution for $l = 7\lambda(-7 \leq v = u/\pi \leq 7)$.

SOLUTION

For a -20 dB side lobe level

$$R_0 \text{ (voltage ratio)} = 10$$

Using (7-26)

$$A = \frac{1}{\pi}\cosh^{-1}(10) = 0.95277$$

and by (7-28)

$$\sigma = \frac{5}{\sqrt{(0.95277)^2 + (5 - 0.5)^2}} = 1.0871$$

The nulls are given by (7-29) or

$$v_n = u_n/\pi = \pm 1.17, \pm 1.932, \pm 2.91, \pm 3.943, \pm 5.00, \pm 6.00, \pm 7.00, \ldots$$

The corresponding null angles for $l = 7\lambda$ are

$$\theta_n = 80.38^\circ\,(99.62^\circ), 73.98^\circ\,(106.02^\circ), 65.45^\circ\,(114.55^\circ),$$
$$55.71^\circ\,(124.29^\circ), 44.41^\circ\,(135.59^\circ), \text{ and } 31.00^\circ\,(149.00^\circ)$$

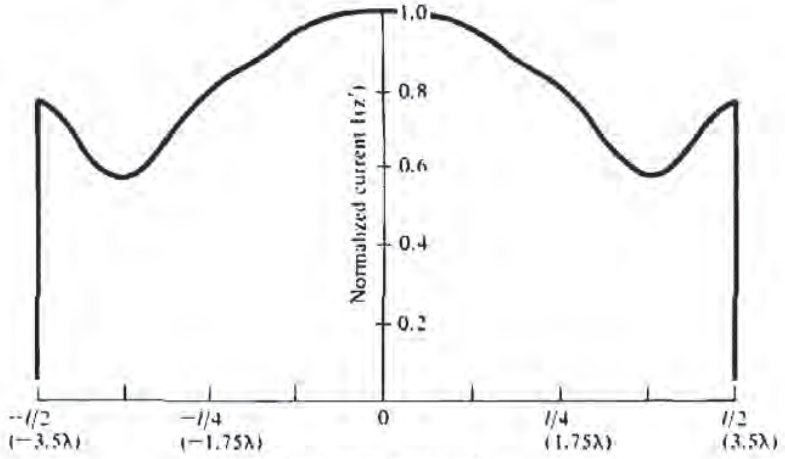
The half-power beamwidth for $l = 7\lambda$ is found using (7-31), or

$$\Theta_0 = 7.95^\circ$$

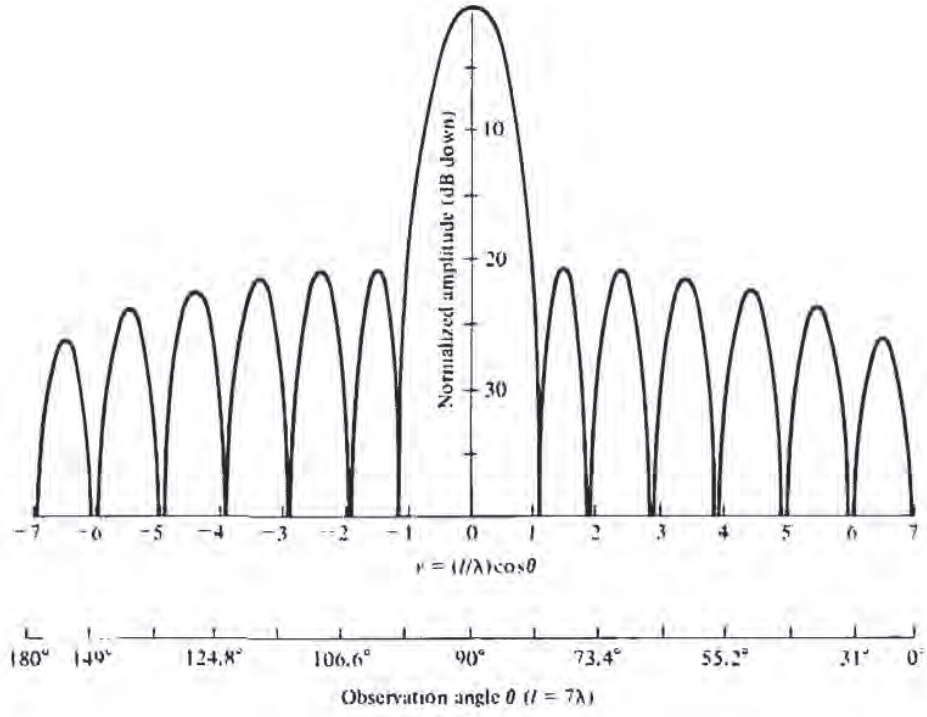
The source distribution, as computed using (7-30) and (7-30a), is displayed in Figure 7.9(a). The corresponding radiation pattern for $-7 \leq v = u/\pi \leq 7$ ($0^\circ \leq \theta \leq 180^\circ$ for $l = 7\lambda$) is shown in Figure 7.9(b).

All the computed parameters compare well with results reported in [5] and [16].

INTEL-1045
U.S. Patent 7,151,430



(a) Current distribution



(b) Space factor

Figure 7.9 Normalized current distribution and far-field space factor pattern for a −20 dB side lobe and $\bar{n} = 5$ Taylor (Tschebyscheff error) line-source of $l = 7\lambda$.

7.7 TAYLOR LINE-SOURCE (ONE-PARAMETER)

The Dolph-Tschebyscheff array design of Section 6.8.3 yields minor lobes of equal intensity while the Taylor (Tschebyscheff error) produces a pattern whose inner minor lobes are maintained at a constant level and the remaining ones decrease monotonically. For some applications, such as radar and low-noise systems, it is desirable to

INTEL-1045
U.S. Patent 7,151,430

sacrifice some beamwidth and low inner minor lobes to have all the minor lobes decay as the angle increases on either side of the main beam. In radar applications this is preferable because interfering or spurious signals would be reduced further when they try to enter through the decaying minor lobes. Thus any significant contributions from interfering signals would be through the pattern in the vicinity of the major lobe. Since in practice it is easier to maintain pattern symmetry around the main lobe, it is also possible to recognize that such signals are false targets. In low-noise applications, it is also desirable to have minor lobes that decay away from the main beam in order to diminish the radiation accepted through them from the relatively "hot" ground.

A continuous line-source distribution that yields decaying minor lobes and, in addition, controls the amplitude of the side lobe is that introduced by Taylor [6] in an unpublished classic memorandum. It is referred to as the *Taylor (one-parameter)* design and its source distribution is given by

$$I_n(z') = \begin{cases} J_0\left[j\pi B\sqrt{1-\left(\dfrac{2z'}{l}\right)^2}\right] & -l/2 \le z' \le +l/2 \\ 0 & \text{elsewhere} \end{cases} \tag{7-32}$$

where J_0 is the Bessel function of the first kind of order zero, l is the total length of the continuous source [see Figure 7.1(a)], and B is a constant to be determined from the specified side lobe level.

The space factor associated with (7-32) can be obtained by using (7-1). After some intricate mathematical manipulations, utilizing Gegenbauer's finite integral and Gegenbauer polynomials [17], the space factor for a Taylor amplitude distribution line-source with uniform phase [$\phi_n(z') = \phi_0 = 0$] can be written as

$$\mathrm{SF}(\theta) = \begin{cases} l\dfrac{\sinh[\sqrt{(\pi B)^2 - u^2}]}{\sqrt{(\pi B)^2 - u^2}}, & u^2 < (\pi B)^2 \\ l\dfrac{\sin[\sqrt{u^2 - (\pi B)^2}]}{\sqrt{u^2 - (\pi B)^2}}, & u^2 > (\pi B)^2 \end{cases} \tag{7-33}$$

where

$$u = \pi\frac{l}{\lambda}\cos\theta \tag{7-33a}$$

B = constant determined from side lobe level

l = line-source dimension

The derivation of (7-33) is assigned as an exercise to the reader (Problem 7.17). When $(\pi B)^2 > u^2$, (7-33) represents the region near the main lobe. The minor lobes are represented by $(\pi B)^2 < u^2$ in (7-33). Either form of (7-33) can be obtained from the other by knowing that (see Appendix VI)

$$\begin{aligned} \sin(jx) &= j\sinh(x) \\ \sinh(jx) &= j\sin(x) \end{aligned} \tag{7-34}$$

INTEL-1045
U.S. Patent 7,151,430

When $u = 0$ ($\theta = \pi/2$ and maximum radiation), the normalized pattern height is equal to

$$(\mathrm{SF})_{\max} = \frac{\sinh(\pi B)}{\pi B} = H_0 \tag{7-35}$$

For $u^2 \gg (\pi B)^2$, the normalized form of (7-33) reduces to

$$\mathrm{SF}(\theta) = \frac{\sin[\sqrt{u^2 - (\pi B)^2}]}{\sqrt{u^2 - (\pi B)^2}} \approx \frac{\sin(u)}{u} \qquad u \gg \pi B \tag{7-36}$$

and it is identical to the pattern of a uniform distribution. The maximum height H_1 of the side lobe of (7-36) is $H_1 = 0.217233$ (or 13.2 dB down from the maximum), and it occurs when (see Appendix I)

$$[u^2 - (\pi B)^2]^{1/2} = u = 4.494 \tag{7-37}$$

Using (7-35), the maximum voltage height of the side lobe (relative to the maximum H_0 of the major lobe) is equal to

$$\frac{H_1}{H_0} = \frac{1}{R_0} = \frac{0.217233}{\sinh(\pi B)/(\pi B)} \tag{7-38}$$

or

$$\boxed{R_0 = \frac{1}{0.217233}\frac{\sinh(\pi B)}{\pi B} = 4.603\frac{\sinh(\pi B)}{\pi B}} \tag{7-38a}$$

Equation (7-38a) can be used to find the constant B when the intensity ratio R_0 of the major-to-the-side lobe is specified. Values of B for typical side lobe levels are

SIDE LOBE LEVEL (dB)	−10	−15	−20	−25	−30	−35	−40
B	$j0.4597$	0.3558	0.7386	1.0229	1.2761	1.5136	1.7415

The disadvantage of designing an array with decaying minor lobes as compared to a design with equal minor lobe level (Dolph-Tschebyscheff), is that it yields about 12 to 15% greater half-power beamwidth. However such a loss in beamwidth is a small penalty to pay when the extreme minor lobes decrease as $1/u$.

To illustrate the principles, let us consider an example.

***Example* 7.7**

Given a continuous line-source, whose total length is 4λ, design a Taylor distribution array whose side lobe is 30 dB down from the maximum of the major lobe.

(a) Find the constant B.

(b) Plot the pattern (in dB) of the continuous line-source distribution.

INTEL-1045
U.S. Patent 7,151,430

(c) For a spacing of $\lambda/4$ between the elements, find the number of discrete isotropic elements needed to approximate the continuous source. Assume that the two extreme elements are placed at the edges of the continuous line source.

(d) Find the normalized coefficients of the discrete array of part (c).

(e) Write the array factor of the discrete array of parts (c) and (d).

(f) Plot the array factor (in dB) of the discrete array of part (e).

(g) For a corresponding Dolph-Tschebyscheff array, find the normalized coefficients of the discrete elements.

(h) Compare the patterns of the Taylor continuous line-source distribution and discretized array, and the corresponding Dolph-Tschebyscheff discrete element array.

SOLUTION

For a -30 dB maximum side lobe, the voltage ratio of the major-to-the-side lobe level is equal to

$$30 = 20 \log_{10}(R_0) \Rightarrow R_0 = 31.62$$

(a) The constant B is obtained using (7-38a) or

$$R_0 = 31.62 = 4.603 \frac{\sinh(\pi B)}{\pi B} \Rightarrow B = 1.2761$$

(b) The normalized space factor pattern is obtained using (7-33), and it is shown plotted in Figure 7.10.

(c) For $d = \lambda/4$ and with elements at the extremes, the number of elements is 17.

(d) The coefficients are obtained using (7-32). Since we have an odd number of elements, their positioning and excitation coefficients are those shown in Figure 6.17(b). Thus the total excitation coefficient of the center element is

$$2a_1 = I_n(z')\big|_{z'=0} = J_0(j4.009) = 11.400 \Rightarrow a_1 = 5.70$$

The coefficients of the elements on either side of the center element are identical (because of symmetry), and they are obtained from

$$a_2 = I(z')\big|_{z'=\pm\lambda/4} = J_0(j3.977) = 11.106$$

The coefficients of the other elements are obtained in a similar manner, and they are given by

$$a_3 = 10.192$$
$$a_4 = 8.889$$
$$a_5 = 7.195$$
$$a_6 = 5.426$$
$$a_7 = 3.694$$
$$a_8 = 2.202$$
$$a_9 = 1.000$$

INTEL-1045
U.S. Patent 7,151,430

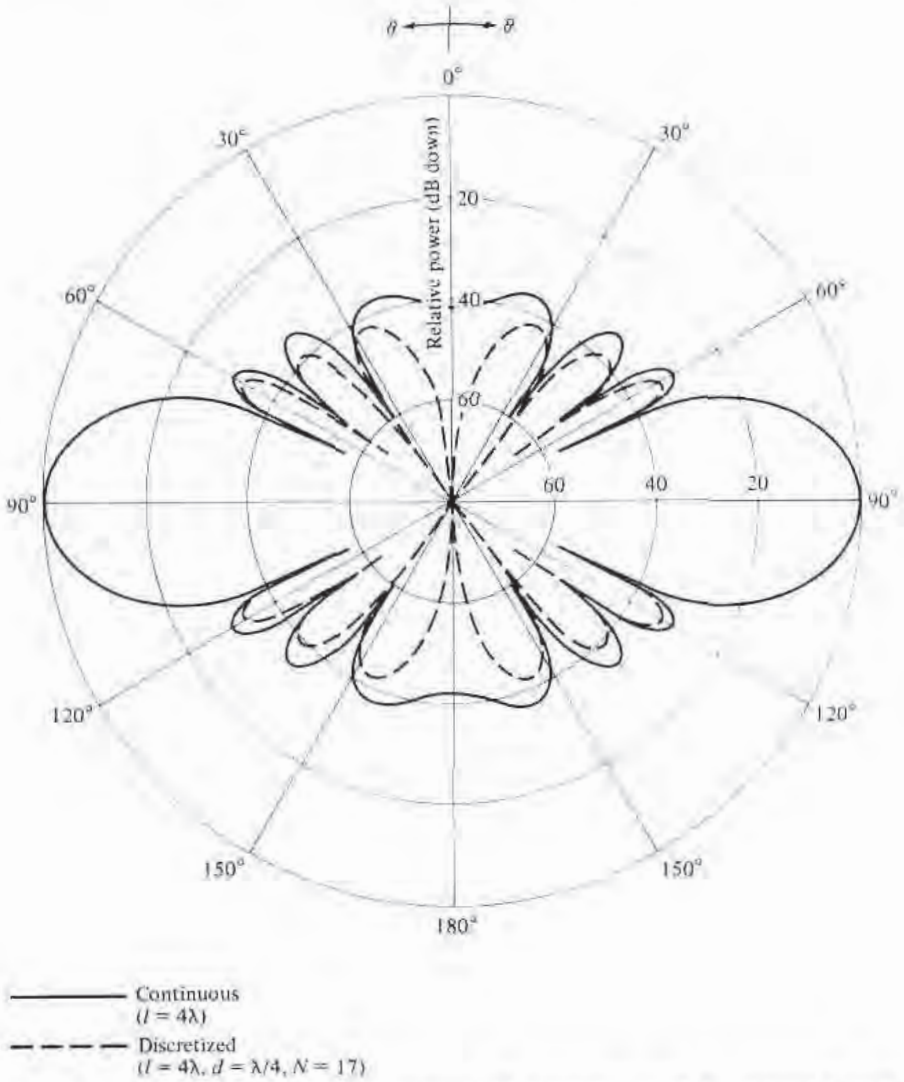


Figure 7.10 Far-field amplitude patterns of continuous and discretized Taylor *(one-parameter) distributions.*

(e) The array factor is given by (6-61b) and (6-61c), or

$$(\mathrm{AF})_{17} = \sum_{n=1}^{9} a_n \cos[2(n-1)u]$$

$$u = \pi \frac{d}{\lambda} \cos\theta = \frac{\pi}{4} \cos\theta$$

where the coefficients (a_n's) are those found in part (d).

(f) The normalized pattern (in dB) of the discretized distribution (discrete element array) is shown in Figure 7.10.

(g) The normalized coefficients of a 17-element Dolph-Tschebyscheff array, with -30 dB side lobes, are obtained using the method outlined in the Design Section of Section 6.8.3 and are given by

INTEL-1045
U.S. Patent 7,151,430

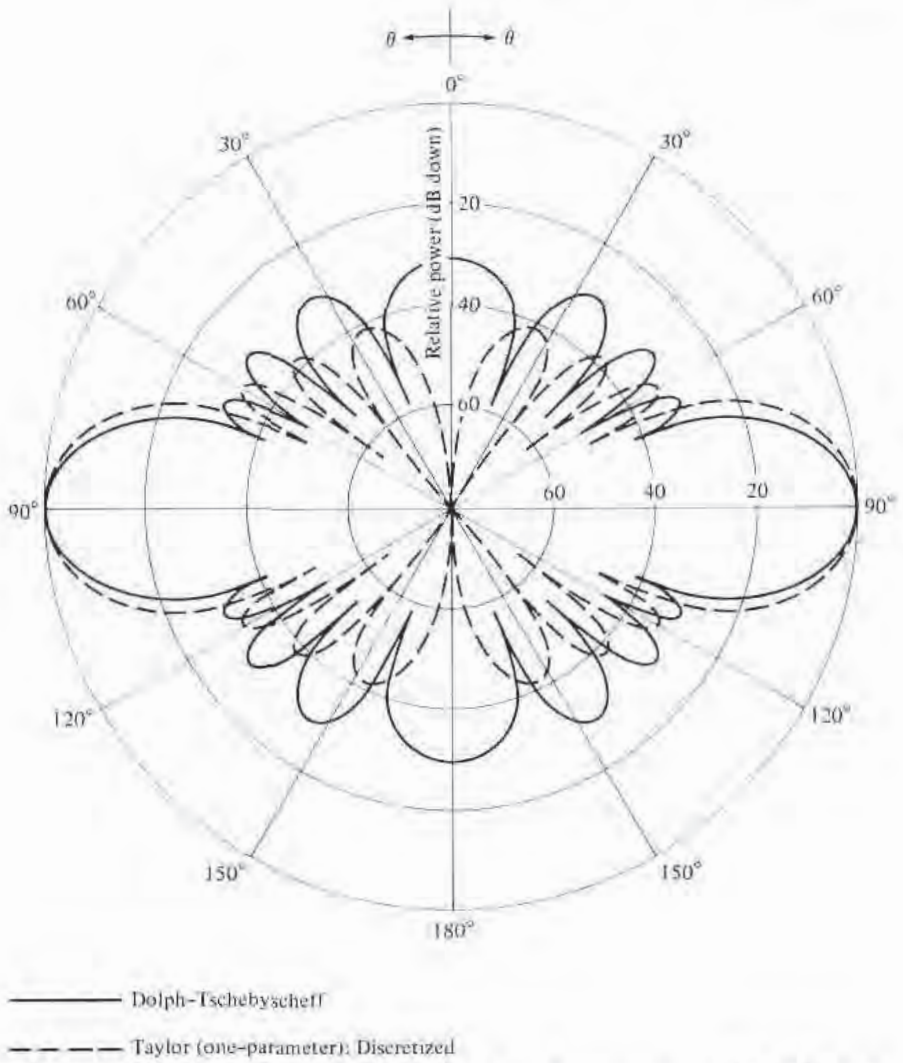


Figure 7.11 Far-field amplitude patterns of Taylor (discretized) and Dolph-Tschebyscheff distributions ($l = 4\lambda$, $d = \lambda/4$, $N = 17$).

UNNORMALIZED	NORMALIZED
$a_1 = 2.858$	$a_{1n} = 1.680$
$a_2 = 5.597$	$a_{2n} = 3.290$
$a_3 = 5.249$	$a_{3n} = 3.086$
$a_4 = 4.706$	$a_{4n} = 2.767$
$a_5 = 4.022$	$a_{5n} = 2.364$
$a_6 = 3.258$	$a_{6n} = 1.915$
$a_7 = 2.481$	$a_{7n} = 1.459$
$a_8 = 1.750$	$a_{8n} = 1.029$
$a_9 = 1.701$	$a_{9n} = 1.000$

As with the discretized Taylor distribution array, the coefficients are symmetrical, and the form of the array factor is that given in part (e).

(h) The normalized pattern (in dB) is plotted in Figure 7.11 where it is compared

INTEL-1045
U.S. Patent 7,151,430

with that of the discretized Taylor distribution. From the patterns in Figures 7.10 and 7.11, it can be concluded that

1. the main lobe of the continuous line-source Taylor design is well approximated by the discretized distribution with a $\lambda/4$ spacing between the elements. Even the minor lobes are well represented, and a better approximation can be obtained with more elements and smaller spacing between them.
2. the Taylor distribution array pattern has a wider main lobe than the corresponding Dolph-Tschebyscheff, but it displays decreasing minor lobes away from the main beam.

A larger spacing between the elements does not approximate the continuous distribution as accurately. The design of Taylor and Dolph-Tschebyscheff arrays for $l = 4\lambda$ and $d = \lambda/2(N = 9)$ is assigned as a problem at the end of the chapter (Problem 7.18).

To qualitatively assess the performance between uniform, binomial, Dolph-Tschebyscheff, and Taylor (one-parameter) array designs, the amplitude distribution of each has been plotted in Figure 7.12(a). It is assumed that $l = 4\lambda$, $d = \lambda/4$, $N = 17$, and the maximum side lobe is 30 dB down. The coefficients are normalized with respect to the amplitude of the corresponding element at the center of that array.

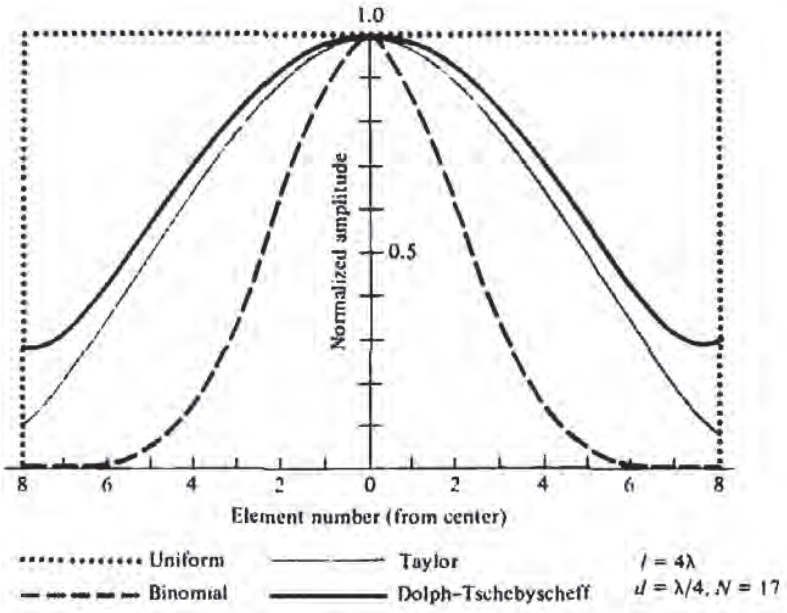
The binomial design possesses the smoothest amplitude distribution (between 1 and 0) from the center to the edges (the amplitude toward the edges is vanishingly small). Because of this characteristic, the binomial array displays the smallest side lobes followed, in order, by the Taylor, Tschebyscheff, and the uniform arrays. In contrast, the uniform array possesses the smallest half-power beamwidth followed, in order, by the Tschebyscheff, Taylor, and binomial arrays. As a rule of thumb, the array with the smoothest amplitude distribution (from the center to the edges) has the smallest side lobes and the larger half-power beamwidths. The best design is a trade-off between side lobe level and beamwidth.

7.8 TRIANGULAR, COSINE, AND COSINE-SQUARED AMPLITUDE DISTRIBUTIONS

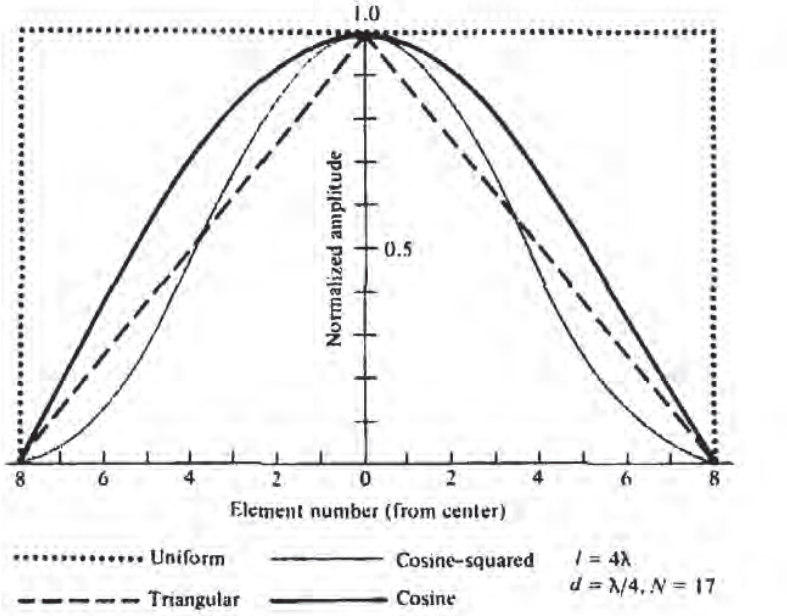
Some other very common and simple line-source amplitude distributions are those of the triangular, cosine, cosine-squared, cosine on-a-pedestal, cosine-squared on-a-pedestal, Gaussian, inverse taper, and edge. Instead of including many details, the pattern, half-power beamwidth, first-null beamwidth, magnitude of side lobes, and directivity for uniform, triangular, cosine, and cosine-squared amplitude distributions (with constant phase) are summarized in Table 7.1 [18], [19].

The normalized coefficients for a uniform, triangular, cosine, and cosine-squared arrays of $l = 4\lambda$, $d = \lambda/4$, $N = 17$ are shown plotted in Figure 7.12(b). The array with the smallest side lobes and the larger half-power beamwidth is the cosine-squared, because it possesses the smoothest distribution. It is followed, in order, by the triangular, cosine, and uniform distributions. This is verified by examining the characteristics in Table 7.1.

INTEL-1045
U.S. Patent 7,151,430



(a) Amplitude distribution of uniform, binomial, Taylor, and Dolph–Tschebyscheff discrete-element arrays



(b) Amplitude distribution of uniform, triangular, cosine, and cosine squared discrete-element arrays

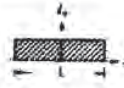
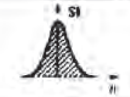
Figure 7.12 Amplitude distribution of nonuniform amplitude linear arrays.

Cosine on-a-pedestal distribution is obtained by the superposition of the uniform and the cosine distributions. Thus it can be represented by

$$I_n(z') = \begin{cases} I_0 + I_2 \cos\left(\dfrac{\pi}{l} z'\right), & -l/2 \le z' \le l/2 \\ 0 & \text{elsewhere} \end{cases} \tag{7-39}$$

INTEL-1045
U.S. Patent 7,151,430

Table 7.1 RADIATION CHARACTERISTICS FOR LINE SOURCES AND LINEAR ARRAYS WITH UNIFORM, TRIANGULAR, COSINE, AND COSINE-SQUARED DISTRIBUTIONS

Distribution	Uniform	Triangular	Cosine	Cosine-Squared
Distribution I_n (analytical)	I_0	$I_1\left(1 - \frac{2}{l}\lvert z'\rvert\right)$	$I_2 \cos\left(\frac{\pi}{l} z'\right)$	$I_3 \cos^2\left(\frac{\pi}{l} z'\right)$
Distribution (graphical)				
Space factor (SF) $u = \left(\frac{\pi l}{\lambda}\right) \cos\theta$	$I_0 l \frac{\sin(u)}{u}$	$I_1 \frac{l}{2}\left[\frac{\sin\left(\frac{u}{2}\right)}{\frac{u}{2}}\right]^2$	$I_2 l \frac{\pi}{2} \frac{\cos(u)}{(\pi/2)^2 - u^2}$	$I_3 \frac{l}{2} \frac{\sin(u)}{u}\left[\frac{\pi^2}{\pi^2 - u^2}\right]$
Space factor |SF|				
Half-power beamwidth (degrees) $l \gg \lambda$	$\frac{50.6}{(l/\lambda)}$	$\frac{73.4}{(l/\lambda)}$	$\frac{68.8}{(l/\lambda)}$	$\frac{83.2}{(l/\lambda)}$
First null beamwidth (degrees) $l \gg \lambda$	$\frac{114.6}{(l/\lambda)}$	$\frac{229.2}{(l/\lambda)}$	$\frac{171.9}{(l/\lambda)}$	$\frac{229.2}{(l/\lambda)}$
First side lobe max. (to main max.) (dB)	−13.2	−26.4	−23.2	−31.5
Directivity factor (l large)	$2\left(\frac{l}{\lambda}\right)$	$0.75\left[2\left(\frac{l}{\lambda}\right)\right]$	$0.810\left[2\left(\frac{l}{\lambda}\right)\right]$	$0.667\left[2\left(\frac{l}{\lambda}\right)\right]$

INTEL-1045
U.S. Patent 7,151,430

where I_0 and I_2 are constants. The space factor pattern of such a distribution is obtained by the addition of the patterns of the uniform and the cosine distributions found in Table 7.1. That is,

$$\mathrm{SF}(\theta) = I_0 l \frac{\sin(u)}{u} + I_2 \frac{\pi l}{2} \frac{\cos u}{(\pi/2)^2 - u^2} \tag{7-40}$$

A similar procedure is used to represent and analyze a cosine-squared on-a-pedestal distribution.

7.9 LINE-SOURCE PHASE DISTRIBUTIONS

The amplitude distributions of the previous section were assumed to have uniform phase variations throughout the physical extent of the source. Practical radiators (such as reflectors, lenses, horns, etc.) have nonuniform phase fronts caused by one or more of the following:

1. displacement of the reflector feed from the focus
2. distortion of the reflector or lens surface
3. feeds whose wave fronts are not ideally cylindrical or spherical (as they are usually presumed to be)
4. physical geometry of the radiator

These are usually referred to *phase errors*, and they are more evident in radiators with tilted beams.

To simplify the analytical formulations, most of the phase fronts are represented with linear, quadratic, or cubic distributions. Each of the phase distributions can be associated with each of the amplitude distributions. In (7-1), the phase distribution of the source is represented by $\phi_n(z')$. For linear, quadratic, and cubic phase variations, $\phi_n(z')$ takes the form of

$$\textit{linear:} \quad \phi_1(z') = \beta_1 \frac{2}{l} z', \qquad -l/2 \le z' \le l/2 \tag{7-41a}$$

$$\textit{quadratic:} \quad \phi_2(z') = \beta_2 \left(\frac{2}{l}\right)^2 z'^2, \qquad -l/2 \le z' \le l/2 \tag{7-41b}$$

$$\textit{cubic:} \quad \phi_3(z') = \beta_3 \left(\frac{2}{l}\right)^3 z'^3, \qquad -l/2 \le z' \le l/2 \tag{7-41c}$$

and it is shown plotted in Figure 7.13. The quadratic distribution is used to represent the phase variations at the aperture of a horn and of defocused (along the symmetry axis) reflector and lens antennas.

The space factor patterns corresponding to the phase distributions of (7-41a)–(7-41c) can be obtained by using (7-1). Because the analytical formulations become lengthy and complex, especially for the quadratic and cubic distributions, they will not be included here. Instead, a general guideline of their effects will be summarized [18], [19].

Linear phase distributions have a tendency to tilt the main beam of an antenna by an angle θ_0 and to form an asymmetrical pattern. The pattern of this distribution can be obtained by replacing the u (for uniform phase) in Table 7.1 by $(u - \theta_0)$. In general, the half-power beamwidth of the tilted pattern is increased by $1/\cos\theta_0$ while the directivity is decreased by $\cos\theta_0$. This becomes more apparent by realizing that

INTEL-1045
U.S. Patent 7,151,430

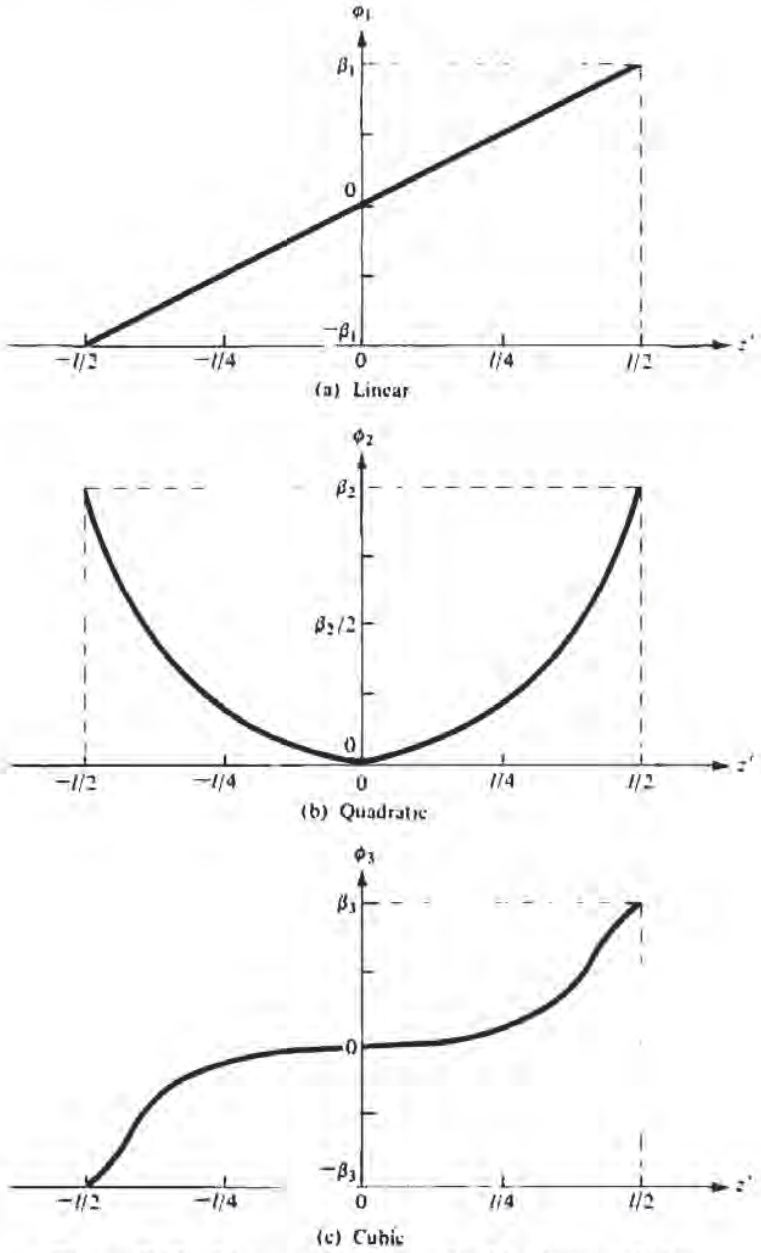


Figure 7.13 Linear, quadratic, and cubic phase variations.

the projected length of the line source toward the maximum is reduced by $\cos\theta_0$. Thus the effective length of the source is reduced.

Quadratic phase errors lead primarily to a reduction of directivity, and an increase in side lobe level on either side of the main lobe. The symmetry of the original pattern is maintained. In addition, for moderate phase variations, ideal nulls in the patterns disappear. Thus the minor lobes blend into each other and into the main beam, and they represent shoulders of the main beam instead of appearing as separate lobes. Analytical formulations for quadratic phase distributions were introduced in Chapter 13 on horn antennas.

Cubic phase distributions introduce not only a tilt in the beam but also decrease

INTEL-1045
U.S. Patent 7,151,430

the directivity. The newly formed patterns are asymmetrical. The minor lobes on one side are increased in magnitude and those on the other side are reduced in intensity.

7.10 CONTINUOUS APERTURE SOURCES

Space factors for aperture (two-dimensional) sources can be introduced in a similar manner as in Section 7.2.1 for line-sources.

7.10.1 Rectangular Aperture

Referring to the geometry of Figure 6.23(b), the space factor for a two-dimensional rectangular distribution along the x-y plane is given by

$$\boxed{\text{SF} = \int_{-l_y/2}^{l_y/2}\int_{-l_x/2}^{l_x/2} A_n(x', y')e^{j[kx'\sin\theta\cos\phi + ky'\sin\theta\sin\phi + \phi_n(x',y')]}\,dx'dy'} \tag{7-42}$$

where l_x and l_y are, respectively, the linear dimensions of the rectangular aperture along the x and y axes. $A_n(x', y')$ and $\phi_n(x', y')$ represent, respectively, the amplitude and phase distributions on the aperture.

For many practical antennas (such as waveguides, horns, etc.) the aperture distribution (amplitude and phase) is separable. That is,

$$A_n(x', y') = I_x(x')I_y(y') \tag{7-42a}$$

$$\phi_n(x', y') = \phi_x(x') + \phi_y(y') \tag{7-42b}$$

so that (7-42) can be written as

$$\text{SF} = S_xS_y \tag{7-43}$$

where

$$S_x = \int_{-l_x/2}^{l_x/2} I_x(x')e^{j[kx'\sin\theta\cos\phi + \phi_x(x')]}\,dx' \tag{7-43a}$$

$$S_y = \int_{-l_y/2}^{l_y/2} I_y(y')e^{j[ky'\sin\theta\sin\phi + \phi_y(y')]}\,dy' \tag{7-43b}$$

which is analogous to the array factor of (6-85)–(6-85b) for discrete-element arrays.

The evaluation of (7-42) can be accomplished either analytically or graphically. If the distribution is separable, as in (7-42a) and (7-42b), the evaluation can be performed using the results of a line-source distribution.

The total field of the aperture antenna is equal to the product of the element and space factors. As for the line sources, the element factor for apertures depends on the type of current density and its orientation.

7.10.2 Circular Aperture

The space factor for a circular aperture can be obtained in a similar manner as for the rectangular distribution. Referring to the geometry of Figure 6.32, the space factor for a circular aperture with radius a can be written as

INTEL-1045
U.S. Patent 7,151,430

Table 7.2 RADIATION CHARACTERISTICS FOR CIRCULAR APERTURES AND CIRCULAR PLANAR ARRAYS WITH CIRCULAR SYMMETRY AND TAPERED DISTRIBUTION

Distribution	Uniform	Radial Taper	Radial Taper Squared
Distribution (analytical)	$I_0\left[1-\left(\frac{\rho'}{a}\right)^2\right]^0$	$I_1\left[1-\left(\frac{\rho'}{a}\right)^2\right]^1$	$I_2\left[1-\left(\frac{\rho'}{a}\right)^2\right]^2$
Distribution (graphical)			
Space factor (SF) $u=\left(2\pi\frac{a}{\lambda}\right)\sin\theta$	$I_0 2\pi a^2\frac{J_1(u)}{u}$	$I_1 4\pi a^2\frac{J_2(u)}{u}$	$I_2 16\pi a^2\frac{J_3(u)}{u}$
Half-power beamwidth (degrees) $a\gg\lambda$	$\frac{29.2}{(a/\lambda)}$	$\frac{36.4}{(a/\lambda)}$	$\frac{42.1}{(a/\lambda)}$
First null beamwidth (degrees) $a\gg\lambda$	$\frac{69.9}{(a/\lambda)}$	$\frac{93.4}{(a/\lambda)}$	$\frac{116.3}{(a/\lambda)}$
First side lobe max. (to main max.) (dB)	−17.6	−24.6	−30.6
Directivity factor	$\left(\frac{2\pi a}{\lambda}\right)^2$	$0.75\left(\frac{2\pi a}{\lambda}\right)^2$	$0.56\left(\frac{2\pi a}{\lambda}\right)^2$

$$\mathrm{SF}(\theta,\phi)=\int_0^{2\pi}\int_0^a A_n(\rho',\phi')e^{j[k\rho'\sin\theta\cos(\phi-\phi')+\zeta_n(\rho',\phi')]}\rho'\,d\rho'\,d\phi' \tag{7-44}$$

where ρ' is the radial distance ($0\le\rho'\le a$), ϕ' is the azimuthal angle over the aperture ($0\le\phi'\le 2\pi$ for $0\le\rho'\le a$), and $A_n(\rho',\phi')$ and $\zeta_n(\rho',\phi')$ represent, respectively, the amplitude and phase distributions over the aperture. Equation (7-44) is analogous to the array factor of (6-112a) for discrete elements.

If the aperture distribution has uniform phase [$\zeta_n(\rho',\phi')=\zeta_0=0$] and azimuthal amplitude symmetry [$A_n(\rho',\phi')=A_n(\rho')$], (7-44) reduces, by using (5-48), to

$$\mathrm{SF}(\theta)=2\pi\int_0^a A_n(\rho')J_0(k\rho'\sin\theta)\rho'd\rho' \tag{7-45}$$

where $J_0(x)$ is the Bessel function of the first kind and of order zero.

Many practical antennas, such as a parabolic reflector, have distributions that taper toward the edges of the apertures. These distributions can be approximated reasonably well by functions of the form

INTEL-1045
U.S. Patent 7,151,430

$$A_n(\rho') = \begin{cases} \left[1 - \left(\frac{\rho'}{a}\right)^2\right]^n & 0 \le \rho' \le a, \quad n = 0, 1, 2, 3, \ldots \\ 0 & \text{elsewhere} \end{cases} \tag{7-46}$$

For $n = 0$, (7-46) reduces to a uniform distribution.

The radiation characteristics of circular apertures or planar circular arrays with distributions (7-46) with $n = 0, 1, 2$ are shown tabulated in Table 7.2 [19]. It is apparent, as before, that distributions with lower taper toward the edges (larger values of n) have smaller side lobes but larger beamwidths. In design, a compromise between side lobe level and beamwidth is necessary.

References

1. S. A. Schelkunoff, "A Mathematical Theory of Linear Arrays," *Bell System Technical Journal*, Vol. 22, pp. 80–107, 1943.
2. H. G. Booker and P. C. Clemmow, "The Concept of an Angular Spectrum of Plane Waves, and Its Relation to That of Polar Diagram and Aperture Distribution," *Proc. IEE* (London), Paper No. 922, Radio Section, Vol. 97, pt. III, pp. 11–17, January 1950.
3. P. M. Woodward, "A Method for Calculating the Field over a Plane Aperture Required to Produce a Given Polar Diagram," *J. IEE*, Vol. 93, pt. IIIA, pp. 1554–1558, 1946.
4. P. M. Woodward and J. D. Lawson, "The Theoretical Precision with Which an Arbitrary Radiation-Pattern May Be Obtained from a Source of a Finite Size," *J. IEE*, Vol. 95, Pt. III, No. 37, pp. 363–370, September 1948.
5. T. T. Taylor, "Design of Line-Source Antennas for Narrow Beamwidth and Low Sidelobes," *IRE Trans. Antennas Propagat.*, Vol. AP-3, No. 1, pp. 16–28, January 1955.
6. T. T. Taylor, "One Parameter Family of Line Sources Producing Modified $\text{Sin}(\pi u)/\pi u$ Patterns," *Hughes Aircraft Co. Tech. Mem. 324, Culver City, Calif., Contract AF* 19(604)-262-F-14, September 4, 1953.
7. R. S. Elliott, "On Discretizing Continuous Aperture Distributions," *IEEE Trans. Antennas Propagat.*, Vol. AP-25, No. 5, pp. 617–621, September 1977.
8. R. C. Hansen (ed.), *Microwave Scanning Antennas*, Vol. I, Academic Press, New York, 1964, p. 56.
9. J. Ruze, "Physical Limitations on Antennas," MIT Research Lab., Electronics Tech. Rept. 248, October 30, 1952.
10. M. I. Skolnik, *Introduction to Radar Systems*, McGraw-Hill, New York, 1962, pp. 320–330.
11. R. S. Elliott, "Criticisms of the Woodward-Lawson Method," *IEEE Antennas and Propagation Society Newsletter*, Vol. 30, p. 43, June 1988.
12. H. Steyskal, "The Woodward-Lawson Method: A Second Opinion," *IEEE Antennas and Propagation Society Newsletter*, Vol. 30, p. 48, October 1988.
13. R. S. Elliott, "More on the Woodward-Lawson Method," *IEEE Antennas and Propagation Society Newsletter*, Vol. 30, pp. 28–29, December 1988.
14. H. Steyskal, "The Woodward-Lawson Method-To Bury or Not to Bury," *IEEE Antennas and Propagation Society Newsletter*, Vol. 31, pp. 35–36, February 1989.
15. H. J. Orchard, R. S. Elliott, and G. J. Stern, "Optimizing the Synthesis of Shaped Beam Antenna Patterns," *IEE Proceedings*, Part H, pp. 63–68, 1985.
16. R. S. Elliott, "Design of Line Source Antennas for Narrow Beamwidth and Asymmetric Low Sidelobes," *IEEE Trans. Antennas Propagat.*, Vol. AP-23, No. 1, pp. 100–107, January 1975.
17. G. N. Watson, *A Treatise on the Theory of Bessel Functions*, 2nd. Ed., Cambridge University Press, London, pp. 50 and 379, 1966.
18. S. Silver (ed.), *Microwave Antenna Theory and Design*, MIT Radiation Laboratory Series, Vol. 12, McGraw-Hill, New York, 1965, Chapter 6, pp. 169–199.

INTEL-1045
U.S. Patent 7,151,430

19. R. C. Johnson and H. Jasik (eds.), *Antenna Engineering Handbook*, 2nd. Ed., McGraw-Hill, New York, 1984, pp. 2-14 to 2-41.

PROBLEMS

7.1. A three-element array is placed along the z-axis. Assuming the spacing between the elements is $d = \lambda/4$ and the relative amplitude excitation is equal to $a_1 = 1$, $a_2 = 2$, $a_3 = 1$,
(a) find the angles where the array factor vanishes when $\beta = 0$, $\pi/2$, π, and $3\pi/2$
(b) plot the relative pattern for each array factor
Use Schelkunoff's method.

7.2. Design a linear array of isotropic elements placed along the z-axis such that the zeros of the array factor occur at $\theta = 0°$, 60°, and 120°. Assume that the elements are spaced $\lambda/4$ apart and that the progressive phase shift between them is 0°.
(a) Find the required number of elements.
(b) Determine their excitation coefficients.
(c) Write the array factor.
(d) Plot the array factor pattern to verify the validity of the design.

7.3. The z-plane array factor of an array of isotropic elements placed along the z-axis is given by

$$\text{AF} = z(z^4 - 1)$$

Determine the
(a) number of elements of the array. If there are any elements with zero excitation coefficients (null elements), so indicate
(b) position of each element (including that of null elements) along the z axis
(c) magnitude and phase (in degrees) excitation of each element
(d) angles where the pattern vanishes when the total array length (including null elements) is 2λ

7.4. Repeat Prob. 7.3 when

$$\text{AF} = z(z^3 - 1)$$

7.5. Repeat Example 7.2 when

$$\text{SF}(\theta) = \begin{cases} 1 & 40° \le \theta \le 140° \\ 0 & \text{elsewhere} \end{cases}$$

7.6. Repeat the Fourier transform design of Example 7.2 for a line source along the z-axis whose sectoral pattern is given by

$$\text{SF}(\theta) = \begin{cases} 1 & 60° \le \theta \le 120° \\ 0 & \text{elsewhere} \end{cases}$$

Use $l = 5\lambda$ and 10λ. Compare the reconstructed patterns with the desired one.

7.7. Repeat the Fourier transform design of Problem 7.6 for a linear array with a spacing of $d = \lambda/2$ between the elements and
(a) $N = 11$ elements
(b) $N = 21$ elements

7.8. Repeat the design of Problem 7.6 using the Woodward-Lawson method for line-sources.

7.9. Repeat the design of Problem 7.7 using the Woodward-Lawson method for linear arrays for $N = 10, 20$.

7.10. Design, using the Woodward-Lawson method, a line-source of $l = 5\lambda$ whose space factor pattern is given by

$$\text{SF}(\theta) = \sin^3(\theta) \qquad 0° \le \theta \le 180°$$

Determine the current distribution and compare the reconstructed pattern with the desired pattern.

INTEL-1045
U.S. Patent 7,151,430

7.11. Repeat the design of Problem 7.10 for a linear array of $N = 10$ elements with a spacing of $d = \lambda/2$ between them.

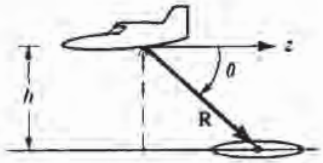
7.12. In target-search, grounding-mapping radars, and in airport beacons it is desirable to have the echo power received from a target, of constant cross section, to be independent of its range R.

Generally, the far-zone field radiated by an antenna is given by

$$|E(R, \theta, \phi)| = C_0 \frac{|F(\theta, \phi)|}{R}$$

where C_0 is a constant. According to the geometry of the figure

$$R = h/\sin(\theta) = h \csc(\theta)$$



For a constant value of ϕ, the radiated field expression reduces to

$$|E(R, \theta, \phi = \phi_0)| = C_0 \frac{|F(\theta, \phi = \phi_0)|}{R} = C_1 \frac{|f(\theta)|}{R}$$

A constant value of field strength can be maintained provided the radar is flying at a constant altitude h and the far-field antenna pattern is equal to

$$f(\theta) = C_2 \csc(\theta)$$

This is referred to as a cosecant pattern, and it is used to compensate for the range variations. For very narrow beam antennas, the total pattern is approximately equal to the space or array factor. Design a line-source, using the Woodward-Lawson method, whose space factor is given by

$$\mathrm{SF}(\theta) = \begin{cases} 0.342 \csc(\theta), & 20^\circ \le \theta \le 60^\circ \\ 0 & \text{elsewhere} \end{cases}$$

Plot the synthesized pattern for $l = 20\lambda$, and compare it with the desired pattern.

7.13. Repeat the design of Problem 7.12 for a linear array of $N = 41$ elements with a spacing of $d = \lambda/2$ between them.

7.14. For some radar search applications, it is more desirable to have an antenna which has a square beam for $0 \le \theta \le \theta_0$, a cosecant pattern for $\theta_0 \le \theta \le \theta_m$, and it is zero elsewhere. Design a line-source, using the Woodward-Lawson method, with a space factor of

$$\mathrm{SF}(\theta) = \begin{cases} 1 & 15^\circ \le \theta < 20^\circ \\ 0.342 \csc(\theta) & 20^\circ \le \theta \le 60^\circ \\ 0 & \text{elsewhere} \end{cases}$$

Plot the reconstructed pattern for $l = 20\lambda$, and compare it with the desired pattern.

7.15. Repeat the design of Problem 7.14, using the Woodward-Lawson method, for a linear array of 41 elements with a spacing of $d = \lambda/2$ between them.

7.16. Design a Taylor (Tschebyscheff error) line-source with a

(a) -25 dB side lobe level and $\bar{n} = 5$

(b) -20 dB side lobe level and $\bar{n} = 10$

For each, find the half-power beamwidth and plot the normalized current distribution and the reconstructed pattern when $l = 10\lambda$.

7.17. Derive (7-33) using (7-1), (7-32), and Gegenbauer's finite integral and polynomials.

INTEL-1045
U.S. Patent 7,151,430

7.18. Repeat the design of Example 7.7 for an array with $l = 4\lambda$, $d = \lambda/2$, $N = 9$.

7.19. Design a broadside five-element, -40 dB side lobe level Taylor (one-parameter) distribution array of isotropic sources. The elements are placed along the x-axis with a spacing of $\lambda/4$ between them. Determine the
(a) normalized excitation coefficients (amplitude and phase) of each element
(b) array factor

7.20. Derive the space factors for uniform, triangular, cosine, and cosine squared line-source continuous distributions. Compare with the results in Table 7.1.

7.21. Compute the half-power beamwidth, first null beamwidth, first side lobe level (in dB), and directivity of a linear array of closely spaced elements with overall length of 4λ when its amplitude distribution is
(a) uniform (b) triangular
(c) cosine (d) cosine squared

7.22. Derive the space factors for the uniform radial taper, and radial taper-squared circular aperture continuous distributions. Compare with the results in Table 7.2.

7.23. Compute the half-power beamwidth, first null beamwidth, first side lobe level (in dB), and gain factor of a circular planar array of closely spaced elements, with radius of 2λ when its amplitude distribution is
(a) uniform
(b) radial taper
(c) radial taper-squared

INTEL-1045
U.S. Patent 7,151,430

CHAPTER 8

INTEGRAL EQUATIONS, MOMENT METHOD, AND SELF AND MUTUAL IMPEDANCES

8.1 INTRODUCTION

In Chapter 2 it was shown, by the Thévenin and Norton equivalent circuits of Figures 2.21 and 2.22, that an antenna can be represented by an equivalent impedance $Z_A[Z_A = (R_r + R_L) + jX_A]$. The equivalent impedance is attached across two terminals (terminals $a - b$ in Figures 2.21 and 2.22) which are used to connect the antenna to a generator, receiver, or transmission line. In general, this impedance is called the *driving-point* impedance. However, when the antenna is radiating in an unbounded medium, in the absence of any other interfering elements or objects, the driving-point impedance is the same as the *self-impedance* of the antenna. In practice, however, there is always the ground whose presence must be taken into account in determining the antenna driving-point impedance. The self- and driving point impedances each have, in general, a real and an imaginary part. The real part is designated as the resistance and the imaginary part is called the reactance.

The impedance of an antenna depends on many factors including its frequency of operation, its geometry, its method of excitation, and its proximity to the surrounding objects. Because of their complex geometries, only a limited number of practical antennas have been investigated analytically. For many others, the input impedance has been determined experimentally.

The impedance of an antenna at a point is defined as the ratio of the electric to the magnetic fields at that point; alternatively, at a pair of terminals it is defined as the ratio of the voltage to the current across those terminals. There are many methods that can be used to calculate the impedance of an antenna [1]. Generally, these can be classified into three catogories: (1) the boundary-value method, (2) the transmission-line method, and (3) the Poynting vector method. Extensive and brief discussions and comparisons of these methods have been reported [1], [2].

The boundary-value approach is the most basic, and it treats the antenna as a boundary-value problem. The solution to this is obtained by enforcing the boundary

INTEL-1045
U.S. Patent 7,151,430

conditions (usually that the tangential electric field components vanish at the conducting surface). In turn, the current distribution and finally the impedance (ratio of applied emf to current) are determined, with no assumptions as to their distribution, as solutions to the problem. The principal disadvantage of this method is that it has limited applications. It can only be applied and solved exactly on simplified geometrical shapes where the scalar wave equation is separable.

The transmission-line method, which has been used extensively by Schelkunoff [3], treats the antenna as a transmission line, and it is most convenient for the biconical antenna. Since it utilizes tangential electric field boundary conditions for its solution, this technique may also be classified as a boundary-value method.

The basic approach to the Poynting vector method is to integrate the Poynting vector (power density) over a closed surface. The closed surface chosen is usually either a sphere of a very large radius r ($r \geq 2D^2/\lambda$ where D is the largest dimension of the antenna) or a surface that coincides with the surface of the antenna. The large sphere closed surface method has been introduced in Chapters 4 and 5, but it lends itself to calculations only of the real part of the antenna impedance (radiation resistance). The method that utilizes the antenna surface has been designated as the induced emf method, and it has been utilized [4]–[6] for the calculation of antenna impedances.

The impedance of an antenna can also be found using an integral equation with a numerical technique solution, which is widely referred to as the *Integral Equation-Method of Moments* [7]–[14]. This method, which in the late 1960s was extended to include electromagnetic problems, is analytically simple, it is versatile, but it requires large amounts of computation. The limitation of this technique is usually the speed and storage capacity of the computer.

In this chapter the integral equation method, with a Moment Method numerical solution, will be introduced and used first to find the self- and driving-point impedances, and mutual impedance of wire type of antennas. This method casts the solution for the induced current in the form of an integral (hence its name) where the unknown induced current density is part of the integrand. Numerical techniques, such as the *Moment Method* [7]–[14], can then be used to solve the current density. In particular two classical integral equations for linear elements, *Pocklington's and Hallén's Integral Equations*, will be introduced. This approach is very general, and it can be used with todays modern computational methods and equipment to compute the characteristics of complex configurations of antenna elements, including skewed arrangements. For special cases, closed form expressions for the self, driving point, and mutual impedances will be presented using the induced emf method. This method is limited to classical geometries, such as straight wires and arrays of collinear and parallel straight wires.

8.2 INTEGRAL EQUATION METHOD

The objective of the Integral Equation (IE) method for radiation or scattering is to cast the solution for the unknown current density, which is induced on the surface of the radiation scatterer, in the form of an integral equation where the unknown induced current density is part of the integrand. The integral equation is then solved for the unknown induced current density using numerical techniques such as the *Moment Method* (MM). To demonstrate this technique, we will initially consider some specific problems. For introduction, we will start with an electrostatics problem and follow it with time-harmonic problems.

INTEL-1045
U.S. Patent 7,151,430

8.2.1 Electrostatic Charge Distribution

In electrostatics, the problem of finding the potential that is due to a given charge distribution is often considered. In physical situations, however, it is seldom possible to specify a charge distribution. Whereas we may connect a conducting body to a voltage source, and thus specify the potential throughout the body, the distribution of charge is obvious only for a few rotationally symmetric geometries. In this section we will consider an integral equation approach to solve for the electric charge distribution once the electric potential is specified. Some of the material here and in other sections is drawn from [15], [16].

From statics we know that a linear electric charge distribution $\rho(r')$ creates an electric potential, $V(r)$, according to [17]

$$V(r) = \frac{1}{4\pi\epsilon_0} \int_{\substack{\text{source} \\ \text{(charge)}}} \frac{\rho(r')}{R}\, dl' \tag{8-1}$$

where $r'(x', y', z')$ denotes the source coordinates, $r(x, y, z)$ denotes the observation coordinates, dl' is the path of integration, and R is the distance from any one point on the source to the observation point, which is generally represented by

$$R(r, r') = |\mathbf{r} - \mathbf{r}'| = \sqrt{(x - x')^2 + (y - y')^2 + (z - z')^2} \tag{8-1a}$$

We see that (8-1) may be used to calculate the potentials that are due to any known line charge density. However, the charge distribution on most configurations of practical interest, i.e., complex geometries, is not usually known, even when the potential on the source is given. It is the nontrivial problem of determining the charge distribution, for a specified potential, that is to be solved here using an integral equation-numerial solution approach.

A. Finite Straight Wire

Consider a straight wire of length l and radius a, placed along the y axis, as shown in Figure 8-1(a). The wire is given a normalized constant electric potential of 1 V.

Note that (8-1) is valid everywhere, including on the wire itself ($V_{\text{wire}} = 1$ V). Thus, choosing the observation along the wire axis ($x = z = 0$) and representing the charge density on the surface of the wire, (8-1) can be expressed as

$$1 = \frac{1}{4\pi\epsilon_0} \int_0^l \frac{\rho(y')}{R(y, y')}\, dy', \quad 0 \le y \le l \tag{8-2}$$

where

$$R(y, y') = R(r, r')\big|_{x=z=0} = \sqrt{(y - y')^2 + [(x')^2 + (z')^2]}$$

$$= \sqrt{(y - y')^2 + a^2} \tag{8-2a}$$

The observation point is chosen along the wire axis and the charge density is represented along the surface of the wire to avoid $R(y, y') = 0$, which would introduce a singularity in the integrand of (8-2).

It is necessary to solve (8-2) for the unknown $\rho(y')$ (an inversion problem). Equation (8-2) is an integral equation that can be used to find the charge density $\rho(y')$ based on the 1-V potential. The solution may be reached numerically by reducing (8-2) to a series of linear algebraic equations that may be solved by conventional matrix equation techniques. To facilitate this, let us approximate the unknown charge

INTEL-1045
U.S. Patent 7,151,430

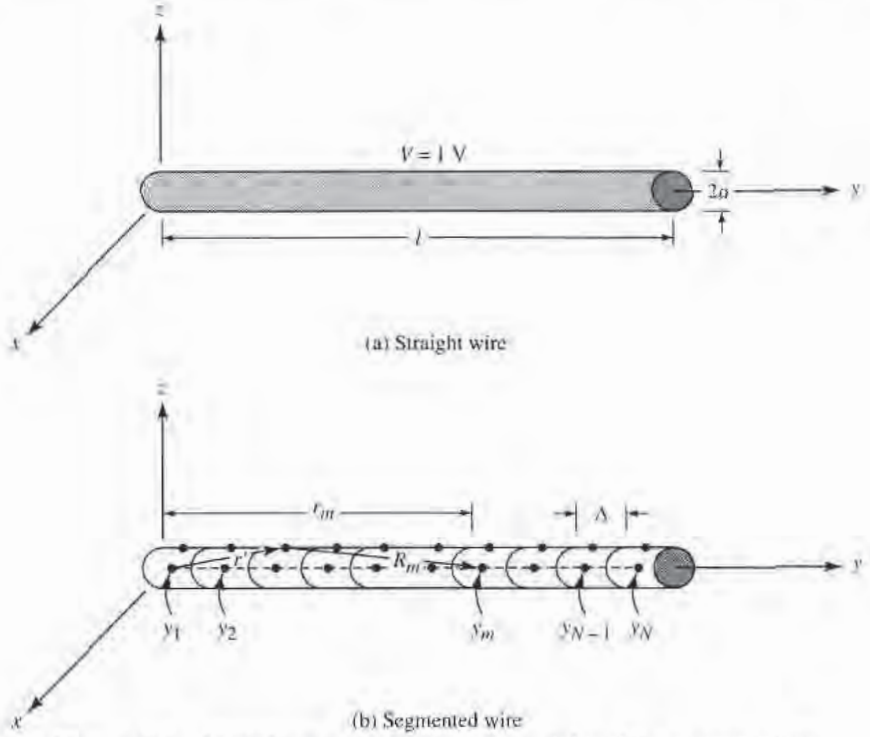


Figure 8.1 Straight wire of constant potential and its segmentation.

distribution $\rho(y')$ by an expansion of N known terms with constant, but unknown, coefficients, that is,

$$\rho(y') = \sum_{n=1}^{N} a_n g_n(y') \tag{8-3}$$

Thus, (8-2) may be written, using (8-3), as

$$4\pi\epsilon_0 = \int_0^l \frac{1}{R(y, y')} \left[\sum_{n=1}^{N} a_n g_n(y') \right] dy' \tag{8-4}$$

Because (8-4) is a nonsingular integral, its integration and summation can be interchanged, and it can be written as

$$4\pi\epsilon_0 = \sum_{n=1}^{N} a_n \int_0^l \frac{g_n(y')}{\sqrt{(y - y')^2 + a^2}} dy' \tag{8-4a}$$

The wire is now divided into N uniform segments, each of length $\Delta = l/N$, as illustrated in Figure 8.1(b). The $g_n(y')$ functions in the expansion (8-3) are chosen for their ability to accurately model the unknown quantity, while minimizing computation. They are often referred to as *basis* (or expansion) functions, and they will be discussed further in Section 8.2.3. To avoid complexity in this solution, subdomain piecewise constant (or "pulse") functions will be used. These functions, shown in Figure 8.5, are defined to be of a constant value over one segment and zero elsewhere, or

$$g_n(y') = \begin{cases} 0 & y' < (n-1)\Delta \\ 1 & (n-1)\Delta \le y' \le n\Delta \\ 0 & n\Delta < y' \end{cases} \tag{8-5}$$

INTEL-1045
U.S. Patent 7,151,430

Many other basis functions are possible, some of which will be introduced later in *Section 8.2.3.*

Replacing y in (8-4) by a fixed point such as y_m, results in an integrand that is solely a function of y', so the integral may be evaluated. Obviously, (8-4) leads to one equation with N unknowns a_n written as

$$4\pi\epsilon_0 = a_1 \int_0^{\Delta} \frac{g_1(y')}{R(y_m, y')} dy' + a_2 \int_{\Delta}^{2\Delta} \frac{g_2(y')}{R(y_m, y')} dy' + \cdots + a_n \int_{(n-1)\Delta}^{n\Delta} \frac{g_n(y')}{R(y_m, y')} dy' + \cdots + a_N \int_{(N-1)\Delta}^{l} \frac{g_N(y')}{R(y_m, y')} dy' \tag{8-6}$$

In order to obtain a solution for these N amplitude constants, N linearly independent equations are necessary. These equations may be produced by choosing N observation points y_m each at the center of each Δ length element as shown in Figure 8.1(b). This results in one equation of the form of (8-6) corresponding to each observation point. For N such points, we can reduce (8-6) to

$$\begin{aligned} 4\pi\epsilon_0 &= a_1 \int_0^{\Delta} \frac{g_1(y')}{R(y_1, y')} dy' + \cdots + a_N \int_{(N-1)\Delta}^{l} \frac{g_N(y')}{R(y_1, y')} dy' \\ &\vdots \\ 4\pi\epsilon_0 &= a_1 \int_0^{\Delta} \frac{g_1(y')}{R(y_N, y')} dy' + \cdots + a_N \int_{(N-1)\Delta}^{l} \frac{g_N(y')}{R(y_N, y')} dy' \end{aligned} \tag{8-6a}$$

We may write (8-6a) more concisely using matrix notation as

$$[V_m] = [Z_{mn}][I_n] \tag{8-7}$$

where each Z_{mn} term is equal to

$$\begin{aligned} Z_{mn} &= \int_0^{l} \frac{g_n(y')}{\sqrt{(y_m - y')^2 + a^2}} dy' \\ &= \int_{(n-1)\Delta}^{n\Delta} \frac{1}{\sqrt{(y_m - y')^2 + a^2}} dy' \end{aligned} \tag{8-7a}$$

and

$$[I_n] = [a_n] \tag{8-7b}$$

$$[V_m] = [4\pi\epsilon_0]. \tag{8-7c}$$

The V_m column matrix has all terms equal to $4\pi\epsilon_0$, and the $I_n = a_n$ values are the unknown charge distribution coefficients. Solving (8-7) for $[I_n]$ gives

$$[I_n] = [a_n] = [Z_{mn}]^{-1}[V_m] \tag{8-8}$$

Either (8-7) or (8-8) may readily be solved on a digital computer by using any of a number of matrix inversion or equation solving routines. Whereas the integral involved here may be evaluated in closed form by making appropriate approximations, this is not usually possible with more complicated problems. Efficient numerical integral computer subroutines are commonly available in easy-to-use forms.

INTEL-1045
U.S. Patent 7,151,430

One closed form evaluation of (8-7a) is to reduce the integral and represent it by

$$Z_{mn} = \begin{cases} 2 \ln\left(\dfrac{\dfrac{\Delta}{2} + \sqrt{a^2 + \left(\dfrac{\Delta}{2}\right)^2}}{a}\right) & m = n \qquad (8\text{-}9a) \\ \ln\left\{\dfrac{d_{mn}^{+} + [(d_{mn}^{+})^2 + a^2]^{1/2}}{d_{mn}^{-} + [(d_{mn}^{-})^2 + a^2]^{1/2}}\right\} & m \neq n \text{ but } |m - n| \leq 2 \qquad (8\text{-}9b) \\ \ln\left(\dfrac{d_{mn}^{+}}{d_{mn}^{-}}\right) & |m - n| > 2 \qquad (8\text{-}9c) \end{cases}$$

where

$$d_{mn}^{+} = l_m + \frac{\Delta}{2} \qquad (8\text{-}9d)$$

$$d_{mn}^{-} = l_m - \frac{\Delta}{2} \qquad (8\text{-}9e)$$

l_m is the distance between the mth matching point and the center of the nth source point.

In summary, the solution of (8-2) for the charge distribution on a wire has been accomplished by approximating the unknown with some basis functions, dividing the wire into segments, and then sequentially enforcing (8-2) at the center of each segment to form a set of linear equations.

Even for the relatively simple straight wire geometry we have discussed, the exact form of the charge distribution is not intuitively apparent. To illustrate the principles of the numerical solution, an example is now presented.

Example 8.1

A 1-m long straight wire of radius $a = 0.001$ m is maintained at a constant potential of 1 V. Determine the linear charge distribution on the wire by dividing the length into 5 and 20 uniform segments. Assume subdomain pulse basis functions.

SOLUTION

1. $N = 5$. When the 1-m long wire is divided into five uniform segments each of length $\Delta = 0.2$ m, (8-7) reduces to

$$\begin{bmatrix} 10.60 & 1.10 & 0.51 & 0.34 & 0.25 \\ 1.10 & 10.60 & 1.10 & 0.51 & 0.34 \\ 0.51 & 1.10 & 10.60 & 1.10 & 0.51 \\ 0.34 & 0.51 & 1.10 & 10.60 & 1.10 \\ 0.25 & 0.34 & 0.51 & 1.10 & 10.60 \end{bmatrix} \begin{bmatrix} a_1 \\ a_2 \\ a_3 \\ a_4 \\ a_5 \end{bmatrix} = \begin{bmatrix} 1.11 \times 10^{-10} \\ 1.11 \times 10^{-10} \\ \vdots \\ 1.11 \times 10^{-10} \end{bmatrix}$$

Inverting this matrix leads to the amplitude coefficients and subsequent charge distribution of

$$a_1 = 8.81 pC/m$$

$$a_2 = 8.09 pC/m$$

INTEL-1045
U.S. Patent 7,151,430

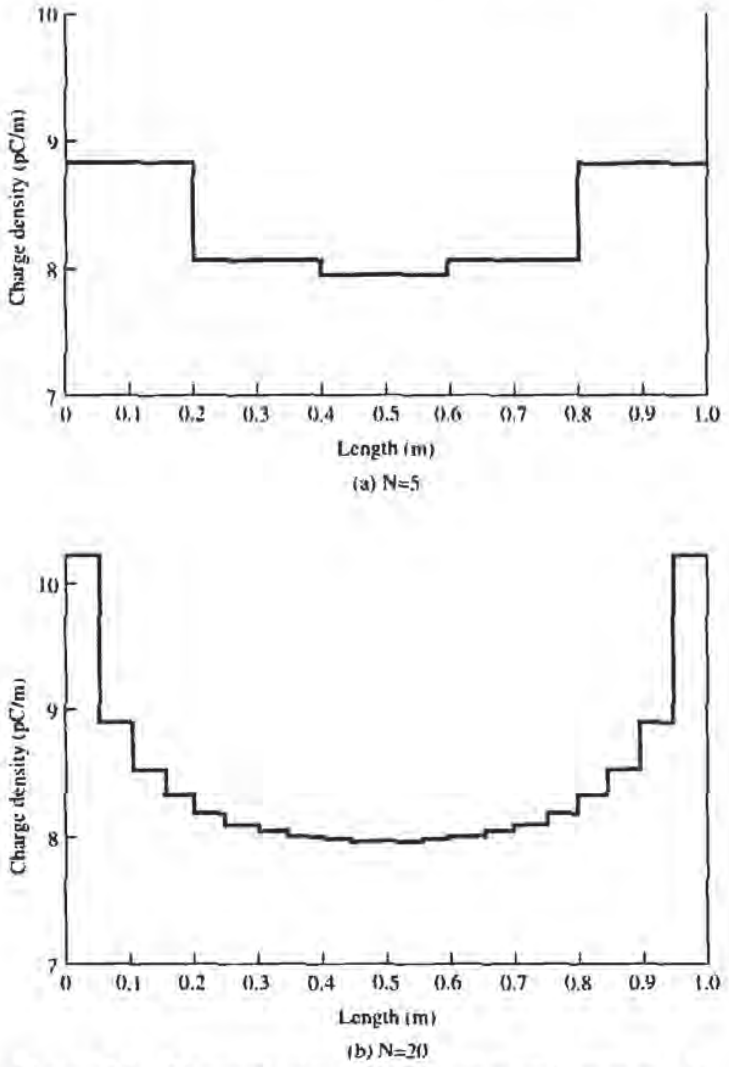


Figure 8.2 Charge distribution on a 1-m straight wire at 1 V.

$$a_3 = 7.97pC/m$$
$$a_4 = 8.09pC/m$$
$$a_5 = 8.81pC/m$$

The charge distribution is shown in Figure 8.2(a).

2. *$N = 20$. Increasing the number of segments to 20 results in a much smoother* distribution, as shown plotted in Figure 8.2(b). As more segments are used, a better approximation of the actual charge distribution is attained, which has smaller discontinuities over the length of the wire.

B. Bent Wire

In order to illustrate the solution of a more complex structure, let us analyze a body composed of two noncollinear straight wires; that is, a bent wire. If a straight wire is bent, the charge distribution will be altered, although the solution to find it will differ

INTEL-1045
U.S. Patent 7,151,430

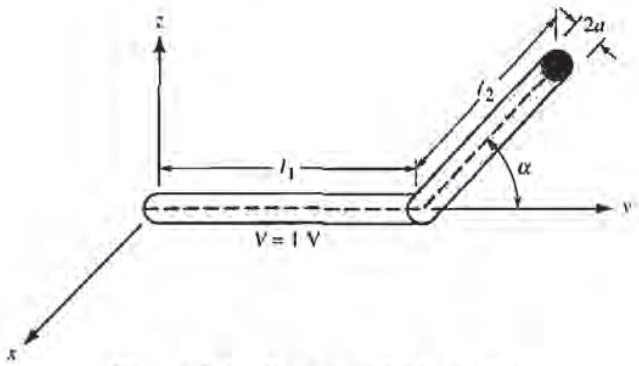


Figure 8.3 Geometry for bent wire.

only slightly from the straight wire case. We will assume a bend of angle α, which remains on the yz-plane, as shown in Figure 8.3.

For the first segment l_1 of the wire, the distance R can be represented by (8-2a). However, for the second segment l_2 we can express the distance as

$$R = \sqrt{(y - y')^2 + (z - z')^2} \tag{8-10}$$

Also because of the bend, the integral in (8-7a) must be separated into two parts of

$$Z_{mn} = \int_0^{l_1} \frac{\rho_n(l_1')}{R} dl_1' + \int_0^{l_2} \frac{\rho_n(l_2')}{R} dl_2' \tag{8-11}$$

where l_1 and l_2 are measured along the corresponding straight sections from their left ends.

Example 8.2

Repeat Example 8.1 assuming that the wire has been bent 90° at its midpoint. Subdivide the wire into 20 uniform segments.

SOLUTION

The charge distribution for this case, calculated using (8-10) and (8-11), is plotted in Figure 8.4 for $N = 20$ segments. Note that the charge is relatively more concentrated near the ends of this structure than was the case for a straight wire of Figure 8.2(b). Further, the overall density, and thus capacitance, on the structure has decreased.

Arbitrary wire configurations, including numerous ends and even curved sections, may be analyzed by the methods already outlined here. As with the simple bent wire, the only alterations generally necessary are those required to describe the geometry analytically.

INTEL-1045
U.S. Patent 7,151,430

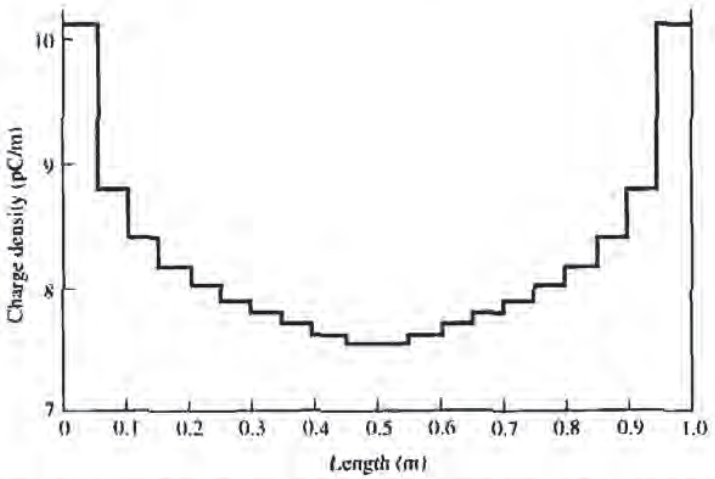


Figure 8.4 Charge distribution on a 1-m bent wire ($\alpha = 90°$, $N = 20$).

8.2.2 Integral Equation

Equation (8-2) for the 1-V potential on a wire of length l is an integral equation, which can be used to solve for the charge distribution. Numerically this is accomplished using a method, which is usually referred to as *Moment Method* or *Method of Moments* [7]–[14]. To solve (8-2) numerically the unknown charge density $\rho(y')$ is represented by N terms, as given by (8-3). In (8-3) $g_n(y')$ are a set of N known functions, usually referred to as *basis* or *expansion* functions, while a_n represents a set of N constant, but unknown, coefficients. The basis or expansion functions are chosen to best represent the unknown charge distribution.

Equation (8-2) is valid at every point on the wire. By enforcing (8-2) at N discrete but different points on the wire, the integral equation of (8-2) is reduced to a set of N linearly independent algebraic equations, as given by (8-6a). This set is generalized by (8-7)–(8-7c), which is solved for the unknown coefficients a_n by (8-8) using matrix inversion techniques. Since the system of N linear equations each with N unknowns, as given by (8-6a)–(8-8), was derived by applying the boundary condition (constant 1-V potential) at N discrete points on the wire, the technique is referred to as *point-matching* (or *collocation*) method [7], [8]. Thus, by finding the elements of the $[V]$ and $[Z]$, and then the inverse $[Z]^{-1}$ matrices, we can then determine the coefficients a_n of the $[I]$ matrix using (8-8). This in turn allows us to approximate the charge distribution $\rho(y')$ using (8-3). This was demonstrated by Examples 8.1 and 8.2 for the straight and bent wires, respectively.

In general, there are many forms of integral equations. For time-harmonic electromagnetics, two of the most popular integral equations are the *electric field integral equation* (EFIE) and the *magnetic field integral equation* (MFIE) [14]. The EFIE enforces the boundary condition on the tangential electric field while the MFIE enforces the boundary condition on the tangential components of the magnetic field. The EFIE is valid for both closed or open surfaces while the MFIE is valid for closed surfaces. These integral equations can be used for both radiation and scattering problems. Two- and three-dimensional EFIE and MFIE equations for TE and TM polarizations are derived and demonstrated in [14]. For radiation problems, especially wire antennas, two popular EFIEs are the Pocklington Integral Equation and the Hallén

INTEL-1045
U.S. Patent 7,151,430

Integral Equation. Both of these will be discussed and demonstrated in the section that follows.

8.3 FINITE DIAMETER WIRES

In this section we want to derive and apply two classic three-dimensional integral equations, referred to as *Pocklington's integrodifferential equation* and *Hallén's integral equation* [18]–[26], that can be used most conveniently to find the current distribution on conducting wires. Hallén's equation is usually restricted to the use of a *delta-gap* voltage source model at the feed of a wire antenna. Pocklington's equation, however, is more general and it is adaptable to many types of feed sources (through alteration of its excitation function or excitation matrix), including a magnetic frill [27]. In addition, Hallén's equation requires the inversion of an $N + 1$ order matrix (where N is the number of divisions of the wire) while Pocklington's equation requires the inversion of an N order matrix.

For very thin wires, the current distribution is usually assumed to be of sinusoidal form as given by (4-56). For finite diameter wires (usually diameters d of $d > 0.05\lambda$), the sinusoidal current distribution is representative but not accurate. To find a more accurate current distribution on a cylindrical wire, an integral equation is usually derived and solved. Previously, solutions to the integral equation were obtained using iterative methods [20]; presently, it is most convenient to use moment method techniques [7]–[9].

If we know the voltage at the feed terminals of a wire antenna and find the current distribution, the input impedance and radiation pattern can then be obtained. Similarly, if a wave impinges upon the surface of a wire scatterer, it induces a current density that in turn is used to find the scattered field. Whereas the linear wire is simple, most of the information presented here can be readily extended to more complicated structures.

8.3.1 Pocklington's Integral Equation

To derive Pocklington's integral equation, refer to Figure 8.5. Although this derivation is general, it can be used either when the wire is a scatterer or an antenna. Let us assume that an incident wave impinges on the surface of a conducting wire, as shown in Figure 8.5(a), and it is referred to as the *incident electric field* $\mathbf{E}^i(\mathbf{r})$. When the wire is an antenna, the incident field is produced by the feed at the gap, as shown in Figure 8.7. Part of the incident field impinges on the wire and induces on its surface a linear current density $\mathbf{J}_s$ (amperes per meter). The induced current density $\mathbf{J}_s$ reradiates and produces an electric field that is referred to as the *scattered electric field* $\mathbf{E}^s(\mathbf{r})$. Therefore, at any point in space the total electric field $\mathbf{E}^t(\mathbf{r})$ is the sum of the incident and scattered fields, or

$$\mathbf{E}^t(\mathbf{r}) = \mathbf{E}^i(\mathbf{r}) + \mathbf{E}^s(\mathbf{r}) \tag{8-12}$$

where

$\mathbf{E}^t(\mathbf{r})$ = total electric field
$\mathbf{E}^i(\mathbf{r})$ = incident electric field
$\mathbf{E}^s(\mathbf{r})$ = scattered electric field

When the observation point is moved to the surface of the wire ($r = r_s$) and the wire is perfectly conducting, the total tangential electric field vanishes. In cylindrical

INTEL-1045
U.S. Patent 7,151,430

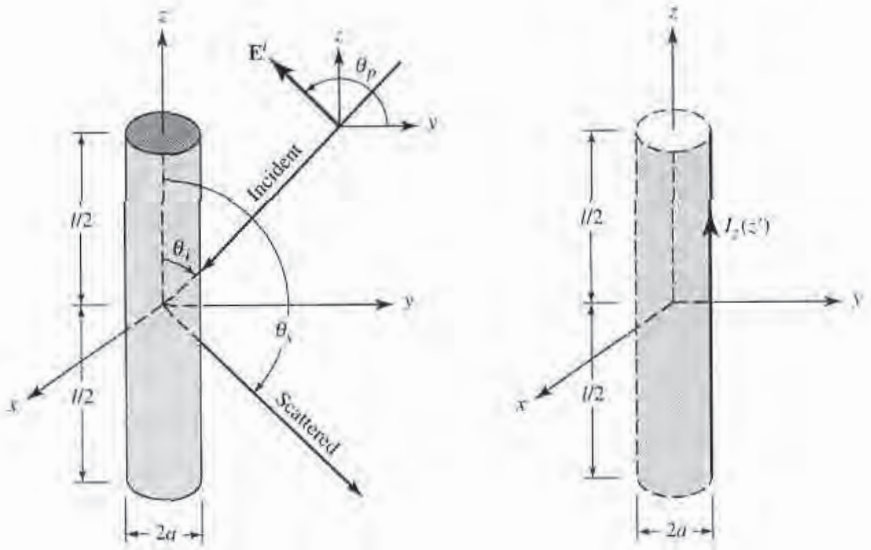


Figure 8.5 Uniform plane wave obliquely incident on a conducting wire.

coordinates, the electric field radiated by the dipole has a radial component (E_ρ) and a tangential component (E_z). These are represented by (8-55a) and (8-55b). Therefore on the surface of the wire the tangential component of (8-12) reduces to

$$E_z^t(r = r_s) = E_z^i(r = r_s) + E_z^s(r = r_s) = 0 \tag{8-13}$$

or

$$E_z^s(r = r_s) = -E_z^i(r = r_s) \tag{8-13a}$$

In general, the scattered electric field generated by the induced current density $\mathbf{J}_s$ is given by (3-15), or

$$\begin{aligned} \mathbf{E}^s(\mathbf{r}) &= -j\omega\mathbf{A} - j\frac{1}{\omega\mu\epsilon}\nabla(\nabla\cdot\mathbf{A}) \\ &= -j\frac{1}{\omega\mu\epsilon}[k^2\,\mathbf{A} + \nabla(\nabla\cdot\mathbf{A})] \end{aligned} \tag{8-14}$$

However, for observations at the wire surface only the z component of (8-14) is needed, and we can write it as

$$E_z^s(r) = -j\frac{1}{\omega\mu\epsilon}\left(k^2 A_z + \frac{\partial^2 A_z}{\partial z^2}\right) \tag{8-15}$$

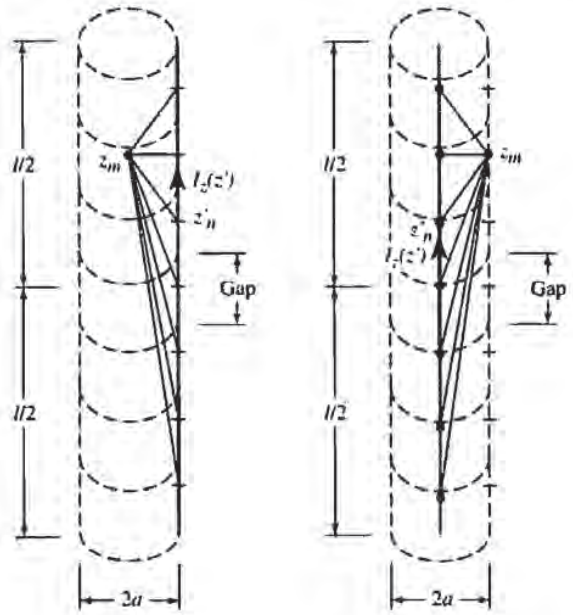
According to (3-51) and neglecting edge effects

$$A_z = \frac{\mu}{4\pi}\iint_S J_z\frac{e^{-jkR}}{R}\,ds' = \frac{\mu}{4\pi}\int_{-l/2}^{+l/2}\int_0^{2\pi} J_z\frac{e^{-jkR}}{R}\,a\,d\phi'\,dz' \tag{8-16}$$

If the wire is very thin, the current density J_z is not a function of the azimuthal angle ϕ, and we can write it as

$$2\pi a J_z = I_z(z') \Rightarrow J_z = \frac{1}{2\pi a}I_z(z') \tag{8-17}$$

INTEL-1045
U.S. Patent 7,151,430



(a) On the surface (b) Along the center

Figure 8.6 Dipole segmentation and its equivalent current.

where $I_z(z')$ is assumed to be an equivalent filament line-source current located a radial distance $\rho = a$ from the z axis, as shown in Figure 8.6(a). Thus (8-16) reduces to

$$A_z = \frac{\mu}{4\pi}\int_{-l/2}^{+l/2}\left[\frac{1}{2\pi a}\int_0^{2\pi} I_z(z')\frac{e^{-jkR}}{R}a\,d\phi'\right]dz' \tag{8-18}$$

$$\begin{aligned} R &= \sqrt{(x-x')^2 + (y-y')^2 + (z-z')^2} \\ &= \sqrt{(\rho^2 + a^2 - 2\rho a\cos(\phi-\phi') + (z-z')^2} \end{aligned} \tag{8-18a}$$

where ρ is the radial distance to the observation point and a is the radius.

Because of the symmetry of the scatterer, the observations are not a function of ϕ. For simplicity, let us then choose $\phi = 0$. For observations on the surface $\rho = a$ of the scatterer (8-18) and (8-18a) reduce to

$$\begin{aligned} A_z(\rho = a) &= \mu\int_{-l/2}^{+l/2} I_z(z')\left(\frac{1}{2\pi}\int_0^{2\pi}\frac{e^{-jkR}}{4\pi R}d\phi'\right)dz' \\ &= \mu\int_{-l/2}^{+l/2} I_z(z')G(z,z')\,dz' \end{aligned} \tag{8-19}$$

$$G(z,z') = \frac{1}{2\pi}\int_0^{2\pi}\frac{e^{-jkR}}{4\pi R}d\phi' \tag{8-19a}$$

$$R(\rho = a) = \sqrt{4a^2\sin^2\left(\frac{\phi'}{2}\right) + (z-z')^2} \tag{8-19b}$$

INTEL-1045
U.S. Patent 7,151,430

Thus for observations at the surface $\rho = a$ of the scatterer, the z component of the scattered electric field can be expressed as

$$E_z^s(\rho = a) = -j\frac{1}{\omega\epsilon}\left(k^2 + \frac{d^2}{dz^2}\right)\int_{-l/2}^{+l/2} I_z(z')G(z, z')\,dz' \tag{8-20}$$

which by using (8-13a) reduces to

$$-j\frac{1}{\omega\epsilon}\left(\frac{d^2}{dz^2} + k^2\right)\int_{-l/2}^{+l/2} I_z(z')G(z, z')\,dz' = -E_z^i(\rho = a) \tag{8-21}$$

or

$$\left(\frac{d^2}{dz^2} + k^2\right)\int_{-l/2}^{+l/2} I_z(z')G(z, z')\,dz' = -j\omega\epsilon E_z^i(\rho = a) \tag{8-21a}$$

Interchanging integration with differentiation, we can rewrite (8-21a) as

$$\int_{-l/2}^{+l/2} I_z(z')\left[\left(\frac{\partial^2}{\partial z^2} + k^2\right)G(z, z')\right]dz' = -j\omega\epsilon E_z^i(\rho = a) \tag{8-22}$$

where $G(z, z')$ is given by (8-19a).

Equation (8-22) is referred to as *Pocklington's integral equation* [1], and it can be used to determine the equivalent filamentary line-source current of the wire, and thus current density on the wire, by knowing the incident field on the surface of the wire.

If we assume that the wire is very thin ($a \ll \lambda$) such that (8-19a) reduces to

$$G(z, z') = G(R) = \frac{e^{-jkR}}{4\pi R} \tag{8-23}$$

(8-22) can also be expressed in a more convenient form as [22]

$$\int_{-l/2}^{+l/2} I_z(z')\frac{e^{-jkR}}{4\pi R^5}[(1 + jkR)(2R^2 - 3a^2) + (kaR)^2]\,dz' = -j\omega\epsilon E_z^i(\rho = a) \tag{8-24}$$

where for observations along the center of the wire ($\rho = 0$)

$$R = \sqrt{a^2 + (z - z')^2} \tag{8-24a}$$

In (8-22) or (8-24), $I_z(z')$ represents the equivalent filamentary line-source current located on the surface of the wire, as shown in Figure 8.5(b), and it is obtained by knowing the incident electric field on the surface of the wire. By point-matching techniques, this is solved by matching the boundary conditions at discrete points on the surface of the wire. Often it is easier to choose the matching points to be at the interior of the wire, especially along the axis as shown in Figure 8.6(a), where $I_z(z')$ is located on the surface of the wire. By reciprocity, the configuration of Figure 8.6(a) is analogous to that of Figure 8.6(b) where the equivalent filamentary line-source current is assumed to be located along the center axis of the wire and the matching points are selected on the surface of the wire. Either of the two configurations can be used to determine the equivalent filamentary line-source current $I_z(z')$; the choice is left to the individual.

INTEL-1045
U.S. Patent 7,151,430

8.3.2 Hallén's Integral Equation

Referring again to Figure 8.5(a), let us assume that the length of the cylinder is much larger than its radius ($l \gg a$) and its radius is much smaller than the wavelength ($a \ll \lambda$) so that the effects of the end faces of the cylinder can be neglected. Therefore the boundary conditions for a wire with infinite conductivity are those of vanishing total tangential **E** fields on the surface of the cylinder and vanishing current at the ends of the cylinder [$I_z(z' = \pm l/2) = 0$].

Since only an electric current density flows on the cylinder and it is directed along the z axis ($\mathbf{J} = \hat{\mathbf{a}}_z J_z$), then according to (3-14) and (3-51) $\mathbf{A} = \hat{\mathbf{a}}_z A_z(z')$, which for small radii is assumed to be only a function of z'. Thus (3-15) reduces to

$$E_z^i = -j\omega A_z - j\frac{1}{\omega\mu\epsilon}\frac{\partial^2 A_z}{\partial z^2} = -j\frac{1}{\omega\mu\epsilon}\left[\frac{d^2A_z}{dz^2} + \omega^2\mu\epsilon A_z\right] \tag{8-25}$$

Since the total tangential electric field E_z^i vanishes on the surface of the cylinder, (8-25) reduces to

$$\frac{d^2A_z}{dz^2} + k^2A_z = 0 \tag{8-25a}$$

Because the current density on the cylinder is symmetrical [$J_z(z') = J_z(-z')$], the potential A_z is also symmetrical (i.e., $A_z(z') = A_z(-z')$]. Thus the solution of (8-25a) is given by

$$A_z(z) = -j\sqrt{\mu\epsilon}[B_1\cos(kz) + C_1\sin(k|z|)] \tag{8-26}$$

where B_1 and C_1 are constants. For a current-carrying wire, its potential is also given by (3-53). Equating (8-26) to (3-53) leads to

$$\int_{-l/2}^{+l/2} I_z(z')\frac{e^{-jkR}}{4\pi R}dz' = -j\sqrt{\frac{\epsilon}{\mu}}[B_1\cos(kz) + C_1\sin(k|z|)] \tag{8-27}$$

If a voltage V_i is applied at the input terminals of the wire, it can be shown that the constant $C_1 = V_i/2$. The constant B_1 is determined from the boundary condition that requires the current to vanish at the end points of the wire.

Equation (8-27) is referred to as *Hallén's integral equation* for a perfectly conducting wire. It was derived by solving the differential equation (3-15) or (8-25a) with the enforcement of the appropriate boundary conditions.

8.3.3 Source Modeling

Let us assume that the wire of Figure 8.5 is symmetrically fed by a voltage source, as shown in Figure 8.7(a), and the element acting as a dipole antenna. To use, for example, Pocklington's integrodifferential equation (8-22) or (8-23) we need to know how to express $E_z^i(\rho = a)$. Traditionally there have been two methods used to model the excitation to represent $E_z^i(\rho = a, 0 \le \phi \le 2\pi, -l/2 \le z \le +l/2)$ at all points on the surface of the dipole: One is referred to as the *delta-gap* excitation and the other as the *equivalent magnetic ring current* (better known as *magnetic frill generator*) [27].

INTEL-1045
U.S. Patent 7,151,430

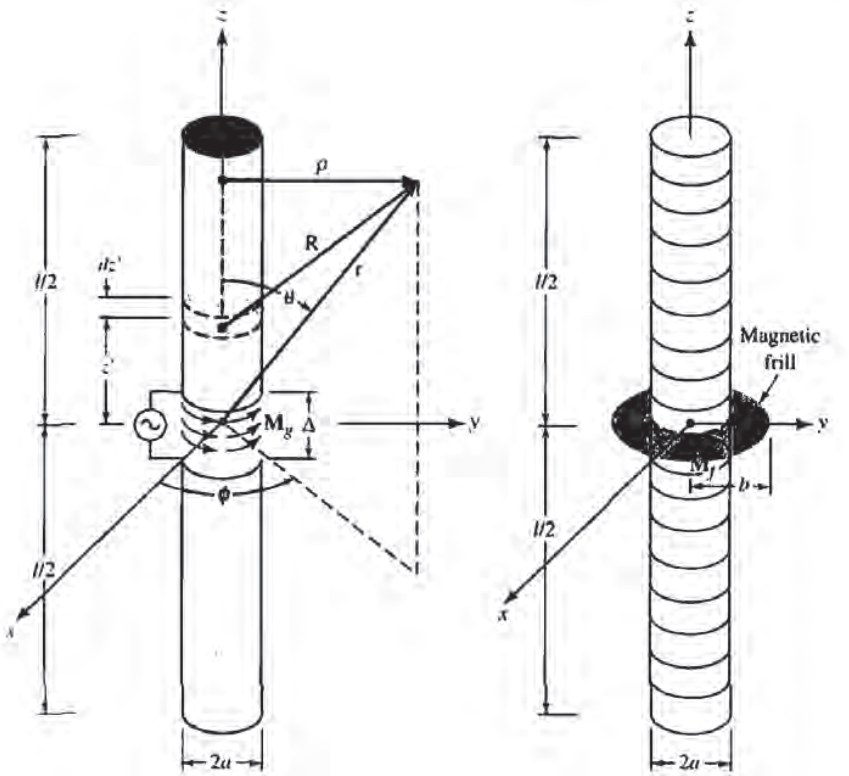


Figure 8.7 Cylindrical dipole, its segmentation, and gap modeling.

A. Delta Gap

The delta-gap source modeling is the simplest and most widely used of the two, but it is also the least accurate, especially for impedances. Usually it is most accurate for smaller width gaps. Using the delta gap, it is assumed that the excitation voltage at the feed terminals is of a constant V_i value and zero elsewhere. Therefore the incident electric field $E_z^i(\rho = a,\ 0 \le \phi \le 2\pi,\ -l/2 \le z \le +l/2)$ is also a constant (V_i/Δ where Δ is the gap width) over the feed gap and zero elsewhere, hence the name delta gap. For the delta-gap model, the feed gap Δ of Figure 8.7(a) is replaced by a narrow band of strips of equivalent magnetic current density of

$$\mathbf{M}_g = -\hat{\mathbf{n}} \times \mathbf{E}^i = -\hat{\mathbf{a}}_\rho \times \hat{\mathbf{a}}_z \frac{V_i}{\Delta} = \hat{\mathbf{a}}_\phi \frac{V_i}{\Delta} \qquad -\frac{\Delta}{2} \le z' \le \frac{\Delta}{2} \tag{8-28}$$

The magnetic current density $\mathbf{M}_g$ is sketched in Figure 8.7(a).

B. Magnetic Frill Generator

The magnetic frill generator was introduced to calculate the near- as well as the far-zone fields from coaxial apertures [27]. To use this model, the feed gap is replaced with a circumferentially directed magnetic current density that exists over an annular aperture with inner radius a, which is usually chosen to be the radius of the wire, and an outer radius b, as shown in Figure 8.7(b). Since the dipole is usually fed by transmission lines, the outer radius b of the equivalent annular aperture of the magnetic frill generator is found using the expression for the characteristic impedance of the transmission line.

INTEL-1045
U.S. Patent 7,151,430

Over the annular aperture of the magnetic frill generator, the electric field is represented by the TEM mode field distribution of a coaxial transmission line given by

$$\mathbf{E}_f = \hat{\mathbf{a}}_\rho \frac{V_i}{2\rho' \ln(b/a)} \quad a \le \rho' \le b \tag{8-29}$$

Therefore the corresponding equivalent magnetic current density $\mathbf{M}_f$ for the magnetic frill generator used to represent the aperture is equal to

$$\mathbf{M}_f = -2\hat{\mathbf{n}} \times \mathbf{E}_f = -2\hat{\mathbf{a}}_z \times \hat{\mathbf{a}}_\rho E_\rho = -\hat{\mathbf{a}}_\phi \frac{V_i}{\rho' \ln(b/a)} \quad a \le \rho' \le b \tag{8-30}$$

The fields generated by the magnetic frill generator of (8-30) on the surface of the wire are found by using [27]

$$\begin{aligned} E_z^i\left(\rho = a, 0 \le \phi \le 2\pi, -\frac{l}{2} \le z \le \frac{l}{2}\right) &\simeq -V_i\left(\frac{k(b^2 - a^2)e^{-jkR_0}}{8\ln(b/a)R_0^2}\left\{2\left[\frac{1}{kR_0} + j\left(1 - \frac{b^2 - a^2}{2R_0^2}\right)\right]\right.\right. \\ &+ \frac{a^2}{R_0}\left[\left(\frac{1}{kR_0} + j\left(1 - \frac{(b^2 + a^2)}{2R_0^2}\right)\right)\left(-jk - \frac{2}{R_0}\right)\right. \\ &\left.\left.\left. + \left(-\frac{1}{kR_0^2} + j\frac{b^2 + a^2}{R_0^3}\right)\right]\right\}\right) \end{aligned} \tag{8-31}$$

where

$$R_0 = \sqrt{z^2 + a^2} \tag{8-31a}$$

The fields generated on the surface of the wire computed using (8-31) can be approximated by those found along the axis ($\rho = 0$). Doing this leads to a simpler expression of the form [27]

$$E_z^i\left(\rho = 0, -\frac{l}{2} \le z \le \frac{l}{2}\right) = -\frac{V_i}{2\ln(b/a)}\left[\frac{e^{-jkR_1}}{R_1} - \frac{e^{-jkR_2}}{R_2}\right] \tag{8-32}$$

where

$$R_1 = \sqrt{z^2 + a^2} \tag{8-32a}$$

$$R_2 = \sqrt{z^2 + b^2} \tag{8-32b}$$

To compare the results using the two source modelings (delta-gap and magnetic-frill generator), an example is performed.

Example 8.3

For a center-fed linear dipole of $l = 0.47\lambda$ and $a = 0.005\lambda$, determine the induced voltage along the length of the dipole based on the incident electric field of the magnetic frill of (8-32). Subdivide the wire into 21 segments ($N = 21$). Compare the induced voltage distribution based on the magnetic frill to that of the delta gap. Assume a 50-ohm characteristic impedance with free space between the conductors for the annular feed.

INTEL-1045
U.S. Patent 7,151,430

SOLUTION

Since the characteristic impedance of the annular aperture is 50 ohms, then

$$Z_c = \sqrt{\frac{\mu_0}{\epsilon_0}}\frac{\ln(b/a)}{2\pi} = 50 \quad \Rightarrow \quad \frac{b}{a} = 2.3$$

Subdividing the total length ($l = 0.47\lambda$) of the dipole to 21 segments makes

$$\Delta = \frac{0.47\lambda}{21} = 0.0224\lambda$$

Using (8-32) to compute E_z^i, the corresponding induced voltages obtained by multiplying the value of $-E_z^i$ at each segment by the length of the segment are listed in Table 8.1, where they are compared with those of the delta gap. In Table 8.1 $n = 1$ represents the outermost segment and $n = 11$ represents the center segment. Because of the symmetry, only values for the center segment and half of the other segments are shown. Although the two distributions are not identical, the magnetic-frill distribution voltages decay quite rapidly away from the center segment and they very quickly reach almost vanishing values.

Table 8.1 UNNORMALIZED AND NORMALIZED DIPOLE INDUCED VOLTAGE† DIFFERENCES FOR DELTA-GAP AND MAGNETIC-FRILL GENERATOR ($l = 0.47\lambda$, $a = 0.005\lambda$, $N = 21$)

Segment Number n	Delta-Gap Voltage		Magnetic Frill Generator Voltage			
	Unnormalized	Normalized	Unnormalized		Normalized	
1	0	0	1.11×10^{-4}	$-26.03°$	7.30×10^{-5}	$-26.03°$
2	0	0	1.42×10^{-4}	$-20.87°$	9.34×10^{-5}	$-20.87°$
3	0	0	1.89×10^{-4}	$-16.13°$	1.24×10^{-4}	$-16.13°$
4	0	0	2.62×10^{-4}	$-11.90°$	1.72×10^{-4}	$-11.90°$
5	0	0	3.88×10^{-4}	$-8.23°$	2.55×10^{-4}	$-8.23°$
6	0	0	6.23×10^{-4}	$-5.22°$	4.10×10^{-4}	$-5.22°$
7	0	0	1.14×10^{-3}	$-2.91°$	7.5×10^{-4}	$-2.91°$
8	0	0	2.52×10^{-3}	$-1.33°$	1.66×10^{-3}	$-1.33°$
9	0	0	7.89×10^{-3}	$-0.43°$	5.19×10^{-3}	$-0.43°$
10	0	0	5.25×10^{-2}	$-0.06°$	3.46×10^{-2}	$-0.06°$
11	1	1	1.52	0°	1.0	0°

†Voltage differences as defined here represent the product of the incident electric field at the center of each segment and the corresponding segment length.

8.4 MOMENT METHOD SOLUTION

Equations (8-22), (8-24), and (8-27) each has the form of

$$F(g) = h \tag{8-33}$$

where F is a known linear operator, h is a known excitation function, and g is the response function. For (8-22) F is an integrodifferential operator while for (8-24) and (8-27) it is an integral operator. The objective here is to determine g once F and h are specified.

INTEL-1045
U.S. Patent 7,151,430

While the inverse problem is often intractable in closed form, the linearity of the operator F makes a numerical solution possible. One technique, known as the Moment Method [7]–[14] requires that the unknown response function be expanded as a linear combination of N terms and written as

$$g(z') \simeq a_1 g_1(z') + a_2 g_2(z') + \cdots + a_N g_N(z') = \sum_{n=1}^{N} a_n g_n(z') \tag{8-34}$$

Each a_n is an unknown constant and each $g_n(z')$ is a known function usually referred to as a *basis* or *expansion* function. The domain of the $g_n(z')$ functions is the same as that of $g(z')$. Substituting (8-34) into (8-33) and using the linearity of the F operator reduces (8-33) to

$$\sum_{n=1}^{N} a_n F(g_n) = h \tag{8-35}$$

The basis functions g_n are chosen so that each $F(g_n)$ in (8-35) can be evaluated conveniently, preferably in closed form or at the very least numerically. The only task remaining then is to find the a_n unknown constants.

Expansion of (8-35) leads to one equation with N unknowns. It alone is not sufficient to determine the N unknown a_n ($n = 1, 2, \ldots, N$) constants. To resolve the N constants, it is necessary to have N linearly independent equations. This can be accomplished by evaluating (8-35) (e.g., applying boundary conditions) at N different points. This is referred to as *point-matching* (or *collocation*). Doing this, (8-35) takes the form of

$$\sum_{n=1}^{N} I_n F(g_n) = h_m, \qquad m = 1, 2, \ldots, N \tag{8-36}$$

In matrix form, (8-36) can be expressed as

$$[Z_{mn}][I_n] = [V_m] \tag{8-37}$$

where

$$Z_{mn} = F(g_n) \tag{8-37a}$$

$$I_n = a_n \tag{8-37b}$$

$$V_m = h_m \tag{8-37c}$$

The unknown coefficients a_n can be found by solving (8-37) using matrix inversion techniques, or

$$[I_n] = [Z_{mn}]^{-1}[V_m] \tag{8-38}$$

8.4.1 Basis Functions

One very important step in any numerical solution is the choice of basis functions. In general, one chooses as basis functions the set that has the ability to accurately represent and resemble the anticipated unknown function, while minimizing the computational effort required to employ it [28]–[30]. Do not choose basis functions with smoother properties than the unknown being represented.

Theoretically, there are many possible basis sets. However, only a limited number

INTEL-1045
U.S. Patent 7,151,430

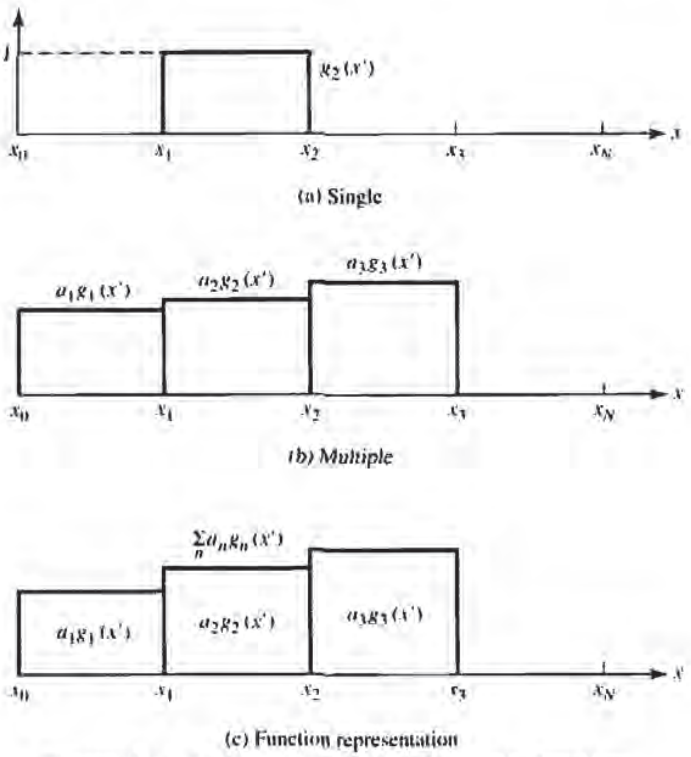


Figure 8.8 Piecewise constant subdomain functions.

are used in practice. These sets may be divided into two general classes. The first class consists of subdomain functions, which are nonzero only over a part of the domain of the function $g(x')$; its domain is the surface of the structure. The second class contains entire domain functions that exist over the entire domain of the unknown function. The entire domain basis function expansion is analogous to the well-known Fourier series expansion method.

A. Subdomain Functions

Of the two types of basis functions, subdomain functions are the most common. Unlike entire domain bases, they may be used without prior knowledge of the nature of the function that they must represent.

The subdomain approach involves subdivision of the structure into N nonoverlapping segments, as illustrated on the axis in Figure 8.8(a). For clarity, the segments are shown here to be collinear and of equal length, although neither condition is necessary. The basis functions are defined in conjunction with the limits of one or more of the segments.

Perhaps the most common of these basis functions is the conceptually simple piecewise constant, or "pulse" function, shown in Figure 8.8(a). It is defined by

Piecewise Constant

$$g_n(x') = \begin{cases} 1 & x'_{n-1} \le x' \le x'_n \\ 0 & \text{elsewhere} \end{cases} \tag{8-39}$$

INTEL-1045
U.S. Patent 7,151,430

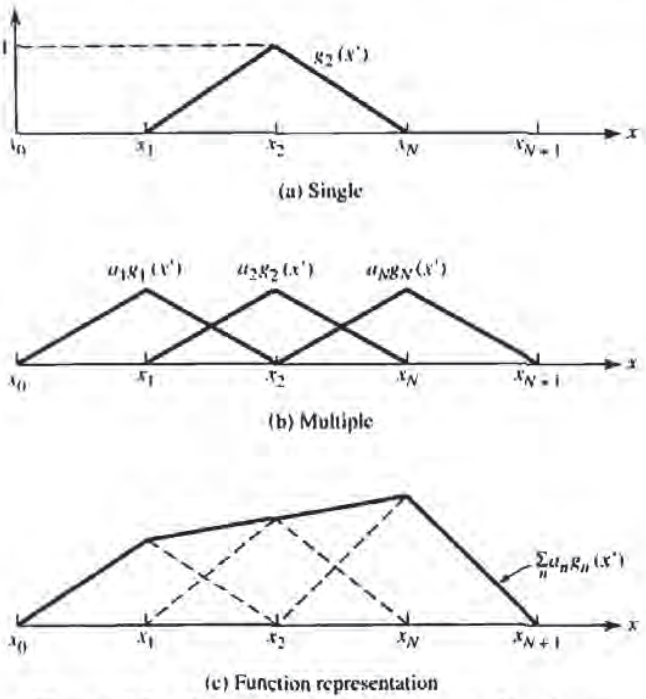


Figure 8.9 Piecewise linear subdomain functions.

Once the associated coefficients are determined, this function will produce a staircase representation of the unknown function, similar to that in Figures 8.8(b) and (c).

Another common basis set is the piecewise linear, or "triangle," functions seen in Figure 8.9(a). These are defined by

Piecewise Linear

$$g_n(x') = \begin{cases} \dfrac{x' - x'_{n-1}}{x'_n - x'_{n-1}} & x'_{n-1} \le x' \le x'_n \\ \dfrac{x'_{n+1} - x'}{x'_{n+1} - x'_n} & x'_n \le x' \le x'_{n+1} \\ 0 & \text{elsewhere} \end{cases} \tag{8-40}$$

and are seen to cover two segments, and overlap adjacent functions [Figure 8.9(b)]. The resulting representation [Figure 8.9(c)] is smoother than that for "pulses," but at the cost of increased computational complexity.

Increasing the sophistication of subdomain basis functions beyond the level of the "triangle" may not be warranted by the possible improvement in accuracy. However, there are cases where more specialized functions are useful for other reasons. For example, some integral operators may be evaluated without numerical integration when their integrands are multiplied by a $\sin(kx')$ or $\cos(kx')$ function, where x' is the variable of integration. In such examples, considerable advantages in computation time and resistance to errors can be gained by using basis functions like the piecewise sinusoid of Figure 8.10 or truncated cosine of Figure 8.11. These functions are defined by

INTEL-1045
U.S. Patent 7,151,430

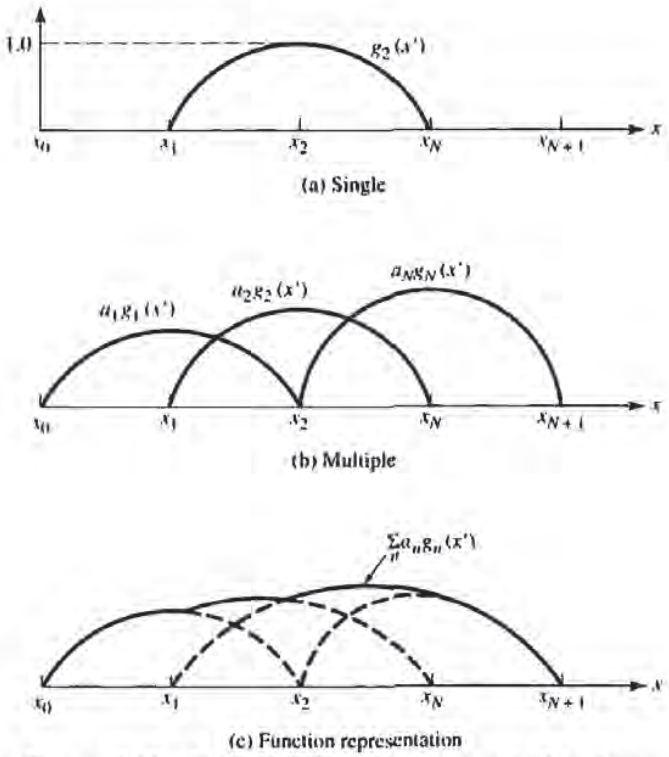


Figure 8.10 Piecewise sinusoids subdomain functions.

Piecewise Sinusoid

$$g_n(x') = \begin{cases} \dfrac{\sin[k(x' - x'_{n-1})]}{\sin[k(x'_n - x'_{n-1})]} & x'_{n-1} \le x' \le x'_n \\ \dfrac{\sin[k(x'_{n+1} - x')]}{\sin[k(x'_{n+1} - x'_n)]} & x'_n \le x' \le x'_{n+1} \\ 0 & \text{elsewhere} \end{cases} \tag{8-41}$$

Truncated Cosine

$$g_n(x') = \begin{cases} \cos\left[k\left(x' - \dfrac{x'_n - x'_{n-1}}{2}\right)\right] & x'_{n-1} \le x' \le x'_n \\ 0 & \text{elsewhere} \end{cases} \tag{8-42}$$

B. Entire Domain Functions

Entire domain basis functions, as their name implies, are defined and are nonzero over the entire length of the structure being considered. Thus no segmentation is involved in their use.

A common entire domain basis set is that of sinusoidal functions, where

Entire Domain

$$g_n(x') = \cos\left[\frac{(2n-1)\pi x'}{l}\right] \qquad -\frac{l}{2} \le x' \le \frac{l}{2} \tag{8-43}$$

INTEL-1045
U.S. Patent 7,151,430

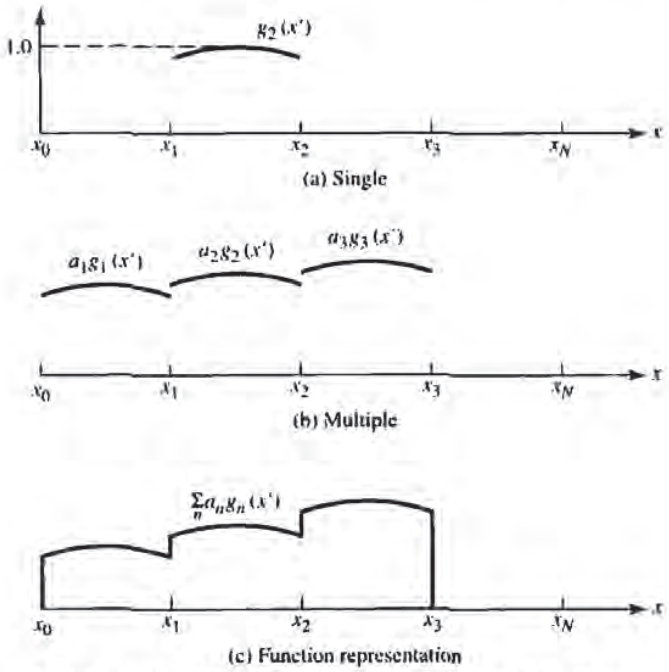


Figure 8.11 Truncated cosines subdomain functions.

Note that this basis set would be particularly useful for modeling the current distribution on a wire dipole, which is known to have primarily sinusoidal distribution. The main advantage of entire domain basis functions lies in problems where the unknown function is assumed *a priori* to follow a known pattern. Such entire-domain functions may render an acceptable representation of the unknown while using far fewer terms in the expansion of (8-34) than would be necessary for subdomain bases. Representation of a function by entire domain cosine and/or sine functions is similar to the Fourier series expansion of arbitrary functions.

Because we are constrained to use a finite number of functions (or modes, as they are sometimes called), entire domain basis functions usually have difficulty in modeling arbitrary or complicated unknown functions.

Entire domain basis functions, sets like (8-43), can be generated using Tschebyscheff, Maclaurin, Legendre, and Hermite polynomials, or other convenient functions.

8.4.2 Weighting (Testing) Functions

To improve the point-matching solution of (8-36), (8-37), or (8-38) an inner product $\langle w, g \rangle$ can be defined which is a scalar operation satisfying the laws of

$$\langle w, g \rangle = \langle g, w \rangle \tag{8-44a}$$

$$\langle bf + cg, w \rangle = b\langle f, w \rangle + c\langle g, w \rangle \tag{8-44b}$$

$$\langle g^*, g \rangle > 0 \quad \text{if } g \neq 0 \tag{8-44c}$$

$$\langle g^*, g \rangle = 0 \quad \text{if } g = 0 \tag{8-44d}$$

INTEL-1045
U.S. Patent 7,151,430

where b and c are scalars and the asterisk (*) indicates complex conjugation. A typical, but not unique, inner product is

$$\langle \mathbf{w}, \mathbf{g} \rangle = \iint_s \mathbf{w}^* \cdot \mathbf{g}\, ds \tag{8-45}$$

where the w's are the *weighting* (*testing*) functions and S is the surface of the structure being analyzed. Note that the functions w and g can be vectors. This technique is better known as the *Moment Method* or *Method of Moments* (MM) [7], [8].

The collocation (point-matching) method is a numerical technique whose solutions satisfy the electromagnetic boundary conditions (e.g., vanishing tangential electric fields on the surface of an electric conductor) only at discrete points. Between these points the boundary conditions may not be satisfied, and we define the deviation as a *residual* (e.g., residual $= \Delta E|_{\tan} = E\text{ (scattered)}|_{\tan} + E\text{ (incident)}|_{\tan} \neq 0$ on the surface of an electric conductor). For a half-wavelength dipole, a typical residual is shown in Figure 8.12(a) for pulse basis functions and point-matching and Figure 8.12(b) exhibits the residual for piecewise sinusoids-Galerkin method [31]. As expected, the pulse basis point-matching exhibits the most ill-behaved residual and the piecewise sinusoids-Galerkin method indicates an improved residual. To minimize the residual in such a way that its overall average over the entire structure approaches zero, the method of *weighted residuals* is utilized in conjunction with the inner product of (8-45). This technique, referred to as the *Moment Method* (MM), does not lead to a vanishing residual at every point on the surface of a conductor, but it forces the boundary conditions to be satisfied in an average sense over the entire surface.

To accomplish this, we define a set of N *weighting* (or testing) functions $\{w_m\} = w_1, w_2, \ldots, w_N$ in the domain of the operator F. Forming the inner product between each of these functions, (8-35) results in

$$\sum_{n=1}^{N} a_n \langle w_m, F(g_n) \rangle = \langle w_m, h \rangle \qquad m = 1, 2, \ldots, N \tag{8-46}$$

This set of N equations may be written in matrix form as

$$[F_{mn}]\,[a_n] = [h_m] \tag{8-47}$$

where

$$[F_{mn}] = \begin{bmatrix} \langle w_1, F(g_1) \rangle & \langle w_1, F(g_2) \rangle & \cdots \\ \langle w_2, F(g_1) \rangle & \langle w_2, F(g_2) \rangle & \\ \vdots & & \vdots \end{bmatrix} \tag{8-47a}$$

$$[a_n] = \begin{bmatrix} a_1 \\ a_2 \\ \vdots \\ a_N \end{bmatrix} \qquad [h_m] = \begin{bmatrix} \langle w_1, h \rangle \\ \langle w_2, h \rangle \\ \vdots \\ \langle w_N, h \rangle \end{bmatrix} \tag{8-47b}$$

The matrix of (8-47) may be solved for the a_n by inversion, and it can be written as

$$[a_n] = [F_{mn}]^{-1}[h_m] \tag{8-48}$$

The choice of weighting functions is important in that the elements of $\{w_n\}$ must be linearly independent, so that the N equations in (8-46) will be linearly independent [7]–[9], [29], [30]. Further, it will generally be advantageous to choose weighting functions that minimize the computations required to evaluate the inner product.

The condition of linear independence between elements and the advantage of

INTEL-1045
U.S. Patent 7,151,430

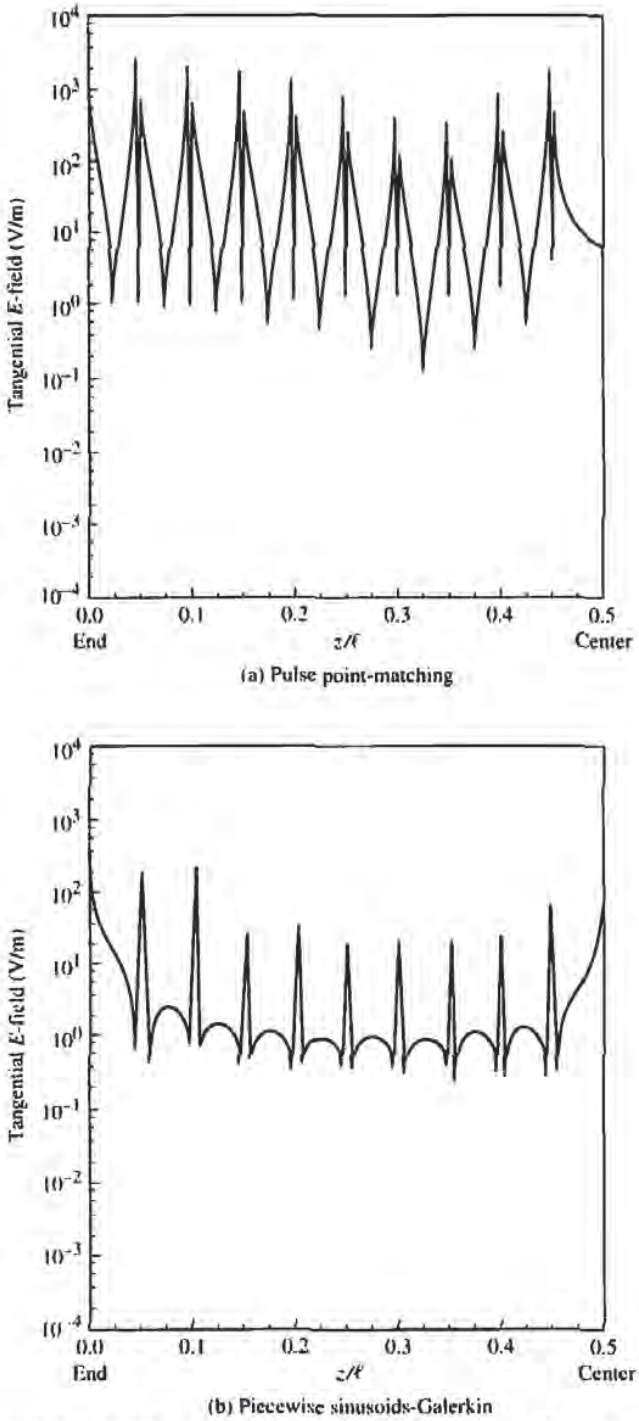


Figure 8.12 Tangential electric field on the conducting surface of a $\lambda/2$ dipole. (SOURCE: E. K. Miller and F. J. Deadrick. "Some computational aspects of thin-wire modeling" in *Numerical and Asymptotic Techniques in Electromagnetics.* 1975, Springer-Verlag.)

computational simplicity are also important characteristics of basis functions. Because of this, similar types of functions are often used for both weighting and expansion. A particular choice of functions may be to let the weighting and basis function be the same, that is, $w_n = g_n$. This technique is known as *Galerkin's method* [32].

INTEL-1045
U.S. Patent 7,151,430

It should be noted that there are N^2 terms to be evaluated in (8-47a). Each term usually requires two or more integrations; at least one to evaluate each $F(g_n)$ and one to perform the inner products of (8-45). When these integrations are to be done numerically, as is often the case, vast amounts of computation time may be necessary. There is, however, a unique set of weighting functions that reduce the number of required integrations. This is the set of Dirac delta weighting functions

$$[w_m] = [\delta(p - p_m)] = [\delta(p - p_1), \delta(p - p_2), \ldots] \tag{8-49}$$

where p specifies a position with respect to some reference (origin) and p_m represents a point at which the boundary condition is enforced. Using (8-45) and (8-49) reduces (8-46) to

$$\begin{aligned} \langle \delta(p - p_m), h \rangle &= \sum_n a_n \langle \delta(p - p_m), F(g_n) \rangle \quad m = 1, 2, \ldots, N \\ \iint_S \delta(p - p_m) h \, ds &= \sum_n a_n \iint_S \delta(p - p_m) F(g_n) \, ds \quad m = 1, 2, \ldots, N \\ h|_{p=p_m} &= \sum_n a_n F(g_n)|_{p=p_m} \quad m = 1, 2, \ldots, N \end{aligned} \tag{8-50}$$

Hence, the only remaining integrations are those specified by $F(g_n)$. This simplification may lead to solutions that would be impractical if other weighting functions were used. Physically, the use of Dirac delta weighting functions is seen as the relaxation of boundary conditions so that they are enforced only at discrete points on the surface of the structure, hence the name point-matching.

An important consideration when using point-matching is the positioning of the N points (p_m). While equally space points often yield good results, much depends on the basis functions used. When using subsectional basis functions in conjunction with point-matching, one match point should be placed on each segment (to maintain linear independence). Placing the points at the center of the segments usually produces the best results. It is important that a match point does not coincide with the "peak" of a triangle or a similar discontinuous function, where the basis function is not differentiably continuous. This may cause errors in some situations.

8.5 SELF IMPEDANCE

The input impedance of an antenna is a very important parameter, and it is used to determine the efficiency of the antenna. In Section 4.5 the real part of the impedance (referred either to the current at the feed terminals or to the current maximum) was found. At that time, because of mathematical complexities, no attempt was made to find the imaginary part (reactance) of the impedance. In this section the self impedance of a linear element will be examined using both the Integral Equation-Moment Method and the induced emf method. The real and imaginary parts of the impedance will be found using both methods.

8.5.1 Integral Equation-Moment Method

To use this method to find the self impedance of a dipole, the first thing to do is to solve the integral equation for the current distribution. This is accomplished using either Pocklington's Integral equation of (8-22) or (8-24) or Hallén's integral equation of (8-27). For Pocklington's integral equation you can use either the delta-gap voltage excitation of (8-28) or the magnetic frill model of (8-31) or (8-32). Hallén's integral equation is based on the delta-gap model of (8-28).

INTEL-1045
U.S. Patent 7,151,430

Once the current distribution is found, using either or both of the integral equations, then the self (input) impedance is determined using the ratio of the voltage to current, or

$$Z_{in} = \frac{V_{in}}{I_{in}} \tag{8-51}$$

A computer program MOMENT METHOD has been developed based on Pocklington's and Hallén's integral equations, and it is found at the end of this chapter. Pocklington's uses both the delta-gap and magnetic-frill models while Hallén's uses only the delta-gap feed model. Both, however, use piecewise constant subdomain functions and point-matching. The program computes the current distribution, normalized amplitude radiation pattern, and input impedance. The user must specify the *length of the wire, its radius (both in wavelengths), and the type of feed modeling* (delta-gap or magnetic-frill) and the number of segments.

To demonstrate the procedure and compare the results using the two-source modelings (delta-gap and magnetic-frill generator) for Pocklington's integral equation, an example is performed.

Example 8.4

Assume a center-fed linear dipole of $l = 0.47\lambda$ and $a = 0.005\lambda$. This is the same element of Example 8.3.

1. Determine the normalized current distribution over the length of the dipole using $N = 21$ segments to subdivide the length. Plot the current distribution.
2. Determine the input impedance using segments of $N = 7, 11, 21, 29, 41, 51, 61, 71$, and 79.

Use Pocklington's integrodifferential equation (8-24) with piecewise constant subdomain basis functions and point-matching to solve the problems, model the gap with one segment, and use both the delta-gap and magnetic-frill generator to model the excitation. Use (8-32) for the magnetic-frill generator. Because the current at the ends of the wire vanishes, the piecewise constant subdomain basis functions are not the most judicious choice. However, because of their simplicity, they are chosen here to illustrate the principles even though the results are not the most accurate. Assume that the characteristic impedance of the annular aperture is 50 ohms and the excitation voltage V_i is 1 V.

SOLUTION

1. The voltage distribution was found in Example 8.3, and it is listed in Table 8.1. The corresponding normalized currents obtained using (8-24) with piecewise constant pulse functions and point-matching technique for both the delta-gap and magnetic frill-generator are shown plotted in Figure 8.13(a). It is apparent that the two distributions are almost identical in shape, and they resemble that of the ideal sinusoidal current distribution which is more valid for very thin wires and very small gaps. The distributions obtained using Pocklington's integral equation do not vanish at the ends because of the use of piecewise constant subdomain basis functions.

INTEL-1045
U.S. Patent 7,151,430

Table 8.2 DIPOLE INPUT IMPEDANCE FOR DELTA-GAP AND MAGNETIC-FRILL GENERATOR USING POCKLINGTON'S INTEGRAL EQUATION ($l = 0.47\lambda$, $a = 0.005\lambda$)

N	Delta Gap	Magnetic Frill
7	$122.8 + j113.9$	$26.8 + j24.9$
11	$94.2 + j49.0$	$32.0 + j16.7$
21	$77.7 - j0.8$	$47.1 - j0.2$
29	$75.4 - j6.6$	$57.4 - j4.5$
41	$75.9 - j2.4$	$68.0 - j1.0$
51	$77.2 + j2.4$	$73.1 + j4.0$
61	$78.6 + j6.1$	$76.2 + j8.5$
71	$79.9 + j7.9$	$77.9 + j11.2$
79	$80.4 + j8.8$	$78.8 + j12.9$

2. The input impedances using both the delta-gap and the magnetic-frill generator are shown listed in Table 8.2. It is evident that the values begin to stabilize and compare favorably to each other once 61 or more segments are used.

To further illustrate the point on the variation of the current distribution on a dipole, it has been computed by Moment Method and plotted in Figure 8.13(b) for $l = \lambda/2$ and $l = \lambda$ for wire radii of a $= 10^{-5}\lambda$ and $10^{-3}\lambda$ where it is compared with that based on the sinusoidal distribution. It is apparent that the radius of the wire does not influence to a large extent the distribution of the $l = \lambda/2$ dipole. However it has a profound effect on the current distribution of the $l = \lambda$ dipole at and near the feed point. Therefore the input impedance of the $l = \lambda$ dipole is quite different for the three cases of Figure 8.13(b), since the zero current at the center of the sinusoidal distribution predicts an infinite impedance. In practice, the impedance is not infinite but is very large.

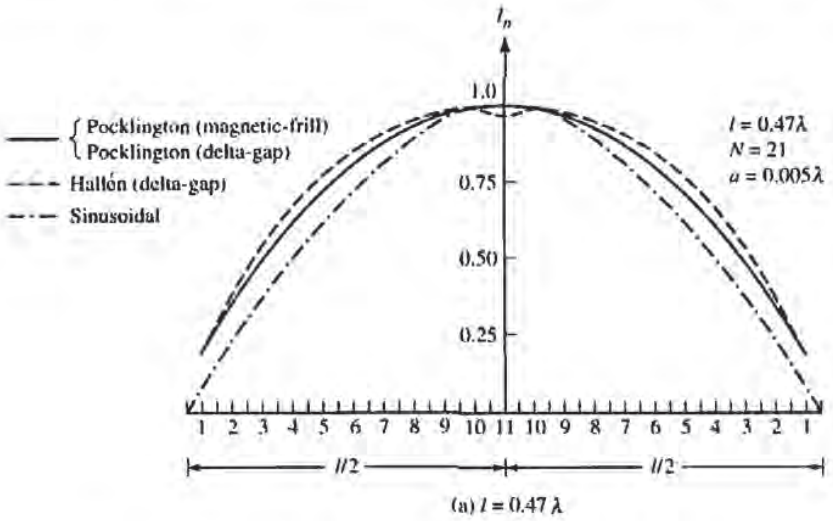
8.5.2 Induced EMF Method

The induced emf method is a classical method to compute the self and mutual impedances [1]–[6], [33]. The method is basically limited to straight, parallel and in echelon elements, and it is more difficult to account accurately for the radius of the wires as well as the gaps at the feeds. However it leads to closed form solutions which provide very good design data. From the analysis of the infinitesimal dipole in Section 4.2, it was shown that the imaginary part of the power density, which contributes to the imaginary power, is dominant in the near-zone of the element and becomes negligible in the far-field. Thus, near-fields of an antenna are required to find its input reactance.

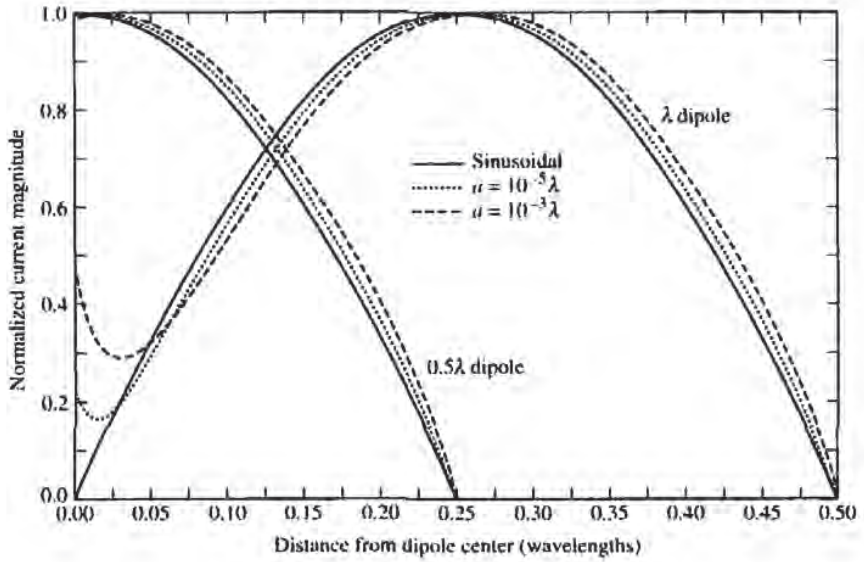
A. Near-Field of Dipole

In Chapter 4 the far-zone electric and magnetic fields radiated by a finite length dipole with a sinusoidal current distribution were found. The observations were restricted in the far-field in order to reduce the mathematical complexities. The expressions of these fields were used to derive the radiation resistance and the input resistance of the

INTEL-1045
U.S. Patent 7,151,430



(a) $l = 0.47\,\lambda$



(b) $l = \lambda/2$ and $l = \lambda$

Figure 8.13 Current distribution on a dipole antenna.

dipole. However, when the input reactance and/or the mutual impedance between elements are desired, the near-fields of the element must be known. It is the intent here to highlight the derivation.

The fields are derived based on the geometry of Figure 8.14. The procedure is identical to that used in Section 4.2.1 for the infinitesimal dipole. The major difference is that the integrations are much more difficult. To minimize long derivations involving complex integrations, only the procedure will be outlined and the final results will be given. The derivation is left as an end of the chapter problems. The details can also be found in the first edition of this book.

To derive the fields, the first thing is to specify the sinusoidal current distribution for a finite dipole which is that of (4-56). Once that is done, then the vector potential **A** of (4-2) is determined. Then the magnetic field is determined using (3-2a), or

INTEL-1045
U.S. Patent 7,151,430

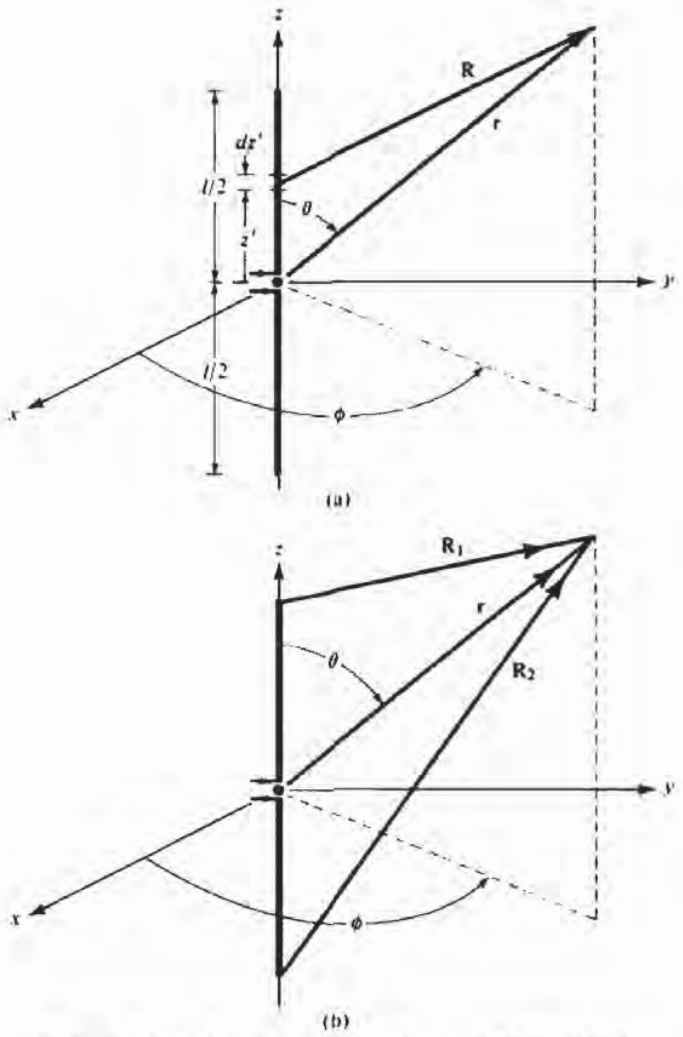


Figure 8.14 Dipole geometry for near-field analysis.

$$\mathbf{H} = \frac{1}{\mu}\nabla \times \mathbf{A} = -\hat{\mathbf{a}}_\phi \frac{1}{\mu}\frac{\partial A_z}{\partial \rho} \tag{8-52}$$

It is recommended that cylindrical coordinates are used. By following this procedure and after some lengthy analytical details, it can be shown by referring to Figure 8.14(b) that the magnetic field radiated by the dipole is

$$\mathbf{H} = \hat{\mathbf{a}}_\phi H_\phi = -\hat{\mathbf{a}}_\phi \frac{I_0}{4\pi j}\frac{1}{y}\left[e^{-jkR_1} + e^{-jkR_2} - 2\cos\left(\frac{kl}{2}\right)e^{-jkr}\right] \tag{8-53}$$

where

$$r = \sqrt{x^2 + y^2 + z^2} = \sqrt{\rho^2 + z^2} \tag{8-53a}$$

$$R_1 = \sqrt{x^2 + y^2 + \left(z - \frac{l}{2}\right)^2} = \sqrt{\rho^2 + \left(z - \frac{l}{2}\right)^2} \tag{8-53b}$$

$$R_2 = \sqrt{x^2 + y^2 + \left(z + \frac{l}{2}\right)^2} = \sqrt{\rho^2 + \left(z + \frac{l}{2}\right)^2} \tag{8-53c}$$

INTEL-1045
U.S. Patent 7,151,430

The corresponding electric field is found using Maxwell's equation of

$$\mathbf{E} = \frac{1}{j\omega\epsilon}\nabla \times \mathbf{H} \tag{8-54}$$

Once this is done, it can be shown that the electric field radiated by the dipole is

$$\mathbf{E} = \hat{\mathbf{a}}_\rho E_\rho + \hat{\mathbf{a}}_z E_z = -\hat{\mathbf{a}}_\rho \frac{1}{j\omega\epsilon}\frac{\partial H_\phi}{\partial z} + \hat{\mathbf{a}}_z \frac{1}{j\omega\epsilon}\frac{1}{\rho}\frac{\partial}{\partial \rho}(\rho H_\phi) \tag{8-55}$$

where

$$E_\rho = E_r = j\frac{\eta I_0}{4\pi y}\left[\left(z - \frac{l}{2}\right)\frac{e^{-jkR_1}}{R_1} + \left(z + \frac{l}{2}\right)\frac{e^{-jkR_2}}{R_2} - 2z\cos\left(\frac{kl}{2}\right)\frac{e^{-jkr}}{r}\right] \tag{8-55a}$$

$$E_z = -j\frac{\eta I_0}{4\pi}\left[\frac{e^{-jkR_1}}{R_1} + \frac{e^{-jkR_2}}{R_2} - 2\cos\left(\frac{kl}{2}\right)\frac{e^{-jkr}}{r}\right] \tag{8-55b}$$

It should be noted that the last term in (8-53), (8-55a), and (8-55b) vanishes when the overall length of the element is an integral number of odd half wavelengths ($l = n\lambda/2$, $n = 1, 3, 5, \ldots$) because $\cos(kl/2) = \cos(n\pi/2) = 0$ for $n = 1, 3, 5, \ldots$.

The fields of (8-53), (8-55a), and (8-55b) were derived assuming a zero radius wire. In practice all wire antennas have a finite radius which in most cases is very small electrically (typically less than $\lambda/200$). Therefore the fields of (8-53), (8-55a), and (8-55b) are good approximations for finite, but small, radius dipoles.

B. Self Impedance

The technique, which is used in this chapter to derived closed form expressions for the self- and driving point impedances of finite linear dipoles, is known as the *induced emf method*. The general approach of this method is to form the Poynting vector using (8-53), (8-55a), and (8-55b), and to integrate it over the surface that coincides with the surface of the antenna (linear dipole) itself. However, the same results can be obtained using a slightly different approach, as will be demonstrated here. The expressions derived using this method are more valid for small radii dipoles. Expressions, which are more accurate for larger radii dipoles, were derived in the previous section based on the Integral Equation-Moment Method.

To find the input impedance of a linear dipole of finite length and radius, shown in Figure 8.15, the tangential electric field component on the surface of the wire is needed. This was derived previously and is represented by (8-55b). Based on the current distribution and tangential electric field along the surface of the wire, the induced potential developed at the terminals of the dipole based on the maximum current is given by

$$\begin{aligned} V_m &= \int_{-\ell/2}^{+\ell/2} dV_m \\ &= -\frac{1}{I_m}\int_{-\ell/2}^{+\ell/2} I_z(\rho = a, z = z')E_z(\rho = a, z = z')\,dz' \end{aligned} \tag{8-56}$$

INTEL-1045
U.S. Patent 7,151,430

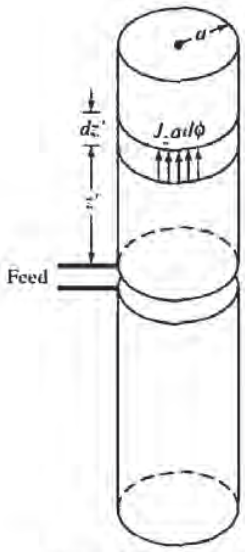


Figure 8.15 Uniform linear current density over cylindrical surface of wire.

where I_m is the maximum current. The input impedance (*referred to at the current maximum* I_m) is defined as

$$Z_{in} = \frac{V_m}{I_m} \tag{8-57}$$

and can be expressed using (8-56) as

$$Z_{in} = -\frac{1}{I_m^2}\int_{-\ell/2}^{\ell/2} I_z(\rho = a, z = z')E_z(\rho = a, z = z')\,dz' \tag{8-57a}$$

Equation (8-57a) can also be obtained by forming the complex power density, integrating it over the surface of the antenna, and then relating the complex power to the terminal and induced voltages [2]. The integration can be performed either over the gap at the terminals or over the surface of the conducting wire.

For a wire dipole, the total current I_z is uniformly distributed around the surface of the wire, and it forms a linear current sheet J_z. The current is concentrated primarily over a very small thickness of the conductor, as shown in Figure 8.15, and it is given, based on (4-56), by

$$I_z = 2\pi a J_z = I_m \sin\left[k\left(\frac{\ell}{2} - |z'|\right)\right] \tag{8-58}$$

Therefore (8-57a) can be written as

$$Z_{in} = -\frac{1}{I_m}\int_{-\ell/2}^{\ell/2} \sin\left[k\left(\frac{\ell}{2} - |z'|\right)\right] E_z(\rho = a, z = z')\,dz' \tag{8-59}$$

For simplicity, it is assumed that the E-field produced on the surface of the wire by a current sheet is the same as if the current were concentrated along a filament placed along the axis of the wire. Then the E-field used in (8-59) is the one obtained along a line parallel to the wire at a distance $\rho = a$ from the filament.

Letting $I_m = I_0$ and substituting (8-55b) into (8-59) it can be shown, after some

INTEL-1045
U.S. Patent 7,151,430

lengthy but straightforward manipulations, that the real and imaginary parts of the input impedance (referred to at the *current maximum*) can be expressed as

$$R_r = R_m = \frac{\eta}{2\pi}\{C + \ln(kl) - C_i(kl) + \frac{1}{2}\sin(kl)[S_i(2kl) - 2S_i(kl)] + \frac{1}{2}\cos(kl)[C + \ln(kl/2) + C_i(2kl) - 2C_i(kl)]\} \tag{8-60a}$$

$$X_m = \frac{\eta}{4\pi}\left\{2S_i(kl) + \cos(kl)[2S_i(kl) - S_i(2kl)] - \sin(kl)\left[2C_i(kl) - C_i(2kl) - C_i\left(\frac{2ka^2}{l}\right)\right]\right\} \tag{8-60b}$$

where $S_i(x)$ and $C_i(x)$ are the sine and cosine integrals of Appendix III. Equation (8-60a) is identical to (4-70). In deriving (8-60a) it was assumed that the radius of the wire is negligible (in this case set to zero), and it has little effect on the overall answer. This is a valid assumption provided $l \gg a$, and it has been confirmed by other methods.

The input resistance and input reactance (*referred to at the current at the input terminals*) can be obtained by a transfer relation given by (4-79), or

$$R_{in} = \left(\frac{I_0}{I_{in}}\right)^2 R_r = \frac{R_r}{\sin^2(kl/2)} \tag{8-61a}$$

$$X_{in} = \left(\frac{I_0}{I_{in}}\right)^2 X_m = \frac{X_m}{\sin^2(kl/2)} \tag{8-61b}$$

For a small dipole the input reactance is given by [34]

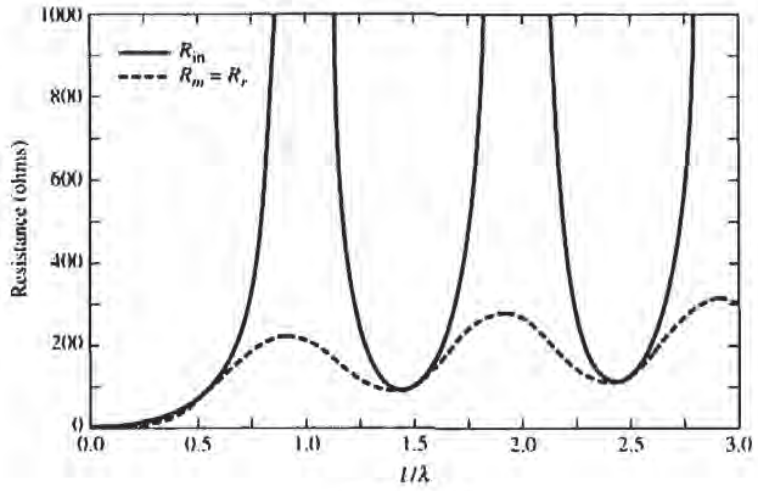
$$X_{in} = X_m = -120\frac{[\ln(l/2a) - 1]}{\tan(kl/2)} \tag{8-62}$$

while its input resistance and radiation resistance are given by (4-37). Plots of the self impedance, both resistance and reactance, based on (8-60a), (8-60b) and (8-61a), (8-61b) for $0 \le l \le 3\lambda$ are shown in Figures 8.16(a,b). The radius of the wire is $10^{-5}\lambda$. It is evident that when the length of the wire is multiples of a wavelength the resistances and reactances become infinite; in practice they are large.

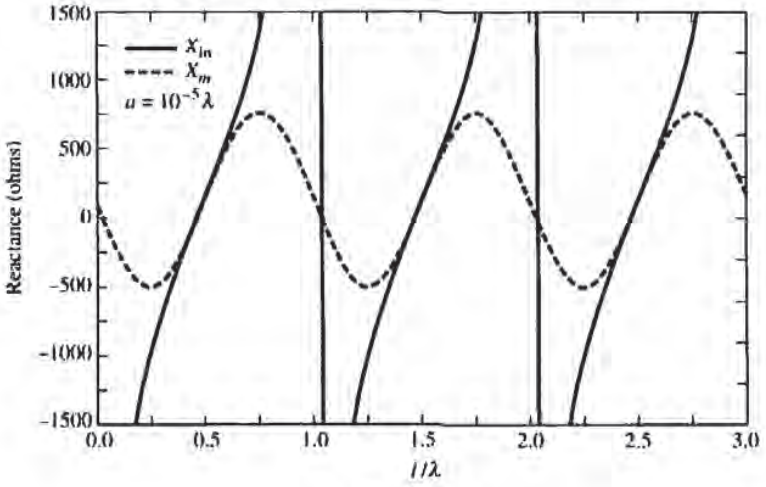
Ideally the radius of the wire does not affect the input resistance, as is indicated by (8-60a). However in practice it does have an effect, although it is not as significant as it is for the input reactance. To examine the effect the radius has on the values of the reactance, its values as given by (8-60) have been plotted in Figure 8.17 for $a = 10^{-5}\lambda$, $10^{-4}\lambda$, $10^{-3}\lambda$, and $10^{-2}\lambda$. The overall length of the wire is taken to be $0 < l \le 3\lambda$. It is apparent that the reactance can be reduced to zero provided the overall length is slightly less than $n\lambda/2$, $n = 1, 3, \ldots$, or slightly greater than $n\lambda/2$, $n = 2, 4, \ldots$. This is commonly done in practice for $l \simeq \lambda/2$ because the input resistance is close to 50 ohms, an almost ideal match for the widely used 50-ohm lines. For small radii, the reactance for $l = \lambda/2$ is equal to 42.5 ohms.

From (8-60b) it is also evident that when $l = n\lambda/2$, $n = 1, 2, 3, \ldots$, the terms within the last bracket do not contribute because $\sin(kl) = \sin(n\pi) = 0$. Thus for dipoles whose overall length is an integral number of half-wavelengths, the radius

INTEL-1045
U.S. Patent 7,151,430



(a) Resistance



(b) Reactance

Figure 8.16 Self-resistance and self-reactance of dipole antenna with wire radius of $10^{-5}\,\lambda$.

has no effect on the antenna reactance. This is illustrated in Figure 8.17 by the intersection points of the curves.

Example 8.5

Using the induced emf method, compute the input reactance for a linear dipole whose lengths are $n\lambda/2$, where $n = 1 - 6$.

SOLUTION

The input reactance for a linear dipole based on the induced emf method is given by (8-60b) whose values are equal to 42.5 for $\lambda/2$, 125.4 for λ, 45.5 for $3\lambda/2$, 133.1 for 2λ, 46.2 for $5\lambda/2$, and 135.8 for 3λ.

INTEL-1045
U.S. Patent 7,151,430

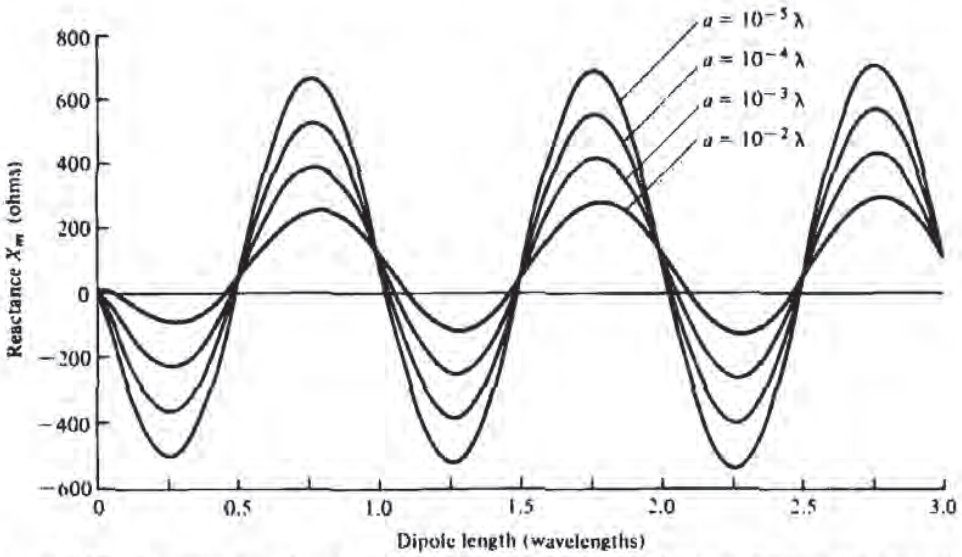


Figure 8.17 Reactance (referred to the current maximum) of linear dipole with sinusoidal current distribution for different wire radii.

8.6 MUTUAL IMPEDANCE BETWEEN LINEAR ELEMENTS

In the previous section, the input impedance of a linear dipole was derived when the element was radiating into an unbounded medium. The presence of an obstacle, which could be another element, would alter the current distribution, the field radiated, and in turn the input impedance of the antenna. Thus the antenna performance depends not only on its own current but also on the current of neighboring elements. For resonant elements with no current excitation of their own, there could be a substantial current induced by radiation from another source. These are known as parasitic elements, as in the case of a Yagi-Uda antenna, and play an important role in the overall performance of the entire antenna system. The antenna designer, therefore, must take into account the interaction and mutual effects between elements. The input impedance of the antenna in the presence of the other elements or obstacles, which will be referred to as *driving-point impedance*, depends upon the self impedance (input impedance in the absence of any obstacle or other element) and the mutual impedance between the driven element and the other obstacles or elements.

To simplify the analysis, it is assumed that the antenna system consists of two elements. The system can be represented by a two-port (four-terminal) network, as shown in Figure 8.18, and by the voltage-current relations

$$\left.\begin{aligned} V_1 &= Z_{11}I_1 + Z_{12}I_2 \\ V_2 &= Z_{21}I_1 + Z_{22}I_2 \end{aligned}\right\} \tag{8-63}$$

where

$$Z_{11} = \left.\frac{V_1}{I_1}\right|_{I_2=0} \tag{8-63a}$$

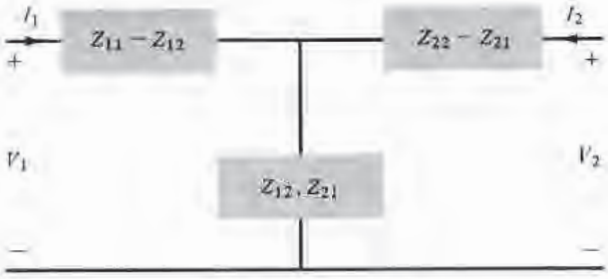
is the input impedance at port #1 with port #2 open-circuited,

$$Z_{12} = \left.\frac{V_1}{I_2}\right|_{I_1=0} \tag{8-63b}$$

INTEL-1045
U.S. Patent 7,151,430



(a) Two-port network



(b) T-network equivalent

Figure 8.18 Two-port network and its *T*-equivalent.

is the mutual impedance at port #1 due to a current at port #2 (with port #1 open-circuited),

$$Z_{21} = \left.\frac{V_2}{I_1}\right|_{I_2=0} \tag{8-63c}$$

is the mutual impedance at port #2 due to a current in port #1 (with port #2 open-circuited),

$$Z_{22} = \left.\frac{V_2}{I_2}\right|_{I_1=0} \tag{8-63d}$$

is the input impedance at port #2 with port #1 open-circuited. For a reciprocal network, $Z_{12} = Z_{21}$.

The impedances Z_{11} and Z_{22} are the input impedances of antennas 1 and 2, respectively, when each is radiating in an unbounded medium. The presence of another element modifies the input impedance and the extent and nature of the effects depends upon (1) the antenna type, (2) the relative placement of the elements, and (3) the type of feed used to excite the elements.

Equation (8-63) can also be written as

$$Z_{1d} = \frac{V_1}{I_1} = Z_{11} + Z_{12}\left(\frac{I_2}{I_1}\right) \tag{8-64a}$$

$$Z_{2d} = \frac{V_2}{I_2} = Z_{22} + Z_{21}\left(\frac{I_1}{I_2}\right) \tag{8-64b}$$

Z_{1d} and Z_{2d} represent the driving point impedances of antennas 1 and 2, respectively. Each driving point impedance depends upon the current ratio I_1/I_2, the mutual impedance, and the self-input impedance (when radiating into an unbounded medium). When attempting to match any antenna, it is the driving point impedance that must be matched. It is, therefore, apparent that the mutual impedance plays an important role in the performance of an antenna and should be investigated. However, the

INTEL-1045
U.S. Patent 7,151,430

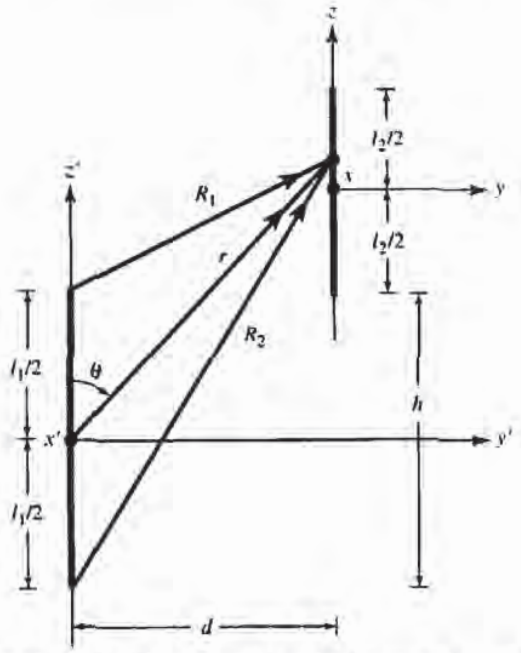


Figure 8.19 Dipole positioning for mutual coupling.

analysis associated with it is usually quite complex and only simplified models can be examined with the induced emf method. Integral Equation-Moment Method techniques can be used for more complex geometries, including skewed arrangements of elements.

Referring to Figure 8.19, the induced open-circuit voltage in antenna 2, *referred to its current at the input terminals*, due to radiation from antenna 1 is given by

$$V_{21} = -\frac{1}{I_{2i}}\int_{-l_2/2}^{l_2/2} E_{z21}(z')I_2(z')\,dz' \tag{8-65}$$

where

$E_{z21}(z')$ = E-field component radiated by antenna 1, which is parallel to antenna 2
$I_2(z')$ = current distribution along antenna 2

Therefore the mutual impedance of (8-63c), (referred to at the *input current* I_{1i} *of antenna 1*), is expressed as

$$Z_{21i} = \frac{V_{21}}{I_{1i}} = -\frac{1}{I_{1i}I_{2i}}\int_{-l_2/2}^{l_2/2} E_{z21}(z')I_2(z')\,dz' \tag{8-66}$$

8.6.1 Integral Equation-Moment Method

To use this method to find the mutual impedance based on (8-66), an integral equation must be formed to find E_{z21}, which is the field radiated by antenna 1 at any point on antenna 2. This integral equation must be a function of the unknown current on antenna 1, and it can be derived using a procedure similar to that used to form Pocklington's Integral Equation of (8-22) or (8-24), or Hallén's Integral Equation of (8-27). The unknown current of antenna 1 can be represented by a series of finite

INTEL-1045
U.S. Patent 7,151,430

number of terms with N unknown coefficients and a set of known (chosen) basis functions. The current $I_2(z)$ must also be expanded into a finite series of N terms with N unknown coefficients and a set of N chosen basis functions. Once each of them is formulated, then they can be used interactively to reduce (8-66) into an $N \times N$ set of linearly independent equations to find the mutual impedance.

To accomplish this requires a lengthy formulation, computer programming, and usually a digital computer. The process usually requires numerical integrations or special functions for the evaluation of the impedance matrices of E_{z21} and the integral of (8-66). There are national computer codes, such as the Numerical Electromagnetics Code (NEC) and the simplified version Mini Numerical Electromagnetics Code (MININEC), for the evaluation of the radiation characteristics, including impedances, of wire antennas [35]–[37]. Both of these are based on an Integral Equation-Moment Method formulation. Information concerning these two codes follows. There are other codes; however, these two seem to be the most popular, especially for wire type antennas.

Another procedure that has been suggested to include mutual effects in arrays of linear elements is to use a convergent iterative algorithm [38], [39]. This method can be used in conjunction with a calculator [38], and it has been used to calculate impedances, patterns and directivities of arrays of dipoles [39].

A. Numerical Electromagnetics Code (NEC)

The Numerical Electromagnetics Code (NEC) is a user-oriented program developed at Lawrence Livermore Laboratory. It is a moment method code for analyzing the interaction of electromagnetic waves with arbitrary structures consisting of conducting wires and surfaces. It combines an integral equation for smooth surfaces with one for wires to provide convenient and accurate modeling for a wide range of applications. The code can model nonradiating networks and transmission lines, perfect and imperfect conductors, lumped element loading, and perfect and imperfect conducting ground planes. It uses the electric field integral equation (EFIE) for thin wires and the magnetic field integral equation (MFIE) for surfaces. The excitation can be either an applied voltage source or an incident plane wave. The program computes induced currents and charges, near- and far-zone electric and magnetic fields, radar cross section, impedances or admittances, gain and directivity, power budget, and antenna-to-antenna coupling.

B. Mini-Numerical Electromagnetics Code (MININEC)

The Mini-Numerical Electromagnetics Code (MININEC) [36], [37] is a user-oriented compact version of the NEC developed at the Naval Ocean Systems Center (NOSC). It is also a moment method code, but coded in BASIC, and has retained the most frequently used options of the NEC. It is intended to be used in mini, micro, and personal computers, as well as work stations, and it is most convenient to analyze wire antennas. It computes currents, and near- and far-field patterns. It also optimizes the feed excitation voltages that yield desired radiation patterns.

Information concerning the NEC and MININEC, and their availability, can be directed to:

Professor Richard W. Adler
Naval Postgraduate School
Code 62 AB
Monterey, California 93943

INTEL-1045
U.S. Patent 7,151,430

8.6.2 Induced EMF Method

The induced emf method is also based on (8-66) except that $I_2(z')$ is assumed to be the ideal current distribution of (4-56) or (8-58) while $E_{z21}(z')$ is the electric field of (8-55b). Using (8-58) and (8-55b), we can express (8-66) as

$$Z_{21i} = \frac{V_{21}}{I_{1i}} = j\frac{\eta I_{1m} I_{2m}}{4\pi I_{1i} I_{2i}} \int_{-l_2/2}^{l_2/2} \sin\left[k\left(\frac{l_2}{2} - |z'|\right)\right]\left[\frac{e^{-jkR_1}}{R_1} + \frac{e^{-jkR_2}}{R_2} - 2\cos\left(k\frac{l_1}{2}\right)\frac{e^{-jkr}}{r}\right] dz' \tag{8-67}$$

where r, R_1, and R_2 are given, respectively, by (8-53a), (8-53b) and (8-53c) but with $y = d$ and $l = l_1$. I_{1m}, I_{2m} and I_{1i}, I_{2i} represent, respectively, the maximum and input currents for antennas 1 and 2. By referring each of the maximum currents to those at the input using (4-78) and assuming free space, we can write (8-67) as

$$Z_{21i} = j\frac{30}{\sin\left(\frac{kl_1}{2}\right)\sin\left(\frac{kl_2}{2}\right)} \int_{-l_2/2}^{l_2/2} \sin\left[k\left(\frac{l_2}{2} - |z'|\right)\right]\left[\frac{e^{-jkR_1}}{R_1} + \frac{e^{-jkR_2}}{R_2} - 2\cos\left(k\frac{l_1}{2}\right)\frac{e^{-jkr}}{r}\right] dz' \tag{8-68}$$

The mutual impedance referred to the current maxima is related to that at the input of (8-68) by

$$Z_{21m} = Z_{21i} \sin\left(\frac{kl_1}{2}\right)\sin\left(\frac{kl_2}{2}\right) \tag{8-69}$$

which for identical elements ($l_1 = l_2 = l$) reduces to

$$Z_{21m} = Z_{21i} \sin^2\left(\frac{kl}{2}\right) \tag{8-70}$$

whose real and imaginary parts are related by

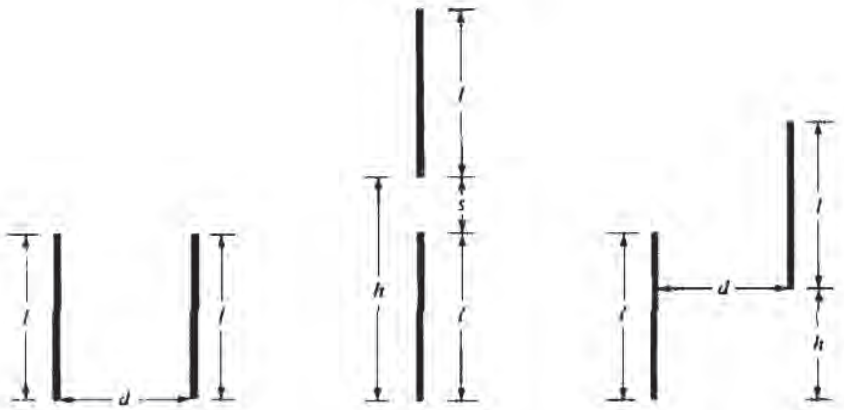
$$R_{21m} = R_{21i} \sin^2\left(\frac{kl}{2}\right) \tag{8-70a}$$

$$X_{21m} = X_{21i} \sin^2\left(\frac{kl}{2}\right) \tag{8-70b}$$

For a two-element array of linear dipoles, there are three classic configurations for which closed-form solutions for (8-68), in terms of sine and cosine integrals, are obtained [33]. These are shown in Figure 8.20, and they are referred to as the *side-by-side* [Fig. 8.20(a)], *collinear* [Fig. 8.20(b)], and *parallel-in-echelon* [Fig. 8.20(c)]. For two identical elements (each with *odd* multiples of $\lambda/2$, $l = n\lambda/2$, $n = 1, 3, 5, \ldots$) (8-70) reduces for each arrangement to the expressions that follow. Expressions for linear elements of any length are much more complex and can be found in [33].

A computer program referred to as SELF AND MUTUAL IMPEDANCES, based on (8-71a)–(8-73i), is included at the end of the chapter.

INTEL-1045
U.S. Patent 7,151,430



(a) Side-by-side (b) Collinear (c) Parallel in echelon

Figure 8.20 Dipole configuration of two identical elements for mutual impedance computations.

Side-by-Side Configuration [Figure 8.20(a)]

$$R_{21m} = \frac{\eta}{4\pi}[2C_i(u_0) - C_i(u_1) - C_i(u_2)] \tag{8-71a}$$

$$X_{21m} = -\frac{\eta}{4\pi}[2S_i(u_0) - S_i(u_1) - S_i(u_2)] \tag{8-71b}$$

$$u_0 = kd \tag{8-71c}$$

$$u_1 = k(\sqrt{d^2 + l^2} + l) \tag{8-71d}$$

$$u_2 = k(\sqrt{d^2 + l^2} - l) \tag{8-71e}$$

Collinear Configuration [Figure 8.20(b)]

$$R_{21m} = -\frac{\eta}{8\pi}\cos(v_0)[-2C_i(2v_0) + C_i(v_2) + C_i(v_1) - \ln(v_3)] + \frac{\eta}{8\pi}\sin(v_0)[2S_i(2v_0) - S_i(v_2) - S_i(v_1)] \tag{8-72a}$$

$$X_{21m} = -\frac{\eta}{8\pi}\cos(v_0)[2S_i(2v_0) - S_i(v_2) - S_i(v_1)] + \frac{\eta}{8\pi}\sin(v_0)[2C_i(2v_0) - C_i(v_2) - C_i(v_1) - \ln(v_3)] \tag{8-72b}$$

$$v_0 = kh \tag{8-72c}$$

$$v_1 = 2k(h + l) \tag{8-72d}$$

$$v_2 = 2k(h - l) \tag{8-72e}$$

$$v_3 = (h^2 - l^2)/h^2 \tag{8-72f}$$

INTEL-1045
U.S. Patent 7,151,430

Parallel-in-Echelon Configuration [Figure 8.20(c)]

$$R_{21m} = -\frac{\eta}{8\pi}\cos(w_0)[-2C_i(w_1) - 2C_i(w_1') + C_i(w_2) + C_i(w_2') + C_i(w_3) + C_i(w_3')] + \frac{\eta}{8\pi}\sin(w_0)[2S_i(w_1) - 2S_i(w_1') - S_i(w_2) + S_i(w_2') - S_i(w_3) + S_i(w_3')] \tag{8-73a}$$

$$X_{21m} = -\frac{\eta}{8\pi}\cos(w_0)[2S_i(w_1) + 2S_i(w_1') - S_i(w_2) - S_i(w_2') - S_i(w_3) - S_i(w_3')] + \frac{\eta}{8\pi}\sin(w_0)[2C_i(w_1) - 2C_i(w_1') - C_i(w_2) + C_i(w_2') - C_i(w_3) + C_i(w_3')] \tag{8-73b}$$

$$w_0 = kh \tag{8-73c}$$

$$w_1 = k(\sqrt{d^2 + h^2} + h) \tag{8-73d}$$

$$w_1' = k(\sqrt{d^2 + h^2} - h) \tag{8-73e}$$

$$w_2 = k[\sqrt{d^2 + (h - l)^2} + (h - l)] \tag{8-73f}$$

$$w_2' = k[\sqrt{d^2 + (h - l)^2} - (h - l)] \tag{8-73g}$$

$$w_3 = k[\sqrt{d^2 + (h + l)^2} + (h + l)] \tag{8-73h}$$

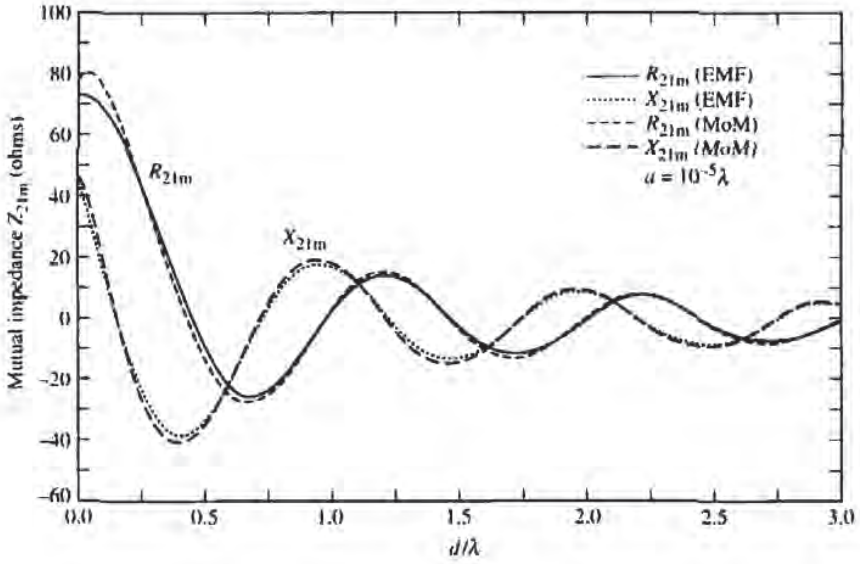
$$w_3' = k[\sqrt{d^2 + (h + l)^2} - (h + l)] \tag{8-73i}$$

The mutual impedance, referred to the current maximum, based on the induced emf method of a side-by-side and a collinear arrangement of two half-wavelength dipoles is shown plotted in Figure 8.21. It is apparent that the side-by-side arrangement exhibits larger mutual effects since the antennas are placed in the direction of maximum radiation. The data is compared with those based on the Moment Method/NEC [35] using a wire with a radius of $10^{-5}\lambda$. A very good agreement is indicated between the two sets because a wire with a radius of $10^{-5}\lambda$ for the MM/NEC is considered very thin. Variations as a function of the radius of the wire for both the side-by-side and collinear arrangements using the MM/NEC are shown, respectively, in Figures 8.22(a,b). Similar sets of data were computed for the parallel-in-echelon arrangement of Figure 8.20(c), and they are shown, respectively, in Figures 8.23(a) and 8.23(b) for $d = \lambda/4$, $0 \le h \le \lambda$ and $h = \lambda/2$, $0 < d < \lambda$ for wire radii of $10^{-5}\lambda$. Again a very good agreement between the induced emf and Moment Method/NEC data is indicated.

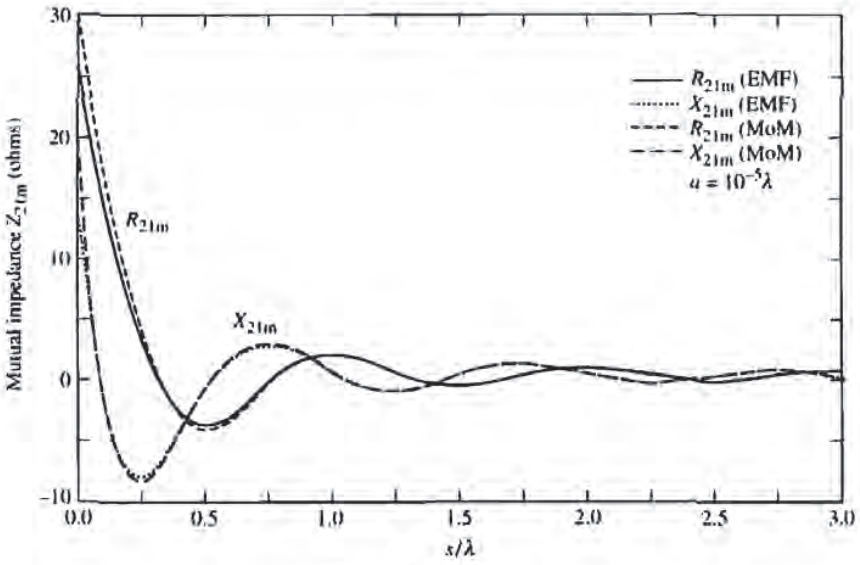
Example 8.6

Two identical linear half-wavelength dipoles are placed in a side-by-side arrangement, as shown in Figure 8.20(a). Assuming that the separation between the elements is $d = 0.35\lambda$, find the driving point impedance of each.

INTEL-1045
U.S. Patent 7,151,430



(a) Side-by-side



(b) Collinear

Figure 8.21 Mutual impedance of two side-by-side and collinear $\lambda/2$ dipoles using the moment method and induced emf method.

SOLUTION

Using (8-64a)

$$Z_{1d} = \frac{V_1}{I_1} = Z_{11} + Z_{12}\left(\frac{I_2}{I_1}\right)$$

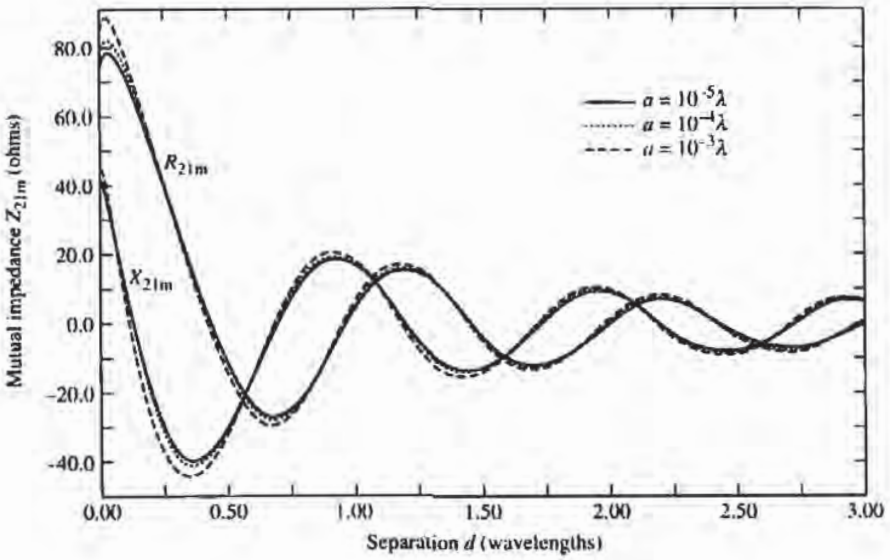
Since the dipoles are identical, $I_1 = I_2$. Thus

$$Z_{1d} = Z_{11} + Z_{12}$$

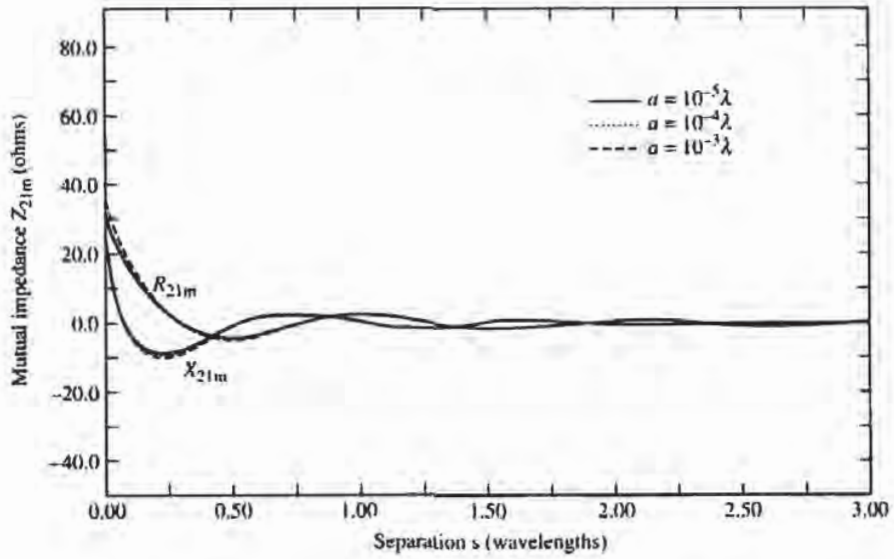
From Figure 8.21(a)

$$Z_{12} = 25 - j38$$

INTEL-1045
U.S. Patent 7,151,430



(a) Side-by-side



(b) Collinear

Figure 8.22 Variations of mutual impedance as a function of wire radius for side-by-side and collinear λ/2 dipole arrangements.

Since

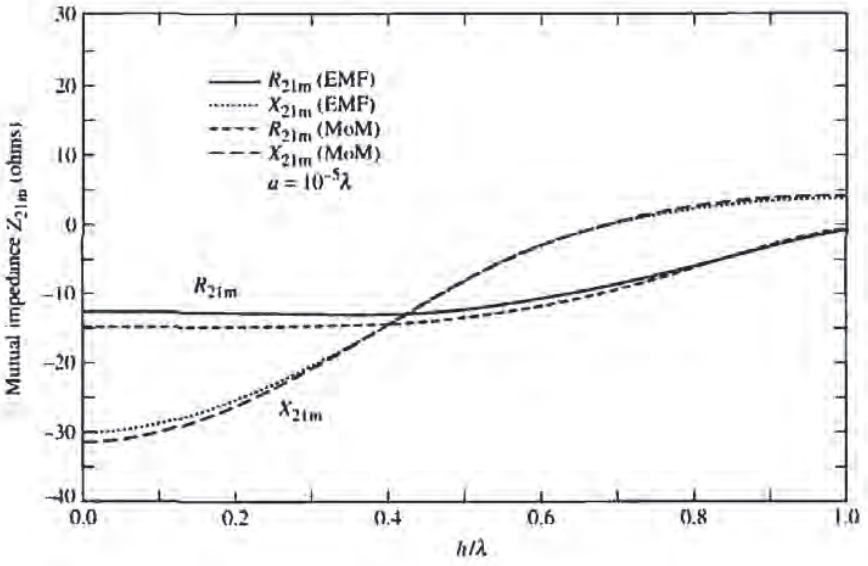
$$Z_{11} = 73 + j42.5$$

Z_{1d} reduces to

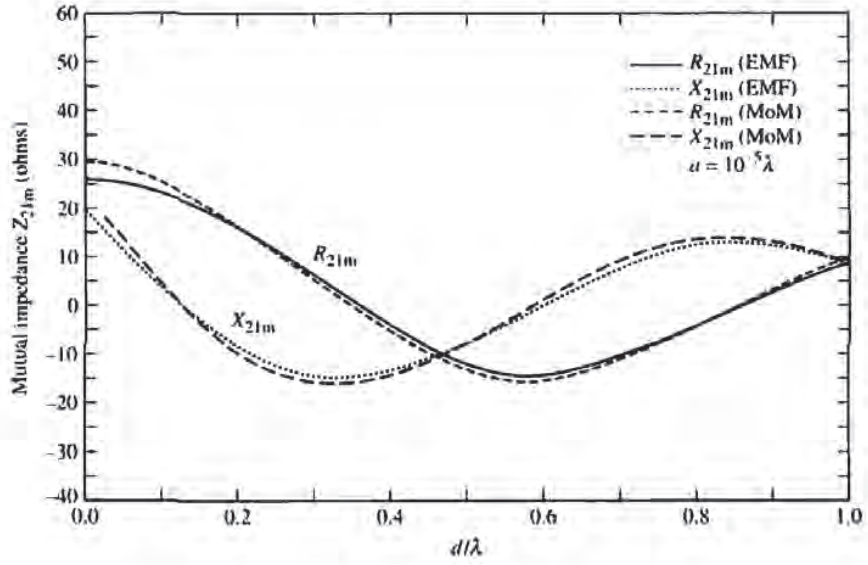
$$Z_{1d} \simeq 98 + j4.5$$

which is also equal to Z_{2d} of (8-64b).

INTEL-1045
U.S. Patent 7,151,430



(a) $d = 0.5\lambda$



(b) $h = 0.5\lambda$

Figure 8.23 Mutual impedance for two parallel-in-echelon λ/2 dipoles with wire radii of 10^{-5} λ.

As discussed in Chapter 2, Section 2.13, maximum power transfer between the generator and the transmitting antenna occurs when their impedances are conjugate-matched. The same is necessary for the receiver and receiving antenna. This ensures maximum power transfer between the transmitter and receiver, when there is no interaction between the antennas. In practice, the input impedance of one antenna depends on the load connected to the other antenna. Under those conditions, the matched loads and maximum coupling can be computed using the Linville method [40], which is used in rf amplifier design. This technique has been incorporated into the NEC [35]. Using this method, maximum coupling is computed using [35]

INTEL-1045
U.S. Patent 7,151,430

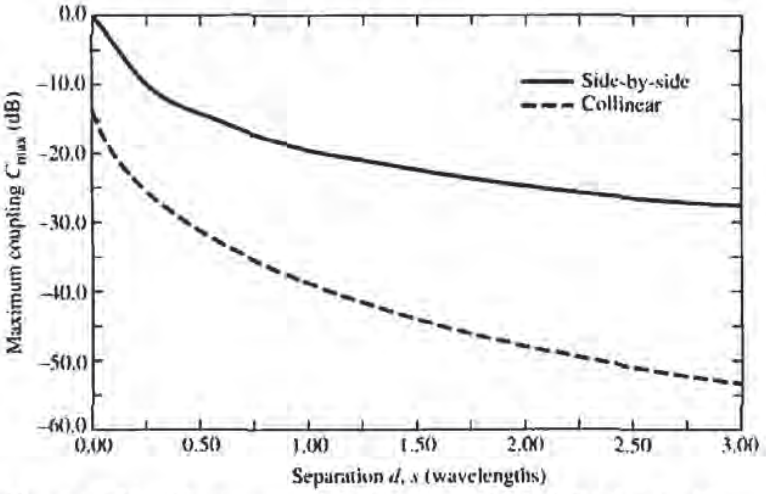


Figure 8.24 Maximum coupling for the two $\lambda/2$ dipoles in side-by-side and collinear arrangements as a function of separation.

$$C_{\max} = \frac{1}{L}[1 - (1 - L^2)^{1/2}] \tag{8-74}$$

where

$$L = \frac{|Y_{12}Y_{21}|}{2\text{Re}(Y_{11})\,\text{Re}(Y_{22}) - \text{Re}(Y_{12}Y_{21})} \tag{8-74a}$$

To ensure maximum coupling, the admittance of the matched load on the receiving antenna should be [35]

$$Y_L = \left[\frac{1 - \rho}{1 + \rho} + 1\right]\text{Re}(Y_{22}) - Y_{22} \tag{8-75}$$

where

$$\rho = \frac{G_{MAX}(Y_{12}Y_{21})^*}{|Y_{12}Y_{21}|} \tag{8-75a}$$

The corresponding input admittance of the transmitting antenna is

$$Y_{in} = Y_{11} - \frac{Y_{21}Y_{12}}{Y_L + Y_{22}} \tag{8-76}$$

Based on (8-74)–(8-76), maximum coupling for two half-wavelength dipoles in side-by-side and collinear arrangements as a function of the element separation (d for side-by-side and s for collinear) was computed using the NEC, and it is shown in Figure 8.24. As expected, the side-by-side arrangement exhibits much stronger coupling, since the elements are placed along the direction of their respective maximum radiation. Similar curves can be computed for the parallel-in-echelon arrangement.

8.7 MUTUAL COUPLING IN ARRAYS

When two antennas are near each other, whether one and/or both are transmitting or receiving, some of the energy that is primarily intended for one ends up at the other.

INTEL-1045
U.S. Patent 7,151,430

The amount depends primarily on the

a. radiation characteristics of each
b. relative separation between them
c. relative orientation of each

There are many different mechanisms that can cause this interchange of energy. For example, even if both antennas are transmitting, some of the energy radiated from each will be received by the other because of the nonideal directional characteristics of practical antennas. Part of the incident energy on one or both antennas may be rescattered in different directions allowing them to behave as secondary transmitters. This interchange of energy is known as "mutual coupling," and in many cases it complicates the analysis and design of an antenna. Furthermore, for most practical configurations, mutual coupling is difficult to predict analytically but must be taken into account because of its significant contribution. Because the mutual effects of any antenna configuration cannot be generalized, in this section we want first to briefly introduce them in a qualitative manner and then examine their general influence on the behavior of the radiation characteristics of the antenna. Most of the material and presentation in this section is followed from a well-written document on this subject [41].

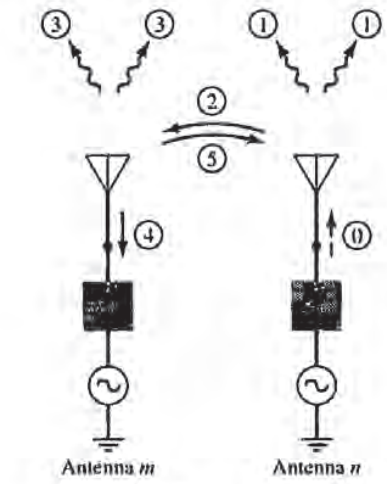
8.7.1 Coupling in the Transmitting Mode

To simplify the discussion, let us assume that two antennas m and n of an array are positioned relative to each other as shown in Figure 8.25(a). The procedure can be extended to a number of elements. If a source is attached to antenna n, the generated energy traveling toward the antenna labeled as (0) will be radiated into space (1) and toward the mth antenna (2). The energy incident on the mth antenna sets up currents which have a tendency to rescatter some of the energy (3) and allow the remaining to travel toward the generator of m (4). Some of the rescattered energy (3) may be redirected back toward antenna n (5). This process can continue indefinitely. The same process would take place if antenna m is excited and antenna n is the parasitic element. If both antennas, m and n, are excited simultaneously, the radiated and rescattered fields by and from each must be added vectorially to arrive at the total field at any observation point. Thus, "*the total contribution to the far-field pattern of a particular element in the array depends not only upon the excitation furnished by its own generator (the direct excitation) but upon the total parasitic excitation as well, which depends upon the couplings from and the excitation of the other generators* [41]."

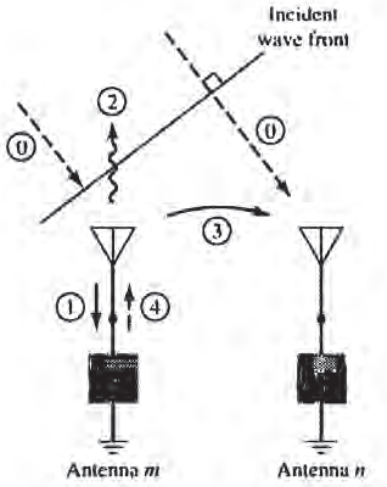
The wave directed from the n to the m antenna and finally toward its generator (4) adds vectorially to the incident and reflected waves of the m antenna itself, thus enhancing the existing standing wave pattern within m. For coherent excitations, the coupled wave (4) due to source n differs from the reflected one in m only in phase and amplitude. The manner in which these two waves interact depends on the coupling between them and the excitation of each. It is evident then that the vector sum of these two waves will influence the input impedance looking in at the terminals of antenna m and will be a function of the position and excitation of antenna n. This coupling effect is commonly modeled as a change in the apparent driving impedance of the elements and it is usually referred to as *mutual impedance variation.*

To demonstrate the usefulness of the driving impedance variation, let us assume

INTEL-1045
U.S. Patent 7,151,430



(a) Transmitting



(b) Receiving

Figure 8.25 Transmitting mode coupling paths between antennas m and n (Reprinted with permission of MIT Lincoln Laboratory, Lexington, MA).

that a set of elements in an array are excited. For a given element in the array, the generator impedance that is optimum in the sense of maximizing the radiated power for that element is that which would be a conjugate impedance match at the element terminals. This is accomplished by setting a reflected wave which is equal in amplitude and phase to the backwards traveling waves induced due to the coupling. Even though this is not the generator impedance which is a match to a given element when all other elements are not excited, it does achieve maximum power transfer.

To minimize confusion, let us adopt the following terminology [41]:

1. *Antenna impedance:* The impedance looking into a single isolated element.
2. *Passive driving impedance:* The impedance looking into a single element of an array with all other elements of the array passively terminated in their normal generator impedance unless otherwise specified.
3. *Active driving impedance:* The impedance looking into a single element of an array with all other elements of the array excited.

INTEL-1045
U.S. Patent 7,151,430

Since the passive driving impedance is of minor practical importance and differs only slightly from the antenna impedance, the term *driving impedance* will be used to indicate *active* driving impedance, unless otherwise specified.

Since the driving impedance for a given element is a function of the placement and excitation of the other elements, then *optimum generator impedance that maximizes array radiation efficiency (gain) varies with array excitation.* These changes, with element excitation variations, constitute one of the principal aggravations in electronic scanning arrays.

8.7.2 Coupling in the Receiving Mode

To illustrate the coupling mechanism in the receiving mode, let us again assume that the antenna system consists of two passively loaded elements of a large number, as shown in Figure 8.25(b). Assume that a plane wave (0) is incident, and it strikes antenna m first where it causes current flow. Part of the incident wave will be rescattered into space as (2), the other will be directed toward antenna n as (3) where it will add vectorially with the incident wave (0), and part will travel into its feed as (1). It is then evident that the amount of energy received by each element of an antenna array is the vector sum of the direct waves and those that are coupled to it parasitically from the other elements.

The amount of energy that is absorbed and reradiated by each element depends on its match to its terminating impedance. Thus, the amount of energy received by any element depends upon its terminating impedance as well as that of the other elements. In order to maximize the amount of energy extracted from an incident wave, we like to minimize the total backscattered (2) energy into space by properly choosing the terminating impedance. This actually can be accomplished by mismatching the receiver itself relative to the antenna so that the reflected wave back to the antenna (4) is cancelled by the rescattered wave, had the receiver been matched to the actual impedance of each antenna.

As a result of the previous discussion, it is evident that mutual coupling plays an important role in the performance of an antenna. However, the analysis and understanding of it may not be that simple.

8.7.3 Mutual Coupling on Array Performance

The effects of the mutual coupling on the performance of an array depends upon the

a. antenna type and its design parameters
b. relative positioning of the elements in the array
c. feed of the array elements
d. scan volume of the array

These design parameters influence the performance of the antenna array by varying its element impedance, reflection coefficients, and overall antenna pattern. In a finite-element array, the multipath routes the energy follows because of mutual coupling will alter the pattern in the absence of these interactions. However, for a very large regular array (array with elements placed at regular intervals on a grid and of sufficient numbers so that edge effects can be ignored), the relative shape of the pattern will be the same with and without coupling interactions. It will only require a scaling up or down in amplitude while preserving the shape. This, however, is not true for irregular placed elements or for small regular arrays where edge effects become dominant.

INTEL-1045
U.S. Patent 7,151,430

8.7.4 Coupling in an Infinite Regular Array

The analysis and understanding of coupling can be considerably simplified by considering an infinite regular array. Although such an array is not physically realizable, it does provide an insight and in many cases answers of practical importance. For the infinite regular array we assume that

a. all the elements are placed at regular intervals
b. all the elements are identical
c. all the elements have uniform (equal) amplitude excitation
d. there can be a linear relative phasing between the elements in the two orthogonal directions

The geometry of such an array is shown in Figure 6.23 with its array factor given by (6-87) or (6-88). This simplified model will be used to analyze the coupling and describes fairly accurately the behavior of most elements in arrays of modest to large size placed on flat or slowly curve surfaces with smoothly varying amplitude and phase taper.

To assess the behavior of the element driving impedance as a function of scan angle, we can write the terminal voltage of any one element in terms of the currents flowing in the others, assuming a single-mode operation, as

$$V_{mn} = \sum_{p} \sum_{q} Z_{mn,pq} I_{pq} \tag{8-77}$$

where $Z_{mn,pq}$ defines the terminal voltage at antenna mn due to a unity current in element pq when the current in all the other elements is zero. Thus the $Z_{mn,pq}$ terms represent the *mutual impedances* when the indices mn and pq are not identical. The *driving impedance* of the mnth element is defined as

$$Z_{Dmn} = \frac{V_{mn}}{I_{mn}} = \sum_{p} \sum_{q} Z_{mn,pq} \frac{I_{pq}}{I_{mn}} \tag{8-78}$$

Since we assumed that the amplitude excitation of the elements of the array was uniform and the phase linear, we can write that

$$I_{pq} = I_{00} e^{j(p\beta_x + q\beta_y)} \tag{8-79a}$$

$$I_{mn} = I_{00} e^{j(m\beta_x + n\beta_y)} \tag{8-79b}$$

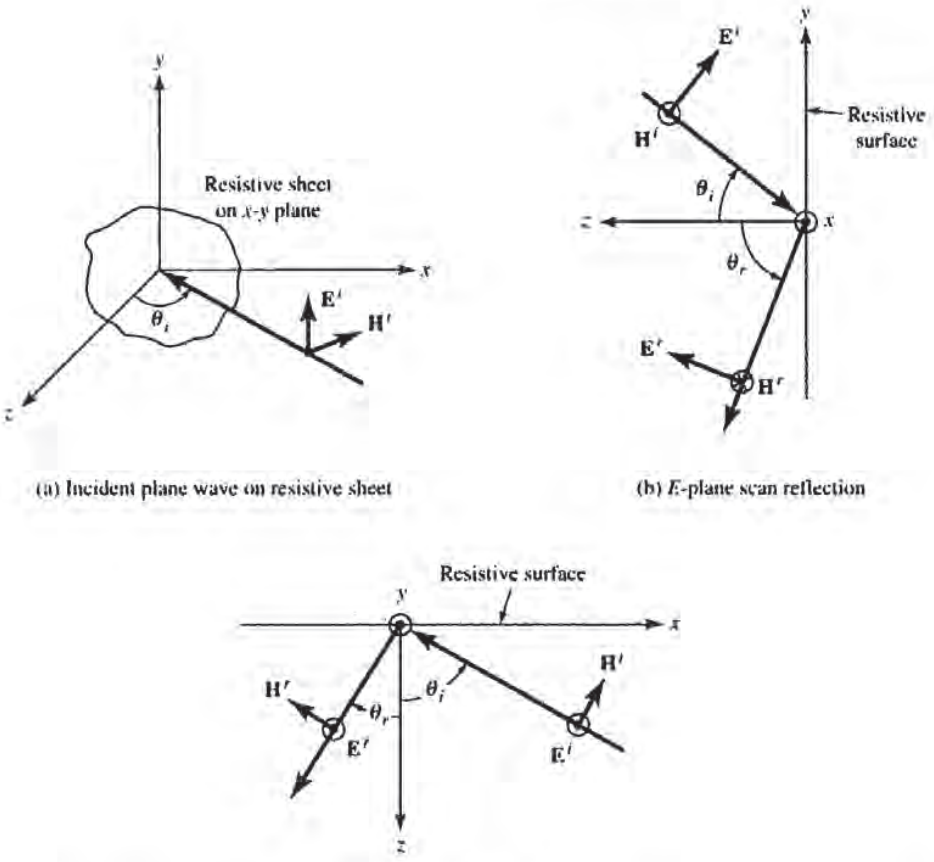
Thus, (8-78) reduces to

$$Z_{Dmn} = \sum_{p} \sum_{q} Z_{mn,pq} e^{j(p-m)\beta_x} e^{j(q-n)\beta_y} \tag{8-80}$$

It is evident that the driving point impedance of mn element is equal to the vector sum of the element self impedance ($mn = pq$) and the phased mutual impedances between it and the other elements ($mn \neq pq$). The element self impedance ($mn = pq$) is obtained when all other elements are open-circuited so that the current at their feed points is zero [$I_{pq}(pq \neq mn) = 0$]. For most practical antennas, physically this is almost equivalent to removing the pq elements and finding the impedance of a single isolated element.

A consequence of the mutual coupling problem is the change of the array impedance with scan angle. In order not to obscure the basic principle with the complexity of the problem, this can best be illustrated by examining the behavior of the reflection

INTEL-1045
U.S. Patent 7,151,430



(a) Incident plane wave on resistive sheet

(b) *E*-plane scan reflection

(c) *H*-plane scan reflection

Figure 8.26 Geometry for plane wave reflection from resistive sheet. (Reprinted with permission of MIT Lincoln Laboratory, Lexington, MA.)

coefficient of a uniform plane wave in free-space incident on a resistive sheet of infinite extent backed by an open circuit so that there are no transmitted fields through the sheet, as shown in Figure 8.26(a). Although the open circuit is not physically realizable, nevertheless the model is useful. This is accomplished by choosing the surface resistivity of the sheet to be that of free-space ($\eta_0 = 120\pi$) so that the sheet is an exact match for a normally incident wave. Referring to Figure 8.26(b) for an *E*-plane scan and Figure 8.26(c) for an *H*-plane scan, we impose that at the boundary ($z = 0$ for all x and y) the ratio of the total tangential electric field to the total tangential magnetic field is equal to the surface impedance of the sheet. The same procedure is used in electromagnetics to derive the Fresnel reflection and transmission coefficients from planar interfaces for vertical and horizontal polarizations [14].

Referring to Figure 8.26(b), we can write that the incident and reflected waves for the **E**- and **H**-fields as

$$\mathbf{E}^i = E_0^i(\hat{\mathbf{a}}_y \cos\theta_i - \hat{\mathbf{a}}_z \sin\theta_i)e^{+jk_0(y\sin\theta_i + z\cos\theta_i)} \tag{8-81a}$$

$$\mathbf{H}^i = \hat{\mathbf{a}}_x H_0^i e^{+jk_0(y\sin\theta_i + z\cos\theta_i)} \tag{8-81b}$$

$$\mathbf{E}^r = E_0^r(\hat{\mathbf{a}}_y \cos\theta_r + \hat{\mathbf{a}}_z \sin\theta_r)e^{-jk_0(-y\sin\theta_r + z\cos\theta_r)} \tag{8-81c}$$

$$\mathbf{H}^r = -\hat{\mathbf{a}}_x H_0^r e^{-jk_0(-y\sin\theta_r + z\cos\theta_r)} \tag{8-81d}$$

INTEL-1045
U.S. Patent 7,151,430

Applying boundary conditions on the tangential components of the electric and magnetic field of (8-81a)–(8-81d) gives

$$\eta_0 = \frac{E_{\tan}}{H_{\tan}} = \frac{E_0^i \cos\theta_i e^{jk_0 y \sin\theta_i} + E_0^r \cos\theta_r e^{jk_0 y \sin\theta_r}}{H_0^i e^{jk_0 y \sin\theta_i} - H_0^r e^{jk_0 y \sin\theta_i}} \tag{8-82}$$

Since

$$H_0^i = \frac{E_0^i}{\eta_0} \tag{8-82a}$$

$$H_0^r = \frac{E_0^r}{\eta_0} \tag{8-82b}$$

we can write (8-82) as

$$E_0^i(\cos\theta_i - 1)e^{jk_0 y \sin\theta_i} = -E_0^r(\cos\theta_r + 1)e^{jk_0 y \sin\theta_r} \tag{8-83}$$

whose only solution independent of y occurs when $\theta_r = \theta_i$. Thus,

$$\Gamma_e = \frac{E_0^r}{E_0^i} = \frac{1 - \cos\theta_i}{1 + \cos\theta_i} = \tan^2\left(\frac{\theta_i}{2}\right) \tag{8-84}$$

which can also be written as

$$\Gamma_e = \frac{E_0^r}{E_0^i} = \frac{1 - \cos\theta_i}{1 + \cos\theta_i} = \frac{\dfrac{1}{\cos\theta_i} - 1}{\dfrac{1}{\cos\theta_i} + 1} = \frac{Z_e - 1}{Z_e + 1} \tag{8-85}$$

By comparison with the reflection coefficient Γ of a transmission line with a normalized load $\bar{Z}_L$

$$\Gamma = \frac{\bar{Z}_L - 1}{\bar{Z}_L + 1} \tag{8-86}$$

the sheet represents an impedance to the wave that varies as

$$Z_e = \frac{1}{\cos\theta_i} \tag{8-87}$$

This is usually referred to as a *normalized directional impedance.*

Referring to Figure 8.26(c), it can be shown that for the H-plane scan the reflection coefficient is

$$\Gamma_h = -\frac{1 - \cos\theta_i}{1 + \cos\theta_i} = -\tan^2\left(\frac{\theta_i}{2}\right) \tag{8-88}$$

and the sheet represents to the wave an impedance that varies as

$$Z_h = \cos\theta_i \tag{8-89}$$

It is clear that even for such a simple problem of a plane wave impinging on a resistive sheet, there is a change, as a function of the scan angle, of the apparent impedance that the resistive sheet represents to the wave.

To illustrate the practical importance of the resistive sheet problem, the computed reflection coefficient magnitude for the E- and H-plane scans for arrays of half-

INTEL-1045
U.S. Patent 7,151,430

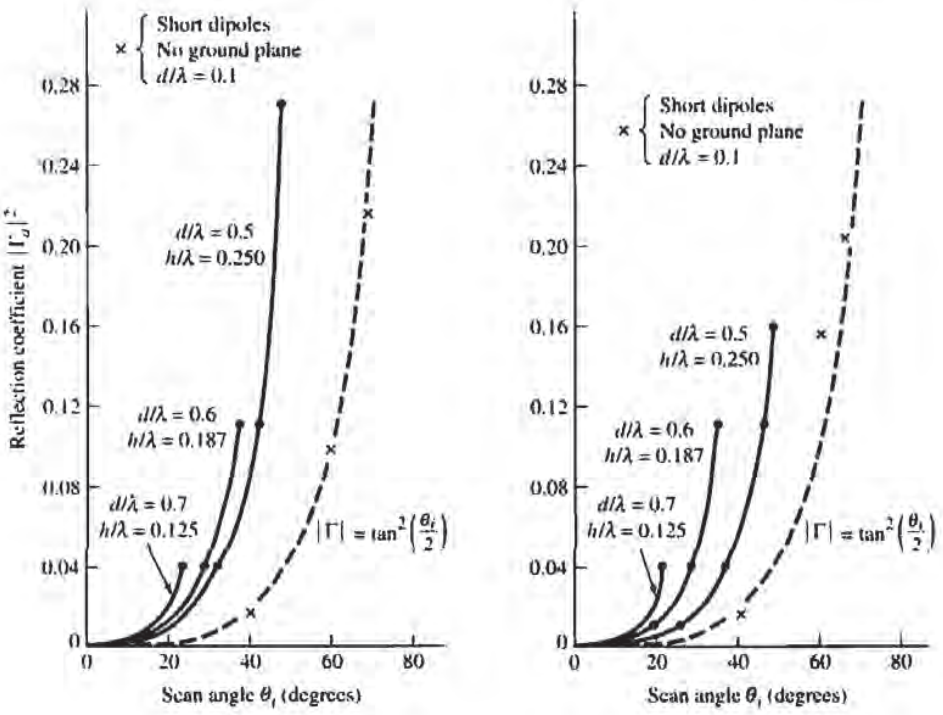


Figure 8.27 Magnitude of reflection coefficient as a function of principal plane scan angle. (Reprinted with permission of MIT Lincoln Laboratory, Lexington, MA.)

wavelength dipoles for various spacings $d(d = d_x = d_y)$ and height h above a ground plane are shown in Figures 8.27(a,b) [41]. The height h was chosen to minimize the mismatch in the principal planes of scan. The curves are discontinued at the angles where major lobes are equally disposed about broadside and retrace themselves beyond that point. The angles of discontinuity become smaller for wider spacings. It is also evident that the reflection coefficient for a given scan angle in the principal plane becomes smaller as the elements are brought closer together. In the same figures and indicated by small x's is the reflection coefficient of the central element of a large array of short dipoles with a spacing of $d_x = d_y = 0.1\lambda$ but without a ground plane. The resistive sheet reflection coefficient is also plotted for comparison purposes. It should be noted that the results of Figure 8.27 were computed assuming the generator impedance is matched to the element driving impedance when the array's major lobe was toward broadside. This requires the tuning of the driving reactance for broadside conditions, which for small spacings is exceedingly large.

8.7.5 Grating Lobes Considerations

Because of the periodic nature of an infinite array, the impedance behavior as a function of scan volume for different elements and interelement spacing can be described in the form of an infinite series. This is accomplished by expressing the radiated and stored (real and reactive) powers in the vicinity of the array in terms of the current, field distribution or pattern, of a typical element. The analysis, which was pioneered by Wheeler [42]; Edelberg and Oliner [43], [44]; and Stark [45] is straightforward, but it will not be included here because it requires a knowledge of Fourier

INTEL-1045
U.S. Patent 7,151,430

transforms, and it is beyond the scope of the book at this point. However, some qualitative results will be briefly discussed.

It was shown in Section 6.10.1 that *grating lobes* in an array can be formed provided (6-89a) and (6-89b) are satisfied. This was illustrated by the three-dimensional pattern of Figure 6.29. It was indicated there that additional grating lobes can be formed by increasing the interelement spacing. The grating lobes disappear as the spacing recedes toward zero. In general, grating lobes can be moved into and out of the visible region by controlling the spacing and/or relative phase between the elements.

The dependence of the element driving impedance $Z_D(\beta_x, \beta_y)$ on the pointing direction (scan) of the main beam of the array is demonstrated by examining it for different elements, spacings, and the presence of a ground plane. The discussion is restricted to planar arrays and the impedance variations are illustrated for the *E*-, *H*-, and *D*-planes. We define *D*- as the diagonal plane (45° from the *E*- and *H*-planes) and θ_e, θ_h, and θ_d as the angles of the main beam from broadside for the *E*-, *H*- and *D*-planes, respectively.

If the elements are polarized in the *y*-direction, then according to (6-90a) and (6-90b) the progressive phase shifts between the elements must be

$$\begin{aligned} \beta_x &= 0 \\ \beta_y &= -kd_y \sin\theta_e \end{aligned} \qquad E\text{-plane scan } (\phi_0 = 90°,\ \theta_0 = \theta_e) \tag{8-90}$$

$$\begin{aligned} \beta_x &= -kd_x \sin\theta_h \\ \beta_y &= 0 \end{aligned} \qquad H\text{-plane scan } (\phi_0 = 0°,\ \theta_0 = \theta_h) \tag{8-91}$$

$$\left(\frac{\beta_x}{d_x}\right)^2 + \left(\frac{\beta_y}{d_y}\right)^2 = k \sin\theta_d \qquad D\text{-plane scan } (\phi_0 = 45°,\ \theta_0 = \theta_d) \tag{8-92}$$

To make the presentation of the results more uniform, the element driving impedance $Z_D(\theta)$ is displayed on a Smith chart in a normalized form

$$Z_D(\theta)_{\text{norm}} = \frac{Z_D(\theta) - jX_D(0)}{R_D(0)} \tag{8-93}$$

where

$$Z_D(\theta) = R_D(\theta) + jX_D(\theta) \tag{8-93a}$$

$$\begin{aligned} R_D(0) &= R_D(\theta = 0°) \\ X_D(0) &= X_D(\theta = 0°) \end{aligned} \qquad \text{beam pointed at broadside} \tag{8-93b}$$

In Figure 8.28, we display the normalized driving impedance in the *E*-, *H*- and *D*-planes for a planar array of half-wavelength dipoles ($l = 0.5\lambda$) spaced $d_x = d_y = 0.55\lambda$ [41]. The *E*- and *H*-planes are discontinued at 65°. Physically that angle corresponds to a grating lobe at −65°, symmetrically disposed relative to the main beam. Scanning beyond that point is equivalent to moving the main beam in from 65° or retracing the curve.

For a VSWR of 3:1, the half-wavelength dipole array of Figure 8.28 can be scanned up to 45° in the *H*-plane, 79° in the *D*-plane, and anywhere in the *E*-plane; for a VSWR of 2:1, then the maximum scan angles are 50° in the *E*-plane, 40° in the *H*-plane, and 77° in the *D*-plane. For a small dipole ($l = 0.1\lambda$) the maximum scans are 47° in the *H*-plane, 79° in the *D*-plane, and anywhere for the *E*-plane for a 3:1

INTEL-1045
U.S. Patent 7,151,430

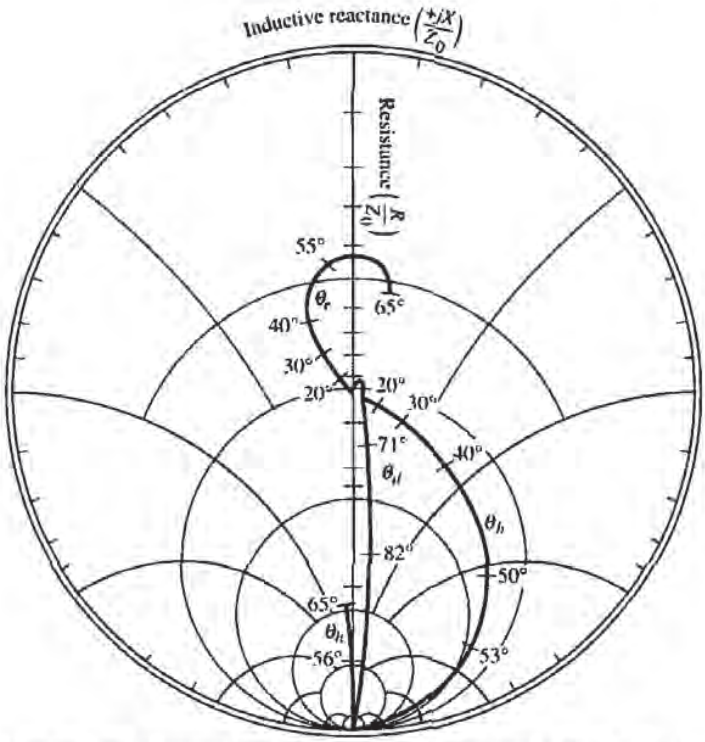


Figure 8.28 Normalized element impedance versus scan angle on the *E*-, *H*-, and *D*-planes for a planar array of half-wavelength dipoles ($\ell = 0.5\lambda$) with $d_x = d_y = 0.55\lambda$ and with no ground plane. (Reprinted with permission of MIT Lincoln Laboratory, Lexington, MA.)

VSWR; maximum scans of 40° in the *H*-plane, 76° in the *D*-plane, and anywhere in the *E*-plane for a 2:1 VSWR. The results are summarized in Table 8.3 [41].

To demonstrate the effects of a ground plane on the element driving impedance, the normalized impedance of the half-wavelength ($l = 0.5\lambda$) dipole arrays, when placed horizontally a height $h = 0.25\lambda$ above an infinite electric ground plane, are displayed in Figure 8.29. Physically, the introduction of the ground plane below the

Table 8.3 MAXIMUM SCAN VOLUME OF SHORT AND HALF-WAVELENGTH DIPOLE PLANAR ARRAY WITH $d_x = d_y = 0.55\lambda$ AND WITHOUT GROUND PLANE FOR VSWRs OF 3:1 AND 2:1
[Reprinted with permission of MIT Lincoln Laboratory, Lexington, MA]

		Maximum Scan Angle	
VSWR	Scan Plane	Short Dipole ($l = 0.1\lambda$)	Half-Wavelength Dipole ($l = 0.5\lambda$)
3:1	*E*-Plane	—	—
	H-Plane	47°	45°
	D-Plane	79°	79°
2:1	*E*-Plane	—	50°
	H-Plane	40°	40°
	D-Plane	76°	77°

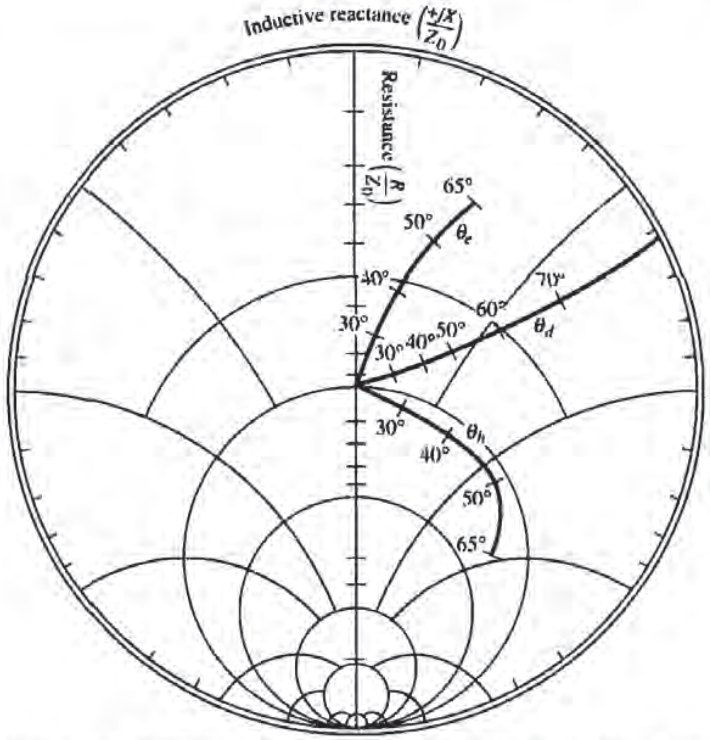


Figure 8.29 Normalized element impedance versus scan angle on the *E*-, *H*-, and *D*-planes for a planar array of half-wavelength ($\ell = 0.5\lambda$) dipoles with $d_x = d_y = 0.55\lambda$ and placed $h = 0.25\lambda$ above a ground plane. (Reprinted with permission of MIT Lincoln Laboratory, Lexington, MA.)

horizontal electric dipoles prevents them from radiating along the ground plane, so the impedance is continuous when a grating lobe moves into the visible region. The maximum scan angles for VSWR's of 3:1 and 2:1 are shown listed in Table 8.4 [41].

The impedances of a short dipole ($l = 0.1\lambda$) are similar to those of the half-wavelength dipole shown in Figures 8.28 and 8.29. The most striking variation in

Table 8.4 MAXIMUM SCAN VOLUME OF SHORT AND HALF-WAVELENGTH DIPOLE PLANAR ARRAY WITH $d_x = d_y = 0.55\lambda$ AND WITH GROUND PLANE ($h = 0.25\lambda$) FOR VSWRs OF 3:1 AND 2:1
[Reprinted with permission of MIT Lincoln Laboratory, Lexington, MA]

		Maximum Scan Angle	
VSWR	Scan Plane	Short Dipole ($l = 0.1\lambda$)	Half-Wavelength Dipole ($l = 0.5\lambda$)
3:1	*E*-Plane	55°	50°
	H-Plane	50°	50°
	D-Plane	62°	62°
2:1	*E*-Plane	45°	40°
	H-Plane	40°	40°
	D-Plane	52°	50°

INTEL-1045
U.S. Patent 7,151,430

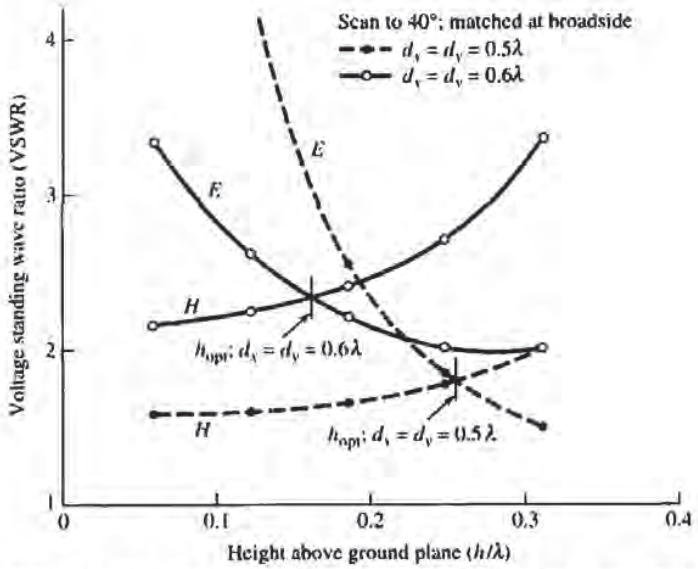


Figure 8.30 VSWR at θ_{max} versus height above ground plane for two large planar square arrays of half-wavelength ($\ell = 0.5\lambda$) dipoles. (Reprinted with permission of MIT Lincoln Laboratory, Lexington, MA.)

impedance of a given array of dipoles is accomplished by the introduction of the ground plane particularly for scan angles near grating-lobe formation.

By comparing the results of Tables 8.3 and 8.4 it is evident that if for dipole arrays the element spacing for allowing grating lobes to appear marginally is used as a design criterion, placing the arrays above a ground plane would give vastly better (but still poor) VSWR performance at extreme scans. If, however, the element spacing is chosen to maintain the maximum VSWR below a given value, there appears little difference between the elements but results in a smaller maximum scan for a given element spacing.

To examine the effect the height h above the ground plane has on the maximum VSWR (within a specified scan volume), the maximum VSWR as a function of the height for E- and H-plane scans of two large square arrays of half-wavelength dipoles with $d_x = d_y = 0.5\lambda$ and $d_x = d_y = 0.6\lambda$ spacing between the elements are displayed in Figure 8.30. The maximum scan angle is 40° and the arrays are assumed to be matched at broadside. It is evident from the results that as the height is decreased the maximum E-plane mismatch becomes very large while that of the H-plane decreases monotonically. The optimum height which leads to equal maximum mismatches in the E- and H-planes of scan for a given scan volume is determined by the spacing between the elements. The optimum heights for the two arrays are indicated in Figure 8.30.

It can be concluded that when an array is placed at its optimum height above the ground plane for a given scan volume and the spacing between the elements of the array is smaller than that required by the grating lobes, that array will exhibit less impedance variations than the one which just satisfies the scan volume requirement.

To demonstrate the variations of the input reflection coefficient, and thus of the input impedance, of an infinite array as a function of scan angle, the input reflection coefficient of an infinite array of circular microstrip patches matched at broadside is shown in Figure 8.31 for the E-plane and H-plane [46]. The variations are due mainly to coupling between the elements. The variations are more pronounced for the

INTEL-1045
U.S. Patent 7,151,430

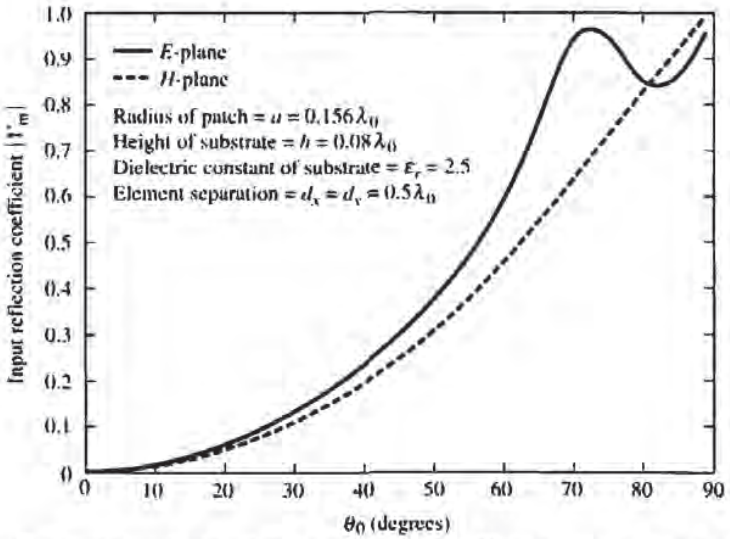


Figure 8.31 Typical magnitude of input reflection coefficient versus scan angle in *E*- and *H*-planes for infinite array of microstrip patches (courtesy J. T. Aberle and F. Zavosh).

E-plane than for the *H*-plane. For microstrip patches, coupling is attributed to space waves (with $1/r$ radial variations), higher order waves (with $1/\rho^2$ radial variations), surface waves (with $1/\rho^2$ radial variations), and leaky waves [with $\exp(-\lambda\rho)/\rho^{1/2}$ radial variations]. As is shown in Chapter 14 and Figures 14.36, 14.37, the variations of the reflection coefficient can be reduced by suppressing the surface waves supported by the substrate using cavities to back the patches [46]. The variations of the reflection coefficient as a function of scan angle can lead, due to large values of the reflection coefficient (ideally unity), to what is usually referred as *array scan blindness* [47]–[50]. This is evident for the *E*-plane near 72°–73° and is due to excitation in that plane of a leaky-wave mode, which is not as strongly excited as the scan angle increases beyond those values. Scan blindness is reached at a scan angle of 90°. Also there can be degradation of side lobe level and main beam shape due to the large variations of the reflection coefficient.

Scan blindness is attributed to slow waves which are supported by the structure of the antenna array. These structures may take the form of dielectric layers (such as radomes, superstrates and substrates) over the face of the array, or metallic grids or fence structures. The scan blindness has been referred to as a "forced surface wave" [47], [48], or a "leaky wave" [49], resonant response of the slow wave structure by the phased array. For the microstrip arrays, the substrate layer supports a slow surface wave which contributes to scan blindness [50].

References

1. R. E. Burgess, "Aerial Characteristics," *Wireless Engr.*, Vol. 21, pp. 154–160, April 1944.
2. J. D. Kraus, *Antennas*, McGraw-Hill, New York, 1988, Chapters 9, 10, pp. 359–434.
3. S. A. Schelkunoff and H. T. Friis, *Antennas: Theory and Practice*, Wiley, New York, 1952, pp. 213–242.
4. A. A. Pistolkors, "The Radiation Resistance of Beam Antennas," *Proc. IRE*, Vol. 17, pp. 562–579, March 1929.
5. R. Bechmann, "On the Calculation of Radiation Resistance of Antennas and Antenna Combinations," *Proc. IRE*, Vol. 19, pp. 461–466, March 1931.

INTEL-1045
U.S. Patent 7,151,430

6. P. S. Carter, "Circuit Relations in Radiation Systems and Applications to Antenna Problems," *Proc. IRE*, Vol. 20, pp. 1004–1041, June 1932.
7. R. F. Harrington, "Matrix Methods for Field Problems," *Proc. IEEE*, Vol. 55, No. 2, pp. 136–149, February 1967.
8. R. F. Harrington, *Field Computation by Moment Methods*, Macmillan, New York, 1968.
9. J. H. Richmond, "Digital Computer Solutions of the Rigorous Equations for Scattering Problems," *Proc. IEEE*, Vol. 53, pp. 796–804, August 1965.
10. L. L. Tsai, "Moment Methods in Electromagnetics for Undergraduates," *IEEE Trans. on Education*, Vol. E-21, No. 1, pp. 14–22, February 1978.
11. R. Mittra (Ed.), *Computer Techniques for Electromagnetics*, Pergamon, New York, 1973.
12. J. Moore and R. Pizer, *Moment Methods in Electromagnetics*, John Wiley and Sons, New York, 1984.
13. J. J. H. Wang, *Generalized Moment Methods in Electromagnetics*, John Wiley and Sons, New York, 1991.
14. C. A. Balanis, *Advanced Engineering Electromagnetics*, John Wiley and Sons, New York, 1989.
15. J. D. Lilly, "Application of The Moment Method to Antenna Analysis," MSEE Thesis, Department of Electrical Engineering, West Virginia University, 1980.
16. J. D. Lilly and C. A. Balanis, "Current Distributions, Input Impedances, and Radiation Patterns of Wire Antennas," North American Radio Science Meeting of URSI, Université Laval, Quebec, Canada, June 2–6, 1980.
17. D. K. Cheng, *Field and Wave Electromagnetics*, Addison-Wesley, Reading, MA, 1989, p. 97.
18. H. C. Pocklington, "Electrical Oscillations in Wire," *Cambridge Philos. Soc. Proc.*, Vol. 9, pp. 324–332, 1897.
19. E. Hallén, "Theoretical investigations into the transmitting and receiving qualities of antennae," *Nova Acta Regiae Soc. Sci. Upsaliensis*, Ser. IV, No. 4, pp. 1–44, 1938.
20. R. King and C. W. Harrison, Jr., "The distribution of current along a symmetric center-driven antenna," *Proc. IRE*, Vol. 31, pp. 548–567, October 1943.
21. J. H. Richmond, "A Wire-Grid Model for Scattering by Conducting Bodies," *IEEE Trans. Antennas Propagat.*, Vol. AP-14, No. 6, pp. 782–786, November 1966.
22. G. A. Thiele, "Wire Antennas," in *Computer Techniques for Electromagnetics*, R. Mittra (Ed.), Pergamon, New York, Chapter 2, pp. 7–70, 1973.
23. C. M. Butler and D. R. Wilton, "Evaluation of Potential Integral at Singularity of Exact Kernel in Thin-Wire Calculations," *IEEE Trans. Antennas Propagat.*, Vol. AP-23, No. 2, pp. 293–295, March 1975.
24. L. W. Pearson and C. M. Butler, "Inadequacies of Collocation Solutions to Pocklington-Type Models of Thin-Wire Structures," *IEEE Trans. Antennas Propagat.*, Vol. AP-23, No. 2, pp. 293–298, March 1975.
25. C. M. Butler and D. R. Wilton, "Analysis of Various Numerical Techniques Applied to Thin-Wire Scatterers," *IEEE Trans. Antennas Propagat.*, Vol. AP-23, No. 4, pp. 534–540, July 1975.
26. D. R. Wilton and C. M. Butler, "Efficient Numerical Techniques for Solving Pocklington's Equation and their Relationships to Other Methods," *IEEE Trans. Antennas Propagat.*, Vol. AP-24, No. 1, pp. 83–86, January 1976.
27. L. L. Tsai, "A Numerical Solution for the Near and Far Fields of an Annular Ring of Magnetic Current," *IEEE Trans. Antennas Propagat.*, Vol. AP-20, No. 5, pp. 569–576, September 1972.
28. R. Mittra and C. A. Klein, "Stability and Convergence of Moment Method Solutions," in *Numerical and Asymptotic Techniques in Electromagnetics*, R. Mittra (Ed.), Springer-Verlag, New York, 1975, Chapter 5, pp. 129–163.
29. T. K. Sarkar, "A Note on the Choice Weighting Functions in the Method of Moments," *IEEE Trans. Antennas Propagat.*, Vol. AP-33, No. 4, pp. 436–441, April 1985.
30. T. K. Sarkar, A. R. Djordjević and E. Arvas, "On the Choice of Expansion and Weighting

INTEL-1045
U.S. Patent 7,151,430

Functions in the Numerical Solution of Operator Equations," *IEEE Trans. Antennas Propagat.*, Vol. AP-33, No. 9, pp. 988–996, September 1985.
31. E. K. Miller and F. J. Deadrick, "Some Computational Aspects of Thin-Wire Modeling," in *Numerical and Asymptotic Techniques in Electromagnetics*, R. Mittra (Ed.), Springer-Verlag, New York, 1975, Chapter 4, pp. 89–127.
32. L. Kantorovich and G. Akilov, *Functional Analysis in Normed Spaces*, Pergamon, Oxford, pp. 586–587, 1964.
33. H. E. King, "Mutual Impedance of Unequal Length Antennas in Echelon," *IRE Trans. Antennas Propagat.*, Vol. AP-5, pp. 306–313, July 1957.
34. R. C. Hansen, "Fundamental Limitations in Antennas," *Proc. IEEE*, Vol. 69, No. 2, pp. 170–182, February 1981.
35. G. J. Burke and A. J. Poggio, "Numerical Electromagnetics Code (NEC)-method of moments," Technical Document 11, Naval Ocean Systems Center, San Diego, Calif., January 1981.
36. A. J. Julian, J. M. Logan, and J. W. Rockway, "MININEC: A Mini-Numerical Electromagnetics Code," Technical Document 516, Naval Ocean Systems Center, San Diego, Calif, September 6, 1982.
37. J. Rockway, J. Logan, D. Tam, and S. Li, *The MININEC SYSTEM: Microcomputer Analysis of Wire Antennas*, Artech House, 1988.
38. J. A. G. Malherbe, "Calculator Program for Mutual Impedance," *Microwave Journal*, (Euro-Global Ed.), pp. 82-H–82-M, February 1984.
39. J. A. G. Malherbe, "Analysis of a Linear Antenna Array Including the Effects of Mutual Coupling," *IEEE Trans. Education*, Vol. 32, No. 1, pp. 29–34, February 1989.
40. D. Rubin, *The Linville Method of High Frequency Transistor Amplifier Design*, Naval Weapons Center, NWCCL TP 845, Corona Labs., Corona, CA. March 1969.
41. J. L. Allen and B. L. Diamond, "Mutual Coupling in Array Antennas," Technical Report EDS-66-443, Lincoln Lab., MIT, October 4, 1966.
42. H. A. Wheeler, "The Radiation Resistance of an Antenna in an Infinite Array or Waveguide," *Proc. IRE*, Vol. 48, pp. 478–487, April 1948.
43. S. Edelberg and A. A. Oliner, "Mutual Coupling Effects in Large Antenna Arrays, Part I," *IRE Trans. Antennas Propagat.*, Vol. AP-8, No. 3, pp. 286–297, May 1960.
44. S. Edelberg and A. A. Olinder, "Mutual Coupling Effects in Large Antenna Arrays," Part II," *IRE Trans. Antennas Propagat.*, Vol. AP-8, No. 4, pp. 360–367, July 1960.
45. L. Stark, "Radiation Impedance of a Dipole in an Infinite Planar Phased Array," *Radio Science*, Vol. 3, pp. 361–375, 1966.
46. F. Zavosh and J. T. Aberle, "Infinite Phased Arrays of Cavity-Backed Patches," *IEEE Trans. Antennas Propagat.*, Vol. 42, No. 3, pp. 390–394, March 1994.
47. N. Amitay, V. Galindo, and C. P. Wu, *Theory and Analysis of Phased Array Antennas*, John Wiley and Sons, New York, 1972.
48. L. Stark, "Microwave Theory of Phased-Array Antennas—A Review," *Proc. IEEE*, Vol. 62, pp. 1661–1701, December 1974.
49. G. H. Knittel, A. Hessel and A. A. Oliner, "Element Pattern Nulls in Phased Arrays and Their Relation to Guided Waves," *Proc. IEEE*, Vol. 56, pp. 1822–1836, November 1968.
50. D. M. Pozar and D. H. Schaubert, "Scan Blindness in Infinite Phased Arrays of Printed Dipoles," *IEEE Trans. Antennas Propagat.*, Vol. AP-32, No. 6, pp. 602–610, June 1984.

PROBLEMS

8.1. Derive Pocklington's integral equation 8-24 using (8-22) and (8-23).
8.2. Derive the solution of (8-26) to the differential equation of (8-25a). Show that Hallén's integral equation can be written as (8-27).
8.3. Show that the incident tangential electric field (E_z^i) generated on the surface of a wire of radius a by a magnetic field generator of (8-30) is given by (8-31).
8.4. Reduce (8-31) to (8-32) valid only along the z axis ($\rho = 0$).

INTEL-1045
U.S. Patent 7,151,430

8.5. For the center-fed dipole of Example 8.3 write the [Z] matrix for $N = 21$ using for the gap the delta-gap generator and the magnetic-frill generator. Use the computer program MOMENT METHOD (POCKLINGTON) at the end of the chapter.

8.6. For an infinitesimal center-fed dipole of $\ell = \lambda/50$ of radius $a = 0.005\lambda$, derive the input impedance using Pocklington's integral equation with piecewise constant subdomain basis functions and point-matching. Use $N = 21$ and model the gap as a delta-gap generator and as a magnetic-frill generator. Use the MOMENT METHOD (POCKLINGTON) computer program at the end of the chapter.

8.7. Using the MOMENT METHOD (HALLÉN) computer program at the end of the chapter, compute the input impedance of a $\lambda/4$ and $3\lambda/4$ dipole with an l/d ratio of $l/d = 50$ and 25. Use 20 subsections. Compare the results with the impedances of a dipole with $l/d = 10^9$. Plot the current distribution and the far-field pattern of each dipole.

8.8. Derive (8-53)–(8-55b) using (8-52), (3-2a), and (4-56).

8.9. For a linear dipole with sinusoidal current distribution, radiating in free-space, find the radiation Z_{im} and the input Z_{in} impedances when $a = \lambda/20$. Verify using the computer program SELF AND MUTUAL IMPEDANCES at the end of the chapter.
(a) $l = \lambda/4$ (b) $l = \lambda/2$
(c) $l = 3\lambda/4$ (d) $l = \lambda$

8.10. A $\lambda/2$ dipole of finite radius is not self-resonant. However, if the dipole is somewhat less than $\lambda/2$, it becomes self-resonant. For a dipole with radius of $a = \lambda/200$ radiating in free-space, find the
(a) *nearest length by which the $\lambda/2$ dipole becomes self-resonant*
(b) radiation resistance (referred to the current maximum) of the new resonant dipole
(c) input resistance
(d) VSWR when the dipole is connected to a 50-ohm line

8.11. Find the length, at the first resonance, of linear dipoles with wire radii of
(a) $10^{-5}\lambda$ (b) $10^{-4}\lambda$
(c) $10^{-3}\lambda$ (d) $10^{-2}\lambda$
Compute the radiation resistance of each.

8.12. A quarter-wavelength monopole of radius $a = 10^{-2}\lambda$ is placed upon an infinite ground plane. Determine the
(a) impedance of the monopole
(b) *length by which it must be shortened to become self-resonant (first resonance)*
(c) impedance of the monopole when its length is that given in part b.
(d) VSWR when the monopole of part b is connected to a 50-ohm line.

8.13. For two half-wavelength dipoles radiating in free-space, compute (using equations, *not* curves) the mutual impedance Z_{21_m} referred to the current maximum for
(a) side-by-side arrangement with $d = \lambda/4$
(b) collinear configuration with $s = \lambda/4$
Verify using the computer program SELF AND MUTUAL IMPEDANCES at the end of the chapter.

8.14. Two identical linear $\lambda/2$ dipoles are placed in a collinear arrangement a distance $s = 0.35\lambda$ apart. Find the driving point impedance of each. Verify using the computer *program SELF AND MUTUAL IMPEDANCES at the end of the chapter.*

8.15. Two identical linear $\lambda/2$ dipoles are placed in a collinear arrangement. Find the spacings between them so that the driving point impedance of each has the smallest reactive part.

INTEL-1045
U.S. Patent 7,151,430

```
C*****************************************************************
C
C THIS IS A FORTRAN MOMENT METHOD PROGRAM USING
C
C     I.  POCKLINGTON'S [Equ. (8-24)]
C     II. HALLEN'S [Equ. (8-27)]
C
C INTEGRAL EQUATIONS TO COMPUTE THE:
C
C     A. CURRENT DISTRIBUTION
C     B. INPUT IMPEDANCE
C     C. NORMALIZED AMPLITUDE RADIATION PATTERN
C
C OF A LINEAR SYMMETRICALLY EXCITED DIPOLE.
C
C THIS PROGRAM USES PULSE EXPANSION FOR THE ELECTRIC
C CURRENT MODE AND POINT-MATCHING THE ELECTRIC
C FIELD AT THE CENTER OF EACH WIRE SEGMENT
C
C DELTA-GAP FEED MODEL IS USED IN BOTH FORMULATIONS.
C IN ADDITION, MAGNETIC-FRILL GENERATOR IS AVAILABLE IN
C THE POCKLINGTON'S INTEGRAL EQUATION
C
C
C     OPTION I.  POCKLINGTON'S INTEGRAL EQUATION
C     OPTION II. HALLEN'S INTEGRAL EQUATION
C
C          **INPUT PARAMETERS
C          1. TL  =  TOTAL LENGTH OF THE DIPOLE (in wavelengths)
C          2. RA  =  RADIUS OF THE WIRE (in wavelengths)
C          3. NM  =  TOTAL NUMBER OF SUBSECTIONS
C                    (must be an odd integer)
C          4. IEX =  OPTION TO USE EITHER MAGNETIC-FRILL
C                    GENERATOR OR DELTA-GAP FEED
C             IEX =  1: MAGNETIC-FRILL GENERATOR
C             IEX =  2: DELTA-GAP FEED
C
C          **NOTE
C          IGNORE INPUT PARAMETER IEX WHEN CHOOSING OPTION II
C          (i.e., HALLEN'S FORMULATION)
C
C*****************************************************************
```


INTEL-1045
U.S. Patent 7,151,430

COMPUTER PROGRAM - SELF AND MUTUAL IMPEDANCES

```
C**********************************************************************
C
C THIS IS A FORTRAN PROGRAM THAT COMPUTES THE:
C
C     I.  SELF IMPEDANCE FOR ANY LENGTH DIPOLE
C     II. MUTUAL IMPEDANCE BETWEEN TWO IDENTICAL
C         LINEAR DIPOLES
C
C BASED ON THE INDUCED EMF METHOD AND THE IDEAL CURRENT
C DISTRIBUTION OF EQUATION (4-56)
C
C THE IMPEDANCES CAN BE COMPUTED BASED EITHER ON THE CURRENT
C AT THE INPUT, OR ON THE CURRENT MAXIMUM:
C
C     I. SELF IMPEDANCE (INPUT IMPEDANCE)
C
C          1. BASED ON CURRENT AT THE INPUT:
C               Zin  = Rin + j Xin
C               Rin  = INPUT RESISTANCE [Equs.(8-60a) and (8-61a)]
C               Xin  = INPUT REACTANCE [Equs.(8-60b) and (8-61b)]
C
C          2. BASED ON CURRENT MAXIMUM:
C               Zinm = Rinm + j Xinm
C               Rinm = SELF RESISTANCE [Equ. (8-60a)]
C               Xinm = SELF REACTANCE [Equ. (8-60b)]
C
C     II. MUTUAL IMPEDANCE
C
C          1. BASED ON CURRENT AT THE INPUT:
C               Z21i = R21i + j X21i [Equ. (8-68)]
C               R21i = MUTUAL RESISTANCE
C               X21i = MUTUAL REACTANCE
C
C          2. BASED ON CURRENT MAXIMUM:
C               Z21m = R21m + j X21m [Equ. (8-70)]
C               R21m = MUTUAL RESISTANCE
C               X21m = MUTUAL REACTANCE
C
C THE DIPOLES FOR MUTUAL IMPEDANCE COMPUTATIONS MUST BE
C IDENTICAL WITH LENGTH OF ODD MULTIPLES OF λ/2
C (l = nλ/2, n = 1,3,5,..).
C
C
C     OPTION I.  SELF IMPEDANCE (INPUT IMPEDANCE)
C
C          **ARRAY INPUT PARAMETERS
C          1. l  = LENGTH OF THE DIPOLE
C          2. a  = RADIUS OF THE DIPOLE
C
C                                                  (continued on next page)
```


INTEL-1045
U.S. Patent 7,151,430

```
C                                                          (continued)
C
C
C     OPTION II.  MUTUAL IMPEDANCE
C
C       CHOICE A: SIDE-BY-SIDE [see Fig. 8.19(a)]
C
C          **ARRAY INPUT PARAMETERS
C          1. l  = LENGTH OF THE DIPOLES
C          2. d  = HORIZONTAL DISPLACEMENT OF DIPOLES
C
C       CHOICE B: COLLINEAR [see Fig. 8.19(b)]
C
C          **ARRAY INPUT PARAMETERS
C          1. l  = LENGTH OF THE DIPOLES
C          2. h  = VERTICAL DISPLACEMENT OF DIPOLES
C
C       CHOICE C: PARALLEL-IN-ECHELON [see Fig. 8.19(c)]
C
C          **ARRAY INPUT PARAMETERS
C          1. l  = LENGTH OF THE DIPOLE
C          2. h  = VERTICAL DISPLACEMENT OF DIPOLES
C          2. d  = HORIZONTAL DISPLACEMENT OF DIPOLES
C
C
C       **NOTE
C       ALL THE INPUT DATA ARE IN WAVELENGTHS.
C
C*****************************************************************
```


INTEL-1045
U.S. Patent 7,151,430

CHAPTER 9

BROADBAND DIPOLES AND MATCHING TECHNIQUES

9.1 INTRODUCTION

In Chapter 4 the radiation properties (pattern, directivity, input impedance, mutual impedance, etc.) of very thin wire antennas were investigated by assuming that the current distribution, which in most cases is sinusoidal, is known. In practice, infinitely thin (electrically) wires are not realizable but can be approximated. In addition, their radiation characteristics (such as pattern, impedance, gain, etc.) are very sensitive to frequency. The degree to which they change as a function of frequency depends on the antenna bandwidth. For applications that require coverage of a broad range of frequencies, such as television reception of all channels, wide-band antennas are needed. There are numerous antenna configurations, especially of arrays, that can be used to produce wide bandwidths. Some simple and inexpensive dipole configurations, including the conical and cylindrical dipoles, can be used to accomplish this to some degree.

For a finite diameter wire (usually $d > 0.05\lambda$) the current distribution may not be sinusoidal and its effect on the radiation pattern of the antenna is usually negligible. However, it has been shown that the current distribution has a pronounced effect on the input impedance of the wire antenna, especially when its length is such that a near null in current occurs at its input terminals. The effects are much less severe when a near current maximum occurs at the input terminals.

Historically there have been three methods that were used to take into account the finite conductor thickness. The first method treats the problem as boundary-value problem [1], the second as a tapered transmission line or electromagnetic horn [2], and the third finds the current distribution on the wire from an integral equation [3]. The boundary-value approach is well suited for idealistic symmetrical geometries (e.g., ellipsoids, prolate spheroids) which cannot be used effectively to approximate more practical geometries such as the cylinder. The method expresses the fields in terms of an infinite series of free oscillations or natural modes whose coefficients are chosen to satisfy the conditions of the driving source. For the assumed idealized configurations, the method does lead to very reliable data, but it is very difficult to know how to approximate more practical geometries (such as a cylinder) by the more

INTEL-1045
U.S. Patent 7,151,430

idealized configurations (such as the prolate spheroid). For these reasons the boundary-value method is not very practical and will not be pursued any further in this text.

In the second method Schelkunoff represents the antenna as a two-wire uniformly tapered transmission line, each wire of conical geometry, to form a biconical antenna. Its solution is obtained by applying transmission line theory (incident and reflected waves), so well known to the average engineer. The analysis begins by first finding the radiated fields which in turn are used, in conjunction with transmission line theory, to find the input impedance.

For the third technique, the main objectives are to find the current distribution on the antenna and in turn the input impedance. These were accomplished by Hallén by deriving an integral equation for the current distribution whose approximate solution, of different orders, was obtained by iteration and application of boundary conditions. Once a solution for the current is formed, the input impedance is determined by knowing the applied voltage at the feed terminals.

The details of the second method will follow in summary form. The integral equation technique of Hallén, along with that of Pocklington, form the basis of Moment Method techniques which were discussed in Chapter 8.

9.2 BICONICAL ANTENNA

One simple configuration that can be used to achieve broadband characteristics is the biconical antenna formed by placing two cones of infinite extent together, as shown in Figure 9.1(a). This can be thought to represent a uniformly tapered transmission line. The application of a voltage V_i at the input terminals will produce outgoing spherical waves, as shown in Figure 9.1(b), which in turn produce at any point $(r, \theta = \theta_c, \phi)$ a current I along the surface of the cone and voltage V between the cones (Figure 9.2). These can then be used to find the characteristic impedance of the transmission line, which is also equal to the input impedance of an infinite geometry. Modifications to this expression, to take into account the finite lengths of the cones, will be made using transmission line analogy.

9.2.1 Radiated Fields

The analysis begins by first finding the radiated **E**- and **H**-fields between the cones, assuming dominant TEM mode excitation (**E** and **H** are transverse to the direction of propagation). Once these are determined for any point (r, θ, ϕ), the voltage V and current I at any point on the surface of the cone $(r, \theta = \theta_c, \phi)$ will be formed. From Faraday's law we can write that

$$\nabla \times \mathbf{E} = -j\omega\mu\mathbf{H} \tag{9-1}$$

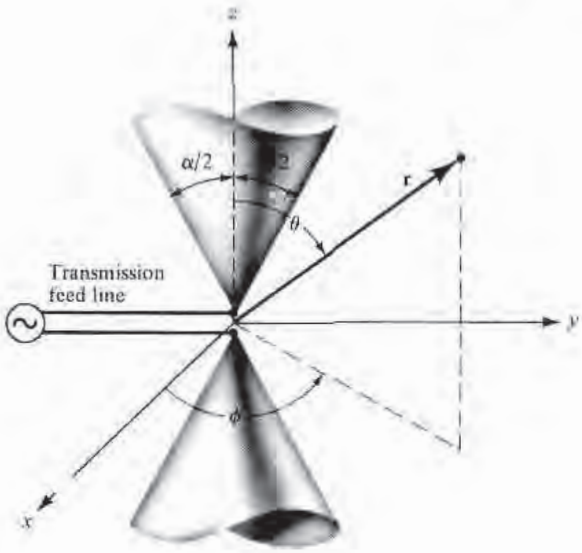
which when expanded in spherical coordinates and assuming that the **E**-field has only an E_θ component independent of ϕ, reduces to

$$\nabla \times \mathbf{E} = \hat{\mathbf{a}}_\phi \frac{1}{r}\frac{\partial}{\partial r}(rE_\theta) = -j\omega\mu(\hat{\mathbf{a}}_r H_r + \hat{\mathbf{a}}_\theta H_\theta + \hat{\mathbf{a}}_\phi H_\phi) \tag{9-2}$$

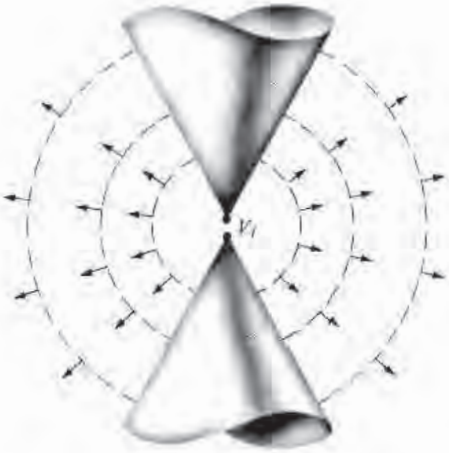
Since **H** only has an H_ϕ component, necessary to form the TEM mode with E_θ, (9-2) can be written as

$$\frac{1}{r}\frac{\partial}{\partial r}(rE_\theta) = -j\omega\mu H_\phi \tag{9-2a}$$

INTEL-1045
U.S. Patent 7,151,430



(a) Biconical geometry



(b) Spherical waves

Figure 9.1 Biconical antenna geometry and radiated spherical waves.

From Ampere's law we have that

$$\nabla \times \mathbf{H} = +j\omega\epsilon\mathbf{E} \tag{9-3}$$

which when expanded in spherical coordinates, and assuming only E_θ and H_ϕ components independent of ϕ, reduces to

$$\hat{\mathbf{a}}_r \frac{1}{r^2 \sin\theta}\left[\frac{\partial}{\partial\theta}(r\sin\theta H_\phi)\right] - \hat{\mathbf{a}}_\theta \frac{1}{r\sin\theta}\left[\frac{\partial}{\partial r}(r\sin\theta H_\phi)\right] = +j\omega\epsilon(\hat{\mathbf{a}}_\theta E_\theta) \tag{9-4}$$

which can also be written as

$$\frac{\partial}{\partial\theta}(r\sin\theta H_\phi) = 0 \tag{9-4a}$$

$$\frac{1}{r\sin\theta}\frac{\partial}{\partial r}(r\sin\theta H_\phi) = -j\omega\epsilon E_\theta \tag{9-4b}$$

INTEL-1045
U.S. Patent 7,151,430

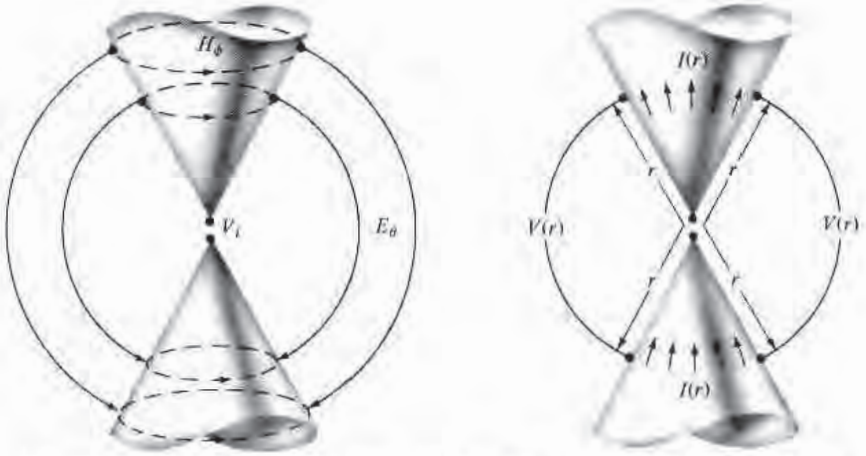


Figure 9.2 Electric and magnetic fields, and associated voltages and currents, for a biconical antenna.

Rewriting (9-4b) as

$$\frac{1}{r}\frac{\partial}{\partial r}(rH_\phi) = -j\omega\epsilon E_\theta \tag{9-5}$$

and substituting it into (9-2a) we form a differential equation for H_ϕ as

$$-\frac{1}{j\omega\epsilon r}\frac{\partial}{\partial r}\left[\frac{\partial}{\partial r}(rH_\phi)\right] = -j\omega\mu H_\phi \tag{9-6}$$

or

$$\frac{\partial^2}{\partial r^2}(rH_\phi) = -\omega^2\mu\epsilon(rH_\phi) = -k^2(rH_\phi) \tag{9-6a}$$

A solution for (9-6a) must be obtained to satisfy (9-4a). To meet the condition of (9-4a), the θ variations of H_ϕ must be of the form

$$H_\phi = \frac{f(r)}{\sin\theta} \tag{9-7}$$

A solution of (9-6a), which also meets the requirements of (9-7) and represents an outward traveling wave, is

$$H_\phi = \frac{H_0}{\sin\theta}\frac{e^{-jkr}}{r} \tag{9-8}$$

where

$$f(r) = H_0\frac{e^{-jkr}}{r} \tag{9-8a}$$

An inward traveling wave is also a solution but does not apply to the infinitely long structure.

INTEL-1045
U.S. Patent 7,151,430

Since the field is of TEM mode, the electric field is related to the magnetic field by the intrinsic impedance, and we can write it as

$$E_\theta = \eta H_\phi = \eta \frac{H_0}{\sin\theta}\frac{e^{-jkr}}{r} \tag{9-9}$$

In Figure 9.2(a) we have sketched the electric and magnetic field lines in the space between the two conical structures. The voltage produced between two corresponding points on the cones, a distance r from the origin, is found by

$$V(r) = \int_{\alpha/2}^{\pi-\alpha/2} \mathbf{E}\cdot d\mathbf{l} = \int_{\alpha/2}^{\pi-\alpha/2} (\hat{\mathbf{a}}_\theta E_\theta)\cdot(\hat{\mathbf{a}}_\theta r\,d\theta) = \int_{\alpha/2}^{\pi-\alpha/2} E_\theta r\,d\theta \tag{9-10}$$

or by using (9-9)

$$V(r) = \eta H_0 e^{-jkr}\int_{\alpha/2}^{\pi-\alpha/2}\frac{d\theta}{\sin\theta} = \eta H_0 e^{-jkr}\ln\left[\frac{\cot(\alpha/4)}{\tan(\alpha/4)}\right]$$

$$V(r) = 2\eta H_0 e^{-jkr}\ln\left[\cot\left(\frac{\alpha}{4}\right)\right] \tag{9-10a}$$

The current on the surface of the cones, a distance r from the origin, is found by using (9-8) as

$$I(r) = \int_0^{2\pi} H_\phi r\sin\theta\,d\phi = H_0 e^{-jkr}\int_0^{2\pi} d\phi = 2\pi H_0 e^{-jkr} \tag{9-11}$$

In Figure 9.2(b) we have sketched the voltage and current at a distance r from the origin.

9.2.2 Input Impedance

A. Infinite Cones

Using the voltage of (9-10a) and the current of (9-11), we can write the characteristic impedance as

$$Z_c = \frac{V(r)}{I(r)} = \frac{\eta}{\pi}\ln\left[\cot\left(\frac{\alpha}{4}\right)\right] \tag{9-12}$$

Since the characteristic impedance is not a function of the radial distance r, it also represents the input impedance at the antenna feed terminals of the infinite structure. For a free-space medium, (9-12) reduces to

$$\boxed{Z_c = Z_{in} = 120\ln\left[\cot\left(\frac{\alpha}{4}\right)\right]} \tag{9-12a}$$

which is a pure resistance. For small cone angles

$$Z_{in} = \frac{\eta}{\pi}\ln\left[\cot\left(\frac{\alpha}{4}\right)\right] = \frac{\eta}{\pi}\ln\left[\frac{1}{\tan(\alpha/4)}\right] \simeq \frac{\eta}{\pi}\ln\left(\frac{4}{\alpha}\right) \tag{9-12b}$$

Variations of Z_{in} as a function of the half-cone angle $\alpha/2$ are shown plotted in Figure 9.3(a) for $0° < \alpha/2 \leq 90°$ and in Figure 9.3(b) in an expanded scale for

INTEL-1045
U.S. Patent 7,151,430

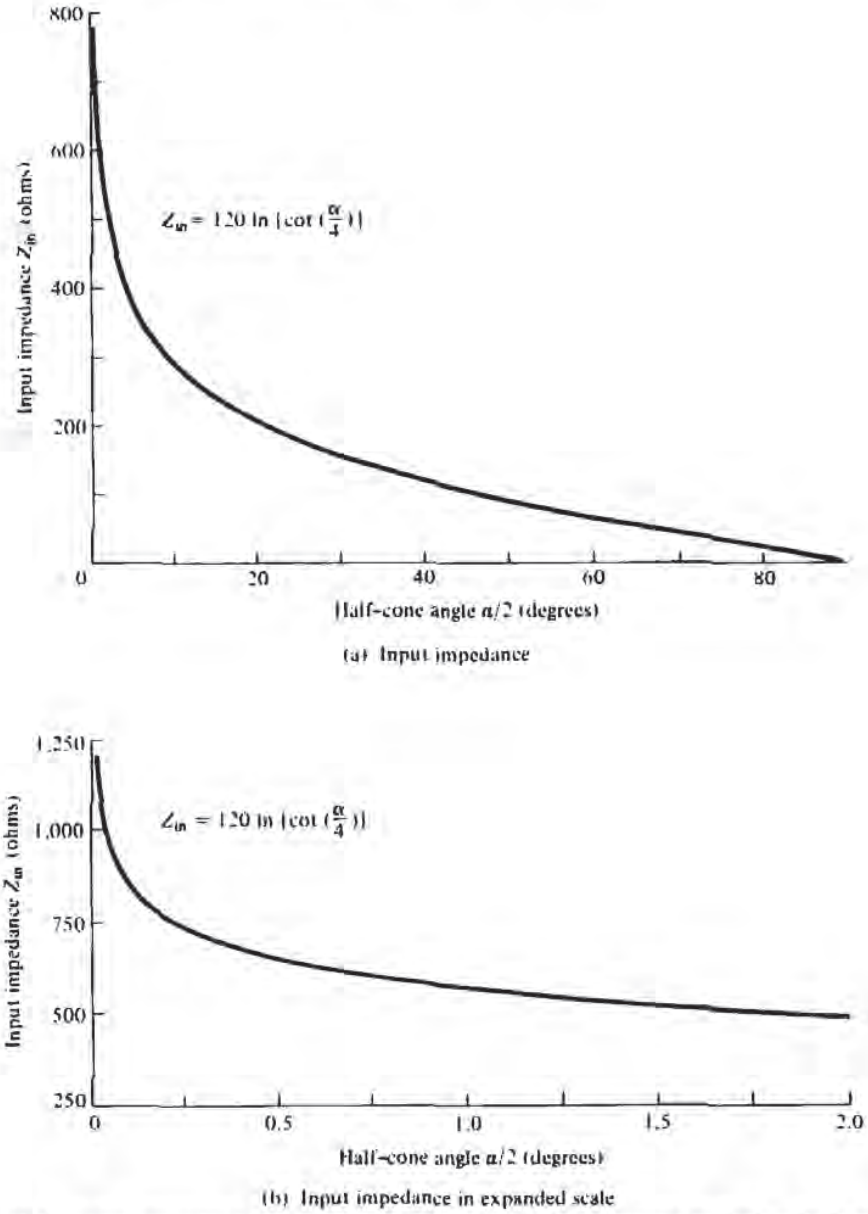


Figure 9.3 Input impedance of an infinitely long biconical antenna radiating in free-space.

$0° < \alpha/2 \leq 2°$. Although the half-cone angle is not very critical in the design, it is usually chosen so that the characteristic impedance of the biconical configuration is nearly the same as that of the transmission line to which it will be attached. Small angle biconical antennas are not very practical but wide-angle configurations ($30° < \alpha/2 < 60°$) are frequently used as broadband antennas.

The radiation resistance of (9-12) can also be obtained by first finding the total radiated power

$$P_{rad} = \oiint_S \mathbf{W}_{av} \cdot d\mathbf{s} = \int_0^{2\pi} \int_{\alpha/2}^{\pi-\alpha/2} \frac{|E|^2}{2\eta} r^2 \sin\theta \, d\theta \, d\phi = \pi\eta |H_0|^2 \int_0^{\pi-\alpha/2} \frac{d\theta}{\sin\theta}$$

INTEL-1045
U.S. Patent 7,151,430

$$P_{\text{rad}} = 2\pi\eta|H_0|^2 \ln\left[\cot\left(\frac{\alpha}{4}\right)\right] \tag{9-13}$$

and by using (9-11) evaluated at $r = 0$ we form

$$\boxed{R_r = \frac{2P_{\text{rad}}}{|I(0)|^2} = \frac{\eta}{\pi}\ln\left[\cot\left(\frac{\alpha}{4}\right)\right]} \tag{9-14}$$

which is identical to (9-12).

B. Finite Cones

The input impedance of (9-12) or (9-14) is for an infinitely long structure. To take into account the finite dimensions in determining the input impedance, Schelkunoff [2] has devised an ingenious method where he assumes that for a finite length cone ($r = l/2$) some of the energy along the surface of the cone is reflected while the remaining is radiated. Near the equator most of the energy is radiated. This can be viewed as a load impedance connected across the ends of the cones. The electrical equivalent is a transmission line of characteristic impedance Z_c terminated in a load impedance Z_L. Computed values [4] for the input resistance and reactance of small angle cones are shown in Figure 9.4. It is apparent that the antenna becomes more broadband (its resistance and reactance variations are less severe) as the cone angle increases.

The biconical antenna represents one of the canonical problems in antenna theory, and its model is well suited for examining general characteristics of dipole-type antennas.

C. Unipole

Whenever one of the cones is mounted on an infinite plane conductor (i.e., the lower cone is replaced by a ground plane), it forms a unipole and its input impedance is one-half of the two-cone structure. Input impedances for unipoles of various cone angles as a function of the antenna length l have been measured [5]. Radiation patterns of biconical dipoles fed by coaxial lines have been computed by Papas and King [6].

9.3 TRIANGULAR SHEET, BOW-TIE, AND WIRE SIMULATION

Because of their broadband characteristics, biconical antennas have been employed for many years in the VHF and UHF frequency ranges. However, the solid or shell biconial structure is so massive for most frequencies of operation that it is impractical to use. Because of its attractive radiation characteristics, compared to those of other single antennas, realistic variations to its mechanical structure have been sought while retaining as much of the desired electrical features as possible.

Geometrical approximations to the solid or shell conical unipole or biconical antenna are the triangular sheet and bow-tie antennas shown in Figures 9.5(a) and (b), respectively, each fabricated from sheet metal. The triangular sheet has been investigated experimentally by Brown and Woodward [5]. Each of these antennas can also be simulated by a wire along the periphery of its surface which reduces significantly the weight and wind resistance of the structure. The computed input impedances and radiation patterns of wire bow-tie antennas, when mounted above a ground plane,

INTEL-1045
U.S. Patent 7,151,430

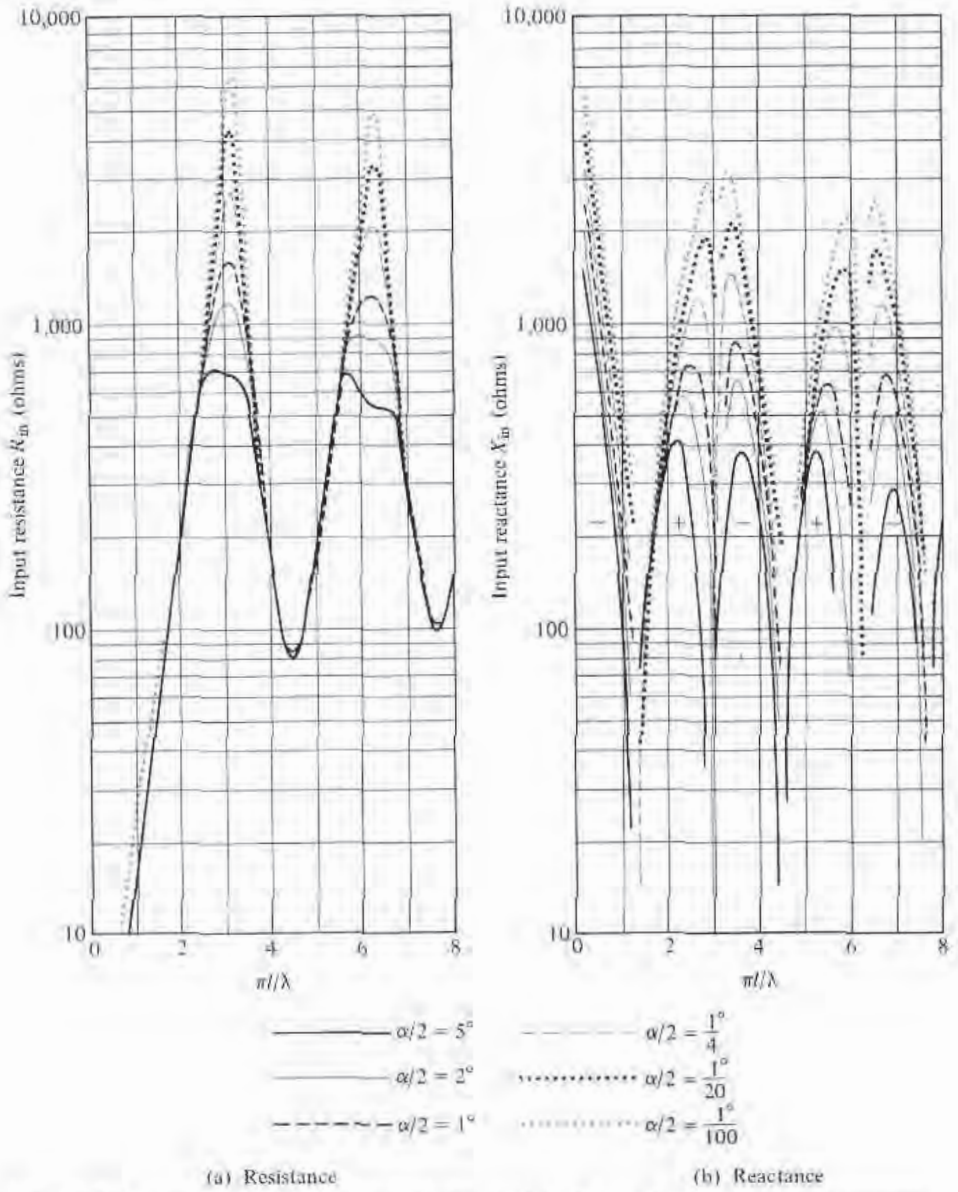
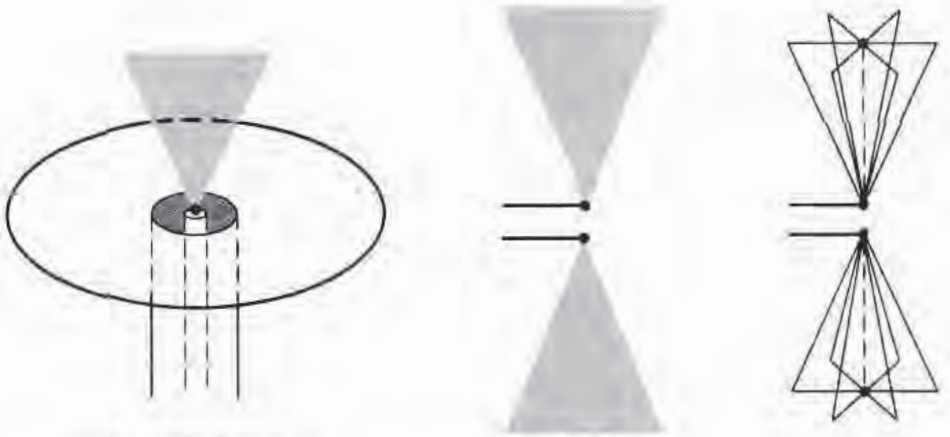


Figure 9.4 *Input impedance (at feed terminals) of finite length biconical antenna.* (SOURCE: H. Jasik (ed.), *Antenna Engineering Handbook*, McGraw-Hill, New York, 1961, Chapter 3)

have been computed using the Moment Method [7]. The impedance is shown plotted in Figure 9.6. A comparison of the results of Figure 9.6 with those of reference [5] reveals that the bow-tie antenna does not exhibit as broadband characteristics (i.e., nearly constant resistance and essentially zero reactance over a large frequency range) as the corresponding solid biconical antenna for $30° < \alpha < 90°$. Also for a given flare angle the resistance and reactance of the bow-tie wire structure fluctuate more than for a triangular sheet antenna. Thus the wire bow-tie is very narrowband as compared to the biconical surface of revolution or triangular sheet antenna.

In order to simulate better the attractive surface of revolution of a biconical antenna by low-mass structures, multielement intersecting wire bow-ties were employed as shown in Figure 9.5(c). It has been shown that eight or more intersecting

INTEL-1045
U.S. Patent 7,151,430



(a) Triangular sheet (b) Bow-tie (c) Wire simulation

Figure 9.5 Triangular sheet, bow-tie, and wire simulation of biconical antenna.

wire-constructed bow-ties can approximate reasonably well the radiation characteristics of a conical body-of-revolution antenna.

9.4 CYLINDRICAL DIPOLE

Another simple and inexpensive antenna whose radiation characteristics are frequency dependent is a cylindrical dipole (i.e., a wire of finite diameter and length) of the form shown in Figure 9.7. Thick dipoles are considered broadband while thin dipoles are more narrowband. This geometry can be considered to be a special form of the biconical antenna when $\alpha = 0°$. A thorough analysis of the current, impedance, pattern, and other radiation characteristics can be performed using the Moment Method. With that technique the antenna is analyzed in terms of integral formulations of the Hallén and Pocklington type which can be evaluated quite efficiently by the Moment Method. The analytical formulation of the Moment Method has been presented in Chapter 8. In this section we want to present, in summary form, some of its performance characteristics.

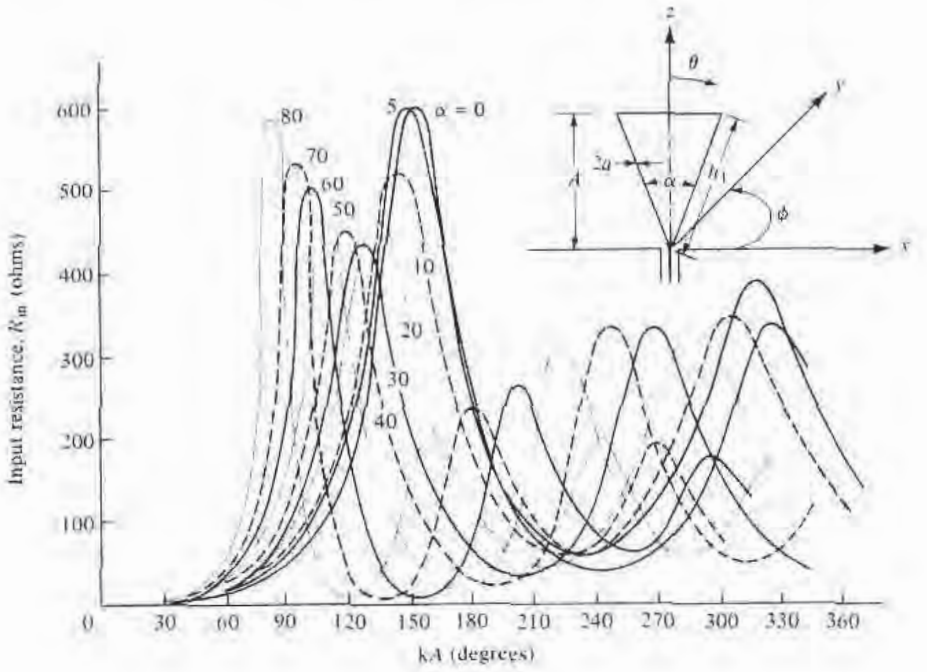
9.4.1 Bandwidth

As has been pointed out previously, a very thin linear dipole has very narrowband input impedance characteristics. Any small perturbations in the operating frequency will result in large changes in its operational behavior. One method by which its acceptable operational bandwidth can be enlarged will be to decrease the l/d ratio. For a given antenna, this can be accomplished by holding the length the same and increasing the diameter of the wire. For example, an antenna with a $l/d = 5{,}000$ has an acceptable bandwidth of about 3%, which is a small fraction of the center frequency. An antenna of the same length but with a $l/d = 260$ has a bandwidth of about 30%.

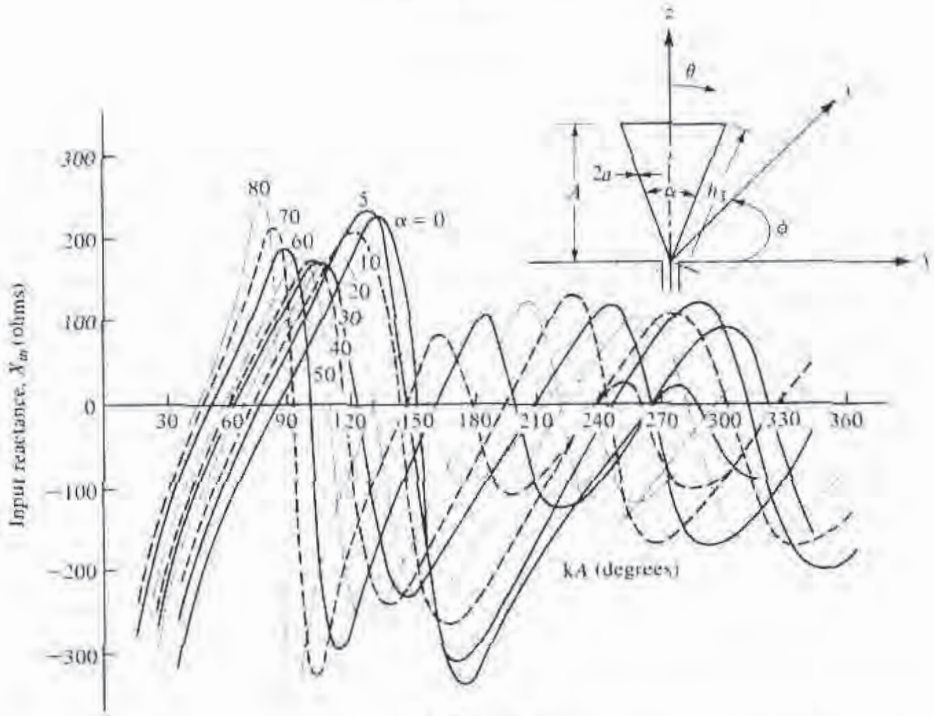
9.4.2 Input Impedance

The input impedance (resistance and reactance) of a very thin dipole of length l and diameter d can be computed using (8-60a)–(8-61b). As the radius of the wire increases,

INTEL-1045
U.S. Patent 7,151,430



(a) Resistance



(b) Reactance

Figure 9.6 Computed impedance of wire bow-tie (or wire unipole) as a function of length for various included angles. (SOURCE: C. E. Smith, C. M. Butler, and K. R. Umashankar. "Characteristics of Wire Biconical Antenna," *Microwave Journal*, pp. 37–40, September 1979)

INTEL-1045
U.S. Patent 7,151,430

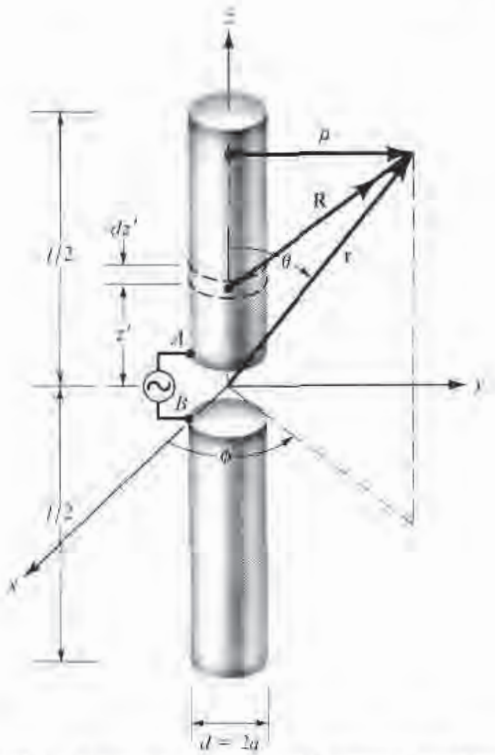


Figure 9.7 Center-fed cylindrical antenna configuration.

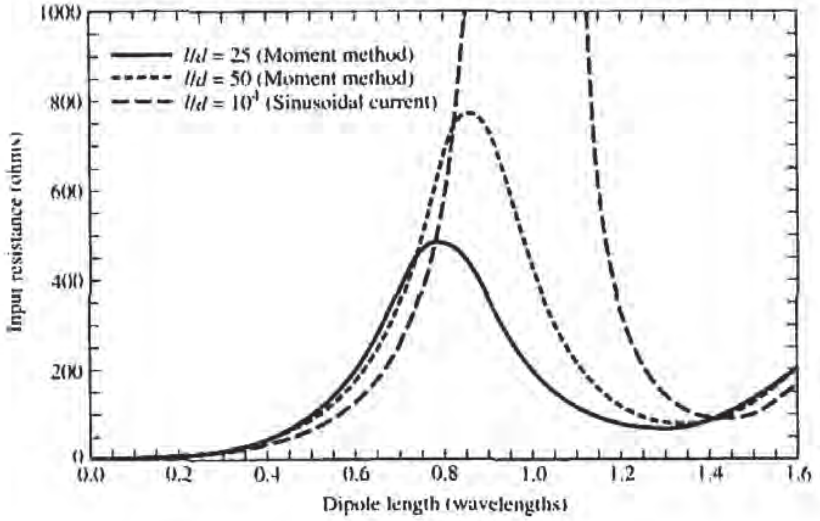
these equations become inaccurate. However, using integral equation analyses such as the Moment Method of Chapter 8, input impedances can be computed for wires with different l/d ratios. In general, it has been observed that for a given length wire its impedance variations become less sensitive as a function of frequency as the l/d ratio decreases. Thus more broadband characteristics can be obtained by increasing the diameter of a given wire. To demonstrate this, in Figures 9.8(a) and (b) we have plotted, as a function of length, the input resistance and reactance of dipoles with $l/d = 10^4(\Omega = 19.81)$, $50(\Omega = 9.21)$, and $25(\Omega = 6.44)$ where $\Omega = 2\ln(2l/d)$. For $l/d = 10^4$ the values were computed using (8-60a) and (8-61a) and then transferred to the input terminals by (8-60b) and (8-61b), respectively. The others were computed using the Moment Method techniques of Chapter 8. It is noted that the variations of each are less pronounced as the l/d ratio decreases, thus providing greater bandwidth.

Measured input resistances and reactances for a wide range of constant l/d ratios have been reported [8]. These curves are for a cylindrical antenna driven by a coaxial cable mounted on a large ground plane on the earth's surface. Thus they represent half of the input impedance of a center-fed cylindrical dipole radiating in free-space. The variations of the antenna's electrical length were obtained by varying the frequency while the length-to-diameter (l/d) ratio was held constant.

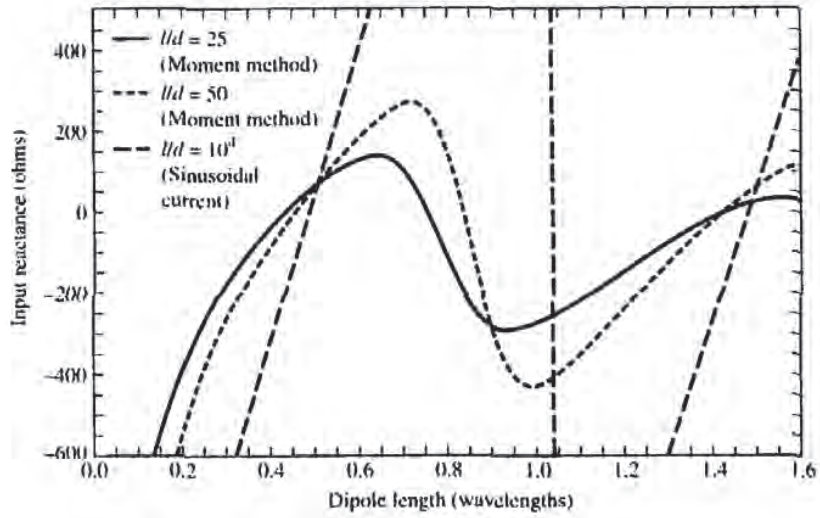
9.4.3. Resonance and Ground Plane Simulation

The imaginary part of the input impedance of a linear dipole can be eliminated by making the total length, l, of the wire slightly less than an integral number of half-wavelengths (i.e., l slight less than $n\lambda/2$, $n = 1, 2, 3, 4, \ldots$). The amount of reduction in length, is a function of the radius of the wire, and it can be determined for thin

INTEL-1045
U.S. Patent 7,151,430



(a) Input resistance



(b) Input reactance

Figure 9.8 (a) Input resistance and reactance of wire dipoles.

wires iteratively using (8-60b) and (8-61b). At the resonance length, the resistance can then be determined using (8-60a) and (8-61a). Empirical equations for approximating the length, impedance, and the order of resonance of the cylindrical dipoles are found in Table 9.1 [9]. R_n is called the natural resistance and represents the geometric mean resistance at an odd resonance and at the next higher even resonance. For a cylindrical stub above a ground plane, as shown in Figure 9.9, the corresponding values are listed in Table 9.2 [9].

To reduce the wind resistance, to simplify the design, and to minimize the costs, a ground plane is often simulated, especially at low frequencies, by crossed wires as shown in Figure 9.9(b). Usually only two crossed wires (four radials) are employed. A larger number of radials results in a better simulation of the ground plane. Ground planes are also simulated by wire mesh. The spacing between the wires is usually

INTEL-1045
U.S. Patent 7,151,430

Table 9.1 CYLINDRICAL DIPOLE RESONANCES

	First Resonance	Second Resonance	Third Resonance	Fourth Resonance
LENGTH	$0.48\lambda F$	$0.96\lambda F$	$1.44\lambda F$	$1.92\lambda F$
RESISTANCE (ohms)	67	$\frac{R_n^2}{67}$	95	$\frac{R_n^2}{95}$

$$F = \frac{l/2a}{1 + l/2a}; \quad R_n = 150 \log_{10}(l/2a)$$

selected to be equal or smaller than $\lambda/10$. The flat or shaped reflecting surfaces for UHF educational TV are usually realized approximately by using wire mesh.

9.4.4 Radiation Patterns

The theory for the patterns of infinitesimally thin wires was developed in Chapter 4. Although accurate patterns for finite diameter wires can be computed using current distributions obtained by the Moment Method of Chapter 8, the patterns calculated using ideal sinusoidal current distributions, valid for infinitely small diameters, provide a good first-order approximation even for relatively thick cylinders. To illustrate this, in Figure 9.10 we have plotted the relative patterns for $l = 3\lambda/2$ with $l/d = 10^4(\Omega = 19.81)$, $50(\Omega = 9.21)$, $25(\Omega = 6.44)$, and $8.7(\Omega = 5.71)$, where $\Omega = 2\ \ln(2l/d)$. For $l/d = 10^4$ the current distribution was assumed to be purely sinusoidal, as given by (4-56); for the others, the Moment Method techniques of Chapter 8 were used. The patterns were computed using the Moment Method formulations outlined in Section 8.4. It is noted that the pattern is essentially unaffected by the thickness of the wire in regions of intense radiation. However, as the radius of the wire increases, the minor lobes diminish in intensity and the nulls are replaced by low-level radiation. The same characteristics have been observed for other length dipoles such as $l = \lambda/2$, λ and 2λ. The input impedance for the $l = \lambda/2$ and $l = 3\lambda/2$ dipoles, with $l/d = 10^4$, 50, and 25, is equal to

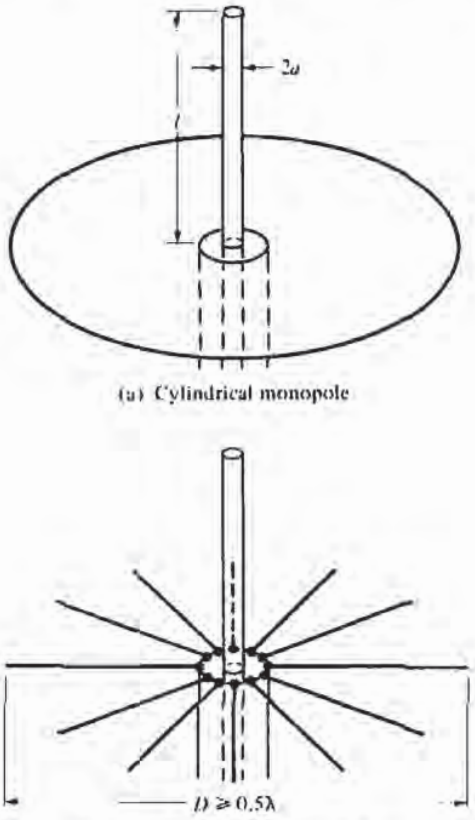
$l = \lambda/2$	$l = 3\lambda/2$	
$Z_{in}(l/d = 10^4) = 73 + j42.5$	$Z_{in}(l/d = 10^4) = 105.49 + j45.54$	
$Z_{in}(l/d = 50) = 85.8 + j54.9$	$Z_{in}(l/d = 50) = 103.3 + j9.2$	(9-15)
$Z_{in}(l/d = 25) = 88.4 + j27.5$	$Z_{in}(l/d = 25) = 106.8 + j4.9$	

Table 9.2 CYLINDRICAL STUB RESONANCES

	First Resonance	Second Resonance	Third Resonance	Fourth Resonance
LENGTH	$0.24\lambda F'$	$0.48\lambda F'$	$0.72\lambda F'$	$0.96\lambda F'$
RESISTANCE (ohms)	34	$\frac{(R_n')^2}{34}$	48	$\frac{(R_n')^2}{48}$

$$F' = \frac{l/a}{1 + l/a}; \quad R_n' = 75 \log_{10}(l/a)$$

INTEL-1045
U.S. Patent 7,151,430



(a) Cylindrical monopole

(b) Wire simulation of ground plane

Figure 9.9 Cylindrical monopole above circular solid and wire-simulated ground planes.

9.4.5 Equivalent Radii

Up to now, the formulations for the current distribution and the input impedance assume that the cross section of the wire is constant and of radius a. An electrical equivalent radius can be obtained for some uniform wires of noncircular cross section. This is demonstrated in Table 9.3 where the actual cross sections and their equivalent radii are illustrated.

The equivalent radius concept can be used to obtain the antenna or scattering characteristics of electrically small wires of arbitrary cross sections. It is accomplished by replacing the noncircular cross section wire with a circular wire whose radius is the "equivalent" radius of the noncircular cross section. In electrostatics, the equivalent radius represents the radius of a circular wire whose capacitance is equal to that of the noncircular geometry. This definition can be used at all frequencies provided the wire remains electrically small. The circle with equivalent radius lies between the circles which circumscribe and inscribe the geometry and which together bound the noncircular cross section.

9.4.6 Dielectric Coating

Up to now it has been assumed that the wire antennas are radiating into free-space. The radiation characteristics of a wire antenna (current distribution, far-field pattern,

INTEL-1045
U.S. Patent 7,151,430

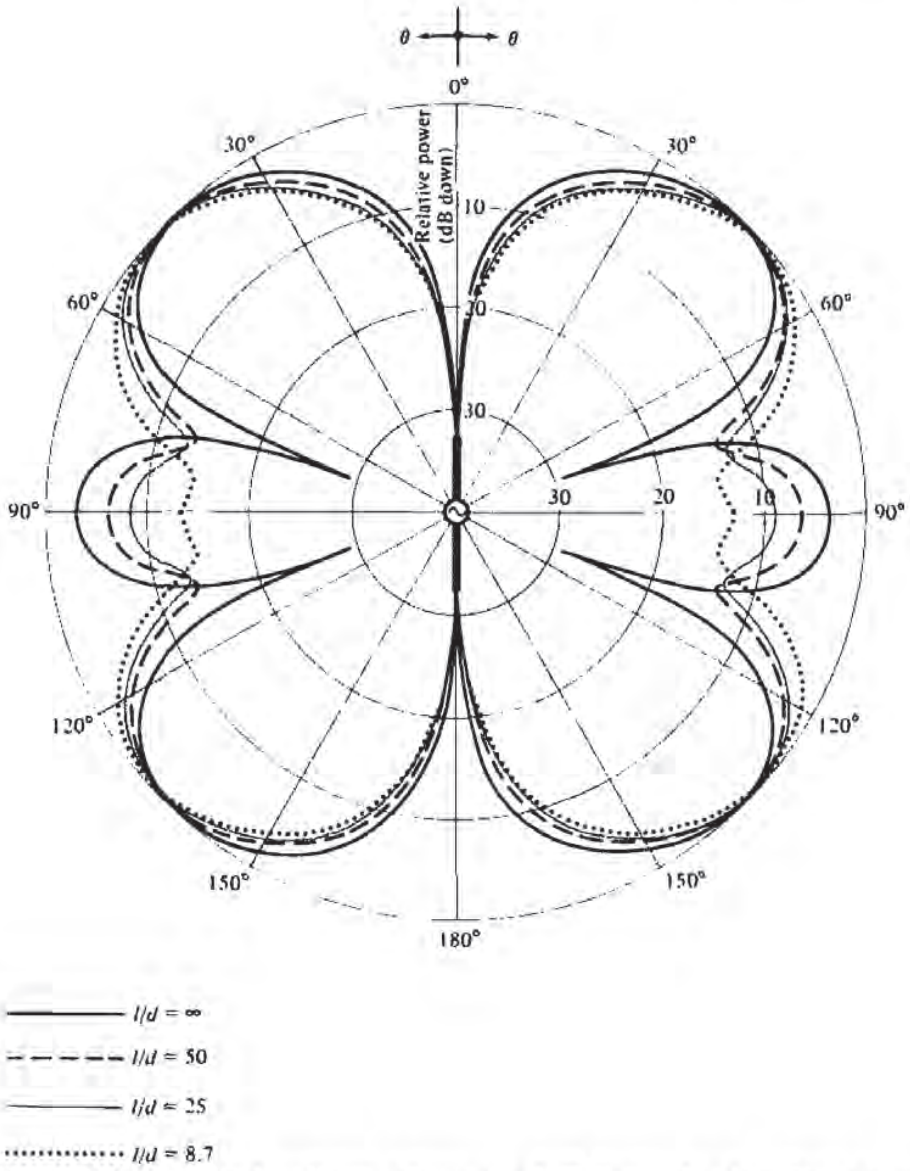


Figure 9.10 Amplitude radiation patterns of a $3\lambda/2$ dipole of various thicknesses.

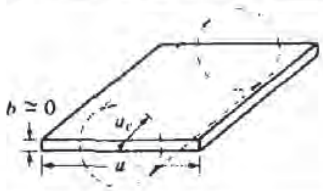
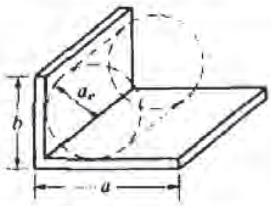
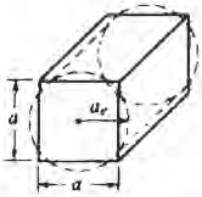
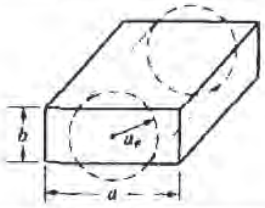
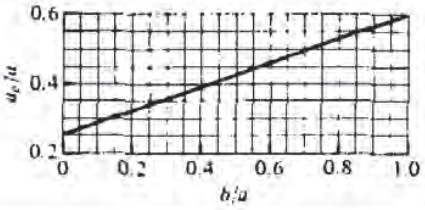
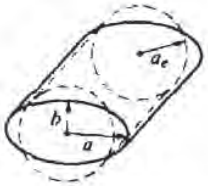
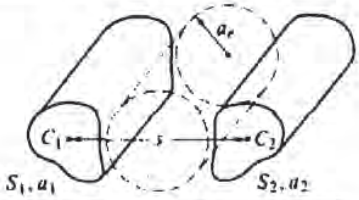
input impedance, bandwidth, radiation efficiency, and effective length) coated with a layer of electrically and magnetically lossless [10] or lossy [11] medium, as shown in Figure 9.11, will be affected unless the layer is very thin compared to the radius and the wavelength. The problem was investigated analytically by the Moment Method and the effects on the radiation characteristics can be presented by defining the two parameters

$$P = \left(\frac{\dot{\epsilon}_r - 1}{\dot{\epsilon}_r}\right) \ln\left(\frac{b}{a}\right) \tag{9-16}$$

$$Q = (\dot{\mu}_r - 1) \ln\left(\frac{b}{a}\right) \tag{9-17}$$

INTEL-1045
U.S. Patent 7,151,430

Table 9.3 CONDUCTOR GEOMETRICAL SHAPES AND THEIR EQUIVALENT CIRCULAR CYLINDER RADII

Geometrical Shape	Electrical Equivalent Radius
	$a_e = 0.25a$
	$a_e = 0.2(a + b)$
	$a_e = 0.59a$
 	
	$a_e = \frac{1}{2}(a + b)$
	$\ln a_e = \frac{1}{(S_1 + S_2)^2} \times \{S_1^2 \ln a_1 + S_2^2 \ln a_2 + 2S_1S_2 \ln s\}$ S_1, S_2 = peripheries of conductors C_1, C_2 a_1, a_2 = equivalent radii of conductors C_1, C_2

INTEL-1045
U.S. Patent 7,151,430

where

$\dot{\epsilon}_r$ = relative (to the ambient medium) complex permittivity
$\dot{\mu}_r$ = relative (to the ambient medium) complex permeability
a = radius of the conducting wire
$b - a$ = thickness of coating

In general:

1. Increasing the real part of either P or Q
   a. increases the peak input admittance
   b. increases the electrical length (lowers the resonant frequency)
   c. narrows the bandwidth
2. Increasing the imaginary part of P or Q
   a. decreases the peak input admittance
   b. decreases the electrical length (increases the resonant frequency)
   c. increases the bandwidth
   d. accentuates the power dissipated (decreases the radiation efficiency)
   e. accentuates the traveling wave component of the current distribution

Thus the optimum bandwidth of the antenna can be achieved by choosing a lossy dielectric material with maximum imaginary parts of P and Q and minimum real parts. However, doing this decreases the radiation efficiency. In practice, a trade-off between bandwidth and efficiency is usually required. This is not a very efficient technique to broadband the antenna.

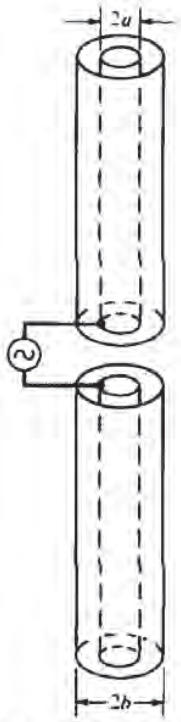


Figure 9.11 Coated linear dipole.

INTEL-1045
U.S. Patent 7,151,430

9.5 FOLDED DIPOLE

To achieve good directional pattern characteristics and at the same time provide good matching to practical coaxial lines with 50- or 75-ohm characteristic impedances, the length of a single wire element is usually chosen to be $\lambda/4 \leq l < \lambda$. The most widely used dipole is that whose overall length is $l \simeq \lambda/2$, and which has an input impedance of $Z_{in} \simeq 73 + j42.5$ and directivity of $D_0 \simeq 1.643$. In practice, there are other very common transmission lines whose characteristic impedance is much higher than 50 or 75 ohms. For example, a "twin lead" transmission line (usually two parallel wires separated by about $\frac{5}{16}$ in. and embedded in a low-loss plastic material used for support and spacing) is widely used for TV applications and has a characteristic impedance of about 300 ohms.

In order to provide good matching characteristics, variations of the single dipole element must be used. One simple geometry that can achieve this is a folded wire which forms a very thin ($s \ll \lambda$) rectangular loop as shown in Figure 9.12(a). This antenna, when the spacing between the two larger sides is very small (usually $s < 0.05\lambda$), is known as a folded dipole and it serves as a step-up impedance transformer (approximately by a factor of 4 when $l = \lambda/2$) of the single element impedance. Thus when $l = \lambda/2$ and the antenna is resonant, impedances on the order of about 300 ohms can be achieved, and it would be ideal for connections to "twin-lead" transmission lines.

A folded dipole operates basically as an unbalanced transmission line, and it can be analyzed by assuming that its current is decomposed into two distinct modes: a transmission line mode [Figure 9.12(b)] and an antenna mode [Figure 9.12(c)]. This type of an analytic model can be used to predict accurately the input impedance provided the longer parallel wires are close together electrically ($s \ll \lambda$).

To derive an equation for the input impedance, let us refer to the modeling of Figure 9.12. For the transmission line mode of Figure 9.12(b), the input impedance at the terminals $a - b$ or $e - f$, looking toward the shorted ends, is obtained from the impedance transfer equation

$$Z_t = Z_0 \left[\frac{Z_L + jZ_0 \tan(kl')}{Z_0 + jZ_L \tan(kl')} \right]_{\substack{l' = l/2 \\ Z_L = 0}} = jZ_0 \tan\left(k\frac{l}{2}\right) \tag{9-18}$$

where Z_0 is the characteristic impedance of a two-wire transmission line

$$Z_0 = \frac{\eta}{\pi} \cosh^{-1}\left(\frac{s/2}{a}\right) = \frac{\eta}{\pi} \ln\left[\frac{s/2 + \sqrt{(s/2)^2 - a^2}}{a}\right] \tag{9-19}$$

which can be approximated for $s/2 \gg a$ by

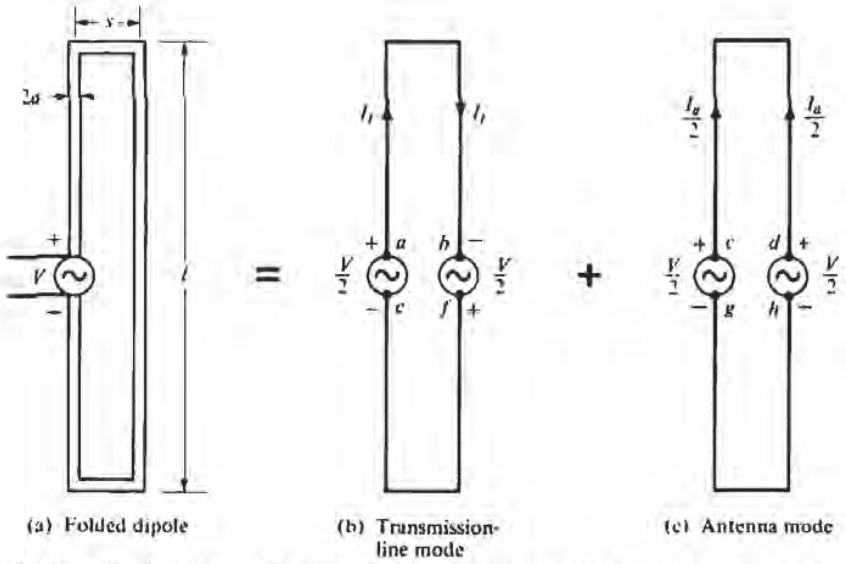
$$Z_0 = \frac{\eta}{\pi} \ln\left[\frac{s/2 + \sqrt{(s/2)^2 - a^2}}{a}\right] \simeq \frac{\eta}{\pi} \ln\left(\frac{s}{a}\right) = 0.733\eta \log_{10}\left(\frac{s}{a}\right) \tag{9-19a}$$

Since the voltage between the points a and b is $V/2$, and it is applied to a transmission line of length $l/2$, the transmission line current is given by

$$I_t = \frac{V/2}{Z_t} \tag{9-20}$$

For the antenna mode of Figure 9.12(c), the generator points $c - d$ and $g - h$ are each at the same potential and can be connected, without loss of generality, to form a dipole. Each leg of the dipole is formed by a pair of closely spaced wires

INTEL-1045
U.S. Patent 7,151,430



(a) Folded dipole (b) Transmission-line mode (c) Antenna mode

Figure 9.12 Folded dipole and its equivalent transmission line and antenna mode models. (SOURCE: G. A. Thiele, E. P. Ekelman, Jr., and L. W. Henderson, "On the Accuracy of the Transmission Line Model for Folded Dipole," *IEEE Trans. Antennas Propagat.*, Vol. AP-28, No. 5, pp. 700–703, September 1980. © (1980) IEEE)

($s \ll \lambda$) extending from the feed ($c - d$ or $g - h$) to the shorted end. Thus the current for the antenna mode is given by

$$I_a = \frac{V/2}{Z_d} \tag{9-21}$$

where Z_d is the input impedance of a linear dipole of length l and diameter d computed using (8-60a)–(8-61b). For the configuration of Figure 9.12(c), the radius that is used to compute Z_d for the dipole can be either the half-spacing between the wires ($s/2$) or an equivalent radius a_e. The equivalent radius a_e is related to the actual wire radius a by (from Table 9.3)

$$\ln(a_e) = \tfrac{1}{2}\ln(a) + \tfrac{1}{2}\ln(s) = \ln(a) + \tfrac{1}{2}\ln\left(\frac{s}{a}\right) = \ln\sqrt{as} \tag{9-22}$$

or

$$a_e = \sqrt{as} \tag{9-22a}$$

It should be expected that the equivalent radius yields the most accurate results.

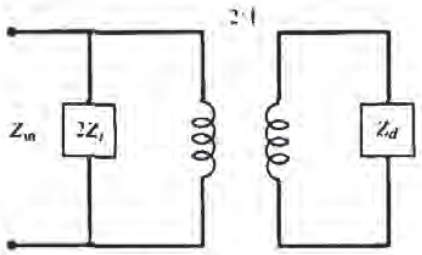
The total current on the feed leg (left side) of the folded dipole of Figure 9.12(a) is given by

$$I_{in} = I_t + \frac{I_a}{2} = \frac{V}{2Z_t} + \frac{V}{4Z_d} = \frac{V(2Z_d + Z_t)}{4Z_tZ_d} \tag{9-23}$$

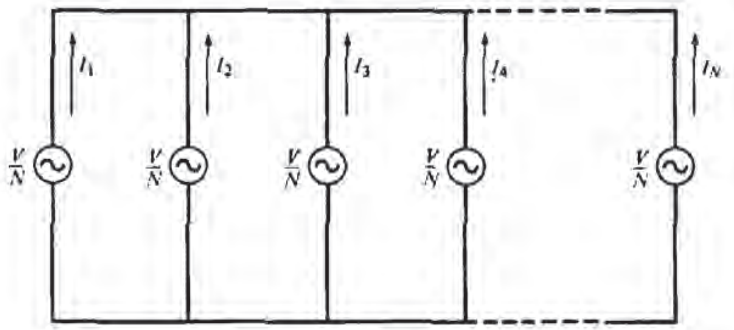
and the input impedance at the feed by

$$\boxed{Z_{in} = \frac{V}{I_{in}} = \frac{2Z_t(4Z_d)}{2Z_t + 4Z_d} = \frac{4Z_tZ_d}{2Z_d + Z_t}} \tag{9-24}$$

INTEL-1045
U.S. Patent 7,151,430



(a) Two-element



(b) N-element

Figure 9.13 Equivalent circuits for two-element and N-element (with equal radii elements) folded dipoles.

Based on (9-24), the folded dipole behaves as the equivalent of Figure 9.13(a) in which the antenna mode impedance is stepped up by a ratio of four. The transformed impedance is then placed in shunt with twice the impedance of the nonradiating (transmission line) mode to result in the input impedance.

When $l = \lambda/2$, it can be shown that (9-24) reduces to

$$\boxed{Z_{in} = 4Z_d} \tag{9-25}$$

or that the impedance of the folded dipole is four times greater than that of an isolated dipole of the same length as one of its sides. This is left as an exercise for the reader (Prob. 9.9).

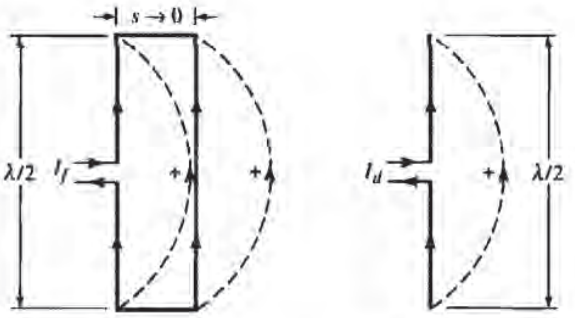
The impedance relation of (9-25) for the $l = \lambda/2$ can also be derived by referring to Figure 9.14. Since for a folded dipole the two vertical arms are closely spaced ($s \ll \lambda$), the current distribution in each is identical as shown in Figure 9.14(a). The equivalent of the folded dipole of Figure 9.14(a) is the ordinary dipole of Figure 9.14(b). Comparing the folded dipole to the ordinary dipole, it is apparent that the currents of the two closely spaced and identical arms of the folded dipole are equal to the one current of the ordinary dipole, or

$$2I_f = I_d \tag{9-26}$$

where I_f is the current of the folded dipole and I_d is the current of the ordinary dipole. Also the input power of the two dipoles are identical, or

$$P_f = \frac{1}{2} I_f^2 Z_f = P_d = \frac{1}{2} I_d^2 Z_d \tag{9-27}$$

INTEL-1045
U.S. Patent 7,151,430



(a) Folded dipole (b) Regular dipole

Figure 9.14 Folded dipole and equivalent regular dipole.

Substituting (9-26) into (9-27) leads to

$$Z_f = 4Z_d \tag{9-28}$$

where Z_f is the impedance of the folded dipole while Z_d is the impedance of the ordinary dipole. Equation (9-28) is identical to (9-25).

To better understand the impedance transformation of closely spaced conductors (of equal diameter) and forming a multielement folded dipole, let us refer to its equivalent circuit in Figure 9.13(b). For N elements, the equivalent voltage at the center of each conductor is V/N and the current in each is I_n, $n = 1, 2, 3, \ldots, N$. Thus the voltage across the first conductor can be represented by

$$\frac{V}{N} = \sum_{n=1}^{N} I_n Z_{1n} \tag{9-29}$$

where Z_{1n} represents the self or mutual impedance between the first and nth element. Because the elements are closely spaced

$$I_n \simeq I_1 \quad \text{and} \quad Z_{1n} \simeq Z_{11} \tag{9-30}$$

for all values of $n = 1, 2, \ldots, N$. Using (9-30), we can write (9-29) as

$$\frac{V}{N} = \sum_{n=1}^{N} I_n Z_{1n} \simeq I_1 \sum_{n=1}^{N} Z_{1n} \simeq N I_1 Z_{11} \tag{9-31}$$

or

$$\boxed{Z_{in} = \frac{V}{I_1} \simeq N^2 Z_{11} = N^2 Z_r} \tag{9-31a}$$

since the self-impedance Z_{11} of the first element is the same as its impedance Z_r in the absence of the other elements. Additional impedance step-up of a single dipole can be obtained by introducing more elements. For a three-element folded dipole with elements of identical diameters and of $l \simeq \lambda/2$, the input impedance would be about nine times greater than that of an isolated element or about 650 ohms. Greater step-up transformations can be obtained by adding more elements; in practice, they are seldom needed. Many other geometrical configurations of a folded dipole can be obtained which would contribute different values of input impedances. Small variations in impedance can be obtained by using elements of slightly different diameters and/or lengths.

INTEL-1045
U.S. Patent 7,151,430

To test the validity of the transmission line model for the folded dipole, a number of computations were made [12] and compared with data obtained by the Moment Method, which is considered to be more accurate. In Figures 9.15(a) and (b) the input resistance and reactance for a two-element folded dipole is plotted as a function of l/λ when the diameter of each wire is $d = 2a = 0.001\lambda$ and the spacing between the elements is $s = 0.00613\lambda$. The characteristic impedance of such a transmission line is 300 ohms. The equivalent radius was used in the calculations of Z_A. An excellent agreement is indicated between the results of the transmission line model and the Moment Method. Computations and comparisons for other spacings ($s = 0.0213\lambda$, $Z_0 = 450$ ohms and $s = 0.0742\lambda$, $Z_0 = 600$ ohms) but with elements of the same diameter ($d = 0.001\lambda$) have been made [12]. It has been shown that as the spacing between the wires increased, the results of the transmission line mode began to disagree with those of the Moment Method. For a given spacing, the accuracy for the characteristic impedance, and in turn for the input impedance, can be improved by increasing the diameter of the wires. The characteristic impedance of a transmission line, as given by (9-19) or (9-19a), depends not on the spacing but on the spacing-to-diameter (s/d) ratio, which is more accurate for smaller s/d. Computations were also made whereby the equivalent radius was not used. The comparisons of these results indicated larger disagreements, thus concluding the necessity of the equivalent radius, especially for the larger wire-to-wire spacings.

A two-element folded dipole is widely used as feed element of TV antennas such as Yagi-Uda antennas. Although the impedance of an isolated folded dipole may be around 300 ohms, its value will be somewhat different when it is used as an element in an array or with a reflector. The folded dipole has better bandwidth characteristics than a single dipole of the same size. Its geometrical arrangement tends to behave as a short parallel stub line which attempts to cancel the off resonance reactance of a single dipole. The folded dipole can be thought to have a bandwidth which is the same as that of a single dipole but with an equivalent radius ($a < a_e < s/2$).

Symmetrical and asymmetrical planar folded dipoles can also be designed and constructed using strips which can be fabricated using printed circuit technology [13]. The input impedance can be varied over a wide range of values by adjusting the width of the strips. In addition, the impedance can be adjusted to match the characteristic impedance of printed circuit transmission lines with four-to-one impedance ratios.

9.6 DISCONE AND CONICAL SKIRT MONOPOLE

There are innumerable variations to the basic geometrical configurations of cones and dipoles, some of which have already been discussed, to obtain broadband characteristics. Two other common radiators that meet this characteristic are the conical skirt monopole and the discone antenna [14] shown in Figures 9.16(a) and (b), respectively.

For each antenna, the overall pattern is essentially the same as that of a linear dipole of length $l < \lambda$ (i.e., a solid of revolution formed by the rotation of a figure-eight) whereas in the horizontal (azimuthal) plane it is nearly omnidirectional. The polarization of each is vertical. Each antenna because of its simple mechanical design, ease of installation, and attractive broadband characteristics has wide applications in the VHF (30–300 MHz) and UHF (300 MHz–3 GHz) spectrum for broadcast, television, and communication applications.

The discone antenna is formed by a disk and a cone. The disk is attached to the center conductor of the coaxial feed line, and it is perpendicular to its axis. The cone is connected at its apex to the outer shield of the coaxial line. The geometrical

INTEL-1045
U.S. Patent 7,151,430

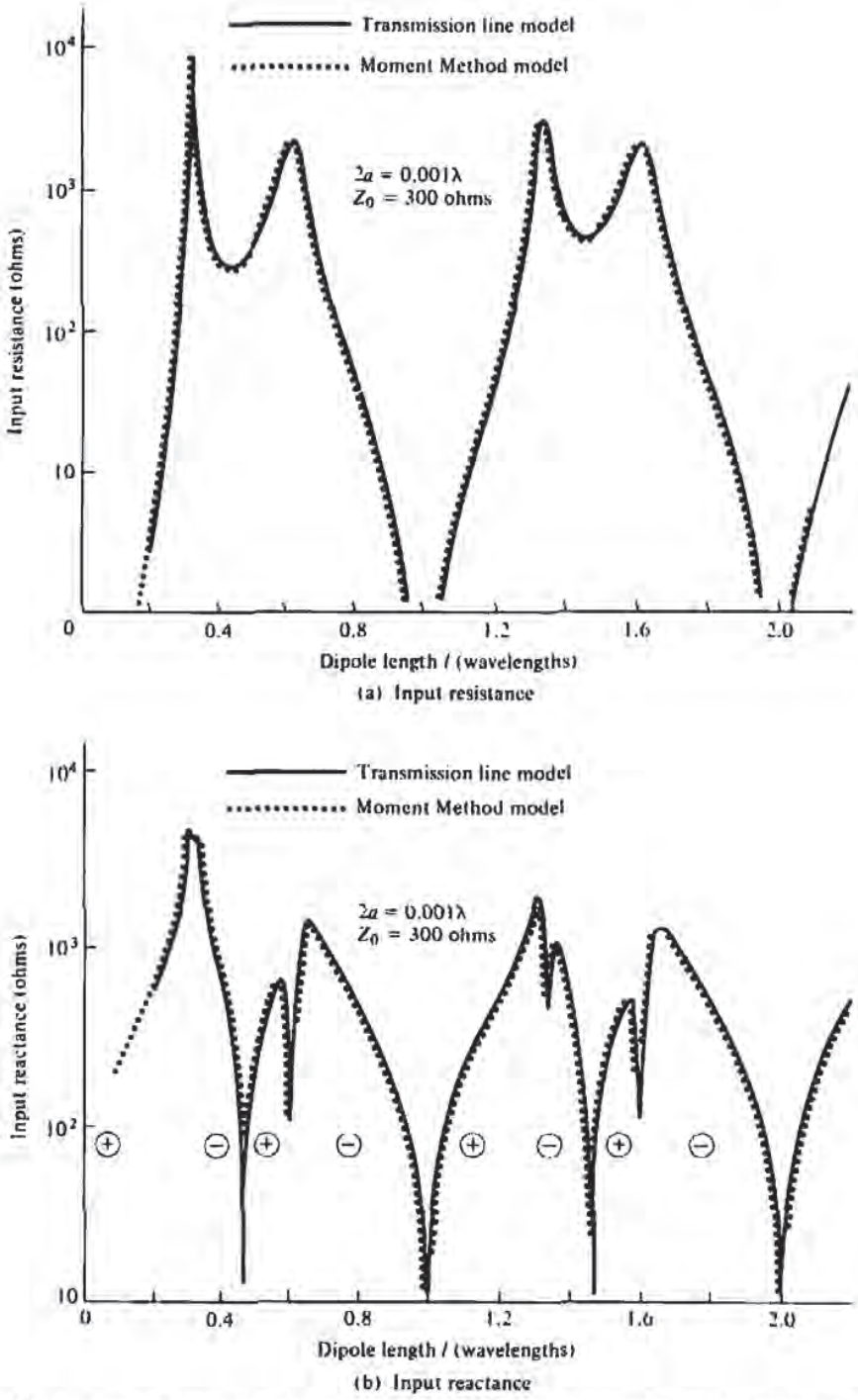


Figure 9.15 Input resistance and reactance of folded dipole. (SOURCE: G. A. Thiele, E. P. Ekelman, Jr., and L. W. Henderson, "On the Accuracy of the Transmission Line Model for Folded Dipole," *IEEE Trans. Antennas Propagat.*, Vol. AP-28, No. 5, pp. 700–703, September 1980. © (1980) IEEE)

INTEL-1045
U.S. Patent 7,151,430

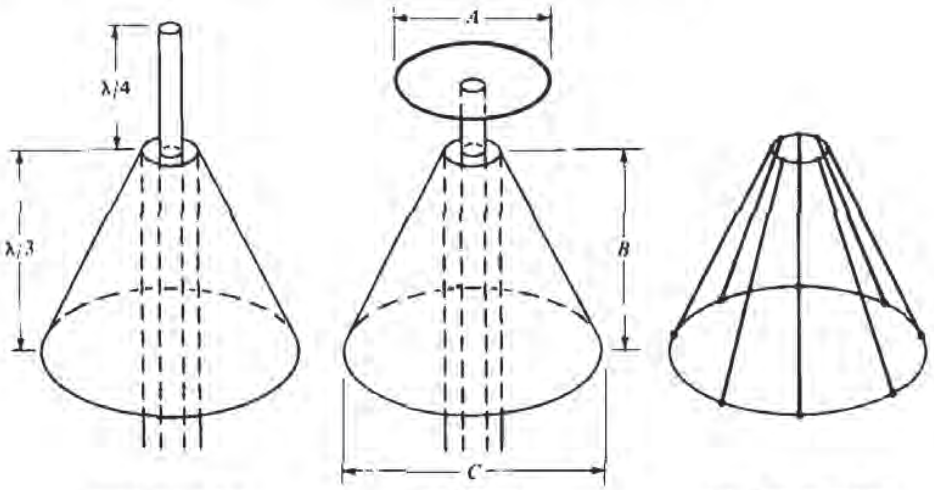


Figure 9.16 Conical skirt monopole, discone, and wire-simulated cone surface.

dimensions and the frequency of operation of two designs [14] are shown in Table 9.4.

In general, the impedance and pattern variations of a discone as a function of frequency are much less severe than those of a dipole of fixed length l. The performance of this antenna as a function of frequency is similar to a high-pass filter. Below an effective cutoff frequency it becomes inefficient, and it produces severe standing waves in the feed line. At cutoff, the slant height of the cone is approximately $\lambda/4$.

Measured elevation (vertical) plane radiation patterns from 250 to 650 MHz, at 50-MHz intervals, have been published [14] for a discone with a cutoff frequency of 200 MHz. No major changes in the "figure-eight" shape of the patterns were evident other than at the high-frequency range where the pattern began to turn downward somewhat.

The conical skirt monopole is similar to the discone except that the disk is replaced by a monopole of length usually $\lambda/4$. Its general behavior also resembles that of the discone. Another way to view the conical skirt monopole is with a $\lambda/4$ monopole mounted above a finite ground plane. The plane has been tilted downward to allow more radiation toward and below the horizontal plane.

To reduce the weight and wind resistance of the cone, its solid surface can be simulated by radial wires, as shown in Figure 9.16(c). This is a usual practice in the simulation of finite size ground planes for monopole antennas. The lengths of the wires used to simulate the ground plane are on the order of about $\lambda/4$ or greater.

9.7 SLEEVE DIPOLE

The radiation patterns of asymmetrically driven wire antennas, with overall length less than a half-wavelength ($l < \lambda/2$), will almost be independent of the point of feed along the wire. However for lengths greater than $\lambda/2$ ($l > \lambda/2$) the current variation along the wire will undergo a phase reversal while maintaining almost sinusoidal amplitude current distribution forced by the boundary conditions at its ends. It would then seem that the input impedance would largely be influenced by the feed point. Even the patterns may be influenced by the point of excitation for antennas with lengths greater than $\lambda/2$.

INTEL-1045
U.S. Patent 7,151,430

Table 9.4 FREQUENCY AND DIMENSIONS OF TWO DESIGNS

Frequency (MHz)	A (cm)	B (cm)	C (cm)
90	45.72	60.96	50.80
200	22.86	31.75	35.56

The input impedance Z_{as} of an asymmetric (off-center) driven dipole is related approximately to the input impedance Z_s at its center by

$$Z_{as} \simeq \frac{Z_s}{\cos^2(k\Delta l)} \tag{9-32}$$

where Δl represents the displacement of the feed from the center. Better accuracy can be obtained using more complicated formulas [15].

An antenna that closely resembles an asymmetric dipole and can be analyzed in a similar manner is a sleeve dipole, shown in Figure 9.17(a). This radiator is essentially the same as that of a base-driven monopole above a ground plane. The outer shield of the coaxial line, which is also connected to the ground plane, has been extended a distance l along the axis of the wire to provide mechanical strength, impedance variations, and extended broadband characteristics.

By introducing the outer sleeve, the excitation gap voltage maintained by the feeding transmission line has been moved upward from the conducting plate ($z = 0$) to $z = h$. The theory of images yields the equivalent symmetrical structure of Figure 9.17(b) in which two generators maintain each equal voltage at $z = \pm h$.

Because of the linearity of Maxwell's equations, the total current in the system will be equal to the sum of the currents maintained independently by each generator in each of the two asymmetric excited radiators [16] shown in Figure 9.17(c). Thus the antenna can be analyzed as the sum of two asymmetrically fed radiators, ignoring the diameter change in each as in Figure 9.17(d). Since the two structures in Figure 9.17(d) are identical at their feed, the input current is

$$I_{in} \simeq I_{as}(z = h) + I_{as}(z = -h) \tag{9-33}$$

where

I_{in} = input current at the feed of the sleeve dipole [Figure 9.17(a)]

$I_{as}(z = h)$ = current of asymmetric structure at $z = h$ [Figure 9.17(d)]

$I_{as}(z = -h)$ = current of asymmetric structure at $z = -h$ [Figure 9.17(d)]

and the input admittance is

$$Y_{in} = \frac{I_{as}(z = h) + I_{as}(z = -h)}{V_{in}} = \frac{I_{as}(z = h)}{V_{in}}\left[1 + \frac{I_{as}(z = -h)}{I_{as}(z = h)}\right]$$
$$= Y_{as}\left[1 + \frac{I_{as}(z = -h)}{I_{as}(z = h)}\right] \tag{9-34}$$

where $Y_{as} = 1/Z_{as}$ as given by (9-32).

Through a number of computations [16], the frequency response of a sleeve dipole

INTEL-1045
U.S. Patent 7,151,430

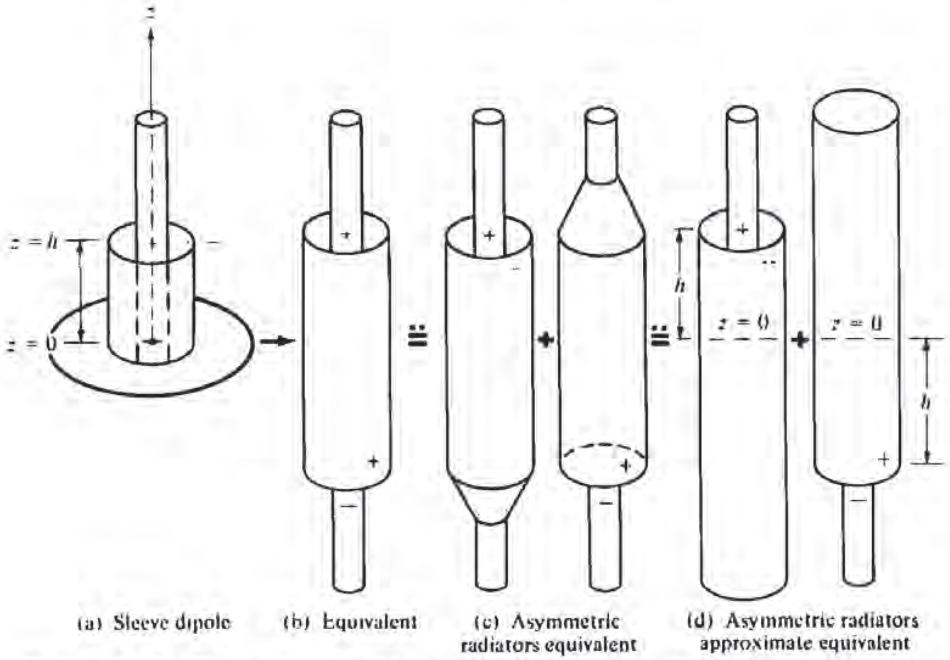


Figure 9.17 Sleeve dipole and its equivalents. (SOURCE: W. L. Weeks, *Antenna Engineering*, McGraw-Hill, New York, 1968)

has been shown to be much superior than either that of a half-wavelength or full-wavelength dipole. Also the standing wave inside the feed line can be maintained reasonably constant by the use of a properly designed reactive matching network.

9.8 MATCHING TECHNIQUES

The operation of an antenna system over a frequency range is not completely dependent upon the frequency response of the antenna element itself but rather on the frequency characteristics of the transmission line-antenna element combination. In practice, the characteristic impedance of the transmission line is usually real whereas that of the antenna element is complex. Also the variation of each as a function of frequency is not the same. Thus efficient coupling-matching networks must be designed which attempt to couple-match the characteristics of the two elements over the desired frequency range.

There are many coupling-matching networks that can be used to connect the transmission line to the antenna element and which can be designed to provide acceptable frequency characteristics. Only a limited number will be introduced here.

9.8.1 Stub-Matching

Ideal matching at a given frequency can be accomplished by placing a short- or open-circuited shunt stub a distance s from the transmission line-antenna element connection, as shown in Figure 9.18(a). Assuming a real characteristic impedance, the length s is controlled so as to make the real part of the antenna element impedance equal to the characteristic impedance. The length l of the shunt line is varied until the susceptance of the stub is equal in magnitude but opposite in phase to the line input susceptance at the point of the transmission line-shunt element connection. The match-

INTEL-1045
U.S. Patent 7,151,430

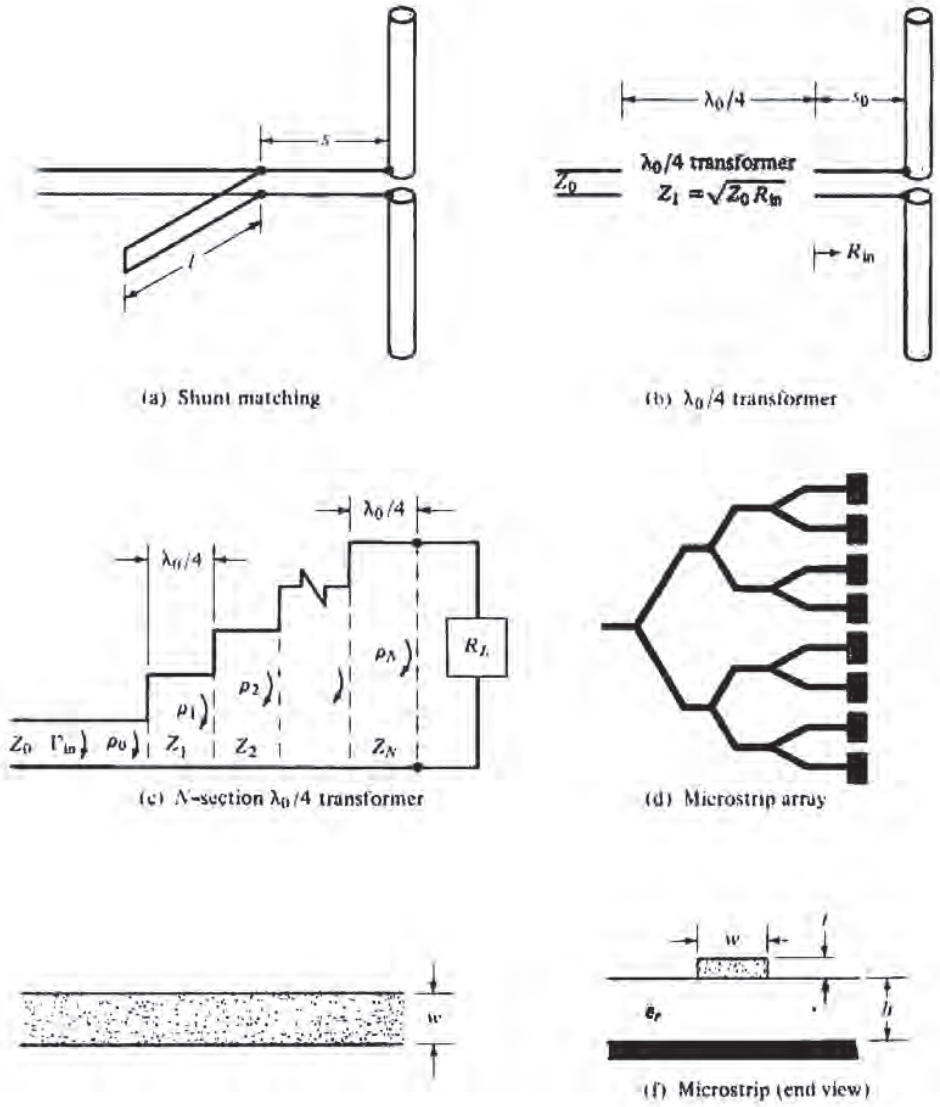


Figure 9.18 Matching and microstrip techniques.

ing procedure is illustrated best graphically with the use of a Smith chart. Analytical methods, on which the Smith chart graphical solution is based, can also be used. The short-circuited stub is more practical because an equivalent short can be created by a pin connection in a coaxial cable or a slider in a waveguide. This preserves the overall length of the stub line for matchings which may require longer length stubs.

A single stub with a variable length l cannot always match all antenna (load) impedances. A double-stub arrangement positioned a fixed distance s from the load, with the length of each stub variable and separated by a constant length d, will match a greater range of antenna impedances. However, a triple-stub configuration will always match all loads.

An excellent treatment of the analytical and graphical methods for the single-, double-, triple-stub, and other matching techniques is presented by Collin [17]. The

INTEL-1045
U.S. Patent 7,151,430

higher-order stub arrangements provide more broad and less sensitive matchings (to frequency variations) but are more complex to implement. Usually a compromise is chosen, such as the double-stub.

9.8.2 Quarter-Wavelength Transformer

A. Single Section

Another technique that can be used to match the antenna to the transmission line is to use a $\lambda/4$ transformer. If the impedance of the antenna is real, the transformer is attached directly to the load. However if the antenna impedance is complex, the transformer is placed a distance s_0 away from the antenna, as shown in Figure 9.18(b). The distance s_0 is chosen so that the input impedance toward the load at s_0 is real and designated as R_{in}. To provide a match, the transformer characteristic impedance Z_1 should be $Z_1 = \sqrt{R_{in}Z_0}$, where Z_0 is the characteristic impedance (real) of the input transmission line. The transformer is usually another transmission line with the desired characteristic impedance.

Because the characteristic impedances of most off-the-shelf transmission lines are limited in range and values, the quarter-wavelength transformer technique is most suitable when used with microstrip transmission lines. In microstrips, the characteristic impedance can be changed by simply varying the width of the center conductor.

B. Multiple Sections

Matchings that are less sensitive to frequency variations and that provide broader bandwidths, require multiple $\lambda/4$ sections. In fact the number and characteristic impedance of each section can be designed so that the reflection coefficient follows, within the desired frequency bandwidth, prescribed variations which are symmetrical about the center frequency. The antenna (load) impedance will again be assumed to be real; if not, the antenna element must be connected to the transformer at a point s_0 along the transmission line where the input impedance is real.

Referring to Figure 9.18(c), the total input reflection coefficient Γ_{in} for an N-section quarter-wavelength transformer with $R_L > Z_0$ can be written approximately as [17]

$$\begin{aligned}\Gamma_{in}(f) &\simeq \rho_0 + \rho_1 e^{-j2\theta} + \rho_2 e^{-j4\theta} + \cdots + \rho_n e^{-j2N\theta} \\ &= \sum_{n=0}^{N} \rho_n e^{-j2n\theta}\end{aligned} \tag{9-35}$$

where

$$\rho_n = \frac{Z_{n+1} - Z_n}{Z_{n+1} + Z_n} \tag{9-35a}$$

$$\theta = k\Delta l = \frac{2\pi}{\lambda}\left(\frac{\lambda_0}{4}\right) = \frac{\pi}{2}\left(\frac{f}{f_0}\right) \tag{9-35b}$$

In (9-35), ρ_n represents the reflection coefficient at the junction of two infinite lines with characteristic impedances Z_n and Z_{n+1}. f_0 represents the designed center frequency, and f the operating frequency. Equation (9-35) is valid provided the ρ_n's at each junction are small ($R_L = Z_0$). If $R_L < Z_0$, the ρ_n's should be replaced by $-\rho_n$'s. For a real load impedance, the ρ_n's and Z_n's will also be real.

INTEL-1045
U.S. Patent 7,151,430

For a symmetrical transformer ($\rho_0 = \rho_N$, $\rho_1 = \rho_{N-1}$, etc.), (9-35) reduces to

$$\Gamma_{in}(f) \simeq 2e^{-jN\theta}[\rho_0 \cos N\theta + \rho_1 \cos(N-2)\theta + \rho_2 \cos(N-4)\theta + \cdots] \quad (9\text{-}36)$$

The last term in (9-36) should be

$$\rho_{[(N-1)/2]}\cos\theta \qquad \text{for } N = \text{odd integer} \quad (9\text{-}36a)$$

$$\tfrac{1}{2}\rho_{(N/2)} \qquad \text{for } N = \text{even integer} \quad (9\text{-}36b)$$

C. Binomial Design

One technique, used to design an N-section $\lambda/4$ transformer, requires that the input reflection coefficient of (9-35) have maximally flat passband characteristics. For this method, the junction reflection coefficients (ρ_n's) are derived using the binomial expansion. Doing this, we can equate (9-35) to

$$\Gamma_{in}(f) = \sum_{n=0}^{N} \rho_n e^{-j2n\theta} = e^{-jN\theta}\frac{R_L - Z_0}{R_L + Z_0}\cos^N(\theta) = 2^{-N}\frac{R_L - Z_0}{R_L + Z_0}\sum_{n=0}^{N} C_n^N e^{-j2n\theta} \quad (9\text{-}37)$$

where

$$C_n^N = \frac{N!}{(N-n)!n!}, \qquad n = 0, 1, 2, \ldots, N \quad (9\text{-}37a)$$

From (9-35)

$$\rho_n = 2^{-N}\frac{R_L - Z_0}{R_L + Z_0}C_n^N \quad (9\text{-}38)$$

For this type of design, the fractional bandwidth $\Delta f/f_0$ is given by

$$\frac{\Delta f}{f_0} = 2\frac{(f_0 - f_m)}{f_0} = 2\left(1 - \frac{f_m}{f_0}\right) = 2\left(1 - \frac{2}{\pi}\theta_m\right) \quad (9\text{-}39)$$

Since

$$\theta_m = \frac{2\pi}{\lambda_m}\left(\frac{\lambda_0}{4}\right) = \frac{\pi}{2}\left(\frac{f_m}{f_0}\right) \quad (9\text{-}40)$$

(9-39) reduces using (9-37) to

$$\frac{\Delta f}{f_0} = 2 - \frac{4}{\pi}\cos^{-1}\left[\frac{\rho_m}{(R_L - Z_0)/(R_L + Z_0)}\right]^{1/N} \quad (9\text{-}41)$$

where ρ_m is the maximum value of reflection coefficient which can be tolerated within the bandwidth.

The usual design procedure is to specify the

1. load impedance (R_L)
2. input characteristic impedance (Z_0)
3. number of sections (N)
4. maximum tolerable reflection coefficient (ρ_m) [or fractional bandwidth ($\Delta f/f_0$)]

and to find the

INTEL-1045
U.S. Patent 7,151,430

1. characteristic impedance of each section
2. fractional bandwidth [or maximum tolerable reflection coefficient (ρ_m)]

To illustrate the principle, let us consider an example.

Example 9.1

A linear dipole with an input impedance of $70 + j37$ is connected to a 50-ohm line. Design a two-section $\lambda/4$ binomial transformer by specifying the characteristic impedance of each section to match the antenna to the line at $f = f_0$. If the input impedance (at the point the transformer is connected) is assumed to remain constant as a function of frequency, determine the maximum reflection coefficient and VSWR within a fractional bandwidth of 0.375.

SOLUTION

Since the antenna impedance is not real, the antenna must be connected to the transformer through a transmission line of length s_0. Assuming a 50-ohm characteristic impedance for that section of the transmission line, the input impedance at $s_0 = 0.062\lambda$ is real and equal to 100 ohms. Using (9-37a) and (9-38)

$$\rho_n = 2^{-N}\frac{R_L - Z_0}{R_L + Z_0}C_n^N = 2^{-N}\frac{R_L - Z_0}{R_L + Z_0}\frac{N!}{(N-n)!n!}$$

which for $N = 2$, $R_L = 100$, $Z_0 = 50$

$$n = 0: \quad \rho_0 = \frac{Z_1 - Z_0}{Z_1 + Z_0} = \frac{1}{12} \rightarrow Z_1 = 1.182Z_0 = 59.09$$

$$n = 1: \quad \rho_1 = \frac{Z_2 - Z_1}{Z_2 + Z_1} = \frac{1}{6} \rightarrow Z_2 = 1.399Z_1 = 82.73$$

For a fractional bandwidth of 0.375 ($\theta_m = 1.276$ rad $= 73.12°$) we can write, using (9-41)

$$\frac{\Delta f}{f_0} = 0.375 = 2 - \frac{4}{\pi}\cos^{-1}\left[\frac{\rho_m}{(R_L - Z_0)/(R_L + Z_0)}\right]^{1/2}$$

which for $R_L = 100$ and $Z_0 = 50$ gives

$$\rho_m = 0.028$$

The maximum voltage standing wave ratio is

$$\text{VSWR}_m = \frac{1 + \rho_m}{1 - \rho_m} = 1.058$$

The magnitude of the reflection coefficient is given by (9-37) as

$$\Gamma_{in} = \rho_{in} = \left|\frac{R_L - Z_0}{R_L + Z_0}\right|\cos^2\theta = \frac{1}{3}\cos^2\left[\frac{2\pi}{\lambda}\left(\frac{\lambda_0}{4}\right)\right] = \frac{1}{3}\cos^2\left[\frac{\pi}{2}\left(\frac{f}{f_0}\right)\right]$$

which is shown plotted in Figure 9.19, and it is compared with the response of a single section $\lambda/4$ transformer.

INTEL-1045
U.S. Patent 7,151,430

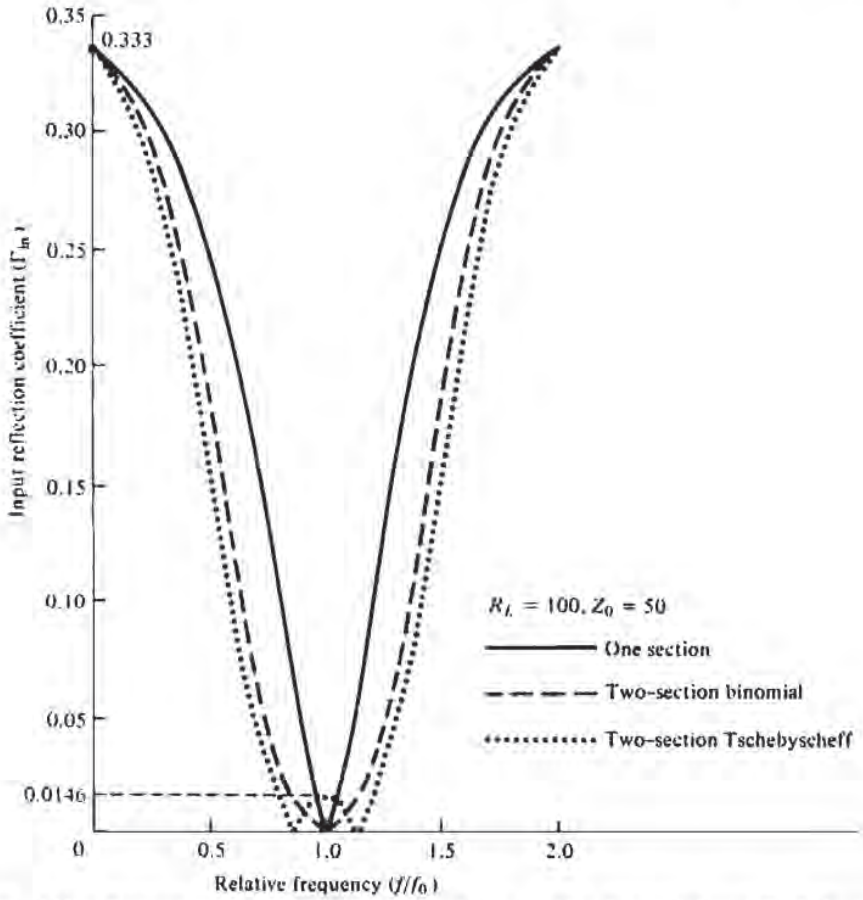


Figure 9.19 Responses of single-section, and two-section binomial and Tschebyscheff quarter-wavelength transformers.

Microstrip designs are ideally suited for antenna arrays, as shown in Figure 9.18(d). In general the characteristic impedance of a microstrip line, whose top and end views are shown in Figures 9.18(e) and (f), respectively, is given by [18].

$$Z_c = \frac{87}{\sqrt{\epsilon_r + 1.41}} \ln\left(\frac{5.98h}{0.8w + t}\right) \qquad \text{for } h < 0.8w \qquad (9\text{-}42)$$

where

ϵ_r = dielectric constant of dielectric substrate (board material)
h = height of substrate
w = width of microstrip center conductor
t = thickness of microstrip center conductor

Thus for constant values of ϵ_r, h, and t, the characteristic impedance can be changed by simply varying the width (w) of the center conductor.

D. Tschebyscheff Design

The reflection coefficient can be made to vary within the bandwidth in an oscillatory manner and have equal-ripple characteristics. This can be accomplished by making

INTEL-1045
U.S. Patent 7,151,430

Γ_{in} behave according to a Tschebyscheff polynomial. For the Tschebyscheff design, the equation that corresponds to (9-37) is

$$\boxed{\Gamma_{in}(f) = e^{-jN\theta}\frac{Z_L - Z_0}{Z_L + Z_0}\frac{T_N(\sec\theta_m \cos\theta)}{T_N(\sec\theta_m)}} \tag{9-43}$$

where $T_N(x)$ is the Tschebyscheff polynomial of order N.

The maximum allowable reflection coefficient occurs at the edges of the passband where $\theta = \theta_m$ and $T_N(\sec\theta_m \cos\theta)|_{\theta=\theta_m} = 1$. Thus

$$\rho_m = \left|\frac{Z_L - Z_0}{Z_L + Z_0}\frac{1}{T_N(\sec\theta_m)}\right| \tag{9-44}$$

The first few Tschebyscheff polynomials are given by (6-69). For $z = \sec\theta_m \cos\theta$, the first three polynomials reduce to

$$\begin{aligned} T_1(\sec\theta_m \cos\theta) &= \sec\theta_m \cos\theta \\ T_2(\sec\theta_m \cos\theta) &= 2(\sec\theta_m \cos\theta)^2 - 1 = \sec^2\theta_m \cos 2\theta + (\sec^2\theta_m - 1) \\ T_3(\sec\theta_m \cos\theta) &= 4(\sec\theta_m \cos\theta)^3 - 3(\sec\theta_m \cos\theta) \\ &= \sec^3\theta_m \cos 3\theta + 3(\sec^3\theta_m - \sec\theta_m)\cos\theta \end{aligned} \tag{9-45}$$

The remaining details of the analysis are found in [17].

The design of Example 9.1 using a Tschebyscheff transformer is assigned as an exercise to the reader (Prob. 9.17). However its response is shown plotted in Figure 9.19 for comparison.

In general, the multiple sections (either binomial or Tschebyscheff) provide greater bandwidths than a single section. As the number of sections increases, the bandwidth also increases. The advantage of the binomial design is that the reflection coefficient values within the bandwidth monotonically decrease from both ends toward the center. Thus the values are always smaller than an acceptable and designed value that occurs at the "skirts" of the bandwidth. For the Tschebyscheff design, the reflection coefficient values within the designed bandwidth are equal or smaller than an acceptable and designed value. The number of times the reflection coefficient reaches the maximum ripple value within the bandwidth is determined by the number of sections. In fact, for an even number of sections the reflection coefficient at the designed center frequency is equal to the maximum allowable value, while for an odd number of sections it is zero. For a maximum tolerable reflection coefficient, the N-section Tschebyscheff transformer provides a larger bandwidth than a corresponding N-section binomial design, or for a given bandwidth the maximum tolerable reflection coefficient is smaller for a Tschebyscheff design.

9.8.3 T-Match

Another effective shunt-matching technique is the T-match connection shown in Figure 9.20(a). With this method the dipole of length l and radius a is connected to the transmission line by another dipole of length l' ($l' < l$) and radius a'. The smaller dipole is "tapped" to the larger one at distances $l'/2$ from the center and the two are separated by a small distance s. The transmission line is connected to the smaller dipole at its center. The T-match connection is a general form of a folded dipole since the two legs are usually not of the same length or diameter. Since the T-match is a

INTEL-1045
U.S. Patent 7,151,430

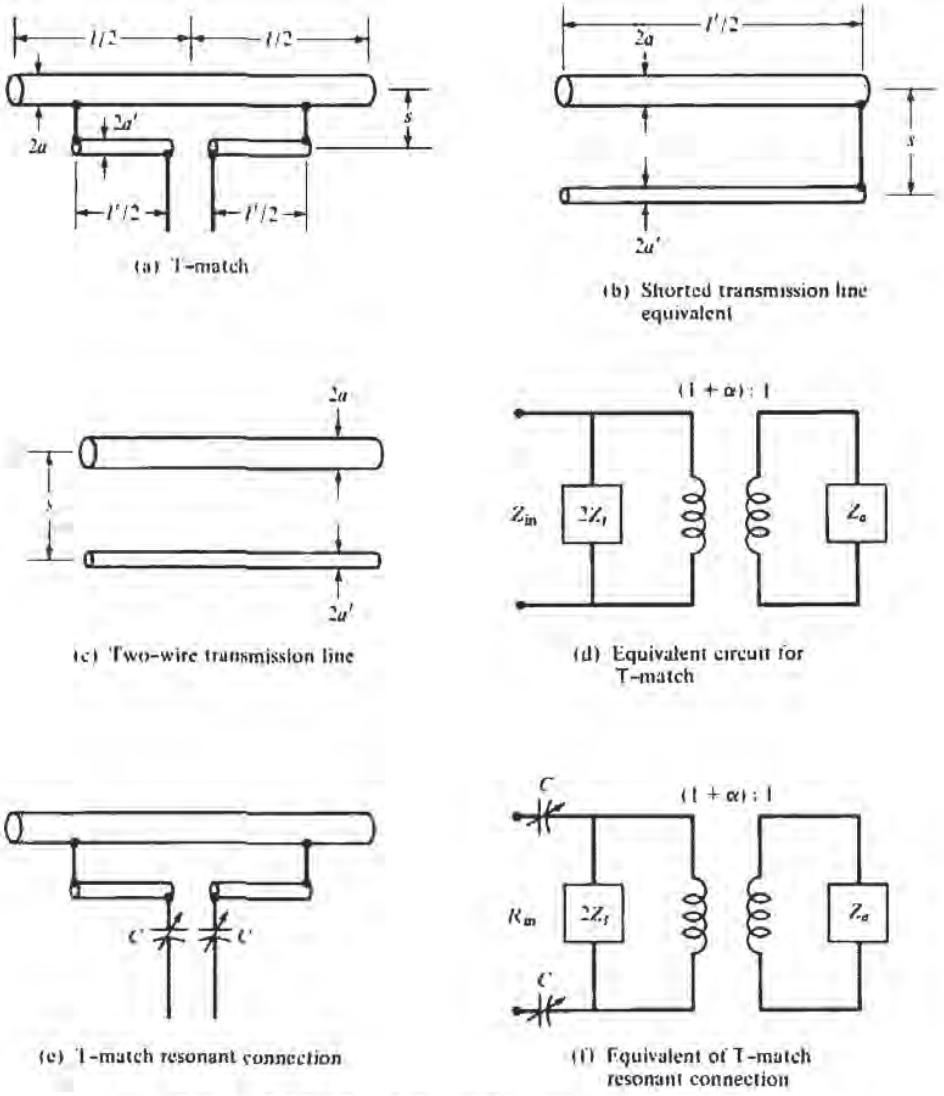


Figure 9.20 T-match and its associated equivalents.

symmetrical and balanced system, it is well suited for use with parallel-conductor transmission lines such as the "twin lead." Coaxial lines, which are unsymmetrical and unbalanced lines, should be connected to dipoles using the gamma match.

The design procedure for the T-match is developed similarly to that of the folded dipole. The T-match is also modeled by transmission line and antenna modes, as shown in Figure 9.12 for the folded dipole. The total current at the input terminals is divided between the two conductors in a way that depends on the relative radii of the two conductors and the spacing between them. Since the two conductors are not in general of the same radius, the antenna mode current division is not unity. Instead, a current division factor is assigned which also applies to the voltage division of the transmission line mode.

Instead of including all the details of the analysis, only the steps that are applicable to a T-match design will be included.

INTEL-1045
U.S. Patent 7,151,430

A. Design Procedure

1. Calculate the current division factor α by

$$\alpha = \frac{\cosh^{-1}\left(\dfrac{v^2 - u^2 + 1}{2v}\right)}{\cosh^{-1}\left(\dfrac{v^2 + u^2 - 1}{2vu}\right)} \simeq \frac{\ln(v)}{\ln(v) - \ln(u)} \tag{9-46}$$

$$u = \frac{a}{a'} \tag{9-46a}$$

$$v = \frac{s}{a'} \tag{9-46b}$$

2. From Table 9.3, the "equivalent" radius of the two-wire arrangement can be written as

$$\ln(a_e) \simeq \frac{1}{(a' + a)^2}\left[a'^2 \ln a' + a^2 \ln a + 2a'a \ln s\right] \tag{9-47}$$

since $S_1 = 2\pi a'$, $S_2 = 2\pi a$. It can be shown that (9-47) reduces to

$$\ln(a_e) \simeq \ln a' + \frac{1}{(1 + u)^2}(u^2 \ln u + 2u \ln v) \tag{9-47a}$$

3. Calculate the impedance at the input terminals for the transmission line mode [i.e., two-wire shorted transmission line of length $l'/2$ with radii a, a' and separation s shown in Figure 9.20(b)]

$$Z_t = jZ_0 \tan\left(k\frac{l'}{2}\right) \tag{9-48}$$

where

$$Z_0 = 60 \cosh^{-1}\left(\frac{s^2 - a^2 - a'^2}{2aa'}\right) \simeq 276 \log_{10}\left(\frac{s}{\sqrt{aa'}}\right) \tag{9-48a}$$

Z_0 is the characteristic impedance of the two-wire transmission line with radii a, a' and separation s, as shown in Figure 9.20(c).

4. The total input impedance, which is a combination of the antenna (radiating) and the transmission (nonradiating) modes, can be written as

$$\boxed{Z_{in} = R_{in} + jX_{in} = \frac{2Z_t[(1 + \alpha)^2 Z_a]}{2Z_t + (1 + \alpha)^2 Z_a}} \tag{9-49}$$

and the input admittance as

$$\boxed{Y_{in} = \frac{1}{Z_{in}} = \frac{Y_a}{(1 + \alpha)^2} + \frac{1}{2Z_t}} \tag{9-50}$$

$Z_a = 1/Y_a$ is the center point free-space input impedance of the antenna in the absence of the T-match connection.

B. Equivalent Circuit

Based upon (9-49) or (9-50), the T-match behaves as the equivalent circuit of Figure 9.20(d) in which the antenna impedance is stepped up by a ratio of $1 + \alpha$,

INTEL-1045
U.S. Patent 7,151,430

and it is placed in shunt with twice the impedance of the nonradiating mode (transmission line) to result in the input impedance. When the current division factor is unity ($\alpha = 1$), the T-match equivalent of Figure 9.20(d) reduces to that of Figure 9.14(a) for the folded dipole.

For $l' \simeq \lambda/2$, the transmission line impedance Z_t is much greater than $(1 + \alpha)^2 Z_a$ and the input impedance of (9-49) reduces to

$$\boxed{Z_{in} \simeq (1 + \alpha)^2 Z_a} \tag{9-51}$$

For two equal radii conductors, the current division factor is unity and (9-51) becomes

$$\boxed{Z_{in} \simeq 4Z_a} \tag{9-52}$$

a relation obtained previously.

The impedance of (9-49) is generally complex. Because each of the lengths ($l'/2$) of the T-match rods are usually selected to be very small (0.03 to 0.06λ), Z_{in} is inductive. To eliminate the reactance (resonate the antenna) at a given center frequency and keep a balanced system, two variable series capacitors are usually used, as shown in Figure 9.20(e). The value of each capacitor is selected so that Z_{in} of (9-49) is equal to $R_{in}(Z_{in} = R_{in})$. To accomplish this

$$\boxed{C = 2C_{in} = \frac{1}{\pi f X_{in}}} \tag{9-53}$$

where f is the center frequency, and C_{in} is the series combination of the two C capacitors. The resonant circuit equivalent is shown in Figure 9.20(f).

The T-match connection of Figure 9.20(e) is used not only to resonate the circuit, but also to make the total input impedance equal to the characteristic impedance of the feed transmission line. This is accomplished by properly selecting the values of $l'/2$ and C (s is not usually varied because the impedance is not very sensitive to it). In most cases, a trial and error procedure is followed. An orderly graphical method using the Smith chart is usually more convenient, and it is demonstrated in the following section for the gamma match.

9.8.4 Gamma Match

Frequently dipole antennas are fed by coaxial cables which are unbalanced transmission lines. A convenient method to connect the dipole or other antennas (Yagi-Uda, log-periodic, etc.) to 50- or 75-ohm "coaxs" and to obtain a match is to use the gamma match arrangement shown in Figure 9.21.

A. Equivalent Circuit

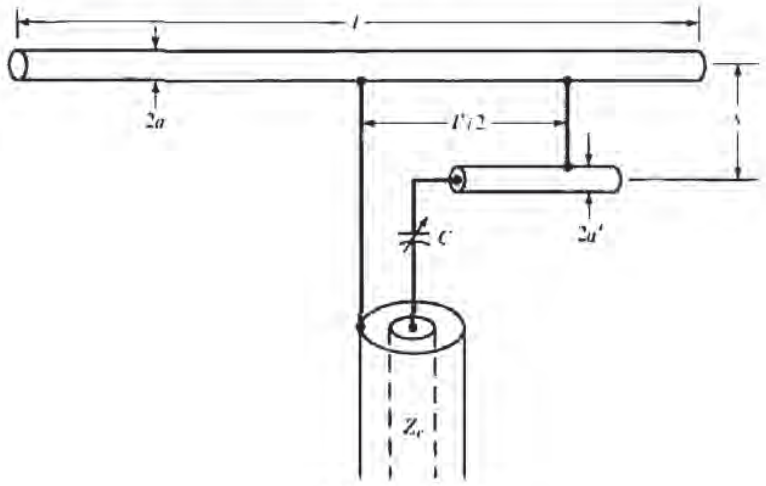
The gamma match is equivalent to half of the T-match, and it also requires a capacitor in series with the gamma rod. The equivalent is shown in Figure 9.21(b), and its input impedance is equal to

$$\boxed{Z_{in} = -jX_c + \frac{Z_g[(1 + \alpha)^2 Z_a]}{2Z_g + (1 + \alpha)^2 Z_a}} \tag{9-54}$$

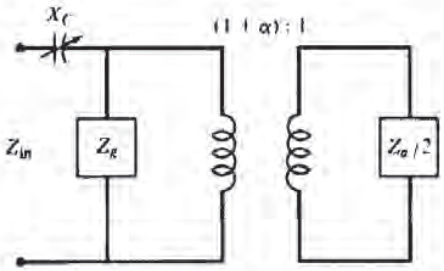
where Z_a is the center point free-space impedance of the antenna in the absence of the gamma match connection. The second term of (9-54) is similar in form to that of (9-49).

The usual problem encountered is that the length of the wire antenna (l) and the

INTEL-1045
U.S. Patent 7,151,430



(a) Gamma match



(b) Equivalent

Figure 9.21 Gamma match and its equivalent.

characteristic impedance of the feed coax (Z_c) are known. What is required are the values of the radii a and a', the length $l'/2$, and the capacitance C which will achieve a match. Since the arrangement is similar to the T-match or folded dipole, its analysis is based on the same theory.

To accomplish the match, a graphical design technique, which is different from that reported in [19] and [20], will be demonstrated. This procedure utilizes the Smith chart, and it is based on the equivalent of Figure 9.21(b). A purely mathematical procedure is also available [21], but it will not be included here.

Because the input impedance is not very sensitive to a, a', and s, the usual procedure is to select their values and keep them fixed. The parameters that are usually varied are then $l'/2$ and C. In practice, $l'/2$ is varied by simply using a sliding clamp to perform the shorted connection at the end of the gamma rod.

The graphical design method assumes that $l'/2$ is given, and C that resonates the circuit is found. If the input resistance is not equal to the characteristic impedance Z_c of the feed line, another value of $l'/2$ is selected, and the procedure is repeated until $R_{in} = Z_c$. The graphical method is suggestive as to how the length $l'/2$ should be changed (smaller or larger) to accomplish the match.

B. Design Procedure

1. Determine the current division factor α by using (9-46)–(9-46b).
2. Find the free-space impedance (in the absence of the gamma match) of the driven element at the center point. Designate it as Z_a.

INTEL-1045
U.S. Patent 7,151,430

3. Divide Z_a by 2 and multiply it by the step-up ratio $(1 + \alpha)^2$. Designate the result as Z_2.

$$Z_2 = R_2 + jX_2 = (1 + \alpha)^2 \frac{Z_a}{2} \tag{9-55}$$

4. Determine the characteristic impedance Z_0 of the transmission line formed by the driven element and the gamma rod using (9-48a).
5. Normalize Z_2 of (9-55) by Z_0 and designate it as z_2.

$$z_2 = \frac{Z_2}{Z_0} = \frac{R_2 + jX_2}{Z_0} = r_2 + jx_2 \tag{9-56}$$

and enter on the Smith chart.

6. Invert z_2 of (9-56) and obtain its equivalent admittance $y_2 = g_2 + jb_2$. On the Smith chart this is accomplished by moving z_2 diagonally across from its position.
7. In shunt with the admittance y_2 from step 6 is an inductive reactance due to the short-circuited transmission line formed by the antenna element and the gamma rod. This is an inductive reactance because the length of the gamma rod is very small (usually 0.03 to 0.06λ), but always much smaller than $\lambda/2$. Obtain its normalized value using

$$z_g = j \tan\left(k \frac{l'}{2}\right) \tag{9-57}$$

and place on Smith chart. The impedance z_g of (9-57) can also be obtained by using exclusively the Smith chart. You begin by locating the short-circuited load at $Z_s = 0 + j0$. Then you move this point a distance $l'/2$ toward the generator, along the outside perimeter of the Smith chart. The new point represents the normalized impedance z_g of (9-57).

8. Invert the impedance from step 7 (z_g) to obtain its equivalent admittance $y_g = g_g + jb_g$. On the Smith chart this is accomplished by moving z_g diagonally across from its position.
9. Add the two parallel admittances (from steps 6 and 8) to obtain the total input admittance at the gamma feed. That is,

$$y_{in} = y_2 + y_g = (g_2 + g_g) + j(b_2 + b_g) \tag{9-58}$$

and locate it on the Smith chart.

10. Invert the normalized input admittance y_{in} of (9-58) to obtain the equivalent normalized input impedance

$$z_{in} = r_{in} + jx_{in} \tag{9-59}$$

11. Obtain the unnormalized input impedance by multiplying z_{in} by Z_0.

$$Z_{in} = R_{in} + jX_{in} = Z_0 z_{in} \tag{9-60}$$

12. Select the capacitor C so that its reactance is equal in magnitude to X_{in}.

$$\frac{1}{\omega C} = \frac{1}{2\pi f_0 C} = X_{in} \tag{9-61}$$

If all the dimensions were chosen properly for a perfect match, the real part R_{in} of (9-60) should be equal to Z_c. If not, change one or more of the dimensions

INTEL-1045
U.S. Patent 7,151,430

(usually the length of the rod) and repeat the procedure until $R_{in} = Z_c$. Practically the capacitor C is chosen to be variable so adjustments can be made with ease to obtain the best possible match.

Example 9.2

The driven element impedance of a 20-m ($f = 15$ MHz; see Appendix VIII) Yagi-Uda antenna has a free-space impedance at its center point of $30.44(1 - j)$ ohms [20]. It is desired to connect it to a 50-ohm coaxial line using a gamma match. The driven element and the gamma rod are made of tubing with diameters of $0.95 \times 10^{-3}\lambda$ (0.75 in. = 1.905 cm) and $3.175 \times 10^{-4}\lambda$ (0.25 in. = 0.635 cm), respectively. The center-to-center separation between the driven element and the rod is $3.81 \times 10^{-3}\lambda$ (3 in. = 7.62 cm). Determine the required capacitance to achieve a match. Begin with a gamma rod length of 0.036λ (28.35 in. = 72.01 cm).

SOLUTION

1. Using (9-46)–(9-46b)

$$u = \frac{a}{a'} = 3 \qquad v = \frac{s}{a'} = \frac{3.81}{0.15875} = 24$$

$$\alpha = \frac{\ln(24)}{\ln(24) - \ln(3)} = 1.528$$

and the step-up ratio

$$(1 + \alpha)^2 = (1 + 1.528)^2 = 6.39$$

2. $Z_a = 30.44(1 - j)$, as given.
3. Using (9-55)

$$Z_2 = (1 + 1.528)^2 \frac{30.44(1 - j)}{2} = 97.25(1 - j)$$

4. $$Z_0 = 276 \log_{10}\left[\frac{2(3.81)}{\sqrt{0.95(0.3175)}}\right] = 315.25 \simeq 315$$

5. $$z_2 = \frac{97.25}{315}(1 - j) = 0.31(1 - j)$$

6. On the Smith chart in Figure 9.22 locate z_2 and invert it to y_2. It leads to

$$y_2 = \frac{1}{z_2} = 1.6(1 + j)$$

7. On the Smith chart locate $z_s = 0 + j0$ and advance it toward the generator a distance 0.036λ to obtain

$$z_g = 0 + j0.23$$

8. From the Smith chart

$$y_g = \frac{1}{z_g} = -j4.35$$

INTEL-1045
U.S. Patent 7,151,430

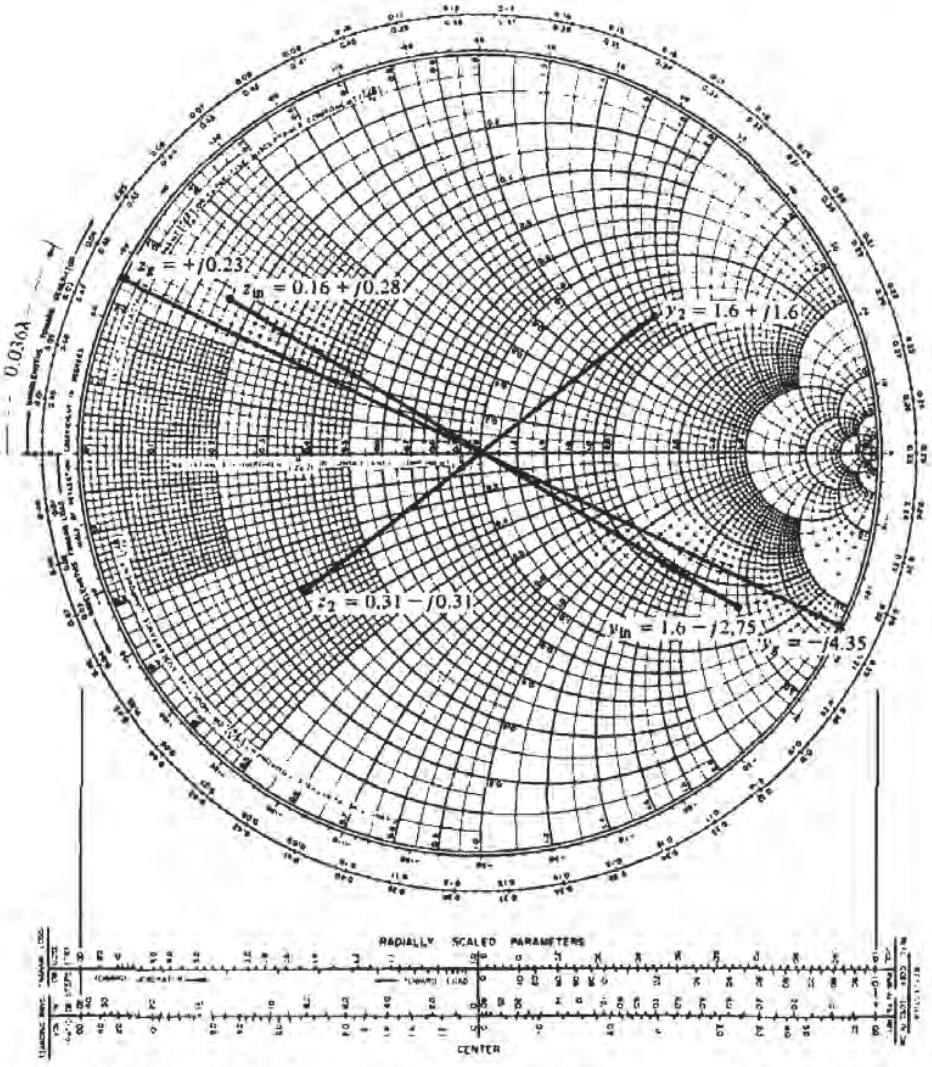


Figure 9.22 Smith chart for Example 9.2. Copyright renewal 1976 by P. H. Smith. Murray Hill, N.J.

9. Add y_2 and y_g

$$y_{in} = y_2 + y_g = 1.6 - j2.75$$

which is located on the Smith chart.

10. Inverting y_{in} on the Smith chart to z_{in} gives

$$z_{in} = 0.16 + j0.28$$

11. Unnormalizing z_{in} by $Z_0 = 315.$ reduces it to

$$Z_{in} = 50.4 + j88.2$$

12. The capacitance should be

$$C = \frac{1}{2\pi f_0(88.2)} = \frac{1}{2\pi(15 \times 10^6)(88.2)}$$
$$= 120.3 \times 10^{-12} \approx 120 \text{ pF}$$

INTEL-1045
U.S. Patent 7,151,430

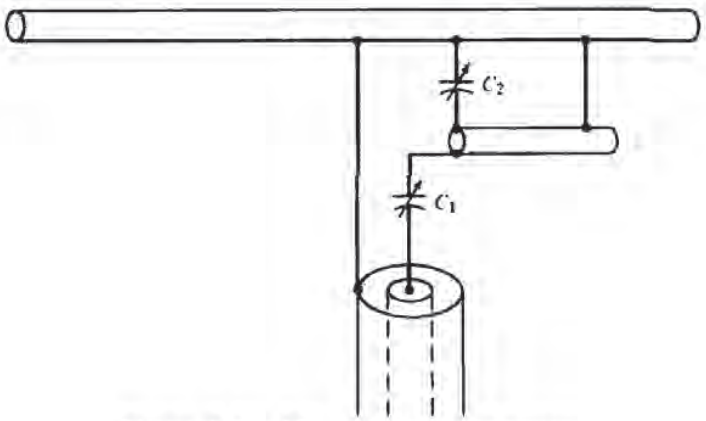


Figure 9.23 Omega match arrangement.

Since $R_{in} = 50.4$ ohms is not exactly equal to $Z_0 = 50$ ohms, one of the physical dimensions (usually the length of the rod) can be changed slightly and then the process can be repeated. However in this case they are so close that for practical purposes this is not required.

9.8.5 Omega Match

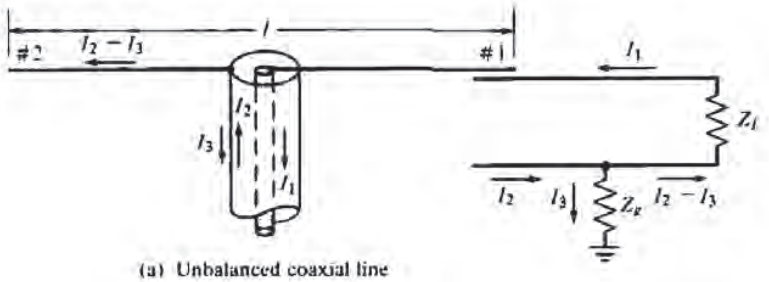
A slightly modified version of the gamma match is the omega match shown in Figure 9.23. The only difference between the two is that in addition to the series capacitor C_1 there is one in shunt C_2 which can aid in achieving the match. Usually the presence of C_2 makes it possible to use a shorter rod or makes it easier to match a resonant driven element. The primary function of C_2 is to change y_{in} in step 9 of the design procedure so that when it is inverted its unnormalized real part is equal to the characteristic impedance of the input transmission line. This will possibly eliminate the need of changing the dimensions of the matching elements, if a match is not achieved.

9.8.6 Baluns and Transformers

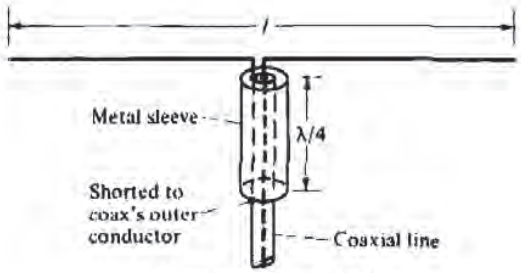
A twin-lead transmission line (two parallel-conductor line) is a symmetrical line whereas a coaxial cable is inherently unbalanced. Because the inner and outer (inside and outside parts of it) conductors of the coax are not coupled to the antenna in the same way, they provide the unbalance. The result is a net current flow to ground on the outside part of the outer conductor. This is shown in Figure 9.24(a) where an electrical equivalent is also indicated. The amount of current flow I_3 on the outside surface of the outer conductor is determined by the impedance Z_g from the outer shield to ground. If Z_g can be made very large, I_3 can be reduced significantly. Devices that can be used to balance inherently unbalanced systems, by canceling or choking the outside current, are known as *baluns* (*bal*ance to *un*balance).

One type of a balun is that shown in Figure 9.24(b), referred to usually as a *bazooka* balun. Mechanically it requires that a $\lambda/4$ in length metal sleeve, and shorted at its one end, encapsulates the coaxial line. Electrically the input impedance at the open end of this $\lambda/4$ shorted transmission line, which is equivalent to Z_g, will be very large (ideally infinity). Thus the current I_3 will be choked, if not completely eliminated, and the system will be nearly balanced.

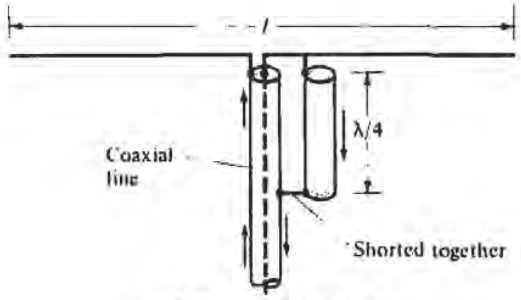
INTEL-1045
U.S. Patent 7,151,430



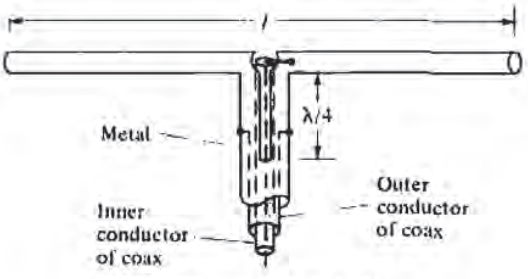
(a) Unbalanced coaxial line



(b) Bazooka balun (1 : 1)



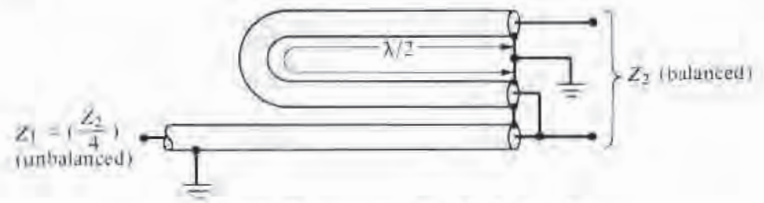
(c) $\lambda/4$ coaxial balun (1 : 1)



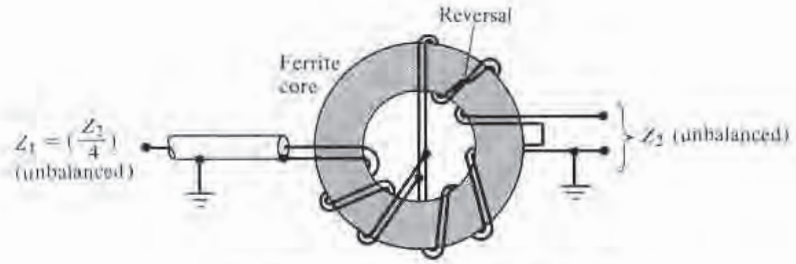
(d) Coaxial balun (1 : 1)

Figure 9.24 Balun configurations.

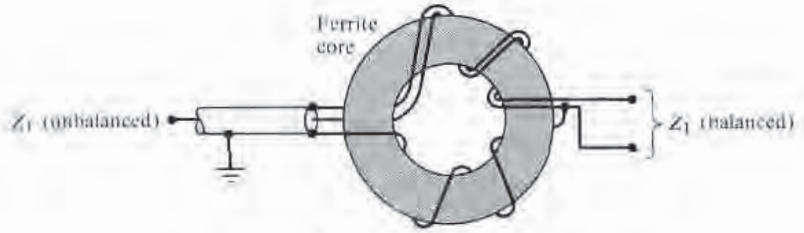
INTEL-1045
U.S. Patent 7,151,430



(a) $\lambda/2$ coaxial balun (4 : 1 or 1 : 4)



(b) Ferrite core transformer (4 : 1 or 1 : 4)



(c) Ferrite core balun (1 : 1)

Figure 9.25 Balun and ferrite core transformers.

Another type of a balun is that shown in Figure 9.24(c). It requires that one end of a $\lambda/4$ section of a transmission line be connected to the outside shield of the main coaxial line while the other is connected to the side of the dipole which is attached to the center conductor. This balun is used to cancel the flow of I_3. The operation of it can be explained as follows: In Figure 9.24(a) the voltages between each side of the dipole and the ground are equal in magnitude but 180° out of phase, thus producing a current flow on the outside of the coaxial line. If the two currents I_1 and I_2 are equal in magnitude, I_3 would be zero. Since terminal #2 of the dipole is connected directly to the shield of the coax while terminal #1 is weakly coupled to it, it produces a much larger current I_2. Thus there is relatively little cancellation in the two currents.

The two currents, I_1 and I_2, can be made equal in magnitude if the center conductor of the coax is connected directly to the outer shield. If this connection is made directly at the antenna terminals, the transmission line and the antenna would be short-circuited, thus eliminating any radiation. However, the indirect parallel conductor connection of Figure 9.24(c) provides the desired current cancelation without eliminating the radiation. The current flow on the outer shield of the main line is canceled at the bottom end of the $\lambda/4$ section (where the two join together) by the equal in magnitude, but opposite in phase, current in the $\lambda/4$ section of the auxiliary line. Ideally then there is no current flow in the outer surface of the outer shield of the remaining part

INTEL-1045
U.S. Patent 7,151,430

of the main coaxial line. It should be stated that the parallel auxiliary line need not be made $\lambda/4$ in length to achieve the balance. It is made $\lambda/4$ to prevent the upsetting of the normal operation of the antenna.

A compact construction of the balun in Figure 9.24(c) is that in Figure 9.24(d). The outside metal sleeve is split and a portion of it is removed on opposite sides. The remaining opposite parts of the outer sleeve represent electrically the two shorted $\lambda/4$ parallel transmission lines of Figure 9.24(c). All of the baluns shown in Figure 9.24 are narrowband devices.

Devices can be constructed which provide not only balancing but also step-up impedance transformations. One such device is the $\lambda/4$ coaxial balun, with a 4:1 impedance transformation, of Figure 9.25(a). The U-shaped section of the coaxial line must be $\lambda/2$ long [22].

Because all the baluns-impedance transformers that were discussed so far are narrowband devices, the bandwidth can be increased by employing ferrite cores in their construction [23]. Two such designs, one a 4:1 or 1:4 transformer and the other a 1:1 balun, are shown in Figures 9.25(b) and (c). The ferrite core has a tendency to maintain high impedance levels over a wide frequency range [24]. A good design and construction can provide bandwidths of 8 or even 10 to 1. Coil coaxial baluns, constructed by coiling the coaxial line itself to form a balun [24], can provide bandwidths of 2 or 3 to 1.

References

1. M. Abraham, "Die electrischen Schwingungen um einen stabformingen Leiter, behandelt nach der Maxwelleschen Theorie," *Ann. Physik*, 66, pp. 435–472, 1898.
2. S. A. Schelkunoff, *Electromagnetic Waves*, Van Nostrand, New York, 1943, Chapter 11.
3. E. Hallén, "Theoretical Investigations into the Transmitting and Receiving Qualities of Antennae," *Nova Acta Regiae Soc. Sci. Upsaliensis*, Ser. IV, 11, No. 4, pp. 1–44, 1938.
4. R. C. Johnson and H. Jasik (eds.), *Antenna Engineering Handbook*, McGraw-Hill, New York, 1984, Chapter 4.
5. G. H. Brown and O. M. Woodward, Jr., "Experimentally Determined Radiation Characteristics of Conical and Triangular Antennas," *RCA Rev.*, Vol. 13, No. 4, p. 425, December 1952.
6. C. H. Papas and R. King, "Radiation from Wide-Angle Conical Antennas Fed by a Coaxial Line," *Proc. IRE*, Vol. 39, p. 1269, November 1949.
7. C. E. Smith, C. M. Butler, and K. R. Umashankar, "Characteristics of a Wire Biconical Antenna," *Microwave Journal*, pp. 37–40, September 1979.
8. G. H. Brown and O. M. Woodward, Jr., "Experimentally Determined Impedance Characteristics of Cylindrical Antennas," *Proc. IRE*, Vol. 33, pp. 257–262, 1945.
9. J. D. Kraus, *Antennas*, McGraw-Hill, New York, 1950, pp. 276–278.
10. J. H. Richmond and E. H. Newman, "Dielectric Coated Wire Antennas," *Radio Science*, Vol. 11, No. 1, pp. 13–20, January 1976.
11. J. Y. P. Lee and K. G. Balmain, "Wire Antennas Coated with Magnetically and Electrically Lossy Material," *Radio Science*, Vol. 14, No. 3, pp. 437–445, May-June 1979.
12. G. A. Thiele, E. P. Ekelman, Jr., and L. W. Henderson, "On the Accuracy of the Transmission Line Model for Folded Dipole," *IEEE Trans. Antennas Propagat.*, Vol. AP-28, No. 5, pp. 700–703, September 1980.
13. R. W. Lampe, "Design Formulas for an Asymmetric Coplanar Strip Folded Dipole," *IEEE Trans. Antennas Propagat.*, Vol. AP-33, No. 9, pp. 1028–1031, September 1985.
14. A. G. Kandoian, "Three New Antenna Types and Their Applications," *Proc. IRE*, Vol. 34, pp. 70W–75W, February 1946.

INTEL-1045
U.S. Patent 7,151,430

15. R. W. King and T. T. Wu, "The Cylindrical Antenna with Arbitrary Driving Point," *IEEE Trans. Antennas Propagat.*, Vol. AP-13, No. 5, pp. 710–718, September 1965.
16. R. W. P. King, "Asymmetric Driven Antennas and the Sleeve Dipole," *Proc. IRE*, Vol. 38, pp. 1154–1164, October 1950.
17. R. E. Collin, *Foundations for Microwave Engineering*, McGraw-Hill, New York, 1992, Chapter 5, pp. 303–386.
18. S. Y. Liao, *Microwave Devices and Circuits*, Prentice-Hall, Englewood Cliffs, New Jersey, 1980, pp. 418–422.
19. D. J. Healey, III, "An Examination of the Gamma Match," *QST*, pp. 11–15, April 1969.
20. *The ARRL Antenna Book*, American Radio Relay League, Inc., Newington, Conn., 1974, pp. 118–121.
21. H. T. Tolles, "How To Design Gamma-Matching Networks," *Ham Radio*, pp. 46–55, May 1973.
22. O. M. Woodward, Jr., "Balance Measurements on Balun Transformers," *Electronics*, Vol. 26, No. 9, September 1953, pp. 188–191.
23. C. L. Ruthroff, "Some Broad-Band Transformers," *Proc. IRE*, Vol. 47, August 1959, pp. 1337–1342.
24. W. L. Weeks, *Antenna Engineering*, McGraw-Hill, New York, 1968, pp. 161–180.

PROBLEMS

9.1. A 300-ohm "twin-lead" transmission line is attached to a biconical antenna.
   (a) Determine the cone angle that will match the line to an infinite length biconical antenna.
   (b) For the cone angle of part (a), determine the two smallest cone lengths that will resonate the antenna.
   (c) For the cone angle and cone lengths from part (b), what is the input VSWR?

9.2. Determine the first two resonant lengths, and the corresponding diameters and input resistances, for dipoles with $l/d = 25$, 50, and 10^4 using
   (a) the data in Figures 9.8(a) and 9.8(b)
   (b) Table 9.1

9.3. Design a resonant cylindrical stub monopole of length l, diameter d, and l/d of 50. Find the length (in λ), diameter (in λ), and the input resistance (in ohms) at the first four resonances.

9.4. A linear dipole of $l/d = 25$, 50, and 10^4 is attached to a 50-ohm line. Determine the VSWR of each l/d when
   (a) $l = \lambda/2$
   (b) $l = \lambda$
   (c) $l = 3\lambda/2$

9.5. Find the equivalent circular radius a_e for a
   (a) very thin flat plate of width $\lambda/10$
   (b) square wire with sides of $\lambda/10$
   (c) rectangular wire with sides of $\lambda/10$ and $\lambda/100$
   (d) elliptical wire with major and minor axes of $\lambda/10$ and $\lambda/20$
   (e) twin-lead transmission line with wire radii of 1.466×10^{-2} cm and separation of 0.8 cm

9.6. Compute the characteristic impedance of a two-wire transmission line with wire diameter of $d = 10^{-3}\lambda$ and center-to-center spacings of
   (a) $6.13 \times 10^{-3}\lambda$
   (b) $2.13 \times 10^{-2}\lambda$
   (c) $7.42 \times 10^{-2}\lambda$

9.7. Verify (9-47) from the expressions listed in Table 9.3.

9.8. To increase its bandwidth, a $\lambda/4$ monopole antenna operating at 1 GHz is made of two side-by-side copper wires ($\sigma = 5.7 \times 10^7$ S/m) of circular cross section. The wires at

INTEL-1045
U.S. Patent 7,151,430

each end of the arm are connected (shorted) electrically together. The radius of each wire is $\lambda/200$ and the separation between them is $\lambda/50$.

(a) What is the effective radius (in meters) of the two wires? Compare with the physical radius of each wire (in meters).

(b) What is the high-frequency loss resistance of each wire? What is the total loss resistance of the two together in a side-by-side shorted at the ends arrangement? What is the loss resistnce based on the effective radius?

(c) What is the radiation efficiency of one wire by itself? Compare with that of the two together in a side-by-side arrangement. What is the radiation efficiency based on the loss resistance of the effective radius?

9.9. Show that the input impedance of a two-element folded dipole of $l = \lambda/2$ is four times greater than that of an isolated element of the same length.

9.10. Design a two-element folded dipole with wire diameter of $10^{-3}\lambda$ and center-to-center spacing of $6.13 \times 10^{-3}\lambda$.

(a) Determine its shortest length for resonance.

(b) Compute the VSWR at the first resonance when it is attached to a 300-ohm line.

9.11. A two-element folded dipole of identical wires has an $l/d = 500$ and a center-to-center spacing of $6.13 \times 10^{-3}\lambda$ between the wires. Compute the

(a) approximate length of a single wire at its first resonance

(b) diameter of the wire at the first resonance

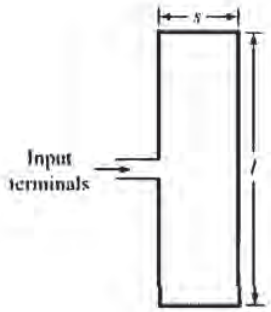
(c) characteristic impedance of the folded dipole transmission line

(d) input impedance of the transmission line mode model

(e) input impedance of the folded dipole using as the radius of the antenna mode (1) the radius of the wire a, (2) the equivalent radius a_e of the wires, (3) half of the center-to-center spacing ($s/2$). Compare the results.

9.12. The input impedance of a 0.47λ folded dipole operating at 10 MHz is

$$Z_{in} = 306 + j75.3$$



To resonate the element, it is proposed to place a lumped element in shunt (parallel) at the input terminals where the impedance is measured.

(a) What kind of an element (capacitor or inductor) should be used to accomplish the requirement?

(b) What is the value of the element (in farads or henries)?

(c) What is the new value of the input impedance?

(d) What is the VSWR when the resonant antenna is connected to a 300-ohm line?

9.13. A half-wavelength, two-element symmetrical folded dipole is connected to a 300-ohm "twin-lead" transmission line. In order for the input impedance of the dipole to be real, an energy storage lumped element is placed across its input terminals. Determine, assuming $f = 100$ MHz, the

(a) capacitance or inductance of the element that must be placed across the terminals.

(b) VSWR at the terminals of the transmission line taking into account the dipole and the energy storage element.

INTEL-1045
U.S. Patent 7,151,430

9.14. A half-wavelength, two-element symmetrical folded dipole whose each wire has a radius of $10^{-3}\lambda$ is connected to a 300-ohm "twin-lead" transmission line. The center-to-center spacing of the two wires is $4 \times 10^{-3}\lambda$. In order for the input impedance of the dipole to be real, determine, assuming $f = 100$ MHz, the
(a) total capacitance C that must be placed in series at the input terminals.
(b) capacitance C_L (two of them) that must be placed in series at each of the input terminals of the dipole in order to keep the antenna symmetrical.
(c) VSWR at the terminals of the transmission line connected to the dipole through the two capacitances.

9.15. An $l = 0.47\lambda$ folded dipole, whose wire radius is $5 \times 10^{-3}\lambda$, is fed by a "twin lead" transmission line with a 300-ohm characteristic impedance. The center-to-center spacing of the two side-by-side wires of the dipole is $s = 0.025\lambda$. The dipole is operating at $f = 10$ MHz. The input impedance of the "regular" dipole of $l = 0.47\lambda$ is $Z_d = 79 + j13$.
(a) Determine the
i. Input impedance of the folded dipole.
ii. Amplification factors of the real and imaginary parts of the input impedance of the folded dipole, compared to the corresponding values of the regular dipole.
iii. Input reflection coefficient.
iv. Input VSWR.
(b) To resonate the folded dipole and keep the system balanced, two capacitors (each C) are connected each symmetrically in series at the input terminals of the folded dipole.
i. What should C be to resonate the dipole?
ii. What is the new reflection coefficient at the input terminals of the "twin lead" line?
iii. What is the new VSWR?

9.16. A $\lambda/2$ dipole is fed asymmetrically at a distance of $\lambda/8$ from one of its ends. Determine its input impedance using (9-32). Compare its value with that obtained using the impedance transfer method of Section 4.5.5.

9.17. Repeat the design of Example 9.1 using a Tschebyscheff transformer.

9.18. Repeat the design of Example 9.1 for a three-section
(a) binomial transformer
(b) Tschebyscheff transformer

9.19. A self-resonant (*first resonance*) half-wavelength dipole of radius $a = 10^{-3}\lambda$ is connected to a 300-ohm "twin-lead" line through a three-section binomial impedance transformer. Determine the impedances of the three-section binomial transformer required to match the resonant dipole to the "twin-lead" line.

9.20. Consider a center-fed thin-wire dipole with wire radius $a = 0.005\lambda$.
(a) Determine the resonant length l (in wavelengths) and corresponding input resistance R_{in} of the antenna using assumed sinusoidal current distribution.
(b) Design a two-section Tschebyscheff quarter-wavelength transformer to match the antenna to a 75-ohm transmission line. Design the transformer to achieve an equal ripple response to R_{in} over a fractional bandwidth of 0.25.
(c) Compare the performance of the matching network in part (b) to an ideal transformer by plotting the input reflection coefficient magnitude versus normalized frequency for $0 \leq f/f_0 \leq 2$ for both cases.

9.21. The free-space impedance at the center point of the driven element of a 15-MHz Yagi-Uda array is $25 - j25$. Assuming the diameters of the wires of a T-match are $1.9 \times 10^{-3}\lambda$(3.8 cm) and $6.35 \times 10^{-4}\lambda$(1.27 cm), the center-to-center spacing between the wires is $7.62 \times 10^{-1}\lambda$(15.24 cm), and the length $l'/2$ of each T-match rod is 0.0285λ (57 cm), find the
(a) input impedance of the T-match
(b) input capacitance C_{in} that will resonate the antenna
(c) capacitance C that must be used in each leg to resonate the antenna

INTEL-1045
U.S. Patent 7,151,430

9.22. The input impedance of a 145.4 MHz Yagi-Uda antenna is $14 + j3$. Design a gamma match using diameters of 0.9525 cm (for the antenna) and 0.2052 cm (for the rod), and center-to-center spacing between the wires of 1.5316 cm. The match is for a 50-ohm input coaxial line. Find the shortest gamma rod length and the required capacitance. First, do the problem analytically. The design must be such that the real part of the designed input impedance is *within 1 ohm* of the required 50 ohms. Second, check your answers with the Smith chart.

9.23. Repeat Problem 9.22 for an input impedance of $14 - j3$.

9.24. A $\lambda/4$ monopole is mounted on a ground plane and has an input impedance of $34 + j17$ at $f = 145.4$ MHz. Design a gamma match to match the monopole to a 50-ohm coaxial line. The wire diameters are identical (0.9525 cm) and the center-to-center spacing is 3.1496 cm. Find the required capacitance and the shortest gamma rod length. First, do the problem analytically. The design must be such that the real part of the designed input impedance is *within 1 ohm* of the required 50 ohms. Second, check your answers with the Smith chart.

9.25. Using a gamma match, a $\lambda/2$ dipole is connected to an amateur 425 MHz radio receiver using a 78-ohm coaxial line. The length of the gamma match is $\lambda/4$ and its wire radius is identical to that of the dipole.
(a) What is the input impedance of the antenna-gamma match arrangement at the input terminals in the absence of a matching capacitor?
(b) To resonate the antenna, a capacitor is placed in series to the arm that is connected to the center conductor of the coaxial line. What is the value of the capacitor?
(c) When the resonant antenna is connected to a 78-ohm coaxial line, what is the magnitude of the reflection coefficient? What is the VSWR?

9.26. A 300 MHz resonant $\lambda/2$ dipole with an input impedance of 67 ohms is connected to a coaxial line through a gamma match. The radii of the wires for the dipole and gamma match, and the spacing between them, are such that the turns ratio of the transformer is 3:1. The characteristic impedance of the transmission line that the dipole and gamma match part form is 250 ohms. The overall length of the gamma match is 0.1λ.
(a) What is the total input impedance at the input terminals of the gamma match?
(b) What value of capacitor placed in series shall be selected so that the new input impedance is real (resonate the load)?

9.27. A T-match is connected to the antennas of Problems 9.22 and 9.23. Assuming that the wire diameters and lengths for each leg of the T-match are those derived for each gamma match, find the
(a) input impedance of the T-match
(b) capacitance C that must be connected in each leg to make the antenna system resonant

9.28. Repeat Problem 9.27 but select the lengths $l'/2$ of the T-match rods so that the input resistance is 300 ohms. Use diameters of 0.1026 cm (for the rod), 0.9525 cm (for the antenna), and center-to-center spacing of 0.7658 cm. This connection is ideal for use with a 300-ohm "twin-lead" line.

INTEL-1045
U.S. Patent 7,151,430

CHAPTER

10

TRAVELING WAVE AND BROADBAND ANTENNAS

10.1 INTRODUCTION

In the previous chapters we have presented the details of classical methods that are used to analyze the radiation characteristics of some of the simplest and most common forms of antennas (i.e., infinitely thin linear and circular wires, broadband dipoles and arrays). In practice there is a myriad of antenna configurations, and it would be almost impossible to consider all of them in this book. In addition, many of these antennas have bizzare types of geometries and it would be almost impractical, if not even impossible, to investigate each in detail. However, the general performance behavior of some of them will be presented in this chapter with a minimum of analytical formulations. Today, comprehensive analytical formulations are available for most of them, but they would require so much space that it would be impractical to include them in this book.

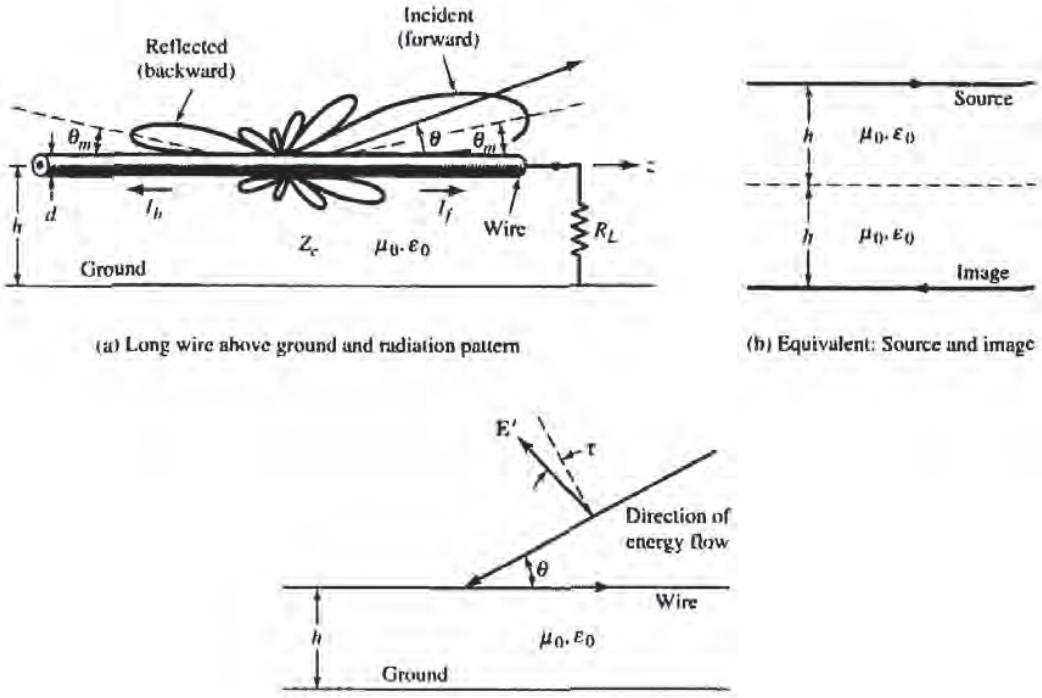
10.2 TRAVELING WAVE ANTENNAS

In Chapter 4, center-fed linear wire antennas were discussed whose amplitude current distribution was

1. constant for infinitesimal dipoles ($l \leq \lambda/50$)
2. linear (triangular) for short dipoles ($\lambda/50 < l \leq \lambda/10$)
3. sinusoidal for long dipoles ($l > \lambda/10$)

In all cases the phase distribution was assumed to be constant. The sinusoidal current distribution of long open-ended linear antennas is a standing wave constructed by two waves of equal amplitude and 180° phase difference at the open-end traveling in opposite directions along its length. The voltage distribution has also a standing wave pattern except that it has maxima (loops) at the end of the line instead of nulls (nodes) as the current. In each pattern, the maxima and minima repeat every integral number of half-wavelengths. There is also a $\lambda/4$ spacing between a null and a maximum in each of the wave patterns. The current and voltage distributions on open-ended wire antennas are similar to the standing wave patterns on open-ended transmission lines.

INTEL-1045
U.S. Patent 7,151,430



(a) Long wire above ground and radiation pattern

(b) Equivalent: Source and image

(c) Wave tilt

Figure 10.1 Beverage (long-wire) antenna above ground.

Linear antennas that exhibit current and voltage standing wave patterns formed by reflections from the open end of the wire are referred to as *standing wave* or *resonant* antennas.

Antennas can be designed which have traveling wave (uniform) patterns in current and voltage. This can be achieved by properly terminating the antenna wire so that the reflections are minimized if not completely eliminated. An example of such an antenna is a long wire that runs horizontal to the earth, as shown in Figure 10.1. The input terminals consist of the ground and one end of the wire. This configuration is known as *Beverage or wave antenna*. There are many other configurations of traveling wave antennas. In general, all antennas whose current and voltage distributions can be represented by one or more traveling waves, usually in the same direction, are referred to as *traveling wave* or *nonresonant* antennas. A progressive phase pattern is usually associated with the current and voltage distributions.

Standing wave antennas, such as the dipole, can be analyzed as traveling wave antennas with waves propagating in opposite directions (forward and backward) and represented by traveling wave currents I_f and I_h in Figure 10.1(a). Besides the long wire antenna there are many examples of traveling wave antennas such as dielectric rod (polyrod), helix, and various surface wave antennas. Aperture antennas, such as reflectors and horns, can also be treated as traveling wave antennas. In addition, arrays of closely spaced radiators (usually less than $\lambda/2$ apart) can also be analyzed as traveling wave antennas by approximating their current or field distribution by a continuous traveling wave. Yagi-Uda, log-periodic, and slots and holes in a waveguide are some examples of discrete-element traveling wave antennas. In general, a traveling wave antenna is usually one that is associated with radiation from a continuous source. An excellent book on traveling wave antennas is one by C. H. Walter [1].

INTEL-1045
U.S. Patent 7,151,430

A traveling wave may be classified as a *slow* wave if its phase velocity v_p ($v_p = \omega/k$, ω = wave angular frequency, k = wave phase constant) is equal or smaller than the velocity of light c in free-space ($v_p/c \leq 1$). A fast wave is one whose phase velocity is greater than the speed of light ($v_p/c > 1$).

In general, there are two types of traveling wave antennas. One is the *surface wave* antenna defined as "an antenna which radiates power flow from discontinuities in the structure that interrupt a bound wave on the antenna surface."* A surface wave antenna is, in general, a slow wave structure whose phase velocity of the traveling wave is equal to or less than the speed of light in free-space ($v_p/c \leq 1$).

For slow wave structures radiation takes place only at nonuniformities, curvatures, and discontinuities. Discontinuities can be either discrete or distributed. One type of discrete discontinuity on a surface wave antenna is a transmission line terminated in an unmatched load, as shown in Figure 10.1(a). A distributed surface wave antenna can be analyzed in terms of the variation of the amplitude and phase of the current along its structure. In general, power flows parallel to the structure, except when losses are present, and for plane structures the fields decay exponentially away from the antenna. Most of the surface-wave antennas are endfire or near-endfire radiators. Practical configurations include line, planar surface, curved, and modulated structures.

Another traveling wave antenna is a *leaky-wave* antenna defined as "an antenna that couples power in small increments per unit length, either continuously or discretely, from a traveling wave structure to free-space"† Leaky-wave antennas continuously lose energy due to radiation, as shown in Figure 10.2 by a slotted rectangular waveguide. The fields decay along the structure in the direction of wave travel and increase in others. Most of them are fast wave structures.

10.2.1 Long Wire

An example of a slow wave traveling antenna is a long wire, as shown in Figure 10.1. An antenna is usually classified as a *long* wire antenna if it is a straight conductor with a length from one to many wavelengths. A long wire antenna has the distinction of being the first traveling wave antenna.

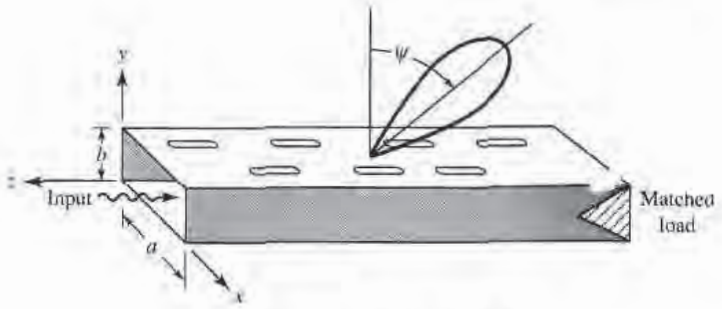
The long wire of Figure 10.1(a), in the presence of the ground, can be analyzed approximately using the equivalent of Figure 10.1(b) where an image is introduced to take into account the presence of the ground. The magnitude and phase of the image are determined using the reflection coefficient for horizontal polarization as given by (4-129). The height h of the antenna above the ground must be chosen so that the reflected wave (or wave from the image), which includes the phase due to reflection is in phase with the direct wave at the angles of desired maximum radiation. However, for typical electrical constitutive parameters of the earth, and especially for observation angles near grazing, the reflection coefficient for horizontal polarization is approximately -1. Therefore the total field radiated by the wire in the presence of the ground can be found by multiplying the field radiated by the wire in free space by the array factor of a two-element array, as was done in Section 4.8.2 and represented by (4-130).

The objective now is to find the field radiated by the long wire in free space. This is accomplished by referring to Figure 10.3. As the wave travels along the wire from the source toward the load, it continuously leaks energy. This can be represented by

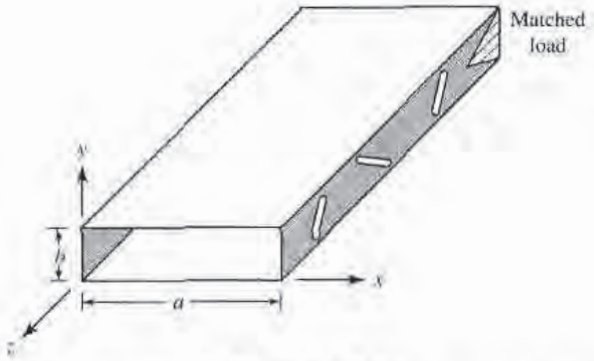
*"IEEE Standard Definitions of Terms for Antennas" (IEEE Std 145-1983), *IEEE Trans. Antennas and Propagat.*, Vol. AP-31, No. 6, Part II, Nov. 1983.

†Ibid.

INTEL-1045
U.S. Patent 7,151,430



(a) Upper wall—longitudinal



(b) Sidewall—inclined

Figure 10.2 Leaky-wave waveguide slots; upper (broad) and side (narrow) walls.

an attenuation coefficient. Therefore the current distribution of the forward traveling wave along the structure can be represented by

$$\mathbf{I}_f = \hat{\mathbf{a}}_z I_z(z')e^{-\gamma(z')z'} = \hat{\mathbf{a}}_z I_0 e^{-[\alpha(z')+jk_z(z')]z'} \tag{10-1}$$

where $\gamma(z')$ is the propagation coefficient [$\gamma(z') = \alpha(z') + jk_z(z')$ where $\alpha(z')$ is the attenuation constant (nepers/meter) while $k_z(z')$ is the phase constant (radians/meter) associated with the traveling wave]. In addition to the losses due to leakage, there are wire and ground losses. The attenuation factor $\alpha(z')$ can also be used to take into account the ohmic losses of the wire as well as ground losses. However, these, especially the ohmic losses, are usually very small and for simplicity are neglected. In addition, when the radiating medium is air, the loss of energy in a long wire ($l \gg \lambda$) due to leakage is also usually very small, and it can also be neglected. Therefore the current distribution of (10-1) can be approximated by

$$\mathbf{I} = \hat{\mathbf{a}}_z I(z')e^{-jk_z z'} = \hat{\mathbf{a}}_z I_0 e^{-jk_z z'} \tag{10-1a}$$

where $I(z') = I_0$ is assumed to be constant. Using techniques outlined and used in Chapter 4, it can be easily shown that in the far-field

$$E_r \simeq E_\phi = H_r = H_\theta = 0 \tag{10-2a}$$

$$E_\theta \simeq j\eta \frac{klI_0 e^{-jkr}}{4\pi r} e^{-j(kl/2)(K-\cos\theta)} \sin\theta \frac{\sin[(kl/2)(\cos\theta - K)]}{(kl/2)(\cos\theta - K)} \tag{10-2b}$$

$$H_\phi \simeq \frac{E_\theta}{\eta} \tag{10-2c}$$

INTEL-1045
U.S. Patent 7,151,430

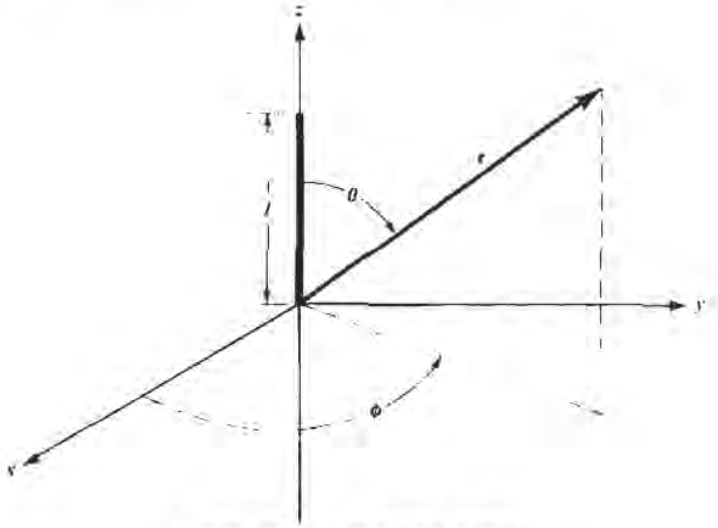


Figure 10.3 Long wire antenna.

where K is used to represent the ratio of the phase constant of the wave along the transmission line (k_z) to that of free-space (k), or

$$K = \frac{k_z}{k} = \frac{\lambda}{\lambda_g} \tag{10-3}$$

λ_g = wavelength of the wave along the transmission line

Assuming a perfect electric conductor for the ground, the total field for Figure 10.1(a) is obtained by multiplying each of (10-2a)–(10-2c) by the array factor sin (kh sin θ).

For $k_z = k$ ($K = 1$) the time-average power density can be written as

$$\mathbf{W}_{av} = \mathbf{W}_{rad} = \hat{\mathbf{a}}_r \eta \frac{|I_0|^2}{8\pi^2 r^2} \frac{\sin^2\theta}{(\cos\theta - 1)^2} \sin^2\left[\frac{kl}{2}(\cos\theta - 1)\right] \tag{10-4}$$

which reduces to

$$\mathbf{W}_{av} = \mathbf{W}_{rad} = \hat{\mathbf{a}}_r \eta \frac{|I_0|^2}{8\pi^2 r^2} \cot^2\left(\frac{\theta}{2}\right) \sin^2\left[\frac{kl}{2}(\cos\theta - 1)\right] \tag{10-5}$$

From (10-5) it is evident that the power distribution of a wire antenna of length l is a multilobe pattern whose number of lobes depend upon its length. Assuming that l is very large such that the variations in the sine function of (10-5) are more rapid than those of the cotangent, the peaks of the lobes occur approximately when

$$\sin^2\left[\frac{kl}{2}(\cos\theta - 1)\right]_{\theta=\theta_m} = 1 \tag{10-6}$$

or

$$\frac{kl}{2}(\cos\theta_m - 1) = \pm\left(\frac{2m+1}{2}\right)\pi, \quad m = 0, 1, 2, 3, \ldots \tag{10-6a}$$

INTEL-1045
U.S. Patent 7,151,430

The angles where the peaks occur are given by

$$\theta_m = \cos^{-1}\left[1 \pm \frac{\lambda}{2l}(2m + 1)\right], \qquad m = 0, 1, 2, 3, \ldots \tag{10-7}$$

The angle where the maximum of the major lobe occurs is given by $m = 0$ (or $2m + 1 = 1$). As l becomes very large ($l \gg \lambda$) the angle of the maximum of the major lobe approaches zero degrees and the structure becomes a near endfire array.

In finding the values of the maxima, the variations of the cotangent term in (10-5) were assumed to be negligible (as compared to those of the sine term). If the effects of the cotangent term were to be included, then the values of the $2m + 1$ term in (10-7) should be

$$2m + 1 = 0.742, 2.93, 4.96, 6.97, 8.99, 11, 13, \ldots \tag{10-8}$$

(instead of 1, 3, 5, 7, 9, ...) for the first, second, third, and so forth maxima. The approximate values approach those of the exact for the higher order lobes.

In a similar manner, the nulls of the pattern can be found and occur when

$$\sin^2\left[\frac{kl}{2}(\cos\theta - 1)\right]_{\theta=\theta_n} = 0 \tag{10-9}$$

or

$$\frac{kl}{2}(\cos\theta_n - 1) = \pm n\pi, \qquad n = 1, 2, 3, 4, \ldots \tag{10-9a}$$

The angles where the nulls occur are given by

$$\theta_n = \cos^{-1}\left(1 \pm n\frac{\lambda}{l}\right), \qquad n = 1, 2, 3, 4, \ldots \tag{10-10}$$

for the first, second, third, and so forth nulls.

The total radiated power can be found by integrating (10-5) over a closed sphere of radius r and reduces to

$$P_{\text{rad}} = \oiint_S \mathbf{W}_{\text{rad}} \cdot d\mathbf{s} = \frac{\eta}{4\pi}|I_0|^2\left[1.415 + \ln\left(\frac{kl}{\pi}\right) - C_i(2kl) + \frac{\sin(2kl)}{2kl}\right] \tag{10-11}$$

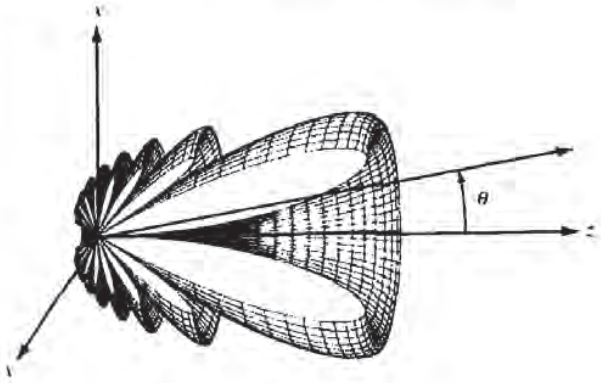
where $C_i(x)$ is the cosine integral of (4-68a). The radiation resistance is then found to be

$$\boxed{R_r = \frac{2P_{\text{rad}}}{|I_0|^2} = \frac{\eta}{2\pi}\left[1.415 + \ln\left(\frac{kl}{\pi}\right) - C_i(2kl) + \frac{\sin(2kl)}{2kl}\right]} \tag{10-12}$$

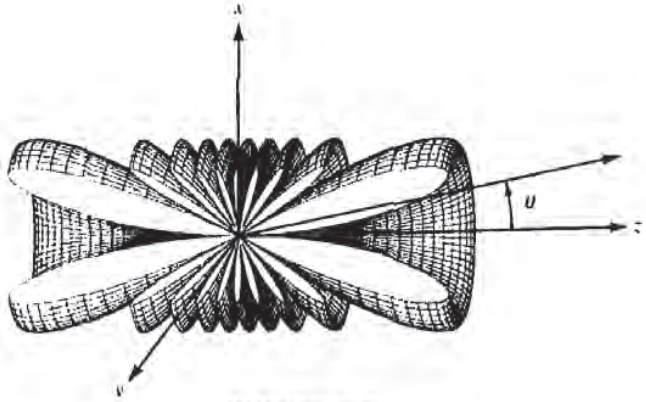
Using (10-5) and (10-11) the directivity can be written as

$$\boxed{D_0 = \frac{4\pi U_{\max}}{P_{\text{rad}}} = \frac{2\cot^2\left[\frac{1}{2}\cos^{-1}\left(1 - \frac{0.371\lambda}{l}\right)\right]}{1.415 + \ln\left(\frac{2l}{\lambda}\right) - C_i(2kl) + \frac{\sin(2kl)}{2kl}}} \tag{10-13}$$

INTEL-1045
U.S. Patent 7,151,430



(a) Traveling wave



(b) Standing wave

Figure 10.4 Three-dimensional free-space amplitude pattern for traveling and standing wave wire antennas of $l = 5\lambda$.

A. Amplitude Patterns, Maxima, and Nulls

To verify some of the derivations and illustrate some of the principles, a number of computations were made. Shown in Figure 10.4(a) is the three-dimensional pattern of a traveling wire antenna with length $l = 5\lambda$ while in Figure 10.4(b) is the three-dimensional pattern for a standing wave wire antenna with length $l = 5\lambda$. The corresponding two- dimensional patterns are shown in Figure 10.5. The pattern of Figure 10.4(a) is formed by the forward traveling wave current $I_f = I_1 e^{-jkz}$ of Figure 10.1(a) while that of Figure 10.4(b) is formed by the forward I_f plus backward I_b traveling wave currents of Figure 10.1(a). The two currents I_f and I_b together form a standing wave: that is, $I_s = I_f + I_b = I_1 e^{-jkz} - I_2 e^{+jkz} = -2jI_0 \sin(kz)$ when $I_2 = I_1 = I_0$. As expected, for the traveling wave antenna of Figure 10.4(a) there is maximum radiation in the forward direction while for the standing wave antenna of Figure 10.4(b) there is maximum radiation in the forward and backward directions. The lobe near the axis of the wire in the directions of travel is the largest. The magnitudes of the other lobes from the main decrease progressively, with an envelope proportional to $\cot^2(\theta/2)$, toward the other direction. The traveling wave antenna is used when it is desired to radiate or receive predominantly from one direction. As the length of the wire increases, the maximum of the main lobe shifts closer toward the axis and the number of lobes increase. This is illustrated in Figure 10.6 for a traveling

INTEL-1045
U.S. Patent 7,151,430

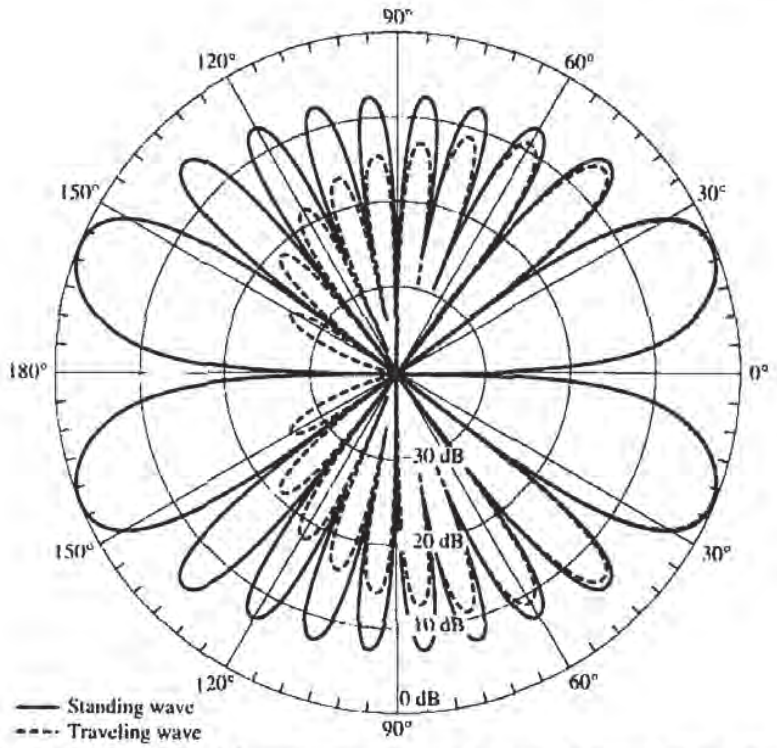


Figure 10.5 Two-dimensional free-space amplitude pattern for traveling and standing wave wire antennas of $l = 5\lambda$.

wave wire antenna with $l = 5\lambda$ and 10λ. The angles of the maxima of the first four lobes, computed using (10-8), are plotted in Figure 10.7(a) for $0.5\lambda \leq l \leq 10\lambda$. The corresponding angles of the first four nulls, computed using (10-10), are shown in Figure 10.7(b) for $0.5\lambda \leq l \leq 10\lambda$. These curves can be used effectively to design long wires when the direction of the maximum or null is desired.

B. Input Impedance

For traveling wave wire antennas the radiation in the opposite direction from the maximum is suppressed by reducing, if not completely eliminating, the current reflected from the end of the wire. This is accomplished by increasing the diameter of the wire or more successfully by properly terminating it to the ground, as shown in Figure 10.1. Ideally a complete elimination of the reflections (perfect match) can only be accomplished if the antenna is elevated only at small heights (compared to the wavelength) above the ground, and it is terminated by a resistive load. The value of the load resistor, to achieve the impedance match, is equal to the characteristic impedance of the wire near the ground (which is found using image theory). For a wire with diameter d and height h above the ground, an approximate value of the termination resistance is obtained from

$$R_L = 138 \log_{10}\left(4\frac{h}{d}\right) \tag{10-14}$$

To achieve a reflection-free termination, the load resistor can be adjusted about this value (usually about 200–300 ohms) until there is no standing wave on the antenna

INTEL-1045
U.S. Patent 7,151,430

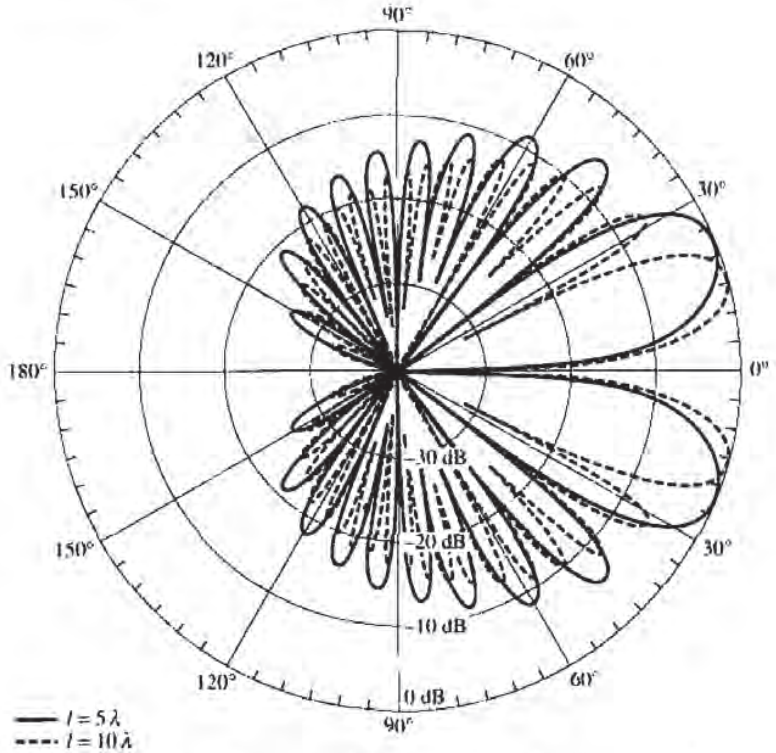


Figure 10.6 Two-dimensional free-space amplitude pattern for traveling wave wire antenna of $l = 5\lambda$ and 10λ.

wire. Therefore the input impedance is the same as the load impedance or the characteristic impedance of the line, as given by (10-14).

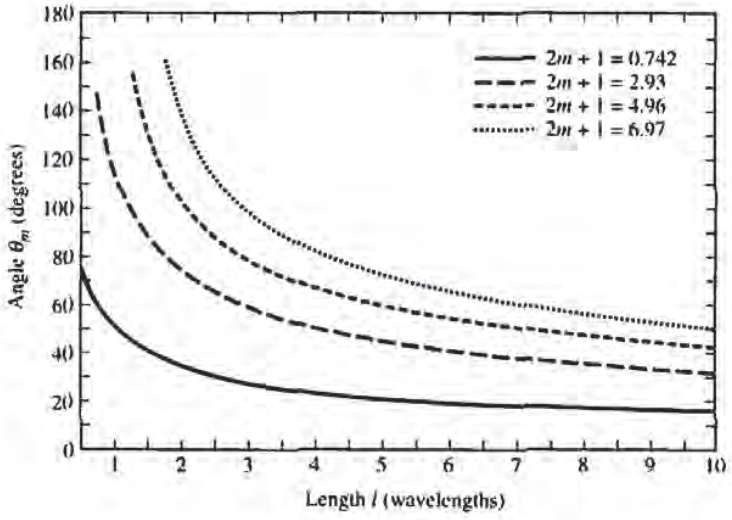
If the antenna is not properly terminated, waves reflected from the load traveling in the opposite direction from the incident waves create a standing wave pattern. Therefore the input impedance of the line is not equal to the load impedance. To find the input impedance, the transmission line impedance transfer equation of (9-18) can be used. Doing this we can write that the impedance at the input terminals of Figure 10.1(a) is

$$Z_{in}(l) = Z_c \left[\frac{R_L + jZ_c \tan(\beta l)}{Z_c + jR_L \tan(\beta l)} \right] \tag{10-15}$$

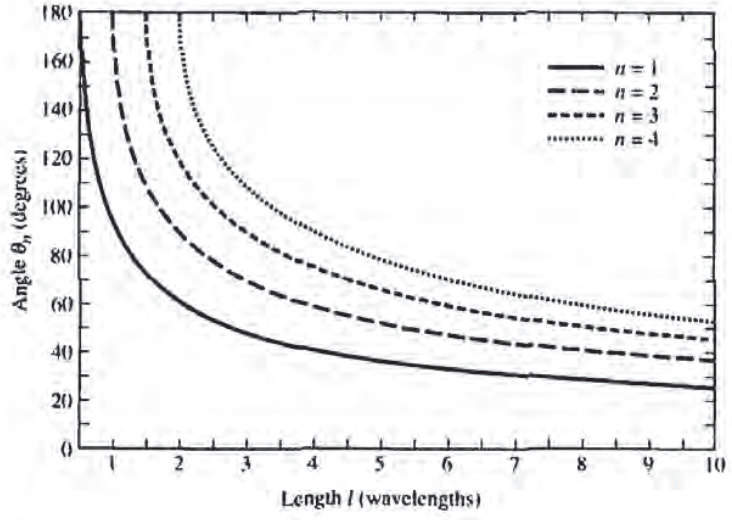
C. Polarization

A long wire antenna is linearly polarized, and it is always parallel to the plane formed by the wire and radial vector from the center of the wire to the observation point. The direction of the linear polarization is not the same in all parts of the pattern, but it is perpendicular to the radial vector (and parallel to the plane formed by it and the wire). Thus the wire antenna of Figure 10.1, when its height above the ground is small compared to the wavelength and its main beam is near the ground, is not an effective element for horizontal polarization. Instead it is usually used to transmit or receive waves that have an appreciable vector component in the vertical plane. This is what is known as a *Beverage antenna* which is used more as a receiving rather than a transmitting element because of its poor radiation efficiency due to power absorbed in the load resistor.

INTEL-1045
U.S. Patent 7,151,430



(a) Maxima



(b) Nulls

Figure 10.7 Angles versus length of wire antenna where maxima and nulls occur.

When a TEM wave travels parallel to an air-conductor interface, it creates a forward wave tilt [2] which is determined by applying the boundary conditions on the tangential fields along the interface. The amount of tilt is a function of the constitutive parameters of the ground. If the conductor is a perfect electric conductor (PEC), then the wave tilt is zero because the tangential electric field vanishes along the PEC. The wave tilt increases with frequency and with ground resistivity. Therefore, for a Beverage wire antenna, shown in Figure 10.1(c) in the receiving mode, reception is influenced by the tilt angle of the incident vertically polarized wavefront, which is formed by the losses of the local ground. The electric field vector of the incident wavefront produces an electric force that is parallel to the wire, which in turn induces a current in the wire. The current flows in the wire toward the receiver, and it is reinforced up to a certain point along the wire by the advancing wavefront. The wave along the wire is transverse magnetic.

INTEL-1045
U.S. Patent 7,151,430

D. Resonant Wires

Resonant wire antennas are formed when the load impedance of Figure 10.1(a) is not matched to the characteristic impedance of the line. This causes reflections which with the incident wave form a standing wave. Resonant antennas, including the dipole, were examined in detail in Chapter 4, and the electric and magnetic field components of a center fed wire of total length l are given, respectively, by (4-62a) and (4-62b). Other radiation characteristics (including directivity, radiation resistance, maximum effective area, etc.) are found in Chapter 4.

Resonant antennas can also be formed using long wires. It can be shown that for *resonant* long wires with lengths odd multiple of half wavelength ($l = n\lambda/2$, $n = 1, 3, 5, \ldots$), the radiation resistance is given approximately (within 0.5 ohms) by [3], [4]

$$R_r = 73 + 69 \log_{10}(n) \tag{10-16}$$

This expression gives a very good answer even for $n = 1$. For the same elements, the angle of maximum radiation is given by

$$\theta_{\max} = \cos^{-1}\left(\frac{n-1}{n}\right) \tag{10-17}$$

This formula is more accurate for small values of n, although it gives good results even for large values of n. It can also be shown that the maximum directivity is related to the radiation resistance by

$$D_0 = \frac{120}{R_r \sin^2 \theta_{\max}} \tag{10-18}$$

The values based on (10-18) are within 0.5 dB from those based on (4-75). It is apparent that all three expressions, (10-16)–(10-18), lead to very good results for the half-wavelength dipole ($n = 1$).

Long wire antennas (both resonant and nonresonant) are very simple, economical, and effective directional antennas with many uses for transmitting and receiving waves in the MF (300 KHz–3 MHz) and HF (3–30 MHz) ranges. Their properties can be enhanced when used in arrays.

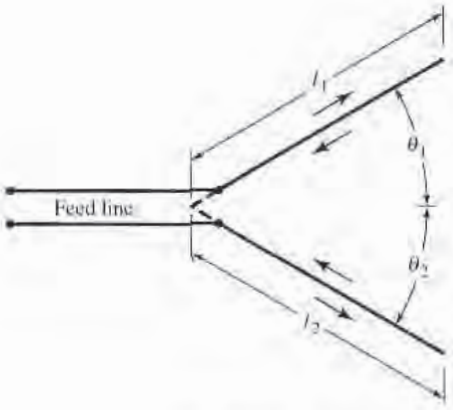
10.2.2 V Antenna

For some applications a single long wire antenna is not very practical because (1) its directivity may be low, (2) its side lobes may be high, and (3) its main beam is inclined at an angle, which is controlled by its length. These and other drawbacks of single long wire antennas can be overcome by utilizing an array of wires.

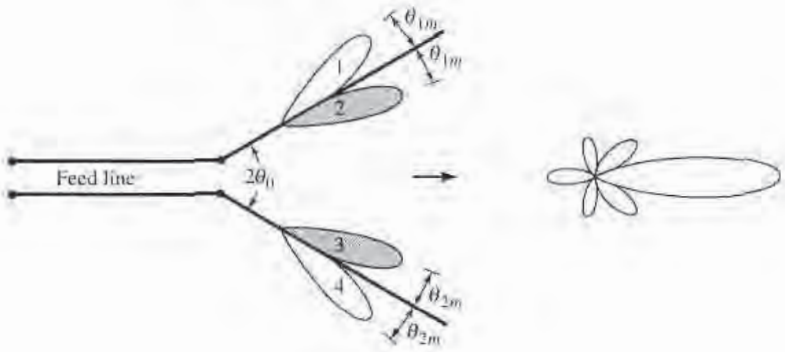
One very practical array of long wires is the V antenna formed by using two wires each with one of its ends connected to a feed line as shown in Figure 10.8(a). In most applications, the plane formed by the legs of the V is parallel to the ground leading to a horizontal V array whose principal polarization is parallel to the ground and the plane of the V. Because of increased sidelobes, the directivity of ordinary linear dipoles begins to diminish for lengths greater than about 1.25λ, as shown in Figure 4.8. However by adjusting the included angle of a V dipole, its directivity can be made greater and its side lobes smaller than those of a corresponding linear dipole. Designs for maximum directivity usually require smaller included angles for longer V's.

Most V antennas are symmetrical ($\theta_1 = \theta_2 = \theta_0$ and $l_1 = l_2 = l$). Also V antennas can be designed to have unidirectional or bidirectional radiation patterns, as

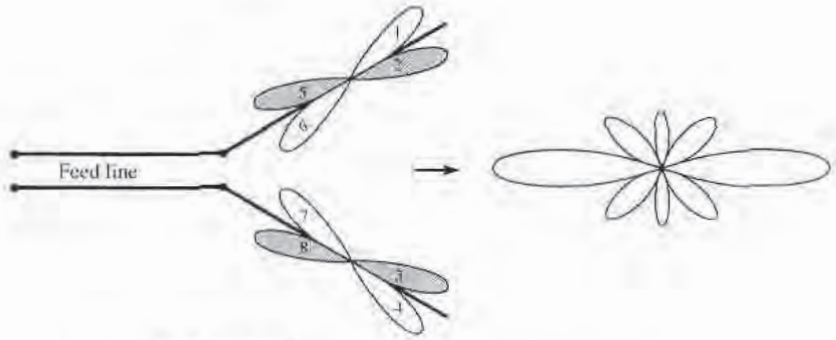
INTEL-1045
U.S. Patent 7,151,430



(a) V antenna



(b) Unidirectional



(c) Bidirectional

Figure 10.8 Unidirectional and bidirectional V antennas.

shown in Figures 10.8(b) and (c), respectively. To achieve the unidirectional characteristics, the wires of the V antenna must be nonresonant which can be accomplished by minimizing if not completely eliminating reflections from the ends of the wire. The reflected waves can be reduced by making the inclined wires of the V relatively thick. In theory, the reflections can even be eliminated by properly terminating the open ends of the V leading to a purely traveling wave antenna. One way of terminating the V antenna will be to attach a load, usually a resistor equal in value to the open-end characteristic impedance of the V-wire transmission line, as shown in Figure

INTEL-1045
U.S. Patent 7,151,430

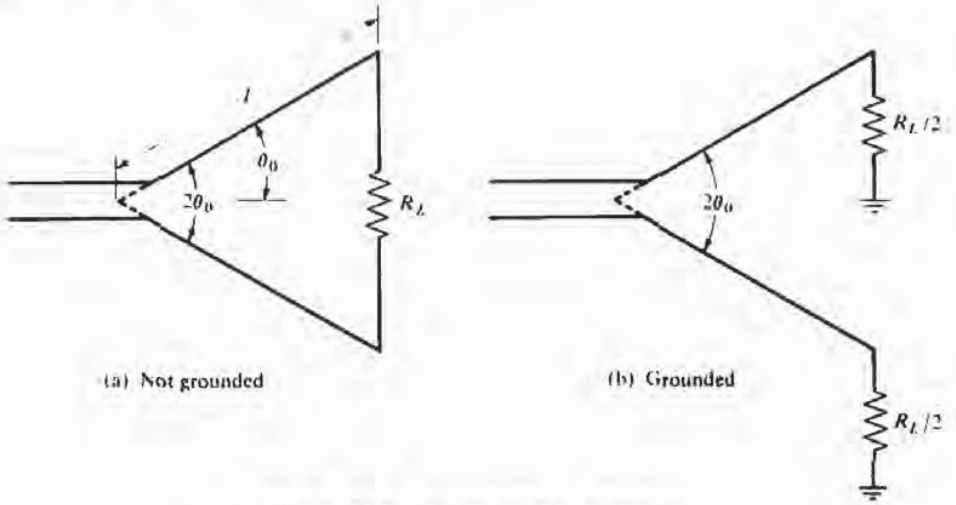


Figure 10.9 Terminated V antennas.

10.9(a). The terminating resistance can also be divided in half and each half connected to the ground leading to the termination of Figure 10.9(b). If the length of each leg of the V is very long (typically $l > 5\lambda$), there will be sufficient leakage of the field along each leg that when the wave reaches the end of the V it will be sufficiently reduced that there will not necessarily be a need for a termination. Of course, termination with a load is not possible without a ground plane.

The patterns of the individual wires of the V antenna are conical in form and are inclined at an angle from their corresponding axes. The angle of inclination is determined by the length of each wire. For the patterns of each leg of a symmetrical V antenna to add in the direction of the line bisecting the angle of the V and to form one major lobe, the total included angle $2\theta_0$ of the V should be equal to $2\theta_m$, which is twice the angle that the cone of maximum radiation of each wire makes with its axis. When this is done, beams 2 and 3 of Figure 10.8(b) are aligned and add constructively. Similarly for Figure 10.8(c), beams 2 and 3 are aligned and add constructively in the forward direction, while beams 5 and 6 are aligned and add constructively in the backward direction. If the total included angle of the V is greater than $2\theta_m$ ($2\theta_0 > 2\theta_m$) the main lobe is split into two distinct beams. However, if $2\theta_0 < 2\theta_m$, then the maximum of the single major lobe is still along the plane that bisects the V but it is tilted upward from the plane of the V. This may be a desired designed characteristic when the antenna is required to transmit waves upward toward the ionosphere for optimum reflection or to receive signals reflected downward by the ionosphere. For optimum operation, typically the included angle is chosen to be approximately $\theta_0 \approx 0.8\theta_m$. When this is done, the reinforcement of the fields from the two legs of the V lead to a total directivity for the V of approximately twice the directivity of one leg of the V.

For a symmetrical V antenna with legs each of length l, there is an optimum included angle which leads to the largest directivity. Design data for optimum included angles of V dipoles were computed [5] using Moment Method techniques and are shown in Figure 10.10(a). The corresponding directivities are shown in Figure 10.10(b). In each figure the dots (·) represent values computed using the Moment Method while the solid curves represent second- or third-order polynomials fitted

INTEL-1045
U.S. Patent 7,151,430

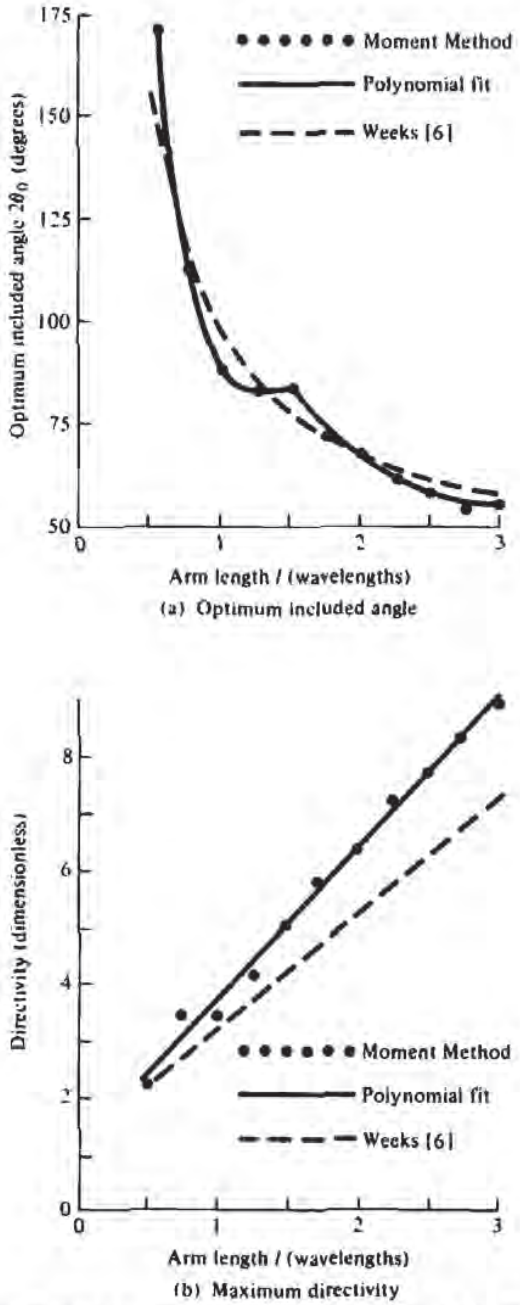


Figure 10.10 Optimum included angle for maximum directivity as a function of arm length for V dipoles. (SOURCE: G. A. Thiele and E. P. Ekelman, Jr., "Design Formulas for Vee Dipoles," *IEEE Trans. Antennas Propagat.*, Vol. AP-28, pp. 588–590, July 1980. © (1980) IEEE)

INTEL-1045
U.S. Patent 7,151,430

through the computed data. The polynomials for optimum included angles and maximum directivities are given by

$$2\theta_0 = \begin{cases} -149.3\left(\frac{l}{\lambda}\right)^3 + 603.4\left(\frac{l}{\lambda}\right)^2 - 809.5\left(\frac{l}{\lambda}\right) + 443.6 & \text{for } 0.5 \le l/\lambda \le 1.5 \quad \text{(10-19a)} \\ 13.39\left(\frac{l}{\lambda}\right)^2 - 78.27\left(\frac{l}{\lambda}\right) + 169.77 & \text{for } 1.5 \le l/\lambda \le 3 \quad \text{(10-19b)} \end{cases}$$

$$D_0 = 2.94\left(\frac{l}{\lambda}\right) + 1.15 \qquad \text{for } 0.5 \le l/\lambda \le 3 \qquad \text{(10-20)}$$

The dashed curves represent data obtained from empirical formulas [6]. The corresponding input impedances of the V's are slightly smaller than those of straight dipoles.

Another form of a V antenna is shown in the insert of Figure 10.11(a). The V is formed by a monopole wire, bent at an angle over a ground plane, and by its image shown dashed. The included angle of the V as well as the length can be used to tune the antenna. For included angles greater than 120° ($2\theta_0 > 120°$), the antenna exhibits primarily vertical polarization with radiation patterns almost identical to those of straight dipoles. As the included angle becomes smaller than about 120°, a horizontally polarized field component is excited which tends to fill the pattern toward the horizontal direction, making it a very attractive communication antenna for aircraft. The computed impedance of the ground plane and free-space V configurations obtained by the Moment Method [7] is shown plotted in Figure 10.11(a).

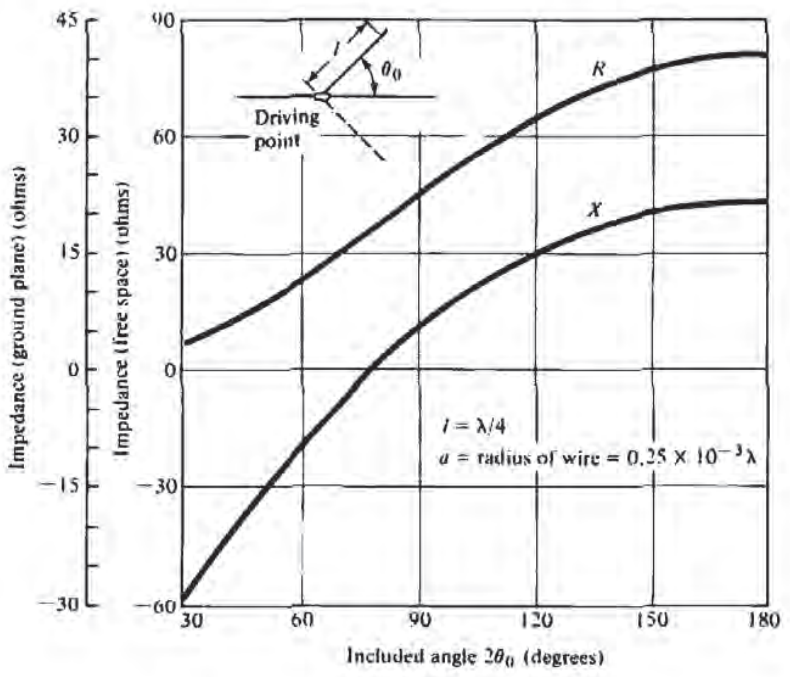
Another practical form of a dipole antenna, particularly useful for airplane or ground-plane applications, is the 90° bent wire configuration of Figure 10.11(b). The computed impedance of the antenna, obtained also by the Moment Method [7], is shown plotted in Figure 10.11(b). This antenna can be tuned by adjusting its perpendicular and parallel lengths h_1 and h_2. The radiation pattern in the plane of the antenna is nearly omnidirectional for $h_1 \le 0.1\lambda$. For $h_1 > 0.1\lambda$ the pattern approaches that of vertical $\lambda/2$ dipole.

10.2.3 Rhombic Antenna

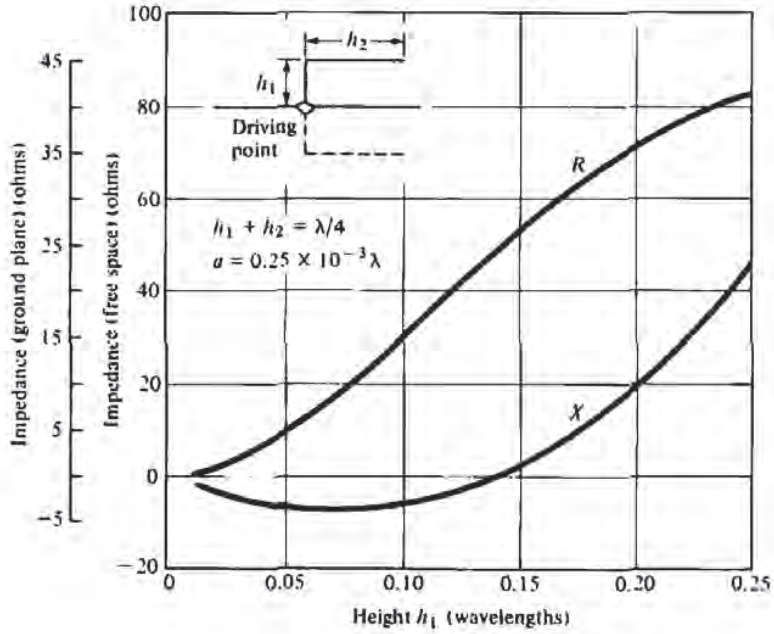
A. Geometry and Radiation Characteristics

Two V antennas can be connected at their open ends to form a diamond or rhombic antenna, as shown in Figure 10.12(a). The antenna is usually terminated at one end in a resistor, usually about 600–800 ohms, in order to reduce if not eliminate reflections. However, if each leg is long enough (typically greater than 5λ) sufficient leakage occurs along each leg that the wave that reaches the far end of the rhombus is sufficiently reduced that it may not be necessary to terminate the rhombus. To achieve the single main lobe, beams 2, 3, 6, and 7 are aligned and add constructively. The other end is used to feed the antenna. Another configuration of a rhombus is that of Figure 9.12(b) which is formed by an inverted V and its image (shown dashed). The inverted V is connected to the ground through a resistor. As with the V antennas, the pattern of rhombic antennas can be controlled by varying the element lengths, angles

INTEL-1045
U.S. Patent 7,151,430



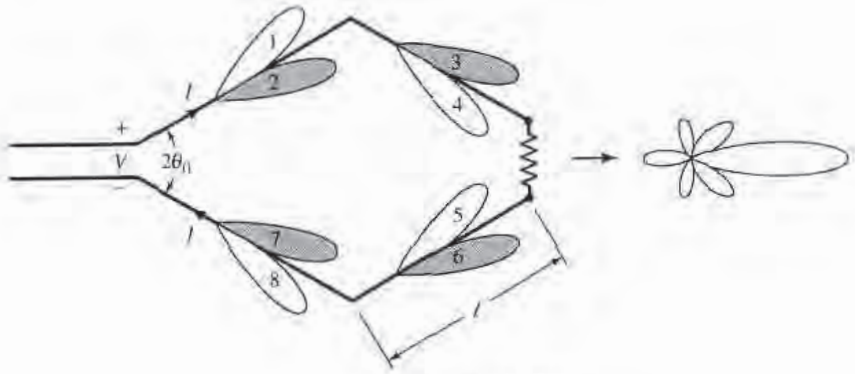
(a) V antenna



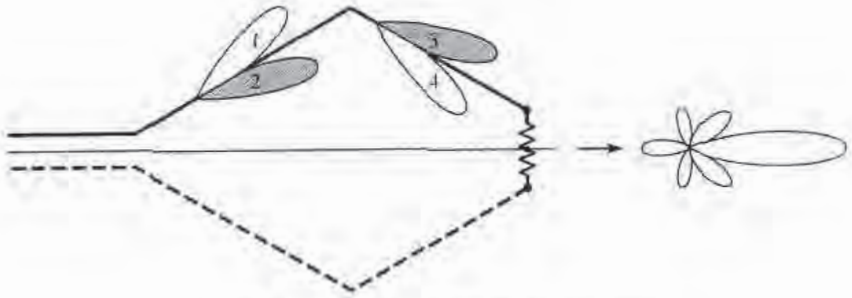
(b) Bent wire

Figure 10.11 Computed impedance ($R + jX$) of V and bent wire antennas above ground. (SOURCE: D. G. Fink (ed.), *Electronics Engineer's Handbook*, Chapter 18 (by W. F. Croswell), McGraw-Hill, New York, 1975)

INTEL-1045
U.S. Patent 7,151,430



(a) Rhombus formed by 2 V's



(b) Rhombus formed by inverted V over ground

Figure 10.12 Rhombic antenna configurations.

between elements, and the plane of the rhombus. Rhombic antennas are usually preferred over V's for nonresonant and unidirectional pattern applications because they are less difficult to terminate. Additional directivity and reduction in side lobes can be obtained by stacking, vertically or horizontally, a number of rhombic and/or V antennas to form arrays.

The field radiated by a rhombus can be found by adding the fields radiated by its four legs. For a symmetrical rhombus with equal legs, this can be accomplished using array theory and pattern multiplication. When this is done, a number of design equations can be derived [8]–[11]. For this design, the plane formed by the rhombus is placed parallel and a height h above a perfect electric conductor.

B. Design Equations

Let us assume that it is desired to design a rhombus such that the maximum of the main lobe of the pattern, in a plane which bisects the V of the rhombus, is directed at an angle ψ_0 above the ground plane. The design can be optimized if the height h is selected according to

$$\frac{h_m}{\lambda_0} = \frac{m}{4\cos(90^\circ - \psi_0)}, \qquad m = 1, 3, 5, \ldots \tag{10-21}$$

with $m = 1$ representing the minimum height.

INTEL-1045
U.S. Patent 7,151,430

The minimum optimum length of each leg of a symmetrical rhombus must be selected according to

$$\frac{l}{\lambda_0} = \frac{0.371}{1 - \sin(90^\circ - \psi_0)\cos\theta_0} \tag{10-22}$$

The best choice for the included angle of the rhombus is selected to satisfy

$$\theta_0 = \cos^{-1}[\sin(90^\circ - \psi_0)] \tag{10-23}$$

10.3 BROADBAND ANTENNAS

In Chapter 9 broadband dipole antennas were discussed. There are numerous other antenna designs that exhibit greater broadband characteristics than those of the dipoles. Some of these antenna can also provide circular polarization, a desired extra feature for many applications. In this section we want to discuss briefly some of the most popular broadband antennas.

10.3.1 Helical Antenna

Another basic, simple, and practical configuration of an electromagnetic radiator is that of a conducting wire wound in the form of a screw thread forming a helix, as shown in Figure 10.13. In most cases the helix is used with a ground plane. The ground plane can take different forms. One is for the ground to be flat, as shown in Figure 10.13. Typically the diameter of the ground plane should be at least $3\lambda/4$. However, the ground plane can also be cupped in the form of a cylindrical cavity or in the form of a frustrum cavity [8]. In addition, the helix is usually connected to the center conductor of a coaxial transmission line at the feed point with the outer conductor of the line attached to the ground plane.

The geometrical configuration of a helix consists usually of N turns, diameter D and spacing S between each turn. The total length of the antenna is $L = NS$ while the total length of the wire is $L_n = NL_0 = N\sqrt{S^2 + C^2}$ where $L_0 = \sqrt{S^2 + C^2}$ is the length of the wire between each turn and $C = \pi D$ is the circumference of the helix. Another important parameter is the pitch angle α which is the angle formed by a line tangent to the helix wire and a plane perpendicular to the helix axis. The pitch angle is defined by

$$\boxed{\alpha = \tan^{-1}\left(\frac{S}{\pi D}\right) = \tan^{-1}\left(\frac{S}{C}\right)} \tag{10-24}$$

When $\alpha = 0^\circ$, then the winding is flattened and the helix reduces to a loop antenna of N turns. On the other hand, when $\alpha = 90^\circ$ then the helix reduces to a linear wire. When $0^\circ < \alpha < 90^\circ$, then a true helix is formed with a circumference greater than zero but less than the circumference when the helix is reduced to a loop ($\alpha = 0^\circ$).

The radiation characteristics of the antenna can be varied by controlling the size of its geometrical properties compared to the wavelength. The input impedance is critically dependent upon the pitch angle and the size of the conducting wire, especially near the feed point, and it can be adjusted by controlling their values. The general polarization of the antenna is elliptical. However circular and linear polarizations can be achieved over different frequency ranges.

INTEL-1045
U.S. Patent 7,151,430

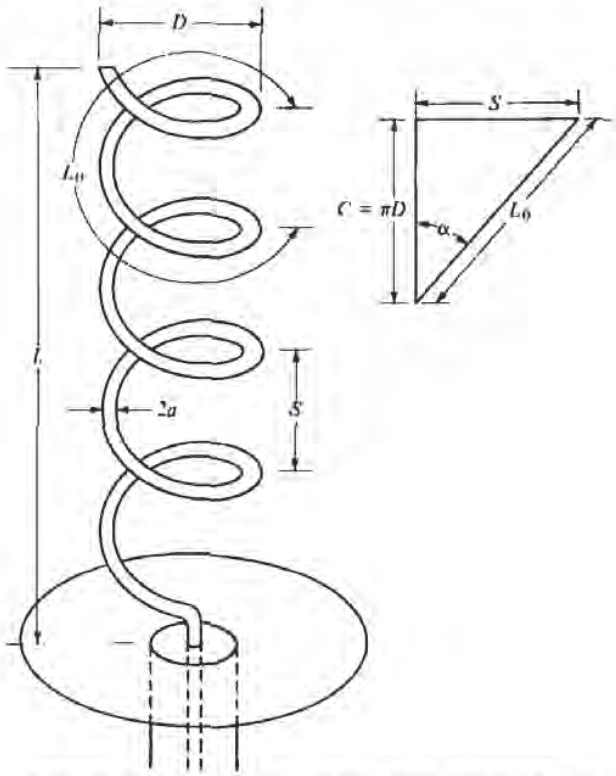


Figure 10.13 Helical antenna with ground plane.

The helical antenna can operate in many modes; however the two principal ones are the normal (broadside) and the axial (endfire) modes. The axial (endfire) mode is usually the most practical because it can achieve circular polarization over a wider bandwidth (usually 2:1) and it is more efficient.

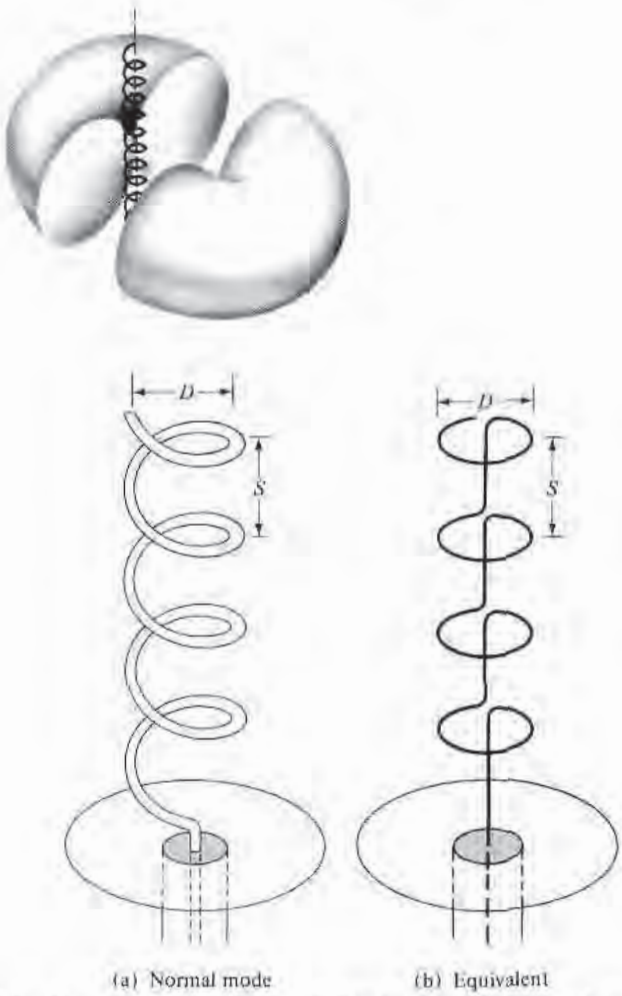
Because an elliptically polarized antenna can be represented as the sum of two orthogonal linear components in time-phase quadrature, a helix can always receive a signal transmitted from a rotating linearly polarized antenna. Therefore helices are usually positioned on the ground for space telemetry applications of satellites, space probes, and ballistic missiles to transmit or receive signals that have undergone Faraday rotation by traveling through the ionosphere.

A. Normal Mode

In the normal mode of operation the field radiated by the antenna is maximum in a plane normal to the helix axis and minimum along its axis, as shown sketched in Figure 10.14(a), which is a figure-eight rotated about its axis similar to that of a linear dipole of $l < \lambda$ or a small loop ($a \ll \lambda$). To achieve the normal mode of operation, the dimensions of the helix are usually small compared to the wavelength (i.e., $NL_0 \ll \lambda$).

The geometry of the helix reduces to a loop of diameter D when the pitch angle approaches zero and to a linear wire of length S when it approaches 90°. Since the limiting geometries of the helix are a loop and a dipole, the far-field radiated by a small helix in the normal mode can be described in terms of E_θ and E_ϕ components of the dipole and loop, respectively. In the normal mode, it can be thought that the helix consists of N small loops and N short dipoles connected together in series as

INTEL-1045
U.S. Patent 7,151,430



(a) Normal mode (b) Equivalent

Figure 10.14 Normal (broadside) mode for helical antenna and its equivalent.

shown in Figure 10.14(b). The fields are obtained by superposition of the fields from these elemental radiators. The planes of the loops are parallel to each other and perpendicular to the axes of the vertical dipoles. The axes of the loops and dipoles coincide with the axis of the helix.

Since in the normal mode the helix dimensions are small, the current throughout its length can be assumed to be constant and its relative far-field pattern to be independent of the number of loops and short dipoles. Thus its operation can be described accurately by the sum of the fields radiated by a small loop of radius D and a short dipole of length S, with its axis perpendicular to the plane of the loop, and each with the same constant current distribution.

The far-zone electric field radiated by a short dipole of length S and constant current I_0 is E_θ, and it is given by (4-26a) as

$$E_\theta = j\eta \frac{kI_0 S e^{-jkr}}{4\pi r} \sin\theta \tag{10-25}$$

where l is being replaced by S. In addition the electric field radiated by a loop is E_ϕ, and it is given by (5-27b) as

INTEL-1045
U.S. Patent 7,151,430

$$E_\phi = \eta \frac{k^2(D/2)^2 I_0 e^{-jkr}}{4r} \sin\theta \tag{10-26}$$

where $D/2$ is substituted for a. A comparison of (10-25) and (10-26) indicates that *the two components are in time-phase quadrature, a necessary but not sufficient* condition for circular or elliptical polarization.

The ratio of the magnitudes of the E_θ and E_ϕ components is defined as the axial ratio (AR), and it is given by

$$\boxed{\text{AR} = \frac{|E_\theta|}{|E_\phi|} = \frac{4S}{\pi k D^2} = \frac{2\lambda S}{(\pi D)^2}} \tag{10-27}$$

By varying the D and/or S the axial ratio attains values of $0 \le \text{AR} \le \infty$. The value of AR = 0 is a special case and occurs when $E_\theta = 0$ leading to a linearly polarized wave of horizontal polarization (the helix is a loop). When AR = ∞, $E_\phi = 0$ and the radiated wave is linearly polarized with vertical polarization (the helix is a vertical dipole). Another special case is the one when AR is unity (AR = 1) and occurs when

$$\frac{2\lambda S}{(\pi D)^2} = 1 \tag{10-28}$$

or

$$\boxed{C = \pi D = \sqrt{2S\lambda}} \tag{10-28a}$$

for which

$$\boxed{\tan\alpha = \frac{S}{\pi D} = \frac{\pi D}{2\lambda}} \tag{10-29}$$

When the dimensional parameters of the helix satisfy the above relation, the radiated field is circularly polarized in *all directions* other than $\theta = 0°$ where the fields vanish.

When the dimensions of the helix do not satisfy any of the above special cases, the field radiated by the antenna is not circularly polarized. The progression of polarization change can be described geometrically by beginning with the pitch angle of zero degrees ($\alpha = 0°$), which reduces the helix to a loop with linear horizontal polarization. As α increases, the polarization becomes ellipitical with the major axis being horizontally polarized. When α, is such that $C/\lambda = \sqrt{2S/\lambda}$, AR = 1 and we have circular polarization. For greater values of α, the polarization again becomes elliptical but with the major axis vertically polarized. Finally when $\alpha = 90°$ the helix reduces to a linearly polarized vertical dipole.

To achieve the normal mode of operation, it has been assumed that the current throughout the length of the helix is of constant magnitude and phase. This is satisfied to a large extent provided the total length of the helix wire NL_0 is very small compared to the wavelength ($L_n \ll \lambda$) and its end is terminated properly to reduce multiple reflections. Because of the critical dependence of its radiation characteristics on its geometrical dimensions, which must be very small compared to the wavelength, this mode of operation is very narrow in bandwidth and its radiation efficiency is very small. Practically this mode of operation is limited, and it is seldom utilized.

INTEL-1045
U.S. Patent 7,151,430

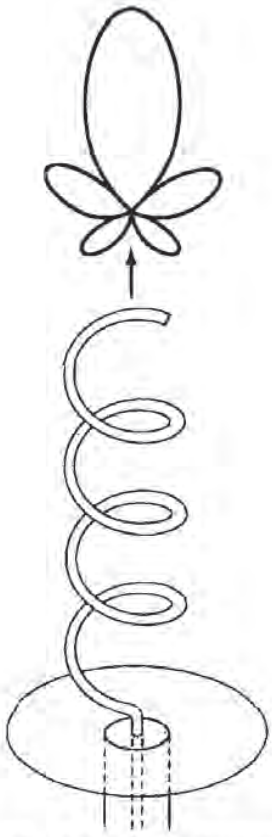


Figure 10.15 Axial (endfire) mode of helix.

B. Axial Mode

A more practical mode of operation, which can be generated with great ease, is the axial or endfire mode. In this mode of operation, there is only one major lobe and its maximum radiation intensity is along the axis of the helix, as shown in Figure 10.15. The minor lobes are at oblique angles to the axis.

To excite this mode, the diameter D and spacing S must be large fractions of the wavelength. To achieve circular polarization, primarily in the major lobe, the circumference of the helix must be in the $\frac{3}{4} < C/\lambda < \frac{4}{3}$ range (with $C/\lambda = 1$ near optimum), and the spacing about $S \simeq \lambda/4$. The pitch angle is usually $12° \leq \alpha \leq 14°$. Most often the antenna is used in conjunction with a ground plane, whose diameter is at least $\lambda/2$, and it is fed by a coaxial line. However other types of feeds (such as waveguides and dielectric rods) are possible, especially at microwave frequencies. The dimensions of the helix for this mode of operation are not as critical, thus resulting in a greater bandwidth.

C. Design Procedure

The terminal impedance of a helix radiating in the axial mode is nearly resistive with values between 100 and 200 ohms. Smaller values, even near 50 ohms, can be obtained by properly designing the feed. Empirical expressions, based on a large number of measurements, have been derived [8] and they are used to determine a number of parameters. The input impedance (purely resistive) is obtained by

INTEL-1045
U.S. Patent 7,151,430

$$R \simeq 140\left(\frac{C}{\lambda}\right) \tag{10-30}$$

which is accurate to about ±20%, the half-power beamwidth by

$$\text{HPBW (degrees)} \simeq \frac{52\lambda^{3/2}}{C\sqrt{NS}} \tag{10-31}$$

the beamwidth between nulls by

$$\text{FNBW (degrees)} \simeq \frac{115\lambda^{3/2}}{C\sqrt{NS}} \tag{10-32}$$

the directivity by

$$D_0 \text{ (dimensionless)} \simeq 15N\frac{C^2S}{\lambda^3} \tag{10-33}$$

the axial ratio (for the condition of increased directivity) by

$$\text{AR} = \frac{2N + 1}{2N} \tag{10-34}$$

and the normalized far-field pattern by

$$E = \sin\left(\frac{\pi}{2N}\right)\cos\theta\frac{\sin[(N/2)\psi]}{\sin[\psi/2]} \tag{10-35}$$

where

$$\psi = k_0\left(S\cos\theta - \frac{L_0}{p}\right) \tag{10-35a}$$

$$p = \frac{L_0/\lambda_0}{S/\lambda_0 + 1} \qquad \text{For ordinary end-fire radiation} \tag{10-35b}$$

$$p = \frac{L_0/\lambda_0}{S/\lambda_0 + \left(\frac{2N + 1}{2N}\right)} \qquad \text{For Hansen-Woodyard end-fire radiation} \tag{10-35c}$$

All these relations are approximately valid provided $12° < \alpha < 14°$, $\frac{3}{4} < C/\lambda < \frac{4}{3}$, and $N > 3$.

The far-field pattern of the helix, as given by (10-35), has been developed by assuming that the helix consists of an array of N identical turns (each of nonuniform current and identical to that of the others), a uniform spacing S between them, and the elements are placed along the z-axis. The $\cos\theta$ term in (10-35) represents the field pattern of a single turn, and the last term in (10-35) is the array factor of a uniform array of N elements. The total field is obtained by multiplying the field from one turn with the array factor (pattern multiplication).

INTEL-1045
U.S. Patent 7,151,430

The value of p in (10-35a) is the ratio of the wave velocity along the helix wire to that in free space, and it is selected according to (10-35b) for ordinary end-fire radiation or (10-35c) for Hansen-Woodyard end-fire radiation. These are derived as follows.

For ordinary end-fire the relative phase ψ among the various turns of the helix (elements of the array) is given by (6-7a), or

$$\psi = k_0 S \cos\theta + \beta \tag{10-36}$$

where $d = S$ is the spacing between the turns of the helix. For an end-fire design, the radiation from each one of the turns along $\theta = 0°$ must be in-phase. Since the wave along the helix wire between turns travels a distance L_0 with a wave velocity $v = pv_0$ ($p > 1$ where v_0 is the wave velocity in free space) and the desired maximum radiation is along $\theta = 0°$, then (10-36) for *ordinary end-fire* radiation is equal to

$$\psi = (k_0 S \cos\theta - kL_0)_{\theta=0°} = k_0\left(S - \frac{L_0}{p}\right) = -2\pi m, \quad m = 0, 1, 2, \ldots \tag{10-37}$$

Solving (10-37) for p leads to

$$p = \frac{L_0/\lambda_0}{S/\lambda_0 + m} \tag{10-38}$$

For $m = 0$ and $p = 1$, $L_0 = S$. This corresponds to a straight wire ($\alpha = 90°$), and not a helix. Therefore the next value is $m = 1$, and it corresponds to the first transmission mode for a helix. Substituting $m = 1$ in (10-38) leads to

$$p = \frac{L_0/\lambda_0}{S/\lambda_0 + 1} \tag{10-38a}$$

which is that of (10-35b).

In a similar manner, it can be shown that for Hansen-Woodyard end-fire radiation (10-37) is equal to

$$\psi = (k_0 S \cos\theta - kL_0)_{\theta=0°} = k_0\left(S - \frac{L_0}{p}\right) = -\left(2\pi m + \frac{\pi}{N}\right), \quad m = 0, 1, 2, \ldots \tag{10-39}$$

which when solved for p leads to

$$p = \frac{L_0/\lambda_0}{S/\lambda_0 + \left(\dfrac{2mN + 1}{2N}\right)} \tag{10-40}$$

For $m = 1$, (10-40) reduces to

$$p = \frac{L_0/\lambda_0}{S/\lambda_0 + \left(\dfrac{2N + 1}{2N}\right)} \tag{10-40a}$$

which is identical to (10-35c).

D. Feed Design

The nominal impedance of a helical antenna operating in the axial mode, computed using (10-30), is 100–200 ohms. However, many practical transmission lines (such

INTEL-1045
U.S. Patent 7,151,430

as a coax) have characteristic impedance of about 50 ohms. In order to provide a better match, the input impedance of the helix must be reduced to near that value. There may be a number of ways by which this can be accomplished. One way to effectively control the input impedance of the helix is to properly design the first 1/4 turn of the helix which is next to the feed [8], [12]. To bring the input impedance of the helix from nearly 150 ohms down to 50 ohms, the wire of the first 1/4 turn should be flat in the form of a strip and the transition into a helix should be very gradual. This is accomplished by making the wire from the feed, at the beginning of the formation of the helix, in the form of a strip of width w by flattening it and nearly touching the ground plane which is covered with a dielectric slab of height [2]

$$h = \frac{w}{\frac{377}{\sqrt{\epsilon_r}\, Z_0} - 2} \tag{10-41}$$

where

w = width of strip conductor of the helix starting at the feed

ϵ_r = dielectric constant of the dielectric slab covering the ground plane

Z_0 = characteristic impedance of the input transmission line

Typically the strip configuration of the helix transitions from the strip to the regular circular wire and the designed pitch angle of the helix very gradually within the first 1/4–1/2 turn.

This modification decreases the characteristic impedance of the conductor-ground plane effective transmission line, and it provides a lower impedance over a substantial but reduced bandwidth. For example, a 50-ohm helix has a VSWR of less than 2:1 over a 40% bandwidth compared to a 70% bandwidth for a 140-ohm helix. In addition, the 50-ohm helix has a VSWR of less than 1.2:1 over a 12% bandwidth as contrasted to a 20% bandwidth for one of 140 ohms.

A simple and effective way of increasing the thickness of the conductor near the feed point will be to bond a thin metal strip to the helix conductor [12]. For example, a metal strip 70-mm wide was used to provide a 50-ohm impedance in a helix whose conducting wire was 13-mm in diameter and it was operating at 230.77 MHz.

10.3.2 Electric-Magnetic Dipole

It has been shown in the previous section that the circular polarization of a helical antenna operating in the normal mode was achieved by assuming that the geometry of the helix is represented by a number of horizontal small loops and vertical infinitesimal dipoles. It would then seem reasonable that an antenna with only one loop and a single vertical dipole would, in theory, represent a radiator with an elliptical polarization. Ideally circular polarization, in all space, can be achieved if the current in each element can be controlled, by dividing the available power equally between the dipole and the loop, so that the magnitude of the field intensity radiated by each is equal.

Experimental models of such an antenna were designed and built [13] one operating around 350 MHz and the other near 1.2 GHz. A sketch of one of them is shown in Figure 10.16. The measured VSWR in the 1.15–1.32 GHz frequency range was less than 2:1.

This type of an antenna is very useful in UHF communication networks where considerable amount of fading may exist. In such cases the fading of the horizontal

INTEL-1045
U.S. Patent 7,151,430

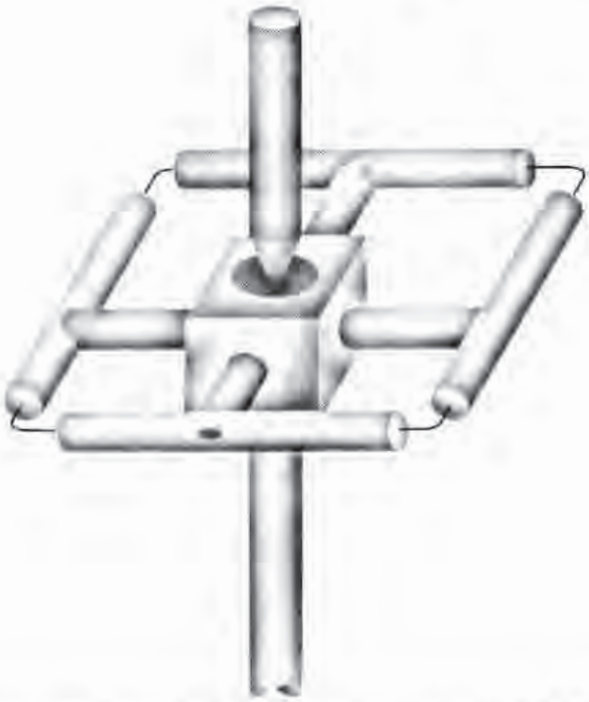


Figure 10.16 Electric-magnetic dipole configuration. (SOURCE: A. G. Kandoian, "Three New Antenna Types and Their Applications," *Proc. IRE*, Vol. 34, pp. 70W–75W, February 1946. © (1946) IEEE)

and vertical components are affected differently and will not vary in the same manner. Hopefully, even in severe cases, there will always be one component all the time which is being affected less than the other, thus providing continuous communication. The same results would apply in VHF and/or UHF broadcasting. In addition, a transmitting antenna of this type would also provide the versatility to receive with horizontally or vertically polarized elements, providing a convenience in the architectural design of the receiving station.

10.3.3 Yagi-Uda Array of Linear Elements

Another very practical radiator in the HF (3–30 MHz), VHF (30–300 MHz), and UHF (300–3,000 MHz) ranges is the Yagi-Uda antenna. This antenna consists of a number of linear dipole elements, as shown in Figure 10.17, one of which is energized directly by a feed transmission line while the others act as parasitic radiators whose currents are induced by mutual coupling. The most common feed element for a Yagi-Uda antenna is a folded dipole. This radiator is exclusively designed to operate as an endfire array, and this is accomplished by having the parasitic elements in the forward beam act as directors while those in the rear act as reflectors. Yagi designated the row of directors as a "wave canal." The Yagi-Uda array is widely used as a home TV antenna; so it should be familiar to most of the readers, if not to the general public.

The original design and operating principles of this radiator were first described in Japanese in articles published in the Journal of I.E.E. of Japan by S. Uda of the Tohoku Imperial University in Japan [14]. In a later, but more widely circulated and read article [15], one of Professor Uda's colleagues H. Yagi described the operation of the same radiator in English. This paper has been considered a classic, and it was

INTEL-1045
U.S. Patent 7,151,430

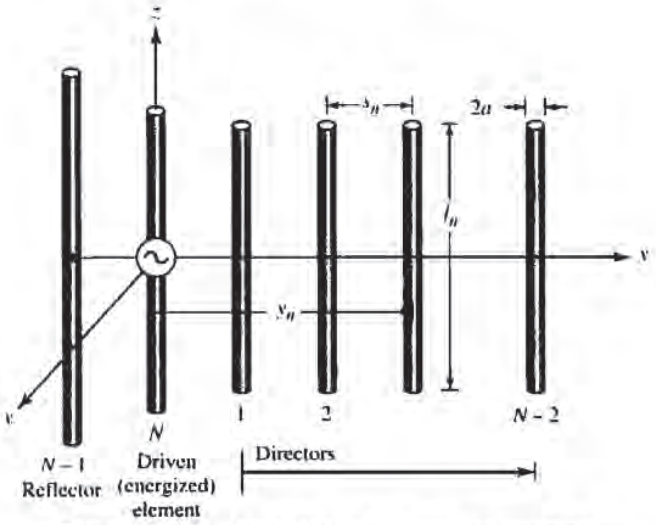


Figure 10.17 Yagi-Uda antenna configuration.

reprinted in 1984 in its original form in the *Proceedings of the IEEE* [15] as part of IEEE's centennial celebration. Despite the fact that Yagi in his English written paper acknowledged the work of Professor Uda on beam radiators at a wavelength of 4.4 m, it became customary throughout the world to refer to this radiator as a *Yagi* antenna, a generic term in the antenna dictionary. However, in order for the name to reflect more appropriately the contributions of both inventors, it should be called a *Yagi-Uda* antenna, a name that will be adopted in this book. Although the work of Uda and Yagi was done in the early 1920s and published in the middle 1920s, full acclaim in the United States was not received until 1928 when Yagi visited the United States and presented papers at meetings of the Institute of Radio Engineers (IRE) in New York, Washington, and Hartford. In addition, his work was published in the *Proceedings of IRE*, June 1928, where J. H. Dellinger, Chief of Radio Division, Bureau of Standards, Washington, D.C., and himself a pioneer of radio waves, characterized as "exceptionally fundamental" and wrote "I have never listened to a paper that I felt so sure was destined to be a classic." So true!!

The Yagi-Uda antenna has received exhaustive analytical and experimental investigations in the open literature and elsewhere. It would be impractical to list all the contributors, many of whom we may not be aware. However, we will attempt to summarize the salient point of the analysis, describe the general operation of the radiator, and present some design data.

To achieve the endfire beam formation, the parasitic elements in the direction of the beam are somewhat smaller in length than the feed element. Typically the driven element is resonant with its length slightly less than $\lambda/2$ (usually 0.45–0.49λ) whereas the lengths of the directors will be about 0.4 to 0.45λ. However, the directors are not necessarily of the same length and/or diameter. The separation between the directors is typically 0.3 to 0.4λ, and it is not necessarily uniform for optimum designs. It has been shown experimentally that for a Yagi-Uda array of 6λ total length the overall gain was independent of director spacing up to about 0.3λ. A significant drop (5–7 dB) in gain was noted for director spacings greater than 0.3λ. For that antenna, the gain was also independent of the radii of the directors up to about 0.024λ. The length of

INTEL-1045
U.S. Patent 7,151,430

the reflector is somewhat greater than that of the feed. In addition, the separation between the driven element and the reflector is somewhat smaller than the spacing between the driven element and the nearest director, and it is found to be near optimum at 0.25λ.

Since the length of each director is smaller than its corresponding resonant length, the impedance of each is capacitive and its current leads the induced emf. Similarly the impedances of the reflectors is inductive and the phases of the currents lag those of the induced emfs. The total phase of the currents in the directors and reflectors is not determined solely by their lengths but also by their spacing to the adjacent elements. Thus, properly spaced elements with lengths slightly less than their corresponding resonant lengths (less than $\lambda/2$) act as directors because they form an array with currents approximately equal in magnitude and with equal progressive phase shifts which will reinforce the field of the energized element toward the directors. Similarly, a properly spaced element with a length of $\lambda/2$ or slightly greater will act as a reflector. Thus a Yagi-Uda array may be regarded as a structure supporting a traveling wave whose performance is determined by the current distribution in each element and the phase velocity of the traveling wave. It should be noted that the previous discussion on the lengths of the directors, reflectors, and driven elements is based on the first resonance. Higher resonances are available near lengths of λ, $3\lambda/2$, and so forth, but are seldom used.

In practice, the major role of the reflector is played by the first element next to the one energized, and very little in the performance of a Yagi-Uda antenna is gained if more than one (at the most two) elements are used as reflectors. However, considerable improvements can be achieved if more directors are added to the array. Practically there is a limit beyond which very little is gained by the addition of more directors because of the progressive reduction in magnitude of the induced currents on the more extreme elements. Usually most antennas have about 6 to 12 directors. However, many arrays have been designed and built with 30 to 40 elements. Array lengths on the order of 6λ have been mentioned [16] as typical. A gain (relative to isotropic) of about 5 to 9 per wavelength is typical for such arrays, which would make the overall gain on the order of about 30 to 54 (14.8–17.3 dB) typical.

The radiation characteristics that are usually of interest in a Yagi-Uda antenna are the *forward and backward gains, input impedance, bandwidth, front-to-back ratio,* and *magnitude of minor lobes.* The lengths and diameters of the directors and reflectors, as well as their respective spacings, determine the optimum characteritics. For a number of years optimum designs were accomplished experimentally. However, with the advent of high-speed computers many different numerical techniques, based on analytical formulations, have been utilized to derive the geometrical dimensions of the array for optimum operational performance. Usually Yagi-Uda arrays have low input impedance and relatively narrow bandwidth (on the order of about 2%). Improvements in both can be achieved at the expense of others (such as gain, magnitude of minor lobes, etc.). Usually a compromise is made, and it depends on the particular design. One way to increase the input impedance without affecting the performance of other parameters is to use an impedance step-up element as a feed (such as a two-element folded dipole with a step-up ratio of about 4). Front-to-back ratios of about 30 ($\simeq$15 dB) can be achieved at wider than optimum element spacings, but they usually are compromised somewhat to improve other desirable characteristics. For optimum designs, the minor lobes are about 30% or less (-5.23 dB or smaller) of the maximum.

INTEL-1045
U.S. Patent 7,151,430

The Yagi-Uda array can be summarized by saying that its performance can be considered in three parts:

1. the reflector-feeder arrangement
2. the feeder
3. the rows of directors

It has been concluded, numerically and experimentally, that the reflector spacing and size have (1) negligible effects on the forward gain and (2) large effects on the backward gain (front-to-back ratio) and input impedance, and they can be used to control or optimize antenna parameters without affecting the gain significantly. The feeder length and radius has a small effect on the forward gain but a large effect on the backward gain and input impedance. Its geometry is usually chosen to control the input impedance that most commonly is made real (resonant element). The size and spacing of the directors have a large effect on the forward gain, backward gain, and input impedance, and they are considered to be the most critical elements of the array.

Yagi-Uda arrays are quite common in practice because they are lightweight, simple to build, low cost, and provide moderately desirable characteristics (including a unidirectional beam) for many applications. The design for a small number of elements (typically five or six) is simple but the design becomes quite critical if a large number of elements are used to achieve a high directivity. To increase the directivity of a Yagi-Uda array or to reduce the beamwidth in the *E*-plane, several rows of Yagi-Uda arrays can be used [17] to form a curtain antenna. To neutralize the effects of the feed transmission line, an odd number of rows is usually used.

A. Theory: Integral Equation-Moment Method

There have been many experimental [18], [19] investigations and analytical [20]–[29] formulations of the Yagi-Uda array. A method [24] based on rigorous integral equations for the electric field radiated by the elements in the array will be presented and it will be used to describe the complex current distributions on all the elements, the phase velocity, and the corresponding radiation patterns. The method is similar to that of [24], which is based on Pocklington's integral equation of (8-24) while the one presented here follows that of [24] but is based on Pocklington's integral equation of (8-22) and formulated by Tirkas [25]. Mutual interactions are also included and, in principle, there are no restrictions on the number of elements. However, for computational purposes, point-matching numerical methods, based on the techniques of Section 8.4, are used to evaluate and satisfy the integral equation at discrete points on the axis of each element rather than everywhere on the surface of every element. The number of discrete points where boundary conditions are matched must be sufficient in number to allow the computed data to compare well with experimental results.

The theory is based on Pocklington's integral equation of (8-22) for the total field generated by an electric current source radiating in an unbounded free space, or

$$\int_{-l/2}^{l/2} I(z')\left(\frac{\partial^2}{\partial z^2} + k^2\right)\frac{e^{-jkR}}{R}\,dz' = j4\pi\omega\epsilon_0 E_z^i \tag{10-42}$$

where

$$R = \sqrt{(x - x')^2 + (y - y')^2 + (z - z')^2} \tag{10-42a}$$

INTEL-1045
U.S. Patent 7,151,430

Since

$$\frac{\partial^2}{\partial z^2}\left(\frac{e^{-jkR}}{R}\right) = \frac{\partial^2}{\partial z'^2}\left(\frac{e^{-jkR}}{R}\right) \tag{10-43}$$

(10-42) reduces to

$$\int_{-l/2}^{+l/2} I(z')\frac{\partial^2}{\partial z'^2}\left(\frac{e^{-jkR}}{R}\right)dz' + k^2\int_{-l/2}^{+l/2} I(z')\frac{e^{-jkR}}{R}\,dz' = j4\pi\omega\epsilon_0 E_z^i \tag{10-44}$$

We will now concentrate in the integration of the first term of (10-44). Integrating the first term of (10-44) by parts where

$$u = I(z') \tag{10-45}$$

$$du = \frac{dI(z')}{dz'}\,dz' \tag{10-45a}$$

$$dv = \frac{\partial^2}{\partial z'^2}\left(\frac{e^{-jkR}}{R}\right)dz' = \frac{\partial}{\partial z'}\left[\frac{\partial}{\partial z'}\left(\frac{e^{-jkR}}{R}\right)\right]dz' \tag{10-46}$$

$$v = \frac{\partial}{\partial z'}\left(\frac{e^{-jkR}}{R}\right) \tag{10-46a}$$

reduces it to

$$\int_{-l/2}^{+l/2} I(z')\frac{\partial^2}{\partial z'^2}\left(\frac{e^{-jkR}}{R}\right)dz' = I(z')\left[\frac{\partial}{\partial z'}\left(\frac{e^{-jkR}}{R}\right)\right]\Bigg|_{-l/2}^{+l/2} - \int_{-l/2}^{+l/2}\frac{\partial}{\partial z'}\left(\frac{e^{-jkR}}{R}\right)\frac{dI(z')}{dz'}\,dz' \tag{10-47}$$

Since we require that the current at the ends of each wire vanish [i.e., $I_z(z' = +l/2) = I_z(z' = -l/2) = 0$], (10-47) reduces to

$$\int_{-l/2}^{+l/2} I(z')\frac{\partial^2}{\partial z'^2}\left(\frac{e^{-jkR}}{R}\right)dz' = -\int_{-l/2}^{+l/2}\frac{\partial}{\partial z'}\left(\frac{e^{-jkR}}{R}\right)dz'\frac{dI(z')}{dz'} \tag{10-48}$$

Integrating (10-48) by parts where

$$u = \frac{dI(z')}{dz'} \tag{10-49}$$

$$du = \frac{d^2I(z')}{dz'^2}\,dz' \tag{10-49a}$$

$$dv = \frac{\partial}{\partial z'}\left(\frac{e^{-jkR}}{R}\right)dz' \tag{10-50}$$

$$v = \frac{e^{-jkR}}{R} \tag{10-50a}$$

INTEL-1045
U.S. Patent 7,151,430

reduces (10-48) to

$$\int_{-l/2}^{+l/2} I(z')\frac{\partial^2}{\partial z'^2}\left(\frac{e^{-jkR}}{R}\right)dz' = -\frac{dI(z')}{dz'}\frac{e^{-jkR}}{R}\bigg|_{-l/2}^{+l/2} + \int_{-l/2}^{+l/2}\frac{d^2I(z')}{dz'^2}\frac{e^{-jkR}}{R}dz' \tag{10-51}$$

When (10-51) is substituted for the first term of (10-44) reduces (10-44) to

$$-\frac{dI(z')}{dz'}\frac{e^{-jkR}}{R}\bigg|_{l/2}^{-l/2} + \int_{-l/2}^{+l/2}\left[k^2I(z') + \frac{d^2I(z')}{dz'^2}\right]\frac{e^{-jkR}}{R}dz' = j4\pi\omega\epsilon_0 E_z^i \tag{10-52}$$

For small diameter wires the current on each element can be approximated by a finite series of odd-ordered even modes. Thus, the current on the nth element can be written as a Fourier series expansion of the form [26]

$$I_n(z') = \sum_{m=1}^{M} I_{nm}\cos\left[(2m-1)\frac{\pi z'}{l_n}\right] \tag{10-53}$$

where I_{nm} represents the complex current coefficient of mode m on element n and l_n represents the corresponding length of the n element. Taking the first and second derivatives of (10-53) and substituting them, along with (10-53), into (10-52) reduces it to

$$\sum_{m=1}^{M} I_{nm}\left\{\frac{(2m-1)\pi}{l_n}\sin\left[(2m-1)\frac{\pi z_n'}{l_n}\right]\frac{e^{-jkR}}{R}\bigg|_{-l_n/2}^{+l_n/2} + \left[k^2 - \frac{(2m-1)^2\pi^2}{l_n^2}\right] \times \int_{-l_n/2}^{+l_n/2}\cos\left[(2m-1)\frac{\pi z_n'}{l_n}\right]\frac{e^{-jkR}}{R}dz_n'\right\} = j4\pi\omega\epsilon_0 E_z^i \tag{10-54}$$

Since the cosine is an even function, (10-54) can be reduced by integrating over only $0 \le z' \le l/2$ to

$$\sum_{m=1}^{M} I_{nm}\left\{(-1)^{m+1}\frac{(2m-1)\pi}{l_n}G_2\left(x, x', y, y'/z, \frac{l_n}{2}\right) + \left[k^2 - \frac{(2m-1)^2\pi^2}{l_n^2}\right] \times \int_0^{l_n/2} G_2(x, x', y, y'/z, z_n')\cos\left[\frac{(2m-1)\pi z_n'}{l_n}\right]dz_n'\right\} = j4\pi\omega\epsilon_0 E_z^i \tag{10-55}$$

where

$$G_2(x, x', y, y'/z, z_n') = \frac{e^{-jkR_-}}{R_-} + \frac{e^{-jkR_+}}{R_+} \tag{10-55a}$$

$$R_\pm = \sqrt{(x - x')^2 + (y - y')^2 + a^2 + (z \pm z')^2} \tag{10-55b}$$

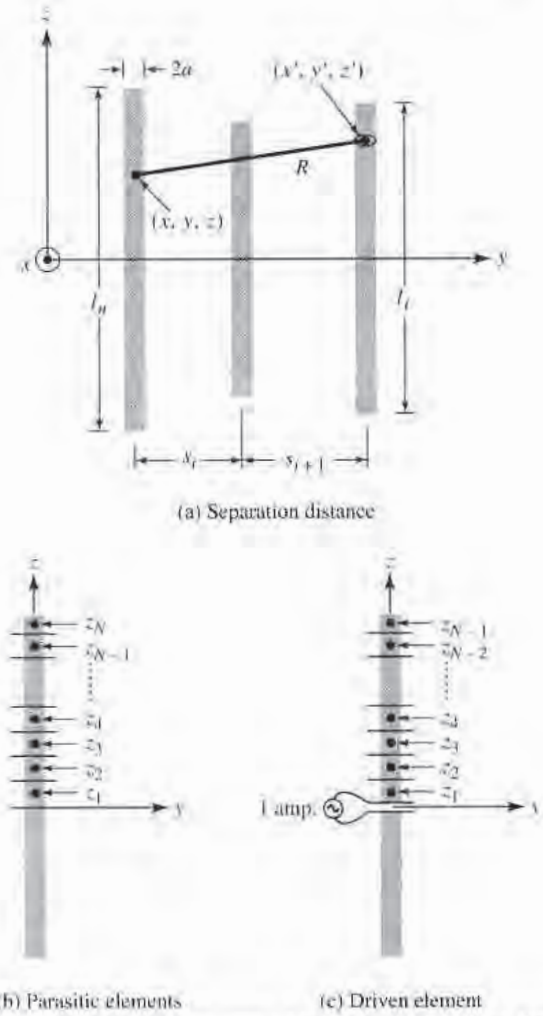
$n = 1, 2, 3, \ldots, N$
N = total number of elements

where

$R_\pm$ is the distance from the center of each wire radius to the center of any other wire, as shown in Figure 10.18(a).

The integral equation of (10-55) is valid for each element, and it assumes that the

INTEL-1045
U.S. Patent 7,151,430



(a) Separation distance

(b) Parasitic elements (c) Driven element

Figure 10.18 Geometry of Yagi–Uda array for Moment Method formulation (SOURCE: G. A. Thiele, "Yagi-Uda Type Antennas," *IEEE Trans. Antennas Propagat.*, Vol. AP-17, No. 1, pp. 24–31, January 1969. © (1969) IEEE)

number M of current modes is the same for each element. To apply the Moment Method solution to the integral equation of (10-55), each wire element is subdivided in M segments. On each element, other than the driven element, the matching is done at the center of the wire, and it is required that E_z^t of (10-55) vanishes at each matching point of each segment [i.e., $E_z^t(z = z_i) = 0$], as shown in Figure 10.18(b). On the driven element the matching is done on the surface of the wire, and it is required that E_z^t of (10-55) vanishes at $M - 1$ points, even though there are m modes, and it excludes the segment at the feed as shown in Figure 10.18(c). This generates $M - 1$ equations. The Mth equation on the feed element is generated by the constraint that the normalized current for all M modes at the feed point ($z' = 0$) of the driven element is equal to unity [24], [26], or

$$\sum_{m=1}^{M} I_{nm}(z' = 0)\Big|_{n=N} = 1 \tag{10-56}$$

INTEL-1045
U.S. Patent 7,151,430

Based on the above procedure, a system of linear equations is generated by taking into account the interaction of

a. each mode in each wire segment with each segment on the same wire.
b. each mode in each wire segment with each segment on the other wires.

This system of linear equations is then solved to find the complex amplitude coefficients of the current distribution in each wire as represented by (10-53). This is demonstrated in [24] for a three-element array (one director, one reflector and the driven element) with two modes in each wire.

B. Far-Field Pattern

Once the current distribution is found, the far-zone field generated by each element can be found using the techniques outlined in Chapter 3. The total field of the entire Yagi-Uda array is obtained by summing the contributions from each.

Using the procedure outlined in Chapter 3, the far-zone electric field generated by the M modes of the nth element oriented parallel to the z axis is given by

$$E_{\theta n} \simeq -j\omega A_{\theta n} \tag{10-57}$$

$$\begin{aligned} A_{\theta n} &\simeq -\frac{\mu e^{-jkr}}{4\pi r}\sin\theta \int_{-l_n/2}^{+l_n/2} I_n e^{jk(x_n \sin\theta\cos\phi + y_n \sin\theta\sin\phi + z_n' \cos\theta)}\, dz_n' \\ &\simeq -\frac{\mu e^{-jkr}}{4\pi r}\sin\theta \left[e^{jk(x_n \sin\theta\cos\phi + y_n \sin\theta\sin\phi)} \int_{-l_n/2}^{+l_n/2} I_n e^{jkz_n' \cos\theta}\, dz_n' \right] \end{aligned} \tag{10-57a}$$

where x_n, y_n represent the position of the nth element. The total field is then obtained by summing the contributions from each of the N elements, and it can be written as

$$E_\theta = \sum_{n=1}^{N} E_{\theta n} = -j\omega A_\theta \tag{10-58}$$

$$\begin{aligned} A_\theta = \sum_{n=1}^{N} A_{\theta n} = -\frac{\mu e^{-jkr}}{4\pi r}\sin\theta \sum_{n=1}^{N} \Bigg\{ & e^{jk(x_n \sin\theta\cos\phi + y_n \sin\theta\sin\phi)} \\ & \times \left[\int_{-l_n/2}^{+l_n/2} I_n e^{jkz_n' \cos\theta}\, dz_n' \right] \Bigg\} \end{aligned} \tag{10-58a}$$

For each wire, the current is represented by (10-53). Therefore the last integral in (10-58a) can be written as

$$\int_{-l_n/2}^{+l_n/2} I_n e^{jkz_n' \cos\theta}\, dz_n' = \sum_{m=1}^{M} I_{nm} \int_{-l_n/2}^{+l_n/2} \cos\left[\frac{(2m-1)\pi z_n'}{l_n}\right] e^{jkz_n' \cos\theta}\, dz_n' \tag{10-59}$$

Since the cosine is an even function, (10-59) can also be expressed as

$$\begin{aligned} \int_{-l_n/2}^{+l_n/2} I_n e^{jkz_n' \cos\theta}\, dz_n' = \sum_{m=1}^{M} I_{nm} \int_{0}^{+l_n/2} & 2\cos\left[\frac{(2m-1)\pi z_n'}{l_n}\right] \\ & \times \left[\frac{e^{jkz_n' \cos\theta} + e^{-jkz_n' \cos\theta}}{2}\right] dz_n' \end{aligned}$$

(Equation continues on top of page 521.)

INTEL-1045
U.S. Patent 7,151,430

$$= \sum_{m=1}^{M} I_{nm} \int_0^{+l_n/2} 2\cos\left[\frac{(2m-1)\pi z_n'}{l_n}\right] \times \cos(kz_n' \cos\theta)\, dz_n' \tag{10-60}$$

Using the trigonometric identity

$$2\cos(\alpha)\cos(\beta) = \cos(\alpha+\beta) + \cos(\alpha-\beta) \tag{10-61}$$

(10-60) can be rewritten as

$$\int_{-l_n/2}^{+l_n/2} I_n e^{jkz_n'\cos\theta}\, dz_n' = \sum_{m=1}^{M} I_{nm} \left\{ \int_0^{+l_n/2} \cos\left[\frac{(2m-1)\pi}{l_n} + k\cos\theta\right] z_n'\, dz_n' + \int_0^{+l_n/2} \cos\left[\frac{(2m-1)\pi}{l_n} - k\cos\theta\right] z_n'\, dz_n' \right. \tag{10-62}$$

Since

$$\int_0^{\alpha/2} \cos[(b \pm c)z]\, dz = \frac{\alpha}{2} \frac{\sin[(b \pm c)\frac{\alpha}{2}]}{(b \pm c)\frac{\alpha}{2}} \tag{10-63}$$

(10-62) can be reduced to

$$\int_{-l_n/2}^{+l_n/2} I_n e^{jkz_n'\cos\theta}\, dz_n' = \sum_{m=1}^{M} I_{nm} \left[\frac{\sin(Z^+)}{Z^+} + \frac{\sin(Z^-)}{Z^-}\right] \frac{l_n}{2} \tag{10-64}$$

$$Z^+ = \left[\frac{(2m-1)\pi}{l_n} + k\cos\theta\right] \frac{l_n}{2} \tag{10-64a}$$

$$Z^- = \left[\frac{(2m-1)\pi}{l_n} - k\cos\theta\right] \frac{l_n}{2} \tag{10-64b}$$

Thus, the total field represented by (10-58) and (10-58a) can be written as

$$E_\theta = \sum_{n=1}^{N} E_{\theta n} = -j\omega A \tag{10-65}$$

$$A_\theta = \sum_{n=1}^{N} A_{\theta n} = -\frac{\mu e^{-jkr}}{4\pi r} \sin\theta \sum_{n=1}^{N} \left\{ e^{jk(x_n \sin\theta\cos\phi + y_n \sin\theta\sin\phi)} \cdot \sum_{m=1}^{M} I_{nm} \left[\frac{\sin(Z^+)}{Z^+} + \frac{\sin(Z^-)}{Z^-}\right] \right\} \frac{l_n}{2} \tag{10-65a}$$

There have been other analyses [27], [28] based on the integral equation formulation that allows the conversion to algebraic equations. In order not to belabor further the analytical formulations, which in call cases are complicated because of the antenna structure, it is appropriate at this time to present some results and indicate design procedures.

C. Computer Program and Results

Based on the preceding formulation, a computer program has been developed [25] that computes the E- and H-plane patterns, their corresponding half-power beamwidths, and the directivity of the Yagi-Uda array. The program is included at the end of this chapter. The input parameters include the total number of elements (N), the

INTEL-1045
U.S. Patent 7,151,430

number of current modes in each element (M), the length of each element, and the spacing between the elements. The program assumes one reflector, one driven element, and $N - 2$ directors. For the development of the formulation and computer program, the numbering system ($n = 1, 2, \ldots, N$) for the elements begins with the first director ($n = 1$), second director ($n = 2$), etc. The reflector is represented by the next to the last element ($n = N - 1$), while the driven element is designated as the last element ($n = N$), as shown in Figure 10.17.

One Yagi-Uda array design is considered here, which is the same as one of the two included in [24]; the other one is assigned as an end of the chapter problem. The patterns, beamwidths, and directivities were computed based on the computer program developed here.

Example 10.1

Design a Yagi-Uda array of 15 elements (13 directors, one reflector and the exciter). Compute and plot the E- and H-plane patterns, normalized current at the center of each element, and directivity and front-to-back ratio as a function of reflector spacing and director spacing. Use the computer program at the end of the chapter. The dimensions of the array are as follows.

$$
\begin{aligned}
N = \text{total number of elements} &= 15 \\
\text{number of directors} &= 13 \\
\text{number of reflectors} &= 1 \\
\text{number of exciters} &= 1 \\
\text{total length of reflector} &= 0.5\lambda \\
\text{total length of feeder} &= 0.47\lambda \\
\text{total length of each director} &= 0.406\lambda \\
\text{spacing between reflector and feeder} &= 0.25\lambda \\
\text{spacing between adjacent directors} &= 0.34\lambda \\
a = \text{radius of wires} &= 0.003\lambda
\end{aligned}
$$

SOLUTION

Using the computer program at the end of the chapter, the computed E- and H-plane patterns of this design are shown in Figure 10.19. The corresponding beamwidths are: E-plane ($\Theta_e = 26.98°$), H-plane ($\Theta_h = 27.96°$) while the directivity is 14.64 dB. A plot of the current at the center of each element versus position of the element is shown in Figure 10.20; the current of the feed element at its center is unity, as required by (10-56). One important *figure-of-merit* in Yagi-Uda array is the *front-to-back* ratio of the pattern $[20 \log_{10} E(\theta = 90°, \phi = 90°)/E(\theta = 90°, \phi = 270°)]$ as a function of the spacing of the reflector with respect to the feeder. This, along with the directivity, is shown in Figure 10.21 for spacing from 0.1λ–0.5λ. For this design, the maximum front-to-back ratio occurs for a reflector spacing of about 0.23λ while the directivity is monotonically decreasing very gradually, from about 15.2 dB at a spacing of 0.1λ down to about 10.4 dB at a spacing of 0.5λ.

Another important parametric investigation is the variation of the front-to-back ratio and directivity as a function of director spacing. This is shown in Figure 10.22 for spacings from 0.1λ to 0.5λ. It is apparent that the directivity exhibits a slight increase from about 12 dB at a spacing of about 0.1λ to about 15.3 dB at a spacing of about 0.45λ. A steep drop in directivity occurs for spacings greater than about

INTEL-1045
U.S. Patent 7,151,430

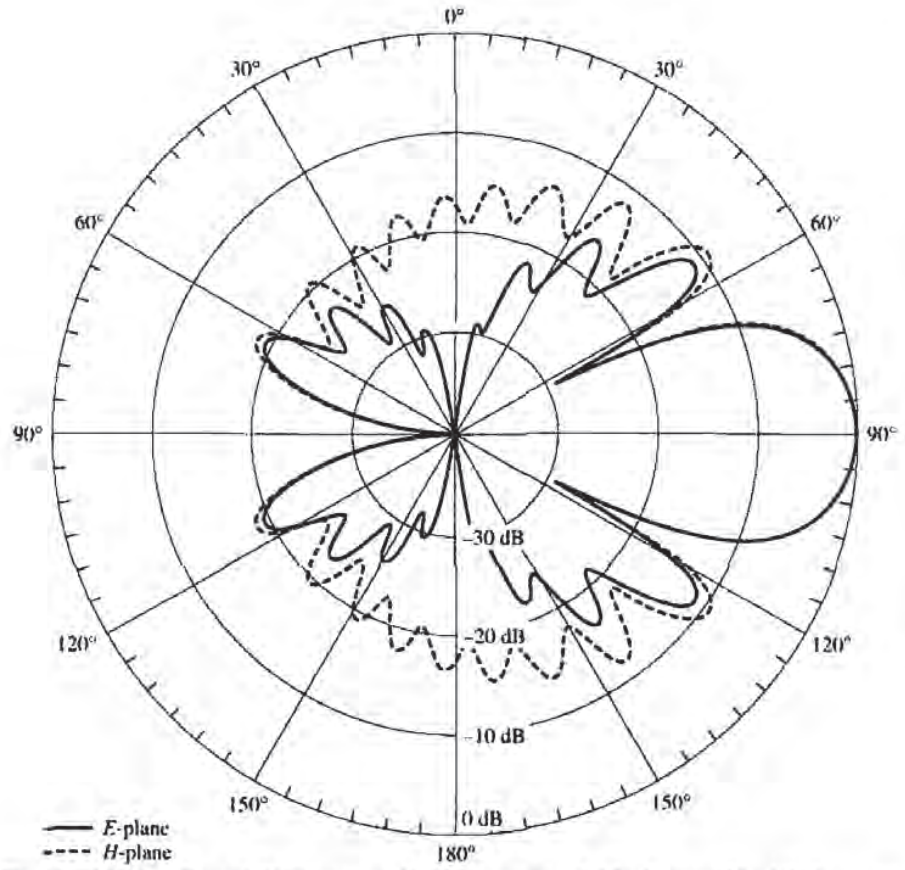


Figure 10.19 *E*- and *H*-plane amplitude patterns of 15-element Yagi-Uda array.

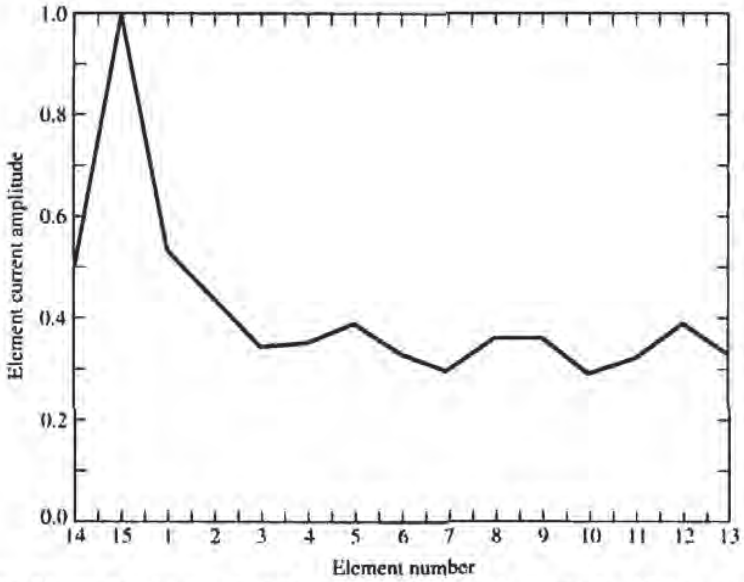


Figure 10.20 Normalized current at the center of each element of a 15-element Yagi-Uda array.

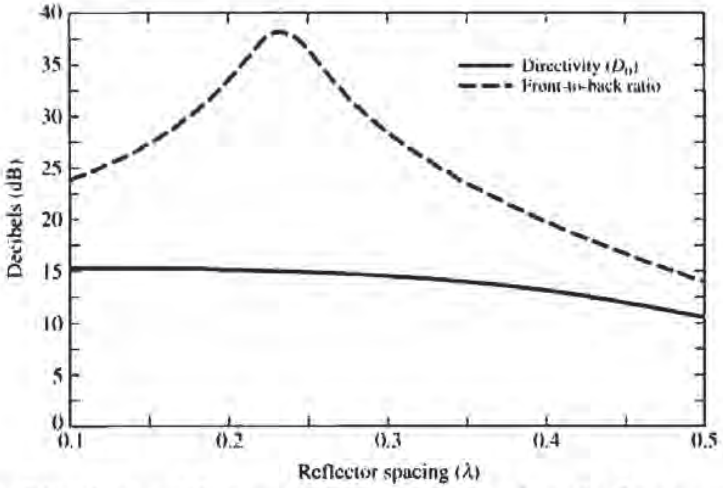


Figure 10.21 Directivity and front-to-back ratio, as a function of reflector spacing, of a 15-element Yagi-Uda array.

0.45λ. This agrees with the conclusion arrived at in [18] and [27] that large reductions in directivity occur in Yagi-Uda array designs for spacings greater than about 0.4λ. For this design, the variations of the front-to-back ratio are much more sensitive as a function of director spacing, as shown in Figure 10.22; excursions on the order of 20–25 dB are evident for changes in spacing of about 0.05λ. Such variations in front-to-back ratio as shown in Figure 10.22, as a function of director spacing, are not evident in Yagi-Uda array designs with a smaller number of elements. However, they are even more pronounced for designs with a larger number of elements. Both of these are demonstrated in design problems assigned at the end of the chapter.

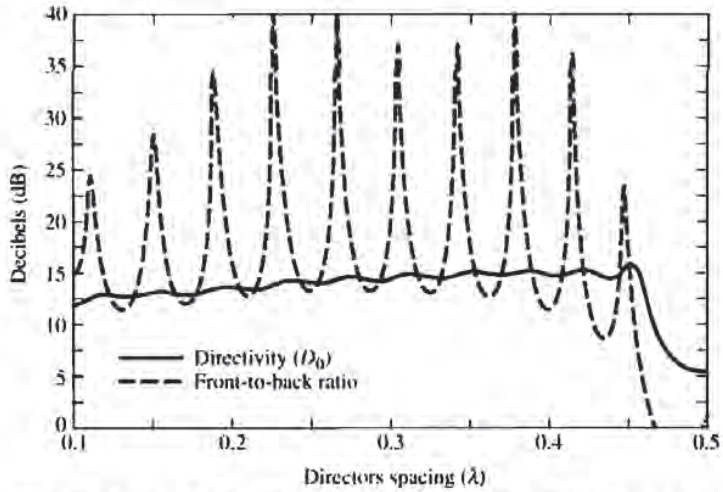


Figure 10.22 Directivity and front-to-back ratio, as a function of director spacing, for 15-element Yagi-Uda array.

INTEL-1045
U.S. Patent 7,151,430

Table 10.1 DIRECTIVITY OPTIMIZATION FOR SIX-ELEMENT YAGI-UDA ARRAY (PERTURBATION OF *DIRECTOR SPACINGS*). $l_1 = 0.51\lambda$, $l_2 = 0.50\lambda$, $l_3 = l_4 = l_5 = l_6 = 0.43\lambda$, $a = 0.003369\lambda$

	s_{21}/λ	s_{32}/λ	s_{43}/λ	s_{54}/λ	s_{65}/λ	Directivity (dB)
INITIAL ARRAY	0.250	0.310	0.310	0.310	0.310	11.21
OPTIMIZED ARRAY	0.250	0.336	0.398	0.310	0.407	12.87

SOURCE: D. K. Cheng and C. A. Chen, "Optimum Spacings for Yagi-Uda Arrays," *IEEE Trans. Antennas Propag.*, Vol. AP-21, pp. 615–623, September 1973. © (1973) IEEE.

D. Optimization

The radiation characteristics of the array can be adjusted by controlling the geometrical parameters of the array. This was demonstrated in Figures 10.21 and 10.22 for the 15-element array using uniform lengths and making uniform variations in spacings. However, these and other array characteristics can be optimized by using nonuniform director lengths and spacings between the directors. For example, the spacing between the directors can be varied while holding the reflector-exciter spacing and the lengths of all elements constant. Such a procedure was used by Cheng and Chen [27] to optimize the directivity of a six-element (four-director, reflector, exciter) array using a perturbational technique. The results of the initial and the optimized (perturbed) array are shown in Table 10.1. For the same array, they allowed all the spacings to vary while maintaining constant all other parameters. The results are shown in Table 10.2.

Another optimization procedure is to maintain the spacings between all the elements constant and vary the lengths so as to optimize the directivity. The results of a six-element array [28] are shown in Table 10.3. The ultimate optimization is to vary both the spacings and lengths. This was accomplished by Chen and Cheng [28] whereby they first optimized the array by varying the spacing, while maintaining the lengths constant. This was followed, on the same array, with perturbations in the lengths while maintaining the optimized spacings constant. The results of this procedure are shown in Table 10.4 with the corresponding H-plane ($\theta = \pi/2$, ϕ) far-field patterns shown in Figure 10.23. In all, improvements in directivity and front-to-back ratio are noted. The ideal optimization will be to allow the lengths and spacings to vary simultaneously. Such an optimization was not performed in [27] or [28], although it could have been done iteratively by repeating the procedure.

Table 10.2 DIRECTIVITY OPTIMIZATION FOR SIX-ELEMENT YAGI-UDA ARRAY (PERTURBATION OF *ALL ELEMENT SPACINGS*). $l_1 = 0.51\lambda$, $l_2 = 0.50\lambda$, $l_3 = l_4 = l_5 = l_6 = 0.43\lambda$, $a = 0.003369\lambda$

	s_{21}/λ	s_{32}/λ	s_{43}/λ	s_{54}/λ	s_{65}/λ	Directivity (dB)
INITIAL ARRAY	0.280	0.310	0.310	0.310	0.310	10.92
OPTIMIZED ARRAY	0.250	0.352	0.355	0.354	0.373	12.89

SOURCE: D. K. Cheng and C. A. Chen, "Optimum Spacings for Yagi-Uda Arrays," *IEEE Trans. Antennas Propag.*, Vol. AP-21, pp. 615–623, September 1973. © (1973) IEEE.

INTEL-1045
U.S. Patent 7,151,430

Table 10.3 DIRECTIVITY OPTIMIZATION FOR SIX-ELEMENT YAGI-UDA ARRAY (PERTURBATION OF *ALL ELEMENT LENGTHS*), $s_{21} = 0.250\lambda$, $s_{32} = s_{43} = s_{54} = s_{65} = 0.310\lambda$, $a = 0.0003369\lambda$

	l_1/λ	l_2/λ	l_3/λ	l_4/λ	l_5/λ	l_6/λ	Directivity (dB)
INITIAL ARRAY	0.510	0.490	0.430	0.430	0.430	0.430	10.93
LENGTH-PERTURBED ARRAY	0.472	0.456	0.438	0.444	0.432	0.404	12.16

SOURCE: C. A. Chen and D. K. Cheng, "Optimum Element Lengths for Yagi-Uda Arrays," *IEEE Trans. Antennas Propag.*, Vol. AP-23, pp. 8–15, January 1975. © (1975) IEEE.

Another parameter that was investigated for the directivity-optimized Yagi-Uda antenna was the frequency bandwidth [29]. The results of such a procedure are shown in Figure 10.24. The antenna was a six-element array optimized at a center frequency f_0. The array was designed, using space perturbations on all the elements, to yield an optimum directivity at f_0. The geometrical parameters are listed in Table 10.2. The 3-dB bandwidth seems to be almost the same for the initial and the optimized arrays. The rapid decrease in the directivity of the initial and optimized arrays at frequencies higher than f_0 and nearly constant values below f_0 may be attributed to the structure of the antenna which can support a "traveling wave" at $f < f_0$ but not at $f > f_0$. It has thus been suggested that an increase in the bandwidth can be achieved if the geometrical dimensions of the antenna are chosen slightly smaller than the optimum.

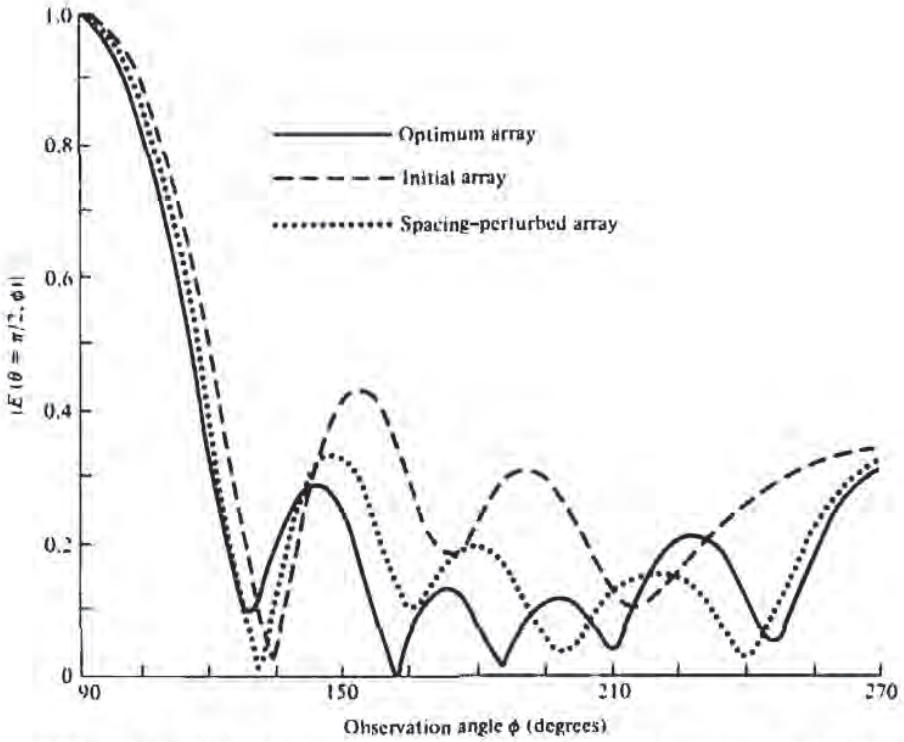


Figure 10.23 Normalized amplitude antenna patterns of initial, perturbed, and optimum six-element Yagi-Uda arrays (Table 10.4). (SOURCE: C. A. Chen and D. K. Cheng, "Optimum Element Lengths for Yagi-Uda Arrays," *IEEE Trans. Antennas Propagat.*, Vol. AP-23, pp. 8–15, January 1975. © (1975) IEEE)

INTEL-1045
U.S. Patent 7,151,430

Table 10.4 DIRECTIVITY OPTIMIZATION FOR SIX-ELEMENT YAGI-UDA ARRAY (PERTURBATION OF *DIRECTOR SPACINGS AND ALL ELEMENT LENGTHS*), $a = 0.003369\lambda$

	l_1/λ	l_2/λ	l_3/λ	l_4/λ	l_5/λ	l_6/λ	s_{21}/λ	s_{32}/λ	s_{43}/λ	s_{54}/λ	s_{65}/λ	Directivity (dB)
INITIAL ARRAY	0.510	0.490	0.430	0.430	0.430	0.430	0.250	0.310	0.310	0.310	0.310	10.93
ARRAY AFTER SPACING PERTURBATION	0.510	0.490	0.430	0.430	0.430	0.430	0.250	0.289	0.406	0.323	0.422	12.83
OPTIMUM ARRAY AFTER SPACING AND LENGTH PERTURBATION	0.472	0.452	0.436	0.430	0.434	0.430	0.250	0.289	0.406	0.323	0.422	13.41

SOURCE: C. A. Chen and D. K. Cheng. "Optimum Element Lengths for Yagi-Uda Arrays," *IEEE Trans. Antennas Propag.*, Vol. AP-23, pp. 8–15, January 1975. © (1975) IEEE.

INTEL-1045
U.S. Patent 7,151,430

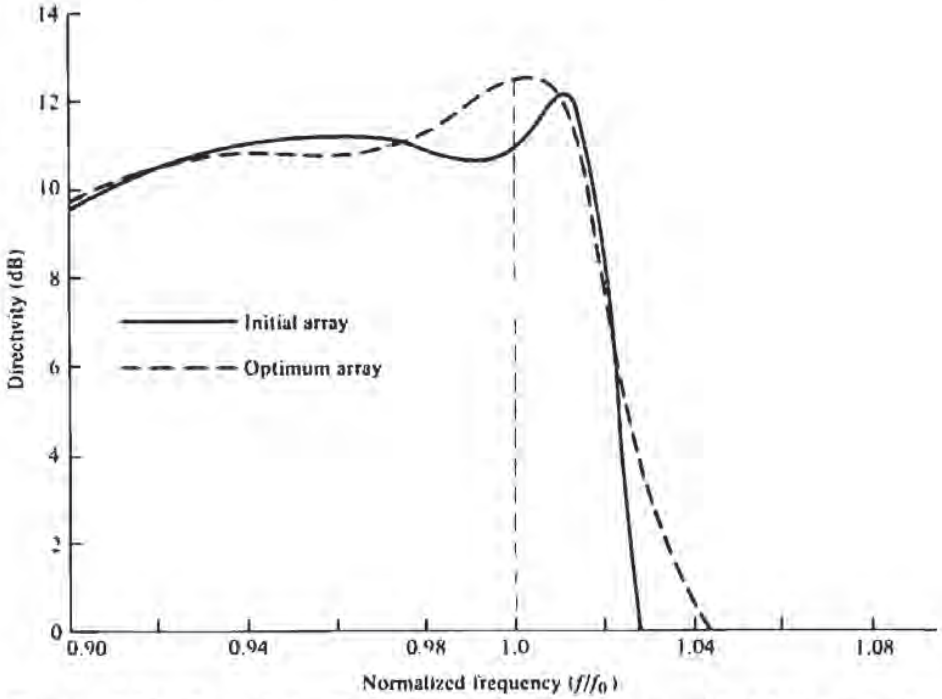


Figure 10.24 Bandwidth of initial and optimum six-element Yagi-Uda array with perturbation of all element spacings (Table 10.2). (SOURCE: N. K. Takla and L.-C. Shen, "Bandwidth of a Yagi Array with Optimum Directivity," *IEEE Trans. Antennas Propagat.*, Vol. AP-25, pp. 913–914, November 1977. © (1977) IEEE)

E. Input Impedance and Matching Techiques

The input impedance of a Yagi-Uda array, measured at the center of the driven element, is usually small and it is strongly influenced by the spacing between the reflector and feed element. For a 13-element array using a resonant driven element, the measured input impedances are listed in Table 10.5 [20]. Some of these values are low for matching to a 50-, 78-, or 300-ohm transmission lines.

There are many techniques that can be used to match a Yagi-Uda array to a transmission line and eventually to the receiver, which in many cases is a television set which has a large impedance (on the order of 300 ohms). Two common matching techniques are the use of the folded dipole, of Section 9.5, as a driven element and simultaneously as an impedance transformer, and the Gamma-match of Section 9.8.4. Which one of the two is used depends primarily on the transmission line from the antenna to the receiver.

The coaxial cable is now widely used as the primary transmission line for television, especially with the wide spread and use of cable TV; in fact, most television sets are already prewired with coaxial cable connections. Therefore, if the coax with a characteristic impedance of about 78 ohms is the transmission line used from the Yagi-Uda antenna to the receiver and since the input impedance of the antenna is typically 30–70 ohms (as illustrated in Table 10.5), the Gamma-match is the most prudent matching technique to use. This has been widely used in commercial designs where a clamp is usually employed to vary the position of the short to achieve a best match.

If, however, a "twin-lead" line with a characteristic impedance of about 300 ohms is used as the transmission line from the antenna to the receiver, as was used

INTEL-1045
U.S. Patent 7,151,430

Table 10.5 INPUT IMPEDANCE OF A 15-ELEMENT YAGI-UDA ARRAY (REFLECTOR LENGTH = 0.5λ; DIRECTOR SPACING = 0.34λ; DIRECTOR LENGTH = 0.406λ)

Reflector Spacing (s_{21}/λ)	Input Impedance (ohms)
0.25	62
0.18	50
0.15	32
0.13	22
0.10	12

widely some years ago, then it would be most prudent to use a folded dipole as the driven element which acts as a step-up impedance transformer of about 4:1 (4:1 when the length of the element is exactly λ/2. This technique is also widely used in commercial designs.

Another way to explain the endfire beam formation and whether the parameters of the Yagi-Uda array are properly adjusted for optimum directivity is by drawing a vector diagram of the progressive phase delay from element-to-element. If the current amplitudes throughout the array are equal, the total phase delay for maximum directivity should be about 180°, as is required by the Hansen-Woodyard criteria for improved endfire radiation. Since the currents in a Yagi-Uda array are not equal in all the elements, the phase velocity of the traveling wave along the antenna structure is not the same from element-to-element but it is always slower than the velocity of light and faster than the corresponding velocity for a Hansen-Woodyard design. For a Yagi-Uda array, the decrease in the phase velocity is a function of the increase in total array length.

In general then, the phase velocity, and in turn the phase shift, of a traveling wave in a Yagi-Uda array structure is controlled by the geometrical dimensions of the array and its elements, and it is not uniform from element-to-element.

F. Design Procedure

A government document [30] has been published which provides extensive data of experimental investigations carried out by the National Bureau of Standards to determine how parasitic element diameter, element length, spacings between elements, supporting booms of different cross-sectional areas, various reflectors, and overall length affect the measured gain. Numerous graphical data is included to facilitate the design of different length antennas to yield maximum gain. In addition, design criteria are presented for stacking Yagi-Uda arrays either one above the other or side-by-side. A step-by-step design procedure has been established in determining the geometrical parameters of a Yagi-Uda array for a desired directivity (over that of a λ/2 dipole mounted at the same height above ground). The included graphs can only be used to design arrays with overall lengths (*from reflector element to last director*) of 0.4, 0.8, 1.2, 2.2, 3.2, and 4.2λ with corresponding directivities of 7.1, 9.2, 10.2, 12.25, 13.4, and 14.2 dB, respectively, and with a diameter-to-wavelength ratio of $0.001 \leq d/\lambda \leq 0.04$. Although the graphs do not cover all possible designs, they do accommodate most practical requests. The driven element used to derive the data was a λ/2 folded dipole, and the measurements were carried out at $f = 400$ MHz. To make the reader aware of the procedure, it will be outlined by the use of an example. The procedure

INTEL-1045
U.S. Patent 7,151,430

Table 10.6 OPTIMIZED UNCOMPENSATED LENGTHS OF PARASITIC ELEMENTS FOR YAGI-UDA ANTENNAS OF SIX DIFFERENT LENGTHS

$d/\lambda = 0.0085$		LENGTH OF YAGI-UDA (IN WAVELENGTHS)					
$s_{12} = 0.2\lambda$		0.4	0.8	1.20	2.2	3.2	4.2
LENGTH OF REFLECTOR (l_1/λ)		0.482	0.482	0.482	0.482	0.482	0.475
LENGTH OF DIRECTORS, λ	l_3	0.442	0.428	0.428	0.432	0.428	0.424
	l_4		0.424	0.420	0.415	0.420	0.424
	l_5		0.428	0.420	0.407	0.407	0.420
	l_6			0.428	0.398	0.398	0.407
	l_7				0.390	0.394	0.403
	l_8				0.390	0.390	0.398
	l_9				0.390	0.386	0.394
	l_{10}				0.390	0.386	0.390
	l_{11}				0.398	0.386	0.390
	l_{12}				0.407	0.386	0.390
	l_{13}					0.386	0.390
	l_{14}					0.386	0.390
	l_{15}					0.386	0.390
	l_{16}					0.386	
	l_{17}					0.386	
SPACING BETWEEN DIRECTORS (s_{ik}/λ)		0.20	0.20	0.25	0.20	0.20	0.308
DIRECTIVITY RELATIVE TO HALF-WAVE DIPOLE (dB)		7.1	9.2	10.2	12.25	13.4	14.2
DESIGN CURVE (SEE FIGURE 10.25)		(*A*)	(*B*)	(*B*)	(*C*)	(*B*)	(*D*)

SOURCE: Peter P. Viezbicke, *Yagi Antenna Design*, NBS Technical Note 688, December 1976.

is identical for all other designs at freqencies where included data can accommodate the specifications.

The heart of the design is the data included in

1. Table 10.6 which represents optimized antenna parameters for six different lengths and for a $d/\lambda = 0.0085$
2. Figure 10.25 which represents *uncompensated* director and reflector lengths for $0.001 \leq d/\lambda \leq 0.04$
3. Figure 10.26 which provides compensation length increase for all the parasitic elements (directors and reflectors) as a function of boom-to-wavelength ratio $0.001 \leq D/\lambda \leq 0.04$

The specified information is usually the center frequency, antenna directivity, d/λ and D/λ ratios, and it is required to find the optimum parasitic element lengths (directors and reflectors). The spacing between the directors is uniform but not the same for all

INTEL-1045
U.S. Patent 7,151,430

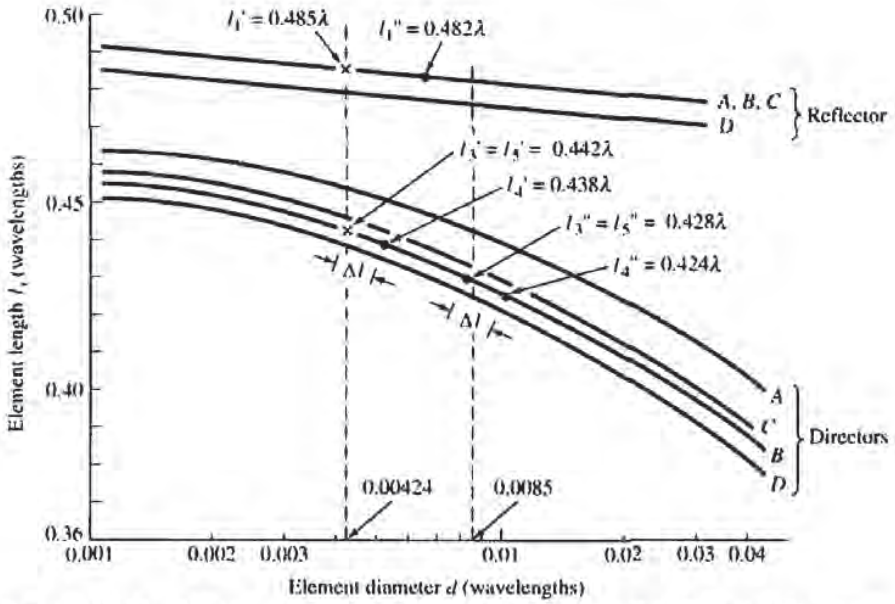


Figure 10.25 Design curves to determine element lengths of Yagi-Uda arrays. (SOURCE: P. P. Viezbicke, "Yagi Antenna Design," NBS Technical Note 688, U.S. Department of Commerce/National Bureau of Standards, December 1976)

designs. However, there is only one reflector and its spacing is $s = 0.2\lambda$ for all designs.

Example 10.2

Design a Yagi-Uda array with a directivity (relative to a $\lambda/2$ dipole at the same height above ground) of 9.2 dB at $f_0 = 50.1$ MHz. The desired diameter of the parasitic elements is 2.54 cm and of the metal supporting boom 5.1 cm. Find the element spacings, lengths, and total array length.

SOLUTION

(a) At $f_0 = 50.1$ MHz the wavelength is $\lambda = 5.988$ m $= 598.8$ cm. Thus $d/\lambda = 2.54/598.8 = 4.24 \times 10^{-3}$ and $D/\lambda = 5.1/598.8 = 8.52 \times 10^{-3}$.

(b) From Table 10.6, the desired array would have a total of five elements (three directors, one reflector, one feeder). For a $d/\lambda = 0.0085$ ratio the optimum uncompensated lengths would be those shown in the second column of Table 10.6 ($l_3 = l_5 = 0.428\lambda$, $l_4 = 0.424\lambda$, and $l_1 = 0.482\lambda$). The overall antenna length would be $L = (0.6 + 0.2)\lambda = 0.8\lambda$, the spacing between directors 0.2λ, and the reflector spacing 0.2λ. It is now desired to find the optimum lengths of the parasitic elements for a $d/\lambda = 0.00424$.

(c) Plot the optimized lengths from Table 10.6 ($l_3'' = l_5'' = 0.428\lambda$, $l_4'' = 0.424\lambda$, and $l_1'' = 0.482\lambda$) on Figure 10.25 and mark them by a dot (·).

(d) In Figure 10.25 draw a vertical line through $d/\lambda = 0.00424$ intersecting curves (B) at director uncompensated lengths $l_3' = l_5' = 0.442\lambda$ and reflector length $l_1' = 0.485\lambda$. Mark these points by an x.

INTEL-1045
U.S. Patent 7,151,430

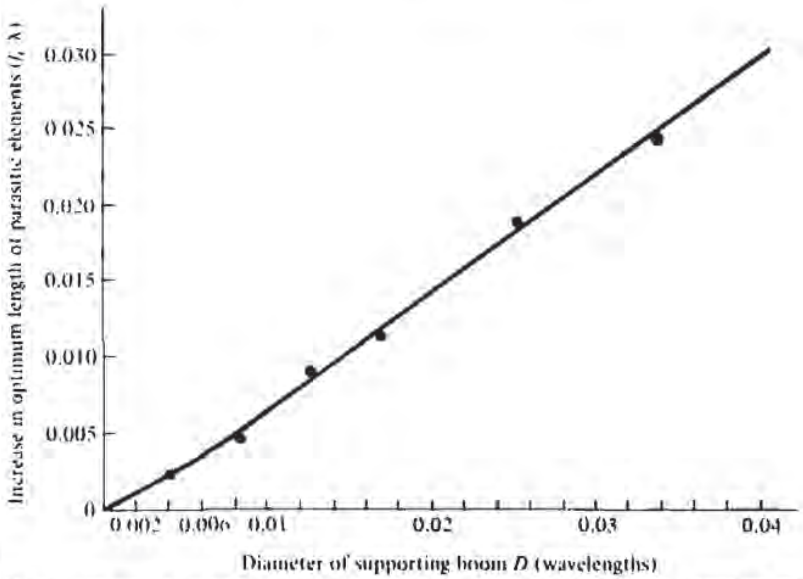


Figure 10.26 Increase in optimum length of parasitic elements as a function of metal boom diameter. (SOURCE: P. P. Viezbicke," Yagi Antenna Design," NBS Technical Note 688, U.S. Department of Commerce/National Bureau of Standards, December 1976)

(e) With a divider, measure the distance (Δl) along director curve (B) between points $l_3'' = l_5'' = 0.428\lambda$ and $l_4'' = 0.424\lambda$. Transpose this distance from the point $l_3' = l_5' = 0.442\lambda$ on curve (B), established in step (d) and marked by an x, downward along the curve and determine the uncompensated length $l_4' = 0.438\lambda$. Thus the boom uncompensated lengths of the array at $f_0 =$ 50.1 MHz are

$$l_3' = l_5' = 0.442\lambda$$
$$l_4' = 0.438\lambda$$
$$l_1' = 0.485\lambda$$

(f) Correct the element lengths to compensate for the boom diameter. From Figure 10.26, a boom diameter-to-wavelength ratio of 0.00852 requires a fractional length increase in each element of about 0.005λ. Thus the final lengths of the elements should be

$$l_3 = l_5 = (0.442 + 0.005)\lambda = 0.447\lambda$$
$$l_4 = (0.438 + 0.005)\lambda = 0.443\lambda$$
$$l_1 = (0.485 + 0.005)\lambda = 0.490\lambda$$

The design data were derived from measurements carried out on a nonconducting Plexiglas boom mounted 3λ above the ground. The driven element was a $\lambda/2$ folded dipole matched to a 50-ohm line by a double-stub tuner. All parasitic elements were constructed from aluminum tubing. Using Plexiglas booms, the data were repeatable and represented the same values as air-dielectric booms. However that was not the case for wooden booms because of differences in the moisture, which had a direct affect on the gain. Data on metal booms was also repeatable provided the element lengths were increased to compensate for the metal boom structure.

INTEL-1045
U.S. Patent 7,151,430

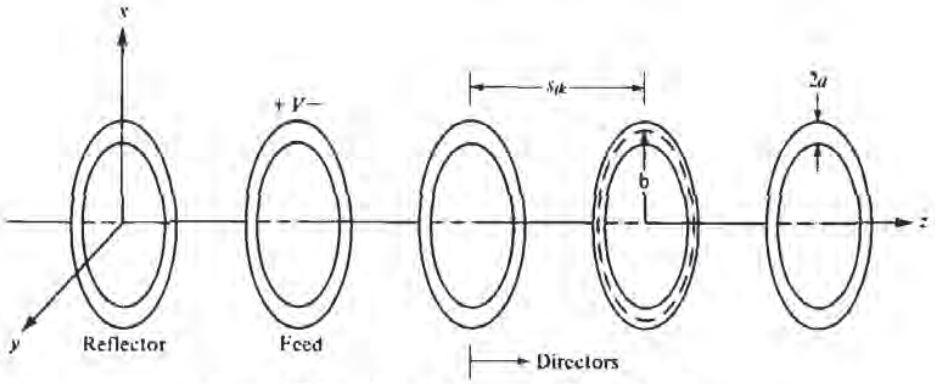


Figure 10.27 Yagi-Uda array of circular loops.

10.3.4 Yagi-Uda Array of Loops

Aside from the dipole, the loop antenna is one of the most basic antenna elements. The pattern of a very small loop is similar to that of a very small dipole and in the far-field region it has a null along its axis. As the circumference of the loop increases, the radiation along its axis increases and reaches near maximum at about one wavelength [31]. Thus loops can be used as the basic elements, instead of the linear dipoles, to form a Yagi-Uda array as shown in Figure 10.27. By properly choosing the dimensions of the loops and their spacing, they can form a unidirectional beam along the axis of the loops and the array.

It has been shown that the radiation characteristics of a two-element loop array, one driven element and a parasitic reflector, resulted in the elimination of corona problems at high altitudes [32]. In addition, the radiation characteristics of loop arrays mounted above ground are less affected by the electrical properties of the soil, as compared with those of dipoles [33]. A two-element loop array also resulted in a 1.8 dB higher gain than a corresponding array of two dipoles [32]. A two-element array of square loops (a feeder and a reflector) in a boxlike construction is called a "cubical quad" or simply a "quad" antenna, and it is very popular in amateur radio applications [34]. The sides of each square loop are $\lambda/4$ (perimeter of λ), and the loops are usually supported by a fiberglass or bamboo cross-arm assembly.

The general performance of a loop Yagi-Uda array is controlled by the same geometrical parameters (reflector, feeder, and director sizes, and spacing between elements), and it is influenced in the same manner as an array of dipoles [35].

In a numerical parametric study of coaxial Yagi-Uda arrays of circular loops [36] of 2 to 10 directors, it has been found that the optimum parameters for *maximum forward gain* were

1. circumference of feeder $2\pi b_2 = 1.1\lambda$, where b_2 is its radius. This radius was chosen so that the input impedance for an isolated element is purely resistive.
2. circumference of the reflector $2\pi b_1 \simeq 1.05\lambda$, where b_1 is its radius. The size of the reflector does not strongly influence the forward gain but has a major effect on the backward gain and input impedance.
3. feeder-reflector spacing of about 0.1λ. Because it has negligible effect on the forward gain, it can be used to control the backward gain and/or the input impedance.
4. circumference of directors $2\pi b \simeq 0.7\lambda$, where b is the radius of any director and

INTEL-1045
U.S. Patent 7,151,430

it was chosen to be the same for all. When the circumference approached a value of one wavelength, the array exhibited its cutoff properties.

5. spacing of directors of about 0.25λ, and it was uniform for all.

The radius a of all the elements was retained constant and was chosen to satisfy $\Omega = 2\ln(2\pi b_2/a) = 11$ where b_2 is the radius of the feeder.

References

1. C. H. Walter. *Traveling Wave Antennas*, McGraw-Hill, New York, 1965.
2. J. D. Kraus, *Electromagnetics*, McGraw-Hill Book Co., New York, 1992.
3. J. G. Brainerd, et. al., *Ultra-High-Frequency Techniques*, Van Nostrand, New York, 1942.
4. L. V. Blake, *Antennas*, John Wiley and Sons, New York, 1966.
5. G. A. Thiele and E. P. Ekelman, Jr., "Design Formulas for Vee Dipoles," *IEEE Trans. Antennas Propagat.*, Vol. AP-28, No. 4, pp. 588–590, July 1980.
6. W. L. Weeks, *Antenna Engineering*, McGraw-Hill, New York, 1968, pp. 140–142.
7. D. G. Fink (ed.), *Electronics Engineers' Handbook*, Chapter 18 (by W. F. Croswell), McGraw-Hill, New York, 1975.
8. J. D. Kraus, *Antennas*, McGraw-Hill, New York, 1988.
9. A. A. de Carvallo, "On the Design of Some Rhombic Antenna Arrays," *IRE Trans. Antennas Propagat.*, Vol. AP-7, pp. 39–46, No. 1, January 1959.
10. E. Bruce, A. C. Beck, and L. R. Lowry, "Horizontal Rhombic Antennas," *Proc. IRE*, Vol. 23, pp. 24–26, January 1935.
11. R. S. Elliott, *Antenna Theory and Design*, Prentice-Hall, Englewood Cliffs, New Jersey, 1981.
12. J. D. Kraus, "A 50-Ohm Input Impedance for Helical Beam Antennas," *IEEE Trans. Antennas Propagat.*, Vol. AP-25, No. 6, p. 913, November 1977.
13. A. G. Kandoian, "Three New Antenna Types and Their Applications," *Proc. IRE*, Vol. 34, pp. 70W–75W, February 1946.
14. S. Uda, "Wireless Beam of Short Electric Waves," *J. IEE*. (Japan), pp. 273–282, March 1926, and pp. 1209–1219, November 1927.
15. H. Yagi, "Beam Transmission of Ultra Short Waves," *Proc. IRE*, Vol. 26, pp. 715–741, June 1928. Also *Proc. IEEE*, Vol. 72, No. 5, pp. 634–645, May 1984.
16. R. M. Fishender and E. R. Wiblin, "Design of Yagi Aerials," *Proc. IEE* (London), pt. 3, Vol. 96, pp. 5–12, January 1949.
17. C. C. Lee and L.-C. Shen, "Coupled Yagi Arrays," *IEEE Trans. Antennas Propagat.*, Vol. AP-25, No. 6, pp. 889–891, November 1977.
18. H. W. Ehrenspeck and H. Poehler, "A New Method for Obtaining Maximum Gain from Yagi Antennas," *IRE Trans. Antennas Propagat.*, Vol. AP-7, pp. 379–386, October 1959.
19. H. E. Green, "Design Data for Short and Medium Length Yagi-Uda Arrays," *Elec. Engrg. Trans. Inst. Engrgs.* (Australia), pp. 1–8, March 1966.
20. W. Wilkinshaw, "Theoretical Treatment of Short Yagi Aerials," *Proc. IEE* (London), pt. 3, Vol. 93, p. 598, 1946.
21. R. J. Mailloux, "The Long Yagi-Uda Array," *IEEE Trans. Antennas Propagat.*, Vol. AP-14, pp. 128–137, March 1966.
22. D. Kajfez, "Nonlinear Optimization Reduces the Sidelobes of Yagi Antennas," *IEEE Trans. Antennas Propagat.*, Vol. AP-21, No. 5, pp. 714–715, September 1973.
23. D. Kajfez, "Nonlinear Optimization Extends the Bandwidth of Yagi Antennas," *IEEE Trans. Antennas Propagat.*, Vol. AP-23, pp. 287–289, March 1975.
24. G. A. Thiele, "Analysis of Yagi-Uda Type Antennas," *IEEE Trans. Antennas Propagat.*, Vol. AP-17, No. 1, pp. 24–31, January 1969.

INTEL-1045
U.S. Patent 7,151,430

25. P. A. Tirkas, Private communication.
26. G. A. Thiele, "Calculation of the Current Distribution on a Thin Linear Antenna," *IEEE Trans. Antennas Propagat.*, Vol. AP-14, No. 5, pp. 648–649, September 1966.
27. D. K. Cheng and C. A. Chen, "Optimum Spacings for Yagi-Uda Arrays," *IEEE Trans. Antennas Propagat.*, Vol. AP-21, No. 5, pp. 615–623, September 1973.
28. C. A. Chen and D. K. Cheng, "Optimum Element Lengths for Yagi-Uda Arrays," *IEEE Trans. Antennas Propagat.*, Vol. AP-23, No. 1, pp. 8–15, January 1975.
29. N. K. Takla and L.-C. Shen, "Bandwidth of a Yagi Array with Optimum Directivity," *IEEE Trans. Antennas Propagat.*, Vol. AP-25, No. 6, pp. 913–914, November 1977.
30. P. P. Viezbicke, "Yagi Antenna Design," NBS Technical Note 688, U.S. Department of Commerce/National Bureau of Standards, December 1968.
31. S. Adachi and Y. Mushiake, "Studies of Large Circular Loop Antennas," Sci. Rep. Research Institute of Tohoku University (RITU), B,9,2, pp. 79–103, 1957.
32. J. E. Lindsay, Jr., "A Parasitic End-fire Array of Circular Loop Elements," *IEEE Trans. Antennas Propagat.*, Vol. AP-15, No. 5, pp. 697–698, September 1967.
33. E. Ledinegg, W. Paponsek, and H. L. Brueckmann, "Low-Frequency Loop Antenna Arrays: Ground Reaction and Mutual Interaction," *IEEE Trans. Antennas Propagat.*, Vol. AP-21, No. 1, pp. 1–8, January 1973.
34. D. DeMaw (ed.), *The Radio Amateur's Handbook*, American Radio Relay League, p. 20-18, 56th ed., 1979.
35. A. Shoamanesh and L. Shafai, "Properties of Coaxial Yagi Loop Arrays," *IEEE Trans. Antennas Propagat.*, Vol. AP-26, No. 4, pp. 547–550, July 1978.
36. A. Shoamanesh and L. Shafai, "Design Data for Coaxial Yagi Array of Circular Loops," *IEEE Trans. Antennas Propagat.*, Vol. AP-27, No. 5, pp. 711–713, September 1979.

PROBLEMS

10.1. Given the current distribution of (10-1a), show that the
(a) far-zone electric field intensity is given by (10-2a) and (10-2b)
(b) average power density is given by (10-4) and (10-5)
(c) radiated power is given by (10-11)

10.2. Determine the phase velocity (compared to free-space) of the wave on a Beverage antenna (terminated long wire) of length $l = 50\lambda$ so that the maximum occurs at angles of
(a) 10°
(b) 20°
from the axis of the wire.

10.3. The current distribution on a terminated and matched long linear (traveling wave) antenna of length l, positioned along the x-axis and fed at its one end, is given by

$$\mathbf{I} = \hat{\mathbf{a}}_x I_0 e^{-jkx'}, \quad 0 \le x' \le l$$

Find the far field electric and magnetic field components in *standard spherical coordinates.*

10.4. A long linear (traveling wave) antenna of length l, positioned along the z-axis and fed at the $z = 0$ end, is terminated in a load at the $z = l$ end. There is a nonzero reflection at the load such that the current distribution on the wire is given by

$$I(z) = I_0 \frac{e^{-jkz} + R\, e^{jkz}}{1 + R}, \quad 0 \le z \le l$$

Determine as a function of R and l the
(a) far-zone spherical electric field components
(b) radiation intensity in the $\theta = \pi/2$ direction

10.5. Design a Beverage antenna so that the first maximum occurs at 10° from its axis.

INTEL-1045
U.S. Patent 7,151,430

Assuming the phase velocity of the wave on the line is the same as that of free-space, find the
(a) lengths (exact and approximate) to accomplish that
(b) angles (exact and approximate) where the next six maxima occur
(c) angles (exact and approximate) where the nulls, between the maxima found in parts (a) and (b), occur
(d) radiation resistance using the exact and approximate lengths
(e) directivity using the exact and approximate lengths

10.6. It is desired to place the first maximum of a long wire traveling wave antenna at an angle of 25° from the axis of the wire. For the wire antenna, find the
(a) exact required length
(b) radiation resistance
(c) directivity (*in dB*)
The wire is radiating into free space.

10.7. Compute the directivity of a long wire with lengths of $l = 2\lambda$ and 3λ.

10.8. A long wire of diameter d is placed (in the air) at a height h above the ground.
(a) Find its characteristic impedance assuming $h \gg d$.
(b) Compare this value with (10-14).

10.9. Beverage (long wire) antennas are used for over-the-horizon communication where the maximum of the main beam is pointed few degrees above the horizon. Assuming the wire antenna of length l and radius $\lambda/200$ is placed horizontally parallel to the z-axis a height $h = \lambda/20$ above a flat, perfect electric conducting plane of infinite extent (x-axis is perpendicular to the ground plane).
(a) Derive the array factor for the equivalent two-element array.
(b) What is the normalized total electric field of the wire in the presence of the conducting plane?
(c) What value of load resistance should be placed at the terminating end to eliminate any reflections and not create a standing wave?

10.10. Compute the optimum directivities of a V antenna with leg lengths of $l = 2\lambda$ and $l = 3\lambda$. Compare these values with those of Problem 10.7.

10.11. Design a symmetrical V antenna so that its optimum directivity is 8 dB. Find the lengths of each leg (in λ) and the total included angle of the V (in degrees).

10.12. Repeat the design of Problem 10.11 for an optimum directivity of 5 dB.

10.13. It is desired to design a V-dipole with a maximized directivity. The length of each arm is 0.5λ (overall length of the entire V-dipole is λ). To meet the requirements of the design, what is the
(a) total included angle of the V-dipole (in degrees)?
(b) directivity (in dB)?
(c) gain (in dB) if the overall antenna efficiency is 35%?

10.14. Ten identical elements of V antennas are placed along the z-axis to form a *uniform broadside* array. Each element is designed to have a maximum directivity of 9 dB. Assuming each element is placed so that its maximum is also broadside ($\theta = 90°$) and the elements are spaced $\lambda/4$ apart, find the
(a) arm length of each V (in λ)
(b) included angle (in degrees) of each V
(c) approximate total directivity of the array (in dB)

10.15. Design a resonant 90° bent, $\lambda/4$ long, $0.25 \times 10^{-3}\lambda$ radius wire antenna placed above a ground plane. Find the
(a) height where the bent must be made
(b) input resistance of the antenna
(c) VSWR when the antenna is connected to a 50-ohm line

10.16. Design a five-turn helical antenna which at 400 MHz operates in the normal mode. The spacing between turns is $\lambda/50$. It is desired that the antenna possesses circular polarization. Determine the

INTEL-1045
U.S. Patent 7,151,430

(a) circumference of the helix (in λ and in meters)
(b) length of a single turn (in λ and in meters)
(c) overall length of the entire helix (in λ and in meters)
(d) pitch angle (in degrees)

10.17. Design a five-turn helical antenna which at 300 MHz operates in the axial mode and possesses circular polarization in the major lobe. Determine the
(a) near optimum circumference (in λ and in meters)
(b) spacing (in λ and in meters) for near optimum pitch angle design
(c) input impedance
(d) half-power beamwidth (in degrees), first null beamwidth (in degrees), directivity (dimensionless and in dB), and axial ratio
(e) VSWR when the antenna is connected to 50- and 75-ohm coaxial lines

10.18. For Problem 10.17, plot, using the 2-D ANTENNA PATTERN PLOTTER: RECTANGULAR-POLAR computer program at the end of Chapter 2, the normalized polar amplitude pattern (in dB) assuming phasing for
(a) ordinary end-fire
(b) Hansen-Woodyard end-fire
(c) $p = 1$

10.19. For Problem 10.17, compute the directivity (in dB) using the computer program DIRECTIVITY at the end of Chapter 2 assuming phasing for
(a) ordinary end-fire
(b) Hansen-Woodyard end-fire
(c) $p = 1$
Compare with the value obtained using (10-33).

10.20. Repeat the design of Problem 10.17 at a frequency of 500 MHz.

10.21. Design an end-fire right-hand circularly polarized helix having a half-power beamwidth of 45°, pitch angle of 13°, and a circumference of 60 cm at a frequency of 500 MHz. Determine the
(a) turns needed
(b) directivity (in dB)
(c) axial ratio
(d) lower and upper frequencies of the bandwidth over which the required parameters remain relatively constant
(e) input impedance at the center frequency and the edges of the band from part (d).

10.22. Design a helical antenna with a directivity of 15 dB that is operating in the axial mode and whose polarization is nearly circular. The spacing between the turns is $\lambda/10$. Determine the
(a) Number of turns.
(b) Axial ratio, *both as an dimensionless quantity and in dB.*
(c) Directivity (in dB) based on Kraus' formula and Tai & Pereira's formula. How do they compare with the desired value?
(d) Progressive phase shifts (in degrees) between the turns to achieve the axial mode radiation.

10.23. Design a 10-turn helical antenna so that at the center frequency of 10 GHz, the circumference of each turn is 0.95λ. Assuming a pitch angle of 14°, determine the
(a) mode in which the antenna operates
(b) half-power beamwidth (in degrees)
(c) directivity (in dB). Compare this answer with what you get using Kraus' formula.

10.24. A *lossless* 10-turn helical antenna with a circumference of *one-wavelength* is connected to a 78-ohm coaxial line, and it is used as a transmitting antenna in a 500-MHz spacecraft communication system. The spacing between turns is $\lambda/10$. The power in the coaxial line from the transmitter is 5 watts. Assuming the antenna is lossless:

INTEL-1045
U.S. Patent 7,151,430

(a) What is radiated power?
(b) If the antenna were isotropic, what would the power density (watts/m^2) be at a distance of 10 kilometers?
(c) What is the power density (in watts/m^2) at the same distance when the transmitting antenna is the 10-turn helix and the observations are made along the maximum of the major lobe?
(d) If at 10 kilometers along the maximum of the major lobe an identical 10-turn helix was placed as a receiving antenna, which was polarization-matched to the incoming wave, what is the maximum power (in watts) that can be received?

10.25. A 20-turn helical antenna operating in the axial mode is used as a transmitting antenna in a 500-MHz long distance communication system. The receiving antenna is a linearly polarized element. Because the transmitting and receiving elements are not matched in polarization, approximately how many dB of losses are introduced because of polarization mismatch?

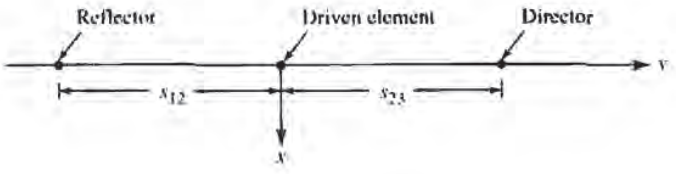
10.26. A Yagi-Uda array of linear elements is used as a TV antenna receiving primarily channel 8 whose center frequency is 183 MHz. With a regular resonant $\lambda/2$ dipole as the feed element in the array, the input impedance is approximately 68 ohms. The antenna is to be connected to the TV using a "twin-lead" line with a characteristic impedance of nearly 300 ohms. At the center frequency of 183 MHz
(a) what should the smallest input impedance of the array be if it is desired to maintain a VSWR equal or less than 1.1?
(b) what is the best way to modify the present feed to meet the desired VSWR specifications? Be very specific in explaining why your recommendation will accomplish this.

10.27. Evaluate approximately the effect of the spacing between the director and driven element in the three-element Yagi-Uda array shown in the accompanying figure. Assume that the far-zone (radiated) field of the antenna is given by

$$E_\theta = \sin\theta \left[1 - e^{-j\pi/8} e^{-jks_{12}\sin\theta\sin\phi} - e^{j\pi/8} e^{+jks_{23}\sin\theta\sin\phi} \right]$$

where s_{12} is the spacing between the reflector and the driven element, and s_{23} is the spacing between the director and the driven element. For this problem, set $s_{12} = 0.2\lambda$ and let $s_{23} = 0.15\lambda, 0.20\lambda, 0.25\lambda$.
(a) Generate polar plots of the radiation power patterns in both E- and H-planes. Normalize the power pattern to its value for $\theta = \pi/2$ and $\phi = \pi/2$. Generate two plots, one for E-plane and one for H-plane.
(b) Compute the front-to-back ratio (FBR) in the E-plane given by

$$FBR|_{E-plane} = \frac{P_n\left(\theta = \frac{\pi}{2}, \phi = \frac{\pi}{2}\right)}{P_n\left(\theta = \frac{\pi}{2}, \phi = \frac{-\pi}{2}\right)}$$



Leave your answers for both parts in terms of numbers, not dB.

INTEL-1045
U.S. Patent 7,151,430

10.28. Analyze a 27-element Yagi-Uda array, using the computer program YAGI-UDA ARRAY at the end of this chapter, having the following specifications:

N = total number of elements	= 27
Number of directors	= 25
Number of reflectors	= 1
Total length of reflector	= 0.5λ
Total length of feeder	= 0.47λ
Total length of each director	= 0.406λ
Spacing between reflector and feeder	= 0.125λ
Spacing between adjacent directors	= 0.34λ
a = radius of wires	= 0.003λ

Use 8 modes for each element. Compute the
(a) far-field E- and H-plane amplitude patterns (in dB).
(b) directivity of the array (in dB).
(c) E-plane half-power beamwidth (in degrees).
(d) H-plane half-power beamwidth (in degrees).
(e) E-plane front-to-back ratio (in dB).
(f) H-plane front to back ratio (in dB).

10.29. Repeat the analysis of Problem 10.28 for a three-element array having the following specifications:

N = total number of elements	= 3
Number of directors	= 1
Number of reflectors	= 1
Total length of reflector	= 0.5λ
Total length of feeder	= 0.475λ
Total length of director	= 0.45λ
Spacing between reflector and feeder	= 0.2λ
Spacing between feeder and director	= 0.16λ
a = radius of wires	= 0.005λ

Use 8 modes for each element.

10.30. Design a Yagi-Uda array of linear dipoles to cover all the VHF TV channels (starting with 54 MHz for channel 2 and ending with 216 MHz for channel 13. See Appendix IX). Perform the design at $f_0 = 216$ MHz. Since the gain is not affected appreciably at $f < f_0$, as Figure 10.24 indicates, this design should accommodate all frequencies below 216 MHz. The gain of the antenna should be 14.4 dB (above isotropic). The elements and the supporting boom should be made of aluminum tubing with outside diameters of $\frac{3}{8}$ in. ($\simeq$ 0.95 cm) and $\frac{3}{4}$ in. ($\simeq$ 1.90 cm), respectively. Find the number of elements, their lengths and spacings, and the total length of the array (in λ, meters, and feet).

10.31. Repeat the design of Problem 10.30 for each of the following:
(a) VHF-TV channels 2–6 (54–88 MHz. See Appendix IX)
(b) VHF-TV channels 7–13 (174–216 MHz. See Appendix IX)

10.32. Design a Yagi-Uda antenna to cover the entire FM band of 88–108 MHz (100 channels spaced at 200 KHz apart. See Appendix IX). The desired gain is 12.35 dB (above isotropic). Perform the design at $f_0 = 108$ MHz. The elements and the supporting boom should be made of aluminum tubing with outside diameters of $\frac{1}{8}$ in. ($\simeq$ 0.95

INTEL-1045
U.S. Patent 7,151,430

cm) and $\frac{3}{4}$ in. ($\simeq$ 1.90 cm), respectively. Find the number of elements, their lengths and spacings, and the total length of the array (in λ, meters, and feet).

10.33. Design a Yagi-Uda antenna to cover the UHF TV channels (512–806 MHz. See Appendix IX). The desired gain is 12.35 dB (above isotropic). Perform the design at f_0 = 806 MHz. The elements and the supporting boom should be made of wire with outside diameters of $\frac{1}{32}$ in. ($\simeq$ 0.2375 cm) and $\frac{1}{16}$ in. ($\simeq$ 0.475 cm), respectively. Find the number of elements, their lengths and spacings, and the total length of the array (in λ, meters, and feet).

INTEL-1045
U.S. Patent 7,151,430

COMPUTER PROGRAM - YAGI-UDA ARRAY

```
C*****************************************************************
C THIS IS A FORTRAN PROGRAM THAT COMPUTES, FOR THE YAGI-UDA
C ANTENNA ARRAY, THE:
C
C   I.  FAR-ZONE E- AND H-PLANE AMPLITUDE PATTERNS (in dB)
C   II.  DIRECTIVITY OF THE ARRAY (in dB)
C   III. E-PLANE HALF-POWER BEAMWIDTH (in degrees)
C   IV. H-PLANE HALF-POWER BEAMWIDTH (in degrees)
C   V.  E-PLANE FRONT-TO-BACK RATIO (in dB)
C   VI. H-PLANE FRONT-TO-BACK RATIO (in dB)
C
C THE PROGRAM IS BASED ON POCKLINGTON'S INTEGRAL
C EQUATION FORMULATION OF SECTION 10.3.3, EQUATIONS
C (10-42) - (10-65a). M ENTIRE DOMAIN COSINUSOIDAL (FOURIER)
C BASIS MODES ARE USED FOR EACH OF THE ANTENNA
C ELEMENTS.
C
C
C       **INPUT PARAMETERS
C       1. M      = NUMBER OF ENTIRE DOMAIN BASIS MODES
C       2. N      = NUMBER OF ANTENNA ELEMENTS
C       3. L      = LENGTH OF EACH ELEMENT l_n (in λ)
C       4. ALPHA  = RADIUS OF EACH ELEMENT a (in λ)
C       5. S      = SEPARATION BETWEEN THE ELEMENTS s_n (in λ)
C
C       **NOTES
C       1. REFER TO FIGURE 10.17 FOR THE GEOMETRY.
C       2. DRIVEN ELEMENT IS AT THE ORIGIN.
C       3. FIRST ELEMENT (N = 1) IS THE FIRST DIRECTOR.
C       4. REFLECTOR IS THE N-1 ELEMENT; ONLY ONE REFLECTOR.
C       5. DRIVEN ELEMENT IS N.
C       6. THE RADIUS OF ALL THE ELEMENTS IS THE SAME.
C
C*****************************************************************
```


INTEL-1045
U.S. Patent 7,151,430

CHAPTER

11

FREQUENCY INDEPENDENT ANTENNAS AND ANTENNA MINIATURIZATION

11.1 INTRODUCTION

The numerous applications of electromagnetics to the advances of technology have necessitated the exploration and utilization of most of the electromagnetic spectrum. In addition, the advent of broadband systems have demanded the design of broadband radiators. The use of simple, small, lightweight, and economical antennas, designed to operate over the entire frequency band of a given system, would be most desirable. Although in practice all the desired features and benefits cannot usually be derived from a single radiator, most can effectively be accommodated. Previous to the 1950s, antennas with broadband pattern and impedance characteristics had bandwidths not greater than 2:1. In the 1950s, a breakthrough in antenna evolution was made which extended the bandwidth to as great as 40:1 or more. The antennas introduced by the breakthrough were referred to as *frequency independent*, and they had geometries that were specified by angles. These antennas are primarily used in the 10–10,000 MHz region in a variety of practical applications such as TV, point-to-point communication, feeds for reflectors and lenses, and so forth.

In antenna scale modeling, characteristics such as impedance, pattern, polarization, and so forth, are invariant to a change of the physical size if a similar change is also made in the operating frequency or wavelength. For example, if *all* the physical dimensions are *reduced* by a factor of two, the performance of the antenna will remain unchanged if the operating frequency is *increased* by a factor of two. In other words, the performance is invariant if the electrical dimensions remain unchanged. This is the principle on which antenna scale model measurements are made. For a complete and thorough discussion of scaling, the reader is referred to Section 16.10 entitled "Scale Model Measurements."

The scaling characteristics of antenna model measurements also indicate that if the shape of the antenna were completely specified by angles, its performance would have to be independent of frequency [1]. The infinite biconical dipole of Figure 9.1 is one such structure. To make infinite structures more practical, the designs usually

INTEL-1045
U.S. Patent 7,151,430

require that the current on the structure decrease with distance away from the input terminals. After a certain point the current is negligible, and the structure beyond that point to infinity can be truncated and removed. Practically then the truncated antenna has a lower cutoff frequency above which its radiation characteristics are the same as those of the infinite structure. The lower cutoff frequency is that for which the current at the point of truncation becomes negligible. The upper cutoff is limited to frequencies for which the dimensions of the feed transmission line cease to look like a "point" (usually about $\lambda_2/8$ where λ_2 is the wavelength at the highest desirable frequency). Practical bandwidths are on the order of about 40:1. Even higher ratios (i.e., 1,000:1) can be achieved in antenna design but they are not necessary, since they would far exceed the bandwidths of receivers and transmitters.

Even though the shape of the biconical antenna can be completely specified by angles, the current on its structure does not diminish with distance away from the input terminals, and its pattern does not have a limiting form with frequency. This can be seen by examining the current distribution as given by (9-11). It is evident that there are phase but no amplitude variations with the radial distance r. Thus the biconical structure cannot be truncated to form a frequency independent antenna. In practice, however, antenna shapes exist which satisfy the general shape equation, as proposed by Rumsey [1], to have frequency independent characteristics in pattern, impedance, polarization, and so forth, and with current distribution which diminishes rapidly.

Rumsey's general equation will first be developed, and it will be used as the unifying concept to link the major forms of frequency independent antennas. Classical shapes of such antennas include the equiangular geometries of planar and conical spiral structures investigated thoroughly by Dyson [2], [3], and the logarithmically periodic structures proposed and developed by DuHamel and Isbell [4], [5].

Fundamental limitations in electrically small antennas will be discussed in Section 11.5. These will be derived using spherical mode theory, with the antenna enclosed in a virtual sphere. Minimum Q curves, which place limits on the achievable bandwidth, will be included.

11.2 THEORY

The analytical treatment of frequency independent antennas presented here parallels that introduced by Rumsey [1] and simplified by Elliott [6] for three-dimensional configurations.

We begin by assuming that an antenna, whose geometry is best described by the spherical coordinates (r, θ, ϕ), has both terminals infinitely close to the origin and each is symmetrically disposed along the $\theta = 0, \pi$-axes. It is assumed that the antenna is perfectly conducting, it is surrounded by an infinite homogeneous and isotropic medium, and its surface or an edge on its surface is described by a curve

$$r = F(\theta, \phi) \tag{11-1}$$

where r represents the distance along the surface or edge. If the antenna is to be scaled to a frequency that is K times lower than the original frequency, the antenna's physical surface must be made K times greater to maintain the same electrical dimensions. Thus the new surface is described by

$$r' = KF(\theta, \phi) \tag{11-2}$$

The new and old surfaces are identical; that is, not only are they similar but they are also congruent (if both surfaces are infinite). Congruence can be established only by

INTEL-1045
U.S. Patent 7,151,430

rotation in ϕ. Translation is not allowed because the terminals of both surfaces are at the origin. Rotation in θ is prohibited because both terminals are symmetrically disposed along the $\theta = 0, \pi$-axes.

For the second antenna to achieve congruence with the first, it must be rotated by an angle C so that

$$KF(\theta, \phi) = F(\theta, \phi + C) \tag{11-3}$$

The angle of rotation C depends on K but neither depends on θ or ϕ. Physical congruence implies that the original antenna electrically would behave the same at both frequencies. However the radiation pattern will be rotated azimuthally through an angle C. For unrestricted values of K ($0 \leq K \leq \infty$), the pattern will rotate by C in ϕ with frequency, because C depends on K, but its shape will be unaltered. Thus the impedance and pattern will be frequency independent.

To obtain the functional representation of $F(\theta, \phi)$, both sides of (11-3) are differentiated with respect to C to yield

$$\begin{aligned} \frac{d}{dC}[KF(\theta, \phi)] &= \frac{dK}{dC}F(\theta, \phi) = \frac{\partial}{\partial C}[F(\theta, \phi + C)] \\ &= \frac{\partial}{\partial(\phi + C)}[F(\theta, \phi + C)] \end{aligned} \tag{11-4}$$

and with respect to ϕ to give

$$\begin{aligned} \frac{\partial}{\partial \phi}[KF(\theta, \phi)] &= K\frac{\partial F(\theta, \phi)}{\partial \phi} = \frac{\partial}{\partial \phi}[F(\theta, \phi + C)] \\ &= \frac{\partial}{\partial(\phi + C)}[F(\theta, \phi + C)] \end{aligned} \tag{11-5}$$

Equating (11-5) to (11-4) yields

$$\frac{dK}{dC}F(\theta, \phi) = K\frac{\partial F(\theta, \phi)}{\partial \phi} \tag{11-6}$$

Using (11-1) we can write (11-6) as

$$\frac{1}{K}\frac{dK}{dC} = \frac{1}{r}\frac{\partial r}{\partial \phi} \tag{11-7}$$

Since the left side of (11-7) is independent of θ and ϕ, a general solution for the surface $r = F(\theta, \phi)$ of the antenna is

$$r = F(\theta, \phi) = e^{a\phi}f(\theta) \tag{11-8}$$

where

$$a = \frac{1}{K}\frac{dK}{dC} \tag{11-8a}$$

and $f(\theta)$ is a completely arbitrary function.

Thus for any antenna to have frequency independent characteristics, its surface must be described by (11-8). This can be accomplished by specifying the function $f(\theta)$ or its derivatives. Subsequently, interesting, practical, and extremely useful antenna configurations will be introduced whose surfaces are described by (11-8).

INTEL-1045
U.S. Patent 7,151,430

11.3 EQUIANGULAR SPIRAL ANTENNAS

The equiangular spiral is one geometrical configuration whose surface can be described by angles. It thus fulfills all the requirements for shapes that can be used to design frequency independent antennas. Since a curve along its surface extends to infinity, it is necessary to designate the length of the arm to specify a finite size antenna. The lowest frequency of operation occurs when the total arm length is comparable to the wavelength [2]. For all frequencies above this, the pattern and impedance characteristics are frequency independent.

11.3.1 Planar Spiral

The shape of an equiangular plane spiral curve can be derived by letting the derivative of $f(\theta)$ in (11-8) be

$$\frac{df}{d\theta} = f'(\theta) = A\delta\left(\frac{\pi}{2} - \theta\right) \tag{11-9}$$

where A is a constant and δ is the Dirac delta function. Using (11-9) reduces (11-8) to

$$r|_{\theta=\pi/2} = \rho = \begin{cases} Ae^{a\phi} = \rho_0 e^{a(\phi-\phi_0)} & \theta = \pi/2 \\ 0 & \text{elsewhere} \end{cases} \tag{11-10}$$

where

$$A = \rho_0 e^{-a\phi_0} \tag{11-10a}$$

In wavelengths, (11-10) can be written as

$$\rho_\lambda = \frac{\rho}{\lambda} = \frac{A}{\lambda}e^{a\phi} = Ae^{a[\phi - \ln(\lambda)/a]} = Ae^{a(\phi-\phi_1)} \tag{11-11}$$

where

$$\phi_1 = \frac{1}{a}\ln(\lambda) \tag{11-11a}$$

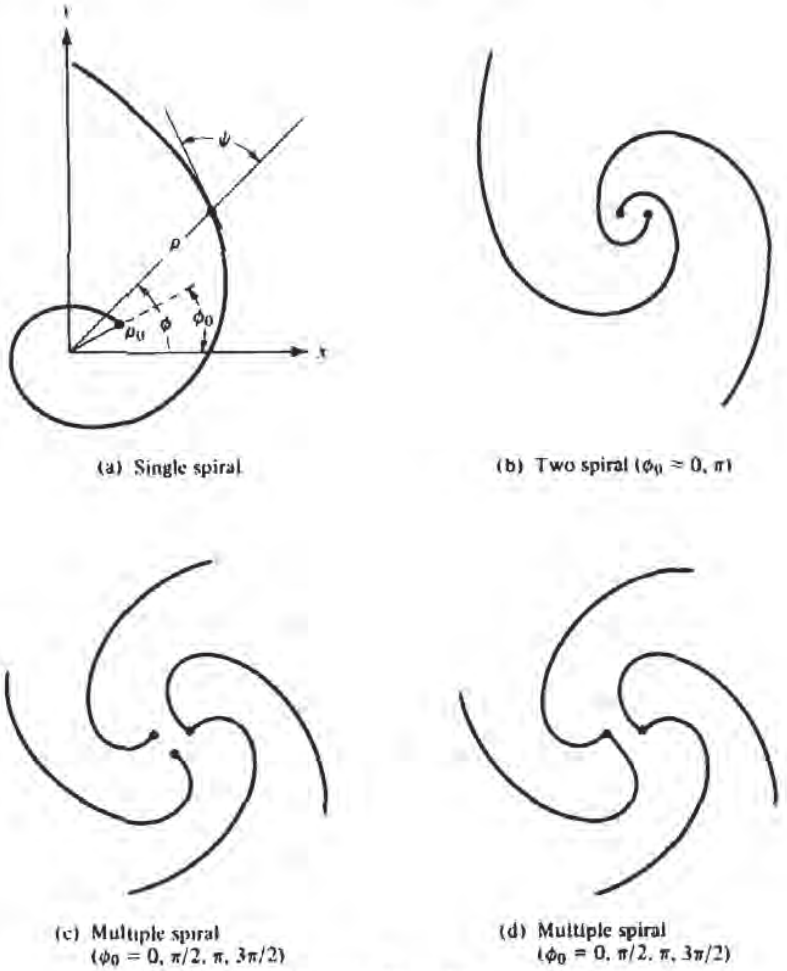
Another form of (11-10) is

$$\phi = \frac{1}{a}\ln\left(\frac{\rho}{A}\right) = \tan\psi \ln\left(\frac{\rho}{A}\right) = \tan\psi(\ln\rho - \ln A) \tag{11-12}$$

where $1/a$ is the rate of expansion of the spiral and ψ is the angle between the radial distance ρ and the tangent to the spiral, as shown in Figure 11.1(a).

It is evident from (11-11) that changing the wavelength is equivalent to varying ϕ_0 which results in nothing more than a pure rotation of the infinite structure pattern. Within limitations imposed by the arm length, similar characteristics have been observed for finite structures. The same result can be concluded by examining (11-12). Increasing the logarithm of the frequency ($\ln f$) by C_0 is equivalent to rotating the structure by $C_0 \tan\psi$. As a result, the pattern is merely rotated but otherwise unaltered. Thus we have frequency independent antennas.

INTEL-1045
U.S. Patent 7,151,430



(a) Single spiral

(b) Two spiral ($\phi_0 = 0, \pi$)

(c) Multiple spiral ($\phi_0 = 0, \pi/2, \pi, 3\pi/2$)

(d) Multiple spiral ($\phi_0 = 0, \pi/2, \pi, 3\pi/2$)

Figure 11.1 Spiral wire antennas.

The total length L of the spiral can be calculated by

$$L = \int_{\rho_0}^{\rho_1} \left[\rho^2 \left(\frac{d\phi}{d\rho} \right)^2 + 1 \right]^{1/2} d\rho \tag{11-13}$$

which reduces, using (11-10), to

$$\boxed{L = (\rho_1 - \rho_0) \sqrt{1 + \frac{1}{a^2}}} \tag{11-14}$$

where ρ_0 and ρ_1 represent the inner and outer radii of the spiral.

Various geometrical arrangements of the spiral have been used to form different antenna systems. If ϕ_0 in (11-10) is 0 and π, the spiral wire antenna takes the form of Figure 11.1(b). The arrangements of Figures 11.1(c) and 11.1(d) are each obtained when $\phi_0 = 0, \pi/2, \pi$, and $3\pi/2$. Numerous other combinations are possible.

An equiangular metallic solid surface, designated as P, can be created by defining the curves of its edges, using (11-10), as

$$\rho_2 = \rho_2' e^{a\phi} \tag{11-15a}$$

$$\rho_3 = \rho_3' e^{a\phi} = \rho_2' e^{a(\phi - \delta)} \tag{11-15b}$$

INTEL-1045
U.S. Patent 7,151,430

where

$$\rho_3' = \rho_2' e^{-a\delta} \tag{11-15c}$$

such that

$$K = \frac{\rho_3}{\rho_2} = e^{-a\delta} < 1 \tag{11-16}$$

The two curves, which specify the edges of the conducting surface, are of identical relative shape with one magnified relative to the other or rotated by an angle δ with respect to the other. The magnification or rotation allows the arm of conductor P to have a finite width, as shown in Figure 11.2(a).

The metallic arm of a second conductor, designated as Q, can be defined by

$$\rho_4 = \rho_4' e^{a\phi} = \rho_2' e^{a(\phi - \pi)} \tag{11-17}$$

where

$$\rho_4' = \rho_2' e^{-a\pi} \tag{11-17a}$$

$$\rho_5 = \rho_5' e^{a\phi} = \rho_4' e^{a(\phi - \delta)} = \rho_2' e^{a(\phi - \pi - \delta)} \tag{11-18}$$

where

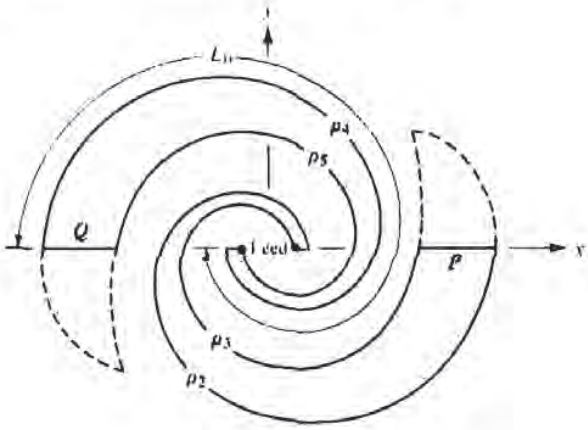
$$\rho_5' = \rho_4' e^{-a\delta} = \rho_2' e^{-a(\pi + \delta)} \tag{11-18a}$$

The system composed of the two conducting arms, P and Q, constitutes a balanced system, and it is shown in Figure 11.2(a). The finite size of the structure is specified by the fixed spiraling length L_0 along the centerline of the arm. The entire structure can be completely specified by the rotation angle δ, the arm length L_0, the rate of spiral $1/a$, and the terminal size ρ_2'. However, it has been found that most characteristics can be described adequately by only three; that is, L_0, ρ_2', and $K = e^{-a\delta}$ as given by (11-16). In addition each arm is usually tapered at its end, shown by dashed lines in Figure 11.2(a), to provide a better matching termination.

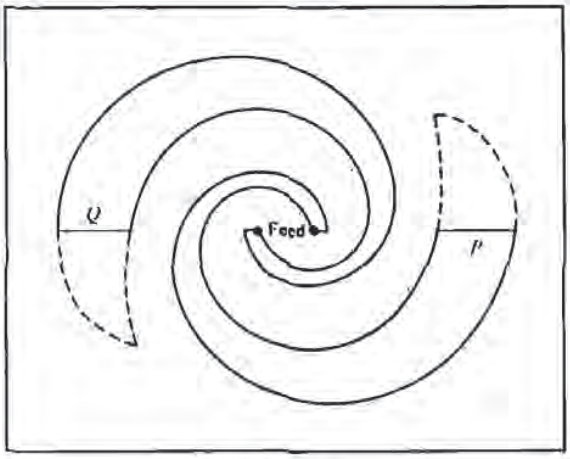
The previous analytical formulations can be used to describe two different antennas. One antenna would consist of two metallic arms suspended in free-space, as shown in Figure 11.2(a), and the other of a spiraling slot on a large conducting plane, as shown in Figure 11.2(b). The second is also usually tapered to provide better matching termination. The slot antenna is the most practical, because it can be conveniently fed by a balanced coaxial arrangement [2] to maintain its overall balancing. The antenna in Figure 11.2(a) with $\delta = \pi/2$ is self-complementary, as defined by Babinet's principle [7], and its input impedance for an infinite structure should be $Z_s = Z_c = 188.5 \simeq 60\pi$ ohms (for discussion of Babinet's Principle see Section 12.8). Experimentally, measured mean input impedances were found to be only about 164 ohms. The difference between theory and experiment is attributed to the finite arm length, finite thickness of the plate, and nonideal feeding conditions.

Spiral slot antennas, with good radiation characteristics, can be built with one-half to three turns. The most optimum design seems to be that with 1.25 to 1.5 turns with an overall length equal to or greater than one wavelength. The rate of expansion should not exceed about 10 per turn. The patterns are bidirectional, single-lobed, broadside (maximum normal to the plane), and must vanish along the directions occupied by the infinite structure. The wave is circularly polarized near the axis of the main lobe over the usable part of the bandwidth. For a fixed cut, the beamwidth will vary with frequency since the pattern rotates. Typical variations are on the order of 10°. In general, however, slot antennas with more broad arms and/or more tightly

INTEL-1045
U.S. Patent 7,151,430



(a) Spiral plate



(b) Spiral slot

Figure 11.2 Spiral plate and slot antennas.

wound spirals exhibit smoother and more uniform patterns with smaller variations in beamwidth with frequency. For symmetrical structures, the pattern is also symmetrical with no tilt to the lobe structure.

To maintain the symmetrical characteristics, the antenna must be fed by an electrically and geometrically balanced line. One method that achieves geometrical balancing requires that the coax is embedded into one of the arms of the spiral. To maintain symmetry, a dummy cable is usually placed into the other arm. No appreciable currents flow on the feed cables because of the rapid attenuation of the fields along the spiral. If the feed line is electrically unbalanced, a balun must be used. This limits the bandwidth of the system.

The polarization of the radiated wave is controlled by the length of the arms. For very low frequencies, such that the total arm length is small compared to the wavelength, the radiated field is linearly polarized. As the frequency increases, the wave becomes elliptically polarized and eventually achieves circular polarization. Since the pattern is essentially unaltered through this frequency range, the polarization change with frequency can be used as a convenient criterion to select the lower cutoff

INTEL-1045
U.S. Patent 7,151,430

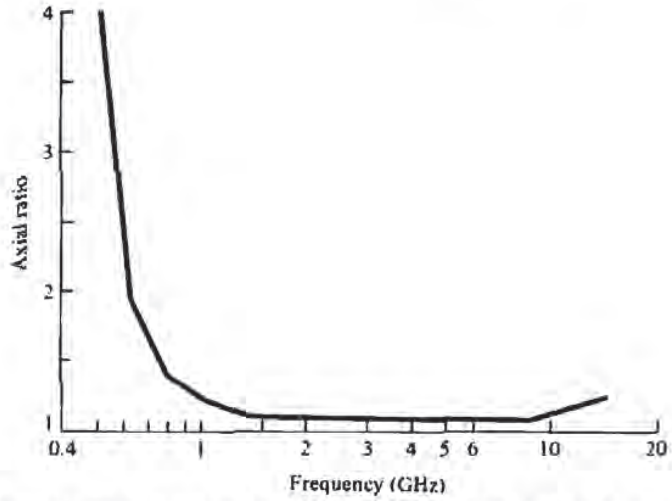


Figure 11.3 On-axis polarization as a function of frequency for one-turn spiral slot. (SOURCE: J. D. Dyson, "The Equiangular Spiral Antenna," *IRE Trans. Antennas Propagat.*, Vol. AP-7, pp. 181–187, April 1959. © (1959) IEEE)

frequency of the usable bandwidth. In many practical cases, this is chosen to be the point where the axial ratio is equal or less than 2 to 1, and it occurs typically when the overall armlength is about one wavelength. A typical variation in axial ratio of the on-axis field as a function of frequency for a one-turn slot antenna is shown in Figure 11.3. The off-axis radiated field has nearly circular polarization over a smaller part of the bandwidth. In addition to the limitation imposed on the bandwidth by the overall length of the arms, another critical factor that can extend or reduce the bandwidth is the construction precision of the feed.

The input impedance of a balanced equiangular slot antenna converges rapidly as the frequency is increased, and it remains reasonably constant for frequencies for which the arm length is greater than about one wavelength. Measured values for a 700–2,500 MHz antenna [2] were about 75–100 ohms with VSWR's of less than 2 to 1 for 50-ohm lines.

For slot antennas radiating in free-space, without dielectric material or cavity backing, typical measured efficiencies are about 98% for arm lengths equal to or greater than one wavelength. Rapid decreases are observed for shorter arms.

11.3.2 Conical Spiral

The shape of a nonplanar spiral can be described by defining the derivative of $f(\theta)$ to be

$$\frac{df}{d\theta} = f'(\theta) = A\delta(\beta - \theta) \tag{11-19}$$

in which β is allowed to take any value in the range $0 \leq \beta \leq \pi$. For a given value of β, (11-19) in conjunction with (11-8) describes a spiral wrapped on a conical surface. The edges of one conical spiral surface are defined by

$$r_2 = r_2' e^{(a \sin \theta_0)\phi} = r_2' e^{b\phi} \tag{11-20a}$$

$$r_3 = r_3' e^{a \sin \theta_0 \phi} = r_2' e^{a \sin \theta_0 (\phi - \delta)} \tag{11-20b}$$

INTEL-1045
U.S. Patent 7,151,430

where

$$r_3' = r_2' e^{-(a \sin \theta_0)\delta} \tag{11-20c}$$

and θ_0 is half of the total included cone angle. Larger values of θ_0 in $0 \leq \theta \leq \pi/2$ represent less tightly wound spirals. These equations correspond to (11-15a)–(11-15c) for the planar surface. The second arm of a balanced system can be defined by shifting each of (11-20a)–(11-20c) by 180°, as was done for the planar surface by (11-17)–(11-18a). A conical spiral metal strip antenna of elliptical polarization is shown in Figure 11.4 [8].

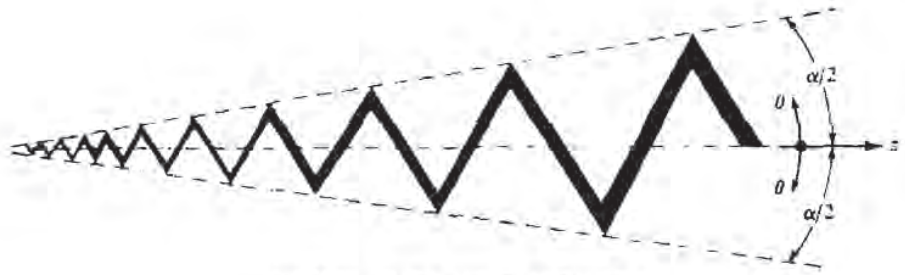
The conducting conical spiral surface can be constructed conveniently by forming, using printed circuit techniques, the conical arms on the dielectric cone which is also used as a support. The feed cable can be bonded to the metal arms which are wrapped around the cone. Symmetry can be preserved by observing the same precautions, like the use of a dummy cable, as was done for the planar surface.

A distinct difference between the planar and conical spirals is that the latter provides unidirectional radiation (single lobe) toward the apex of the cone with the maximum along the axis. Circular polarization and relatively constant impedances are preserved over large bandwidths. Smoother patterns have been observed for unidirectional designs. Conical spirals can be used in conjunction with a ground plane, with a reduction in bandwidth when they are flush-mounted on the plane.

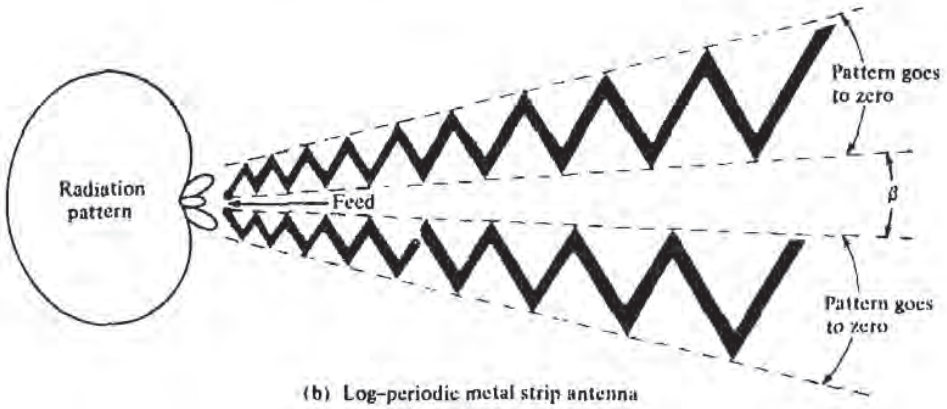


Figure 11.4 Conical spiral metal strip antenna. (SOURCE: *Antennas, Antenna Masts and Mounting Adaptors*, American Electronic Laboratories, Inc., Lansdale, Pa., Catalog 7.5M-7-79. Courtesy of American Electronic Laboratories, Inc., Montgomeryville, PA 18936 USA)

INTEL-1045
U.S. Patent 7,151,430



(a) Metal strip log-periodic configuration



(b) Log-periodic metal strip antenna

Figure 11.5 Typical metal strip log-periodic configuration and antenna structure.

11.4 LOG-PERIODIC ANTENNAS

Another type of an antenna configuration, which closely parallels the frequency independent concept, is the log-periodic structure introduced by DuHamel and Isbell [4]. Because the entire shape of it cannot be solely specified by angles, it is not truly frequency independent.

11.4.1 Planar and Wire Surfaces

A planar log-periodic structure is shown in Figure 11.5(a). It consists of a metal strip whose edges are specified by the angle $\alpha/2$. However, in order to specify the length from the origin to any point on the structure, a distance characteristic must be included.

In spherical coordinates (r, θ, ϕ) the shape of the structure can be written as

$$\theta = \text{periodic function of } [b \ln(r)] \tag{11-21}$$

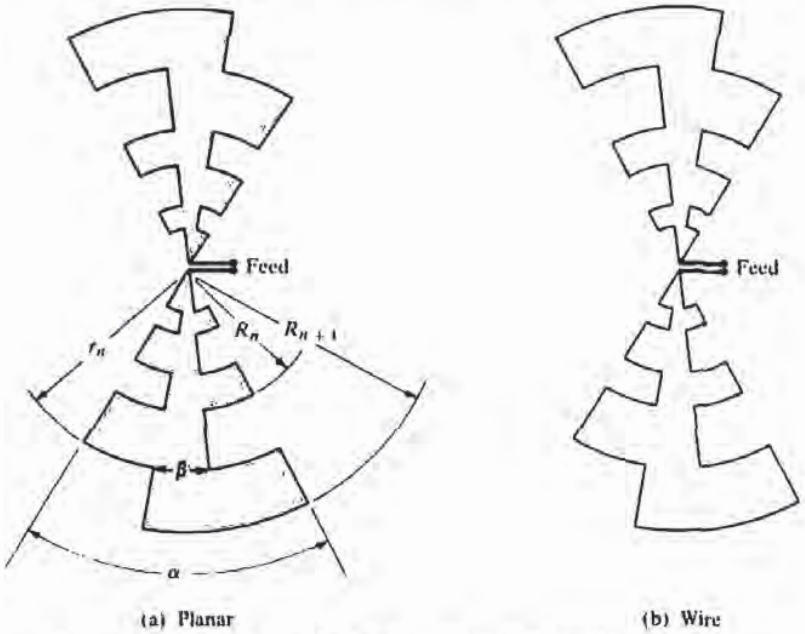
An example of it would be

$$\theta = \theta_0 \sin\left[b \ln\left(\frac{r}{r_0}\right)\right] \tag{11-22}$$

It is evident from (11-22) that the values of θ are repeated whenever the logarithm of the radial frequency $\ln(\omega) = \ln(2\pi f)$ differs by $2\pi/b$. The performance of the system is then periodic as a function of the logarithm of the frequency; thus the name *logarithmic-periodic or log-periodic.*

A typical log-periodic antenna configuration is shown in Figure 11.5(b). It consists of two coplanar arms of the Figure 11.5(a) geometry. The pattern is unidirectional

INTEL-1045
U.S. Patent 7,151,430



(a) Planar (b) Wire

Figure 11.6 Planar and wire logarithmically periodic antennas.

toward the apex of the cone formed by the two arms, and it is linearly polarized. Although the patterns of this and other log-periodic structures are not completely frequency independent, the amplitude variations of certain designs are very slight. Thus practically they are frequency independent.

Log-periodic wire antennas were introduced by DuHamel [4]. While investigating the current distribution on log-periodic surface structures of the form shown in Figure 11.6(a), he discovered that the fields on the conductors attenuated very sharply with distance. This suggested that perhaps there was a strong current concentration at or near the edges of the conductors. Thus removing part of the inner surface to form a wire antenna as shown in Figure 11.6(b) should not seriously degrade the performance of the antenna. To verify this, a wire antenna, with geometrical shape identical to the pattern formed by the edges of the conducting surface, was built and it was investigated experimentally. As predicted, it was found that the performance of this antenna was almost identical to that of Figure 11.6(a); thus the discovery of a much simpler, lighter in weight, cheaper, and less wind resistant antenna. Nonplanar geometries in the form of a V, formed by bending one arm relative to the other, are also widely used.

If the wires or the edges of the plates are linear (instead of curved), the geometries of Figure 11.6 reduce, respectively, to the trapezoidal tooth log-periodic structures of Figure 11.7. These simplifications result in more convenient fabrication geometries with no loss in operational performance. There are numerous other bizarre but practical configurations of log-periodic structures, including log-periodic arrays.

If the geometries of Figure 11.6 use uniform periodic teeth, we define the geometric ratio of the log-periodic structure by

$$\tau = \frac{R_n}{R_{n+1}} \tag{11-23}$$

INTEL-1045
U.S. Patent 7,151,430

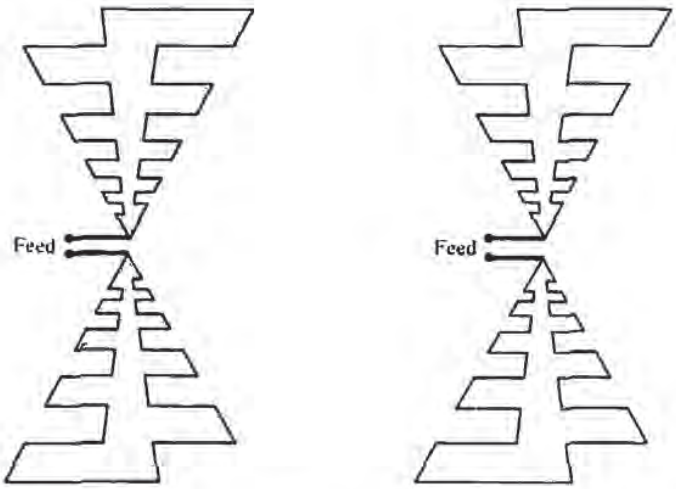


Figure 11.7 Planar and wire trapezoidal toothed log-periodic antennas.

and the width of the antenna slot by

$$\chi = \frac{r_n}{R_{n+1}} \tag{11-24}$$

The geometric ratio τ of (11-23) defines the period of operation. For example, if two frequencies f_1 and f_2 are one period apart, they are related to the geometric ratio τ by

$$\tau = \frac{f_1}{f_2}, \quad f_2 > f_1 \tag{11-25}$$

Extensive studies on the performance of the antenna of Figure 11.6(b) as a function of α, β, τ, and χ, have been performed [9]. In general, these structures performed almost as well as the planar and conical structures. The only major difference is that the log-periodic configurations are linearly polarized instead of circular.

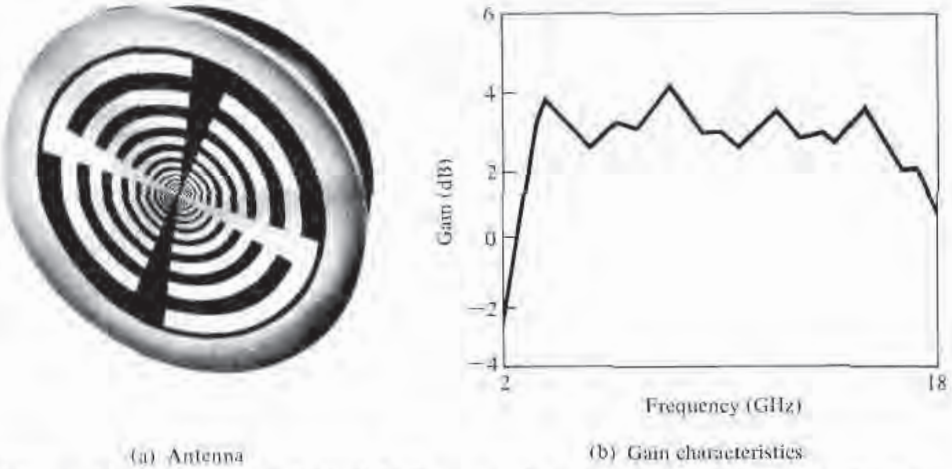
A commercial lightweight, cavity-backed, linearly polarized, flush-mounted log-periodic slot antenna and its associated gain characteristics are shown in Figures 11.8(a) and (b) [8]. Typical electrical characteristics are: VSWR—2:1; *E*-plane beamwidth—70°; *H*-plane beamwidth—70°. The maximum diameter of the cavity is about 2.4 in. (6.1 cm), the depth is 1.75 in. (4.445 cm), and the weight is near 5 oz (0.14 kg).

11.4.2 Dipole Array

To the layman, the most recognized log-periodic antenna structure is the configuration introduced by Isbell [5] which is shown in Figure 11.9(a). It consists of a sequence of side-by-side parallel linear dipoles forming a coplanar array. Although this antenna has similar directivities as the Yagi-Uda array (7–12 dB), they are achievable and maintained over much wider bandwidths. There are, however, major differences between them.

While the geometrical dimensions of the Yagi-Uda array elements do not follow any set pattern, the lengths (l_n's), spacings (R_n's), diameters (d_n's), and even gap

INTEL-1045
U.S. Patent 7,151,430



(a) Antenna (b) Gain characteristics

Figure 11.8 Linearly polarized flush-mounted cavity-backed log-periodic slot antenna and typical gain characteristics. (SOURCE: *Antennas, Antenna Masts and Mounting Adaptors,* American Electronic Laboratories, Inc., Lansdale, Pa., Catalog 7.5M-7-79. Courtesy of American Electronic Laboratories, Inc., Montgomeryville, PA 18936 USA)

spacings at dipole centers (s_n's) of the log-periodic array increase logarithmically as defined by the inverse of the geometric ratio τ. That is,

$$\frac{1}{\tau} = \frac{l_2}{l_1} = \frac{l_{n+1}}{l_n} = \frac{R_2}{R_1} = \frac{R_{n+1}}{R_n} = \frac{d_2}{d_1} = \frac{d_{n+1}}{d_n} = \frac{s_2}{s_1} = \frac{s_{n+1}}{s_n} \tag{11-26}$$

Another parameter that is usually associated with a dipole array is the spacing factor σ defined by

$$\sigma = \frac{R_{n+1} - R_n}{2l_{n+1}} \tag{11-26a}$$

Straight lines through the dipole ends meet to form an angle 2α which is a characteristic of frequency independent structures.

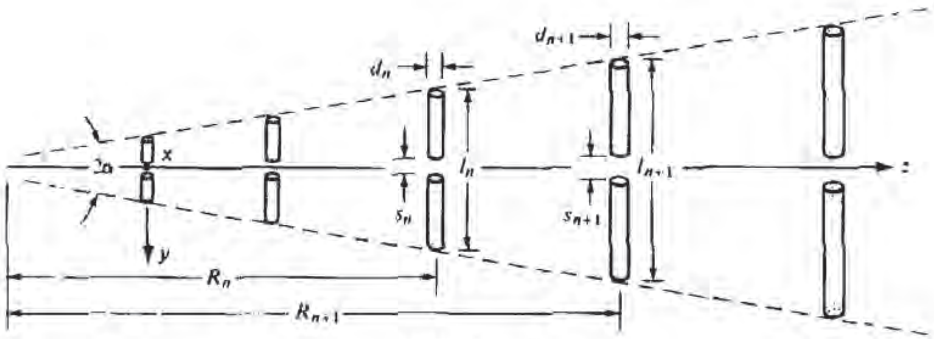
Because it is usually very difficult to obtain wires or tubing of many different diameters and to maintain tolerances of very small gap spacings, constant dimensions in these can be used. These relatively minor factors will not sufficiently degrade the overall performance.

While only one element of the Yagi-Uda array is directly energized by the feed line, while the others operate in a parasitic mode, all the elements of the log-periodic array are connected. There are two basic methods, as shown in Figures 11.9(b) and 11.9(c), which could be used to connect and feed the elements of a log-periodic dipole array. In both cases the antenna is fed at the small end of the structure.

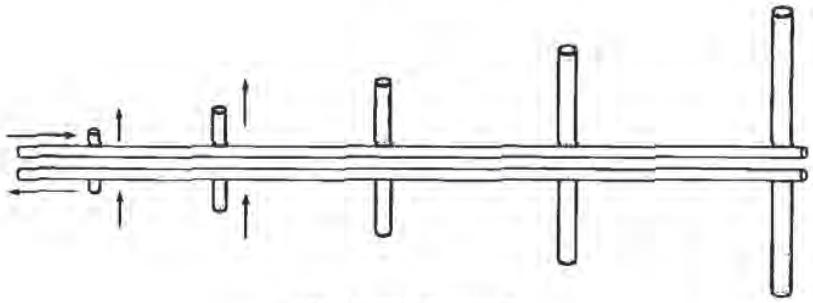
The currents in the elements of Figure 11.9(b) have the same phase relationship as the terminal phases. If in addition the elements are closely spaced, the phase progression of the currents is to the right. This produces an endfire beam in the direction of the longer elements and interference effects to the pattern result.

It was recognized that by mechanically crisscrossing or transposing the feed between adjacent elements, as shown in Figure 11.9(c), a 180° phase is added to the terminal of each element. Since the phase between the adjacent closely spaced short elements is almost in opposition, very little energy is radiated by them and their

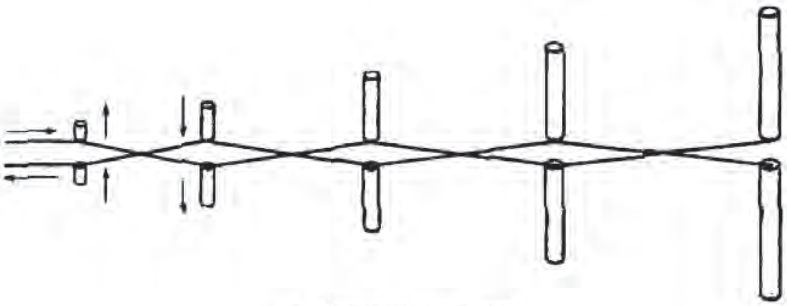
INTEL-1045
U.S. Patent 7,151,430



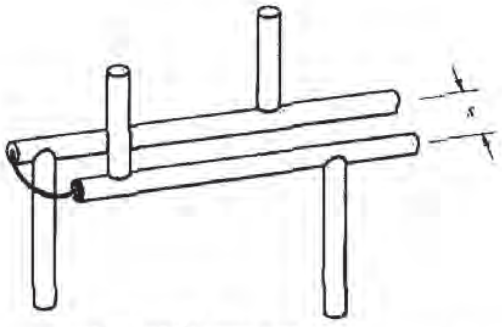
(a) Dipole array



(b) Straight connection



(c) Crisscross connection



(d) Coaxial connection

Figure 11.9 Log-periodic dipole array and associated connections.

INTEL-1045
U.S. Patent 7,151,430

interference effects are negligible. However, at the same time, the longer and larger spaced elements radiate. The mechanical phase reversal between these elements produces a phase progression so that the energy is beamed endfire in the direction of the shorter elements. The most active elements for this feed arrangement are those that are near resonant with a combined radiation pattern toward the vertex of the array.

The feed arrangement of Figure 11.9(c) is convenient provided the input feed line is a balanced line like the two-conductor transmission line. Using a coaxial cable as a feed line, a practical method to achieve the 180° phase reversal between adjacent elements is shown in Figure 11.9(d). This feed arrangement provides a built-in broadband balun resulting in a balanced overall system. The elements and the feeder line of this array are usually made of piping. The coaxial cable is brought to the feed through the hollow part of one of the feeder line pipes. While the outside conductor of the coax is connected to that conductor at the feed, its inner conductor is extended and it is connected to the other pipe of the feeder line.

If the geometrical pattern of the log-periodic array, as defined by (11-26), is to be maintained to achieve a truly log-periodic configuration, an infinite structure would result. However, to be useful as a practical broadband radiator, the structure is truncated at both ends. This limits the frequency of operation to a given bandwidth.

The cutoff frequencies of the truncated structure can be determined by the electrical lengths of the longest and shortest elements of the structure. The lower cutoff frequency occurs approximately when the longest element is $\lambda/2$; however, the high cutoff frequency occurs when the shortest element is nearly $\lambda/2$ only when the active region is very narrow. Usually it extends beyond that element. The active region of the log-periodic dipole array is near the elements whose lengths are nearly or slightly smaller than $\lambda/2$. The role of active elements is passed from the longer to the shorter elements as the frequency increases. Also the energy from the shorter active elements traveling toward the longer inactive elements decreases very rapidly so that a negligible amount is reflected from the truncated end. The movement of the active region of the antenna, and its associated phase center, is an undesirable characteristic in the design of feeds for reflector and lens antennas.

The decrease of energy toward the longer inactive elements is demonstrated in Figure 11.10(a). The curves represent typical computed and measured transmission line voltages (amplitude and phase) on a log-periodic dipole array [10] as a function of distance from its apex. These are feeder-line voltages at the base of the elements of an array with $\tau = 0.95$, $\sigma = 0.0564$, $N = 13$, and $l_n/d_n = 177$. The frequency of operation is such that element No. 10 is $\lambda/2$. The amplitude voltage is nearly constant from the first (the feed) to the eighth element while the corresponding phase is uniformly progressive. Very rapid decreases in amplitude and nonlinear phase variations are noted beyond the eighth element.

The region of constant voltage along the structure is referred to as the *transmission region*, because it resembles that of a matched transmission line. Along the structure, there is about 150° phase change for every $\lambda/4$ free-space length of transmission line. This indicates that the phase velocity of the wave traveling along the structure is $v_p = 0.6u_0$, where u_0 is the free-space velocity. The smaller velocity results from the shunt capacitive loading of the line by the smaller elements. The loading is almost constant per unit length because there are larger spacings between the longer elements.

The corresponding current distribution is shown in Figure 11.10(b). It is noted that the rapid decrease in voltage is associated with strong current excitation of elements 7–10 followed by a rapid decline. The region of high current excitation is

INTEL-1045
U.S. Patent 7,151,430

Figure 11.10 Measured and computed voltage and current distributions on a log-periodic dipole array of 13 elements with frequency such that $l_{10} = \lambda/2$. (SOURCE: R. L. Carrel, "Analysis and Design of the Log-Periodic Dipole Antenna," Ph.D. Dissertation, Elec. Eng. Dept., University of Illinois, 1961, University Microfilms, Inc., Ann Arbor, Michigan)

INTEL-1045
U.S. Patent 7,151,430

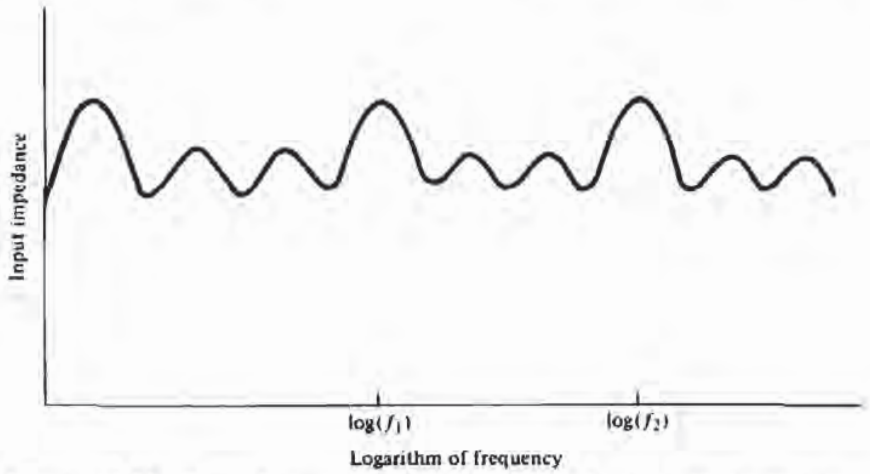


Figure 11.11 Typical input impedance variation of a log-periodic antenna as a function of the logarithm of the frequency.

designated as the *active region*, and it encompasses 4 to 5 elements for this design. The voltage and current excitations of the longer elements (beyond the ninth) are relatively small, reassuring that the truncated larger end of the structure is not affecting the performance. The smaller elements, because of their length, are not excited effectively. As the frequency changes, the relative voltage and current patterns remain essentially the same, but they move toward the direction of the active region.

There is a linear increase in current phase, especially in the active region, from the shorter to the longer elements. This phase shift progression is opposite in direction to that of an unloaded line. It suggests that on the log-periodic antenna structure there is a wave that travels toward the feed forming a unidirectional endfire pattern toward the vertex.

The radiated wave of a single log-periodic dipole array is linearly polarized, and it has horizontal polarization when the plane of the antenna is parallel to the ground. Bidirectional patterns and circular polarization can be obtained by phasing multiple log-periodic dipole arrays. For these, the overall effective phase center can be maintained at the feed.

If the input impedance of a log-periodic antenna is plotted as a function of frequency, it will be repetitive. However, if it is plotted as a function of the *logarithm* of the frequency, it will be *periodic* (not necessarily sinusoidal) with each cycle being exactly identical to the preceding one. Hence the name *log-periodic*, because the variations are *periodic* with respect to the *logarithm* of the frequency. A typical variation of the impedance as a function of frequency is shown in Figure 11.11. Other parameters that undergo similar variations are the pattern, directivity, beamwidth, and side lobe level.

The periodicity of the structure does not ensure broadband operation. However, if the variations of the impedance, pattern, directivity, and so forth within one cycle are made sufficiently small and acceptable for the corresponding bandwidth of the cycle, broadband characteristics are ensured within acceptable limits of variation. The total bandwidth is determined by the number of repetitive cycles for the given truncated structure.

The relative frequency span Δ of each cycle is determined by the geometric ratio

INTEL-1045
U.S. Patent 7,151,430

TABLE 11.1 INPUT RESISTANCES (R_{in} IN OHMS) AND DIRECTIVITIES (dB ABOVE ISOTROPIC) FOR LOG-PERIODIC DIPOLE ARRAYS

α	$\tau = 0.81$		$\tau = 0.89$		$\tau = 0.95$	
	R_{in}(ohms)	D_0(dB)	R_{in}(ohms)	D_0(dB)	R_{in}(ohms)	D_0(dB)
10	98	—	82	9.8	77.5	10.7
12.5	—	—	77	—	—	—
15	—	7.2	—	—	—	—
17.5	—	—	76	7.7	62	8.8
20	—	—	74	—	—	—
25	—	—	63	7.2	—	8.0
30	80	—	64	—	54	—
35	—	—	56	6.5	—	—
45	65	5.2	59	6.2	—	—

SOURCE: D. E. Isbell, "Log Periodic Dipole Arrays," *IRE Trans. Antennas Propagat.*, Vol. AP-8, pp. 260–267, May 1960, © (1960) IEEE.

as defined by (11-25) and (11-26).* Taking the logarithm of both sides in (11-25) reduces to

$$\Delta = \ln(f_2) - \ln(f_1) = \ln\left(\frac{1}{\tau}\right) \tag{11-27}$$

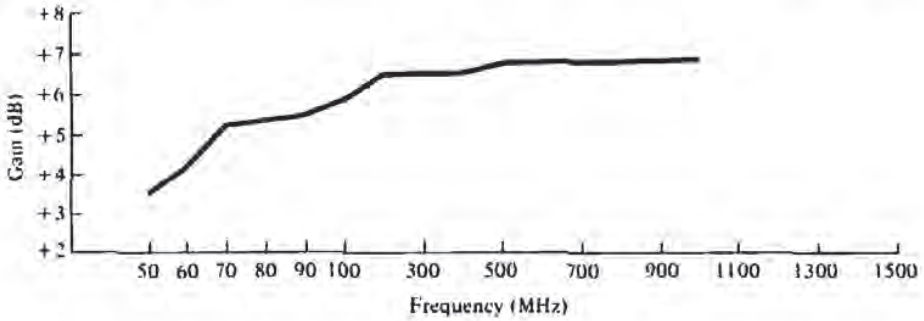
The variations that occur within a given cycle ($f_1 \le f \le f_2 = f_1/\tau$) will repeat identically at other cycles of the bandwidth defined by $f_1/\tau^{n-1} \le f \le f_1/\tau^n$, $n = 1, 2, 3, \ldots$.

Typical designs of log-periodic dipole arrays have apex half angles of $10° \le \alpha \le 45°$ and $0.95 \ge \tau \ge 0.7$. There is a relation between the values of α and τ. As α increases, the corresponding τ values decrease, and vice versa. Larger values of α or smaller values of τ result in more compact designs which require smaller number of elements separated by larger distances. In contrast, smaller values of α or larger values of τ require a larger number of elements that are closer together. For this type of a design, there are more elements in the active region which are nearly $\lambda/2$. Therefore the variations of the impedance and other characteristics as a function of frequency are smaller, because of the smoother transition between the elements, and the gains are larger.

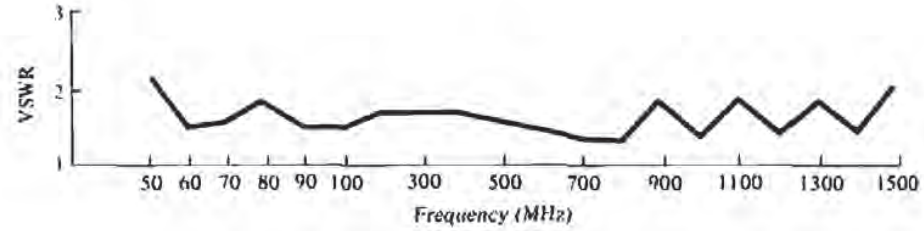
Experimental models of log-periodic dipole arrays have been built and measurements were made [5]. The input impedances (purely resistive) and corresponding directivities (*above isotropic*) for three different designs are listed in Table 11.1. Larger directivities can be achieved by arraying multiple log-periodic dipole arrays. There are other configurations of log-periodic dipole array designs, including those with V instead of linear elements [11]. This array provides moderate bandwidths with good directivities at the higher frequencies, and it is widely used as a single TV antenna covering the entire frequency spectrum from the lowest VHF channel (54 MHz) to the highest UHF (806 MHz). Typical gain, VSWR, and E- and H-plane half-

*In some cases, the impedance (but not the pattern) may vary with a period which is one-half of (11-27). That is, $\Delta = \frac{1}{2}\ln(1/\tau)$.

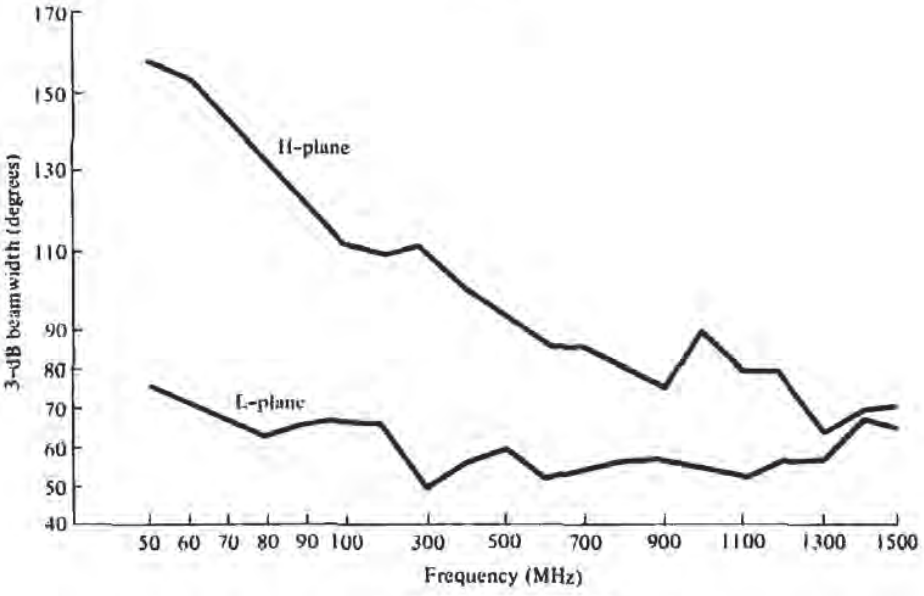
INTEL-1045
U.S. Patent 7,151,430



(a) Gain



(b) VSWR



(c) Half-power beamwidth

Figure 11.12 Typical gain, VSWR, and half-power beamwidth of commercial log-periodic dipole arrays. (SOURCE: *Antennas, Antenna Masts and Mounting Adaptors*, American Electronic Laboratories, Inc., Lansdale, Pa., Catalog 7.5M-7-79. Courtesy of American Electronic Laboratories, Inc., Montgomeryville, PA 18936 USA)

power beamwidths of commercial log-periodic dipole arrays are shown in Figures 11.12(a), (b), (c), respectively [8]. The overall length of each of these antennas is about 105 in. (266.70 cm) while the largest element in each has an overall length of about 122 in. (309.88 cm). The weight of each antenna is about 31 lb (≈14 kg).

INTEL-1045
U.S. Patent 7,151,430

11.4.3 Design of Dipole Array

The ultimate goal of any antenna configuration is the design that meets certain specifications. Probably the most introductory, complete, and practical design procedure for a log-periodic dipole array is that by Carrel [10]. To aid in the design, he has a set of curves and nomographs. The general configuration of a log-periodic array is described in terms of the design parameters τ, α, and σ related by

$$\alpha = \tan^{-1}\left[\frac{1-\tau}{4\sigma}\right] \tag{11-28}$$

Once two of them are specified, the other can be found. Directivity (in dB) contour curves as a function of τ for various values of σ are shown in Figure 11.13.

The original directivity contour curves in [10] are in error because the expression for the E-plane field pattern in [10] is in error. To correct the error, the leading $\sin(\theta)$ function in front of the summation sign of equation 47 in [10] should be in the denominator and not in the numerator [i.e., replace $\sin\theta$ by $1/\sin(\theta)$] [12]. The influence of this error in the contours of Figure 11.13 is variable and leads to 1–2 dB higher directivities. However it has been suggested that, as an average, the directivity of each original contour curve be reduced by about 1 dB. This has been implemented already, and the curves in Figure 11.13 are more accurate as they now appear.

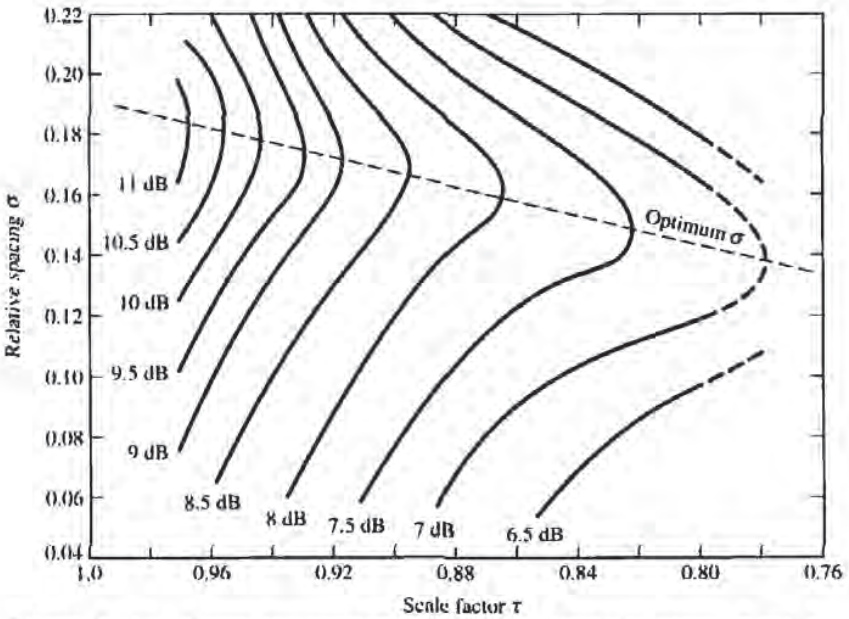


Figure 11.13 Computed contours of constant directivity versus σ and τ for log periodic dipole arrays. (SOURCE: R. L. Carrel, "Analysis and Design of the Log-Periodic Dipole Antenna," Ph.D. Dissertation, Elec. Eng. Dept., University of Illinois, 1961, University Microfilms, Inc., Ann Arbor Michigan)

Note: The initial curves led to designs whose directivities are 1-2 dB too high. They have been reduced by an average of 1dB (see P. C. Butson and G. T. Thompson, "A Note on the Calculation of the Gain of Log-Periodic Dipole Antennas," *IEEE Trans. Antennas Propagat.*, AP-24, pp. 105–106, January 1976).

INTEL-1045
U.S. Patent 7,151,430

A. Design Equations

In this section a number of equations will be introduced that can be used to design a log-periodic dipole array.

While the bandwidth of the system determines the lengths of the shortest and longest elements of the structure, the width of the active region depends on the specific design. Carrel [10] has introduced a semiempirical equation to calculate the bandwidth of the active region B_{ar} related to α and τ by

$$B_{ar} = 1.1 + 7.7(1 - \tau)^2 \cot \alpha \tag{11-29}$$

In practice a slightly larger bandwidth (B_s) is usually designed than that which is required (B). The two are related by

$$B_s = BB_{ar} = B[1.1 + 7.7(1 - \tau)^2 \cot \alpha] \tag{11-30}$$

where

B_s = designed bandwidth
B = desired bandwidth
B_{ar} = active region bandwidth

The total length of the structure L, from the shortest (l_{min}) to the longest (l_{max}) element, is given by

$$L = \frac{\lambda_{max}}{4}\left(1 - \frac{1}{B_s}\right)\cot \alpha \tag{11-31}$$

where

$$\lambda_{max} = 2l_{max} = \frac{v}{f_{min}} \tag{11-31a}$$

From the geometry of the system, the number of elements are determined by

$$N = 1 + \frac{\ln(B_s)}{\ln(1/\tau)} \tag{11-32}$$

The center-to-center spacing s of the feeder line conductors can be determined by specifying the required input impedance (assumed to be real), and the diameter of the dipole elements and the feeder line conductors. To accomplish this, we first define an average characteristic impedance of the elements given by

$$Z_a = 120\left[\ln\left(\frac{l_n}{d_n}\right) - 2.25\right] \tag{11-33}$$

where l_n/d_n is the length-to-diameter ratio of the nth element of the array. For an ideal log-periodic design, this ratio should be the same for all the elements of the array. Practically, however, the elements are usually divided into one, two, three or more groups with all the elements in each group having the same diameter but not the same length. The number of groups is determined by the total number of elements of the array. Usually three groups (for the small, middle, and large elements) should be sufficient.

INTEL-1045
U.S. Patent 7,151,430

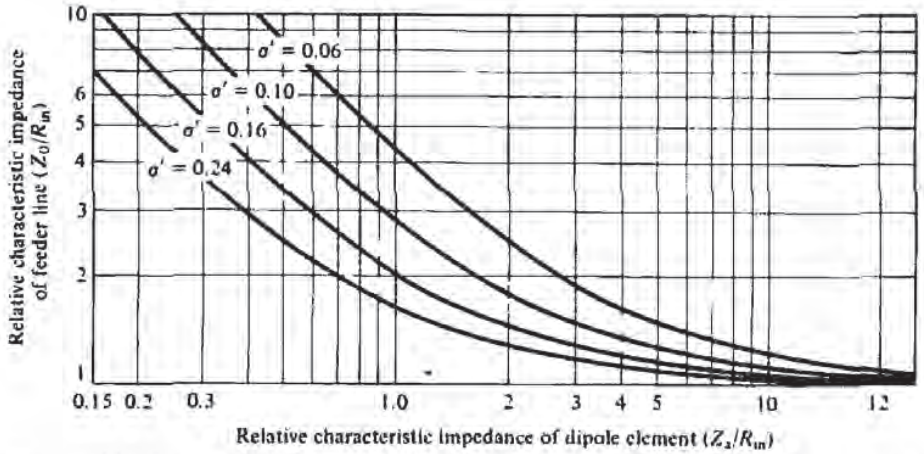


Figure 11.14 Relative characteristic impedance of a feeder line as a function of relative characteristic impedance of dipole element. (SOURCE: R. L. Carrel, "Analysis and Design of the Log-Periodic Dipole Antenna," Ph.D. Dissertation, Elec. Eng. Dept., University of Illinois, 1961, University Microfilms, Inc., Ann Arbor, Michigan)

The effective loading of the dipole elements on the input line is characterized by the graphs shown in Figure 11.14 where

$\sigma' = \sigma/\sqrt{\tau}$ = relative mean spacing

Z_a = average characteristic impedance of the elements

R_{in} = input impedance (real)

Z_0 = characteristic impedance of the feeder line

The center-to-center spacing s between the two rods of the feeder line, each of identical diameter d, is determined by

$$s = d \cosh\left(\frac{Z_0}{120}\right) \tag{11-34}$$

B. Design Procedure

A design procedure is outlined here, based on the equations introduced above and in the previous page, and assumes that the directivity (in dB), input impedance R_{in} (real), diameter of elements of feeder line (d), and the lower and upper frequencies ($B = f_{max}/f_{min}$) of the bandwidth are specified. It then proceeds as follows:

1. Given D_0 (dB), determine σ and τ from Figure 11.13.
2. Determine α using (11-28).
3. Determine B_{ar} using (11-29) and B_s using (11-30).
4. Find L using (11-31) and N using (11-32).
5. Determine Z_a using (11-33) and $\sigma' = \sigma/\sqrt{\tau}$.
6. Determine Z_0/R_{in} using Figure 11.14.
7. Find s using (11-34).

INTEL-1045
U.S. Patent 7,151,430

Example 11.1

Design a log-periodic dipole antenna, of the form shown in Figure 11.9(d), to cover all the VHF TV channels (starting with 54 MHz for channel 2 and ending with 216 MHz for channel 13. See Appendix IX.) The desired directivity is 8 dB and the input impedance is 50 ohms (ideal for a match to 50-ohm coaxial cable). The elements should be made of aluminum tubing with $\frac{1}{4}$ in. (1.9 cm) outside diameter for the largest element and the feeder line and $\frac{3}{16}$ in. (0.48 cm) for the smallest element. These diameters yield identical l/d ratios for the smallest and largest elements.

SOLUTION

1. From Figure 11.13, for $D_0 = 8$ dB the optimum σ is $\sigma = 0.157$ and the corresponding τ is $\tau = 0.865$.
2. Using (11-28)

$$\alpha = \tan^{-1}\left[\frac{1 - 0.865}{4(0.157)}\right] = 12.13^\circ \simeq 12^\circ$$

3. Using (11-29)

$$B_{ar} = 1.1 + 7.7(1 - 0.865)^2 \cot(12.13^\circ) = 1.753$$

and from (11-30)

$$B_s = BB_{ar} = \frac{216}{54}(1.753) = 4(1.753) = 7.01$$

4. Using (11-31a)

$$\lambda_{max} = \frac{v}{f_{min}} = \frac{3 \times 10^8}{54 \times 10^6} = 5.556 \text{ m } (18.227 \text{ ft})$$

From (11-31)

$$L = \frac{5.556}{4}\left(1 - \frac{1}{7.01}\right)\cot(12.13^\circ) = 5.541 \text{ m } (18.178 \text{ ft})$$

and from (11-32)

$$N = 1 + \frac{\ln(7.01)}{\ln(1/0.865)} = 14.43 \text{ (14 or 15 elements)}$$

5. $$\sigma' = \frac{\sigma}{\sqrt{\tau}} = \frac{0.157}{\sqrt{0.865}} = 0.169$$

At the lowest frequency

$$l_{max} = \frac{\lambda_{max}}{2} = \frac{18.227}{2} = 9.1135 \text{ ft}$$

$$\frac{l_{max}}{d_{max}} = \frac{9.1135(12)}{0.75} = 145.816$$

Using (11-33)

$$Z_a = 120[\ln(145.816) - 2.25] = 327.88 \text{ ohms}$$

INTEL-1045
U.S. Patent 7,151,430

Thus

$$\frac{Z_a}{R_{in}} = \frac{327.88}{50} = 6.558$$

6. From Figure 11.14

$$Z_0 = 1.2R_{in} = 1.2(50) = 60 \text{ ohms}$$

7. Using (11-34), assuming the feeder line conductor is made of the same size tubing as the largest element of the array, the center-to-center spacing of the feeder conductors is

$$s = \frac{3}{4}\cosh\left(\frac{60}{120}\right) = 0.846 \simeq 0.85 \text{ in.}$$

which allows for a 0.1-in. separation between their conducting surfaces.

For such a high-gain antenna, this is obviously a good practical design. If a lower gain is specified and designed for, a smaller length will result.

C. Design and Analysis Computer Program

A computer program entitled LOG-PERIODIC DIPOLE ARRAY has been developed based on the design equations of (11-28)–(11-34), and Figures 11.13 and 11.14, to design a log-periodic dipole array whose geometry is shown in Figure 11.9(a). Although most of the program is based on the same design equations as outlined in the design subsection, this program takes into account more design specifications than those included in the previous design procedure, and it is more elaborate. Once the design is completed, the computer program can be used to analyze the design of the antenna. It is included at the end of this chapter, and the listing is found in the computer disc available with this book. The program has been developed based on input specifications, which are listed in the program at the end of the chapter. It can be used as a design tool to determine the geometry of the array (including the number of elements and their corresponding lengths, diameters, and positions) along with the radiation characteristics of the array (including input impedance, VSWR, directivity, front-to-back ratio, E- and H-plane patterns, etc.) based on desired specifications. The input data includes the desired directivity, lower and upper frequency of the operating band, length-to-diameter ratio of the elements, characteristic impedance of the input transmission line, desired input impedance, termination (load) impedance, etc. These and others are listed in the program at the end of the chapter.

The program assumes that the current distribution on each antenna element is sinusoidal. This approximation would be very accurate if the elements were very far from each other. However, in the active region the elements are usually separated by a distance of about 0.1λ when $\alpha = 15°$ and $\tau = 0.9$. Referring to Figure 8.21, one can see that two $\lambda/2$ dipoles separated by 0.1λ have a mutual impedance (almost real) of about 70 ohms. If this mutual impedance is high compared to the resistance of the transmission line (not the characteristic impedance), then the primary method of coupling energy to each antenna will be through the transmission line. If the mutual impedance is high compared to the self-impedance of each element, then the effect on the radiation pattern should be small. In practice, this is usually the case, and the approximation is relatively good. However, an integral equation formulation with a

INTEL-1045
U.S. Patent 7,151,430

Moment Method numerical solution would be more accurate. The program uses (8-60a) for the self-resistance and (8-60b) for the self-reactance. It uses (8-68) for the mutual impedance, which for the side-by-side configuration reduces to the sine and cosine integrals in [13], similar in form to (8-71a)–(8-71e) for the $l = \lambda/2$ dipole.

The geometry of the designed log-periodic dipole array is that of Figure 11.9, except that the program also allows for an input transmission line (connected to the first/shortest element), a termination transmission line (extending beyond the last/longest element), and a termination (load) impedance. The length of the input transmission line changes the phase of computed data (such as voltage, current, reflection coefficient, etc.) while its characteristic impedance is used to calculate the VSWR, which in turn affects the input impedance measured at the source. The voltages and currents are found based on the admittance method of Kyle [14]. The termination transmission line and the termination (load) impedance allow for the insertion of a matching section whose primary purpose is to absorb any energy which manages to continue past the active region. Without the termination (load) impedance, this energy would be reflected along the transmission line back into the active region where it would affect the radiation characteristics of the array design and performance.

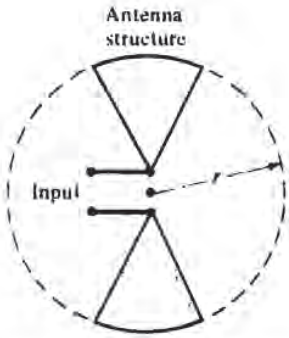
In designing the array, the user has the choice to select σ and τ (but not the directivity) or to select the directivity (but not σ and τ). In the latter case, the program finds σ and τ by assuming an *optimum design* as defined by the dashed line of Figure 11.13. For the geometry of the array, the program assumes that the elements are placed along the z-axis (with the shortest at $z = 0$ and the longest along the positive z-axis). Each linear element of the array is directed along the y-axis (i.e., the array lies on the yz-plane). The angle θ is measured from the z axis toward the xy-plane while angle ϕ is measured from the x-axis (which is normal to the plane of the array) toward the y-axis along the xy-plane. The E-plane of the array is the yz-plane ($\phi = 90°, 270°$; $0° \leq \theta \leq 180°$) while the H-plane is the xz-plane ($\phi = 0°, 180°$; $0° \leq \theta \leq 180°$).

11.5 FUNDAMENTAL LIMITS OF ELECTRICALLY SMALL ANTENNAS

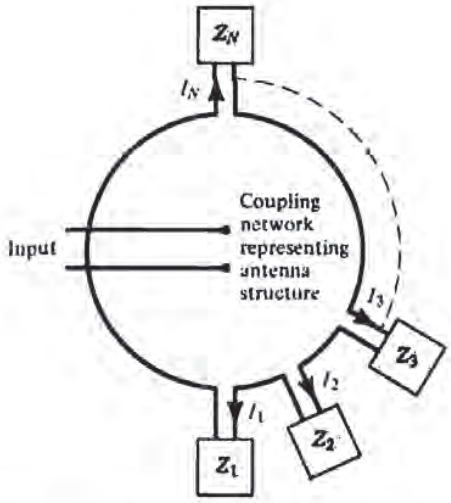
In all areas of electrical engineering, especially in electronic devices and computers, the attention has been shifted toward miniaturization. Electromagnetics, and antennas in particular, are of no exception. A large emphasis in the last few years has been placed toward electrically small antennas, including printed board designs. However, there are fundamental limits as to how small the antenna elements can be made. The basic limitations are imposed by the free-space wavelength to which the antenna element must couple to, which has not been or is expected to be miniaturized [15].

An excellent paper on the fundamental limits in antennas has been published [15], and most of the material in this section is drawn from it. It reviews the limits of electrically small, superdirective, super-resolution, and high-gain antennas. The limits on electrically small antennas are derived by assuming that the entire antenna structure (with a largest linear dimension of $2r$), and its transmission line and oscillator are all enclosed within a sphere of radius r as shown in Figure 11.15(a). Because of the arbitrary current or source distribution of the antenna inside the sphere, its radiated field outside the sphere is expressed as a complete set of orthogonal spherical vector waves or modes. For vertically polarized omnidirectional antennas, only TM_{m0} circularly symmetric (no azimuthal variations) modes are required. Each mode is used to represent a spherical wave which propagates in the outward radial direction. This approach was introduced first by Chu [16], and it was followed by Harrington [17].

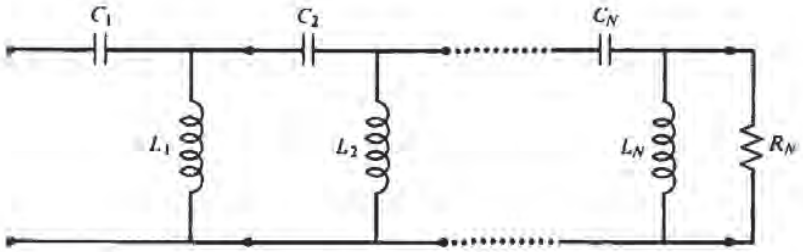
INTEL-1045
U.S. Patent 7,151,430



(a) Biconical antenna within a sphere (after C. J. Chu [13])



(b) Equivalent network of a vertically-polarized omnidirectional antenna (after C. J. Chu [13])



(c) Equivalent circuit for N spherical modes

Figure 11.15 Antenna within a sphere of radius r, and its equivalent circuit modeling. (SOURCE: C. J. Chu, "Physical Limitations of Omnidirectional Antennas," *J. Appl. Phys.*, Vol. 19, pp. 1163–1175, December 1948)

Earlier papers on the fundamental limitations and performance of small antennas were published by Wheeler [18]–[20]. He derived the limits of a small dipole and a small loop (used as a magnetic dipole) from the limitations of a capacitor and an inductor, respectively. The capacitor and inductor were chosen to occupy, respectively, volumes equal to those of the dipole and the loop.

Using the mathematical formulation introduced by Chu [16], the source or current distribution of the antenna system inside the sphere is not uniquely determined by the field distribution outside the sphere. Since it is possible to determine an infinite number of different source or current distributions inside the sphere, for a given field configuration outside the sphere, Chu [16] confined his interest to the most favorable source distribution and its corresponding antenna structure that could exist within the sphere. This approach was taken to minimize the details and to simplify the task of identifying the antenna structure. It was also assumed that the desired current or source distribution minimizes the amount of energy stored inside the sphere so that the input impedance at a given frequency is resistive.

Because the spherical wave modes outside the sphere are orthogonal, the total energy (electric or magnetic) outside the sphere and the complex power transmitted across the closed spherical surface are equal, respectively, to the sum of the energies

INTEL-1045
U.S. Patent 7,151,430

and complex powers associated with each corresponding spherical mode. Therefore there is no coupling, in energy or power, between any two modes outside the sphere. As a result, the space outside the sphere can be replaced by a number of independent equivalent circuits as shown in Figure 11.15(b). The number of equivalent circuits is equal to the number of spherical wave modes outside the sphere, plus one. The terminals of each equivalent circuit are connected to a box which represents the inside of the sphere, and from inside the box a pair of terminals are drawn to represent the input terminals. Using this procedure, the antenna space problem has been reduced to one of equivalent circuits.

The radiated power of the antenna is calculated from the propagating modes while all modes contribute to the reactive power. When the sphere (which encloses the antenna element) becomes very small, there exist no propagating modes. Therefore the Q of the system becomes very large since all modes are evanescent (below cutoff) and contribute very little power. However, unlike closed waveguides, each evanescent mode here has a real part (even though it is very small).

For a lossless antenna (radiation efficiency $e_{cd} = 100\%$), the equivalent circuit of each spherical mode is a single network section with a series C and a shunt L. The total circuit is a ladder network of $L - C$ sections (one for each mode) with a final shunt resistive load, as shown in Figure 11.15(c). The resistive load is used to represent the normalized antenna radiation resistance.

From this circuit structure, the input impedance is found. The Q of each mode is formed by the ratio of its stored to its radiated energy. When several modes are supported, the Q is formed from the contributions of all the modes.

It has been shown that the higher order modes within a sphere of radius r become evanescent when $kr < 1$. Therefore the Q of the system, for the lowest order TM mode, reduces to [15]

$$Q = \frac{1 + 2(kr)^2}{(kr)^3[1 + (kr)^2]} \overset{kr \ll 1}{\simeq} \frac{1}{(kr)^3} \tag{11-35}$$

When two modes are excited, one TE and the other TM, the values of Q are halved. Equation (11-35), which relates the lowest achievable Q to the largest linear dimension of an electrically small antenna, is independent of the geometrical configuration of the antenna within the sphere of radius r. The shape of the radiating element within the bounds of the sphere only determines whether TE, TM, or TE and TM modes are excited. *Therefore (11-35) represents the fundamental limit on the electrical size of an antenna.* In practice, this limit is only approached but is never exceeded or even equaled.

The losses of an antenna can be taken into account by including a loss resistance in series with the radiation resistance, as shown by the equivalent circuits of Figures 2.21(b) and 2.22(b). This influences the Q of the system and the antenna radiation efficiency as given by (2-90).

Computed values of Q versus kr for idealized antennas enclosed within a sphere of radius r, and with radiation efficiences of $e_{cd} = 100$, 50, 10, and 5, are shown plotted in Figure 11.16. These curves represent the minimum values of Q that can be obtained from an antenna whose structure can be enclosed within a sphere of radius r and whose radiated field, outside the sphere, can be represented by a single spherical wave mode.

INTEL-1045
U.S. Patent 7,151,430

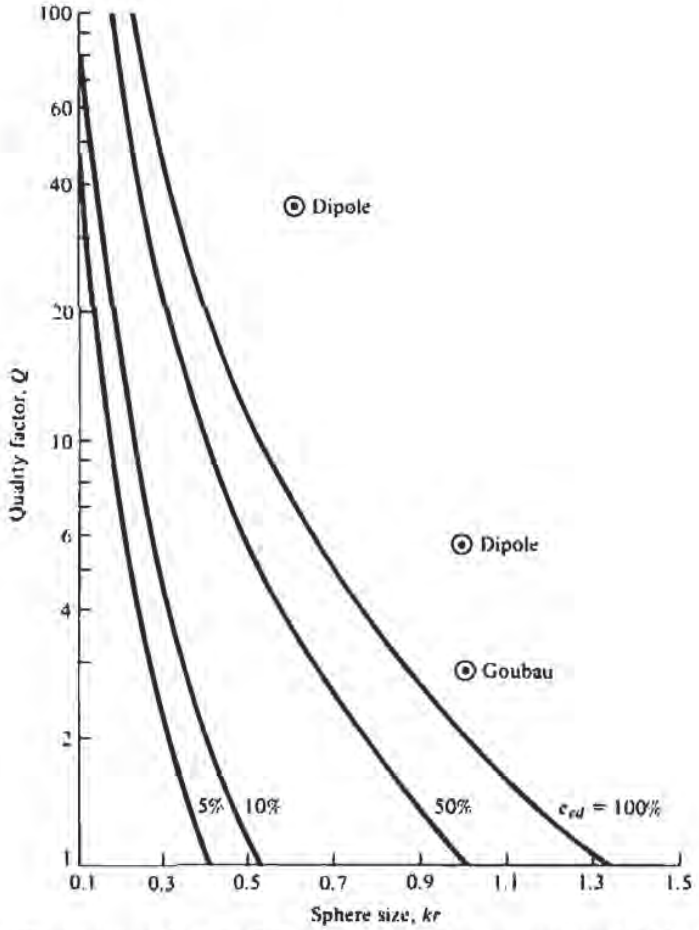


Figure 11.16 Fundamental limits of Q versus antenna size (enclosed within a sphere of radius r) for single-mode antennas of various radiation efficiencies. (SOURCE: R. C. Hansen, "Fundamental Limitations in Antennas," *Proc. IEEE*, Vol. 69, No. 2, February 1981. © (1981) IEEE)

For antennas with equivalent circuits of fixed values, the fractional bandwidth is related to the Q of the system by

$$\text{fractional bandwidth} = \text{FBW} = \frac{\Delta f}{f_0} = \frac{1}{Q} \tag{11-36}$$

where

f_0 = center frequency
Δf = bandwidth

The relationship of (11-36) is valid for $Q \gg 1$ since the equivalent resonant circuit with fixed values is a good approximation for an antenna. For values of $Q < 2$, (11-36) is not accurate.

To compare the results of the minimum Q curves of Figure 11.16 with values of practical antenna structures, data points for a small linear dipole and a Goubau [21]

INTEL-1045
U.S. Patent 7,151,430

antenna are included in the same figure. For a small linear dipole of length l and wire radius a, its impedance is given by [15]

$$Z_{in} = 20\pi^2\left(\frac{l}{\lambda}\right)^2 - j120\frac{\left[\ln\left(\frac{l}{2a}\right) - 1\right]}{\tan\left(\pi\frac{l}{\lambda}\right)} \tag{11-37}$$

and its corresponding Q by

$$Q = \frac{\left[\ln\left(\frac{l}{2a}\right) - 1\right]}{\left(\pi\frac{l}{\lambda}\right)^2 \tan\left(\pi\frac{l}{\lambda}\right)} \tag{11-38}$$

The real part in (11-37) is identical to (4-37). The computed Q values of the small dipole were for $kl/2 = kr \simeq 0.62$ and 1.04 with $l/2a = l/d = 50$, and of the Goubau antenna were for $kr \simeq 1.04$.

It is apparent that the Q's of the dipole are much higher than the corresponding values of the minimum Q curves even for the 100% efficient antennas. However the Goubau antenna, of the same radius sphere, demonstrates a lower value of Q and approaches the values of the 100% minimum Q curve. This indicates that the fractional bandwidth of the Goubau antenna, which is inversely proportional to its Q as defined by (11-36), is higher than that of a dipole enclosed within the same radius sphere. In turn, the bandwidth of an idealized antenna, enclosed within the same sphere, is even larger.

From the above, it is concluded that *the bandwidth of an antenna (which can be closed within a sphere of radius r) can be improved only if the antenna utilizes efficiently, with its geometrical configuration, the available volume within the sphere.* The dipole, being a one-dimensional structure, is a poor utilizer of the available volume within the sphere. However a Goubau antenna, being a clover leaf dipole with coupling loops over a ground plane (or a double cover leaf dipole without a ground plane), is a more effective design for utilizing the available three-dimensional space within the sphere. A design that utilizes the space even more efficiently than the Goubau antenna would possess a lower Q and a higher fractional bandwidth. Ultimately, the values would approach the minimum Q curves. In practice, these curves are only approached but are never exceeded or even equaled.

References

1. V. H. Rumsey, "Frequency Independent Antennas," *1957 IRE National Convention Record*, pt. 1, pp. 114–118.
2. J. D. Dyson, "The Equiangular Spiral Antenna," *IRE Trans. Antennas Propagat.*, Vol. AP-7, pp. 181–187, April 1959.
3. J. D. Dyson, "The Unidirectional Equiangular Spiral Antenna," *IRE Trans. Antennas Propagat.*, Vol. AP-7, pp. 329–334, October 1959.
4. R. H. DuHamel and D. E. Isbell, "Broadband Logarithmically Periodic Antenna Structures," *1957 IRE National Convention Record*, pt. 1, pp. 119–128.
5. D. E. Isbell, "Log Periodic Dipole Arrays," *IRE Trans. Antennas Propagat.*, Vol. AP-8, pp. 260–267, May 1960.

INTEL-1045
U.S. Patent 7,151,430

6. R. S. Elliott, "A View of Frequency Independent Antennas," *The Microwave Journal*, pp. 61–68, December 1962.
7. H. G. Booker, "Slot Aerials and Their Relation to Complementary Wire Aerials," *Journal of IEE* (London), Vol. 93, pt. IIIA, April 1946.
8. *Antennas, Antenna Masts and Mounting Adaptors*, American Electronic Laboratories, Inc., Lansdale, PA, Catalog 7.5M-7-79.
9. R. H. DuHamel and F. R. Ore, "Logarithmically Periodic Antenna Designs," *IRE National Convention Record*, pt. 1, pp. 139–152, 1958.
10. R. L. Carrel, "Analysis and Design of the Log-Periodic Dipole Antenna," Ph.D. Dissertation, Elec. Eng. Dept., University of Illinois, 1961, University Microfilms, Inc., Ann Arbor, MI.
11. P. E. Mayes and R. L. Carrel, "Log-Periodic Resonant-V Arrays," presented at WESCON, San Francisco, California, August 22–25, 1961.
12. P. C. Budson and G. T. Thompson, "A Note on the Calculation of the Gain of Log-Periodic Dipole Antennas," *IEEE Trans. Antennas Propagat.*, AP-24, pp. 105–106, January 1976.
13. H. E. King, "Mutual Impedance of Unequal Length Antennas in Echelon," *IRE Trans. Antennas Propagat.*, Vol. AP-5, pp. 306–313, July 1957.
14. R. H. Kyle, "Mutual Coupling Between Log-Periodic Dipole Antennas," General Electric Tech. Info. Series, Report No. R69ELS-3, December 1968.
15. R. C. Hansen, "Fundamental Limitations in Antennas," *Proc. IEEE*, Vol. 69, No. 2, February 1981.
16. L. J. Chu, "Physical Limitations of Omnidirectional Antennas," *J. Appl. Phys.*, Vol. 19, pp. 1163–1175, December 1948.
17. R. F. Harrington, "Effect of Antenna Size on Gain, Bandwidth, and Efficiency," *J. Res. Nat. Bur. Stand.-D, Radio Propagation*, Vol. 64D, pp. 1–12, January–February 1960.
18. H. A. Wheeler, "Fundamental Limitations of Small Antennas," *Proc. IRE*, pp. 1479–1488, December 1947.
19. H. A. Wheeler, "The Radiansphere Around a Small Antenna," *Proc. IRE*, pp. 1325–1331, August 1959.
20. H. A. Wheeler, "Small Antennas," *IEEE Trans. Antennas Propagat.*, Vol. AP-23, No. 4, pp. 462–469, July 1975.
21. G. Goubau, "Multi-element Monopole Antennas," *Proc. Workshop on Electrically Small Antennas ECOM*, Ft. Monmouth, N. J., pp. 63–67, May 1976.

PROBLEMS

11.1. Design a symmetrical two-wire plane spiral ($\phi_0 = 0, \pi$) at $f = 10$ MHz with total feed terminal separation of $10^{-5}\lambda$. The total length of each spiral should be one wavelength and each wire should be of one turn.
   (a) Determine the rate of spiral of each wire.
   (b) Find the radius (in λ and in meters) of each spiral at its terminal point.
   (c) Plot the geometric shape of one wire. Use meters for its length.

11.2. Verify (11-28).

11.3. Design log-periodic dipole arrays, of the form shown in Figure 11.9(d), each with directivities of 9 dB, input impedance of 75 ohms, and each with the following additional specifications: Cover the (see Appendix IX)
   (a) VHF TV channels 2–13 (54–216 MHz). Use aluminum tubing with outside diameters of $\frac{3}{4}$ in. (1.905 cm) and $\frac{3}{16}$ in. (0.476 cm) for the largest and smallest elements, respectively.
   (b) VHF TV channels 2–6 (54–88 MHz). Use diameters of 1.905 and 1.1169 cm for the largest and smallest elements, respectively.
   (c) VHF TV channels 7–13 (174–216 MHz). Use diameters of 0.6 and 0.476 cm for the largest and smallest elements, respectively.

INTEL-1045
U.S. Patent 7,151,430

(d) UHF TV channels (512–806 MHz). The largest and smallest elements should have diameters of 0.2 and 0.128 cm, respectively.
(e) FM band of 88–108 MHz (100 channels at 200 KHz apart). The largest and smallest elements should have diameters of 1.169 and 0.9525 cm, respectively.

In each design, the feeder line should have the same diameter as the largest element.

11.4. For each design in Problem 11.3, determine the
(a) span of each period over which the radiation characteristics will vary slightly
(b) number of periods (cycles) within the desired bandwidth

11.5. Using the LOG-PERIODIC DIPOLE ARRAY computer program and Appendix IX, design an array which covers the VHF television band. Design the antenna for 7 dBi gain optimized in terms of σ-τ. The antenna should be matched to a 75-ohm coaxial input cable. For this problem, set the input line length to 0 meters, the source resistance to 0 ohms, the termination line length to 0 meters, the termination impedance to 100 Kohms, the length-to-diameter ratio to 40, and the boom diameter to 10 cm. To make the actual input impedance 75 ohms, one must iteratively find the optimal desired input impedance.
(a) Plot the gain, magnitude of the input impedance, and VSWR versus frequency from 30 MHz to 400 MHz.
(b) Based on the ripples in the plot of gain versus frequency, what is τ? Compare this value to the value calculated by the computer program.
(c) Why does the gain decrease rapidly for frequencies less than the lower design frequency yet decrease very slowly for frequencies higher than the upper design frequency?

11.6. For the antenna of Problem 11.5, replace the 100-Kohm load with a 75-ohm resistor.
(a) Plot the gain, magnitude of the input impedance, and VSWR versus frequency from 30 MHz to 400 MHz.
(b) What does the termination resistor do which makes this antenna an improvement over the antenna of Problem 11.5?

11.7. For the antenna of Problem 11.5, replace the 100-Kohm termination (load) with a 75-ohm resistor and make the source resistance 10 ohms. This resistance represents the internal resistance of the power supply as well as losses in the input line.
(a) Plot the gain versus frequency from 30 MHz to 400 MHz.
(b) What is the antenna efficiency of this antenna?
(c) Based on your result from parts (a) and (b), what should the gain versus frequency plot look like for Problem 11.6?

11.8. Design a log-periodic dipole array which operates from 470 MHz to 806 MHz (UHF band) with 8 dBi gain. This antenna should be matched to a 50-ohm cable of length 2 meters with no source resistance. The termination should be left open. Select the length-to-diameter ratio to be 25. At 600 MHz, do the following. Use the computer program at the end of this chapter.
(a) Plot the E- and H- plane patterns.
(b) Calculate the E- and H-plane half-power beamwidths.
(c) Find the front-to-back ratio.
(d) Why does the E-plane pattern have deep nulls while the H-plane pattern does not?

11.9. The overall length of a small linear dipole antenna (like a biconical antenna, or cylindrical dipole, or any other) is λ/π. Assuming the antenna is 100% efficient, what is:
(a) The smallest possible value of Q for an antenna of such a length? Practically it will be larger than that value.
(b) The largest fractional bandwidth ($\Delta f/f_0$ where f_0 is the center frequency)

11.10. It is desired to design a 100% efficient biconical dipole antenna whose overall length is $\lambda/20$. The design guidelines specify a need to optimize the frequency response (bandwidth). To accomplish this, the quality factor Q of the antenna should be minimized. In order to get some indications as to the fundamental limits of the design:
(a) What is the lowest possible limit of the Q for this size antenna?
(b) In order to approach this lower fundamental limit, should the included angle of the biconical antenna be made larger or smaller, and why?

INTEL-1045
U.S. Patent 7,151,430

COMPUTER PROGRAM - LOG-PERIODIC DIPOLE ARRAY

```
C*****************************************************************
C
C     THIS IS A FORTRAN PROGRAM, AND IT DESIGNS AND ANALYZES A
C     LOG-PERIODIC DIPOLE ARRAY BASED ON THE GEOMETRY OF FIGURE
C     11.9(a), THE DATA IN FIGURES 11.13 AND 11.14, AND THE DESIGN
C     EQUATIONS OF (11-28) - (11-34).
C
C     THE USER CAN TAILOR THE DESIGN AND ANALYSIS BY FOLLOWING
C     THE LISTED STEPS AND SELECTING THE APPROPRIATE OPTIONS.
C     FOR MORE DETAILS, SEE THE LPDA.DOC FILE IN THE COMPUTER DISC.
C
C     **DESIGN PROCEDURE
C
C        STEP I: CHOOSE ONE OF THE FOLLOWING OPTIONS
C          . SPECIFY σ AND τ. THIS SETS THE DIRECTIVITY.
C          . SPECIFY THE DIRECTIVITY. THIS SETS σ AND τ FOR
C            OPTIMUM DIRECTIVITY DESIGN.
C        STEP II: CHOOSE ONE OF THE FOLLOWING OPTIONS
C          . CHOOSE THE BOOM SPACING AND BOOM DIAMETER. THIS
C            SETS THE CHARACTERISTIC IMPEDANCE OF THE
C            TRANSMISSION LINE.
C          . CHOOSE THE DESIRED INPUT IMPEDANCE AND BOOM
C            DIAMETER. THIS SETS THE BOOM SPACING.
C        STEP III: CHOOSE ONE OF THE FOLLOWING OPTIONS
C          . ROUND THE CALCULATED ELEMENT DIAMETERS TO THE
C            NEAREST AVAILABLE WIRE DIAMETERS.
C          . DO NOT ROUND THE CALCULATED ELEMENT DIAMETERS.
C
C     AFTER CHOOSING THE DESIGN OPTIONS, PROCEED TO THE
C     ANALYSIS. THE OUTPUT DEPENDS ON ANALYSIS OPTIONS CHOSEN.
C
C     **ANALYSIS PROCEDURE
C
C        STEP IV: SELECT ANY COMBINATION OF THE FOLLOWING OPTIONS
C                 (DO ONE, TWO, THREE OR ALL OF THE FOLLOWING)
C          . NO ANALYSIS
C            OUTPUT: •DESIGN SUMMARY (lists physical parameters and geometry)
C          . ANALYZE DESIGN AT A SINGLE FREQUENCY
C            OUTPUT: •DESIGN SUMMARY (lists physical parameters and geometry)
C                    •E- AND H-PLANE PATTERN ANALYSIS
C                    •CRITICAL PARAMETERS AT ANALYSIS FREQUENCY
C          . ANALYZE DESIGN AT A SINGLE FREQUENCY
C            OUTPUT: •DESIGN SUMMARY (lists physical parameters and geometry)
C                    •CUSTOM-PLANE PATTERN ANALYSIS
C                    •CRITICAL PARAMETERS AT ANALYSIS FREQUENCY
C          . ANALYZE DESIGN OVER A FREQUENCY BAND
C            OUTPUT: •DESIGN SUMMARY (lists physical parameters and geometry)
C                    •CRITICAL PARAMETERS AS A FUNCTION OF
C                     FREQUENCY, INCLUDING GAIN AT BORESIGHT
C
C                                                  (continued on next page)
```


INTEL-1045
U.S. Patent 7,151,430

```
C                                                          (continued)
C
C     TO COMPLETE THE DESIGN AND ANALYSIS OF ANY OPTION, THE
C     FOLLOWING INPUT AND OUTPUT PARAMETERS WILL GENERALLY BE
C     EITHER SPECIFIED OR CALCULATED.  NOT ALL THE PARAMETERS ARE
C     REQUIRED FOR ALL DESIGN AND DESIGN OPTIONS.
C
C      **INPUT PARAMETERS FOR ARRAY DESIGN
C       1. Title    = NAME OF DESIGN
C       2. DO       = DESIRED DIRECTIVITY (dBi)
C       3. Fhigh    = UPPER DESIGN FREQUENCY (MHz)
C       4. Flow     = LOWER DESIGN FREQUENCY (MHz)
C       5. Rs       = SOURCE RESISTANCE (ohms)
C       6. ZCin     = CHARACTERISTIC IMPEDANCE OF INPUT LINE (ohms)
C       7. Rin      = DESIRED INPUT IMPEDANCE (REAL); TYPICALLY
C                     EQUAL TO CHARACTERISTIC IMPEDANCE ZCin
C       8. LLin     = LENGTH OF THE INPUT TRANSMISSION LINE; FROM
C                     THE SOURCE TO FIRST/SHORTEST ELEMENT (m)
C       9. Zout     = TERMINATION IMPEDANCE (ohms); TYPICALLY EQUAL
C                     TO CHARACTERISTIC IMPEDANCE ZCin
C      10. LLout    = LENGTH OF THE TERMINATION TRANSMISSION LINE;
C                     FROM THE LAST-LONGEST ELEMENT TO THE LOAD (m)
C      11. LD       = DESIRED LENGTH-TO-DIAMETER RATIO OF ELEMENTS
C      12. Navail   = NO. OF AVAILABLE ELEMENT DIAMETERS (dimensionless)
C      13. Davail   = DIAMETERS OF AVAILABLE WIRES OR TUBES (cm)
C      14. SB       = CENTER-TO-CENTER BOOM SPACING (cm)
C      15. DB       = DIAMETER OF BOOM TUBES OR WIRES (cm)
C      16. AFSEH    = ANALYSIS FREQ. FOR E- AND H-PATTERNS (MHz)
C      17. AFSC     = ANALYSIS FREQ. FOR CUSTOM PLANE PATTERN (MHz)
C      18. AFhigh   = HIGHEST FREQ. FOR SWEPT FREQUENCY DATA (MHz)
C      19. AFlow    = LOWEST FREQ. FOR SWEPT FREQUENCY DATA (MHz)
C      20. Phi      = ANGLE OF PLANE [(E-, H-) AND/OR CUSTOM] (degrees)
C
C      **PROGRAM OUTPUT OF ARRAY DESIGN
C       1. N        = NUMBER OF ANTENNA ELEMENTS (integer)
C       2. L        = LENGTHS OF ANTENNA ELEMENTS (m)
C       3. ZL       = STATION (POSITION) OF EACH ARRAY ELEMENT (m)
C       4. D        = DIAMETER OF EACH ARRAY ELEMENT (cm)
C       5. VSWR     = VSWR IN INPUT TRANSMISSION LINE
C       6. ZinA     = ACTUAL INPUT IMPEDANCE OF DESIGN (ohms)
C       7. DOA      = ACTUAL DIRECTIVITY OF DESIGN ALONG (dBi)
C       8. PDO      = PEAK DIRECTIVITY ALONG ANY AXIS (dBi)
C       9. FTBR     = FRONT-TO-BACK RATIO OF AMPLITUDE PATTERN (dB)
C      10. FSLL     = FRONT-TO-MAXIMUM SIDE LOBE LEVEL (dB)
C      11. Iin      = CURRENT IN INPUT TRANSMISSION LINE (A)
C      12. Iel      = CURRENTS IN ARRAY ELEMENTS (A)
C      13. Iout     = CURRENT IN TERMINATION TRANSMISSION LINE (A)
C      14. Vin      = VOLTAGE AT THE SOURCE (V)
C      15. Vel      = VOLTAGES OF ARRAY ELEMENTS (V)
C      16. Vout     = VOLTAGE AT THE LOAD (V)
C      17. Epat     = E-PLANE PATTERN (dBi)
C      18. Hpat     = H-PLANE PATTERN (dBi)
C      19. Cpat     = ANY DESIRED CUSTOM PLANE PATTERN (dBi)
C*************************************************************************
```


INTEL-1045
U.S. Patent 7,151,430

CHAPTER

12

APERTURE ANTENNAS

12.1 INTRODUCTION

Aperture antennas are most common at microwave frequencies. There are many different geometrical configurations of an aperture antenna with some of the most popular shown in Figure 1.4. They may take the form of a waveguide or a horn whose aperture may be square, rectangular, circular, elliptical, or any other configuration. Aperture antennas are very practical for space applications, because they can be flush-mounted on the surface of the spacecraft or aircraft. Their opening can be covered with a dielectric material to protect them from environmental conditions. This type of mounting does not disturb the aerodynamic profile of the craft, which in high-speed applications is critical.

In this chapter, the mathematical tools will be developed to analyze the radiation characteristics of aperture antennas. The concepts will be demonstrated by examples and illustrations. Because they are the most practical, emphasis will be given to the rectangular and circular configurations. Due to mathematical complexities, the observations will be restricted to the far-field region. The edge effects, due to the finite size of the ground plane to which the aperture is mounted, can be taken into account by using diffraction methods such as the Geometrical Theory of Diffraction, better known as GTD. This is discussed briefly and only qualitatively in Section 12.10.

The radiation characteristics of wire antennas can be determined once the current distribution on the wire is known. For many configurations, however, the current distribution is not known exactly and only physical intuition or experimental measurements can provide a reasonable approximation to it. This is even more evident in aperture antennas (slits, slots, waveguides, horns, reflectors, lenses). It is therefore expedient to have alternate methods to compute the radiation characteristics of antennas. Emphasis will be placed on techniques that for their solution rely primarily not on the current distribution but on reasonable approximations of the fields on or in the vicinity of the antenna structure. One such technique is the *Field Equivalence Principle*.

12.2 FIELD EQUIVALENCE PRINCIPLE: HUYGENS' PRINCIPLE

The *field equivalence* is a principle by which actual sources, such as an antenna and transmitter, are replaced by equivalent sources. The fictitious sources are said to be

INTEL-1045
U.S. Patent 7,151,430

equivalent within a region because *they produce the same fields within that region.* The formulations of scattering and diffraction problems by the equivalence principle are more suggestive to approximations.

The field equivalence was introduced in 1936 by S. A. Schelkunoff [1], [2], and it is a more rigorous formulation of Huygens' principle [3] which states that "*each point on a primary wavefront can be considered to be a new source of a secondary spherical wave and that a secondary wavefront can be constructed as the envelope of these secondary spherical waves* [4]." The equivalence principle is based on the *uniqueness theorem* which states that "*a field in a lossy region is uniquely specified by the sources within the region plus the tangential components of the electric field over the boundary, or the tangential components of the magnetic field over the boundary, or the former over part of the boundary and the latter over the rest of the boundary* [2], [5]." The field in a lossless medium is considered to be the limit, as the losses go to zero, of the corresponding field in a lossy medium. Thus if the tangential electric and magnetic fields are completely known over a closed surface, the fields in the source-free region can be determined.

By the equivalence principle, the fields outside an imaginary closed surface are obtained by placing over the closed surface suitable electric- and magnetic-current densities which satisfy the boundary conditions. The current densities are selected so that the fields inside the closed surface are zero and outside they are equal to the radiation produced by the actual sources. Thus the technique can be used to obtain the fields radiated outside a closed surface by sources enclosed within it. The formulation is exact but requires integration over the closed surface. The degree of accuracy depends on the knowledge of the tangential components of the fields over the closed surface.

In most applications, the closed surface is selected so that most of it coincides with the conducting parts of the physical structure. This is preferred because the vanishing of the tangential electric field components over the conducting parts of the surface reduces the physical limits of integration.

The equivalence principle is developed by considering an actual radiating source, which electrically is represented by current densities $\mathbf{J}_1$ and $\mathbf{M}_1$, as shown in Figure 12.1(a). The source radiates fields $\mathbf{E}_1$ and $\mathbf{H}_1$ everywhere. However, it is desired to develop a method that will yield the fields outside a closed surface. To accomplish this, a closed surface S is chosen, shown dashed in Figure 12.1(a), which encloses the current densities $\mathbf{J}_1$ and $\mathbf{M}_1$. The volume within S is denoted by V_1 and outside S by V_2. *The primary task will be to replace the original problem, shown in Figure 12.1(a),*

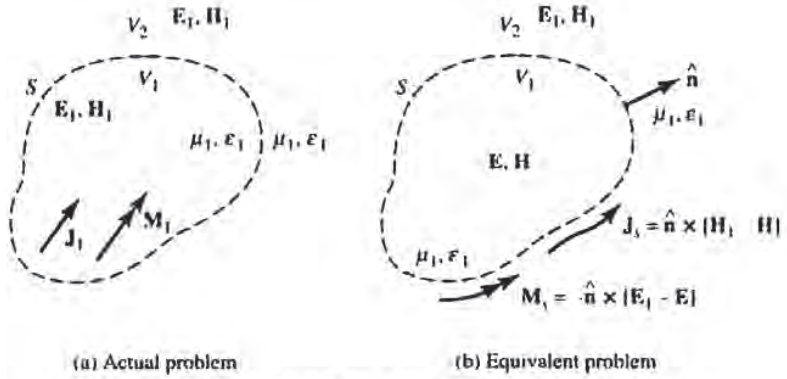


Figure 12.1 Actual and equivalent problem models.

INTEL-1045
U.S. Patent 7,151,430

by an equivalent one which yields the same fields $\mathbf{E}_1$ *and* $\mathbf{H}_1$ *outside* S *(within* V_2*).* The formulation of the problem can be aided eminently if the closed surface is judiciously chosen so that fields over most, if not the entire surface, are known *a priori.*

An equivalent problem of Figure 12.1(a) is shown in Figure 12.1(b). The original sources $\mathbf{J}_1$ and $\mathbf{M}_1$ are removed, and we assume that there exist fields $\mathbf{E}$ and $\mathbf{H}$ inside S and fields $\mathbf{E}_1$ and $\mathbf{H}_1$ outside of S. For these fields to exist within and outside S, they must satisfy the boundary conditions on the tangential electric and magnetic field components. Thus on the imaginary surface S there must exist the *equivalent sources*

$$\mathbf{J}_s = \hat{\mathbf{n}} \times [\mathbf{H}_1 - \mathbf{H}] \tag{12-1}$$

$$\mathbf{M}_s = -\hat{\mathbf{n}} \times [\mathbf{E}_1 - \mathbf{E}] \tag{12-2}$$

and they radiate into an *unbounded space* (same medium everywhere). *The current densities of (12-1) and (12-2) are said to be equivalent only within* V_2*, because they produce the original fields* ($\mathbf{E}_1$, $\mathbf{H}_1$) *only outside S. Fields* $\mathbf{E}$, $\mathbf{H}$, *different from the originals* ($\mathbf{E}_1$, $\mathbf{H}_1$), *result within* V_1. Since the currents of (12-1) and (12-2) radiate in an unbounded space, the fields can be determined using (3-27)–(3-30a) and the geometry of Figure 12.2(a). In Figure 12.2(a), R is the distance from any point on the surface S, where $\mathbf{J}_s$ and $\mathbf{M}_s$ exist, to the observation point.

So far, the tangential components of *both* $\mathbf{E}$ and $\mathbf{H}$ have been used in setting up the equivalent problem. From electromagnetic uniqueness concepts, it is known that the tangential components of only $\mathbf{E}$ or $\mathbf{H}$ are needed to determine the fields. It will be demonstrated that equivalent problems can be found which require only the magnetic current densities (tangential $\mathbf{E}$) or only electric current densities (tangential $\mathbf{H}$). This requires modifications to the equivalent problem of Figure 12.1(b).

Since the fields $\mathbf{E}$, $\mathbf{H}$ within S can be anything (this is not the region of interest), it can be assumed that they are zero. In that case the equivalent problem of Figure 12.1(b) reduces to that of Figure 12.3(a) with the equivalent current densities being equal to

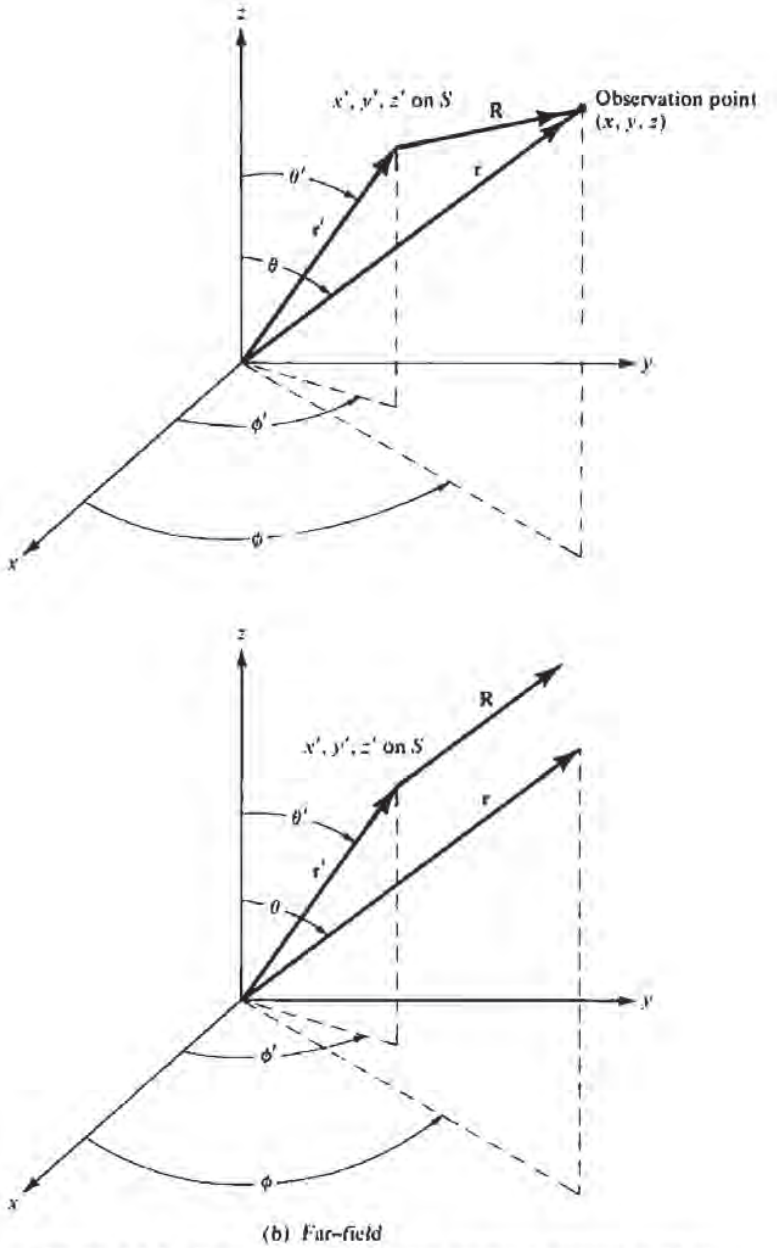
$$\mathbf{J}_s = \hat{\mathbf{n}} \times (\mathbf{H}_1 - \mathbf{H})|_{\mathbf{H}=0} = \hat{\mathbf{n}} \times \mathbf{H}_1 \tag{12-3}$$

$$\mathbf{M}_s = -\hat{\mathbf{n}} \times (\mathbf{E}_1 - \mathbf{E})|_{\mathbf{E}=0} = -\hat{\mathbf{n}} \times \mathbf{E}_1 \tag{12-4}$$

This form of the field equivalence principle is known as *Love's Equivalence Principle* [2], [6]. Since the current densities of (12-3) and (12-4) radiate in an unbounded medium (same μ, ϵ everywhere), they can be used in conjunction with (3-27)–(3-30a) to find the fields everywhere.

Love's Equivalence Principle of Figure 12.3(a) produces a null field within the imaginary surface S. Since the value of the $\mathbf{E} = \mathbf{H} = 0$ within S cannot be disturbed if the properties of the medium within it are changed, let us assume that it is replaced by a perfect electric conductor ($\sigma = \infty$). The introduction of the perfect conductor will have an effect on the equivalent source $\mathbf{J}_s$, and it will prohibit the use of (3-27)–(3-30a) since the current densities no longer radiate into an unbounded medium. Imagine that the geometrical configuration of the electric conductor is identical to the profile of the imaginary surface S, over which $\mathbf{J}_s$ and $\mathbf{M}_s$ exist. As the electric conductor takes its place, as shown in Figure 12.3(b), the electric current density $\mathbf{J}_s$, which is tangent to the surface S, is short-circuited by the electric conductor. Thus the equivalent problem of Figure 12.3(a) reduces to that of Figure 12.3(b). There exists only a magnetic current density $\mathbf{M}_s$ over S, and it radiates in the presence of the electric conductor producing outside S the original fields $\mathbf{E}_1$, $\mathbf{H}_1$. Within S the fields are zero but, as before, this is not a region of interest. The difficulty in trying

INTEL-1045
U.S. Patent 7,151,430



(b) *Far-field*

Figure 12.2 Coordinate system for aperture antenna analysis.

to use the equivalent problem of Figure 12.3(b) is that (3-27)–(3-30a) cannot be used, because the current densities do not radiate into an unbounded medium. The problem of a magnetic current density radiating in the presence of an electric conducting surface must be solved. So it seems that the equivalent problem is just as difficult as the original problem itself.

Before some special simple geometries are considered and some suggestions are made for approximating complex geometries. let us introduce another equivalent problem. Referring to Figure 12.3(a), let us assume that instead of placing a perfect electric conductor within S we introduce a perfect magnetic conductor which will short out the magnetic current density and reduce the equivalent problem to that

INTEL-1045
U.S. Patent 7,151,430

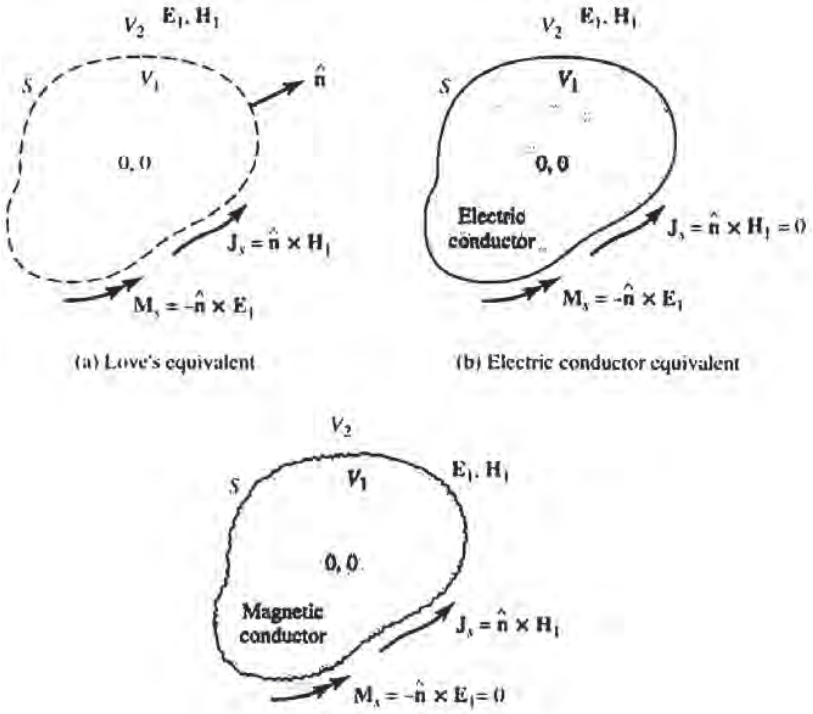


Figure 12.3 Equivalence principle models.

shown in Figure 12.3(c). As was with the equivalent problem of Figure 12.3(b), (3-27)–(3-30a) cannot be used with Figure 12.3(c) and the problem is just as difficult as that of Figure 12.3(b) or the original of Figure 12.1(a).

To begin to see the utility of the field equivalence principle, especially that of Figure 12.3(b), let us assume that the surface of the electric conductor is flat and extends to infinity as shown in Figure 12.4(a). For this geometry, the problem is to determine how a magnetic source radiates in the presence of a flat electric conductor. From image theory, this problem reduces to that of Figure 12.4(b) where an imaginary magnetic source is introduced on the side of the conductor and takes its place (remove conductor). Since the imaginary source is in the same direction as the equivalent source, the equivalent problem of Figure 12.4(b) reduces to that of Figure 12.4(c). The magnetic current density is doubled, it radiates in an unbounded medium, and (3-27)–(3-30a) can be used. The equivalent problem of Figure 12.4(c) yields the correct **E**, **H** fields to the right side of the interface. If the surface of the obstacle is not flat and infinite, but its curvature is large compared to the wavelength, a good approximation is the equivalent problem of Figure 12.3(c).

SUMMARY

In the analysis of electromagnetic problems, many times it is easier to form equivalent problems that yield the same solution within a region of interest. This is the case for scattering, diffraction, and aperture antenna problems. In this chapter, the main interest is in aperture antennas. The concepts will be demonstrated with examples.

The steps that must be used to form an equivalent and solve an aperture problem are as follows:

INTEL-1045
U.S. Patent 7,151,430

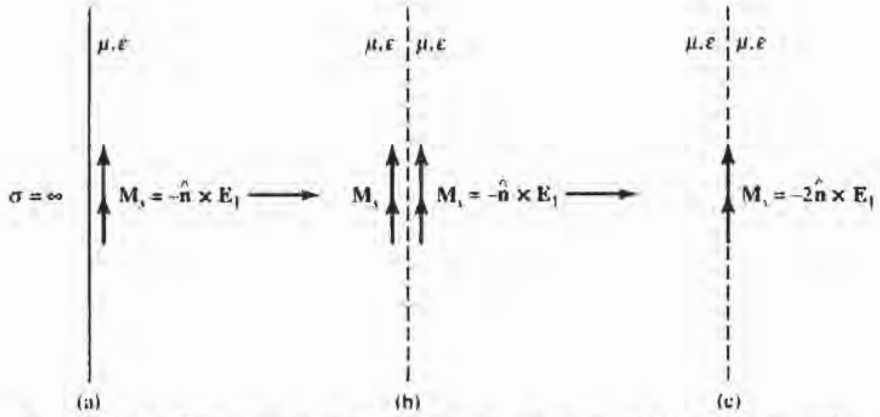


Figure 12.4 Equivalent models for magnetic source radiation near a perfect electric conductor.

1. Select an imaginary surface that encloses the actual sources (the aperture). The surface must be judiciously chosen so that the tangential components of the electric and/or the magnetic field are known, exactly or approximately, over its entire span. In many cases this surface is a flat plane extending to infinity.
2. Over the imaginary surface form equivalent current densities $\mathbf{J}_s$, $\mathbf{M}_s$ which take one of the following forms:
   a. $\mathbf{J}_s$ and $\mathbf{M}_s$ over S assuming that the **E**- and **H**-fields within S are not zero.
   b. or $\mathbf{J}_s$ and $\mathbf{M}_s$ over S assuming that the **E**- and **H**-fields within S are zero (Love's theorem)
   c. or $\mathbf{M}_s$ over S ($\mathbf{J}_s = 0$) assuming that within S the medium is a perfect electric conductor
   d. or $\mathbf{J}_s$ over S ($\mathbf{M}_s = 0$) assuming that within S the medium is a perfect magnetic conductor
3. Solve the equivalent problem. For forms (a) and (b), (3-27)–(3-30a) can be used. For form (c), the problem of a magnetic current source next to a perfect electric conductor must be solved [(3-27)–(3-30a) cannot be used directly, because the current density does not radiate into an unbounded medium]. If the electric conductor is an infinite flat plane the problem can be solved exactly by image theory. For form (d), the problem of an electric current source next to a perfect magnetic conductor must be solved. Again (3-27)–(3-30a) cannot be used directly. If the magnetic conductor is an infinite flat plane, the problem can be solved exactly by image theory.

To demonstrate the usefulness and application of the field equivalence theorem to aperture antenna theory, an example is considered.

Example 12.1

A waveguide aperture is mounted on an infinite ground plane, as shown in Figure 12.5(a). Assuming that the tangential components of the electric field over the aperture are known, and are given by $\mathbf{E}_a$, find an equivalent problem that will yield the same fields **E**, **H** radiated by the aperture to the right side of the interface.

INTEL-1045
U.S. Patent 7,151,430

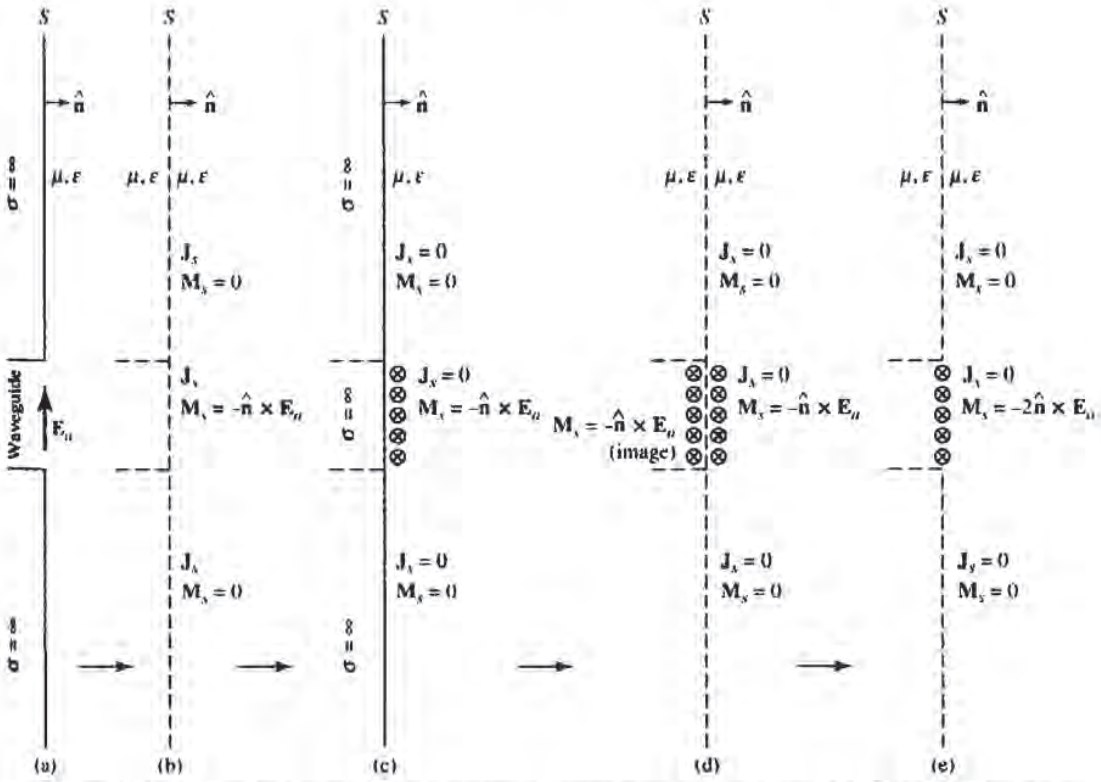


Figure 12.5 Equivalent models for waveguide aperture mounted on an infinite flat electric ground plane.

SOLUTION

First an imaginary closed surface is chosen. For this problem it is appropriate to select a flat plane extending from minus infinity to plus infinity, as shown in Figure 12.5(b). Over the infinite plane, the equivalent current densities $\mathbf{J}_s$ and $\mathbf{M}_s$ are formed. Since the tangential components of $\mathbf{E}$ do not exist outside the aperture, because of vanishing boundary conditions, the magnetic current density $\mathbf{M}_s$ is only nonzero over the aperture. The electric current density $\mathbf{J}_s$ is nonzero everywhere and is yet unknown. Now let us assume that an imaginary flat electric conductor approaches the surface S, and it shorts out the current density $\mathbf{J}_s$ everywhere. $\mathbf{M}_s$ exists only over the space occupied originally by the aperture, and it radiates in the presence of the conductor [see Figure 12.5(c)]. By image theory, the conductor can be removed and replaced by an imaginary (equivalent) source $\mathbf{M}_s$ as shown in Figure 12.5(d), which is analogous to Figure 12.4(b). Finally, the equivalent problem of Figure 12.5(d) reduces to that of Figure 12.5(e), which is analogous to that of Figure 12.4(c). The original problem has been reduced to a very simple equivalent and (3-27)–(3-30a) can be utilized for its solution.

In this chapter the theory will be developed to compute the fields radiated by an aperture, like that shown in Figure 12.5(a), making use of its equivalent of Figure 12.5(e). For other problems, their equivalent forms will not necessarily be the same as that shown in Figure 12.5(e).

INTEL-1045
U.S. Patent 7,151,430

12.3 RADIATION EQUATIONS

In Chapter 3 and in the previous section it was stated that the fields radiated by sources $\mathbf{J}_s$ and $\mathbf{M}_s$ in an unbounded medium can be computed by using (3-27)–(3-30a) where the integration must be performed over the entire surface occupied by $\mathbf{J}_s$ and $\mathbf{M}_s$. These equations yield valid solutions for all observation points [2], [7]. For most problems, the main difficulty is the inability to perform the integrations in (3-27) and (3-28). However for far-field observations, the complexity of the formulation can be reduced.

As was shown in Section 4.4.1, for far-field observations R can most commonly be approximated by

$$R \simeq r - r' \cos\psi \qquad \text{for phase variations} \tag{12-5a}$$

$$R \simeq r \qquad \text{for amplitude variations} \tag{12-5b}$$

where ψ is the angle between the vectors $\mathbf{r}$ and $\mathbf{r}'$, as shown in Figure 12.2(b). The primed coordinates (x', y', z', or r', θ', ϕ') indicate the space occupied by the sources $\mathbf{J}_s$ and $\mathbf{M}_s$, over which integration must be performed. The unprimed coordinates (x, y, z or r, θ, ϕ) represent the observation point. Geometrically the approximation of (12-5a) assumes that the vectors $\mathbf{R}$ and $\mathbf{r}$ are parallel, as shown in Figure 12.2(b).

Using (12-5a) and (12-5b), (3-27) and (3-28) can be written as

$$\mathbf{A} = \frac{\mu}{4\pi}\iint_S \mathbf{J}_s \frac{e^{-jkR}}{R}\,ds' \simeq \frac{\mu e^{-jkr}}{4\pi r}\mathbf{N} \tag{12-6}$$

$$\mathbf{N} = \iint_S \mathbf{J}_s e^{jkr'\cos\psi}\,ds' \tag{12-6a}$$

$$\mathbf{F} = \frac{\epsilon}{4\pi}\iint_S \mathbf{M}_s \frac{e^{-jkR}}{R}\,ds' \simeq \frac{\epsilon e^{-jkr}}{4\pi r}\mathbf{L} \tag{12-7}$$

$$\mathbf{L} = \iint_S \mathbf{M}_s e^{jkr'\cos\psi}\,ds' \tag{12-7a}$$

In Section 3.6 it was shown that in the far-field only the θ and ϕ components of the **E**- and **H**-fields are dominant. Although the radial components are not necessarily zero, they are negligible compared to the θ and ϕ components. Using (3-58a)–(3-59b), the $\mathbf{E}_A$ of (3-29) and $\mathbf{H}_F$ of (3-30) can be written as

$$(E_A)_\theta \simeq -j\omega A_\theta \tag{12-8a}$$

$$(E_A)_\phi \simeq -j\omega A_\phi \tag{12-8b}$$

$$(H_F)_\theta \simeq -j\omega F_\theta \tag{12-8c}$$

$$(H_F)_\phi \simeq -j\omega F_\phi \tag{12-8d}$$

and the $\mathbf{E}_F$ of (3-29) and $\mathbf{H}_A$ of (3-30), with the aid of (12-8a)–(12-8d), as

$$(E_F)_\theta \simeq +\eta(H_F)_\phi = -j\omega\eta F_\phi \tag{12-9a}$$

$$(E_F)_\phi \simeq -\eta(H_F)_\theta = +j\omega\eta F_\theta \tag{12-9b}$$

INTEL-1045
U.S. Patent 7,151,430

$$(H_A)_\theta \simeq -\frac{(E_A)_\phi}{\eta} = +j\omega\frac{A_\phi}{\eta} \tag{12-9c}$$

$$(H_A)_\phi \simeq +\frac{(E_A)_\theta}{\eta} = -j\omega\frac{A_\theta}{\eta} \tag{12-9d}$$

Combining (12-8a)–(12-8d) with (12-9a)–(12-9d), and making use of (12-6)–(12-7a) the total **E**- and **H**-fields can be written as

$$E_r \simeq 0 \tag{12-10a}$$

$$E_\theta \simeq -\frac{jke^{-jkr}}{4\pi r}(L_\phi + \eta N_\theta) \tag{12-10b}$$

$$E_\phi \simeq +\frac{jke^{-jkr}}{4\pi r}(L_\theta - \eta N_\phi) \tag{12-10c}$$

$$H_r \simeq 0 \tag{12-10d}$$

$$H_\theta \simeq \frac{jke^{-jkr}}{4\pi r}\left(N_\phi - \frac{L_\theta}{\eta}\right) \tag{12-10e}$$

$$H_\phi \simeq -\frac{jke^{-jkr}}{4\pi r}\left(N_\theta + \frac{L_\phi}{\eta}\right) \tag{12-10f}$$

The N_θ, N_ϕ, L_θ, and L_ϕ can be obtained from (12-6a) and (12-7a). That is,

$$\mathbf{N} = \iint_S \mathbf{J}_s e^{+jkr'\cos\psi}\,ds' = \iint_S (\hat{\mathbf{a}}_x J_x + \hat{\mathbf{a}}_y J_y + \hat{\mathbf{a}}_z J_z)e^{+jkr'\cos\psi}\,ds' \tag{12-11a}$$

$$\mathbf{L} = \iint_S \mathbf{M}_s e^{+jkr'\cos\psi}\,ds' = \iint_S (\hat{\mathbf{a}}_x M_x + \hat{\mathbf{a}}_y M_y + \hat{\mathbf{a}}_z M_z)e^{+jkr'\cos\psi}\,ds' \tag{12-11b}$$

Using the rectangular-to-spherical component transformation, obtained by taking the inverse (in this case also the transpose) of (4-5), (12-11a) and (12-11b) reduce for the θ and ϕ components to

$$N_\theta = \iint_S [J_x\cos\theta\cos\phi + J_y\cos\theta\sin\phi - J_z\sin\theta]e^{+jkr'\cos\psi}\,ds' \tag{12-12a}$$

$$N_\phi = \iint_S [-J_x\sin\phi + J_y\cos\phi]e^{+jkr'\cos\psi}\,ds' \tag{12-12b}$$

$$L_\theta = \iint_S [M_x\cos\theta\cos\phi + M_y\cos\theta\sin\phi - M_z\sin\theta]e^{+jkr'\cos\psi}\,ds' \tag{12-12c}$$

$$L_\phi = \iint_S [-M_x\sin\phi + M_y\cos\phi]e^{+jkr'\cos\psi}\,ds' \tag{12-12d}$$

SUMMARY

To summarize the results, the procedure that must be followed to solve a problem using the radiation integrals will be outlined. Figures 12.2(a) and 12.2(b) are used to indicate the geometry.

INTEL-1045
U.S. Patent 7,151,430

1. Select a closed surface over which the total electric and magnetic fields $\mathbf{E}_a$ and $\mathbf{H}_a$ are known.
2. Form the equivalent current densities $\mathbf{J}_s$ and $\mathbf{M}_s$ over S using (12-3) and (12-4) with $\mathbf{H}_1 = \mathbf{H}_a$ and $\mathbf{E}_1 = \mathbf{E}_a$.
3. Determine the $\mathbf{A}$ and $\mathbf{F}$ potentials using (12-6)–(12-7a) where the integration is over the closed surface S.
4. Determine the radiated $\mathbf{E}$- and $\mathbf{H}$-fields using (3-29) and (3-30).

The above steps are valid for all regions (near-field and far-field) outside the surface S. If, however, the observation point is in the far-field, steps 3 and 4 can be replaced by 3′ and 4′. That is,

3′. Determine N_θ, N_ϕ, L_θ and L_ϕ using (12-12a)–(12-12d).

4′. Determine the radiated $\mathbf{E}$- and $\mathbf{H}$-fields using (12-10a)–(12-10f).

Some of the steps outlined above can be reduced by a judicious choice of the equivalent model. In the remaining sections of this chapter, the techniques will be applied and demonstrated with examples of rectangular and circular apertures.

12.4 DIRECTIVITY

The directivity of an aperture can be found in a manner similar to that of other antennas. The primary task is to formulate the radiation intensity $U(\theta, \phi)$, using the far-zone electric and magnetic field components, as given by (2-12a) or

$$U(\theta, \phi) = \frac{1}{2}\text{Re}[(\hat{\mathbf{a}}_\theta E_\theta + \hat{\mathbf{a}}_\phi E_\phi) \times (\hat{\mathbf{a}}_\theta H_\theta + \hat{\mathbf{a}}_\phi H_\phi)^*] = \frac{1}{2\eta}(|E_\theta^0|^2 + |E_\phi^0|^2) \tag{12-13}$$

which in normalized form reduces to

$$\boxed{U_n(\theta, \phi) = (|E_\theta^0(\theta, \phi)|^2 + |E_\phi^0(\theta, \phi)|^2) = B_0 F(\theta, \phi)} \tag{12-13a}$$

The directive properties can then be found using (2-19)–(2-22).

Because the radiation intensity $U(\theta, \phi)$ for each aperture antenna will be of a different form, a general equation for the directivity cannot be formed. However, a general FORTRAN computer program, designated as DIRECTIVITY, has been written to compute the directivity of any antenna, including an aperture, once the radiation intensity is specified. The program is based on the formulations of (12-13a), (2-19)–(2-20), and (2-22), and it is shown at the end of Chapter 2. In the main program, it requires the lower and upper limits on θ and ϕ. The radiation intensity for the antenna in question must be specified in the subroutine $U(\theta, \phi, F)$ of the program.

Expressions for the directivity of some simple aperture antennas, rectangular and circular, will be derived in later sections of this chapter.

12.5 RECTANGULAR APERTURES

In practice, the rectangular aperture is probably the most common microwave antenna. Because of its configuration, the rectangular coordinate system is the most convenient system to express the fields at the aperture and to perform the integration. Shown in Figure 12.6 are the three most common and convenient coordinate positions used for the solution of an aperture antenna. In Figure 12.6(a) the aperture lies on the y-z plane,

INTEL-1045
U.S. Patent 7,151,430

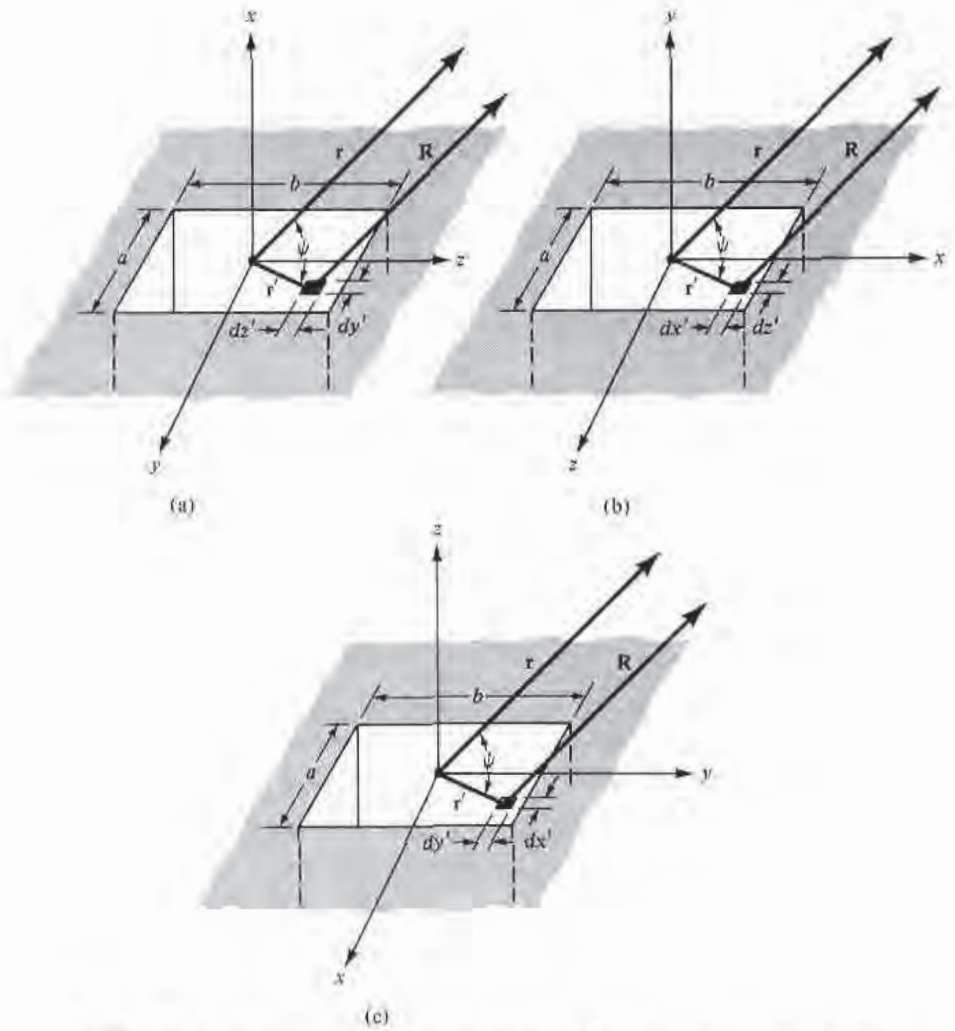


Figure 12.6 Rectangular aperture positions for antenna system analysis.

in Figure 12.6(b) on the x-z plane, and in Figure 12.6(c) on the x-y plane. For a given field distribution, the analytical forms for the fields for each of the arrangements are not the same. However the computed values will be the same, since the physical problem is identical in all cases.

For each of the geometries shown in Figure 12.6, the only difference in the analysis is in the formulation of

1. the components of the equivalent current densities (J_x, J_y, J_z, M_x, M_y, M_z)
2. the difference in paths from the source to the observation point ($r' \cos \psi$)
3. the differential area ds'

In general, the nonzero components of $\mathbf{J}_s$ and $\mathbf{M}_s$ are

$$J_y, J_z, M_y, M_z \quad \text{[Figure 12.6(a)]} \tag{12-14a}$$

$$J_x, J_z, M_x, M_z \quad \text{[Figure 12.6(b)]} \tag{12-14b}$$

$$J_x, J_y, M_x, M_y \quad \text{[Figure 12.6(c)]} \tag{12-14c}$$

INTEL-1045
U.S. Patent 7,151,430

The differential paths take the form of

$$r'\cos\psi = \mathbf{r}'\cdot\hat{\mathbf{a}}_r = (\hat{\mathbf{a}}_y y' + \hat{\mathbf{a}}_z z')\cdot(\hat{\mathbf{a}}_x \sin\theta\cos\phi + \hat{\mathbf{a}}_y \sin\theta\sin\phi + \hat{\mathbf{a}}_z\cos\theta)$$
$$= y'\sin\theta\sin\phi + z'\cos\theta \qquad \text{[Figure 12.6(a)]} \qquad (12\text{-}15a)$$

$$r'\cos\psi = \mathbf{r}'\cdot\hat{\mathbf{a}}_r = (\hat{\mathbf{a}}_x x' + \hat{\mathbf{a}}_z z')\cdot(\hat{\mathbf{a}}_x \sin\theta\cos\phi + \hat{\mathbf{a}}_y \sin\theta\sin\phi + \hat{\mathbf{a}}_z\cos\theta)$$
$$= x'\sin\theta\cos\phi + z'\cos\theta \qquad \text{[Figure 12.6(b)]} \qquad (12\text{-}15b)$$

$$r'\cos\psi = \mathbf{r}'\cdot\hat{\mathbf{a}}_r = (\hat{\mathbf{a}}_x x' + \hat{\mathbf{a}}_y y')\cdot(\hat{\mathbf{a}}_x \sin\theta\cos\phi + \hat{\mathbf{a}}_y \sin\theta\sin\phi + \hat{\mathbf{a}}_z\cos\theta)$$
$$= x'\sin\theta\cos\phi + y'\sin\theta\sin\phi \qquad \text{[Figure 12.6(c)]} \qquad (12\text{-}15c)$$

and the differential areas are represented by

$$ds' = dy'\,dz' \qquad \text{[Figure 12.6(a)]} \qquad (12\text{-}16a)$$
$$ds' = dx'\,dz' \qquad \text{[Figure 12.6(b)]} \qquad (12\text{-}16b)$$
$$ds' = dx'\,dy' \qquad \text{[Figure 12.6(c)]} \qquad (12\text{-}16c)$$

12.5.1 Uniform Distribution on an Infinite Ground Plane

The first aperture examined is a rectangular aperture mounted on an infinite ground plane, as shown in Figure 12.7. To reduce the mathematical complexities, initially the field over the opening is assumed to be constant and given by

$$\mathbf{E}_a = \hat{\mathbf{a}}_y E_0 \qquad -a/2 \le x' \le a/2, \quad -b/2 \le y' \le b/2 \qquad (12\text{-}17)$$

where E_0 is a constant. The task is to find the fields radiated by it, the pattern beamwidths, the side lobe levels of the pattern, and the directivity. To accomplish these, the equivalent will be formed first.

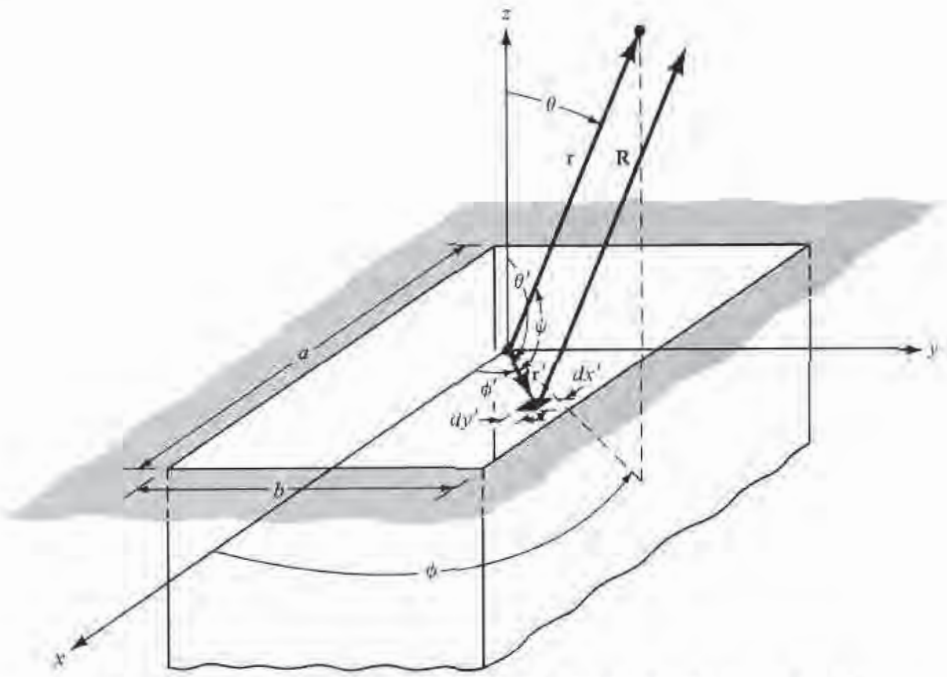


Figure 12.7 Rectangular aperture on an infinite electric ground plane.

INTEL-1045
U.S. Patent 7,151,430

A. Equivalent

To form the equivalent, a closed surface is chosen which extends from $-\infty$ to $+\infty$ on the x-y plane. Since the physical problem of Figure 12.7 is identical to that of Figure 12.5(a), its equivalents are those of Figures 12.5(a)–(e). Using the equivalent of Figure 12.5(e)

$$\mathbf{M}_s = \begin{cases} -2\hat{\mathbf{n}} \times \mathbf{E}_a = -2\hat{\mathbf{a}}_z \times \hat{\mathbf{a}}_y E_0 = +\hat{\mathbf{a}}_x 2E_0 & -a/2 \le x' \le a/2 \\ 0 & -b/2 \le y' \le b/2 \\ & \text{elsewhere} \end{cases} \qquad (12\text{-}18)$$

$$\mathbf{J}_s = 0 \qquad \text{everywhere}$$

B. Radiation Fields: Element and Space Factors

The far-zone fields radiated by the aperture of Figure 12.7 can be found by using (12-10a)–(12-10f), (12-12a)–(12–12d), (12-14c), (12-15c), (12-16c), and (12-18). Thus,

$$N_\theta = N_\phi = 0 \qquad (12\text{-}19)$$

$$L_\theta = \int_{-b/2}^{+b/2} \int_{-a/2}^{+a/2} [M_x \cos\theta \cos\phi]\, e^{jk(x'\sin\theta\cos\phi + y'\sin\theta\sin\phi)}\, dx'\, dy'$$

$$\boxed{L_\theta = \cos\theta\cos\phi \left[\int_{-b/2}^{+b/2} \int_{-a/2}^{+a/2} M_x e^{jk(x'\sin\theta\cos\phi + y'\sin\theta\sin\phi)}\, dx'\, dy' \right]} \qquad (12\text{-}19a)$$

In (12-19a), the integral within the brackets represents the *space factor* for a two-dimensional distribution. It is analogous to the space factor of (4-58a) for a line source (one-dimensional distribution). For the L_θ component of the vector potential $\mathbf{F}$, the *element factor* is equal to the product of the factor outside the brackets in (12-19a) and the factor outside the brackets in (12-10c). The total field is equal to the product of the element and space factors, as defined by (4-59), and expressed in (12-10b) and (12-10c).

Using the integral

$$\int_{-c/2}^{+c/2} e^{j\alpha z}\, dz = c \left[\frac{\sin\left(\frac{\alpha}{2} c\right)}{\frac{\alpha}{2} c} \right] \qquad (12\text{-}20)$$

(12-19a) reduces to

$$L_\theta = 2abE_0 \left[\cos\theta\cos\phi \left(\frac{\sin X}{X}\right)\left(\frac{\sin Y}{Y}\right) \right] \qquad (12\text{-}21)$$

where

$$X = \frac{ka}{2} \sin\theta\cos\phi \qquad (12\text{-}21a)$$

$$Y = \frac{kb}{2} \sin\theta\sin\phi \qquad (12\text{-}21b)$$

Similarly it can be shown that

$$L_\phi = -2abE_0 \left[\sin\phi \left(\frac{\sin X}{X}\right)\left(\frac{\sin Y}{Y}\right) \right] \qquad (12\text{-}22)$$

INTEL-1045
U.S. Patent 7,151,430

Substituting (12-19), (12-21), and (12-22) into (12-10a)–(12-10f), the fields radiated by the aperture can be written as

$$E_r = 0 \tag{12-23a}$$

$$E_\theta = j\frac{abkE_0e^{-jkr}}{2\pi r}\left[\sin\phi\left(\frac{\sin X}{X}\right)\left(\frac{\sin Y}{Y}\right)\right] \tag{12-23b}$$

$$E_\phi = j\frac{abkE_0e^{-jkr}}{2\pi r}\left[\cos\theta\cos\phi\left(\frac{\sin X}{X}\right)\left(\frac{\sin Y}{Y}\right)\right] \tag{12-23c}$$

$$H_r = 0 \tag{12-23d}$$

$$H_\theta = -\frac{E_\phi}{\eta} \tag{12-23e}$$

$$H_\phi = +\frac{E_\theta}{\eta} \tag{12-23f}$$

Equations (12-23a)–(12-23f) represent the three-dimensional distributions of the far-zone fields radiated by the aperture. Experimentally only two-dimensional plots can be measured. To reconstruct experimentally a three-dimensional plot, a series of two-dimensional plots must be made. In many applications, however, only a pair of two-dimensional plots are usually sufficient. These are the principal E- and H-plane patterns whose definition was stated in Section 2.2.2 and illustrated in Figure 2.3.

For the problem in Figure 12.7, the E-plane pattern is on the y-z plane ($\phi = \pi/2$) and the H-plane is on the x-z plane ($\phi = 0$). Thus

E-Plane ($\phi = \pi/2$)

$$E_r = E_\phi = 0 \tag{12-24a}$$

$$E_\theta = j\frac{abkE_0e^{-jkr}}{2\pi r}\left[\frac{\sin\left(\frac{kb}{2}\sin\theta\right)}{\frac{kb}{2}\sin\theta}\right] \tag{12-24b}$$

H-Plane ($\phi = 0$)

$$E_r = E_\theta = 0 \tag{12-25a}$$

$$E_\phi = j\frac{abkE_0e^{-jkr}}{2\pi r}\left\{\cos\theta\left[\frac{\sin\left(\frac{ka}{2}\sin\theta\right)}{\frac{ka}{2}\sin\theta}\right]\right\} \tag{12-25b}$$

To demonstrate the techniques, three-dimensional patterns have been plotted in Figures 12.8 and 12.9. The dimensions of the aperture are indicated in each figure. Multiple lobes appear, because the dimensions of the aperture are greater than one wavelength. The number of lobes increases as the dimensions increase. For the aperture whose dimensions are $a = 3\lambda$ and $b = 2\lambda$ (Figure 12.8), there are a total of five lobes in the principal H-plane and three lobes in the principal E-plane. The pattern in the H-plane is only a function of the dimension a whereas that in the E-plane is only influenced by b. In the E-plane, the side lobe formed on each side of the major lobe is a result of $\lambda < b \leq 2\lambda$. In the H-plane, the first minor lobe on each side of the major lobe is formed when $\lambda < a \leq 2\lambda$ and the second side lobe when $2\lambda < a$

INTEL-1045
U.S. Patent 7,151,430

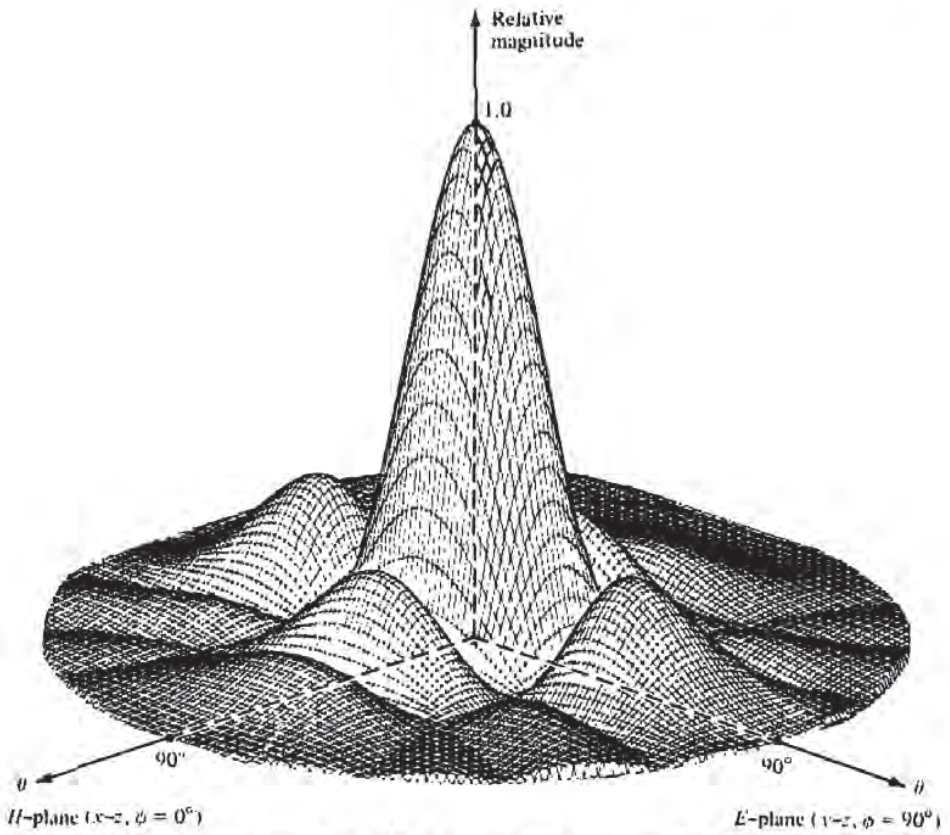


Figure 12.8 Three-dimensional field pattern of a constant field rectangular aperture mounted on an infinite ground plane ($a = 3\lambda$, $b = 2\lambda$).

$\leq 3\lambda$. Additional lobes are formed when one or both of the aperture dimensions increase. This is illustrated in Figure 12.9 for an aperture with $a = b = 3\lambda$.

The two-dimensional principal plane patterns for the aperture with $a = 3\lambda$, $b = 2\lambda$ are shown in Figure 12.10. For this and for all other size apertures mounted on an infinite ground plane, the H-plane patterns along the ground plane vanish. This is dictated by the boundary conditions. The E-plane patterns, in general, do not have to vanish along the ground plane, unless the dimension of the aperture in that plane (in this case b) is a multiple of a wavelength.

The patterns computed above assumed that the aperture was mounted on an infinite ground plane. In practice, infinite ground planes are not realizable, but they can be approximated by large structures. Edge effects, on the patterns of apertures mounted on finite size ground planes, can be accounted for by diffraction techniques. They will be introduced and illustrated in Section 12.9. Computed results, which include diffractions, agree extremely well with measurements [8]–[10].

C. Beamwidths

For the E-plane pattern given by (12-24b), the maximum radiation is directed along the z-axis ($\theta = 0$). The nulls (zeroes) occur when

$$\frac{kb}{2} \sin \theta|_{\theta = \theta_n} = n\pi, \qquad n = 1, 2, 3, \ldots \tag{12-26}$$

INTEL-1045
U.S. Patent 7,151,430

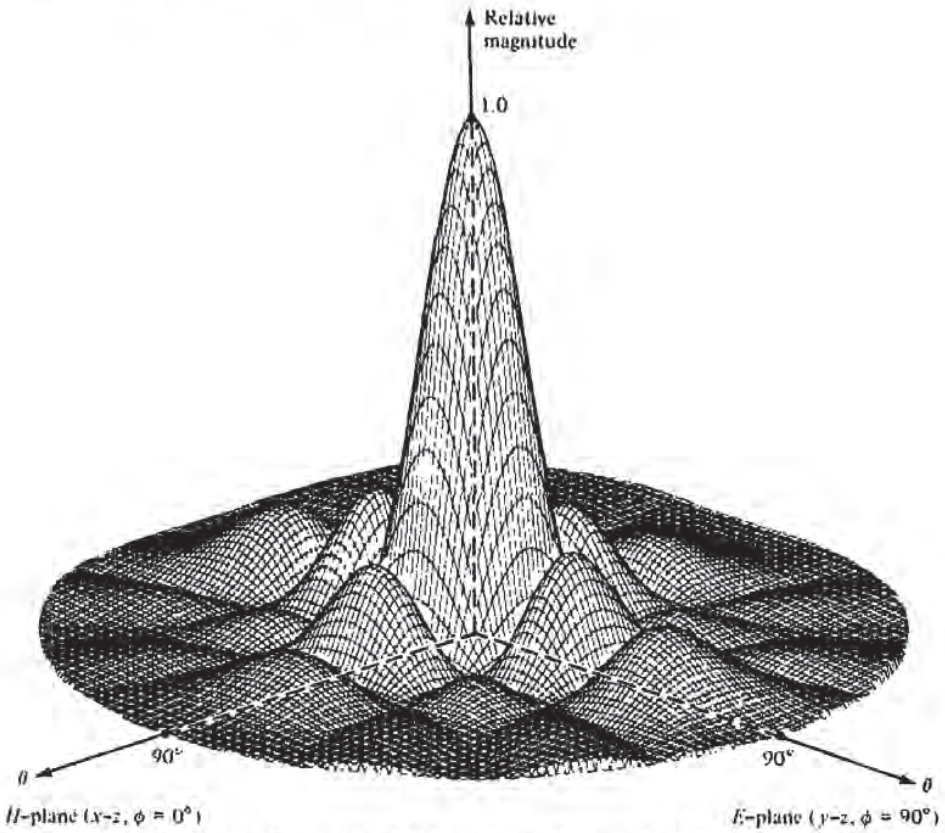


Figure 12.9 Three-dimensional field pattern of a constant field square aperture mounted on an infinite ground plane ($a = b = 3\lambda$).

or at the angles of

$$\theta_n = \sin^{-1}\left(\frac{2n\pi}{kb}\right) = \sin^{-1}\left(\frac{n\lambda}{b}\right) \text{ rad} \qquad (12\text{-}26a)$$

$$= 57.3 \sin^{-1}\left(\frac{n\lambda}{b}\right) \text{ degrees}, \quad n = 1, 2, 3, \ldots$$

If $b \gg n\lambda$, (12-26a) reduces approximately to

$$\theta_n \simeq \frac{n\lambda}{b} \text{ rad} = 57.3\left(\frac{n\lambda}{b}\right) \text{ degrees}, \quad n = 1, 2, 3, \ldots \qquad (12\text{-}26b)$$

The total *beamwidth between nulls* is given by

$$\Theta_n = 2\theta_n = 2\sin^{-1}\left(\frac{n\lambda}{b}\right) \text{ rad}$$

$$= 114.6 \sin^{-1}\left(\frac{n\lambda}{b}\right) \text{ degrees}, \quad n = 1, 2, 3, \ldots \qquad (12\text{-}27)$$

or approximately (for large apertures, $b \gg n\lambda$) by

$$\Theta_n \simeq \frac{2n\lambda}{b} \text{ rad} = 114.6\left(\frac{n\lambda}{b}\right) \text{ degrees}, \quad n = 1, 2, 3, \ldots \qquad (12\text{-}27a)$$

INTEL-1045
U.S. Patent 7,151,430

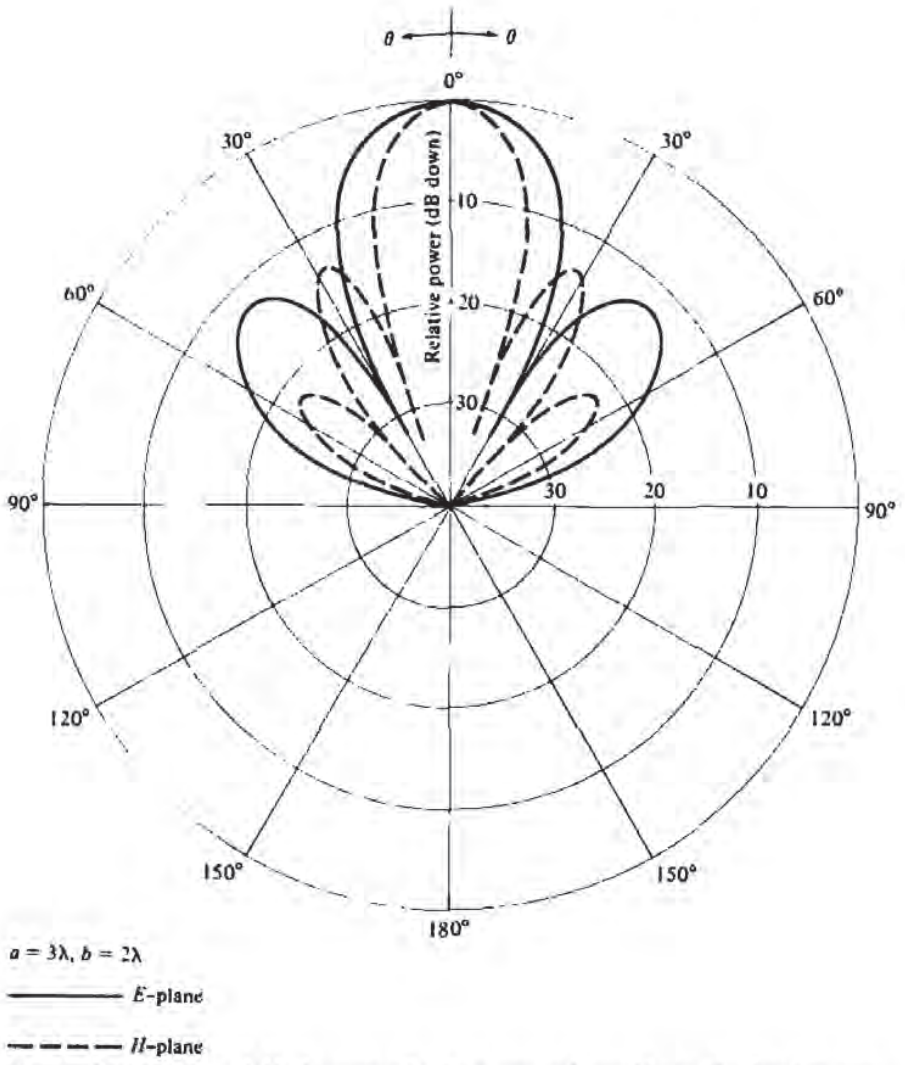


Figure 12.10 *E*- and *H*-plane amplitude patterns for uniform distribution aperture mounted on an infinite ground plane ($a = 3\lambda$, $b = 2\lambda$).

The *first null beamwidth* (FNBW) is obtained by letting $n = 1$.

The half-power point occurs when (see Appendix I)

$$\frac{kb}{2} \sin \theta|_{\theta=\theta_h} = 1.391 \tag{12-28}$$

or at an angle of

$$\theta_h = \sin^{-1}\left(\frac{2.782}{kb}\right) = \sin^{-1}\left(\frac{0.443\lambda}{b}\right) \text{ rad} = 57.3 \sin^{-1}\left(\frac{0.443\lambda}{b}\right) \text{ degrees} \tag{12-28a}$$

If $b \gg 0.443\lambda$, (12-28a) reduces approximately to

$$\theta_h \simeq \left(0.443 \frac{\lambda}{b}\right) \text{ rad} = 25.38 \left(\frac{\lambda}{b}\right) \text{ degrees} \tag{12-28b}$$

INTEL-1045
U.S. Patent 7,151,430

Thus the total *half-power beamwidth* (HPBW) is given by

$$\boxed{\Theta_h = 2\theta_h = 2\sin^{-1}\left(\frac{0.443\lambda}{b}\right)\text{ rad} = 114.6\sin^{-1}\left(\frac{0.443\lambda}{b}\right)\text{ degrees}} \tag{12-29}$$

or approximately (when $b \gg 0.443\lambda$) by

$$\boxed{\Theta_h \simeq \left(0.886\frac{\lambda}{b}\right)\text{ rad} = 50.8\left(\frac{\lambda}{b}\right)\text{ degrees}} \tag{12-29a}$$

The maximum of the first side lobe occurs when (see Appendix I)

$$\frac{kb}{2}\sin\theta\big|_{\theta=\theta_s} = 4.494 \tag{12-30}$$

or at an angle of

$$\theta_s = \sin^{-1}\left(\frac{8.988}{kb}\right) = \sin^{-1}\left(\frac{1.43\lambda}{b}\right)\text{ rad} = 57.3\sin^{-1}\left(\frac{1.43\lambda}{b}\right)\text{ degrees} \tag{12-30a}$$

If $b \gg 1.43\lambda$, (12-30a) reduces to

$$\theta_s \simeq 1.43\left(\frac{\lambda}{b}\right)\text{ rad} = 81.9\left(\frac{\lambda}{b}\right)\text{ degrees} \tag{12-30b}$$

The total beamwidth between first side lobes (FSLBW) is given by

$$\boxed{\Theta_s = 2\theta_s = 2\sin^{-1}\left(\frac{1.43\lambda}{b}\right)\text{ rad} = 114.6\sin^{-1}\left(\frac{1.43\lambda}{b}\right)\text{ degrees}} \tag{12-30c}$$

or approximately (when $b \gg 1.43\lambda$) by

$$\boxed{\Theta_s \simeq 2.86\left(\frac{\lambda}{b}\right)\text{ rad} = 163.8\left(\frac{\lambda}{b}\right)\text{ degrees}} \tag{12-30d}$$

D. Side Lobe Level

The maximum of (12-24b) at the first side lobe is given by (see Appendix I)

$$\boxed{|E_\theta(\theta = \theta_s)| = \left|\frac{\sin(4.494)}{4.494}\right| = 0.217 = -13.26\text{ dB}} \tag{12-31}$$

which is 13.26 dB down from the maximum of the main lobe.

An approximate value of the maximum of the first side lobe can be obtained by assuming that the maximum of (12-24b) occurs when its numerator is maximum. That is, when

$$\frac{kb}{2}\sin\theta\big|_{\theta=\theta_s} \simeq \frac{3\pi}{2} \tag{12-32}$$

INTEL-1045
U.S. Patent 7,151,430

Thus,

$$\boxed{|E_0(\theta = \theta_s)| \simeq \frac{1}{3\pi/2} = 0.212 = -13.47 \text{ dB}} \tag{12-33}$$

These values are very close to the exact ones given by (12-31).

A similar procedure can be followed to find the nulls, 3-dB points, beamwidth between nulls and 3-dB points, angle where the maximum of first side lobe occurs, and its magnitude at that point for the H-plane pattern of (12-25b). A comparison between the E- and H-plane patterns of (12-24b) and (12-25b) shows that they are similar in form except for the additional cos θ term that appears in (12-25b). An examination of the terms in (12-25b) reveals that the cos θ term is a much slower varying function than the $\sin(ka \sin \theta/2)/(ka \sin \theta/2)$ term, especially when a is large.

As a first approximation, (12-26)–(12-33), with b replaced by a, can also be used for the H-plane. More accurate expressions can be obtained by also including the cos θ term. In regions well removed from the major lobe, the inclusion of the cos θ term becomes more essential for accurate results.

E. Directivity

The directivity for the aperture can be found using (12-23a)–(12-23c), (12-13)–(12-13a), and (2-19)–(2-22). The analytical details using this procedure, especially the integration to compute the radiated power (P_{rad}), are more cumbersome.

Because the aperture is mounted on an infinite ground plane, an alternate and much simpler method can be used to compute the radiated power. The average power density is first formed using the fields at the aperture, and it is then integrated over the physical bounds of the opening. The integration is confined to the physical bounds of the opening. Using Figure 12.7 and assuming that the magnetic field at the aperture is given by

$$\mathbf{H}_a = -\hat{\mathbf{a}}_x \frac{E_0}{\eta} \tag{12-34}$$

where η is the intrinsic impedance, the radiated power reduces to

$$P_{rad} = \oiint_S \mathbf{W}_{av} \cdot d\mathbf{s} = \frac{|E_0|^2}{2\eta} \iint_{S_a} ds = ab \frac{|E_0|^2}{2\eta} \tag{12-35}$$

The maximum radiation intensity (U_{max}), using the fields of (12-23a)–(12-23b), occurs toward $\theta = 0°$ and it is equal to

$$U_{max} = \left(\frac{ab}{\lambda}\right)^2 \frac{|E_0|^2}{2\eta} \tag{12-36}$$

Thus the directivity is equal to

$$\boxed{D_0 = \frac{4\pi U_{max}}{P_{rad}} = \frac{4\pi}{\lambda^2} ab = \frac{4\pi}{\lambda^2} A_p = \frac{4\pi}{\lambda^2} A_{em}} \tag{12-37}$$

where

A_p = physical area of the aperture

A_{em} = maximum effective area of the aperture

INTEL-1045
U.S. Patent 7,151,430

Using the definition of (2-110), it is shown that *the physical and maximum effective areas of a constant distribution aperture are equal.*

The beamwidths, side lobe levels, and directivity of this and other apertures are summarized in Table 12.1.

Example 12.2

A rectangular aperture with a constant field distribution, with $a = 3\lambda$ and $b = 2\lambda$, is mounted on an infinite ground plane. Compute the

(a) FNBW in the E-plane
(b) HPBW in the E-plane
(c) FSLBW in the E-plane
(d) FSLMM in the E-plane
(e) directivity using (12-37)
(f) directivity using the DIRECTIVITY computer program at the end of Chapter 2, the fields of (12-23a)–(12-23f), and the formulation of Section 12.4

SOLUTION

(a) Using (12-27)

$$\Theta_1 = 114.6 \sin^{-1}\left(\frac{1}{2}\right) = 114.6(0.524) = 60°$$

(b) Using (12-29)

$$\Theta_h = 114.6 \sin^{-1}\left(\frac{0.443}{2}\right) = 114.6(0.223) = 25.6°$$

(c) Using (12-30c)

$$\Theta_s = 2\theta_s = 114.6 \sin^{-1}\left(\frac{1.43}{2}\right) = 114.6(0.796) = 91.3°$$

(d) Using (12-31)

$$|E_\theta|_{\theta=\theta_1} = 0.217 = -13.26 \text{ dB}$$

(e) Using (12-37)

$$D_0 = 4\pi(3)(2) = 75.4 = 18.77 \text{ dB}$$

(f) Using the computer program at the end of Chapter 2

$$D_0 = 80.4 = 19.05 \text{ dB}$$

The difference in directivity values using (12-37) and the computer program is not attributed to the accuracy of the numerical method. The main contributor is the aperture tangential magnetic field of (12-34), which was assumed to be related to the aperture tangential electric field by the intrinsic impedance. Although this is a good assumption for large size apertures, it is not exact. Therefore the directivity value computed using the computer program should be considered to be the more accurate.

INTEL-1045
U.S. Patent 7,151,430

12.5.2 Uniform Distribution in Space

The second aperture examined is that of Figure 12.7 when it is *not* mounted on an infinite ground plane. The field distribution is given by

$$\left.\begin{aligned} \mathbf{E}_a &= \hat{\mathbf{a}}_y E_0 \\ \mathbf{H}_a &= -\hat{\mathbf{a}}_x \frac{E_0}{\eta} \end{aligned}\right\} \qquad \begin{aligned} -a/2 \le x' \le a/2 \\ -b/2 \le y' \le b/2 \end{aligned} \tag{12-38}$$

where E_0 is a constant. The geometry of the opening for this problem is identical to the previous one. However the equivalents and radiated fields are different, because this time the aperture is not mounted on an infinite ground plane.

A. Equivalent

To form the equivalent, a closed surface is chosen which again extends from $-\infty$ to $+\infty$ on the x-y plane. Over the entire surface $\mathbf{J}_s$ and $\mathbf{M}_s$ are formed. The difficulty encountered in this problem is that both $\mathbf{J}_s$ and $\mathbf{M}_s$ are not zero outside the opening, and expressions for them are not known there. The replacement of the semi-infinite medium to the left of the boundary (negative z) by an imaginary electric or magnetic conductor only eliminates one or the other current densities ($\mathbf{J}_s$ or $\mathbf{M}_s$) but not both. Thus, even though an exact equivalent for this problem exists in principle, it cannot be used practically because the fields outside the opening are not known *a priori*. We are therefore forced to adopt an approximate equivalent.

The usual and most accurate relaxation is to assume that both $\mathbf{E}_a$ and $\mathbf{H}_a$ (and in turn $\mathbf{M}_s$ and $\mathbf{J}_s$) exist over the opening but are zero outside it. It has been shown, by comparison with measurements and other available data, that this approximate equivalent yields the best results.

B. Radiated Fields

Using a procedure similar to that of the previous section, the radiation characteristics of this aperture can be derived. A summary of them is shown in Table 12.1.

The field components of this aperture are identical in form to those of the aperture when it is mounted on an infinite ground plane if the $(1 + \cos\theta)$ term in each component is replaced by 2. Thus for small values of θ (in the main lobe and especially near its maximum), the patterns of the two apertures are almost identical. This procedure can be used, in general, to relate the fields of an aperture when it is and it is not mounted on an infinite ground plane. However, the coordinate system chosen must have the z-axis perpendicular to the aperture.

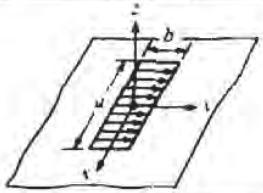
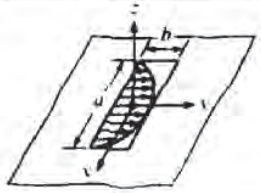
A three-dimensional pattern for an aperture with $a = 3\lambda$, $b = 2\lambda$ was computed, and it is shown in Figure 12.11. The dimensions of this aperture are the same as those of Figure 12.8. However the angular limits over which the radiated fields now exist have been extended to $0° \le \theta \le 180°$. Although the general structures of the two patterns are similar, they are not identical. Becuse of the enlarged space over which fields now exist, additional minor lobes are formed.

C. Beamwidths and Side Lobe Levels

To find the beamwidths and the angle at which the maximum of the side lobe occurs, it is usually assumed that the $(1 + \cos\theta)$ term is a much slower varying function than the $\sin(ka \sin\theta/2)/(ka \sin\theta/2)$ or the $\sin(kb \sin\theta/2)/(kb \sin\theta/2)$ terms. This is an approximation, and it is more valid for large apertures (large a and/or b) and for

INTEL-1045
U.S. Patent 7,151,430

Table 12.1 EQUIVALENTS, FIELDS, BEAMWIDTHS, SIDE LOBE LEVELS, AND DIRECTIVITIES OF RECTANGULAR APERTURES

	Uniform Distribution Aperture on Ground Plane	Uniform Distribution Aperture in Free-Space	TE_{10}-Mode Distribution Aperture on Ground Plane
Aperture distribution of tangential components (analytical)	$\mathbf{E}_a = \hat{\mathbf{a}}_y E_0 \left.\begin{matrix} \\ \end{matrix}\right\} \begin{matrix} -a/2 \le x' \le a/2 \\ -b/2 \le y' \le b/2 \end{matrix}$	$\mathbf{E}_a = \hat{\mathbf{a}}_y E_0$ $\mathbf{H}_a = -\hat{\mathbf{a}}_x \frac{E_0}{\eta} \left.\begin{matrix} \\ \end{matrix}\right\} \begin{matrix} -a/2 \le x' \le a/2 \\ -b/2 \le y' \le b/2 \end{matrix}$	$\mathbf{E}_a = \hat{\mathbf{a}}_y E_0 \cos\left(\frac{\pi}{a}x'\right) \begin{matrix} -a/2 \le x' \le a/2 \\ -b/2 \le y' \le b/2 \end{matrix}$
Aperture distribution of tangential components (graphical)			
Equivalent	$\mathbf{M}_s = \begin{cases} -2\hat{\mathbf{n}} \times \mathbf{E}_a & -a/2 \le x' \le a/2 \\ & -b/2 \le y' \le b/2 \\ 0 & \text{elsewhere} \end{cases}$ $\mathbf{J}_s = 0$ everywhere	$\mathbf{M}_s = -\hat{\mathbf{n}} \times \mathbf{E}_a$ $\mathbf{J}_s = \hat{\mathbf{n}} \times \mathbf{H}_a \left.\begin{matrix} \\ \end{matrix}\right\} \begin{matrix} -a/2 \le x' \le a/2 \\ -b/2 \le y' \le b/2 \end{matrix}$ $\mathbf{M}_s = \mathbf{J}_s = 0$ elsewhere	$\mathbf{M}_s = \begin{cases} -2\hat{\mathbf{n}} \times \mathbf{E}_a & -a/2 \le x' \le a/2 \\ & -b/2 \le y' \le b/2 \\ 0 & \text{elsewhere} \end{cases}$ $\mathbf{J}_s = 0$ everywhere
Far-zone fields $X = \frac{ka}{2}\sin\theta\cos\phi$ $Y = \frac{kb}{2}\sin\theta\sin\phi$ $C = j\frac{abkE_0e^{-jkr}}{2\pi r}$	$E_r = H_r = 0$ $E_\theta = C\sin\phi\frac{\sin X}{X}\frac{\sin Y}{Y}$ $E_\phi = C\cos\theta\cos\phi\frac{\sin X}{X}\frac{\sin Y}{Y}$ $H_\theta = -E_\phi/\eta$ $H_\phi = E_\theta/\eta$	$E_r = H_r = 0$ $E_\theta = \frac{C}{2}\sin\phi(1+\cos\theta)\frac{\sin X}{X}\frac{\sin Y}{Y}$ $E_\phi = \frac{C}{2}\cos\phi(1+\cos\theta)\frac{\sin X}{X}\frac{\sin Y}{Y}$ $H_\theta = -E_\phi/\eta$ $H_\phi = E_\theta/\eta$	$E_r = H_r = 0$ $E_\theta = -\frac{\pi}{2}C\sin\phi\frac{\cos X}{(X)^2 - \left(\frac{\pi}{2}\right)^2}\frac{\sin Y}{Y}$ $E_\phi = -\frac{\pi}{2}C\cos\theta\cos\phi\frac{\cos X}{(X)^2 - \left(\frac{\pi}{2}\right)^2}\frac{\sin Y}{Y}$ $H_\theta = -E_\phi/\eta$ $H_\phi = E_\theta/\eta$

INTEL-1045
U.S. Patent 7,151,430

Table 12.1 (Continued)

Half-power beamwidth (degrees)	*E*-plane $b \gg \lambda$	$\frac{50.6}{b/\lambda}$	$\frac{50.6}{b/\lambda}$	$\frac{50.6}{b/\lambda}$
	H-plane $a \gg \lambda$	$\frac{50.6}{a/\lambda}$	$\frac{50.6}{a/\lambda}$	$\frac{68.8}{a/\lambda}$
First null beamwidth (degrees)	*E*-plane $b \gg \lambda$	$\frac{114.6}{b/\lambda}$	$\frac{114.6}{b/\lambda}$	$\frac{114.6}{b/\lambda}$
	H-plane $a \gg \lambda$	$\frac{114.6}{a/\lambda}$	$\frac{114.6}{a/\lambda}$	$\frac{171.9}{a/\lambda}$
First side lobe max. (to main max.) (dB)	*E*-plane	-13.26	-13.26	-13.26
	H-plane	-13.26 $a \gg \lambda$	-13.26 $a \gg \lambda$	-23 $a \gg \lambda$
Directivity D_0 (dimensionless)		$\frac{4\pi}{\lambda^2}(\text{area}) = 4\pi\left(\frac{ab}{\lambda^2}\right)$	$\frac{4\pi}{\lambda^2}(\text{area}) = 4\pi\left(\frac{ab}{\lambda^2}\right)$	$\frac{8}{\pi^2}\left[4\pi\left(\frac{ab}{\lambda^2}\right)\right] = 0.81\left[4\pi\left(\frac{ab}{\lambda^2}\right)\right]$

INTEL-1045
U.S. Patent 7,151,430

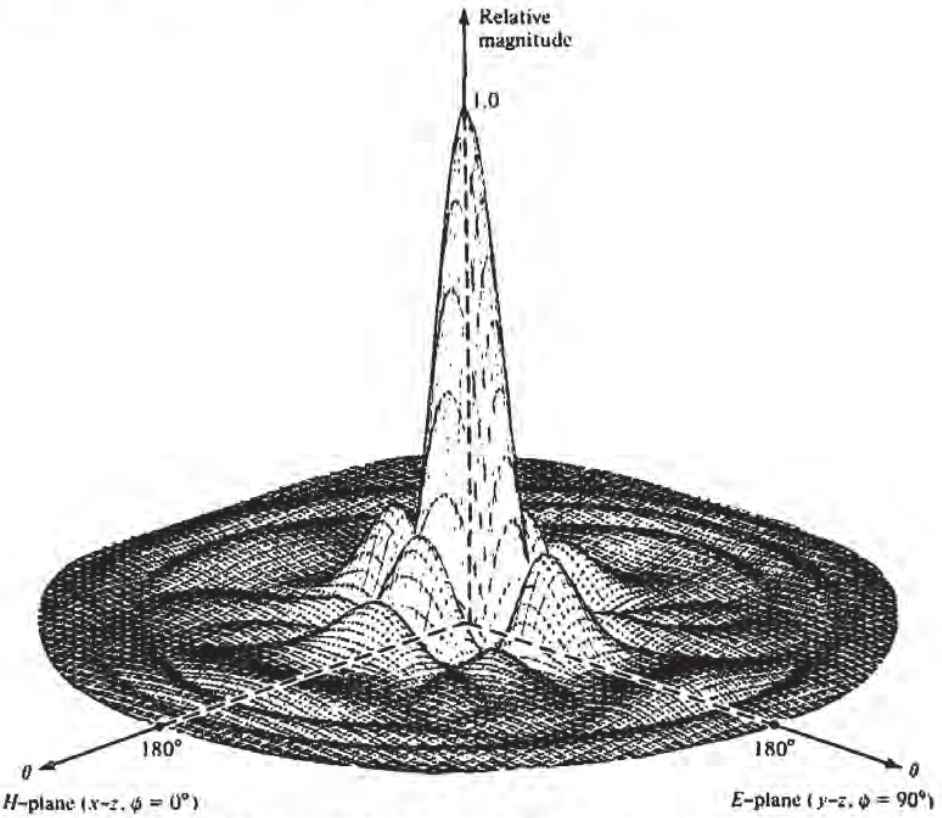


Figure 12.11 Three-dimensional field pattern of a constant field rectangular aperture ($a = 3\lambda$, $b = 2\lambda$).

angles near the main maximum. More accurate results can be obtained by considering the $(1 + \cos\theta)$ term. Thus (12-26)–(12-33) can be used, to a good approximation, to compute the beamwidths and side lobe level. A summary is included in Table 12.1.

D. Directivity

Although the physical geometry of the opening of this problem is identical to that of Section 12.5.1, their directivities are not identical. This is evident by examining their far-zone field expressions or by realizing that the fields outside the aperture along the x-y plane are not exactly the same.

To derive an exact expression for the directivity of this aperture would be a very difficult task. Since the patterns of the apertures are nearly the same, especially at the main lobe, their directivities are almost the same. To verify this, an example is taken.

Example 12.3

Repeat the problem of Example 12.2 for an aperture that is not mounted on an infinite ground plane.

SOLUTION

Since the E-plane patterns of the two apertures are identical, the FNBW, HPBW, FSLBW, and FSLMM are the same. The directivities as computed by (12-37), are

INTEL-1045
U.S. Patent 7,151,430

also the same. Since the fields radiated by the two apertures are not identical, their directivities computed using the far-zone fields will not be exactly the same. Therefore for this problem

$$D_0 \simeq 81.16 \text{ (dimensionless)} = 19.09 \text{ dB}$$

As with Example 12.2, the directivities computed using (12-37) and the computer program do not agree exactly. For this problem, however, neither one is exact. For (12-37), it has been assumed that the aperture tangential magnetic field is related to the aperture tangential electric field by the intrinsic impedance η. This relationship is good but not exact. For the computer program, the formulation is based on the equivalent of this section where the fields outside the aperture were assumed to be negligible. Again this is a good assumption for some problems, but it is not exact.

A summary of the radiation characteristics of this aperture is included in Table 12.1 where it is compared with that of other apertures.

12.5.3 TE_{10}-Mode Distribution on an Infinite Ground Plane

In practice, a commonly used aperture antenna is that of a rectangular waveguide mounted on an infinite ground plane. At the opening, the field is usually approximated by the dominant TE_{10}-mode. Thus

$$\mathbf{E}_a = \hat{\mathbf{a}}_y E_0 \cos\left(\frac{\pi}{a}x'\right) \qquad \begin{cases} -a/2 \le x' \le +a/2 \\ -b/2 \le y' \le +b/2 \end{cases} \tag{12-39}$$

A. Equivalent, Radiated Fields, Beamwidths, and Side Lobe Levels

Because the physical geometry of this antenna is identical to that of Figure 12.7, their equivalents and the procedure to analyze each one are identical. They differ only in the field distribution over the aperture.

The details of the analytical formulation are not included. However, a summary of its radiation characteristics is included in Table 12.1. The E-plane pattern of this aperture is identical in form (with the exception of a normalization factor) to the E-plane of the aperture of Section 12.5.1. This is expected, since the TE_{10}-mode field distribution along the E-plane (y-z plane) is also a constant. That is not the case for the H-plane or at all other points removed from the principal planes. To demonstrate that, a three-dimensional pattern for the TE_{10}-mode aperture with $a = 3\lambda$, $b = 2\lambda$ was computed and it is shown in Figure 12.12. This pattern should be compared with that of Figure 12.8.

The expressions for the beamwidths and side lobe level in the E-plane are identical to those given by (12-26)–(12-33). However those for the H-plane are more complex, and a simple procedure is not available. Computations for the HPBW, FNBW, FSLBW, FSLMM in the E- and H-planes were made, and they are shown graphically in Figures 12.13 and 12.14.

B. Directivity and Aperture Efficiency

The directivity of this aperture is found in the same manner as that of the uniform distribution aperture of Section 12.5.1. Using the aperture electric field of (12-39),

INTEL-1045
U.S. Patent 7,151,430

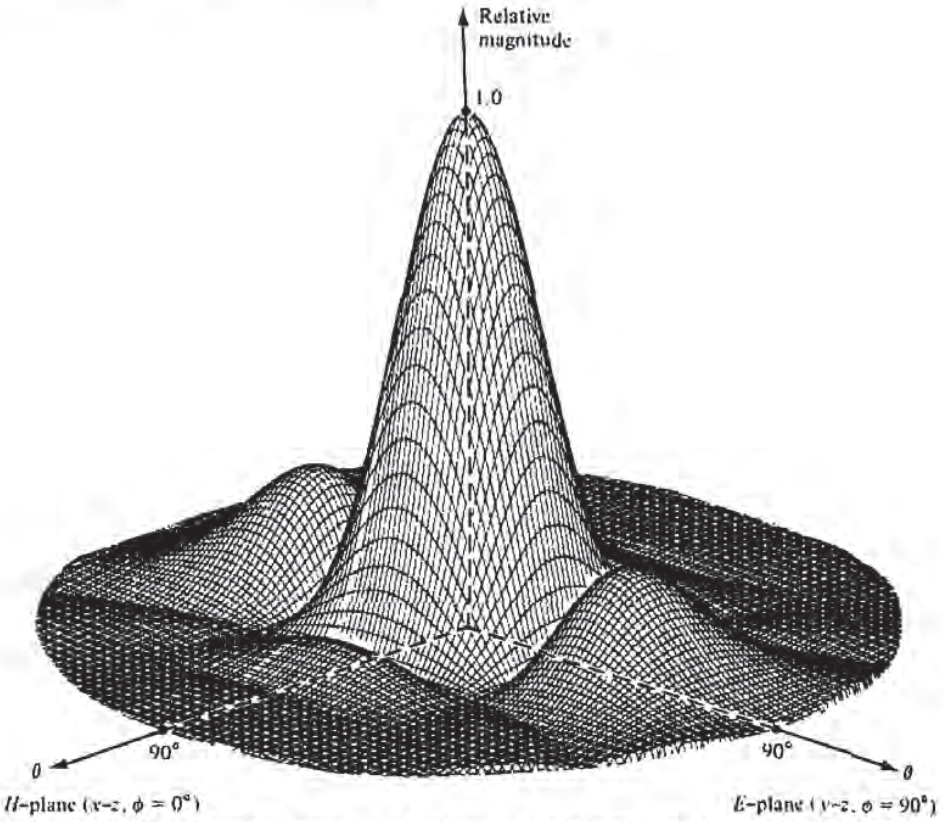


Figure 12.12 Three-dimensional field pattern of a TE_{10}-mode rectangular waveguide mounted on an infinite ground plane ($a = 3\lambda$, $b = 2\lambda$).

and assuming that the aperture magnetic field is related to the electric field by the intrinsic impedance η, the radiated power can be written as

$$P_{\text{rad}} = \oiint_S \mathbf{W}_{\text{av}} \cdot d\mathbf{s} = ab\frac{|E_0|^2}{4\eta} \tag{12-39a}$$

The maximum radiation intensity occurs at $\theta = 0°$, and it is given by

$$U_{\max} = \frac{8}{\pi^2}\left(\frac{ab}{\lambda}\right)^2 \frac{|E_0|^2}{4\eta} \tag{12-39b}$$

Thus the directivity is equal to

$$D_0 = \frac{8}{\pi^2}\left[ab\left(\frac{4\pi}{\lambda^2}\right)\right] = 0.81\left[ab\left(\frac{4\pi}{\lambda^2}\right)\right] = 0.81A_p\left(\frac{4\pi}{\lambda^2}\right) = A_{\text{em}}\left(\frac{4\pi}{\lambda^2}\right) \tag{12-39c}$$

In general, the maximum effective area A_{em} is related to the physical area A_p by

$$A_{\text{em}} = \epsilon_{\text{ap}} A_p, \qquad 0 \le \epsilon_{\text{ap}} \le 1 \tag{12-40}$$

where ϵ_{ap} is the aperture efficiency. For this problem $\epsilon_{\text{ap}} = 8/\pi^2 \simeq 0.81$. The aperture efficiency is a figure-of-merit which indicates how efficiently the physical area of the antenna is utilized. Typically, aperture antennas have aperture efficiencies from about

INTEL-1045
U.S. Patent 7,151,430

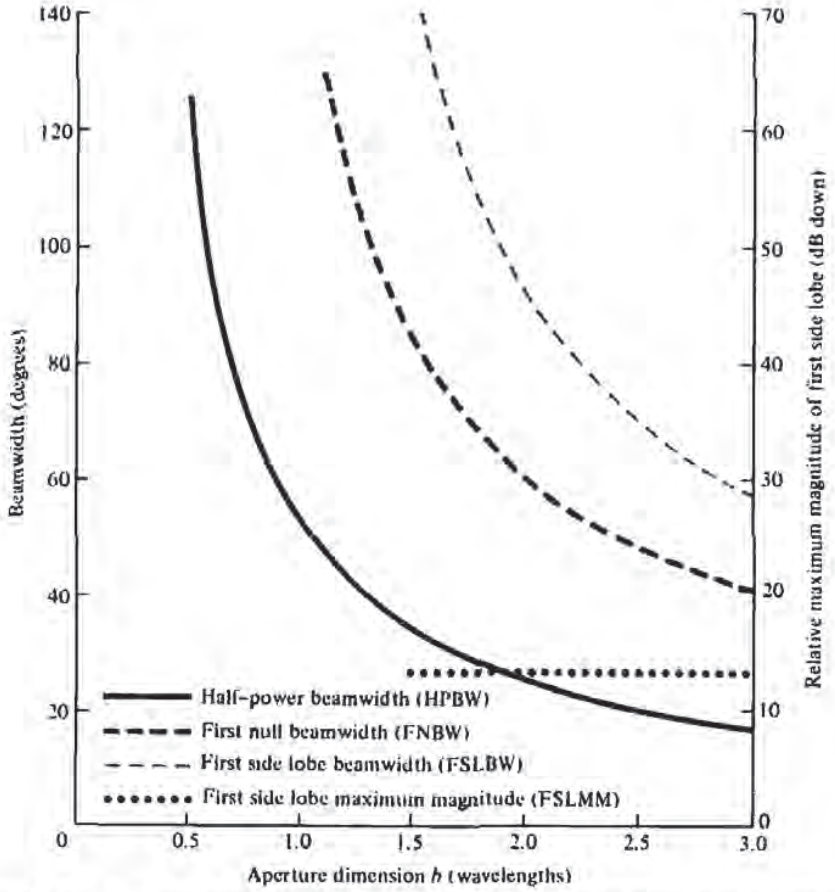


Figure 12.13 E-plane beamwidths and first side lobe relative maximum magnitude for TE_{10}-mode rectangular waveguide mounted on an infinite ground plane.

30% to 90%, horns from 35% to 80% (optimum gain horns have $\epsilon_{ap} = 50\%$), and circular reflectors from 50% to 80%.

For reflectors, the aperture efficiency is a function of many factors. The most prominent are the spillover, amplitude taper, phase distribution, polarization uniformity, blockage, and surface random errors. These are discussed in detail in Section 15.4.1 of Chapter 15.

12.5.4 Beam Efficiency

The beam efficiency for an antenna was introduced in Section 2.10 and was defined by (2-53). When the aperture is mounted on the x-y plane, the beam efficiency can be calculated using (2-54). The beam efficiency can be used to judge the ability of the antenna to discriminate between signals received through its main lobe and those through the minor lobes. Beam efficiencies for rectangular apertures with different aperture field distributions are plotted, versus the half-cone angle θ_1, in Figure 12.15 [11]. The uniform field distribution aperture has the least ability to discriminate between main lobe and minor lobe signals. The aperture radiates in an unbounded medium, and it is not mounted on an infinite ground plane. The lower abscissa scale is in terms of θ_1 (in degrees), and it should be used only when $a = b = 20\lambda$. The upper abscissa scale is in terms of $u|u = (ka/2)\sin\theta_1 = (kb/2)\sin\theta_1|$, and it should be used for any square aperture.

INTEL-1045
U.S. Patent 7,151,430

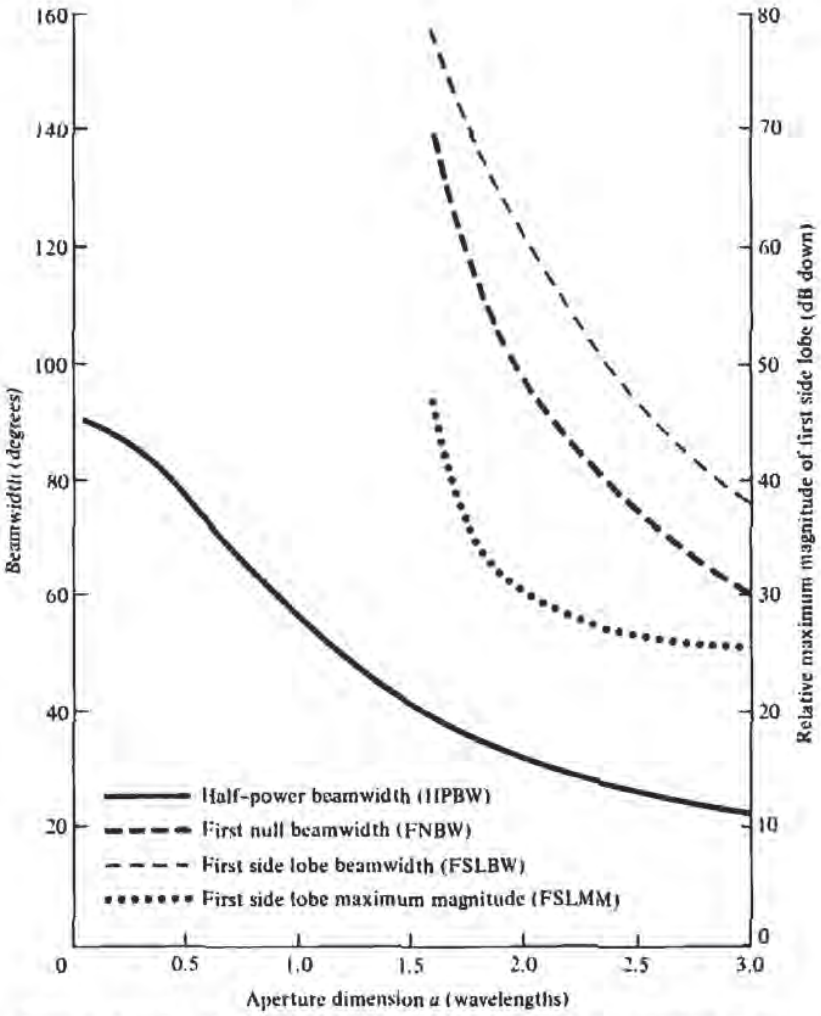


Figure 12.14 *H*-plane beamwidths and first side lobe relative maximum magnitude for TE_{10}-mode rectangular waveguide mounted on an infinite ground plane.

Example 12.4

Determine the beam efficiency, within a cone of half-angle $\theta_1 = 10°$, for a square aperture with uniform field distribution and with

(a) $a = b = 20\lambda$

(b) $a = b = 3\lambda$

SOLUTION

The solution is carried out using the curves of Figure 12.15.

(a) When $a = b = 20\lambda$, the lower abscissa scale can be used. For $\theta_1 = 10°$, the efficiency for the uniform aperture is about 94%.

(b) For $a = b = 3\lambda$ and $\theta_1 = 10°$

$$u = \frac{ka}{2}\sin\theta_1 = 3\pi\sin(10°) = 1.64$$

INTEL-1045
U.S. Patent 7,151,430

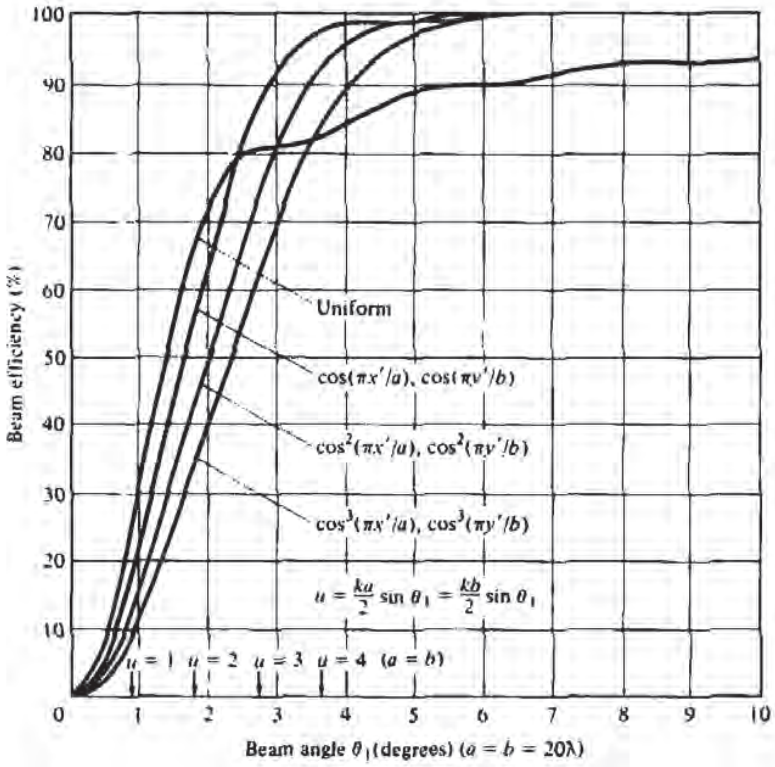


Figure 12.15 Beam efficiency versus half-cone angle θ_1, for a square aperture with different field distributions. The aperture is not mounted on an infinite ground plane. (SOURCE: D. G. Fink (ed.), *Electronics Engineers' Handbook*, Section 18 (by W. F. Croswell), McGraw-Hill, New York, 1975)

Using the upper abscissa scale, the efficiency for the uniform aperture at $u = 1.64$ is about 58%.

12.6 CIRCULAR APERTURES

A widely used microwave antenna is the circular aperture. One of the attractive features of this configuration is its simplicity in construction. In addition, closed form expressions for the fields of all the modes that can exist over the aperture can be obtained.

The procedure followed to determine the fields radiated by a circular aperture is identical to that of the rectangular, as summarized in Section 12.3. The primary differences lie in the formulation of the equivalent current densities (J_x, J_y, J_z, M_x, M_y, M_z), the differential paths from the source to the observation point ($r' \cos \psi$), and the differential area (ds'). Before an example is considered, these differences will be reformulated for the circular aperture.

Because of the circular profile of the aperture, it is often convenient and desirable to adopt cylindrical coordinates for the solution of the fields. In most cases, therefore, the electric and magnetic field components over the circular opening will be known in cylindrical form; that is, E_ρ, E_ϕ, E_z, H_ρ, H_ϕ, and H_z. Thus the components of the equivalent current densities $\mathbf{M}_s$ and $\mathbf{J}_s$ would also be conveniently expressed in cylindrical form (M_ρ, M_ϕ, M_z, J_ρ, J_ϕ, J_z). In addition, the required integration over the

INTEL-1045
U.S. Patent 7,151,430